frontiers | Research Topics

Women in science: Chemistry 2021

Edited by
Valeria Conte, Franziska Luise Emmerling, Zoe Pikramenou, Lihong Jing, Kamila Kočí, Xi Chen and Elena Vladimirovna Boldyreva

Published in
Frontiers in Chemistry

ISSN 1664-8714
ISBN 978-2-83251-279-1
DOI 10.3389/978-2-83251-279-1

About Frontiers

Frontiers is more than just an open access publisher of scholarly articles: it is a pioneering approach to the world of academia, radically improving the way scholarly research is managed. The grand vision of Frontiers is a world where all people have an equal opportunity to seek, share and generate knowledge. Frontiers provides immediate and permanent online open access to all its publications, but this alone is not enough to realize our grand goals.

Frontiers journal series

The Frontiers journal series is a multi-tier and interdisciplinary set of open-access, online journals, promising a paradigm shift from the current review, selection and dissemination processes in academic publishing. All Frontiers journals are driven by researchers for researchers; therefore, they constitute a service to the scholarly community. At the same time, the *Frontiers journal series* operates on a revolutionary invention, the tiered publishing system, initially addressing specific communities of scholars, and gradually climbing up to broader public understanding, thus serving the interests of the lay society, too.

Dedication to quality

Each Frontiers article is a landmark of the highest quality, thanks to genuinely collaborative interactions between authors and review editors, who include some of the world's best academicians. Research must be certified by peers before entering a stream of knowledge that may eventually reach the public - and shape society; therefore, Frontiers only applies the most rigorous and unbiased reviews. Frontiers revolutionizes research publishing by freely delivering the most outstanding research, evaluated with no bias from both the academic and social point of view. By applying the most advanced information technologies, Frontiers is catapulting scholarly publishing into a new generation.

What are Frontiers Research Topics?

Frontiers Research Topics are very popular trademarks of the *Frontiers journals series*: they are collections of at least ten articles, all centered on a particular subject. With their unique mix of varied contributions from Original Research to Review Articles, Frontiers Research Topics unify the most influential researchers, the latest key findings and historical advances in a hot research area.

Find out more on how to host your own Frontiers Research Topic or contribute to one as an author by contacting the Frontiers editorial office: frontiersin.org/about/contact

Women in Science: Chemistry 2021

Topic editors

Valeria Conte — University of Rome Tor Vergata, Italy

Franziska Luise Emmerling — Federal Institute for Materials Research and Testing (BAM), Germany

Zoe Pikramenou — University of Birmingham, United Kingdom

Lihong Jing — Institute of Chemistry, Chinese Academy of Sciences (CAS), China

Kamila Kočí — VŠB-Technical University of Ostrava, Czechia

Xi Chen — Oak Ridge National Laboratory (DOE), United States

Elena Vladimirovna Boldyreva — Novosibirsk State University, Russia

Citation

Conte, V., Emmerling, F. L., Pikramenou, Z., Jing, L., Kočí, K., Chen, X., Boldyreva, E. V., eds. (2023). *Women in science: Chemistry 2021*. Lausanne: Frontiers Media SA. doi: 10.3389/978-2-83251-279-1

Table of contents

frontiers in Chemistry

ORIGINAL RESEARCH
published: 20 July 2021
doi: 10.3389/fchem.2021.726357

Towards Computational Screening for New Energetic Molecules: Calculation of Heat of Formation and Determination of Bond Strengths by Local Mode Analysis

Imogen L. Christopher[1], *Adam A. L. Michalchuk*[2], *Colin R. Pulham*[1] *and Carole A. Morrison*[1]*

[1]*EaStCHEM School of Chemistry, University of Edinburgh, Edinburgh, United Kingdom,* [2]*Federal Institute for Materials Research and Testing (BAM), Berlin, Germany*

OPEN ACCESS

Edited by:
Elena Vladimirovna Boldyreva, Novosibirsk State University, Russia

Reviewed by:
German Perlovich, Institute of Solution Chemistry (RAS), Russia
Vladimir Tsirelson, D. Mendeleyev University of Chemical Technology of Russia, Russia
Jernej Stare, National Institute of Chemistry, Slovenia

***Correspondence:**
Carole A. Morrison
c.morrison@ed.ac.uk

Specialty section:
This article was submitted to Theoretical and Computational Chemistry, a section of the journal Frontiers in Chemistry

Received: *16 June 2021*
Accepted: *02 July 2021*
Published: *20 July 2021*

Citation:
Christopher IL, Michalchuk AAL, Pulham CR and Morrison CA (2021) Towards Computational Screening for New Energetic Molecules: Calculation of Heat of Formation and Determination of Bond Strengths by Local Mode Analysis. Front. Chem. 9:726357. doi: 10.3389/fchem.2021.726357

The reliable determination of gas-phase and solid-state heats of formation are important considerations in energetic materials research. Herein, the ability of PM7 to calculate the gas-phase heats of formation for CNHO-only and inorganic compounds has been critically evaluated, and for the former, comparisons drawn with isodesmic equations and atom equivalence methods. Routes to obtain solid-state heats of formation for a range of single-component molecular solids, salts, and co-crystals were also evaluated. Finally, local vibrational mode analysis has been used to calculate bond length/force constant curves for seven different chemical bonds occurring in CHNO-containing molecules, which allow for rapid identification of the weakest bond, opening up great potential to rationalise decomposition pathways. Both metrics are important tools in rationalising the design of new energetic materials through computational screening processes.

Keywords: heat of formation, computational screening, lattice energy calculations, local force constants, energetic materials

INTRODUCTION

Energetic materials (explosives, propellants, pyrotechnics and gas generators, EMs) are characterised by their ability to rapidly convert chemical potential energy into kinetic energy. Safety is of paramount importance in this field and takes precedence over performance, such that only a limited number of EMs have found employment in civilian and military applications. Many of the well-established EMs, however, do not comply with increasing environmental and public health regulations (Cumming, 2017), which fuels the need to develop new non-toxic and environmentally benign EMs that do not compromise on safety or performance metrics.

Computational screening presents an attractive route in the new materials pipeline, as it offers a cost-effective way to assess candidates prior to synthesis. This is particularly desirable in the field of EMs where safety testing (such as impact, spark and friction sensitivity measurements) typically require gram-scale quantities of compounds to be synthesised. This is potentially very hazardous work when the material is novel and may initiate on the slightest perturbation.

Having access to reliable predictive models also opens up routes to the rational design of new EMs, by offering a path towards understanding structure-property relationships. Previous work in our group has focused on the ability to predict the impact sensitivities of EMs using first principles simulations, and our methods, which are based on a vibrational up-pumping model, have

demonstrated success for a range of structurally diverse materials that exhibit widely varying sensitivities to initiation (Michalchuk et al., 2018a; Michalchuk et al., 2019; Michalchuk et al., 2021). This predictive model highlighted the importance of low energy (*ca*. 200 ± 50 to 600 ± 150 cm^{-1}) molecular vibrational modes to channel (up-pump) the energy arising from the phonon scattering of the many low energy lattice mode vibrations which become vibrationally hot following a mechanically-induced shock event. Trapping this energy in the low energy molecular vibrations induces large amplitude vibrations that distort the molecular structure to the degree that electronic changes occur: band gaps narrow, electrons flow, and unstable species emerge all on the timescale of a molecular vibration (Michalchuk et al., 2018b). This marks the start of initiation. It therefore follows that crystal lattices with a high density of low-lying molecular vibrations will likely be sensitive to shock and impact-induced initiation. The reverse also holds true: crystal lattices that are vibrationally sparse in this region will likely be shock and impact-insensitive, and are thus safer to handle.

Predicting impact sensitivities is only one aspect of an EM computational screening process. Also of key importance is the stored energy in the molecule, which can be gleaned from the solid-state heat of formation energy, $\Delta H_{f(s)}$. This provides a route to calculate the heat of combustion, which in turn allows prediction of several parameters including the detonation pressure and the velocity and heat of explosion (Politzer et al., 2003), using thermo-chemical software methods such as CHEETAH (Fried and Souers, 1994) or EXPLO-5 (Suceska, 2004).

Multiple routes to calculating $\Delta H_{f(s)}$ have been previously proposed in the literature. Our purpose here is to signpost the current state of the art, and to show its application to EMs. The first step in calculating $\Delta H_{f(s)}$ begins with the gas-phase heat of formation, $\Delta H_{f(g)}$, and various methods have been proposed for this over the years. For instance, Benson's group increment theory (BIGT) exploited experimental heats of formation for individual groups of atoms to develop group equivalence values for linear and branched alkanes and alkenes (Benson and Buss, 1958). While impressive at the time of inception, its application is limited to the types of molecules represented in the training set, and so it has limited scope beyond this area. More recently, quantitative structure-property relationship (QSPR) models have been realised as a powerful tool to explore the relationships that link molecular structure to material properties. Vatani et al. (2007) devised a new QSPR method for predicting heats of formation for over 1,000 organic molecules, covering almost all organic functional groups. However, transition-metal and main-group elements were not included in the training set, so whilst excellent results were obtained, widespread application is again limited.

Within the field of EMs isodesmic reaction equations (Hehre et al., 1970; Ponomarev and Takhistov, 1997) and the atom- and group-equivalence methods (Byrd and Rice, 2006) are commonly applied. The former relies on a reaction equation where the types of chemical bonds in the reactants and products are conserved, and the heats of formation are known for all other molecules in the reaction except the one unknown (Cramer, 2004). Any intrinsic error associated with calculating any particular chemical bond is thereby cancelled out, meaning that relatively low-level computational methods can be employed to give fairly accurate results (Hehre et al., 1970). This method has been employed in computational chemistry for over 50 years, with recent developments automating the generation of parts of the isodesmic reaction equation (Chan et al., 2020). However, as a general technique it has found little application beyond CHNO-containing molecules.

The atom-equivalence method developed by Byrd and Rice is an advance on BGIT and has been extensively applied to EMs (Singh et al., 2014a; Singh et al., 2014b; Axthammer et al., 2015; Piercey et al., 2016), but is again restricted to CHNO-containing molecules. Here atom equivalence energy values for the four atoms were determined through comparison of experimental heats of formation for molecules in a training set and their computationally derived molecular energies (Byrd and Rice, 2006). This method works well, reporting root mean square deviation of 12.6 kJ mol^{-1} and is arguably more efficient than the isodesmic equation route, as it requires just the optimised energy of the molecule of interest expressed at a prescribed quantum mechanical model chemistry. A further advantage is the absence of any reliance on further experimental data. However, the continued application to CHNO-only molecules limits its application in a computational screening programme for new EMs which should have the flexibility to draw upon main-group and transition-metal elements.

Given the limitations of these two methods, herein we have pursued the use of PM7 to determine $\Delta H_{f(g)}$ (Stewart, 2013). This has been shown by Wan et al. to out-perform previous semi-empirical methods for a set of 142 organic molecules (Wan et al., 2020). Elioff et al. evaluated its capabilities compared to both the isodesmic and the group equivalence methods for nitrogen-containing organic molecules (Elioff et al., 2016). While the outcome showed that PM7 was the least accurate of the three (R^2 line of best fit against experimental data = 0.986, compared to 0.999 and 0.995 for the isodesmic and atom equivalence methods, respectively), it still performs relatively well, and has the advantage of being an easily deployed method that can be used for any molecule containing atoms from H–La and Lu–Bi. Fomin et al. (2017) tested the PM7 method alongside other semi-empirical methods, namely PM6, PM5, PM3, AM/1, and MNDO, for calculating $\Delta H_{f(g)}$ for copper and alkaline Earth metal complexes. They concluded that PM6 and PM7 both perform well, reporting R^2 values of 0.961 and 0.960, respectively. While these results are encouraging, further validation for the accurate prediction of $\Delta H_{f(g)}$ for a broader range of inorganic molecules would be welcome and will be provided here. The PM7 method also carries the advantage that no further calculations beyond a geometry optimisation are required, which renders it attractive as part of a high throughput study. Moreover, semi-empirical calculation methods have a wide application and user base, and are being continuously improved (Wan et al., 2020).

Converting $\Delta H_{f(g)}$ to $\Delta H_{f(s)}$ requires the addition of an intermolecular interaction energy term, as captured by the sublimation energy, ΔH_{sub}, or the lattice energy, ΔH_L

(formally, $\Delta H_L = -\Delta H_{sub} - 2RT$). For single-component molecular solids, Politzer et al. have developed a route to determine ΔH_{sub} from consideration of the electrostatic potential (ESP) (Politzer et al., 1997; Politzer et al., 1998). While they have applied this analysis to estimate many liquid, solid, and solution parameters dependent on non-covalent interactions (Politzer and Murray, 1998; Politzer and Murray, 2002) it is their relationship to calculate ΔH_{sub} which is most relevant here. The method was developed initially using a training set of 34 CHNO-containing molecules, and further parametrised by Byrd et al. using a training set of 38 CHNO-containing energetic molecules (Byrd and Rice, 2006). The ESP method tested here uses the parameters proposed by Byrd, as parameterisation was carried out at using the B3LYP/6-31G* computational model, rather than the HF/STO-5G* level originally used by Politzer. In addition, Byrd's training set included functional groups more likely to be present in EMs (e.g., azides and nitro groups).

For salts, an attractive route to $\Delta H_{f(s)}$ from $\Delta H_{f(g)}$ is *via* calculation of ΔH_L using the method developed by Jenkins et al. (1999), Jenkins et al. (2002) that relies only on knowledge of the molecular (formula unit) volume and the stoichiometry of the salt. This method has been used by Gao et al. (2007) to compare the estimated values of $\Delta H_{f(s)}$ for 33 energetic salts to their respective experimental values, using the G2 method to calculate the $\Delta H_{f(g)}$ terms for the ions based on their proton or electron affinities. They reported $R^2 = 0.983$, with a maximum deviation of 158.5 kJ mol^{-1}.

Co-crystals are an important development in the field of EMs (Kennedy and Pulham, 2018). While acknowledging that predicting whether or not a stable co-crystal will form from its single-component species is in itself the greater challenge, having the ability to predict $\Delta H_{f(s)}$ for known materials is also important. This is particularly true for EM research, where creating materials that can store large amounts of chemical energy is an essential requirement. Previous attempts have met with limited success. For instance, Zhang et al. (2016), Bozkuş et al. (2019) both used an atomisation energy method (Curtiss et al., 1997) which can formally only be used to calculate the heat of formation of gas-phase species. Ma et al. (2017) used isodesmic equations to calculate $\Delta H_{f(g)}$ for the co-formers of a CL-20/MTNP co-crystal, and then predicted ΔH_{sub} using a relationship based on the melting point of the co-crystal. While this method is promising, its application is limited if the melting point is not known. Gavezzotti developed the PIXEL method to calculate ΔH_L as a sum of Coulombic, polarisation, dispersion and repulsion intermolecular energies in a crystal structure and has been shown to have the correlation $R^2 = 0.845$ between experimental and calculated ΔH_L for 154 organic crystal structures (Gavezzotti, 2011). The method was recently expanded to include parameterisation for transition metal complexes (Maloney et al., 2015). Another route to obtaining ΔH_L is through the more computationally demanding dispersion-corrected density functional theory (DFT-D) (Morrison and Siddick, 2003; Feng and Li, 2006; Brandenburg et al., 2015; Fan et al., 2017). For the specific example of co-crystals considered here, as it is uncommon to measure $\Delta H_{f(s)}$ we shall compute formation enthalpies using both PIXEL and DFT-D for direct comparison.

In addition to having reliable routes to predict $\Delta H_{f(s)}$, having knowledge of the strengths of the individual bonds within a molecule is also valuable information at the EM molecular design stage, as it can provide information on the first-stage initiation pathway. Historically, intramolecular bond strengths have been calculated through heterolytic bond cleavage reactions, but this proves problematic beyond the first bond breaking reaction, as each subsequent bond breakage reaction is performed on increasingly unstable molecular fragments (Cremer et al., 2000), or requires a separate bond breaking reaction for each bond to be investigated (Zou et al., 2012). This is particularly problematic for ring systems, where breaking one bond introduces additional strain in the remaining bonds, such that isolating one bond becomes an impossible task. Alternatively, computation of the bond force constants offers a direct route to determining the bond strengths of all bonds within a molecule without recourse to molecular fragmentation. However, the normal modes of molecular vibration, from which the force constants are extracted, are commonly a complex mix of bond stretching, angle bending and twisting motions, meaning that pure bond force constants can rarely be obtained. Recent developments by Konkoli and Cremer (Konkoli and Cremer, 1998a; Konkoli and Cremer, 1998b; Kraka et al., 2020) have allowed for the mass decoupling of the normal modes of vibration, to recast the eigenvectors onto a new set of modes, termed the local modes of vibration, that correlate directly with individual bond stretches, angle bends etc. Their work has shown that the resulting local-mode force constants thus obtained are a direct measure of bond strength (Kraka and Cremer, 2019). Thus performing local mode analysis across a broad range of molecules (both energetic and non-energetic) provides information on the relationship between bond length and bond strength of the most common chemical bonds in EMs, which has the potential to be utilised for molecular design.

Herein, a set of 20 CHNO-containing molecules and a further 31 inorganic molecules was constructed to benchmark the PM7 method against isodesmic equation reactions and the atom equivalence method to calculate $\Delta H_{f(g)}$. Additionally, methods for converting $\Delta H_{f(g)}$ to $\Delta H_{f(s)}$ using the methods proposed by Byrd, Jenkins, and by the PIXEL method/DFT-D for single-component molecular crystals, salts and co-crystals, respectively, were also pursued for 48 compounds. Local vibrational mode analysis has also been carried out on 30 molecules containing chemical bonds found in energetic molecules, to evaluate bond length/strength relationships and to ascertain the likely weakest bonds in energetic molecules. Finally, both parameters have been highlighted for their potential to be included in a computational screening program for new energetic materials.

COMPUTATIONAL METHODS

All optimization and vibrational frequency calculations were performed at the B3LYP/6-31G* level, as implemented in Gaussian16 (Frisch et al., 2016).

Gas-Phase Heat of Formation: Isodesmic Equations

Equations were devised to ensure the type of chemical bonds were conserved, and that the heats of formation of all other molecules in the equation were known (see **Supplementary Table 2**). The heat of reaction, ΔH_R, is then calculated according to **Eq. 1**.

$$\Delta H_R = \Delta E_0 + \Delta ZPE + \Delta H_T + \Delta nRT \quad (1)$$

Where ΔE_0 is the change in energy between the products and reactants, ΔZPE is the change in the zero-point energies between products and reactants, and ΔH_T is the thermal correction from 0 to 298 K. As the number of atoms remain constant in the reaction, ΔnRT equals zero. The calculated heat of reaction is then equated to **Eq. 2**. Assuming the molecule of interest is a reactant in the isodesmic equation then its heat of formation is calculated by subtracting the known heats of formation of the other reactants and products from ΔH_R.

$$\Delta H_R = \sum \Delta H_{f\,(g)products} + \sum \Delta H_{f\,(g)reactants} \quad (2)$$

Gas-Phase Heat of Formation: Atom Equivalence Method

Formation energies were determined according to **Eq. 3**, where E is the optimised energy of the molecule, n_j is the number of atoms of type j and e_j is the atom equivalence value of atom j, as determined by Byrd and Rice (Byrd and Rice, 2006).

$$\Delta H_{f\,(g)} = E - \sum n_j e_j \quad (3)$$

Gas-Phase Heat of Formation: PM7

PM7 (Stewart, 2013) method was utilised as presented in Gaussian 16, using geometries optimised to global minima from the previously mentioned calculations for improved accuracy. For molecules containing third row and higher atoms, the SCF = YQC algorithm was used, as suggested in the PM7 documentation.

Solid-State Heat of Formation: Single-Component Solids

The solid heat of formation for single component materials were calculated using **Eq. 4**, where $\Delta H_{f(g)}$ was calculated using PM7 as described above, and ΔH_{sub} was calculated using the ESP method as described by **Eq. 5**.

$$\Delta H_{f\,(s)} = \Delta H_{f\,(g)} - \Delta H_{sub} \quad (4)$$

$$\Delta H_{sub} = a\,(SA)^2 + b\sqrt{\sigma_{tot}^2 \nu} + c \quad (5)$$

Where a, b and c are semi-empirically deduced fitting parameters proposed by Byrd et al. (Byrd and Rice, 2006) SA is the surface area of the 0.001 electron.bohr^{-3} isosurface of the electrostatic potential of the molecule, σ_{tot}^2 is the measure of variablity of electronic potential on the surface, and ν is the degree of balance between the positive and negative charges on the isosurface. The latter three parameters were calculated using Multiwfn (Lu and Chen, 2012).

Solid-State Heat of Formation: Salts

For the energetic salts $\Delta H_{f(s)}$ was calculated from **Eq. 6**, where $\Delta H_{f(g)}$ of the cations and anions were calculated using PM7 as described above.

$$\Delta H_{f\,(s)} = \Delta H_{f\,(g)\,(cation)} + \Delta H_{f\,(g)\,(anion)} - \Delta H_L \quad (6)$$

Here, ΔH_L is expressed by **Eq. 7**, as proposed by Jenkins et al. (2002).

$$\Delta H_L = U_{pot} + \left[p\,(n_m/2 - 2) + q\,(n_x/2 - 2)\right]RT \quad (7)$$

Where n_m and n_x are constants that depend on the nature of the ions, and are set to 3 for monoatomic ions, 5 for linear polyatomic ions and 6 for non-linear polyatomic ions. The variables p and q denote the relative charges of the respective ions. The term U_{pot} denotes the lattice potential energy and in turn is defined by **Eq. 8**.

$$U_{pot} = \alpha\,(V_m)^{\frac{1}{3}} + \beta \quad (8)$$

Where V_m denotes the molecular volume (V_{cell}/Z), in nm^3, and the remaining coefficients α and β are fitting terms provided by Jenkins et al. and which vary depending on the charge ratio of the salt.

Solid-State Heat of formation: Co-Crystals

For lattice enthalpies calculated using PIXEL (Gavezzotti, 2005), calculations were set up using MrPIXEL (Reeves et al., 2020) within the Mercury interface, distributed with the Cambridge Structural Database (CSD) (Macrae et al., 2008; Groom et al., 2016). Hydrogen atom positions were set to the CSD normalised positions. For DFT-D, geometry optimisation calculations were performed using CASTEP17 (Clark et al., 2005) using the Perdew-Burke-Ernzerhof functional (Perdew et al., 1996) with a plane-wave basis set with a cut-off energy of 900 eV, which demonstrated convergence to 1 meV.atom^{-1}. Norm-conserving pseudopotentials were used throughout, with a k-point spacing of 0.05 Å^{-1}. The Tkatchenko-Scheffler dispersion correction scheme was applied. Lattice energies were determined by comparing the optimized energy values for the crystal structure with the energy for individual co-formers, modelled as effectively gas phase by removing all but one of the co-former molecules from the optimized crystal structure and computing a single point energy value using the same computational model as applied to the co-crystal. In cases where a unit cell vector was short, such that interactions with the nearest neighbour replica may occur (taken to be <5 Å), the smallest unit cell vector was doubled to

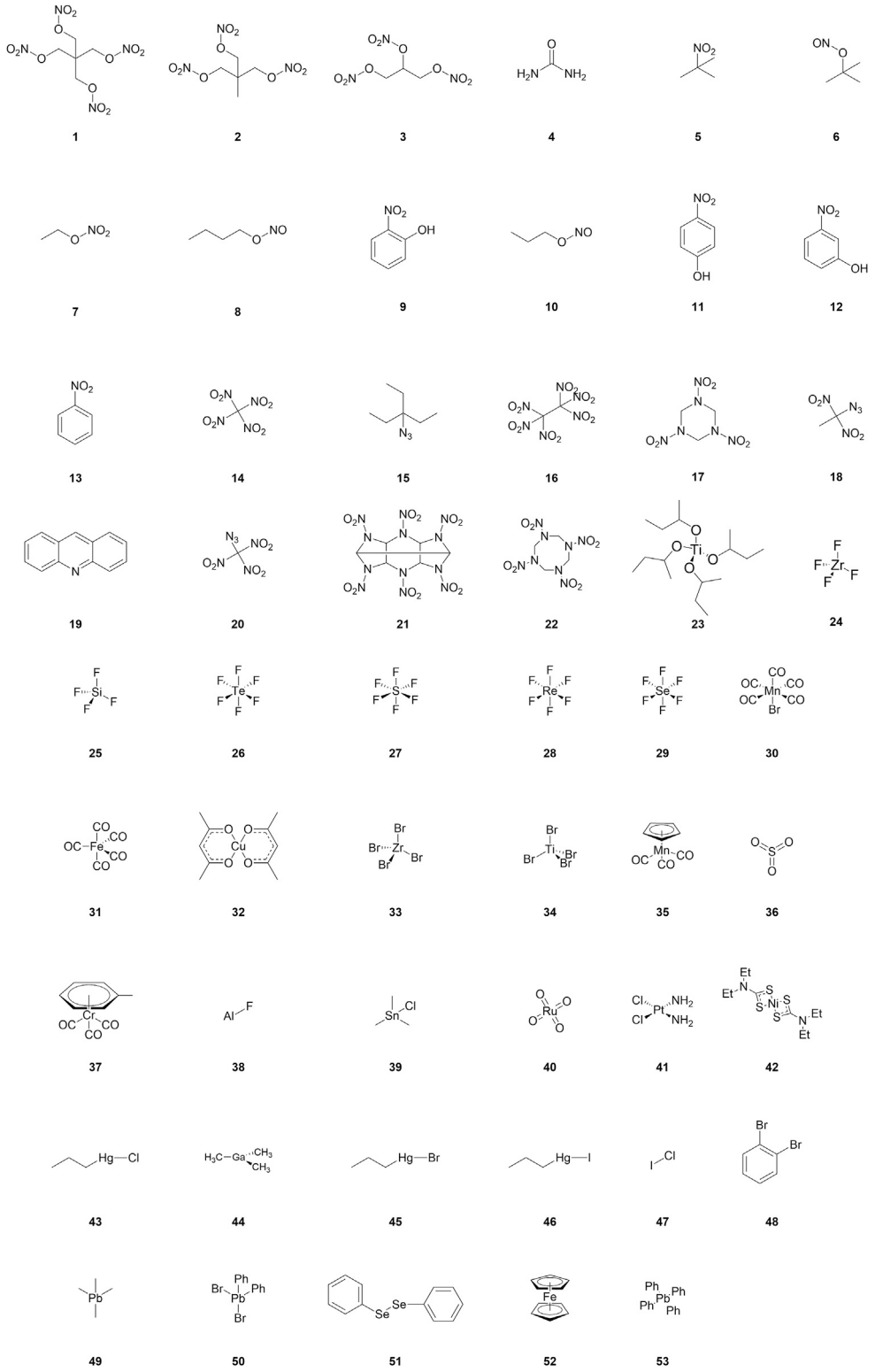

FIGURE 1 | Molecules, salts and co-crystals employed in heat of formation energy calculations.

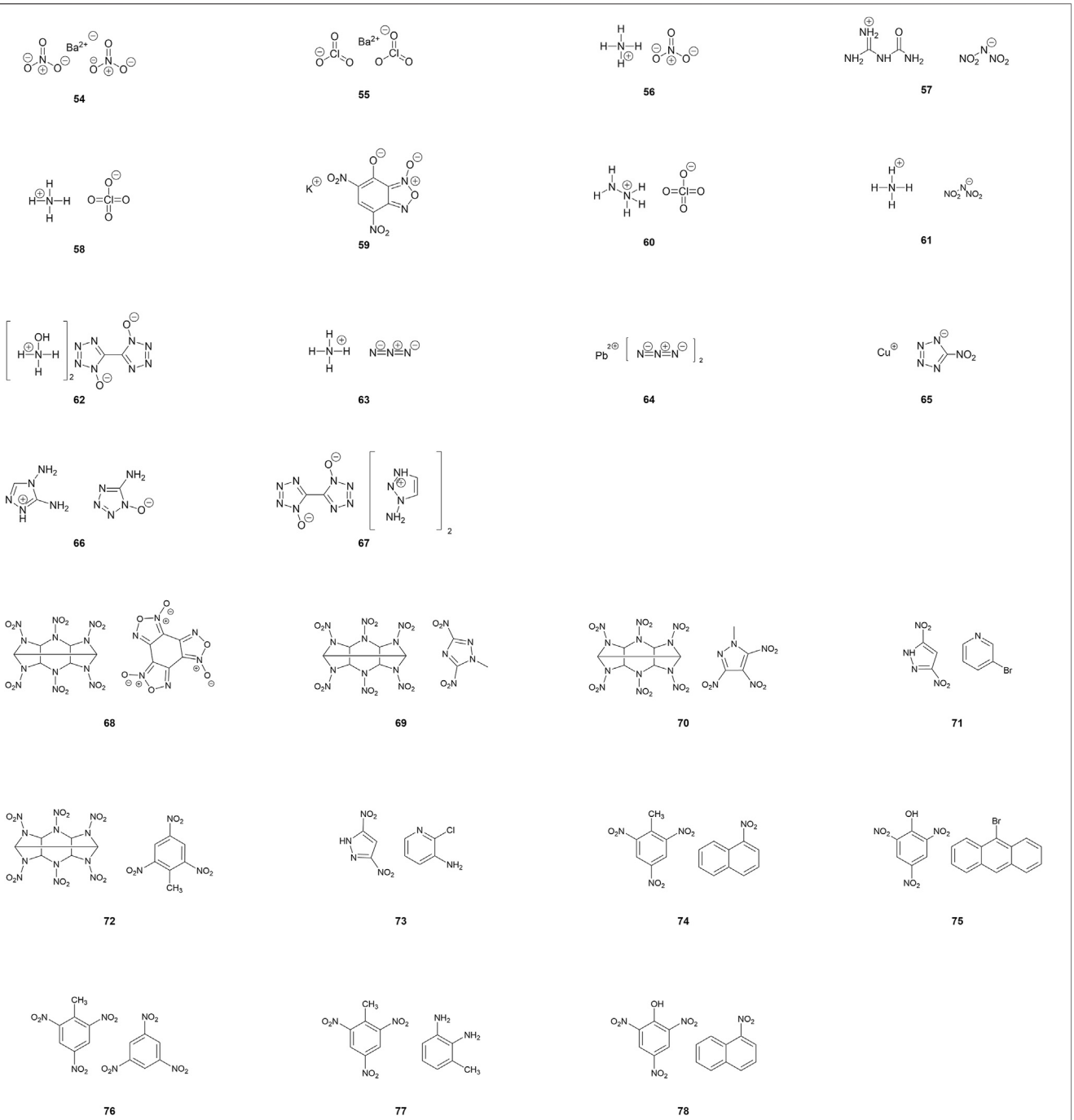

FIGURE 1 | (Continued).

ensure zero interaction. This was the case for **64**, **70** and **76**. Lattice enthalpies were then calculated using **Eq. 9**.

$$\Delta H_L = \frac{E_{cell}}{Z} - E_{co-former1} - E_{co-fomer2} \quad (9)$$

Where E_{cell} is the energy of the unit cell of the co-crystal and $E_{co-fomer1,2}$ is the energy of each of the co-formers modelled in the "gas phase" and Z is the number of molecular units in the co-crystal. The $\Delta H_{f(g)}$ terms, to convert the ΔH_L terms to $\Delta H_{f(s)}$, were calculated using PM7 as documented above.

Lattice enthalpies of individual co-formers were calculated by adding the thermodynamic correction shown in **Eq. 10** to the sublimation enthalpies calculated using the ESP method described above.

$$\Delta H_L = -\Delta H_{sub} - 2RT \quad (10)$$

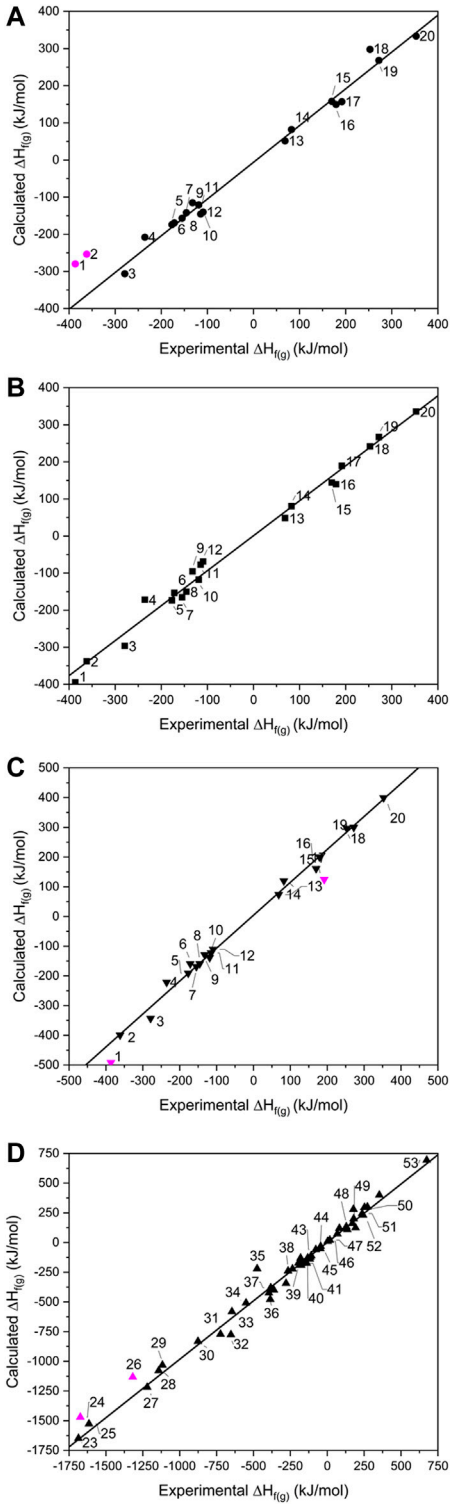

FIGURE 2 | Showing calculated *vs.* experimental gas phase heats of formation for the **(A)** isodesmic, **(B)** atom equivalence, **(C)** PM7 for **1**–**20** and **(D)** PM7 for **23–53**. Data points omitted from the lines of best fit are shown in pink.

Local Mode Force Constants

These were calculated using LMODEA (Kraka et al., 2020), following geometry optimisation and vibrational frequency calculation, for the 31 CHNO-containing molecules listed in **Supplementary Table 6**.

RESULTS AND DISCUSSION

Calculating Gas Phase Heats of Formation

To test the three different methods for calculating $\Delta H_{f(g)}$ molecules **1**–**20** (see **Figure 1** and **Supplementary Table 1**), were considered. Molecules were chosen as they had reliably reported experimental $\Delta H_{f(g)}$ available in the literature, and their less complex nature meant that the construction of isodesmic reaction equations was relatively straightforward (reported in full in **Supplementary Table 2**). As the PM7 method permits inorganic molecules to be studied, a further set of molecules which comprised main group and transition metal elements (**23**–**53**) was also studied. Notably, examples include molecules containing lead, copper and halogens, which are commonly found in EMs.

While the majority of CHNO-containing molecules investigated here have already been reported by Elioff et al. (2016), our process differs in that all molecules were first optimised at the 6-31G*/B3LYP level, followed by a single-point energy evaluation at PM7. In addition, the data set includes a further 4 molecules, namely **1, 2, 4,** and **19**, which incorporates the important EMs PETN (**1**), TMETN (**2**) into the test set. Calculation of $\Delta H_{f(g)}$ for the 31 inorganic molecules (**23**–**53**) by PM7 has not been reported before.

When calculated values of $\Delta H_{f(g)}$ are compared against experimental data (**Figure 2**), the two largest outliers for the isodesmic equation method (**Figure 2A** and **Supplementary Table 3**) were PETN and TMETN (**1** and **2** respectively), which deviate from the experimental values by 106.8 and 108.0 kJ mol^{-1}, respectively. Both data points were disregarded when carrying out linear fitting, which otherwise returned an R^2 value of 0.994, and the gradient of the fitted line, $m = 0.989$. The reasons for failure for data points **1** and **2** must rest with either the experimental formation energies and/or the geometry optimisations of PETN and TMETN, or the geometry optimisation and/or experimental formation energy of another molecule defined in their respective isodesmic equations. The atom equivalence method (shown in **Figure 2B**) performs considerably better for these two compounds, which suggests that the experimental formation energies and the geometry optimizations, for both PETN and TMETN, are reliable. The isodesmic reactions constructed for these two molecules both include $C(CH_3)_4$, which is absent in all other isodesmic equations constructed for the test set (see **Supplementary Table 2**). Careful checking of the simulated geometry, to ensure the configuration obtained refers to the global minimum, suggests that the error most likely rests with the experimental heat of formation for $C(CH_3)_4$. This highlights a fundamental weakness with the

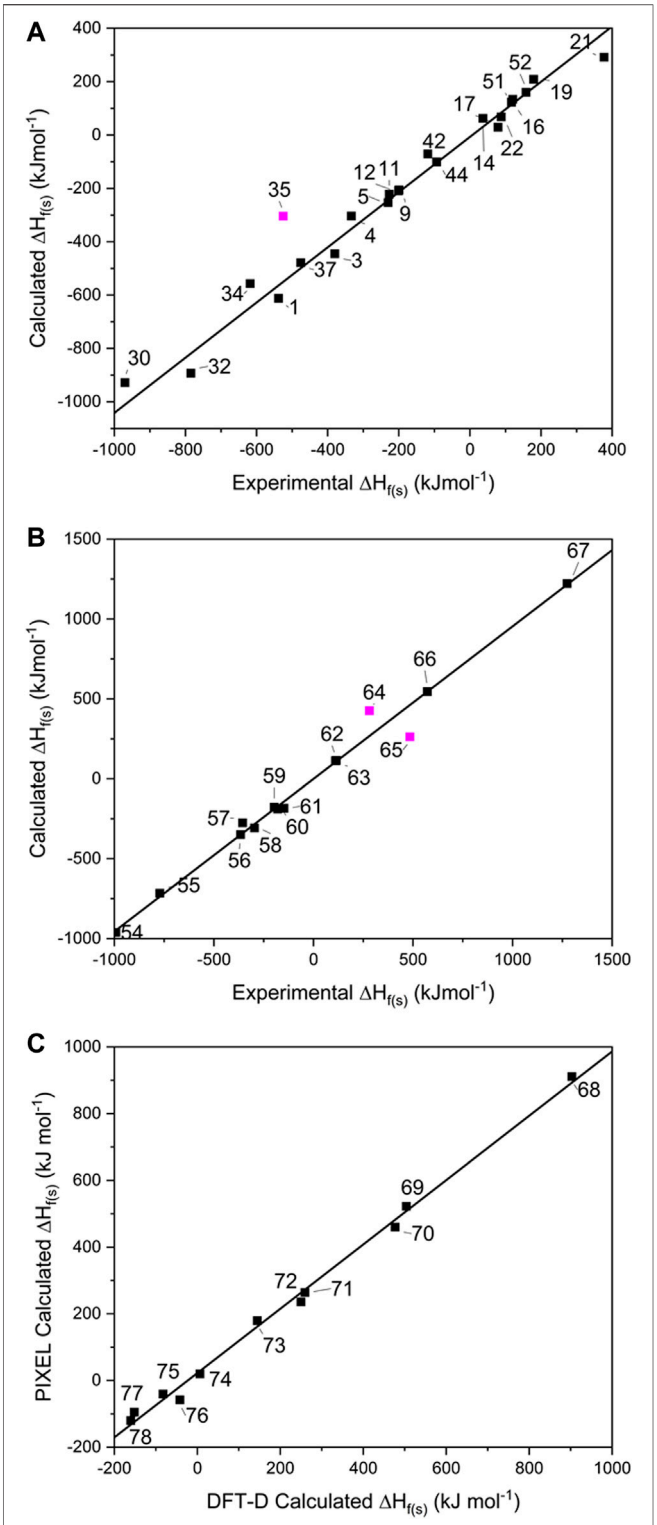

FIGURE 3 | Showing the calculated solid heats of formation for **(A)** single component crystals, **(B)** salts and **(C)** co-crystals. Data points omitted from the lines of best fit are shown in pink.

isodesmic equation route, in that any error with any one term in the equation will render the calculated $\Delta H_{f(g)}$ for the target molecule as unreliable.

Using the atom equivalence method, no outliers where identified, showing the strength of this method for CHNO-containing molecules. This gave an R^2 value of 0.994 (m = 0.943), indicating that the atom equivalence method performs just as well as the isodesmic method.

Turning to the PM7 results (**Figure 2C**), PETN (**1**) again represents the largest deviation, with the semi-empirical method over-estimating the experimental value by 91.2 kJ mol^{-1}. RDX (**17**) also appears to be less reliably calculated by this method, compared to the other two routes. Discarding **1** and **17** from the test set gives a line of best fit with R^2 = 0.993 (m = 1.083), suggesting overall that this method provides a similar level of accuracy compared to the isodesmic reaction and atom equivalence methods. The correlation with experimental data here is better than that reported by Elioff et al. (2016) (R^2 = 0.986) and considering the high overlap of molecules in test sets used, the improvement is likely due to the B3LYP/6-31G* geometry optimization step, as Elioff et al. relied on the PM7 method for structure optimisation as well as energy calculation. For the inorganic molecule list, **23–53,** which were tackled by PM7 only, the R^2 value increased slightly to 0.995, with the gradient of the line of best fit improved considerably [m = 0.983; omitting the largest outliers ZrF_4 (**24**) and TeF_6 (**26**), which deviate from experimental values by 186 and 203 kJ mol^{-1}, respectively], suggesting its performance is just as reliable for inorganic molecules as it is for organic molecules. It is unclear why ZrF_4 and TeF_6 deviate so much from the expected values. Other related compounds, **25**, **27–29** and **34**, have been calculated accurately (although **26** is the only Te-containing compound and Zr is represented just twice in the data set). The possibility of experimental inaccuracy also cannot be ruled out.

Calculating Solid Heats of Formation

To probe the conversion of $\Delta H_{f(g)}$ to $\Delta H_{f(s)}$, 23 of the single-component EMs were selected from the **1–53** test set for which experimentally determined $\Delta H_{f(s)}$ were available (see **Figure 3A** and **Supplementary Table 1**), and further pursued using the ESP method. This includes 14 CHNO-containing molecules and 9 inorganic compounds. Fourteen salts (**54–67** in **Figure 1**) were similarly pursued using Jenkins' method, while 11 co-crystals (**68–78** in **Figure 1**) were explored using PIXEL and DFT-D.

For the single-component crystals, $\Delta H_{f(s)}$ calculated using the ESP method offered a line of best fit of R^2 = 0.995, m = 1.100 [omitting one point that lay off the line, $Mn(CO)_3Cp$ (**35**) by 220 kJ mol^{-1}, see **Figure 3A**], indicating a good predictive result has been obtained across a broad spectrum of compounds and broad range of energies.

For the EM salts (**54–67**), application of Jenkins' method gives a line of best fit through the simulated values (see **Figure 3B**) with R^2 = 0.997 (m = 0.955), and a maximum deviation from experimental values of 80.5 kJ mol^{-1} for FOX-12 (**55**). This is

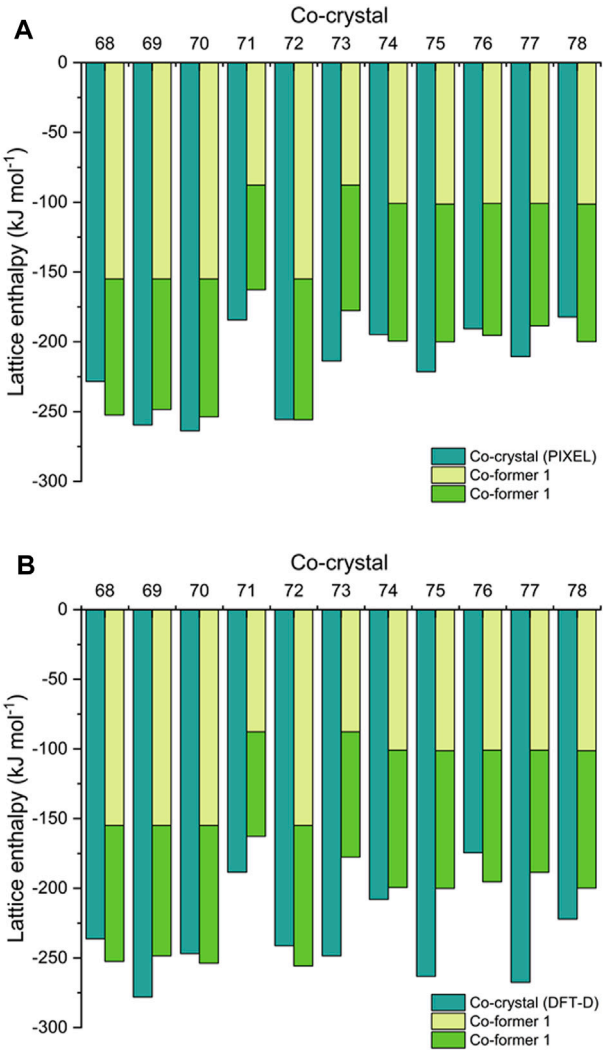

FIGURE 4 | Comparison of calculated lattice enthalpies of co-crystals **68**–**78** by **(A)** PIXEL and **(B)** DFT-D, alongside constituent co-formers.

an improvement in the correlation reported by Gao et al. (2007) who reported an R^2 of 0.984 for a set of 33 inorganic and CHNO EM salts, of which 19 were inorganic and the remainder CHNO. While acknowledging that the improved result obtained here could be due to the smaller test set employed in this work, it could also indicate that the PM7 method, used to calculate the $\Delta H_{f(g)}$ terms for the constituent ions, offered an improvement over the approach adopted by Gao, who relied on isodesmic equations. This latter approach is likely to be particularly problematic here as experimental formation energies of ions are required. Our data set shares two data points with Gao's (salts **56** and **61**); closer inspection of these predictions shows that both $\Delta H_{f(s)}$ values were calculated more accurately here, with **56** deviating from the experimental values by 17 kJ mol^{-1} (Gao's prediction differed by 24.7 kJ mol^{-1}), whereas **61** deviated by only 0.9 kJ mol^{-1} (Gao by 63.5 kJ mol^{-1}). This would therefore appear to support further the use of PM7 to calculate the $\Delta H_{f(g)}$ terms. There are two outliers in this fitting – lead azide (**64**) and DBX-1 (**65**), which deviate from their literature values by 222 and 145 kJ mol^{-1}, respectively. We note that both exist as extended coordination complexes in the solid state, which may contribute towards their poor prediction by Jenkins' method, which was formally devised for salts.

It should be noted that TKX-50 (**62**) has two values for $\Delta H_{f(s)}$ reported in the literature. The most widely reported is 446.6 kJ mol^{-1} (Sabatini and Oyler, 2015), which was the value calculated using Jenkins' method, with the $\Delta H_{f(g)}$ values for the constituent ions calculated using the CBS-4M atomisation method. However, Sinditskii et al. (2015) have argued that this value is questionable when compared to the sum of the enthalpies of formation for the individual components of TKX-50 and when compared with typical heats of reaction between acids and bases. They performed bomb calorimetry experiments and determined $\Delta H_{f(s)}$ to be 111 ± 16 kJ mol^{-1}, far lower than the widely reported calculated value. Our computed value, also derived from the Jenkins' method, but utilising PM7 to calculate the $\Delta H_{f(g)}$ values for the ions, is 112.6 kJ mol^{-1}, showing that the earlier result was in error due to computation of the $\Delta H_{f(g)}$ terms for the molecular ions.

For the 11 energetic co-crystals investigated, ΔH_L was calculated using two different approaches, the quicker PIXEL method, and the more computationally demanding DFT-D method (see **Figure 3C** and **Supplementary Table 6**), as no experimental data was available to benchmark the predictions against. From these results, it was readily apparent that the two methods provide comparable results (R^2 = 0.997, m = 0.964), meaning that both options are viable for co-crystals as part of a computational screening program. PIXEL does present some limitations, however, as it is not applicable to structures where the number of molecules in the crystallographic asymmetric unit exceeds 2; for these larger crystal lattices DFT-D is at present the only realistic solution.

Next, we offer an interesting comparison between the ΔH_L of the co-crystals (from **Eq. 9**) alongside the ΔH_L values for their respective co-formers (from **Eqs. 5**, **10**). This is shown in **Figure 4** (and **Supplementary Tables 1, 6**), from which it is apparent that the sum of the latter gives a reasonable approximation of the former. This is in agreement with Vener et al., who studied a number of co-crystals using DFT-D and hybrid-DFT functionals (Vener et al., 2014). A similar observation was also made by Day et al., who showed using DFT-D simulations that the total energy of 350 organic co-crystals was greater than a linear weighed sum of their single-component counterparts by the order of just *ca.* 8 kJ mol^{-1} (per molecule). This applied to around 95% of their data set, showing that co-crystal formation is overwhelmingly driven by thermodynamics (Taylor and Day, 2018). Estimating ΔH_L for a co-crystal by this quick approximation may help guide the choice of co-formers for EM research, in order to maximize the amount of stored chemical energy. It also would be particularly useful to estimate ΔH_L for co-crystals such as CL-20/HMX, which has a 2:1 ratio of co-formers (Bolton et al., 2012) and thus falls outside the scope of PIXEL calculations. Accordingly, we estimate ΔH_L of CL-20/HMX to be *ca.* −430 kJ mol^{-1} [based on ΔH_L (HMX) + 2 × ΔH_L (CL-20), see **Supplementary Table 1**]. Using DFT-D, the corresponding ΔH_L

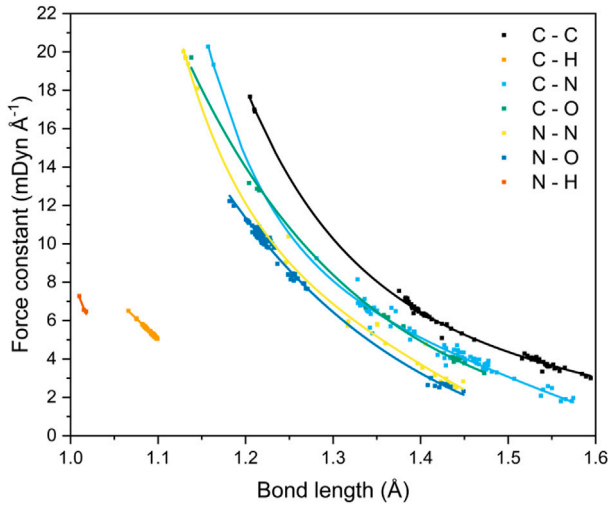

FIGURE 5 | Correlation between bond lengths and local vibrational mode force constants for seven covalent bonding environments.

prediction is -460 kJ mol^{-1}. This results in a predicted $\Delta H_{f(s)}$ of *ca.* 570–600 kJ mol^{-1}. We note that Zhang et al. (2019) estimated a considerably higher value for $\Delta H_{f(s)}$ of 861.9 ± 18.6 kJ mol^{-1}; this was obtained indirectly using a calculated heat of reaction for the formation of solid CL-20/HMX from solid ε-CL-20 and β-HMX, that in turn used a thermochemical cycle based on measured enthalpies of dissolution of all species in acetonitrile, and literature $\Delta H_{f(s)}$ values for ε-CL-20 and β-HMX.

While Day et al. makes a strong case for co-crystallisation being overwhelmingly thermodynamically driven (Taylor and Day, 2018), a recent report by Perlovich suggests that the formation of around 30% of co-crystals are entropically driven (Perlovich, 2020). This work was based on constructing a dataset of 1947 co-crystals for which experimental sublimation energies were available, from which an algorithm to calculate the Gibbs sublimation energy was derived. Our test set of eleven EM co-crystals is too small to add any significant weight to this argument. While in general the predictions show that the lattice energy of the co-crystal does indeed exceed that of the sum of the co-formers (by up to *ca.* 70 kJ mol^{-1}, a similar total energy range reported by Day et al.), for some structures (**68, 74, 76** and **78** by PIXEL, **68**, **72** and **76** by DFT-D) the relationship does not hold, although we note that the energy shortfalls are typically very small. Improving the computational method to improve the accuracy of the comparison (*i.e.,* zero point energy and entropy corrections) (Nyman and Day, 2015) will be considered more broadly in follow up studies. Such corrections could be obtained from calculating full phonon spectra, but these are time consuming to perform and therefore go against the computational screening philosophy which pervades this paper.

In summary, of the three methods tested here for calculating $\Delta H_{f(g)}$, PM7 performs favourably compared with the isodesmic reactions and atom equivalence methods, while offering application to the widest range of molecules. Its strength has also been demonstrated when calculating $\Delta H_{f(s)}$ for single component solids and salts, by the ESP and Jenkins methods, respectively, with predicted values showing excellent correlation with experimental $\Delta H_{f(s)}$ values. Finally, two different methods, PIXEL and DFT-D, were compared for calculating ΔH_L terms for co-crystals and found to give comparable results. Comparison of the calculated ΔH_L terms show that, to a first approximation, the lattice enthalpy of the co-crystal is the sum of the lattice enthalpies of the constituent co-formers. While this does not inform on the likelihood of success for the formation of new co-crystals, it does offer significant new insight in directing co-crystallisation studies to create new EMs with desired $\Delta H_{f(s)}$ values.

Local Force-Constant Calculations

Local vibrational-mode force constants were calculated for all CHNO-containing molecules in the test set, with a further ten EMs added to provide a wider and more comprehensive coverage of bond length values (31 CHNO molecules in total, **Supplementary Table 7**, including the EMs CL-20, RDX, HMX, HNB, NTO, TATB, FOX-7, PETN and nitroglycerin). From this data, a relationship between the bond lengths and force constants (bond strengths) of seven different covalent bonding environments can be drawn (see **Figure 5**).

The data shown here expands upon the relationship that has been established by Kraka et al. for C–C bonds occurring in both gas and solid state geometries.(Kraka et al., 2020). It also mirrors the trends shown by Byler et al. (1987) and Ladd et al. (1964) for C–N bonds and C–O bonds, respectively. The studies by Byler and Ladd analyzed mainly linear molecules in an effort to reduce the effect of coupling of normal vibrational modes. This limitation is elegantly side-stepped by local vibrational mode analysis through the recasting of the normal modes of vibration into the local modes through mass decoupling (Groom et al., 2016; Hehre et al., 1970) Byler et al. reported bond lengths that ranged from 1.122 Å (k = 20.17 mdyn Å^{-1}, $H_3CC–NBCl_3$) to 1.555 Å (k = 3.51 mdyn Å^{-1}, $F_3C–NO$). Their data sit comfortably on our C–N curve, highlighting the power of the local-mode analysis route for obtaining force constants for more complex molecules. Ladd et al. measured the vibrational frequency of the C–O bond stretch for different excited states of carbon monoxide to obtain the relationship between force constant and bond length over the range 1.088–1.396 Å. Their data agree quantitatively with the C–O bond curve shown in **Figure 5** at long bond lengths, but consistently underestimates the force constants at shorter (<1.2 Å) distances, which suggests that measuring the force constants of only excited states of CO has skewed the relationship between bond length and force constant. McKean made extensive studies of the vibrational frequencies of isolated C–H bond stretches, a property which is directly comparable to the local mode of vibration (McKean, 1978; Konkoli et al., 1998; Konkoli and Cremer, 1998a; Larsson and Cremer, 1999), and therefore the force constants, and presented a relationship between C–H bond length and experimentally determined stretching frequencies which mirrors the trend shown here. Cremer et al. (2000) also calculated C–H force constants of adiabatic internal modes (an earlier name for local vibrational modes), their shortest C–H

bond being 1.086 Å with a force constant of 5.58 mdyn $Å^{-1}$. This fits on our line presented in **Figure 5**, which is now further extended to 1.066 Å (and 6.46 mdyn $Å^{-1}$).

A strong correlation of force constant and bond length is observed for all bond types, and decay functions were used to fit trend lines (**Supplementary Table 8**) that returned R^2 values of *ca.* 0.99 for all bond types, with the exception of C–N ($R^2 = 0.98$) and N–H ($R^2 = 0.92$), although the latter corresponds to only four data points and is likely under-represented. Four bond types, C–C, C–N, C–O and N–N, encompass single to triple bond behaviour, and N–O bond types include single and double bonds, as evident from the clustering of data points. The wide range of bond lengths studied give rise to a corresponding wide range of calculated local-force constant values, which for the most part follow the sequence C–C > C–N ≈ C–O > N–N ≈ N–O, although the longer distances associated with single C–N bonds render these interactions on a par with single N–N and N–O bonds. The weakness of the long C–N bond fits with expectation: the rupture of R–NO_2 bonds has been shown to be a critical step in the decomposition of energetic materials (Sharma and Owens, 1979; Sharma et al., 1982; Owens, 1996). The data shown in **Figure 5** are testament to the great potential offered by the local-mode analysis route: it is a quick and straightforward method to compare and contrast the bond strengths of all bonding interactions within a molecule, from which the weakest bond can be unambiguously identified. In essence, the curves shown in **Figure 5** allow a direct mapping between bond length and bond strength to be obtained. For the case of CL-20, a cage nitramine structure comprising 5, 6 and 7 membered C–N rings (compound **21** in **Figure 1**), it has been suggested that the C–N bonds forming the cage can also act as the "trigger linkage," (Sun et al., 2021) in addition to the generally weaker N–NO_2 bonds. This is supported here, with the C–N bonds in the more strained 5-membered rings having force constants similar to the stronger N–NO_2 bonds (3.337 *vs.* 3.151 mdyn $Å^{-1}$, respectively). The less strained 6-membered ring contains stronger C–N bonds, with force constants ranging from 4.088–4.486 mdyn $Å^{-1}$, a considerable increase in strength from the C–N bonds present in the 5-membered rings. The relationship between bond length and force constant presented here therefore has the potential to be applied to molecular design, as the weakest bond in a molecule can be tuned by its surrounding molecular environment.

DATA AVAILABILITY STATEMENT

The original contributions presented in the study are included in the article/**Supplementary Material**, further inquiries can be directed to the corresponding author.

AUTHOR CONTRIBUTIONS

IC performed the calculations. IC and CM wrote the manuscript. All authors analysed the data. AM, CP, and CM directed the research.

FUNDING

This material is based upon work supported by the Air Force Office of Scientific Research under award number FA8655-20-1-7000. We are grateful for computational support from the United Kingdom Materials and Molecular Modelling Hub, which is partially funded by EPSRC (EP/P020194 and EP/T022213), for which access was obtained via the UKCP consortium and funded by EPSRC grant ref EP/P022561/1.

ACKNOWLEDGMENTS

We gratefully acknowledge Prof. E. Kraka (Department of Chemistry, Southern Methodist University, Texas) for early access to their local mode analysis software, LMODEA. IC thanks the University of Edinburgh, School of Chemistry for the award of a PhD studentship. We thank the EaSTCHEM Research Computing Facility and the Edinburgh Computing Data Facility, for access to software and hardware resources, respectively.

SUPPLEMENTARY MATERIAL

The Supplementary Material for this article can be found online at: https://www.frontiersin.org/articles/10.3389/fchem.2021.726357/full#supplementary-material

REFERENCES

Axthammer, Q. J., Krumm, B., and Klapötke, T. M. (2015). Pentaerythritol-based Energetic Materials Related to PETN. *Eur. J. Org. Chem.* 2015, 723–729. doi:10.1002/ejoc.201403265

Benson, S. W., Cruickshank, F. R., Golden, D. M., Haugen, G. R., O'Neal, H. E., Rodgers, A. S., et al. (1969). Additivity Rules for the Estimation of Thermochemical Properties. *Chem. Rev.* 69, 279–324. doi:10.1021/cr60259a002

Bolton, O., Simke, L. R., Pagoria, P. F., and Matzger, A. J. (2012). High Power Explosive with Good Sensitivity: A 2:1 Cocrystal of CL-20:HMX. *Cryst. Growth Des.* 12, 4311–4314. doi:10.1021/cg3010882

Bozkuş, S. I., Hope, K. S., Yüksel, B., Atçeken, N., Nazır, H., Atakol, O., et al. (2019). Characterization and Properties of a Novel Energetic Co-crystal Formed between 2,4,6-Trinitrophenol and 9-Bromoanthracene. *J. Mol. Struct.* 1192, 145–153. doi:10.1016/j.molstruc.2019.04.109

Brandenburg, J. G., Maas, T., and Grimme, S. (2015). Benchmarking DFT and Semiempirical Methods on Structures and Lattice Energies for Ten Ice Polymorphs. *J. Chem. Phys.* 142, 124104–124111. doi:10.1063/1.4916070

Byler, D. M., Susi, H., and Damert, W. C. (1987). Relation between Force Constant and Bond Length for Carbon-Nitrogen Bonds. *Spectrochimica Acta A: Mol. Spectrosc.* 43, 861–863. doi:10.1016/0584-8539(87)80231-3

Byrd, E. F. C., and Rice, B. M. (2006). Improved Prediction of Heats of Formation of Energetic Materials Using Quantum Mechanical Calculations. *J. Phys. Chem. A.* 110, 1005–1013. doi:10.1021/jp0536192

Chan, B., Collins, E., and Raghavachari, K. (2020). Applications of Isodesmic-type Reactions for Computational Thermochemistry. *Wires Comput. Mol. Sci.* 11, 1–18. doi:10.1002/wcms.1501

Clark, S. J., Segall, M. D., Pickard, C. J., Hasnip, P. J., Probert, M. I. J., Refson, K., et al. (2005). First Principles Methods Using CASTEP. *Z. fuer Krist* 220, 567–570. doi:10.1524/zkri.220.5.567.65075

Cramer, C. (2004). *Essentials of Computational Chemistry Theories and Models*. 2nd ed. Chichester: Wiley.

Cremer, D., Wu, A., Larsson, A., and Kraka, E. (2000). Some Thoughts about Bond Energies, Bond Lengths, and Force Constants. *J. Mol. Model.* 6, 396–412. doi:10.1007/PL00010739

Cumming, A. S. (2017). Environmental Aspects of Energetic Materials Use and Disposal. *Chem. Rocket Propulsion*, 727–741. doi:10.1007/978-3-319-27748-6

Curtiss, L. A., Raghavachari, K., Redfern, P. C., and Pople, J. A. (1997). Assessment of Gaussian-2 and Density Functional Theories for the Computation of Enthalpies of Formation. *J. Chem. Phys.* 106, 1063–1079. doi:10.1063/1.473182

Elioff, M. S., Hoy, J., and Bumpus, J. A. (2016). Calculating Heat of Formation Values of Energetic Compounds: A Comparative Study. *Adv. Phys. Chem.*, 2016, 1. doi:10.1155/2016/5082084

Fan, J.-Y., Zheng, Z.-Y., Su, Y., and Zhao, J.-J. (2017). Assessment of Dispersion Correction Methods within Density Functional Theory for Energetic Materials. *Mol. Simulation* 43, 568–574. doi:10.1080/08927022.2017.1293258

Feng, S., and Li, T. (2006). Predicting Lattice Energy of Organic Crystals by Density Functional Theory with Empirically Corrected Dispersion Energy. *J. Chem. Theor. Comput.* 2, 149–156. doi:10.1021/ct050189a

Fomin, V. N., Gogol, D. B., Rozhkovoy, I. E., and Ponomarev, D. L. (2017). Quantum Chemical and Thermodynamic Calculations of Fulvic and Humic Copper Complexes in Reactions of Malachite and Azurite Formation. *Appl. Geochem.* 79, 9–16. doi:10.1016/j.apgeochem.2017.02.002

Fried, L., and Souers, P. (1994). CHEETAH: A Next Generation Thermochemical Code. doi:10.2172/95184

Frisch, M. J., Trucks, G. W., Schlegel, H. B., Scuseria, G. E., Robb, M. A., Cheeseman, J. R., et al. (2016). Gaussian 16, Revision A.03.

Gao, H., Ye, C., Piekarski, C. M., and Shreeve, J. n. M. (2007). Computational Characterization of Energetic Salts. *J. Phys. Chem. C* 111, 10718–10731. doi:10.1021/jp070702b

Gavezzotti, A. (2005). Calculation of Lattice Energies of Organic Crystals: The PIXEL Integration Method in Comparison with More Traditional Methods. *Z. Krist* 220, 499–510. doi:10.1524/zkri.220.5.499.65063

Gavezzotti, A. (2011). Efficient Computer Modeling of Organic Materials. The Atom-Atom, Coulomb-London-Pauli (AA-CLP) Model for Intermolecular Electrostatic-Polarization, Dispersion and Repulsion Energies. *New J. Chem.* 35, 1360–1368. doi:10.1039/c0nj00982b

Groom, C. R., Bruno, I. J., Lightfoot, M. P., and Ward, S. C. (2016). The Cambridge Structural Database. *Acta Crystallogr. Sect B* 72, 171–179. doi:10.1107/S2052520616003954

Hehre, W. J., Ditchfield, R., Radom, L., and Pople, J. A. (1970). Molecular Orbital Theory of the Electronic Structure of Organic Compounds. V. Molecular Theory of Bond Separation. *J. Am. Chem. Soc.* 92, 4796–4801. doi:10.1021/ja00719a006

Jenkins, H. D. B., Roobottom, H. K., Passmore, J., and Glasser, L. (1999). Relationships Among Ionic Lattice Energies, Molecular (Formula Unit) Volumes, and Thermochemical Radii. *Inorg. Chem.* 38, 3609–3620. doi:10.1021/ic9812961

Jenkins, H. D. B., Tudela, D., and Glasser, L. (2002). Lattice Potential Energy Estimation for Complex Ionic Salts from Density Measurements. *Inorg. Chem.* 41, 2364–2367. doi:10.1021/ic011216k

Kennedy, S. R., and Pulham, C. R. (2018). "Chapter 6. Co-crystallization of Energetic Materials," in *In Co-crystals: Preparation, Characterization and Applications Edited*. Editors B. Aakeroy and A. Sinha (London, United Kingdom: The Royal Society of Chemistry), 231–266. doi:10.1039/9781788012874

Konkoli, Z., and Cremer, D. (1998a). A New Way of Analyzing Vibrational Spectra. III. Characterization of normal Vibrational Modes in Terms of Internal Vibrational Modes. *Int. J. Quant. Chem.* 67, 29–40. doi:10.1002/(sici)1097-461x(1998)67:1<29::aid-qua3>3.0.co;2-0

Konkoli, Z., and Cremer, D. (1998b). A New Way of Analyzing Vibrational Spectra. I. Derivation of Adiabatic Internal Modes. *Int. J. Quant. Chem.* 67, 1–9. doi:10.1002/(sici)1097-461x(1998)67:1<1::aid-qua1>3.0.co;2-z

Konkoli, Z., Larsson, J. A., and Cremer, D. (1998). A New Way of Analyzing Vibrational Spectra. IV. Application and Testing of Adiabatic Modes within the Concept of the Characterization of normal Modes. *Int. J. Quant. Chem.* 67, 41–55. doi:10.1002/(sici)1097-461x(1998)67:1<41::aid-qua4>3.0.co;2-z

Kraka, E., and Cremer, D. (2019). Dieter Cremer's Contribution to the Field of Theoretical Chemistry. *Int. J. Quan. Chem.* 119, e25849–28. doi:10.1002/qua.25849

Kraka, E., Zou, W., and Tao, Y. (2020). Decoding Chemical Information from Vibrational Spectroscopy Data: Local Vibrational Mode Theory. *Wires Comput. Mol. Sci.* 10, 1–34. doi:10.1002/wcms.1480

Ladd, J. A., Orville-Thomas, W. J., and Cox, B. C. (1964). Molecular Parameters and Bond Structure-III. Carbon-Oxygen Bonds. *Spectrochimica Acta* 20, 1771–1780. doi:10.1016/0371-1951(64)80180-6

Larsson, J. A., and Cremer, D. (1999). Theoretical Verification and Extension of the McKean Relationship between Bond Lengths and Stretching Frequencies. *J. Mol. Struct.* 485-486, 385–407. doi:10.1016/S0022-2860(99)00093-9

Lu, T., and Chen, F. (2012). Multiwfn: A Multifunctional Wavefunction Analyzer. *J. Comput. Chem.* 33, 580–592. doi:10.1002/jcc.22885

Ma, Q., Jiang, T., Chi, Y., Chen, Y., Wang, J., Huang, J., et al. (2017). A Novel Multi-Nitrogen 2,4,6,8,10,12-Hexanitrohexaazaisowurtzitane-Based Energetic Co-crystal with 1-Methyl-3,4,5-Trinitropyrazole as a Donor: Experimental and Theoretical Investigations of Intermolecular Interactions. *New J. Chem.* 41, 4165–4172. doi:10.1039/c6nj03976f

Macrae, C. F., Bruno, I. J., Chisholm, J. A., Edgington, P. R., Mccabe, P., Pidcock, E., et al. (2008). Mercury CSD 2.0- New Features for the Visualization and Investigation of crystal Structures. *J. Appl. Cryst.* 41, 466–470. doi:10.1107/S0021889807067908

Maloney, A. G. P., Wood, P. A., and Parsons, S. (2015). Intermolecular Interaction Energies in Transition Metal Coordination Compounds. *CrystEngComm* 17, 9300–9310. doi:10.1039/c5ce01522g

McKean, D. C. (1978). Individual CH bond strengths in simple organic compounds: Effects of conformation and substitution. *Chem Soc Rev.* 7, 399–422. doi:10.1039/CS9780700399

Michalchuk, A. A. L., Fincham, P. T., Portius, P., Pulham, C. R., and Morrison, C. A. (2018a). A Pathway to the Athermal Impact Initiation of Energetic Azides. *J. Phys. Chem. C* 122, 19395–19408. doi:10.1021/acs.jpcc.8b05285

Michalchuk, A. A. L., Rudić, S., Pulham, C. R., and Morrison, C. A. (2018b). Vibrationally Induced Metallisation of the Energetic Azide α-NaN3. *Phys. Chem. Chem. Phys.* 20, 29061–29069. doi:10.1039/c8cp06161k

Michalchuk, A. A. L., Hemingway, J., and Morrison, C. A. (2021). Predicting the Impact Sensitivities of Energetic Materials through Zone-center Phonon Up-Pumping. *J. Chem. Phys.* 154, 064105–064111. doi:10.1063/5.0036927

Michalchuk, A. A. L., Trestman, M., Rudić, S., Portius, P., Fincham, P. T., Pulham, C. R., et al. (2019). Predicting the Reactivity of Energetic Materials: an Ab Initio Multi-Phonon Approach. *J. Mater. Chem. A.* 7, 19539–19553. doi:10.1039/c9ta06209b

Morrison, C. A., and Siddick, M. M. (2003). Determining the Strengths of Hydrogen Bonds in Solid-State Ammonia and Urea: Insight from Periodic DFT Calculations. *Chem. Eur. J.* 9, 628–634. doi:10.1002/chem.200390067

Nyman, J., and Day, G. M. (2015). Static and Lattice Vibrational Energy Differences between Polymorphs. *CrystEngComm* 17, 5154–5165. doi:10.1039/c5ce00045a

Owens, F. J. (1996). Calculation of Energy Barriers for Bond Rupture in Some Energetic Molecules. *J. Mol. Struct. THEOCHEM* 370, 11–16. doi:10.1016/S0166-1280(96)04673-8

Perdew, J. P., Burke, K., and Ernzerhof, M. (1996). Generalized Gradient Approximation Made Simple. *Phys. Rev. Lett.* 77, 3865–3868. doi:10.1103/PhysRevLett.77.3865

Perlovich, G. L. (2020). Formation Thermodynamics of Two-Component Molecular Crystals: Polymorphism, Stoichiometry, and Impact of Enantiomers. *Cryst. Growth Des.* 20, 5526–5537. doi:10.1021/acs.cgd.0c00695

Piercey, D. G., Chavez, D. E., Scott, B. L., Imler, G. H., and Parrish, D. A. (2016). An Energetic Triazolo-1,2,4-Triazine and its N-Oxide. *Angew. Chem. Int. Ed.* 55, 15315–15318. doi:10.1002/anie.201608723

Politzer, P., Lane, P., and Concha, M. C. (2003). Computational Approaches to Heats of Formation. *Elsevier B.V* 12, 247–277. doi:10.1016/s1380-7323(03)80011-0

Politzer, P., Murray, J. S., Edward Grice, M., Desalvo, M., and Miller, E. (1997). Calculation of Heats of Sublimation and Solid Phase Heats of Formation. *Mol. Phys.* 91, 923–928. doi:10.1080/002689797171030

Politzer, P., and Murray, J. S. (1998). Relationships between Lattice Energies and Surface Electrostatic Potentials and Areas of Anions. *J. Phys. Chem. A.* 102, 1018–1020. doi:10.1021/jp972885f

Politzer, P., and Murray, J. S. (2002). The Fundamental Nature and Role of the Electrostatic Potential in Atoms and Molecules. *Theor. Chem. Acc. Theor. Comput. Model. (Theoretica Chim. Acta)* 108, 134–142. doi:10.1007/s00214-002-0363-9

Politzer, P., Seminario, J. M., and Concha, M. C. (1998). Statitical Analysis of the Molecular Surfae Electrostatic Potential: an Approach to Describing Noncovalent Interactions in Condensed Phases. *J. Mol. Struct.* 427, 123–129. doi:10.1016/S0166-1280(97)00162-0

Ponomarev, D. A., and Takhistov, V. V. (1997). What Are Isodesmic Reactions? *J. Chem. Educ.* 74, 201–203. doi:10.1021/ed074p201

Reeves, M. G., Wood, P. A., and Parsons, S. (2020). MrPIXEL: Automated Execution of Pixel Calculations via theMercuryinterface. *J. Appl. Cryst.* 53, 1154–1162. doi:10.1107/S1600576720008444

Sabatini, J., and Oyler, K. (2015). Recent Advances in the Synthesis of High Explosive Materials. *Crystals* 6, 5–22. doi:10.3390/cryst6010005

Sharma, J., Garrett, W. L., Owens, F. J., and Vogel, V. L. (1982). X-ray Photoelectron Study of Electronic Structure, Ultraviolet, and Isothermal Decomposition of 1,3,5-Triamino-2,4,6-Trinitrobenzene. *J. Phys. Chem.* 86, 1657–1661. doi:10.1021/j100206a034

Sharma, J., and Owens, F. J. (1979). XPS Study of UV and Shock Decomposed Triamino-Trinitrobenzene. *Chem. Phys. Lett.* 61, 280–282. doi:10.1016/0009-2614(79)80644-2

Sinditskii, V. P., Filatov, S. A., Kolesov, V. I., Kapranov, K. O., Asachenko, A. F., Nechaev, M. S., et al. (2015). Combustion Behavior and Physico-Chemical Properties of Dihydroxylammonium 5,5′-Bistetrazole-1,1′-Diolate (TKX-50). *Thermochim. Acta* 614, 85–92. doi:10.1016/j.tca.2015.06.019

Singh, H. J., Gupta, S., and Sengupta, S. K. (2014a). Computational Studies on Nitramino Derivatives of 1-Amino-1,2-Azaboriridine as High Energetic Material. *RSC Adv.* 4, 40534–40541. doi:10.1039/c4ra06285j

Singh, H. J., Upadhyay, M. K., and Sengupta, S. K. (2014b). Theoretical Studies on Benzo[1,2,4]triazine-Based High-Energy Materials. *J. Mol. Model.* 20, 1–10. doi:10.1007/s00894-014-2205-9

Stewart, J. J. P. (2013). Optimization of Parameters for Semiempirical Methods VI: More Modifications to the NDDO Approximations and Re-optimization of Parameters. *J. Mol. Model.* 19, 1–32. doi:10.1007/s00894-012-1667-x

Suceska, M. (2004). Calculation of Detonation Parameters by EXPLO5 Computer Program. *Mater. Sci. Forum* 465–466, 325–330. doi:10.4028/www.scientific.net/msf.465-466.325

Sun, K.-b., Zhang, S.-h., Ren, F.-d., Hao, Y.-P., and Ba, S.-h. (2021). Theoretical Prediction of the Trigger Linkage, Cage Strain, and Explosive Sensitivity of CL-20 in the External Electric fields. *J. Mol. Model.* 27, 1–20. doi:10.1007/s00894-020-04634-8

Taylor, C. R., and Day, G. M. (2018). Evaluating the Energetic Driving Force for Cocrystal Formation. *Cryst. Growth Des.* 18, 892–904. doi:10.1021/acs.cgd.7b01375

Vatani, A., Mehrpooya, M., and Gharagheizi, F. (2007). Prediction of Standard Enthalpy of Formation by a QSPR Model. *Int. J. Mol. Sci.* 8, 407–432. doi:10.3390/i8050407

Vener, M. V., Levina, E. O., Koloskov, O. A., Rykounov, A. A., Voronin, A. P., and Tsirelson, V. G. (2014). Evaluation of the Lattice Energy of the Two-Component Molecular Crystals Using Solid-State Density Functional Theory. *Cryst. Growth Des.* 14, 4997–5003. doi:10.1021/cg5005243

Wan, Z., Wang, Q. D., and Liang, J. (2020). Accurate Prediction of Standard Enthalpy of Formation Based on Semiempirical Quantum Chemistry Methods with Artificial Neural Network and Molecular Descriptors. *Int. J. Quan. Chem.* 121, 1–16. doi:10.1002/qua.26441

Zhang, S., Zhang, J., Kou, K., Jia, Q., Xu, Y., Liu, N., et al. (2019). Standard Enthalpy of Formation, Thermal Behavior, and Specific Heat Capacity of 2HNIW·HMX Co-crystals. *J. Chem. Eng. Data* 64, 42–50. doi:10.1021/acs.jced.8b00454

Zhang, Z.-B., Li, T., Yin, L., Yin, X., and Zhang, J.-G. (2016). A Novel Insensitive Cocrystal Explosive BTO/ATZ: Preparation and Performance. *RSC Adv.* 6, 76075–76083. doi:10.1039/c6ra14510h

Zou, W., Kalescky, R., Kraka, E., and Cremer, D. (2012). Relating normal Vibrational Modes to Local Vibrational Modes with the Help of an Adiabatic Connection Scheme. *J. Chem. Phys.* 137, 084114. doi:10.1063/1.4747339

Conflict of Interest: The authors declare that the research was conducted in the absence of any commercial or financial relationships that could be construed as a potential conflict of interest.

The handling Editor declared a past co-authorship with the authors (AM, CP, CM)

frontiers in Chemistry

ORIGINAL RESEARCH
published: 03 September 2021
doi: 10.3389/fchem.2021.686788

Synthesis, Mesomorphic, and Solar Energy Characterizations of New Non-Symmetrical Schiff Base Systems

Fowzia S. Alamro[1], *Hoda A. Ahmed*[2,3]*, *Sobhi M. Gomha*[2,4]* *and Mohamed Shaban*[5,6]

[1]Department of Chemistry, College of Science, Princess Nourah bint Abdulrahman University, Riyadh, Saudi Arabia, [2]Department of Chemistry, Faculty of Science, Cairo University, Cairo, Egypt, [3]Chemistry Department, College of Sciences Yanbu, Taibah University, Yanbu, Saudi Arabia, [4]Chemistry Department, Faculty of Science, Islamic University of Madinah, Almadinah-Almonawara, Saudi Arabia, [5]Nanophotonics and Applications Labs, Department of Physics, Faculty of Science, Beni-Suef University, Beni-Suef, Egypt, [6]Department of Physics, Faculty of Science, Islamic University of Madinah, Al-Madinah Al-Munawwarah, Saudi Arabia

New asymmetrical Schiff base series based on lateral methoxy group in a central core, (E)-3-methoxy-4-(((4-methoxyphenyl)imino)methyl)phenyl 4-alkoxybenzoate (**An**), were synthesized and their optical and mesomorphic characteristics were investigated. The lateral OCH_3group was inserted in the central ring in ortho position with respect to the azomethine linkage. FT-IR, and NMR spectroscopy as well as elemental analyses were used to elucidate their molecular structures. Their mesomorphic behaviors were characterized by polarized optical microscopy (POM) and differential scanning calorimetry (DSC). These examinations indicated that all the designed series were monomorphic and possessed nematic (N) mesophase enantiotropically, except **A12** derivative which exhibited monotropic N phase. A comparative study was made between the present investigated series (**An**) and their corresponding isomers (**Bn**). The results revealed that the kind and stability of the mesophase as well as its temperature range are affected by the location and special orientation of the lateral methoxy group electric-resistance, conductance, energy-gap, and Urbach-energy were also reported for the present investigated **An** series. These results revealed that all electrodes exhibit Ohmic properties and electric-resistances in the GΩ range, whereas the electric resistance was decreased from 221.04 to 44.83 GΩ by lengthening the terminal alkoxy-chain to n = 12. The band gap of the **An** series was reduced from 3.43 to 2.89 eV by increasing the terminal chain length from n = 6 to n = 12 carbons. Therefore, controlling the length of the terminal chain can be used to improve the **An** series' electric conductivity and optical absorption, making it suitable for solar energy applications.

Keywords: lateral methoxy, schiff base liquid crystals, nematic phase, optical properties, electrical properties, solar energy

OPEN ACCESS

Edited by:
Franziska Luise Emmerling, Federal Institute for Materials Research and Testing, Germany

Reviewed by:
George A O'Doherty, Northeastern University, United States
Fabio De Moliner, University of Edinburgh, United Kingdom

***Correspondence:**
Hoda A. Ahmed
ahoda@sci.cu.edu.eg
Sobhi M. Gomha
smgomha@iu.edu.sa

Specialty section:
This article was submitted to Organic Chemistry, a section of the journal Frontiers in Chemistry

Received: *27 March 2021*
Accepted: *08 July 2021*
Published: *03 September 2021*

Citation:
Alamro FS, Ahmed HA, Gomha SM and Shaban M (2021) Synthesis, Mesomorphic, and Solar Energy Characterizations of New Non-Symmetrical Schiff Base Systems. Front. Chem. 9:686788. doi: 10.3389/fchem.2021.686788

INTRODUCTION

Today, numerous applications are being found for liquid crystals (LCs) due to their ability to undergo molecular orientation changes, such as electromagnetic fields, optical displays, surface modifications, and solar energy applications (Meng et al., 2018; You et al., 2019; Olaleru et al., 2020). On the other hand, the development of LC structural shapes with specific characteristics for certain applications remains a crucial challenge which needs wide information about the correlation between structural

shape and mesomorphic properties, as well as their effect on the involved mechanisms of phase transitions (Lagerwall and Giesselmann, 2006).

Recently, the small molecule solar cells have exhibited great potential (Badgujar et al., 2016; Bin et al., 2017; Qiu et al., 2017; Bin et al., 2018; Li et al., 2018). Organic solar cells are cost-effective compared to traditional photovoltaic cells. Numerous studies on the applications of organic compounds for photosensitizers in solar cells have been reported (Meng et al., 2018; You et al., 2019; Olaleru et al., 2020). Innovative characteristics of organic solar cells as flexibility, cheap, and ease of use have attracted considerable attention from technological engineers and researchers. Furthermore, modern organic solar cells are low coast and having excellent efficiency (Meng et al., 2018). Due to the applications of solar energy, such as catalytic photo-degradation of dyes, solar hydrogen-generation, photo-electrochemical water splitting, and solar cells, band gap engineering and optical property control are critical parameters of interest (Ahmed and Abdalla, 2020; Helmy et al., 2020; Mohamed et al., 2020; Shaban and El Sayed, 2020; Shaban et al., 2020).

Huge numbers of rod-like thermotropic LCs, with rigid cores containing two or more aromatic rings and terminal flexible chains, have been reported (Kelker and Scheurle, 1969; Sharma and Patel, 2017; Kato et al., 2018). Most of these studies were based on azomethine linkages (Ahmed et al., 2018; Al-Mutabagani et al., 2021; Altowyan et al., 2021; El-atawy et al., 2021). The insertion of high polar compact lateral or terminal groups to main architecture influences the thermal and physical properties of the resulting LC material, such as phase transition temperatures, dielectric anisotropy, and the dipole moment (Jessy et al., 2018; Mishra et al., 2018; Saccone et al., 2018; Zaki et al., 2018; Zaki, 2019). Generally, the intermolecular separation increases due to the addition of lateral substituent, which widens the mesogenic cores and consequently leads to a reduction in lateral interactions (Naoum et al., 1997; Saad and Nessim, 1999; Naoum et al., 2010). However, as the breadth/length of the molecule will increment the thermal stability of produced phases decreases (Luckhurst and Gray, 1979). The small size of the lateral substituent enables its attachment into mesomorphic geometrics without being sterically disrupted, so liquid crystalline mesophases can still be observed. On the other hand, the terminal flexible chain group plays an essential role in the mesomorphic behaviors of synthesized materials (Yeap et al., 2004; Takezoe and Takanishi, 2006). As the length of the flexible terminal chain increases, the molecules tend to be oriented in a parallel alignment (Henderson and Imrie, 2011).

This study aims to synthesize new azomethine derivatives of di-methoxy groups having changeable lengths of the terminal alkoxy-group (n), namely, (E)-3-methoxy-4-(((4-methoxyphenyl)imino)methyl)phenyl 4-alkoxybenzoate, ***An.***

The methoxy substituent is attached to a Schiff base terminal phenyl linker, while the other CH_3O group is present into the central of structure as a laterally polar moiety. Moreover, the study aims to investigate the impact of lengthen of alkoxy chain on the mesomorphic properties of synthesized homologues. In addition, a comparison is conducted between the present investigated series and the previously reported isomers to evaluate the impact of exchanging the location of terminal polar groups on the mesomorphic behavior. The research also aims to study their optical and electric behaviors.

EXPERIMENTAL

Synthesis

Many reports have revealed that hydrazones and imines are valuable materials for medicinal and synthetic applications (Gomha and Riyadh, 2011; Abu-Melha et al., 2020; Gomha et al., 2020a; Gomha et al., 2020b; Ouf et al., 2020; Sayed et al., 2020; Gomha et al., 2021; Sayed et al., 2021). The following **Scheme 1** shows the synthesis of a series of novel lateral CH3O materials **3** and **An**:

Details for synthesis of (E)-3-methoxy-4-(((4-methoxyphenyl)imino)methyl)phenol (3) and (E)-3-methoxy-4-(((4-methoxyphenyl)imino)methyl)phenyl 4-alkoxybenzoate, An are included in the **Supplementary Material**.

^{1}H-NMR, ^{13}C-NMR, Infrared spectra (IR), and elemental analyses for the investigated materials were in agreement with the assigned structures. ^{1}H-NMR data showed the expected ratios (**Figure 1**, **Figure 2**, and **Figure 3**). The physical data of products **A*n*** are listed below:

(E)-3-Methoxy-4-(((4-methoxyphenyl)imino)methyl) phenyl 4-(hexyloxy)benzoate (A6)

Yield: 87.3%; mp 103–105 ˚C, FTIR (ύ, cm^{-1}): 3,016, 2,944 (C-H), 1,737 (C=O), 1,622 (C=N). ^{1}H-NMR (400 MHz, DMSO): δ/ppm: 0.80–0.85 (t, 3H, $\underline{CH_3}(CH_2)_3CH_2CH_2O$-), 1.26–1.40 (m, 6H, $CH_3\underline{(CH_2)_3}CH_2CH_2O$-), 1.67–1.73 (m, 2H, $CH_3(CH_2)_3\underline{CH_2}CH_2O$-), 3.74 (s, 3H, $O\underline{CH_3}$), 3.79 (s, 3H, $O\underline{CH_3}$), 4.03–4.05 (t, 2H, $CH_3(CH_2)_3CH_2\underline{CH_2}O$-), 6.93–6.96 (d, 2H, Ar–H), 7.06–7.11(d, 2H, Ar–H), 7.26–7.30 (m, 3H, Ar–H), 7.47–7.50 (d, 1H, Ar–H), 7.66 (s, 1H, Ar–H), 8.00–8.03 (d, 2H, Ar–H), 8.61 (s, 1H, CH = N) ppm; ^{13}C-NMR (400 MHz, DMSO): δ/ppm: 13.90 (CH_3), 22.06, 25.09, 28.44, 30.96 (CH_2), 55.29, 55.87 (OCH_3), 68.01 (CH_2-O), 110.93, 114.43, 114.72, 120.33, 122.01, 122.45, 123.47, 132.10, 135.28, 141.77, 143.93, 151.38, 157.61 (Ar-C), 157.99 (C=N), 163.26 (Ar-C-OR), 163.49 (C=O) ppm. Anal. Calcd. for $C_{28}H_{31}NO_5$ (461.55): C, 72.86; H, 6.77; N, 3.03. Found: C, 72.73; H, 6.61; N, 2.93%.

(E)-4-(((4-Methoxyphenyl)imino) methyl)-3-methoxyphenyl 4-(octyloxy)benzoate (A8)

Yield: 89.7%; mp 96–97˚C, FTIR (ύ, cm^{-1}): 3,038, 2,929 (C-H), 1733 (C=O), 1,613 (C=N). ^{1}H-NMR (400 MHz, DMSO): δ/ppm: 0.80–0.82 (t, 3H, $CH_3(CH_2)_5CH_2CH_2O$-), 1.19–1.60 (m, 10H, $CH_3(CH_2)_5CH_2CH_2O$-), 1.76–1.78 (m, 2H, $CH_3(CH_2)_5\underline{CH_2}CH_2O$-), 3.79 (s, 3H, $O\underline{CH_3}$), 3.79 (s, 3H, $O\underline{CH_3}$), 4.01–4.04 (t, 2H, $CH_3(CH_2)_5CH_2\underline{CH_2}O$-), 6.53–6.54 (d, 2H, Ar–H), 7.06–7.08 (d, 2H, Ar–H), 7.28–7.32 (m, 3H, Ar–H), 7.42 (d, 1H, Ar–H), 7.68–7.69 (s, 1H, Ar–H), 8.01–8.06 (d, 2H, Ar–H), 8.60 (s, 1H, CH = N) ppm; ^{13}C-NMR (400 MHz, DMSO): δ/ppm: 14.48 (CH_3), 22.62, 24.55, 25.48, 25.96, 29.19, 31.77 (CH_2), 55.21, 56.43 (OCH_3), 68.53 (CH_2-O), 107.21, 111.79, 115.25, 123.08, 123.39, 124.09, 129.69, 132.64, 139.50, 142.81, 149.68, 150.62, 151.97 (Ar-C), 154.48 (C=N), 161.28 (Ar-

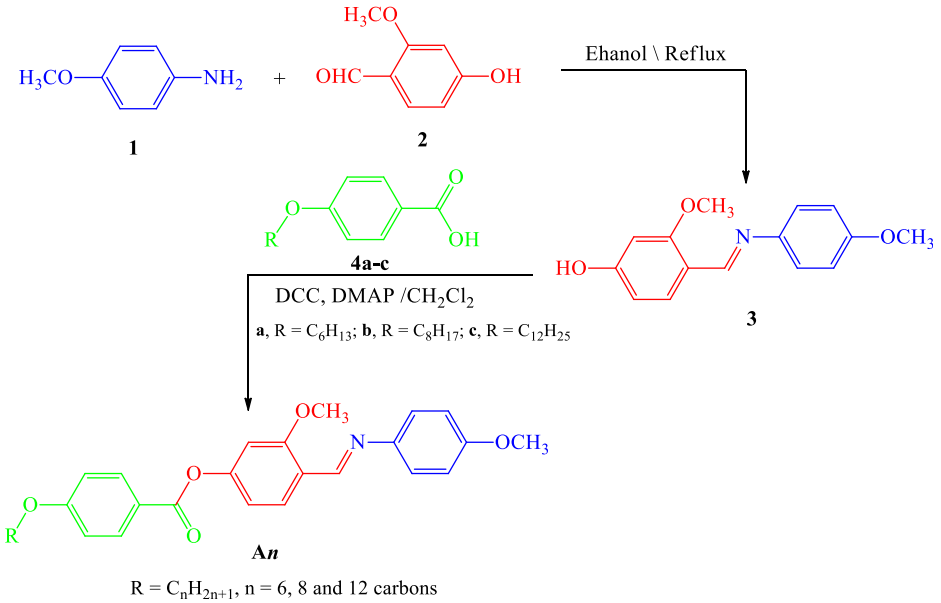

Scheme 1 | Synthesis way of materials An.

C-OR), 163.82 (C=O) ppm. Anal. Calcd. for $C_{30}H_{35}NO_5$ (489.60): C, 73.59; H, 7.21; N, 2.86. Found: C, 73.42; H, 7.09; N, 2.68%.

(E)-4-(((4-methoxyhenyl)imino) methyl)-3-methoxyphenyl 4-(dodecyloxy) benzoate(A12)

Yield: 86.0%; mp 88–89°C, FTIR (ύ, cm^{-1}): 3,018, 2,925 (C-H), 1731 (C=O), 1,608 (C=N). ^{1}H-NMR (400 MHz, DMSO): δ/ppm: 0.80–0.84 (t, 3H, $CH_3(CH_2)_9CH_2CH_2O$-), 1.22–1.36 (m, 18H, $CH_3(CH_2)_9CH_2CH_2O$-), 1.69–1.72 (m, 2H, $CH_3(CH_2)_9\underline{CH_2}CH_2O$-), 3.74 (s, 3H, $O\underline{CH_3}$), 3.79 (s, 3H, OCH_3), 4.02–4.04 (t, 2H, $CH_3(CH_2)_9\underline{CH_2}CH_2O$-), 6.95–6.96 (d, 2H, Ar–H), 7.05–7.07(d, 2H, Ar–H), 7.26–7.32 (m, 3H, Ar–H), 7.48–7.50 (d, 1H, Ar–H), 7.68 (s, 1H, Ar–H), 8.01–8.03 (d, 2H, Ar–H), 8.61 (s, 1H, CH = N) ppm; ^{13}C-NMR (400 MHz, DMSO): δ/ppm: 13.97 (CH_3), 22.10, 24.02, 24.96, 25.44, 28.49, 28.67, 28.72, 31.24, 34.50 (CH_2), 55.32, 55.89 (OCH_3), 68.02 (CH_2-O), 110.97, 114.45, 114.74, 120.35, 122.02, 122.47, 123.49, 132.12, 135.30, 141.78, 143.94, 151.39, 157.63 (Ar-C), 158.01(C=N), 163.28 (Ar-C-OR), 163.51 (C=O) ppm. Anal. Calcd. for $C_{34}H_{43}NO_5$ (545.71): C, 74.83; H, 7.94; N, 2.57. Found: C, 74.71; H, 7.84; N, 2.39%.

RESULTS AND DISCUSSION

Mesomorphic Investigations of Present Series, An

The mesophase characteristics of the synthesized have been investigated via POM and DSC. **Figure 4** shows representative DSC thermograms of homologue **A8** upon heating and cooling cycles. It was observed that the phase transitions from Cr→ N, and N→ I on heating and reversed on cooling for the short chain length **A6** derivative. Transition peaks changed according to the molecular geometry of the designed materials, **An**. Significant endothermic and exothermic peaks were observed to be dependent on the length of the terminal alkoxy chain (n), and were ascribed to mesomorphic transition. Optical images of **A6** and **A10** derivatives under POM are depicted in **Figure 5**. Schlieren/threads textures of the nematic phase were identified upon heating and cooling scans. The mesomorphic transition temperatures, as derived from DSC evaluations, and their associated enthalpies for all the synthesized compounds, **An**, are summarized in **Table 1**. The impact of the terminal length of the attached flexible group on their mesomorphic properties is displayed in **Figure 4**. Results in **Table 1** and **Figure 6** show that all investigated members of the group **An** are monomorphic and possess enantiotropic N phase, except the longer chain compound **A16** which is monotropic nematogenic. In addition, the homologues **An** series exhibit a wide nematogenic range and stability dependent on their terminal chain length, where the **A16** derivative has the lowest nematic stability. The melting transition of the present compounds, as usual, varies irregularly with the terminal chain length (n). From **Figure 6**, the shortest chain length derivative (**A6**) exhibits the highest nematic thermal stability and temperature range 163.6 and 49.1 °C, respectively. The A8 sample also possesses N phase enantiotrpoically with N stability and range nearly 144.9 and 32.8°C, respectively. Moreover, the derivative **A10** has the lowest melting temperature 79.8°C, and possesses less enantiotropic thermal nematic stability (122.3°C). The compound bearing the longest chain terminal length (**A12**)

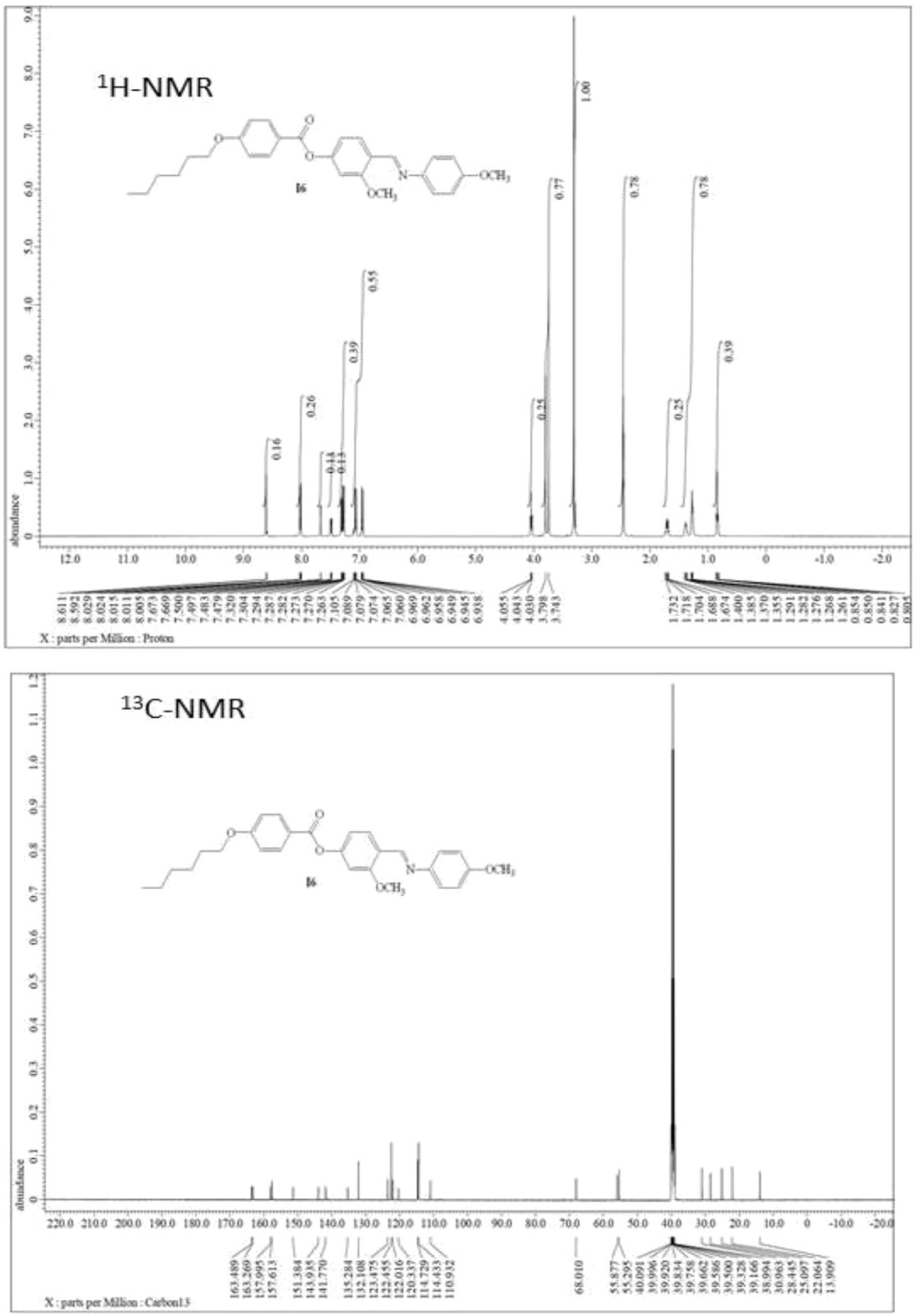

FIGURE 1 | NMR spectra of material **A6**.

has the lowest thermal nematic stability, so its phase appears monotropically. The geometry, polarizability, and the dipole moment of the designed materials are profoundly affected by the mesomeric kind of the terminals. In expansion, the mesomorphic character is impacted by an increase within the polarity and/or polarizability of the mesogenic part. Moreover, the decrement in N

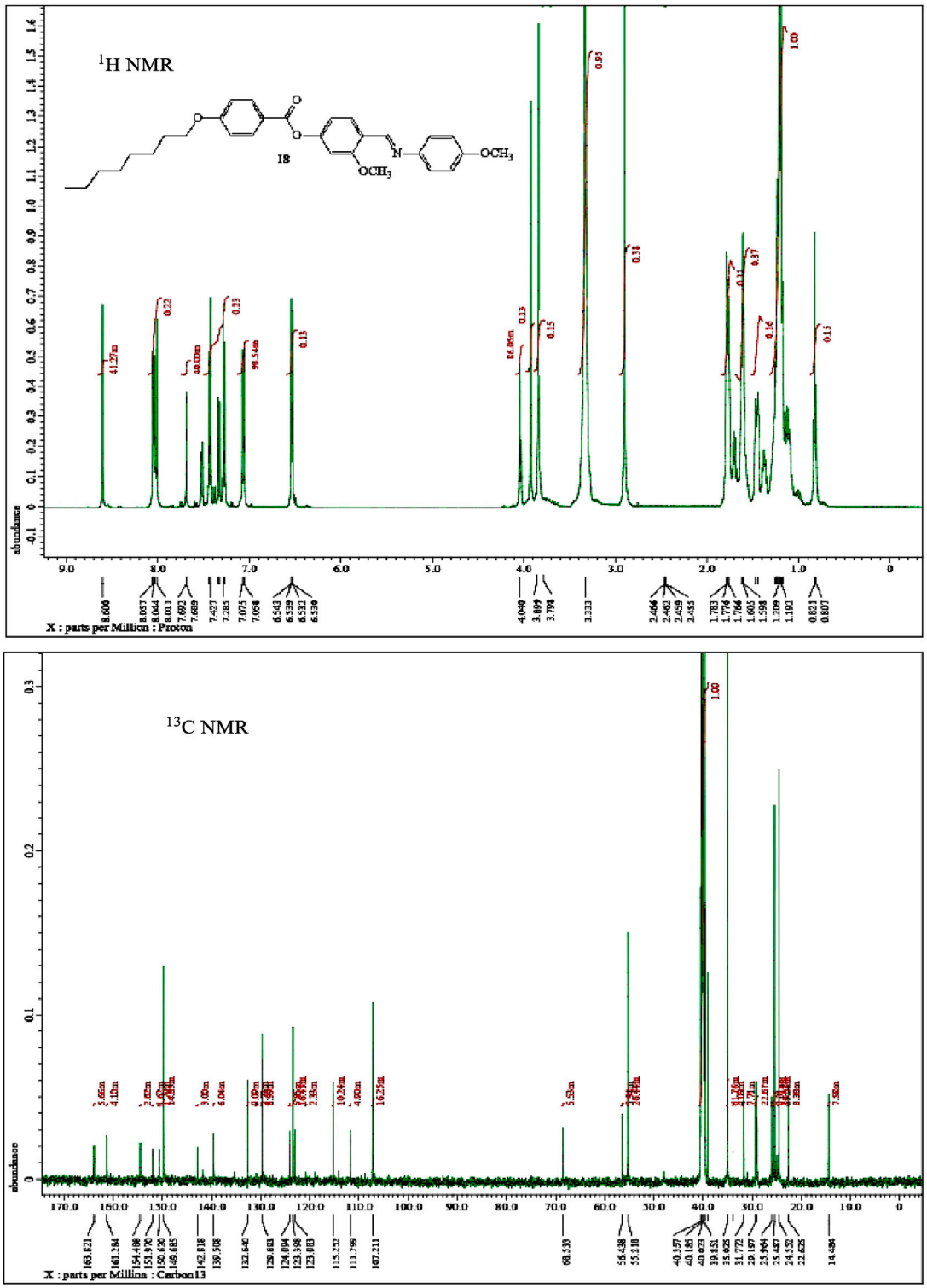

FIGURE 2 | NMR spectra of material **A8**.

stability with the increasing length of the terminal chains (**Figure 6**) is associated with the increment of the dilution of interactions within the mesogenic units as well as the increment of the volume fraction of the alkoxy chains (Walker et al., 2019). The nematic range of the present series decreases in the order: **A6** > **A10** > **A8** > **A12**. The phase character of calamitic molecules is specifically affected by

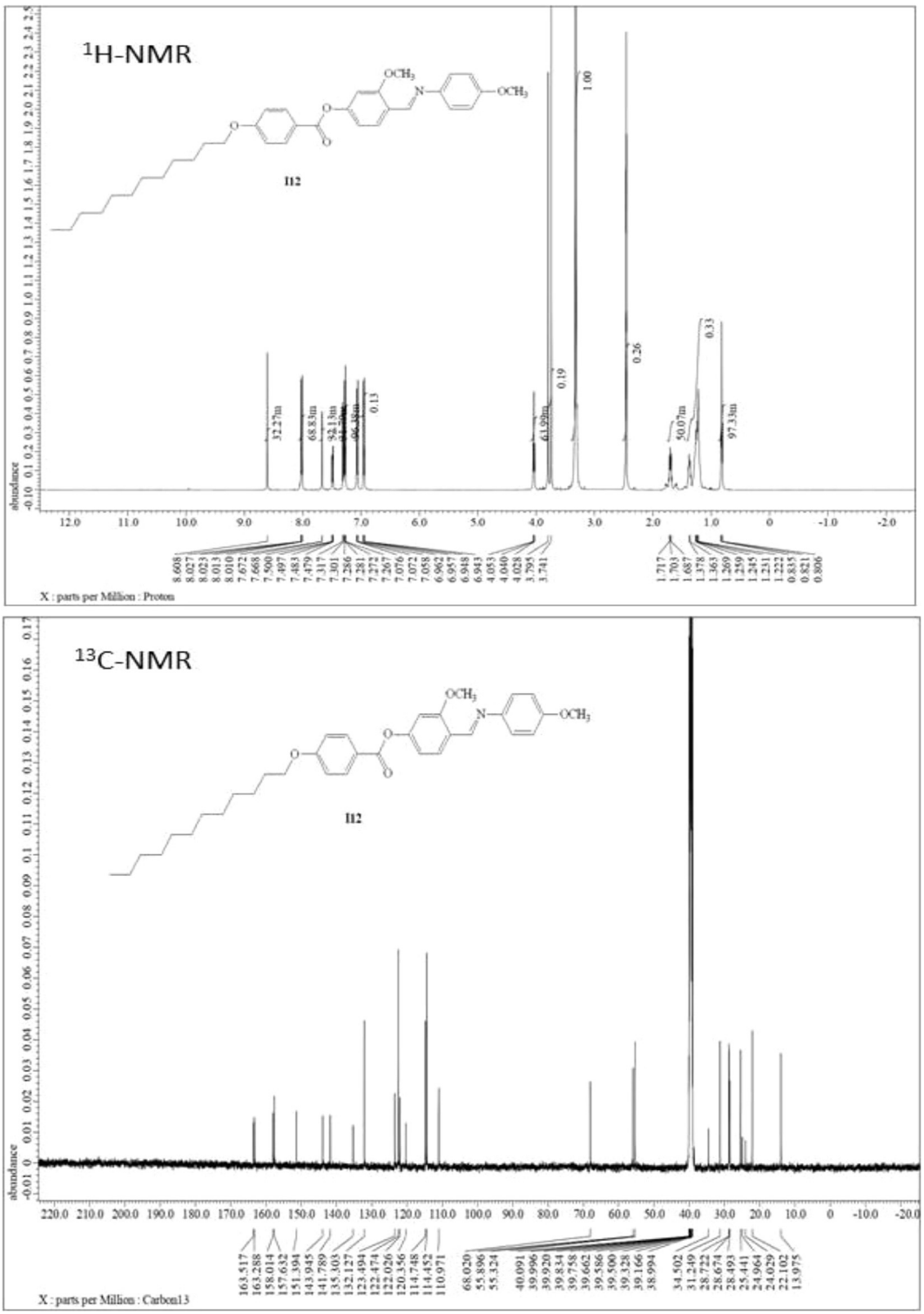

FIGURE 3 | NMR spectra of material **A12**.

molecular-molecular interactions that mainly depend on their shapes and the location of the polar lateral and terminal attached groups.

The normalized entropy changes, $\Delta S_{N\text{-}I}/R$, of the present investigated series (**An**) are summarized in **Table 1**. The data indicated that independent of the terminal alkoxy chains length,

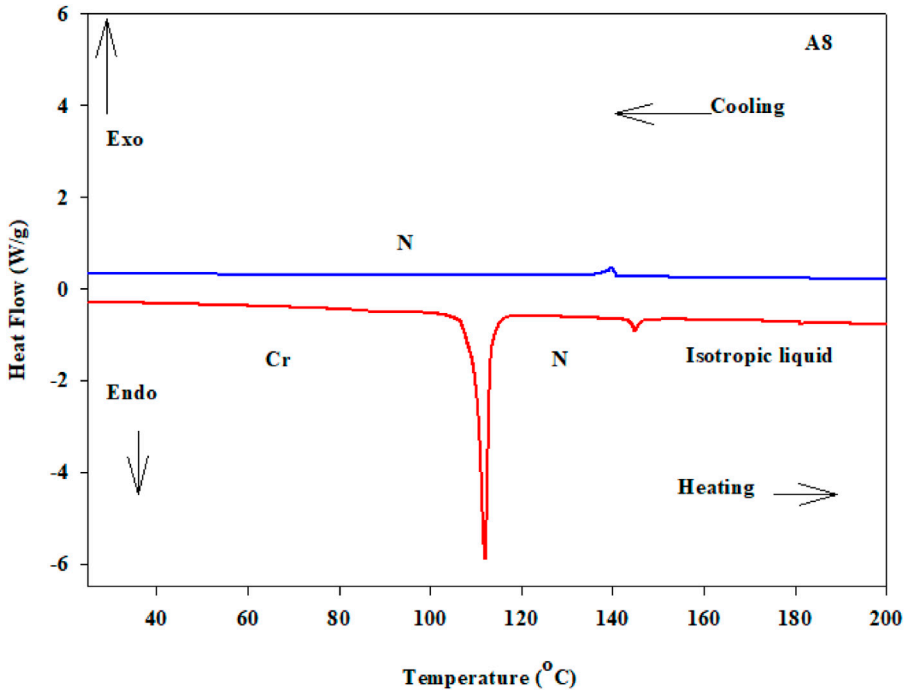

FIGURE 4 | DSC thermograms of derivative **A8** with heating /cooling rate of ±10°C/min.

the entropy of N-I transitions show small values with irregular trends that mainly depend on the type of terminal and lateral substituents. Their relatively lower values may be due to the formation of molecular biaxiality (Henderson et al., 2001; Chan et al., 2012; Lee et al., 2012). These results are inconsistent with the previous investigations for dimeric LC materials based on pyrene derivatives (Attard et al., 1992; Attard and Imrie, 1992). Also, the stereo configuration of the lateral methoxy group plays an essential role in the molecular separations. Furthermore, the thermal cis-trans isomerization of the Schiff base linker has an essential role in the observed lower entropy changes, as reported before (Attard et al., 1990; Imrie et al., 1993; Henderson et al., 2001).

Effect of Position of Lateral Methoxy Group in the Mesomorphic Properties

To investigate the effect of the location of lateral CH_3O groups on the phase and thermal properties of the materials, a comparison was made between the presently investigated series **An** and their previously corresponding isomers **Bn** (Vora and Gupta, 1982) for their mesomorphic properties. The comparison indicated that the thermal stability of the produced phase varies according to the improved molecular dipole moment and polarizability of the lateral methoxy group, which are dependent upon their position. The mesomorphic properties are nearly the same for the shortest terminal chain derivatives ($n = 6$ and $n = 8$) for both groups, while the longest chain compounds **B10** and **B12** have higher thermal stability than **A10** and **A12**, respectively. It could be concluded that the observed nematic range and stability depend on the location and special orientation of the lateral CH_3O moiety which was inserted in the mesogenic molecular part.

Electric Properties

The investigated **An** series' electrical properties and current-voltage (I–V) characteristics are measured from −10 to 10 V at different scan steps; 1.0, 0.5, 0.1, 0.05, and 0.01 V; and shown in **Figures 7A,C**. The trends are almost linear (Ohmic behaviors). As a consequence, the resistances of the **An** electrodes are almost constant and unaffected by the current passing through them. Polymeric and organic systems act like Schottky diodes at low voltage, according to recent research. However, as shown in **Figure 7B**, the relationship between log (I) and $V^{1/2}$ is non-linear in the current study, implying that our **An** electrodes do not behave like Schottky diodes. **Figure 7A** shows how increasing the applied voltage and increasing the terminal alkoxy-chain length to 12 increased the current intensity. The current intensity for the **An** series increased to 0.24 nA@10V when the applied voltage was increased to 10 V and the terminal alkoxy-chain length was increased to 12. As the scan step increased from 0.01 to 1 V, the current intensity is slightly increased, **Figure 7C**. The resistance of the **An** series is decreased by increasing the terminal alkoxy-chain length to 12. The values of the resistance are decreased from 221.04 GΩ for **A6** to 44.83 GΩ for **A12**. The electric resistance of **A10** film is decreased from 191.42 to 144.13 GΩ by increasing the scan step from 0.01 to 1 V as shown in **Figure 7D**. The values of the electric conductance (σ) were obtained and shown in **Supplementary Figure S2** (**Supplementary Material**) and **Table 2**. The value of the electrical conductance is increased

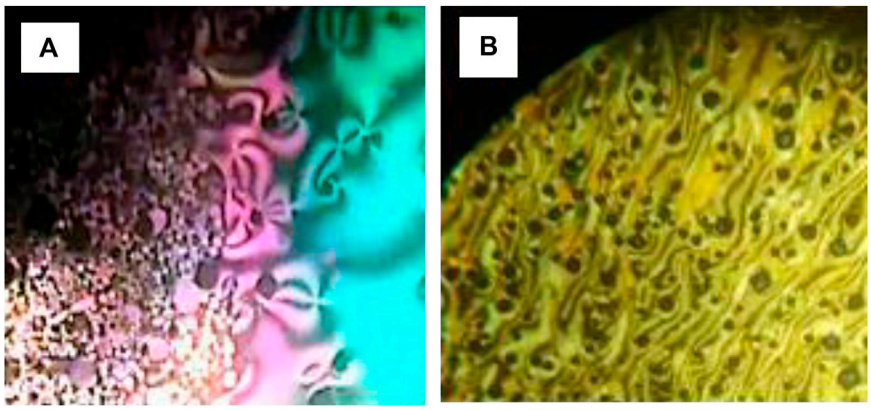

FIGURE 5 | Nematic phase textures upon heating observed under POM for compounds **(A) A6** at 155.0°C and **(B) A10** at 115.0°C.

TABLE 1 | Temperatures of mesomorphic transitions, °C (enthalpy **ΔH**, kJ/mole), mesophase range (**ΔT**, °C), and the normalized-entropy, **ΔS**/R, of transition for investigated series **An**.

Comp	$T_{Cr\text{-}N}$	$\Delta H_{Cr\text{-}N}$	$T_{N\text{-}I}$	$\Delta H_{N\text{-}I}$	ΔT	$\Delta S_{N\text{-}I}/R$
A6	114.5	48.43	163.6	1.15	49.1	0.32
A8	112.1	46.06	144.9	1.61	32.8	0.46
A10	79.8	56.05	122.3	1.04	42.5	0.32
A12	106.5	53.94	102.8[a]	1.02	3.7	0.33

Cr-N = solid to the nematic mesophase transition.
N-I = nematic to the isotropic liquid mesophase transition.
[a]*Monotropic phase.*

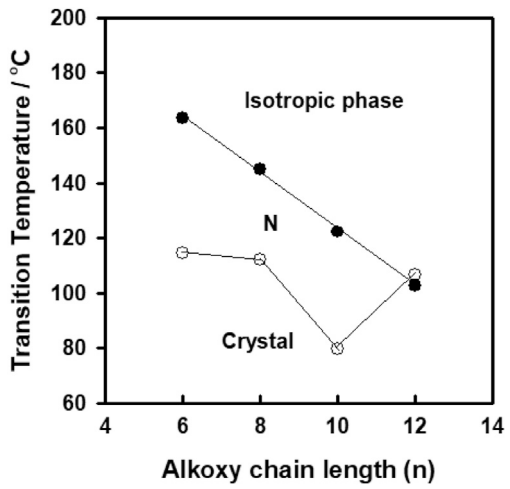

FIGURE 6 | Effect of terminal alkoxy-group on the mesophase behavior of the series **An**.

from 4.52 pS to 22.3 pS by increasing the terminal alkoxy-chain length from $n = 6$ to $n = 12$ carbons, as shown in **Table 2**, since the electrical conductance depends mainly on the number and mobility of charge carriers (Rathi et al., 2017; Kumar et al., 2018). By increasing the scan step from 0.01 to 1 V, the film conductance is increased from 5.22 to 6.94 pS. This indicates the coherent photocurrent generation, which is the basis of the photovoltaic cell (Bian et al., 2020).

Optical Spectra and Energy Gap Calculation

The wavelength of incident light and the length of the **An** series' terminal alkoxy-chain influence the transmittance and absorbance spectra of the **An** series, as shown in **Figures 8A,B**. All films showed transmission close to zero up to 400 nm, then the transmission increased and became less than 20% for **An** samples in the visible light region, **Figure 8A**. The transmission increased exponentially in the near IR region to reach maxima of ~50, 66, 10, and 4% at 1,244 nm for **A6**, **A8**, **A10**, and **A12** electrodes. After that, the transmission decreased as the wavelength increased. The absorbance spectra in **Figure 8B** show that **An** has strong absorption behavior in the UV/Vis region up to ~860 nm. For the present **An series,** all films displayed very strong absorbance in the UV region up to ~400 nm and the strongest absorbance was observed for **A6** and the widest band was observed for **A8**. The absorbance then dropped to a plateau from 400 to 860 nm, then dropped again to a minimum absorbance of around 1,250 nm. **Figure 8B** shows strong and wide absorption bands centered at ~341.6, 340.4, 333.6, and 315.5 nm for **A12**, **A10**, **A8**, and **A6**, respectively, which is blue-shifted by decreasing the terminal alkoxy-chain length of the prepared **An** series. The bandwidths of these absorption bands are 39.2 nm for **A12**, 101.9 nm for **A10**, 112.9 nm for **A8**, and 54.8 nm for **A6**. The right edge of the absorption band is red-shifted by increasing the terminal alkoxy-chain length in the **An** series. This red-shift is mainly attributed to the size effects, where large size increases spin-orbit coupling and controls the exciton positions (Shaban and El Sayed, 2016). The absorption in the visible and IR region is in the order **A12 > A10 > A8**. This strong absorption and wide absorption band in the visible region is a desirable feature for the designing of energy-efficient solar cells (Liu et al., 2016).

According to the optical absorption theorem, the relationship between absorption coefficient, α_a, and the photon energy, $E_{ph} = h\nu$, $h = 6.625\text{x}10^{-34}$ J/s, for the direct allowed transition is given by (Shaban and El Sayed, 2015):

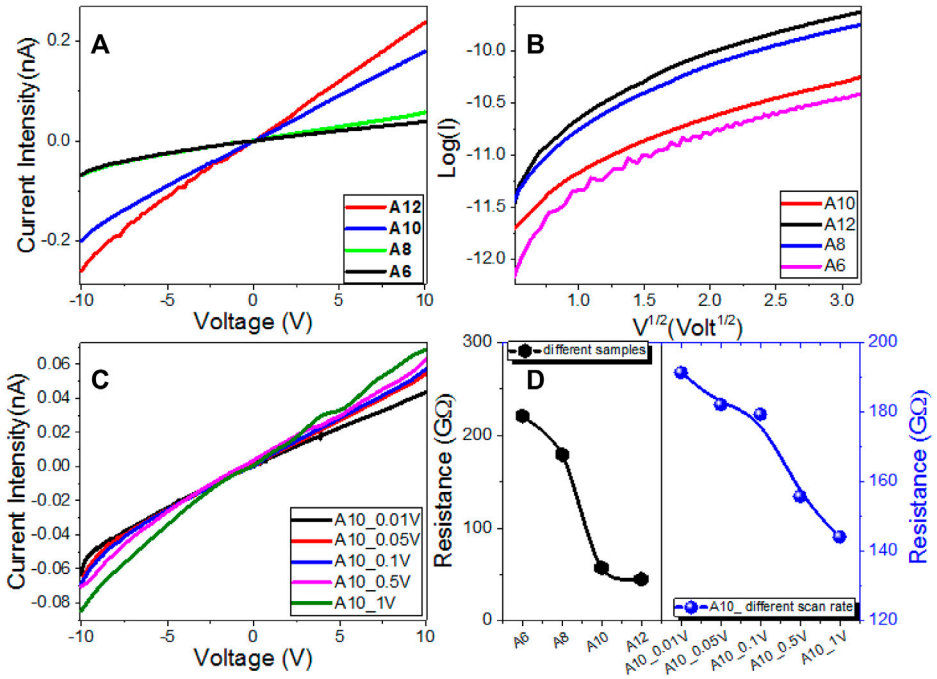

FIGURE 7 | Electrical characteristics of **An** series: **(A)** Current-Voltage characteristics of **An** series, **(B)** Log(I) vs. $V^{0.5}$ For S10 sample at different step scans, **(C)** Current-Voltage characteristics of **A10** sample at different step scans, and **(D)** electric resistance for the **An** samples and **A10 at** different step scans.

TABLE 2 | Values of the electric conductance,**σ,** energy gap, Eg, and Urbach energy, E_U, of **An** series.

Sample	σ (pS)	Eg (eV)	EU (meV)	SD	R^2
A12	22.31	2.89	251.3	3.11	0.9983
A10	17.54	2.91	839.4	8.64	0.9965
A8	5.57	3.01	150.2	2.46	0.9973
A6	4.52	3.43	1,065.0	9.84	0.9975

$$\left(\alpha_a E_{ph}\right)^2 = A\left(E_{ph} - E_g\right) \quad (1)$$

Where E_g is the optical energy gap. The values of direct E_g for **A12**, **A10**, **A8**, and **A6** are obtained by extending the linear segments of the plot of $(\alpha_a E_{ph})^2$ vs. E_{ph} to *zero* as shown in **Figure 9A–D**. The linear part observed for this figure indicates that the transition is performed directly. Interestingly as reported in **Table 2**, there is one direct bandgap for each electrode. The value of the bandgap is decreased from 3.43 to 2.89 eV by increasing the terminal chain length from six carbons (**A6**) to 12 carbons (**A12**). This reduction in the energy gap is ascribed to the influence of the density of localized states and is preferred for solar energy applications (Ahmed and Abdalla, 2020; Helmy et al., 2020; Mohamed et al., 2020; Shaban and El Sayed, 2020; Shaban et al., 2020). This behavior is consistent with the previously

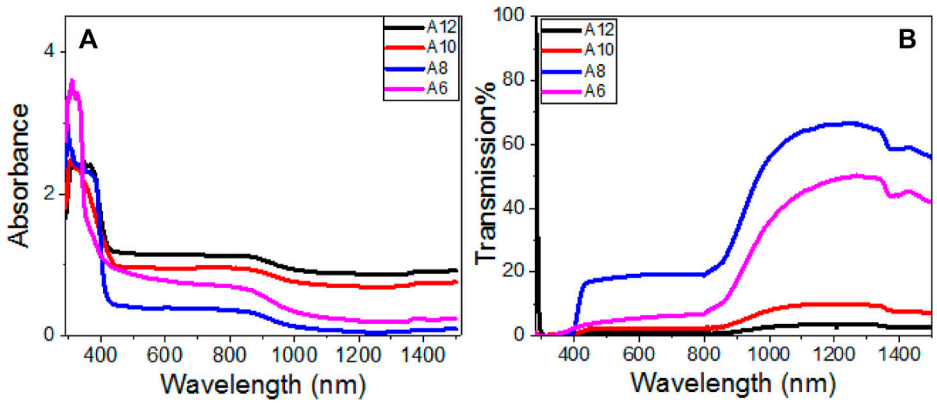

FIGURE 8 | Optical **(A)** absorbance and **(B)** transmittance spectra of **An** films.

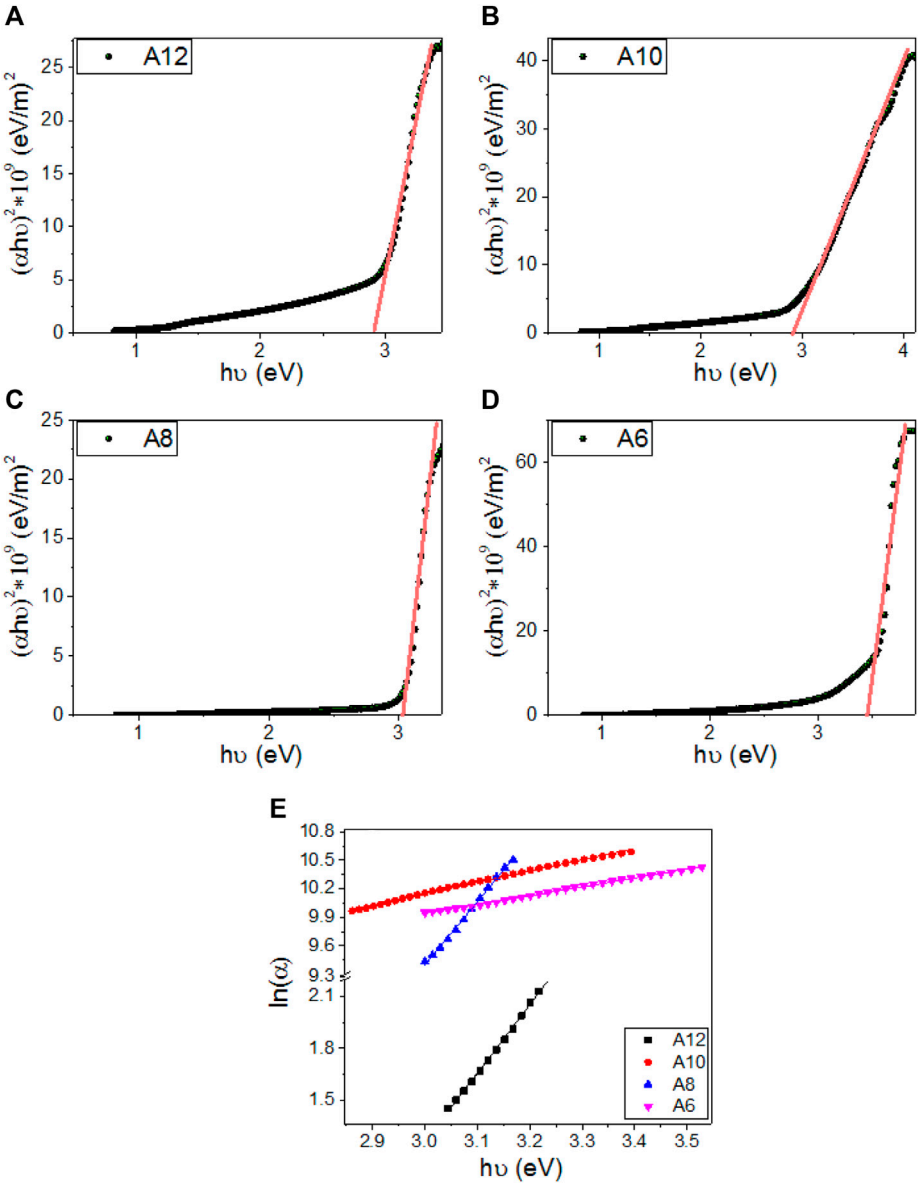

FIGURE 9 | Calculation of energy gap for **(A) A12**, **(B) A10**, **(C) A8**, **(D) A6** derivatives, and **(E)** calculation of Urbach energy for **An** series.

reported studies (Li et al., 2019). The strong absorption in the Visible/IR region and the extension of the bandgap edges are very important for solar energy applications, especially photoelectrochemical hydrogen generation and solar cells (Abdelmoneim et al., 2021; Mohamed et al., 2021; Shaban et al., 2021).

Urbach energy (E_U) refers to the disorder in the material and represents the width of the exponential absorption edge Urbach tail of the valence and conduction bands (El Sayed and Shaban, 2015). The exponential dependency of the E_U can be determined according to the following equation (El Sayed and Shaban, 2015):

$$\alpha_a = \alpha_{ao}\exp\left(E_{ph}/E_u\right) \rightarrow E_u = \delta E_{ph}/\delta\left(ln\left(\alpha_a\right)\right) \quad (2)$$

Where α_{ao} is the band tail parameter that can be given by (Sharma et al., 2014):

$$\alpha_{ao} = \left(4\pi\,\sigma o / x\,\Delta E\,c\right)^{1/2} \quad (3)$$

Where c is the speed of light, σ_o is electrical conductivity at absolute zero, and ΔE represents the width of the tail of the localized state in the forbidden gap. **Figure 9E** shows the plot of ln(α) vs. $h\nu$ for the two band gaps of **A6**, **A8**, **A10**, and **A12**. The values of E_U were obtained from the slopes of the linear fitting of these curves and are reported in **Table 2**. The statistical

parameters, standard deviation (SD) and correlation coefficient (R^2), are also reported in this table. The values are 251.3 ± 3.11 for **A12** and 1,065.0 ± 9.84 for **A6**, which refers to the extension of the bandgap edges to cover a wide range of the spectral range. The minimum value of E_U was reported for **A8**.

Tetracene (**C**) and pentacene (**D**) are small organic molecule semiconductors and most broadly investigated as p-type conjugated compounds in solar cells with high carrier mobilities of up to 0.1 and 3 cm2V-1 s-1, respectively. Due to their planar conjugated geometrical structures, they have a relatively low band energy gap of 1.7 eV. Thus they are suitable to be used as p-type semiconductors in photovoltaics (Mishra and Bäuerle, 2012).

The compounds being studied (**An**) are dielectrics due to their high resistance and energy band-gap values. In the presence of an external electric field, dielectric materials can store electric energy due to their polarization. Specifically, the dielectric energy-storing devices that allow for faster energy delivery (i.e., a quicker charge or discharge time), and hence can have promising applications on hybrid electric vehicles and power pulse devices. In the future, **An** compounds can be further refined by integrating conductive plasmonic nanomaterials to improve the conductivity and minimize the band-gap, allowing these samples to be utilized in solar energy applications such as solar cells, photoelectric cells, and photo-electrochemical cells.

CONCLUSION

New mesomorphic non-symmetrical homologues series based on a lateral CH_3O group in a central core, (E)-3-methoxy-4-(((4-methoxyphenyl)imino)methyl)phenyl 4-alkoxybenzoate (**An**), were synthesized and investigated for their potential in solar energy applications. Molecular structure elucidation for the series was carried out by elemental analyses, FT-IR, and NMR spectroscopy. Examination of their mesomorphic behaviors was conducted *via* DSC and POM which indicated that all the synthesized homologues members are purely nematogenic and possess enantiotropic N mesophase, except the longer terminal chain compound (**A12**) which exhibited monotropic N phase. A comparative study between the present series (**An**) and their corresponding isomers (**Bn**) revealed that the mesophase stability and kind, as well as its temperature range, are affected by the location and special orientation of the lateral CH_3O group. Measurements from the solar energy conversion devices showed that all studied **An** series exhibited Ohmic behavior with electric resistances in the GΩ range. The resistance of the **An** series was decreased by lengthening the terminal alkoxy-chain to n = 12 carbons. The highest electric conductivity, 22.3 pS, was reported for **A12**. The value of the bandgap was reduced from 3.43 to 2.89 eV by increasing the terminal chain length from n = 6 (**A6**) to n = 12 (**A12**). The minimum band edge tail, 150.2 ± 2.46 was reported for the **A8** derivative. Therefore, increasing the length of the terminal chain will increase the **An** series' electric conductivity and optical absorption, making it appropriate for solar energy applications.

DATA AVAILABILITY STATEMENT

The original contributions presented in the study are included in the article/**Supplementary Material**, further inquiries can be directed to the corresponding authors.

AUTHOR CONTRIBUTIONS

Formal analysis, FA, HA, and MS; Funding acquisition, FA, SG, and MS; Methodology, SG and HA; Project administration, FA, HA, and SG; Resources, SG and HA; Writing—original draft, FA, HA, MS, and SG; Writing—review and editing, HA, MS, and SG. All the authors approved the final version.

FUNDING

This research was funded by the Deanship of Scientific Research at Princess Nourah bint Abdulrahman University through the Fast-track Research Funding Program.

ACKNOWLEDGMENTS

The authors acknowledge the Deanship of Scientific Research at Princess Nourah bint Abdulrahman University for financial support through the Fast-track Research Funding Program.

SUPPLEMENTARY MATERIAL

The Supplementary Material for this article can be found online at: https://www.frontiersin.org/articles/10.3389/fchem.2021.686788/full#supplementary-material

REFERENCES

Abdelmoneim, A., Naji, A., Wagenaars, E., and Shaban, M. (2021). Outstanding Stability and Photoelectrochemical Catalytic Performance of (Fe, Ni) Co-Doped Co3O4 Photoelectrodes for Solar Hydrogen Production. *Int. J. Hydrogen Energ.* 46, 12915–12935. doi:10.1016/j.ijhydene.2021.01.113

Abu-Melha, S., Edrees, M. M., Riyadh, S. M., Abdelaziz, M. R., Elfiky, A. A., and Gomha, S. M. (2020). Clean Grinding Technique: A Facile Synthesis and In Silico Antiviral Activity of Hydrazones, Pyrazoles, and Pyrazines Bearing Thiazole Moiety Against SARS-CoV-2 Main Protease (Mpro). *Molecules.* 25, 4565. doi:10.3390/molecules25194565

Ahmed, A., and Abdalla, E. (2020). Mohamed Shaban Simple and Low-Cost Synthesis of Ba-Doped CuO Thin Films for Highly Efficient Solar Generation of Hydrogen. *J. Phys. Chem. C.* 124 (41), 25521. doi:10.1021/acs.jpcc.0c04760

Ahmed, H. A., Hagar, M., and Aljuhani, A. (2018). Mesophase Behavior of New Linear Supramolecular Hydrogen-Bonding Complexes. *RSC Adv.* 8 (61), 34937–34946. doi:10.1039/c8ra07692h

Al-Mutabagani, L. A., Alshabanah, L. A., Ahmed, H. A., Alalawy, H. H., and Al alwani, M. H. (2021). Synthesis, Mesomorphic and Computational

Characterizations of Nematogenic Schiff Base Derivatives in Pure and Mixed State. *Molecules.* 26, 2038. doi:10.3390/molecules26072038

Altowyan, A. S., Ahmed, H. A., Gomha, S. M., and Mostafa, A. M. (2021). Optical and Thermal Investigations of New Schiff Base/Ester Systems in Pure and Mixed States. *Polymers.* 13 (11), 1687. doi:10.3390/polym13111687

Attard, G. S., Garnett, S., Hickman, C. G., Imrie, C. T., and Taylor, L. (1990). Asymmetric Dimeric Liquid Crystals With Charge Transfer Groups. *Liquid Crystals.* 7, 495–508. doi:10.1080/02678299008033826

Attard, G. S., Imrie, C. T., and Karasz, F. E. (1992). Low Molar Mass Liquid-Crystalline Glasses: Preparation and Properties of the .Alpha.-(4-Cyanobiphenyl-4'-oxy)-.Omega.-(1-Pyreniminebenzylidene-4'-Oxy)Alkanes. *Chem. Mater.* 4, 1246–1253. doi:10.1021/cm00024a025

Attard, G. S., and Imrie, C. T. (1992). Liquid-Crystalline and Glass-Forming Dimers Derived From 1-Aminopyrene. *Liquid Crystals.* 11, 785–789. doi:10.1080/02678299208029030

Badgujar, S., Song, C. E., Oh, S., Shin, W. S., Moon, S.-J., Lee, J.-C., et al. (2016). Highly Efficient and Thermally Stable Fullerene-Free Organic Solar Cells Based on a Small Molecule Donor and Acceptor. *J. Mater. Chem. A.* 4, 16335–16340. doi:10.1039/c6ta06367e

Bian, Q., Ma, F., Chen, S., Wei, Q., Su, X., Buyanova, I. A., et al. (2020). Vibronic Coherence Contributes to Photocurrent Generation in Organic Semiconductor Heterojunction Diodes. *Nat. Commun.* 11, 617. doi:10.1038/s41467-020-14476-w

Bin, H., Yang, Y., Zhang, Z.-G., Ye, L., Ghasemi, M., Chen, S., et al. (2017). 9.73% Efficiency Nonfullerene All Organic Small Molecule Solar Cells With Absorption-Complementary Donor and Acceptor. *J. Am. Chem. Soc.* 139, 5085–5094. doi:10.1021/jacs.6b12826

Bin, H., Yao, J., Yang, Y., Angunawela, I., Sun, C., Gao, L., et al. (2018). High-Efficiency All-Small-Molecule Organic Solar Cells Based on an Organic Molecule Donor With Alkylsilyl-Thienyl Conjugated Side Chains. *Adv. Mater.* 30, 1706361. doi:10.1002/adma.201706361

Chan, T.-N., Lu, Z., Yam, W.-S., Yeap, G.-Y., and Imrie, C. T. (2012). Non-Symmetric Liquid Crystal Dimers Containing an Isoflavone Moiety. *Liquid Crystals.* 39, 393–402. doi:10.1080/02678292.2012.658712

El Sayed, A. M., and Shaban, M. (2015). Structural, Optical and Photocatalytic Properties of Fe and (Co, Fe) Co-Doped Copper Oxide Spin Coated Films. *Spectrochimica Acta A: Mol. Biomol. Spectrosc.* 149, 638–646. doi:10.1016/j.saa.2015.05.010

El-atawy, M. A., Naoum, M. M., Al-Zahrani, S. A., and Ahmed, H. A. (2021). New Nitro-Laterally Substituted Azomethine Derivatives; Synthesis, Mesomorphic and Computational Characterizations. *Molecules.* 26, 1927. doi:10.3390/molecules26071927

Gomha, S. M., Abdelhady, H. A., Hassain, D. Z., Abdelmonsef, A. H., El-Naggar, M., Elaasser, M. M., et al. (2021). Thiazole-Based Thiosemicarbazones: Synthesis, Cytotoxicity Evaluation and Molecular Docking Study. *Drug Des. Development Ther.* Vol. 15, 659–677. doi:10.2147/dddt.s291579

Gomha, S. M., Edrees, M. M., Muhammad, Z. A., Kheder, N. A., Abu- Melha, S., and Saad, A. M. (2020a). Synthesis, Characterization, and Antimicrobial Evaluation of Some New 1,4-Dihydropyridines-1,2,4-Triazole Hybrid Compounds. *Polycyclic Aromatic Compounds.*, 1–13. doi:10.1080/10406638.2020.1720751

Gomha, S. M., Muhammad, Z. A., Abdel-aziz, H. M., Matar, I. K., and El-Sayed, A. A. (2020b). Green Synthesis, Molecular Docking and Anticancer Activity of Novel 1,4-Dihydropyridine-3,5-Dicarbohydrazones Under Grind-Stone Chemistry. *Green. Chem. Lett. Rev.* 13, 6–17. doi:10.1080/17518253.2019.1710268

Gomha, S. M., and Riyadh, S. M. (2011). Synthesis Under Microwave Irradiation of [1,2,4]Triazolo[3,4-B] [1,3,4]Thiadiazoles and Other Diazoles Bearing Indole Moieties and Their Antimicrobial Evaluation. *Molecules.* 16, 8244–8256. doi:10.3390/molecules16108244

Helmy, A., Rabia, M., Shaban, M., Ashraf, A. M., Ahmed, S., and Ahmed, A. M. (2020). Graphite/Rolled Graphene Oxide/Carbon Nanotube Photoelectrode for Water Splitting of Exhaust Car Solution. *Int. J. Energ. Res.* 44 (9), 7687–7697. doi:10.1002/er.5501

Henderson, P. A., and Imrie, C. T. (2011). Methylene-Linked Liquid Crystal Dimers and the Twist-Bend Nematic Phase. *Liquid Crystals.* 38 (11-12), 1407–1414. doi:10.1080/02678292.2011.624368

Henderson, P. A., Niemeyer, O., and Imrie, C. T. (2001). Methylene-Linked Liquid Crystal Dimers. *Liquid Crystals.* 28, 463–472. doi:10.1080/02678290010007558

Imrie, C. T., Karasz, F. E., and Attard, G. S. (1993). Comparison of the Mesogenic Properties of Monomeric, Dimeric, and Side-Chain Polymeric Liquid Crystals. *Macromolecules.* 26, 545–550. doi:10.1021/ma00055a021

Jessy, P. J., Radha, S., and Patel, N. (2018). Morphological, Optical and Dielectric Behavior of Chiral Nematic Liquid Crystal Mixture: Study on Effect of Different Amount of Chirality. *J. Mol. Liquids.* 255, 215–223. doi:10.1016/j.molliq.2018.01.160

Kato, T., Uchida, J., Ichikawa, T., and Sakamoto, T. (2018). Functional Liquid Crystals Towards the Next Generation of Materials. *Angew. Chem. Int. Ed.* 57, 4355–4371. doi:10.1002/anie.201711163

Kelker, H., and Scheurle, B. (1969). A Liquid-Crystalline(Nematic) Phase With a Particularly Low Solidification Point. *Angew. Chem. Int. Ed. Engl.* 8 (11), 884–885. doi:10.1002/anie.196908841

Kumar, M., Kumar, S., Upadhyaya, A., Yadav, A., Gupta, S. K., and Singh, A. (2018). Study of Charge Transport in Composite Blend of P3HT and PCBM. *AIP Conf. Proc.* 2018, 050066. doi:10.1063/1.5032721

Lagerwall, J. P. F., and Giesselmann, F. (2006). Current Topics in Smectic Liquid Crystal Research. *ChemPhysChem.* 7, 20–45. doi:10.1002/cphc.200500472

Lee, H.-C., Lu, Z., Henderson, P. A., Achard, M. F., Mahmood, W. A. K., Yeap, G.-Y., et al. (2012). Cholesteryl-Based Liquid Crystal Dimers Containing a Sulfur-Sulfur Link in the Flexible Spacer. *Liquid Crystals.* 39, 259–268. doi:10.1080/02678292.2011.641753

Li, H., Zhao, Y., Fang, J., Zhu, X., Xia, B., Lu, K., et al. (2018). Improve the Performance of the All-Small-Molecule Nonfullerene Organic Solar Cells Through Enhancing the Crystallinity of Acceptors. *Adv. Energ. Mater.* 8, 1702377. doi:10.1002/aenm.201702377

Li, X., Guo, J., Yang, L., Chao, M., Zheng, L., Ma, Z., et al. (2019). Low Bandgap Donor-Acceptor π-Conjugated Polymers From Diarylcyclopentadienone-Fused Naphthalimides. *Front. Chem.* 7, 362. doi:10.3389/fchem.2019.00362

Liu, S., Kan, Z., Thomas, S., Cruciani, F., Brédas, J.-L., and Beaujuge, P. M. (2016). Thieno[3,4-c]Pyrrole-4,6-Dione-3,4-Difluorothiophene Polymer Acceptors for Efficient All-Polymer Bulk Heterojunction Solar Cells. *Angew. Chem. Int. Ed.* 55 (42), 12996–13000. doi:10.1002/anie.201604307

Luckhurst, G., and Gray, G. W. (1979). *The Molecular Physics of Liquid Crystals*. New York, NY: Academic Press.

Meng, L., Zhang, Y., Wan, X., Li, C., Zhang, X., Wang, Y., et al. (2018). Organic and Solution-Processed Tandem Solar Cells With 17.3% Efficiency. *Science.* 361, 1094–1098. doi:10.1126/science.aat2612

Mishra, A., and Bäuerle, P. (2012). Small Molecule Organic Semiconductors on the Move: Promises for Future Solar Energy Technology. *Angew. Chem. Int. Ed.* 51, 2020–2067.þ doi:10.1002/anie.201102326

Mishra, R., Hazarika, J., Hazarika, A., Gogoi, B., Dubey, R., Bhattacharjee, D., et al. (2018). Dielectric Properties of a Strongly Polar Nematic Liquid crystal Compound Doped With Gold Nanoparticles. *Liquid Crystals.* 45, 1661–1671. doi:10.1080/02678292.2018.1478995

Mohamed, F., Rabia, M., and Shaban, M. (2020). Synthesis and Characterization of Biogenic Iron Oxides of Different Nanomorphologies From Pomegranate Peels for Efficient Solar Hydrogen Production. *J. Mater. Res. Technology.* 9 (3), 4255–4271. doi:10.1016/j.jmrt.2020.02.052

Mohamed, H. S. H., Rabia, M., Zhou, X.-G., Qin, X.-S., Khabiri, G., Shaban, M., et al. (2021). Phase-Junction Ag/TiO2 Nanocomposite as Photocathode for H2 Generation. *J. Mater. Sci. Technology.* 83, 179–187. doi:10.1016/j.jmst.2020.12.052

Naoum, M. M., Mohammady, S. Z., and Ahmed, H. A. (2010). Lateral Protrusion and Mesophase Behaviour in Pure and Mixed States of Model Compounds of the Type 4-(4′-Substituted Phenylazo)-2-(or 3-)Methyl Phenyl-4'-Alkoxy Benzoates. *Liquid Crystals.* 37, 1245–1257. doi:10.1080/02678292.2010.497228

Naoum, M. M., Saad, G. R., Nessim, R. I., Abdel-Aziz, T. A., and Seliger, H. (1997). Effect of Molecular Structure on the Phase Behaviour of Some Liquid Crystalline Compounds and Their Binary Mixtures II. 4-Hexadecyloxyphenyl Arylates and Aryl 4-hexadecyloxy Benzoates. *Liquid Crystals.* 23, 789–795. doi:10.1080/026782997207713

Olaleru, S. A., Kirui, J. K., Wamwangi, D., Roro, K. T., and Mwakikunga, B. (2020). Perovskite Solar Cells: The New Epoch in Photovoltaics. *Solar Energy.* 196, 295–309. doi:10.1016/j.solener.2019.12.025

Ouf, S. A., Gomha, S. M., Eweis, M., Ouf, A. S., Sharawy, I. A. A., and Alharbi, S. A. (2020). Antidermatophytic Activity of Some Newly Synthesized Arylhydrazonothiazoles Conjugated with Monoclonal Antibody. *Sci. Rep.* 10, 20863. doi:10.1038/s41598-020-77829-x

Qiu, B., Xue, L., Yang, Y., Bin, H., Zhang, Y., Zhang, C., et al. (2017). All-Small-Molecule Nonfullerene Organic Solar Cells With High Fill Factor and High Efficiency Over 10%. *Chem. Mater.* 29, 7543–7553. doi:10.1021/acs.chemmater.7b02536

Rathi, S., Chauhan, G., Gupta, S. K., Srivastava, R., and Singh, A. (2017). Analysis of Blockade in Charge Transport Across Polymeric Heterojunctions as a Function of Thermal Annealing: A Different Perspective. *J. Elec Materi.* 46, 1235–1247. doi:10.1007/s11664-016-5097-x

Saad, G. R., and Nessim, R. I. (1999). Effect of Molecular Structure on the Phase Behaviour of Some Liquid Crystalline Compounds and Their Binary Mixtures VI[1]. The Effect of Molecular Length. *Liquid Crystals.* 26, 629–636. doi:10.1080/026782999204679

Saccone, M., Kuntze, K., Ahmed, Z., Siiskonen, A., Giese, M., and Priimagi, A. (2018). Ortho-Fluorination of Azophenols Increases the Mesophase Stability of Photoresponsive Hydrogen-Bonded Liquid Crystals. *J. Mater. Chem. C.* 6, 9958–9963. doi:10.1039/c8tc02611d

Sayed, A. R., Gomha, S. M., Taher, E. A., Muhammad, Z. A., El-Seedi, H. R., Gaber, H. M., et al. (2020). One-Pot Synthesis of Novel Thiazoles as Potential Anti-Cancer Agents. *Drug Des. Development Ther.* 14, 1363–1375. doi:10.2147/dddt.s221263

Sayed, R., M Abd El-lateef, H., and Gomha, S. M. (2021). L-Proline Catalyzed Green Synthesis and Anticancer Evaluation of Novel Bioactive Benzil Bis-Hydrazones Under Grinding Technique. *Green. Chem. Lett. Rev.* 14, 179–188. doi:10.1080/17518253.2021.1893392

Shaban, M., and El Sayed, A. M. (2015). Influences of Lead and Magnesium Co-Doping on the Nanostructural, Optical Properties and Wettability of Spin Coated Zinc Oxide Films. *Mater. Sci. Semicond. Process.* 39, 136–147. doi:10.1016/j.mssp.2015.04.008

Shaban, M., and El Sayed, A. M. (2016). Effects of Lanthanum and Sodium on the Structural, Optical and Hydrophilic Properties of Sol-Gel Derived ZnO Films: A Comparative Study. *Mater. Sci. Semiconductor Process.* 41, 323–334. doi:10.1016/j.mssp.2015.09.002

Shaban, M., and El Sayed, A. M. (2020). Influence of the Spin Deposition Parameters and La/Sn Double Doping on the Structural, Optical, and Photoelectrocatalytic Properties of CoCo2O4 Photoelectrodes. *Solar Energ. Mater. Solar Cell.* 217, 110705. doi:10.1016/j.solmat.2020.110705

Shaban, M., Hamd, A., Amin, R. R., Abukhadra, M. R., Khalek, A. A., Khan, A. A. P., et al. (2020). Preparation and Characterization of MCM-48/Nickel Oxide Composite as an Efficient and Reusable Catalyst for the Assessment of Photocatalytic Activity. *Environ. Sci. Pollut. Res.* 27, 32670–32682. doi:10.1007/s11356-020-09431-7

Shaban, M., Rabia, M., Eldakrory, M. G., Maree, R. M., and Ahmed, A. M. (2021). Efficient Photoselectrochemical Hydrogen Production Utilizing of APbI 3 (A = Na, Cs, and Li) Perovskites Nanorods. *Int. J. Energ. Res.* 45, 7436–7446. doi:10.1002/er.6326

Sharma, S., Vyas, S., Periasamy, C., and Chakrabarti, P. (2014). Structural and Optical Characterization of ZnO Thin Films for Optoelectronic Device Applications by RF Sputtering Technique. *Superlattices and Microstructures.* 75, 378–389. doi:10.1016/j.spmi.2014.07.032

Sharma, V. S., and Patel, R. B. (2017). Design and Investigation of Calamatic Liquid Crystals: Schiff Base (–CH□N), Chalcone (–CO–CH□CH–), and Ester (–COO–) Linkage Group Contain Rigid Rod Shape With Various Terminal Parts. *Mol. Crystals Liquid Crystals.* 643 (1), 141–158. doi:10.1080/15421406.2016.1263115

Takezoe, H., and Takanishi, Y. (2006). Bent-core Liquid Crystals: Their Mysterious and Attractive World. *Jpn. J. Appl. Phys.* 45, 597–625. doi:10.1143/jjap.45.597

Vora, R. A., and Gupta, R. (1982). Effect of Lateral Substitution on Mesomorphism: (A) 4(4'-N-Alkoxybenzoyloxy)-3-Methoxy Benzaldehydes (B) 4(4'-N-Alkoxybenzoyloxy)-3-Methoxy Benzylidene-4"-Toluidines (C) 4(4'-N-Alkoxybenzoyloxy)-3-Methoxy Benzylidene-4"-Anisidines. *Mol. Crystals Liquid Crystals.* 80 (1), 119–127. þ. doi:10.1080/00268948208071025

Walker, R., Pociecha, D., Strachan, G. J., Storey, J. M. D., Gorecka, E., and Imrie, C. T. (2019). Molecular Curvature, Specific Intermolecular Interactions and the Twist-bend Nematic Phase: the Synthesis and Characterisation of the 1-(4-Cyanobiphenyl-4-Yl)-6-(4-Alkylanilinebenzylidene-4-Oxy)Hexanes (CB6Om). *Soft Matter.* 15, 3188–3197. doi:10.1039/C9SM00026G

Yeap, G.-Y., Ha, S.-T., Lim, P.-L., Boey, P.-L., Mahmood, W. A. K., Ito, M. M., et al. (2004). Synthesis and Mesomorphic Properties of Schiff Base Esters Ortho-Hydroxy-Para-Alkyloxybenzylidene-Para-Substituted Anilines. *Mol. Crystals Liquid Crystals.* 423, 73–84. doi:10.1080/15421400490494508

You, Y. J., Song, C. E., Hoang, Q. V., Kang, Y., Goo, J. S., Ko, D. H., et al. (2019). Highly Efficient Indoor Organic Photovoltaics With Spectrally Matched Fluorinated Phenylene-Alkoxybenzothiadiazole-Based Wide Bandgap Polymers. *Adv. Funct. Mater.* 29, 1901171. doi:10.1002/adfm.201901171

Zaki, A. A., Ahmed, H. A., and Hagar, M. (2018). Impact of Fluorine Orientation on the Optical Properties of Difluorophenylazophenyl Benzoates Liquid Crystal. *Mater. Chem. Phys.* 216, 316–324. doi:10.1016/j.matchemphys.2018.06.012

Zaki, A. A. (2019). Optical Measurements of Phase Transitions in Difluorophenylazophenyl Benzoate Thermotropic Liquid Crystal With Specific Orientated Fluorine Atoms. *Phase Transitions.* 92, 135–148. doi:10.1080/01411594.2018.1556271

Conflict of Interest: The authors declare that the research was conducted in the absence of any commercial or financial relationships that could be construed as a potential conflict of interest.

Publisher's Note: All claims expressed in this article are solely those of the authors and do not necessarily represent those of their affiliated organizations, or those of the publisher, the editors and the reviewers. Any product that may be evaluated in this article, or claim that may be made by its manufacturer, is not guaranteed or endorsed by the publisher.

frontiers in Chemistry

ORIGINAL RESEARCH
published: 23 September 2021
doi: 10.3389/fchem.2021.754420

Intriguing Heteroleptic Zn^{II} bis(dipyrrinato) Emitters in the Far-Red Region With Large Pseudo-Stokes Shift for Bioimaging

Roberta Tabone[1], *Dominik Feser*[2], *Enrico D. Lemma*[3], *Ute Schepers*[2] *and Claudia Bizzarri*[1]*

[1]Institute of Organic Chemistry, Karlsruhe Institute of Technology (KIT), Karlsruhe, Germany, [2]Institute of Functional Interfaces (IFG), KIT, Eggenstein-Leopoldshafen, Germany, [3]Zoological Institute, Cell and Neurobiology, KIT, Karlsruhe, Germany

Novel heteroleptic Zn^{II} bis(dipyrrinato) complexes were prepared as intriguing emitters. With our tailor-made design, we achieved far-red emissive complexes with a photoluminescence quantum yield up to 45% in dimethylsulfoxide and 70% in toluene. This means that heteroleptic Zn^{II} bis(dipyrrinato) complexes retain very intense emission also in polar solvents, in contrast to their homoleptic counterparts, which we prepared for comparing the photophysical properties. It is evident from the absorption and excitation spectra that heteroleptic complexes present the characteristic features of both ligands: the plain dipyrrin (L_p) and the π-extended dipyrrin (L_π). On the contrary, the emission comes exclusively from the π-extended dipyrrin L_π, suggesting an interligand nonradiative transition that causes a large *pseudo*-Stokes shift (up to 4,600 cm^{-1}). The large *pseudo*-Stokes shifts and the emissive spectral region of these novel heteroleptic Zn^{II} bis(dipyrrinato) complexes are of great interest for bioimaging applications. Thus, their high biocompatibiliy with four different cell lines make them appealing as new fluorophores for cell imaging.

Keywords: bis(dipyrrinato) Zn^{II} complexes, cell-viability, far-red emission, heteroleptic Zn^{II} complexes, large Stokes shift, live-cell imaging, multiplexing

OPEN ACCESS

Edited by:
Ronald K. Castellano, University of Florida, United States

Reviewed by:
Davita L. Watkins, University of Mississippi, United States
Lin Yuan, Hunan University, China

***Correspondence:**
Claudia Bizzarri
bizzarri@kit.edu

Specialty section:
This article was submitted to Supramolecular Chemistry, a section of the journal Frontiers in Chemistry

Received: *06 August 2021*
Accepted: *09 September 2021*
Published: *23 September 2021*

Citation:
Tabone R, Feser D, Lemma ED, Schepers U and Bizzarri C (2021) Intriguing Heteroleptic Zn^{II} bis(dipyrrinato) Emitters in the Far-Red Region With Large Pseudo-Stokes Shift for Bioimaging. Front. Chem. 9:754420. doi: 10.3389/fchem.2021.754420

INTRODUCTION

Far-red and near-infrared (NIR) fluorophores are highly desired probes for bioimaging and sensing applications in living organisms. In fact, they emit in the so-called "*biological imaging window*", where interferences from absorbance by water and proteins and intrinsic autofluorescence are minimal (Weissleder, 2001; Hilderbrand and Weissleder, 2010). Nevertheless, a proper design of far-red/NIR dyes is necessary, as those probes usually suffer from photo-bleaching and low photoluminescence quantum yield (Φ) (Guo et al., 2014). Borondipyrromethene based dyes (BODIPYs) are among the most widely used fluorophore classes used in bioimaging. (Ni and Wu, 2014; Kowada et al., 2015; Grossi et al., 2016; Callaghan et al., 2019; Filatov, 2019; Kaur and Singh, 2019; Qu et al., 2019; Deng et al., 2021). The development of emissive bis(dipyrrinato) zinc complexes have received an increasing momentum only recently, in contrast to BODIPYs, as they were used mainly for supramolecular architectures and coordination polymers (Baudron, 2013; Matsuoka and Nabeshima, 2018; Jiang et al., 2020). With an appropriate design, bright fluorescence can also be achieved from Zn^{II} bis(dipyrrinato) complexes (I.V. Sazanovich, 2004). Even so, homoleptic zinc complexes suffer from an intramolecular electron transfer between the two

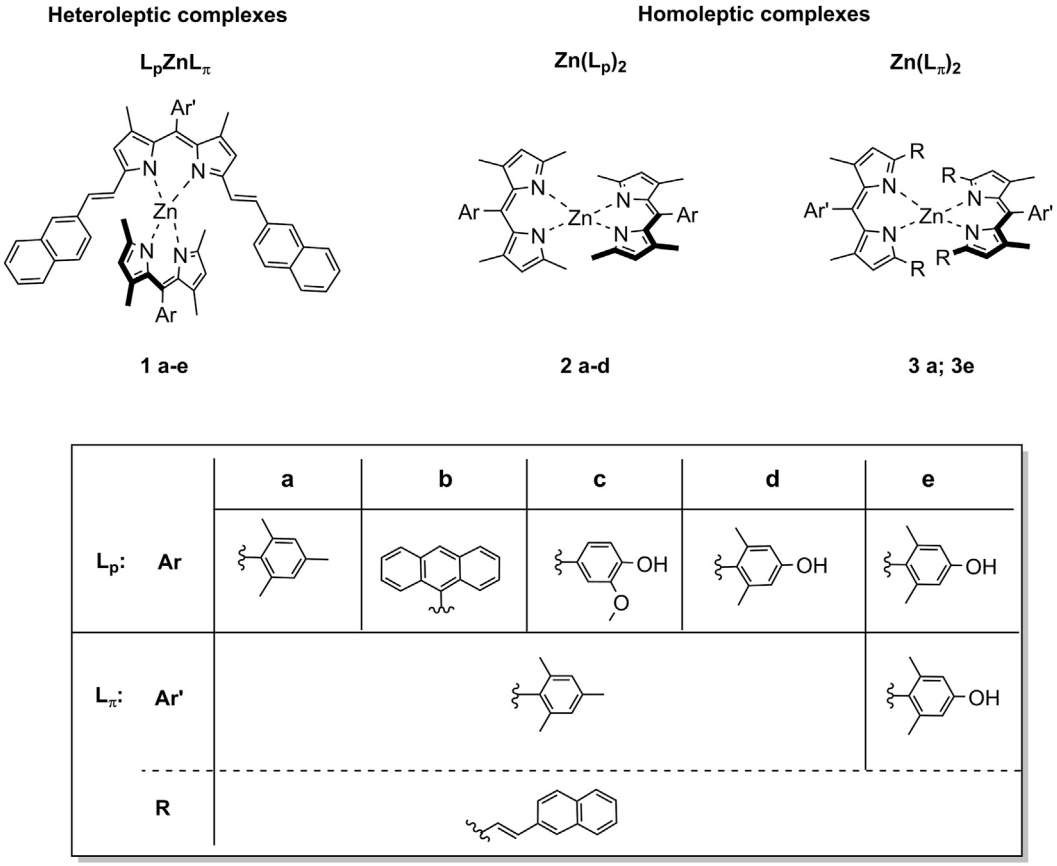

FIGURE 1 | Chemical structures of the new heteroleptic Zn bis(dipyrrinato) complexes **1a-e** presented in this work. For comparison we reported also the study of the homoleptic complexes of type Zn $(L_p)_2$ **2a-d** and of type Zn $(L_\pi)_2$ **3a** and **3e**.

electronically degenerate excited states of the identical dipyrrins. This process causes the population of a non-emissive symmetry-breaking charge transfer state (SBCT) (Trinh et al., 2014). Although SBCT is very appealing in potential applications such as artificial photosynthesis (Alqahtani et al., 2019; Tungulin et al., 2019) or photovoltaics, (Bartynski et al., 2015), it is not advantageous for other applications such as imaging, where high emission also in polar solvents is of utmost importance. A strategy to control this obstacle is encapsulation in nanoparticles (e.g. mesoporous silica) (Sani et al., 2020). Very recently, green-emitting homoleptic bis(dipyrrinato) zinc complexes were employed as selective probes for cancer cells and as photodynamic therapy photosensitisers (Karges et al., 2019a; Karges et al., 2019b; Karges et al., 2020). However, because of their homoleptic nature, encapsulation in polymeric nanoparticles was necessary to overcome the quenching effects in water.

In heteroleptic bis(dipyrrinato) zinc complexes, the electronically excited states of the two dipyrrinato ligands are energetically different. Thus, the absence of degeneracy sets aside the charge-separated state and these complexes are emissive in polar solvents. Our strategy focused on heteroleptic Zn^{II} bis(dipyrrinato) complexes that also benefit from a *pseudo*-Stokes shift (Kusaka et al., 2012; Sakamoto et al., 2016). Although Stokes shifts are defined as the separation in energy between the maxima in absorption and emission of a fluorophore, a *pseudo*-Stokes shift is associated with the difference between the emission and a relative maximum in absorption for an upper-lying excited state, which undergoes a radiation-less deactivation in favour to the lower (and emissive) excited state. Fluorophores with large (*pseudo*)-Stokes shifts are highly desirable in biochemical experiments so that the label emission is at a significant longer wavelength than excitation (e.g. intracellular imaging enabling multiplexing) (Rauf et al., 2010; Jeong et al., 2011; Shcherbakova et al., 2012; Holzapfel et al., 2018). Our new heteroleptic Zn^{II} bis(dipyrrinato) complexes herein presented have intriguing properties to be used as fluorescent emitters for bioimaging.

RESULTS AND DISCUSSION

The synthesis of the plain dipyrrins (L_p) is easily accessible *via* a condensation reaction between the arylaldehyde and two and a half equivalents of 2,4-dimethylpyrrole, followed by oxidation by *p*-chloranil (Loudet and Burgess, 2007). The π-extended

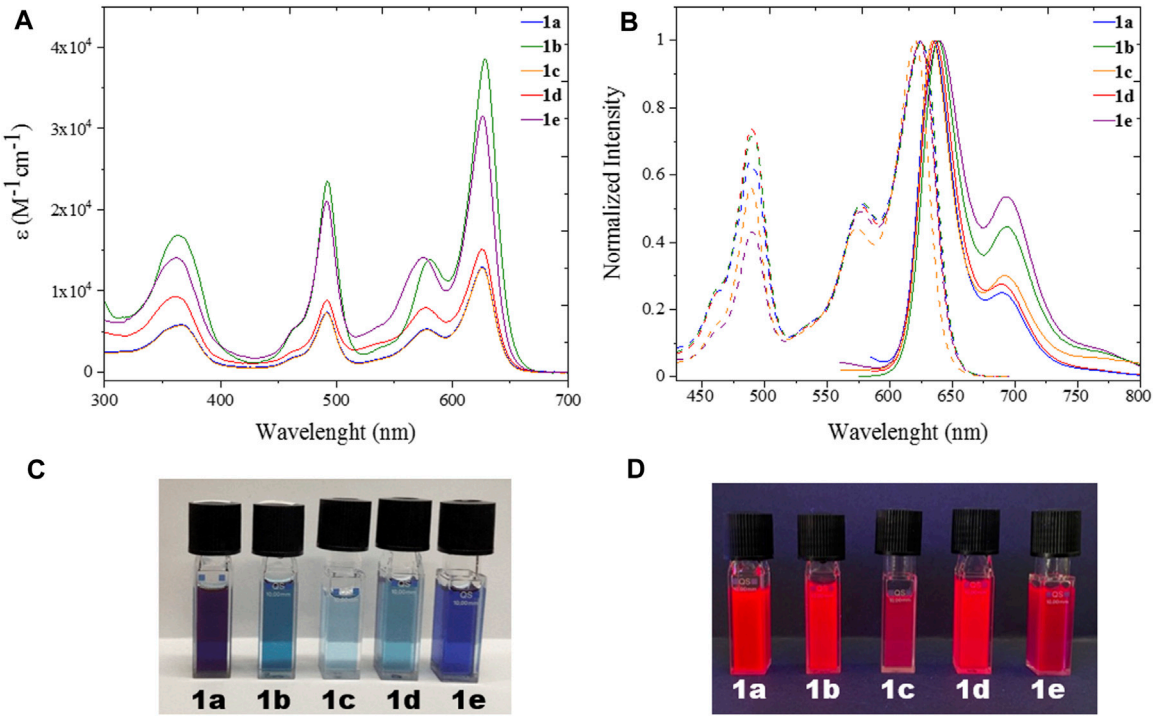

FIGURE 2 | UV **(A)** Uv/Vis absorption spectra with molar absorptivity coefficient (ε) and **(B)** excitation and emission spectra of heteroleptic complexes **1a-e** (λ_{exc} = 570 nm) in spectroscopic DMSO; **(C)** Pictures of **1a-e** in dimethyl sulfoxide solution under ambient (top) and **(D)** UV (bottom) light.

dipyrrins (L_π) were obtained by Knoevenagel condensation of the plain dipyrrins at the methyl groups in *alpha* to the pyrrolic nitrogen with 2-napthalencarbaldehyde, catalysed by acetic acid (Tungulin et al., 2019). By mixing one equivalent of π-extended dipyrrin and one equivalent of a plain dipyrrin with zinc diacetate ($Zn(OAc)_2$) at room temperature, the corresponding new heteroleptic bis(dipyrrinato) Zn^{II} complexes (L_pZnL_π) were obtained with a yield of up to 40%, with chemical structures shown in **Figure 1**. Column chromatography is needed in order to separate the desired complexes from the homoleptic complexes ($Zn(L_p)_2$ and $Zn(L_\pi)_2$) that are also formed in the reaction (**Figure 1**). The homoleptic complexes **2a**, **2b**, and **3a** were already known, (respectively: (Sakamoto et al., 2016; Tsuchiya et al., 2016; Tungulin et al., 2019) while the other homoleptic complexes are presented here for the first time, to the best of our knowledge. We expect them to have a distorted tetrahedral geometry as other bis(dipyrrinato) Zn^{II} complexes (Kusaka et al., 2012; Tsuchiya et al., 2014; Zhang et al., 2018; Zhang et al., 2019).

Photophysical Properties

All five heteroleptic complexes **1a–e** have an intense blue colour in solution (**Figure 2**). Their spectroscopic properties were investigated in a nonpolar solvent, such as toluene (PhMe), and in a polar aprotic solvent, such as dimethyl sulfoxide (DMSO), which will be used for the preparation of the biological assays. In order to understand their photophysical properties, their relative homoleptic complexes were also characterised (see **Figure 3** and **Supplementary Table S1** in ESI). The UV-vis absorbance spectra of complexes **1a–e** have shared features, as shown in **Figures 2**, **3**.

From the absorption spectra, we identify three main electronic transition bands in the heteroleptic complexes **1a–e** (**Table 1**). The broad band at high energy centred at ca. 360 nm is attributed to the electronic transitions localised on the naphthyl vinyl moieties of the π-extended dipyrrins, as they are absent in the plain dipyrrins. It is worth to notice that, in complex **1b**, the characteristic structured band of the anthracenyl moiety is not visible as it is hidden by the aforementioned naphthyl vinyl absorption. This is not the case for the homoleptic complex **2b**, in which spectrum the vibronic structure of the anthracene absorption is clearly visible. The other two main bands are in the visible region, and their profile is reminiscent of the absorption of the dipyrrin ligands. Between these two bands, the one at highest energy presents a shoulder at 465 nm and a relative maximum at ca. 490 nm (e.g.: ε (**1e**) = 2.2 10^4 cm^{-1} M^{-1}).

This absorption is attributed to the singlet ligand centred (^{1}LC) π→π* transition localised on the plain dipyrrin (^1L_pC in **Figure 4**). At longer wavelengths, a very intense absorption at ca. 620 nm (e.g.: ε (**1e**) = 3.3 10^4 cm^{-1} M^{-1}) is present with a shoulder at ca. 575 nm, which is assigned to the π→π* transition and its vibronic coupling localised on the π-expanded dipyrrin ($^1L_\pi C$ in **Figure 4**). The Zn^{II} centre is a d^{10} metal, and it is not involved in the transitions. Furthermore, it is reasonable to expect that the dipyrrinato ligands are almost orthogonal to each other with a weak if not absent exciton

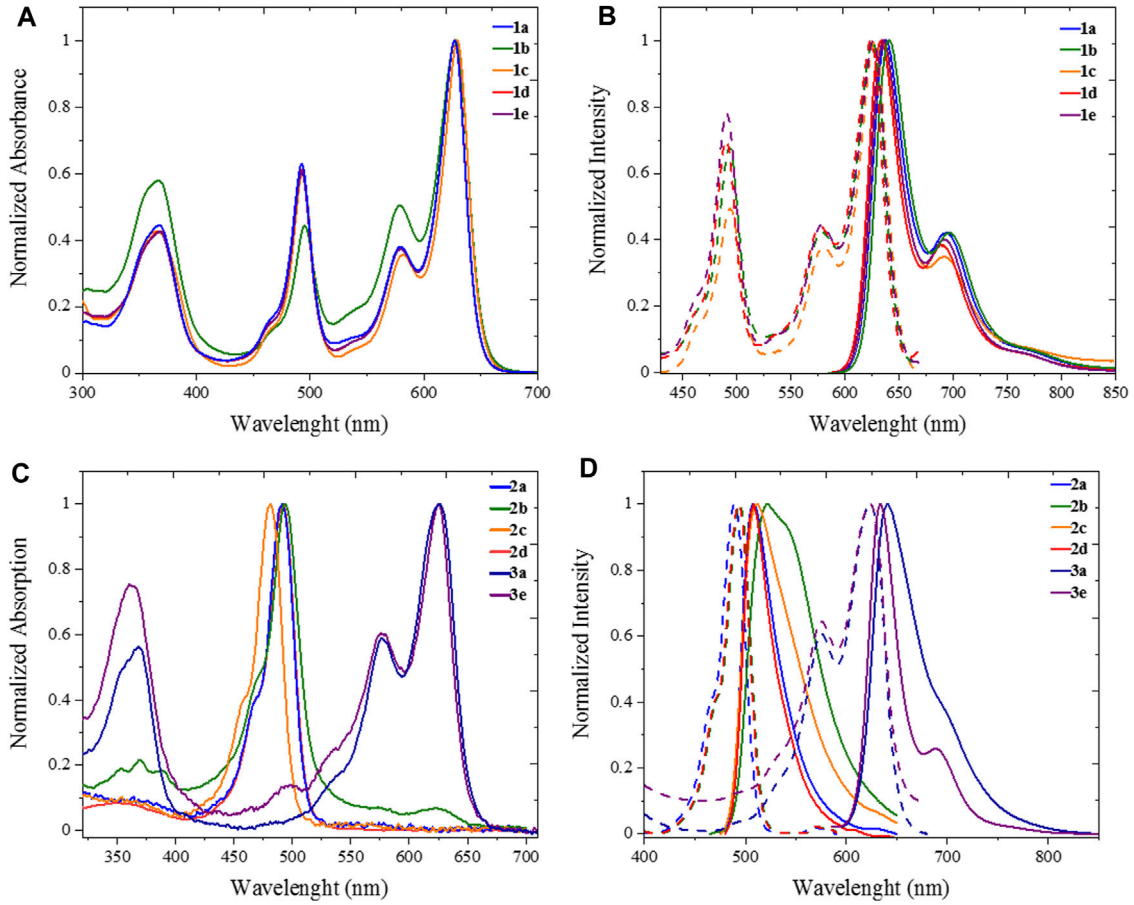

FIGURE 3 | UV Photophysics in spectroscopic toluene for heteroleptic complexes **1a-e** (top) and homoleptic complexes **2a-d**, **3a** and **3e** (bottom). **(A)** Uv/Vis absorption and **(B)** excitation (dashed plot, λ_{em} = 710 nm) emission (solid plot, λ_{exc} = 570) spectra of **1a-e**. **(C)** Uv/Vis absorption and **(D)** excitation (dashed plot, λ_{em} = 600 nm for **2a-d**, λ_{em} = 700 nm for **3a**, **3e**) emission (solid plot, λ_{exc} = 470 nm for **2a-d**, λ_{exc} = 570 nm for **3a**, **3e**).

TABLE 1 | Photophysical properties of heteroleptic Zn^{II} complexes **1a-e**.

Complex	λ_{abs} [a] [nm] (ε [10^4 $M^{-1}cm^{-1}$])	λ_{em} [nm]	$\Delta\nu$ [cm^{-1}] (*Pseudo* $\Delta\nu$ [10^3 cm^{-1}])	Φ [c]	τ [d] [ns]	k_r [10^7 s^{-1}]	k_{nr} [10^7 s^{-1}]
1a	366 (0.54) 491 (0.70) 627 (1.24)	635[a] 638[b]	0.20 (4.62) [a] 0.30 (4.61) [b]	0.44[a] 0.71[b]	3.1[a] 3.5[b]	14.2[a] 20.3[b]	18.1[a] 8.3[b]
1b	364 (1.73) 493 (2.4) 628 (3.89)	639[a] 641[b]	0.27 (4.63) [a] 0.21 (4.51) [b]	0.37[a] 0.55[b]	3.6[a] 4.2[b]	10.3[a] 13.1[b]	17.3[a] 10.7[b]
1c	366 (0.57) 491 (0.72) 626 (1.28)	634[a] 635[b]	0.20 (4.59) [a] 0.17 (4.42) [b]	0.05[a] 0.18[b]	3.0[a] 4.0[b]	1.8[a] 4.5[b]	31.5[a] 20.5[b]
1d	360 (0.95) 492 (0.90) 625 (1.53)	636[a] 634[b]	0.27 (4.62) [a] 0.32 (4.56) [b]	0.46[a] 0.63	2.6[a] 3.8[b]	17.0[a] 16.6[b]	20.0[a] 9.7[b]
1e	361 (1.54) 493 (2.2) 627 (3.28)	640[a] 636[b]	0.32 (4.66) [a] 0.20 (4.53)[b]	0.38[a] 0.45[b]	3.2[a] 3.9[b]	11.9[a] 11.5[b]	19.4[a] 14.1[b]

[a] Measured in DMSO and [b] in toluene. [c] Quantum yields were determined by the relative method, using cresyl violet in methanol as reference (Φ = 0.54).(Brouwer, 2011) [d] Exciting with a NanoLED source at 570 nm.

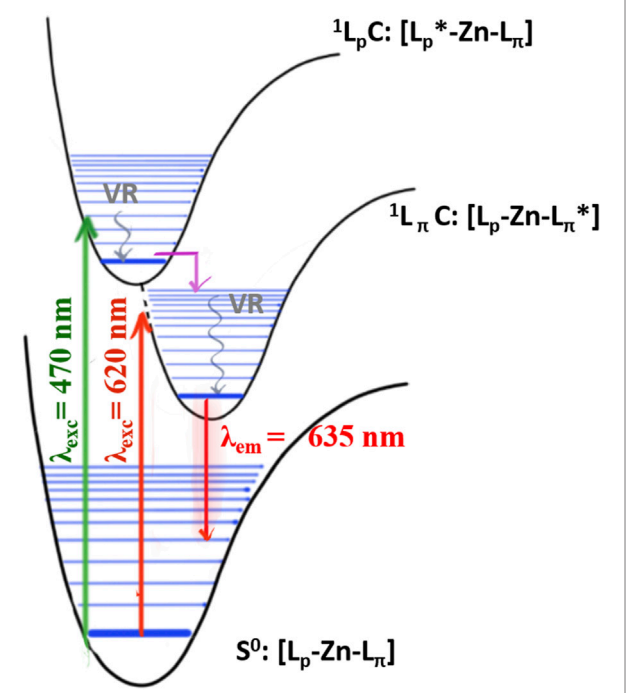

FIGURE 4 | Qualitative Jablonski-diagram for the involved photophysical processes in heteroleptic Zn^{II} complexes. (VR: Vibrational radiation; ^1L_pC: singlet excited state centered on the plain dipyrrin; $^1L_\pi C$: singlet excited state centered on the π-extended dipyrrin. Pink arrow: rapid interligand nonradiative transition).

coupling (Telfer et al., 2011; Trinh et al., 2014). Each complex shows fluorescence in the far-red region (emission centred at 635 nm) and a lower intensity shoulder in the near-infrared region up to 800 nm. The Φ values were measured by the relative method in two solvents: dimethyl sulfoxide (E_T^N: 0.44) and toluene (E_T^N: 0.099) (Reichardt, 1994). In a nonpolar solvent such as toluene, the zinc bis(dipyrrinato) complexes have the highest Φ, with values ranging from 18% for complex **1c** to 70% for complex **1a**. The difference in Φ among complexes **1a–e** has to be ascribed to the distinct aryl group in *meso*-position of the plain dipyrrins. It has been previously proven that the aryl group rotates in respect to the plain of the dipyrrin, allowing nonradiative deactivation unless bulky substituents impede this rotation (I.V. Sazanovich, 2004). In addition to that, the planarity of the chelating dipyrrin might change upon functionalisation, which also influences the rigidity and, therefore, the radiative transitions of the systems (Tungulin et al., 2019). The π-extended dipyrrin is the same for the heteroleptic compounds, besides complex **1e**, which possess a hydroxyl group in position 4 to the 2,6-dimethylphenyl substituent, which is in *para* to the dipyrrin. The presence of this extra hydroxyl group in **1e** with respect to **1d** might induce additional nonradiative processes since Φ in **1e** is slightly lower than the one in **1d** (Φ = 45% and Φ = 63%, respectively). The consistently lower emission efficiency in **1c** is related mainly to the increased rotational freedom of the aryl group in the *meso*-position of the plain dipyrrin. Furthermore, the electron-donating groups such as methoxy and hydroxyl groups induce an additional quenching effect. The homoleptic derivatives are emissive only in toluene (see **Supplementary Table S1**), although their Φ is much lower than their heteroleptic counterparts (e.g. Φ (**2a**): 18%). By comparing the emissions in a polar aprotic solvent such as DMSO, it is possible to assert that the emission energies are not affected by changing the polarity of the medium. In fact, LC transitions are not influenced by different polarities. Heteroleptic zinc bis(dipyrrinato) complexes are not symmetric in their ground and excited states. Therefore, the non-emissive symmetry breaking charge transfer state (SBCT) is not present, which is favoured in the case of homoleptic complexes instead (cf. **Figure 4** and **Supplementary Figure S5**). The intensity of the emission of **1a–e** in DMSO, although reduced in comparison to the values obtained in PhMe, is still very strong with Φ of ca. 40%, except for complex **1c** (Φ = 5%). These values are incredibly appealing for far-red/near-IR emitters, especially because by lowering the emission energies, the nonradiative deactivation paths are much more probable to occur.

The fluorescence decays are monoexponential, and the lifetimes (τ) are close to 3 ns (in DMSO) and 4 ns (in PhMe), with minor differences among the complexes. Radiative rate constants (k_r) are comparable among the heteroleptic Zn^{II} complexes and are higher than the nonradiative ones (k_{nr}) in PhMe and lower in DMSO (except for complex **1c**). Excitation spectra of the investigated complexes show a precise comparison with their relative absorption spectra, meaning that the far-red emission centred on the π-extended dipyrrinato moiety also occurs upon excitation of the plain dipyrrinato moiety (**Figures 2B**, **3B**, and **Supplementary Figure S1**). Thus, the excited state ^1L_pC undergoes a rapid interligand nonradiative transition to populate the lower-lying $^1L_\pi C$ (**Figure 4**). Therefore, upon excitation at shorter wavelength (470 nm), the detected emission is at lower energies (emission maximum at ca. 635 nm). This effect prompts a *pseudo*-Stokes shift of more than 4,600 cm^{-1} (**Table 1**). As the quenching of the plain dipyrrin is total, Nishihara and coworkers suggested a 100% efficient energy transfer from the donor L_p to the acceptor L_π. (Kusaka et al., 2012; Sakamoto et al., 2016). Advanced studies are necessary in order to elucidate the photophysical pathways of these heteroleptic complexes and, currently, we are investigating the involved nonradiative processes by means of transient absorption spectroscopy, which are beyond the scope of the present work.

Further experiments were done by measuring the fluorescence lifetimes of the heteroleptic complexes **1a–e**, using three different excitation wavelengths (455, 570, and 625 nm). For each complex, the obtained decays show identical fittings independently from the excitation energy used (**Supplementary Figure S1**).

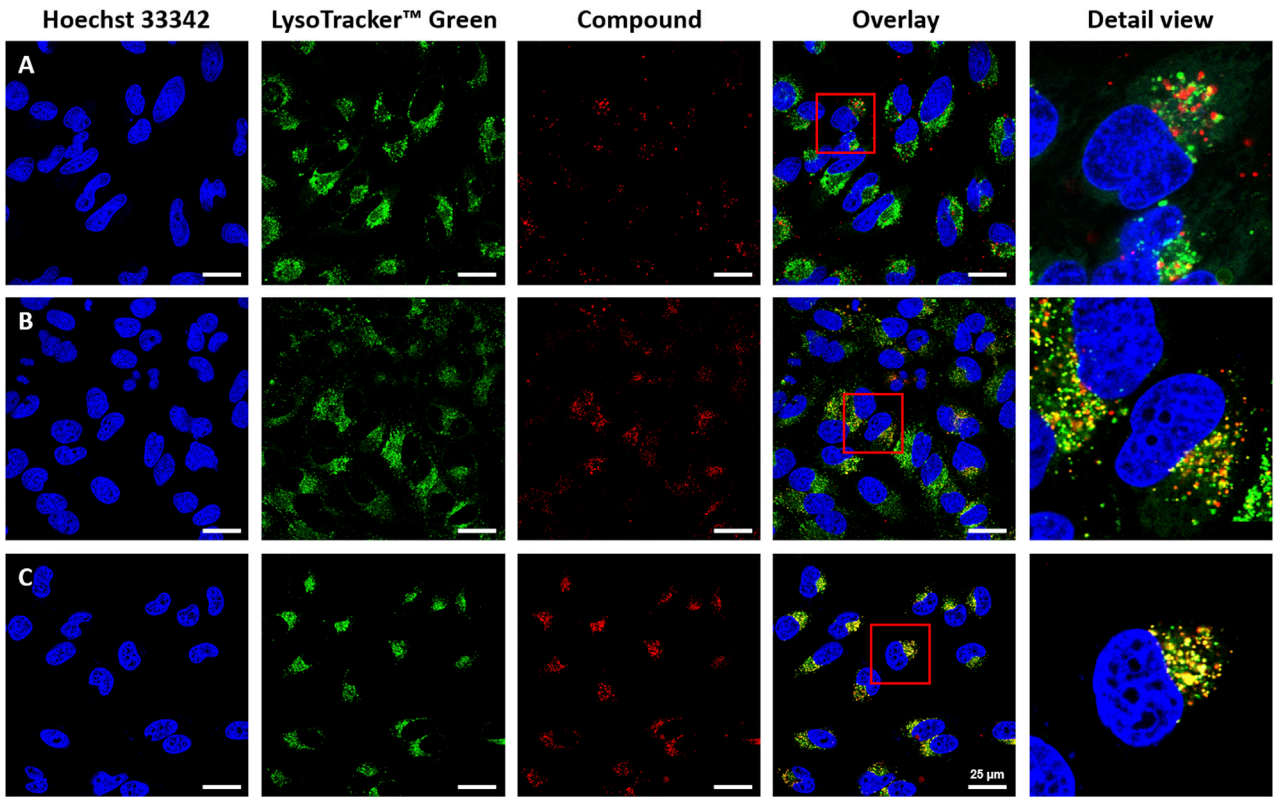

FIGURE 5 | Cellular uptake of heteroleptic bis(dipyrrinato) zinc complexes in HeLa cells (**(A)**: **1a**, **(B)**: **1d**, **(C)**: **1e**). For co-staining of nuclei and endosomes, cells were treated with Hoechst 33,342 (λ_{exc} = 405nm, λ_{em} = 414–462 nm), Lysotracker™ Green (λ_{exc} = 488 nm, λ_{em} 494–545 nm); and Hoechst 33,342, compounds **1a**, **1d**, **1e** (λ_{exc} = 630 nm, λ_{em} = 640–750 nm). Intracellular accumulation of the complexes was detected with fluorescence confocal microscopy using a Leica Stellaris 5 with a white light laser. The overlay is the merged image of the single-channel fluorescence images. Scale bars: 25 µm.

Confocal Laser Microscopy

The emission colors of these new heteroleptic Zn^{II} bis(dipyrrinato) complexes, as well as their high quantum yields also in polar solvents and their large *pseudo*-Stokes Shifts are appealing properties for their exploitation in bioimaging. Before evaluating their biocompatibility, we analysed their stability in different aqueous environments. The UV/vis absorption spectra of the complexes **1a–e** were recorded in Dulbecco Modified Eagle Medium (DMEM) and in deionized water (**Supplementary Figure S3**), using the same concentrations adopted for the confocal laser microscopy, in order to evaluate these the new dyes in media close to the cellular environment. The absorption profiles are stable. The same is true also in aqueous solutions at pH 3.3 and 5.0 (**Supplementary Figure S4**). These conditions were chosen based on the typical pH gradient in endocytic compartments of cells and DMEM is tipically used as cellular medium for cell culture applications. Emission profiles of the compounds in DMEM overlay very well with those measured in organic solvents, while there is a bathochromic shift in water, where the emission maxima are at about 670 nm (**Supplementary Table S1**). Quantum yields of the compounds in aqueous media reflect the extremely large polarity ($E_T^N$of H_2O: 1.00), since the values are up to 3.1% in DMEM and up to 1.7% in water. Furthermore, it should be noted that water causes an additional quenching effect due to hydrogen-bond-assisted nonradiative deactivation (Maillard et al., 2021).

The stability of these complexes was tested at increasing temperatures (**Supplementary Figure S6**. The emission of the complexes is only slightly reduced when going from 20 to 50°C, and this can be ascribed to the increasing collisions with solvent molecules followed by an increase of nonradiative deactivation processes. Thus, our far-red emissive bis(dipyrrinato) zinc complexes are stable in an aqueous solution at different pH values and temperatures. In order to test their biocompatibility in living cells, cell viability and cellular uptake were determined in four different cell types, including primary somatic cells such as human dermal fibroblasts (NHDF), a mouse cell line from embryonic fibroblasts (NIH3T3), and two human cancer cell lines (HeLa, and MCF7). To test the viability, MTT assays were performed by treating 10^4 cells of the respective cell type with different concentrations of the complexes **1a–e** for 72 h at 37°C. For all complexes, the LD_{50} values were >20 µM, showing high biocompatibility (**Supplementary Figure S7**). On the contrary, MTT assays of the single dipyrrin ligand showed a decreased viability already at concentrations lower than 7 µM (**Supplementary Figure S8**). For all these results, we assume high stability of these heteroleptic complexes in the cellular environments.

Since all the complexes showed only negligible toxicity when used to treat the different cell lines, a concentration of 20 µM was chosen

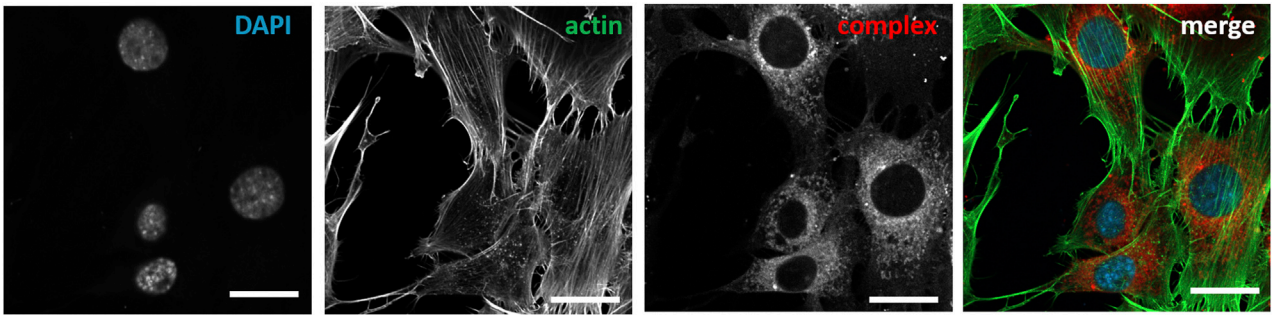

FIGURE 6 | Post-fixation immunochemical staining of nuclei and actin cytoskeleton of NIH3T3 cells treated with compound **1d**. Cells were treated with DAPI (λ_{exc} = 405nm, λ_{em} = 410–470 nm), Actin (λ_{exc} = 488 nm, λ_{em} 490–535 nm); compound **1d** (λ_{exc} = 640 nm, λ_{em} = 656–700 nm).

for the cellular uptake experiments and the live-cell fluorescent imaging (**Figure 5**, **6** and **Supplementary Figures S11–17**). With the best performing complexes **1d** and **1e** we tested their cellular uptake also at different concentrations, such as 1, 10, and 20 μM (**Supplementary Figures S9**, **S10**) It was assumed that due to their hydroxyl groups, a higher water solubility was achieved with complexes **1c**, **1d**, and **1e**. As expected, due to the low Φ of **1c**, this complex is hardly detectable. In contrast, complexes **1d** and **1e** display improved cellular uptake with respect to DMSO controls by virtue of their higher solubility in aqueous solution. Complexes **1a** and **1b** showed decreased cellular uptake. All complexes were taken up by endocytosis at the respective concentrations, leading to an accumulation in the endosomal/lysosomal compartment, which was proven by the counterstaining with Lysotracker Green™ (**Figure 5**) (Canton and Battaglia, 2012; Kolmel et al., 2012).

As a further analysis, confocal live-cell fluorescence microscopy was performed with Mitotracker™ Green. However, no counterstaining with mitochondrial markers was observed (**Supplementary Figures S12–14**). **Figures 5A–C** shows the counterstaining experiments in HeLa cells with Lysotracker Green with Pearson coefficients of 0.85 for **1e**, 0.60 for **1d**, and 0.24 for **1a** (Bolte and Cordelières, 2006). To further test the suitability of these heteroleptic Zn^{II} bis(dipyrrinato) complexes for bioimaging applications, the correlation of incubation time with signal intensity in live-cell imaging and the stability after fixation of cells were also investigated. While differences in the obtained signal intensity could be detected when incubating cells for a period of 0.5, 1.5, and 6 h (**Supplementary Figure S17**, compound **1e**), the complexes showed no decrease in fluorescence intensity after fixation (**Figure 6**). This proves the versatility of these complexes, as they can be used in live-cell imaging and in fixed-cell experiments, e.g. for immunocytochemistry. Moreover, given the photochemical properties of the compounds and the significant *pseudo*-Stokes shift, the excitation of complexes was possible at multiple wavelengths, allowing for the simultaneous excitation of two fluorophores at 488 nm and the detection of their emission at different wavelengths.

CONCLUSION

In the search of promising far-red-emitting fluorophores for bioimaging, we designed and synthesized five new heteroleptic Zn^{II} bis(dipyrrinato) complexes. Their relative homoleptic derivatives were prepared for comparison. We investigated their luminescence in two different solvents: the nonpolar toluene and the polar and water-miscible dimethylsulfoxide. In contrast to the homoleptic derivatives, the heteroleptic complexes feature high emission also in polar aprotic solvent, such as DMSO. We confirmed that emission comes only from the singlet excited state that is centered on the π-extended dipyrrin that has the lowest energy gap. Therefore, those heteroleptic complexes emit in the far-red to NIR region, which is highly desirable for biological investigations. Our heteroleptic Zn^{II} bis(dipyrrinato) are stable in aqueous solutions and at different pH. They presented an endosomal uptake with high cell biocompatibility in four different cell types. Thanks to their large *pseudo*-Stokes shift, these complexes can be excited at multiple wavelengths. Moreover, we demonstrated that they can be used also in fixed-cell experiments. All in one, those results envision heteroleptic Zn^{II} bis(dipyrrinato) complexes as successful fluorophores and motivates further development for exciting application in fluorescence imaging and beyond.

DATA AVAILABILITY STATEMENT

The original contributions presented in the study are included in the article/**Supplementary Material**, further inquiries can be directed to the corresponding author.

AUTHOR CONTRIBUTIONS

Conceptualization: CB. Funding acquisition: CB, US, and EL. Project administration: CB Supervision: CB and US Validation: CB and US Investigation: RT, DF, and EL Writing: all authors.

FUNDING

This research has been funded by the Deutsche Forschungsgemeinschaft (DFG, German Research Foundation) under the Research Training Group GRK 2039 (RT and CB:

project A4; DF and US: project C2) and under Germany's Excellence Strategy via the Excellence Cluster 3D Matter Made to Order (EXC-2082/1—390761711) (US and EDL). The work of EDL has been supported by a postdoctoral research fellowship of the Alexander von Humboldt Foundation.

ACKNOWLEDGMENTS

The authors thank the KIT and the Carl Zeiss Foundation for financial support. Prof. S. Bräse and Prof. H.-A. Wagenknecht (Institute of Organic Chemistry, KIT) and Prof. M. Bastmeyer (Zoological Institute, KIT) are gratefully acknowledged for giving access to the labs and necessary equipment. We acknowledge support by the KIT-Publication Fund of the Karlsruhe Institute of Technology.

SUPPLEMENTARY MATERIAL

The Supplementary Material for this article can be found online at: https://www.frontiersin.org/articles/10.3389/fchem.2021.754420/full#supplementary-material

REFERENCES

Alqahtani, N. Z., Blevins, T. G., and Mccusker, C. E. (2019). Quantifying Triplet State Formation in Zinc Dipyrrin Complexes. *J. Phys. Chem. A.* 123, 10011–10018. doi:10.1021/acs.jpca.9b08682

Bartynski, A. N., Gruber, M., Das, S., Rangan, S., Mollinger, S., Trinh, C., et al. (2015). Symmetry-breaking Charge Transfer in a Zinc Chlorodipyrrin Acceptor for High Open Circuit Voltage Organic Photovoltaics. *J. Am. Chem. Soc.* 137, 5397–5405. doi:10.1021/jacs.5b00146

Baudron, S. A. (2013). Luminescent Dipyrrin Based Metal Complexes. *Dalton Trans.* 42, 7498–7509. doi:10.1039/c3dt50493j

Bolte, S., and Cordelières, F. P. (2006). A Guided Tour into Subcellular Colocalization Analysis in Light Microscopy. *J. Microsc.* 224, 213–232. doi:10.1111/j.1365-2818.2006.01706.x

Brouwer, A. M. (2011). Standards for Photoluminescence Quantum Yield Measurements in Solution (IUPAC Technical Report). *Pure Appl. Chem.* 83, 2213–2228. doi:10.1351/pac-rep-10-09-31

Callaghan, S., Filatov, M. A., Savoie, H., Boyle, R. W., and Senge, M. O. (2019). *In Vitro* cytotoxicity of a Library of BODIPY-Anthracene and -pyrene Dyads for Application in Photodynamic Therapy. *Photochem. Photobiol. Sci.* 18, 495–504. doi:10.1039/c8pp00402a

Canton, I., and Battaglia, G. (2012). Endocytosis at the Nanoscale. *Chem. Soc. Rev.* 41, 2718–2739. doi:10.1039/c2cs15309b

Deng, P., Xiao, F., Wang, Z., and Jin, G. (2021). A Novel BODIPY Quaternary Ammonium Salt-Based Fluorescent Probe: Synthesis, Physical Properties, and Live-Cell Imaging. *Front. Chem.* 9, 650006. doi:10.3389/fchem.2021.650006

Filatov, M. A. (2019). Heavy-atom-free BODIPY Photosensitizers with Intersystem Crossing Mediated by Intramolecular Photoinduced Electron Transfer. *Org. Biomol. Chem.* 18, 10–27. doi:10.1039/c9ob02170a

Grossi, M., Morgunova, M., Cheung, S., Scholz, D., Conroy, E., Terrile, M., et al. (2016). Lysosome Triggered Near-Infrared Fluorescence Imaging of Cellular Trafficking Processes in Real Time. *Nat. Commun.* 7, 10855. doi:10.1038/ncomms10855

Guo, Z., Park, S., Yoon, J., and Shin, I. (2014). Recent Progress in the Development of Near-Infrared Fluorescent Probes for Bioimaging Applications. *Chem. Soc. Rev.* 43, 16–29. doi:10.1039/c3cs60271k

Hilderbrand, S. A., and Weissleder, R. (2010). Near-infrared Fluorescence: Application to *In Vivo* Molecular Imaging. *Curr. Opin. Chem. Biol.* 14, 71–79. doi:10.1016/j.cbpa.2009.09.029

Holzapfel, H. Y., Stern, A. D., Bouhaddou, M., Anglin, C. M., Putur, D., Comer, S., et al. (2018). Fluorescence Multiplexing with Spectral Imaging and Combinatorics. *ACS Comb. Sci.* 20, 653–659. doi:10.1021/acscombsci.8b00101

Jeong, S., Won, N., Lee, J., Bang, J., Yoo, J., Kim, S. G., et al. (2011). Multiplexed Near-Infrared *In Vivo* Imaging Complementarily Using Quantum Dots and Upconverting NaYF4:Yb3+,Tm3+ Nanoparticles. *Chem. Commun.* 47, 8022–8024. doi:10.1039/c1cc12746b

Jiang, Q., Desbois, N., Wang, S., and Gros, C. P. (2020). Recent Developments in Dipyrrin Based Metal Complexes: Self-Assembled Nanoarchitectures and Materials Applications. *J. Porphyrins Phthalocyanines* 24, 646–661. doi:10.1142/s1088424620300025

Karges, J., Basu, U., Blacque, O., Chao, H., and Gasser, G. (2019a). Polymeric Encapsulation of Novel Homoleptic Bis(dipyrrinato) Zinc(II) Complexes with Long Lifetimes for Applications as Photodynamic Therapy Photosensitisers. *Angew. Chem. Int. Ed.* 58, 14334–14340. doi:10.1002/anie.201907856

Karges, J., Blacque, O., Chao, H., and Gasser, G. (2019b). Polymeric Bis(dipyrrinato) Zinc(II) Nanoparticles as Selective Imaging Probes for Lysosomes of Cancer Cells. *Inorg. Chem.* 58, 12422–12432. doi:10.1021/acs.inorgchem.9b02019

Karges, J., Blacque, O., and Gasser, G. (2020). Metal Dipyrrin Complexes as Potential Photosensitizers for Photodynamic Therapy. *Inorg. Chim. Acta* 505. 119482. doi:10.1016/j.ica.2020.119482

Kaur, P., and Singh, K. (2019). Recent Advances in the Application of BODIPY in Bioimaging and Chemosensing. *J. Mater. Chem. C* 7, 11361–11405. doi:10.1039/c9tc03719e

Kölmel, D., Fürniss, D., Susanto, S., Lauer, A., Grabher, C., Bräse, S., et al. (2012). Cell Penetrating Peptoids (CPPos): Synthesis of a Small Combinatorial Library by Using IRORI MiniKans. *Pharmaceuticals* 5, 1265–1281. doi:10.3390/ph5121265

Kowada, T., Maeda, H., and Kikuchi, K. (2015). BODIPY-based Probes for the Fluorescence Imaging of Biomolecules in Living Cells. *Chem. Soc. Rev.* 44, 4953–4972. doi:10.1039/c5cs00030k

Kusaka, S., Sakamoto, R., Kitagawa, Y., Okumura, M., and Nishihara, H. (2012). An Extremely Bright Heteroleptic bis(dipyrrinato)Zinc(II) Complex. *Chem. Asian J.* 7, 907–910. doi:10.1002/asia.201200131

Loudet, A., and Burgess, K. (2007). BODIPY Dyes and Their Derivatives: Syntheses and Spectroscopic Properties. *Chem. Rev.* 107, 4891–4932. doi:10.1021/cr078381n

Maillard, J., Klehs, K., Rumble, C., Vauthey, E., Heilemann, M., and Fürstenberg, A. (2021). Universal Quenching of Common Fluorescent Probes by Water and Alcohols. *Chem. Sci.* 12, 1352–1362. doi:10.1039/d0sc05431c

Matsuoka, R., and Nabeshima, T. (2018). Functional Supramolecular Architectures of Dipyrrin Complexes. *Front. Chem.* 6, 349. doi:10.3389/fchem.2018.00349

Ni, Y., and Wu, J. (2014). Far-red and Near Infrared BODIPY Dyes: Synthesis and Applications for Fluorescent pH Probes and Bio-Imaging. *Org. Biomol. Chem.* 12, 3774–3791. doi:10.1039/c3ob42554a

Qu, X., Song, W., and Shen, Z. (2019). A Highly Selective NIR Fluorescent Turn-On Probe for Hydroxyl Radical and its Application in Living Cell Images. *Front. Chem.* 7, 598. doi:10.3389/fchem.2019.00598

Rauf, S., Glidle, A., and Cooper, J. M. (2010). Application of Quantum Dot Barcodes Prepared Using Biological Self-Assembly to Multiplexed Immunoassays. *Chem. Commun.* 46, 2814–2816. doi:10.1039/b927149j

Reichardt, C. (1994). Solvatochromic Dyes as Solvent Polarity Indicators. *Chem. Rev.* 94, 2319–2358. doi:10.1021/cr00032a005

Sakamoto, R., Iwashima, T., Kögel, J. F., Kusaka, S., Tsuchiya, M., Kitagawa, Y., et al. (2016). Dissymmetric Bis(dipyrrinato)Zinc(II) Complexes: Rich Variety and Bright Red to Near-Infrared Luminescence with a Large Pseudo-stokes Shift. *J. Am. Chem. Soc.* 138, 5666–5677. doi:10.1021/jacs.6b02128

Sani, U., Tungulin, D., Bizzarri, C., and Cucinotta, F. (2020). Turning Weak Emitters into Outstanding Luminescent Materials Using Rigid Host media. *RSC Adv.* 10, 2841–2845. doi:10.1039/c9ra10727d

Sazanovich, I. V., Kirmaier, C., Hindin, E., Yu, L., Bocian, D. F., Lindsey, J. S., et al. (2004). Structural Control of the Excited-State Dynamics of

Bis(dipyrrinato)zinc Complexes: Self-Assembling Chromophores for Light-Harvesting Architectures. *J. Am. Chem. Soc.* 126, 2664–2665. doi:10.1021/ja038763k

Shcherbakova, D. M., Hink, M. A., Joosen, L., Gadella, T. W. J., and Verkhusha, V. V. (2012). An orange Fluorescent Protein with a Large Stokes Shift for Single-Excitation Multicolor FCCS and FRET Imaging. *J. Am. Chem. Soc.* 134, 7913–7923. doi:10.1021/ja3018972

Telfer, S. G., Mclean, T. M., and Waterland, M. R. (2011). Exciton Coupling in Coordination Compounds. *Dalton Trans.* 40, 3097–3108. doi:10.1039/c0dt01226b

Trinh, C., Kirlikovali, K., Das, S., Ener, M. E., Gray, H. B., Djurovich, P., et al. (2014). Symmetry-Breaking Charge Transfer of Visible Light Absorbing Systems: Zinc Dipyrrins. *J. Phys. Chem. C* 118, 21834–21845. doi:10.1021/jp506855t

Tsuchiya, M., Sakamoto, R., Kusaka, S., Kitagawa, Y., Okumura, M., and Nishihara, H. (2014). Asymmetric Dinuclear bis(dipyrrinato)Zinc(II) Complexes: Broad Absorption and Unidirectional Quantitative Exciton Transmission. *Chem. Commun.* 50, 5881–5883. doi:10.1039/c4cc01573h

Tsuchiya, M., Sakamoto, R., Shimada, M., Yamanoi, Y., Hattori, Y., Sugimoto, K., et al. (2016). Bis(dipyrrinato)Zinc(II) Complexes: Emission in the Solid State. *Inorg. Chem.* 55, 5732–5734. doi:10.1021/acs.inorgchem.6b00431

Tungulin, D., Leier, J., Carter, A. B., Powell, A. K., Albuquerque, R. Q., Unterreiner, A. N., et al. (2019). Chasing BODIPY: Enhancement of Luminescence in Homoleptic Bis(dipyrrinato) Zn II Complexes Utilizing Symmetric and Unsymmetrical Dipyrrins. *Chem. Eur. J.* 25, 3816–3827. doi:10.1002/chem.201806330

Weissleder, R. (2001). A Clearer Vision for *In Vivo* Imaging. *Nat. Biotechnol.* 19, 316–317. doi:10.1038/86684

Zhang, F., Baudron, S. A., and Hosseini, M. W. (2018). Symmetrical and Dissymmetrical 2,2′-Bis-Dipyrrin Ligands and Zn(ii) Binuclear Helicates. *New J. Chem.* 42, 6997–7004. doi:10.1039/c8nj00335a

Zhang, F., Fluck, A., Baudron, S. A., and Hosseini, M. W. (2019). Synthesis, crystal Structure and Optical Properties of a Series of Dipyrrins Bearing Peripheral Coordinating Groups and Their BODIPYs and Zn(II) Complexes. *Inorg. Chim. Acta* 494, 216–222. doi:10.1016/j.ica.2019.05.027

Conflict of Interest: The authors declare that the research was conducted in the absence of any commercial or financial relationships that could be construed as a potential conflict of interest.

Publisher's Note: All claims expressed in this article are solely those of the authors and do not necessarily represent those of their affiliated organizations, or those of the publisher, the editors and the reviewers. Any product that may be evaluated in this article, or claim that may be made by its manufacturer, is not guaranteed or endorsed by the publisher.

frontiers in Chemistry

ORIGINAL RESEARCH
published: 15 November 2021
doi: 10.3389/fchem.2021.700956

Design, Synthesis, and Biological Evaluation of Pyrano [2,3-c]-pyrazole–Based RalA Inhibitors Against Hepatocellular Carcinoma

Yuting Wang[1†], Mingyao He[2†], Xiang Li[1,2], Jinlong Chai[2], Qinglin Jiang[3], Cheng Peng[2], Gu He[2]* and Wei Huang[1]**

[1]State Key Laboratory of Southwestern Chinese Medicine Resources, Hospital of Chengdu University of Traditional Chinese Medicine, School of Pharmacy, Chengdu University of Traditional Chinese Medicine, Chengdu, China, [2]State Key Laboratory of Biotherapy and Department of Urology, West China Hospital, Sichuan University, Chengdu, China, [3]School of Pharmacy and Sichuan Province College Key Laboratory of Structure-Specific Small Molecule Drugs, Chengdu Medical College, Chengdu, China

OPEN ACCESS

Edited by:
Laurent G. Désaubry,
INSERM U1260 Nanomedicine régénératrice (RNM), France

Reviewed by:
DR Reshma Rani,
Amity University, India
Rajeev K. Singla,
Sichuan University, China

***Correspondence:**
Qinglin Jiang
jql_cmc@163.com
Gu He
hegu@scu.edu.cn
Wei Huang
huangwei@cdutcm.edu.cn

[†]These authors have contributed equally to this work

Specialty section:
This article was submitted to Medicinal and Pharmaceutical Chemistry, a section of the journal Frontiers in Chemistry

Received: 27 April 2021
Accepted: 29 September 2021
Published: 15 November 2021

Citation:
Wang Y, He M, Li X, Chai J, Jiang Q, Peng C, He G and Huang W (2021) Design, Synthesis, and Biological Evaluation of Pyrano[2,3-c]-pyrazole–Based RalA Inhibitors Against Hepatocellular Carcinoma. Front. Chem. 9:700956. doi: 10.3389/fchem.2021.700956

The activation of Ras small GTPases, including RalA and RalB, plays an important role in carcinogenesis, tumor progress, and metastasis. In the current study, we report the discovery of a series of 6-sulfonylamide-pyrano [2,3-c]-pyrazole derivatives as novel RalA inhibitors. ELISA-based biochemical assay results indicated that compounds **4k**–**4r** suppressed RalA/B binding capacities to their substrates. Cellular proliferation assays indicated that these RalA inhibitors potently inhibited the proliferation of HCC cell lines, including HepG2, SMMC-7721, Hep3B, and Huh-7 cells. Among the evaluated compounds, **4p** displayed good inhibitory capacities on RalA (IC_{50} = 0.22 μM) and HepG2 cells (IC_{50} = 2.28 μM). Overall, our results suggested that a novel small-molecule RalA inhibitor with a 6-sulfonylamide-pyrano [2, 3-c]-pyrazole scaffold suppressed autophagy and cell proliferation in hepatocellular carcinoma, and that it has potential for HCC-targeted therapy.

Keywords: RalA inhibitors, pyrano[2;3-c]-pyrazole, hepatocellular carcinoma, synthesis, autophagy

INTRODUCTION

Hepatocellular carcinoma (HCC) is a primary liver malignancy with one of the highest mortality rates worldwide (Jacobson et al., 2018; Zhou et al., 2018; Paludetto et al., 2019; Siegel et al., 2019). Although significant progress has been made to improve chemotherapy, transcatheter artery chemoembolization (TACE), and targeted HCC therapy, many patients still present recurrences and the development of drug resistance (Xue et al., 2019; Pan et al., 2020; Yu et al., 2020). Therefore, novel targeted therapeutic approaches are required to help overcome these problems. From a molecular-level perspective, an important HCC development factor is the imbalance of major signaling pathways, including Ras, p53, PI3K/Akt, and Wnt/β-catenin (Saha and Giri, 2019; Zhongqi et al., 2019). Ras—a small-molecule GTPase member—has important regulatory functions in cell signal transduction, cytoplasmic skeletal construction, and material transport (Ostrem et al., 2013; Lim et al., 2014; Lito et al., 2016). Notably, recent findings indicated that the Ras gene was mutated in more than 30% of HCC-afflicted patients sampled (Guichard et al., 2012; Lindsay and Blackhall,

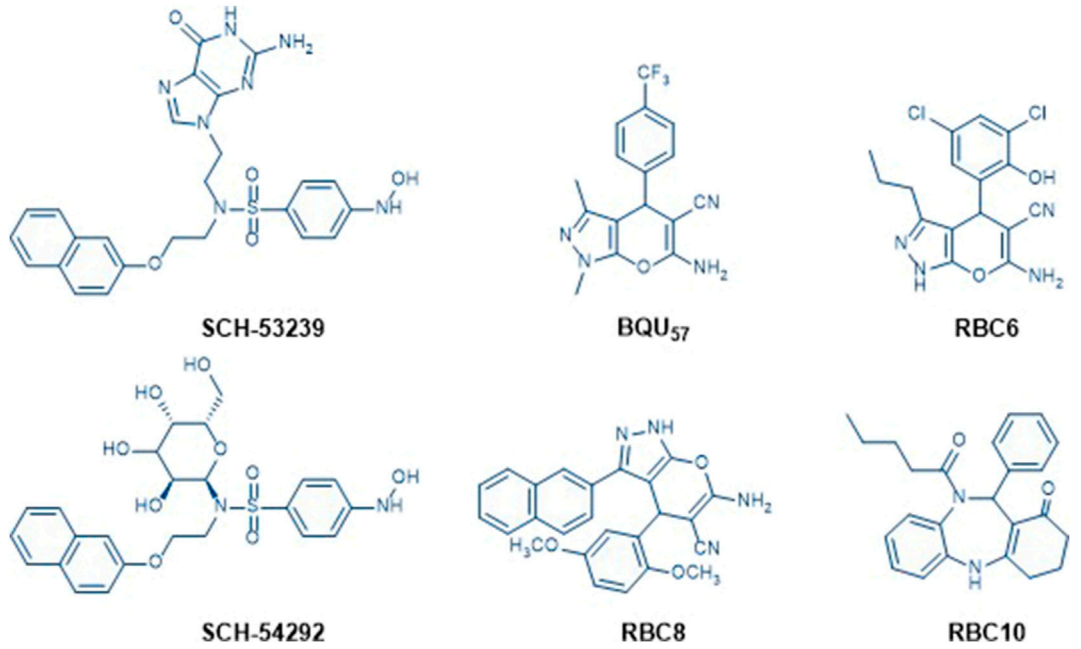

FIGURE 1 | Chemical structures of known Ral inhibitors, including SCH-53239, SCH-54292, BQU57, RBC6, RBC8, and RBC10.

2019; Suzuki et al., 2021). Mutations in the Ras gene have also been detected in various other types of cancers as well, including those for lung cancer, pancreatic cancer, and colon cancer (Zhang et al., 2018; Zhao et al., 2018; Chen et al., 2020). In the subseries of Ras signaling pathways, Ral has one of the most similar structures and functions compared to Ras, reaching up to 50% similarity for their sequences (Yan and Theodorescu, 2018). In the Ral small-GTPase branch, RalA and RalB are closely related G proteins with similar protein structures (Jiang et al., 2016). Their protein structures have an N-terminal free-drifting 11 amino acid sequence, a C-terminal membrane-targeting sequence, and a GTP- binding domain, which facilitate GDP/GTP binding (Zheng et al., 2016). The GTP- binding domain consists of five α-helices, six β-helices, and five loops. Their GTPase activity is low and requires the involvement of GTPase-activating proteins (GAPs) (Tracy et al., 2016). Additionally, the guanylate exchange factor (GEF) plays an important role in GTP/GDP binding and release (Hobbs et al., 2016). Usually, functional Ral members depend on their ability to cycle between activated (phosphorylated) and inactivated (dephosphorylated) Ral states. The Ral inhibitors can be divided into the following cases: targeted to Ral guanine exchange factors (RalGEFs); directly targeted to Ral; targeted to Ral effectors, and combinations of these therapies (Klose et al., 2016).

SCH-53239 was originally designed to inhibit guanine nucleotide exchange and control Ral signaling. A subsequent study elucidated the structure of SCH-53239 and led to the discovery of a derivative with a higher water solubility known as SCH-54292 (Gray et al., 2020). RBC8 has an efficient inhibitory effect on human and mouse platelets, preventing interactions with effector proteins and Ral-binding protein by binding to allosteric sites on GDP-bound Rals, leaving it in an inactive state. These types of compounds include currently reported Ral inhibitors, such as RBC6, RBC10, and BQU5726-27 (**Figure 1**). Prior structure analyses of BQU57 and RBC8 have suggested that the pyrano-fused pyrazole scaffold can bind to the RalA-GDP allosteric site (Alvarado and Giles, 2007; Hamada et al., 2011; Ezzeldin et al., 2014; Yan et al., 2016; Yan and Theodorescu, 2018; Walsh et al., 2019; Bum-Erdene et al., 2020; Xiong et al., 2020). In the current study, following a rationalized approach for strategic drug design, we aimed to develop methods to change the pyrazole ring N-methyl group into a substituted phenyl ring and add a sulfonyl group at the pyrano ring 2-amine group. These adjustments were performed to enhance RalA binding, via a 3-cyanide group and 4-aronmatic ring. The resultant pyrano[2,3-c]-pyrazole derivatives were assayed via their RalA and HCC cellular proliferation inhibitory capacities.

To achieve these objectives we designed and synthesized 6-sulfonamido-pyrano[2,3-c]-pyrazole–based RalA inhibitors. Then, we assayed their performance in HCC-based models *in vitro* and *in vivo*. We used HepG2 cells as vectors for *in vitro* ELISA-based biochemical assays, cell proliferation assays, and autophagy assays. We hypothesized that compound **4p** would suppress RalA/B activation and cellular proliferation, as well as subsequently induce lethal autophagy in HCC-afflicted cells. Furthermore, we hypothesized that compound **4p** would significantly suppress tumor growth using a HepG2 xenograft–based model. Overall, we expected that our findings and novel approach using RalA inhibitors will stimulate novel research that might achieve improved outcomes for targeted HCC therapies.

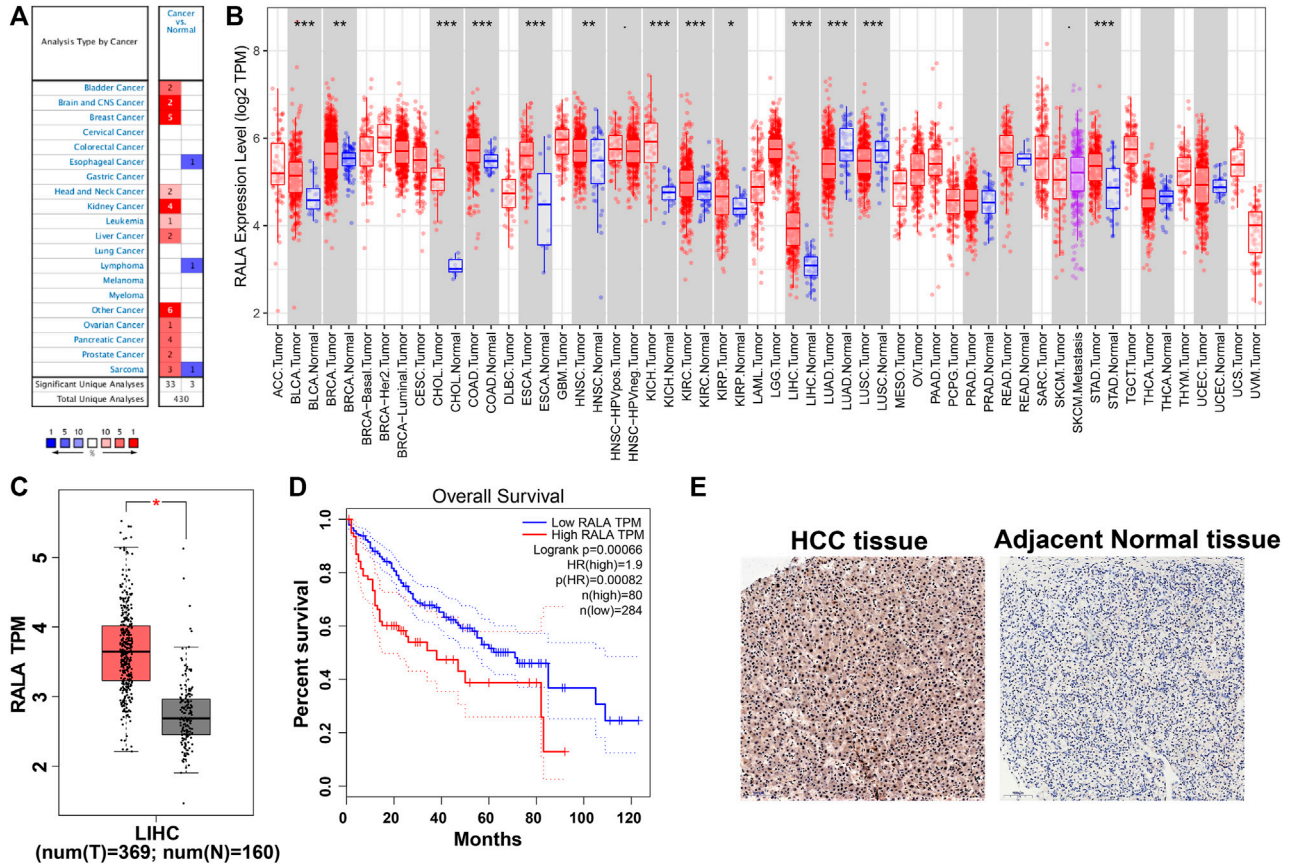

FIGURE 2 | (A) Analysis of the differential RalA expression of various cancer types in the Oncomine database; **(B)** Differential expression profiles of various cancers and RalA in the TCGA database; **(C)** Differential expression of RalA protein in HCC and normal tissues; **(D)** Kalplan–Meier curves of RalA on the overall survival rate of HCC patients in the TCGA database; **(E)** Protein expression levels of RalA in HCC and adjacent normal tissues detected by IHC, scale bar: 100 μm.

RESULTS AND DISCUSSION

We observed that RalA mRNA levels were upregulated in the Oncomine database cancer subtype panels (**Figure 2A**). Results suggested that RalA was overexpressed in different cancer subtypes, including bladder cancer, breast cancer, liver cancer, and prostate cancer (He et al., 2019; Pan et al., 2018). Next, we assessed RalA mRNA expression patterns in the TCGA database. RalA was upregulated in ten TCGA subtype cohorts (fold change >2.0, $p < 0.01$) and was downregulated in two lung cancer cohorts (**Figure 2B**). The analysis of 369 HCC-afflicted tissues and 160 adjacent normal liver tissue samples from data in the TCGA and GTEx databases demonstrated that RalA mRNA expression in HCC-afflicted tissues was 2.67-fold higher than in adjacently sampled normal ones (**Figure 2C**) (Wang et al., 2018; Hao et al., 2019; Wang et al., 2019). Furthermore, the RalA mRNA levels were a significant marker to predict HCC-afflicted patients' prognosis (**Figure 2D**). IHC-derived images of RalA proteins indicated that they were overexpressed in HCC vs. normal liver tissues (**Figure 2E**). Based on these results, we hypothesized that the upregulated RalA may be an attractive target for use in HCC-related therapies.

BQU57 and RBC8 as RalA inhibitors were recently reported (**Figure 3A**) and suggested that they were characterized by a pyran-fused pyrazole scaffold. This type of a scaffold constitutes a core structure that can bind to the RalA-GDP allosteric site, with 2-amino and 3-cyanide groups on the pyran moiety, being key pharmacophores. Pyrano[2,3-c]-pyrazole–based RalA inhibitors' effects on cancer cell proliferation have also been reported. However, we aimed to further develop efficient small-molecule allosteric RalA inhibitors based on these scaffold dynamics. Based on the necessary 5-nitrile-6-amino-pyrano [2, 3-c] pyrazole scaffold, variations in functional groups (R^1 and R^2) were introduced into the core structure, enriching the drug-like skeleton diversity (**Figure 3B**). The resulting compounds may, thus, have great potential to serve as foundations for exploring their uses as novel and efficient RalA inhibitors.

Considering both feasible synthetic routes and the chemical diversity of novel RalA inhibitors, we employed the synthetic route depicted in **Scheme 1**. Briefly, the starting compound (**1a–1o**) was a cyano-olefin formed by aldehyde and Malononitrile reactions via Knoevenagel condensation in the presence of acetic acid and sodium acetate. The corresponding pyrazolone (**2a–2f**) was synthesized from ethyl acetoacetate and

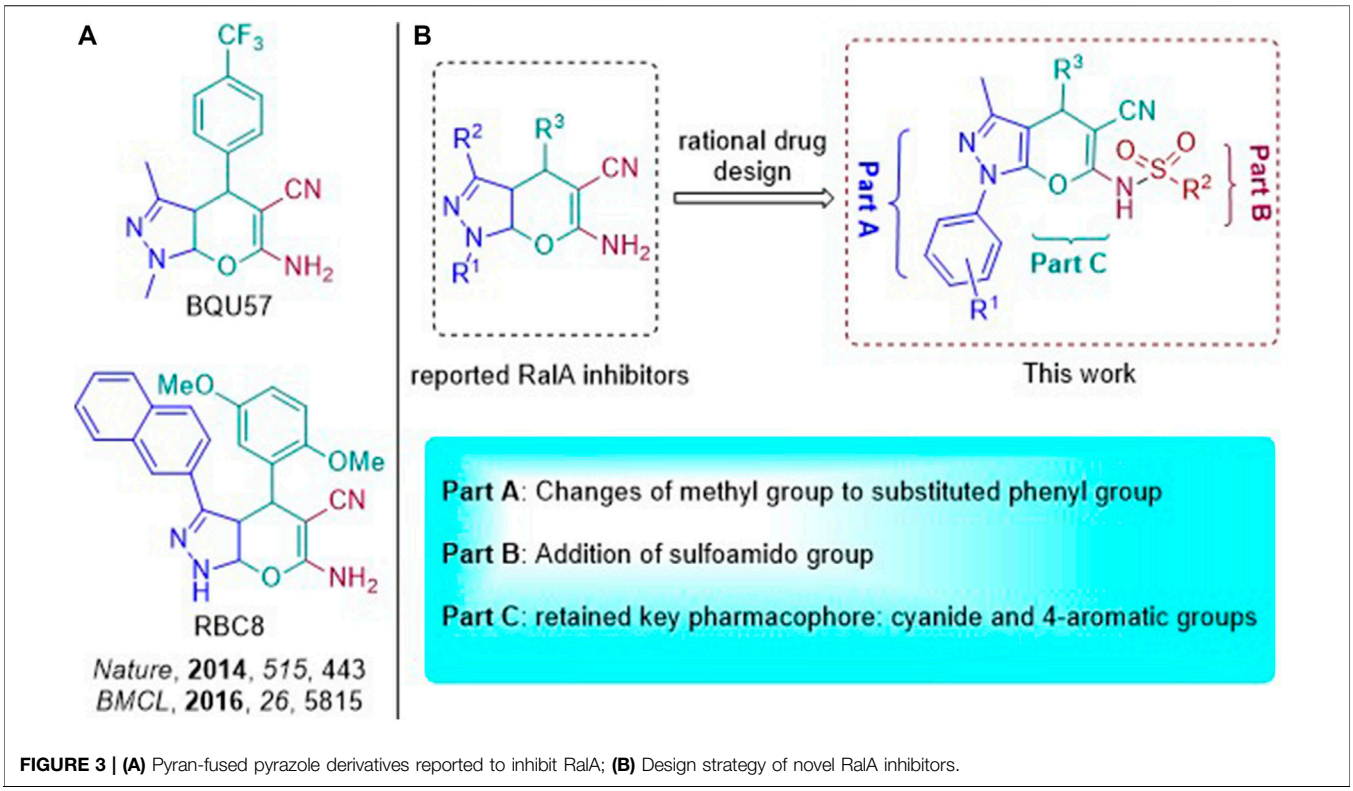

FIGURE 3 | (A) Pyran-fused pyrazole derivatives reported to inhibit RalA; **(B)** Design strategy of novel RalA inhibitors.

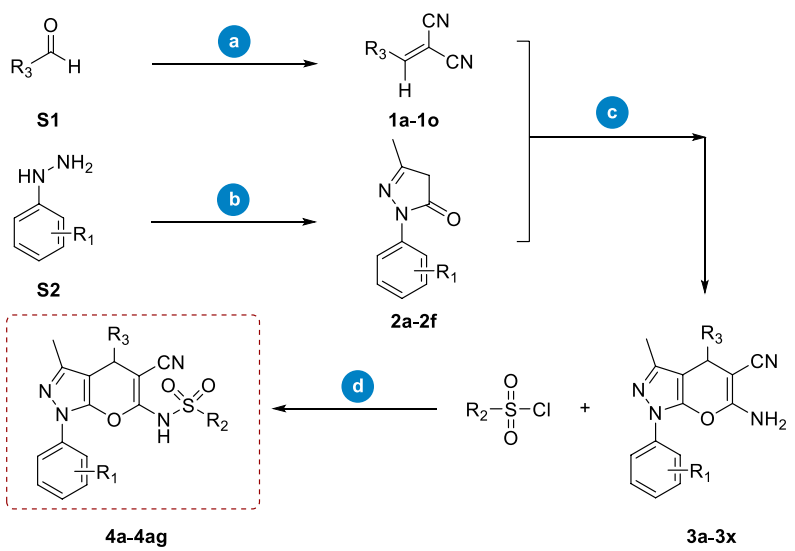

SCHEME 1 | Synthetic route of compounds **4a**–**4ag**. Reagents and conditions: **(A)**. Malononitrile, acetic acid, and CH_3COONa, overnight; **(B)**. Ethyl acetoacetate, acetic acid, and reflux, 4 h; **(C)**. Morpholine and methanol, 40°C, 30 min; **(D)**. DMAP and DCM, 35°C, 12 h.

phenylhydrazine by heating and refluxing acetic acid constituents for 4 h. The **1a–1o** and **2a–2f** compounds were further used as raw materials. Then, morpholine was added into methanol (solvent) followed by heating and stirring for 30 min to form pyrano [2,3-c]pyrazole intermediates (**3a–3x**). Finally, intermediates **3a–3x** reacted with a panel of sulfonyl chloride in the presence of DMAP using dichloromethane (DCM) as a solvent to obtain the target compound 4a–4ag (**Scheme 1**).

The structures of the synthesized target compounds (**4a–4ag**) were characterized by their HR-MS, ^{1}H-NMR, and ^{13}C-NMR spectra. Their RalA/B inhibitory activities at 1.0 μM and cellular proliferation data for HCC cell lines are shown in **Table 1**. When

TABLE 1 | Remaining kinase activities (%) after 1 μM compounds **4a**–**4ag** incubation on RalA and RalB and cell proliferation inhibition.

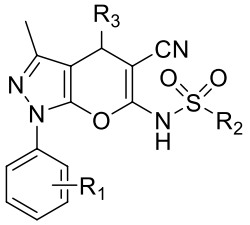

No	R^1	R^2	R^3	% control[a] 1 μM		IC_{50} (μM)	
				RalA	RALB	HepG2	Huh7
4a	H	4-MeC_6H_4	Ph	74	85	>10	>10
4b	H	4-MeC_6H_4	4-MeC_6H_4	75	105	>10	>10
4c	H	4-MeC_6H_4	3-ClC_6H_4	40	69	7.28 ± 0.64	>10
4d	H	4-MeC_6H_4	4-BrC_6H_4	77	89	>10	>10
4e	H	4-MeC_6H_4	4-FC_6H_4	74	76	>10	>10
4f	H	4-MeC_6H_4	3-BrC_6H_4	47	71	8.83 ± 0.75	>10
4g	H	4-MeC_6H_4	3,4-diCl C_6H_3	66	58	>10	>10
4h	H	4-MeC_6H_4	2-F-4-Br C_6H_3	70	83	>10	>10
4i	H	4-MeC_6H_4	4-$MeOC_6H_4$	69	60	>10	>10
4j	H	4-MeC_6H_4	2-furyl	57	70	9.57 ± 1.05	9.94 ± 1.23
4k	H	4-MeC_6H_4	3-pyridyl	32	38	5.63 ± 0.58	6.01 ± 0.57
4l	H	4-MeC_6H_4	4-pyridyl	40	52	9.2 ± 0.89	9.15 ± 1.04
4m	H	4-MeC_6H_4	3-thienyl	45	58	7.2 ± 0.65	>10
4n	H	4-MeC_6H_4	4-$CF_3C_6H_4$	46	59	8.46 ± 0.92	9.58 ± 0.92
4o	H	2-thienyl	4-$CF_3C_6H_4$	36	47	5.32 ± 0.61	>10
4p	H	4-$MeOC_6H_4$	4-$CF_3C_6H_4$	13	22	2.28 ± 0.23	4.31 ± 0.39
4q	H	4-$CF_3C_6H_4$	4-$CF_3C_6H_4$	37	39	8.65 ± 0.97	8.42 ± 0.94
4r	H	2,4-diFC_6H_3	4-$CF_3C_6H_4$	30	43	7.56 ± 0.92	7.39 ± 0.85
4s	2-Cl	4-MeC_6H_4	2-furyl	48	72	9.89 ± 0.81	>10
4t	2-Cl	4-MeC_6H_4	3-pyridyl	46	65	8.28 ± 0.89	>10
4u	2-Cl	4-MeC_6H_4	4-pyridyl	44	50	8.71 ± 0.74	>10
4v	2-Cl	4-MeC_6H_4	3-thienyl	56	78	>10	>10
4w	2-Cl	4-MeC_6H_4	3-$MeOC_6H_4$	51	69	8.87 ± 0.95	>10
4x	2-Cl	Ph	3-$MeOC_6H_4$	59	58	>10	8.93 ± 1.02
4y	2-Cl	4-$MeOC_6H_4$	3-$MeOC_6H_4$	54	73	>10	>10
4z	2-Cl	2-$NO_2C_6H_4$	3-$MeOC_6H_4$	53	60	>10	>10
4aa	2-Cl	3-$NO_2C_6H_4$	3-$MeOC_6H_4$	72	73	>10	>10
4ab	2-Cl	4-$NO_2C_6H_4$	3-$MeOC_6H_4$	60	65	>10	>10
4ac	4-Cl	4-MeC_6H_4	Ph	67	68	>10	>10
4ad	2-Cl	4-MeC_6H_4	Ph	52	64	>10	>10
4ae	4-Me	4-MeC_6H_4	Ph	79	78	>10	>10
4af	2-OMe	4-MeC_6H_4	Ph	73	78	>10	>10
4ag	4-F	4-MeC_6H_4	Ph	66	75	>10	>10

[a]*% control = kinase activity remained.*

TABLE 2 | The IC_{50} values (μM) of compounds **4k**–**4r** on RalA/B and HCC cell lines.

No	Kinase activities (IC_{50}, μM)[a]		Anti-proliferative activities (IC_{50}, μM)[b]			
	RalA	RalB	HepG2	Huh-7	Hep3B	SMMC-7721
4k	0.75 ± 0.09	1.09 ± 0.13	5.63 ± 0.58	6.01 ± 0.57	>10	>10
4l	1.24 ± 0.15	2.64 ± 0.30	9.2 ± 0.89	9.15 ± 1.04	4.39 ± 0.57	5.94 ± 0.77
4m	1.70 ± 0.22	3.86 ± 0.39	7.2 ± 0.65	>10	9.84 ± 1.37	9.60 ± 1.05
4n	1.81 ± 0.19	4.11 ± 0.45	8.46 ± 0.92	9.58 ± 0.92	>10	>10
4o	0.96 ± 0.12	1.93 ± 0.26	5.32 ± 0.61	>10	7.69 ± 0.84	>10
4p	0.22 ± 0.04	0.41 ± 0.07	2.28 ± 0.23	4.31 ± 0.39	2.71 ± 0.27	5.38 ± 0.37
4q	1.02 ± 0.09	1.16 ± 0.19	8.65 ± 0.97	8.42 ± 0.94	7.76 ± 1.00	>10
4r	0.66 ± 0.08	1.49 ± 0.22	7.56 ± 0.92	7.39 ± 0.85	8.30 ± 0.66	>10

[a]*IC_{50} values for enzymatic inhibition of RalA and RalB; Data displayed are the average of at least three independent replicates ±standard deviation.*

[b]*IC_{50} = compound concentration required to inhibit tumor cell proliferation by 50%; Data displayed are the average of at least three independent replicates ±standard deviation.*

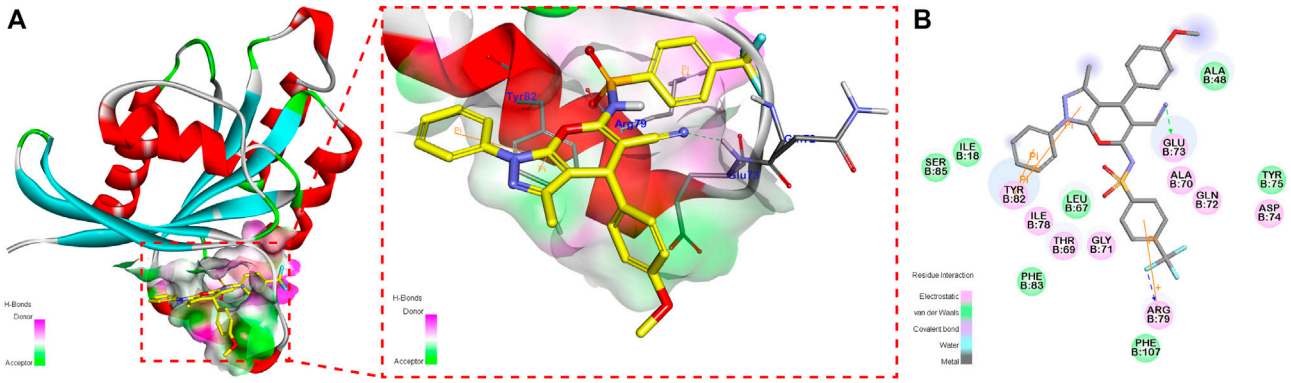

FIGURE 4 | 3D contour **(A)** and 2D contour **(B)** of the binding mode of compound 4p in at the RalA-GDP allosteric site.

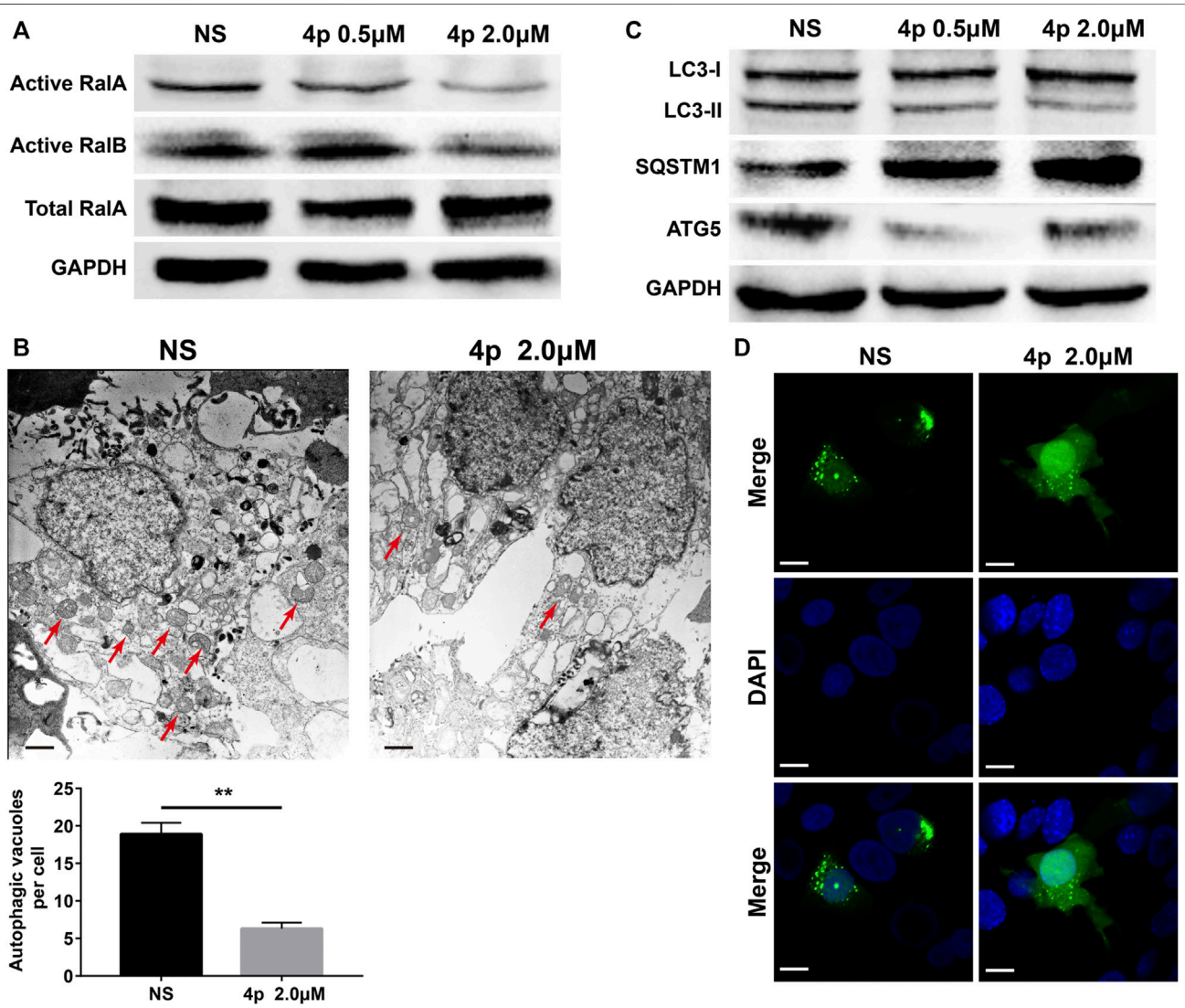

FIGURE 5 | (A) Selective inhibition of **4p** on RalA was observed by the GST pulldown test; **(B)** Transmission electron micrograph of HepG2 cells treated with **4p**, scale bar: 500 nm; **(C)** Western blotting was used to detect the change of the LC3-II/I ratio; **(D)** Formation of autophagosome in GFP-LC3–transfected HepG2 cells induced by 2.0 μM **4p**, scale bar: 6 μm.

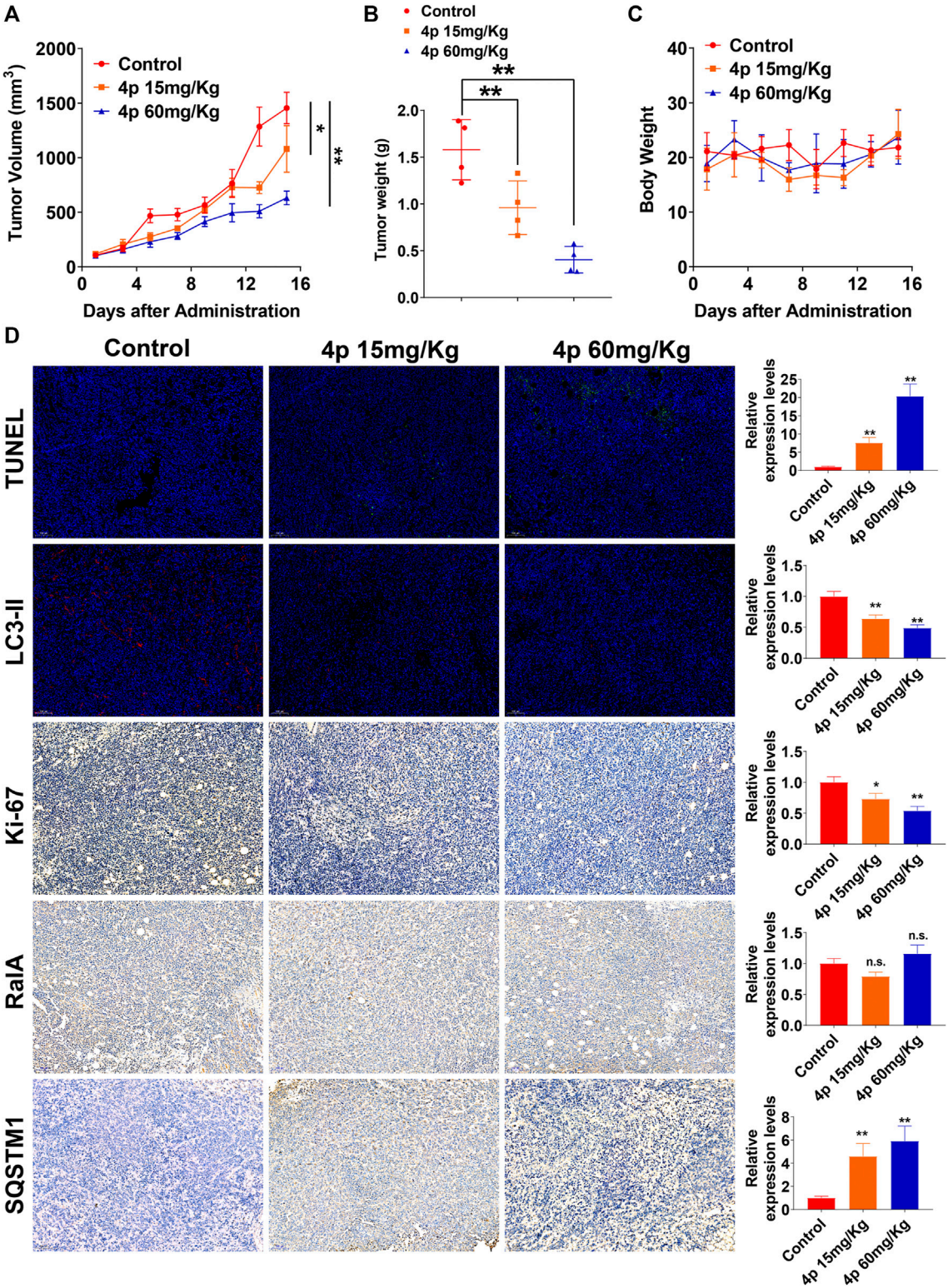

FIGURE 6 | Compound **4p** inhibited tumor growth in a HepG2 xenograft model. **(A)** Tumor volume changes were determined every 2 days after drug administration; **(B)** Tumor weight in each mouse in **(A, C)** The body weight of mice in each group; **(D)** Immunofluorescence and IHC images and analysis of tissue sections stained by TUNEL, Ki-67, RalA, LC3-II, and SQSTM1 in each group, scale bar: 100 μm.

different pyrano [2,3-c]-pyrazole ring–type bioactivities were compared, the remaining RalA/B kinase activity was relatively high for pyran ring substituents with moderate steric hindrance (e.g. benzene rings or halogen-substituted phenyl groups). However, the corresponding HepG2 and Huh7 IC_{50} values were higher than 10 μM. When the 4-substitution of the pyran ring (R^3 substitution) was a 4-trifluoromethyl phenyl or heteroaromatic ring, better activities were observed. Our findings also indicated that the hydrogen atom in the R^1 group was preferred using **4s–4ag**. Any changes at this site, such as halogen, methyl, or methoxyl substitutions led to a loss of RalA/B and HCC cell proliferation inhibitory activities. We found that the p-methoxybenzenesulfonyl group was the R^2 -substituted fragment from compound **4n–4ab** with the highest inhibitory activities against RalA/B and HCC cells. 1.0 μM of **4p** was added before incubation, and only 13 and 22% of RalA and RalB kinase activities were detected, respectively. After compound **4p's** application, its IC_{50} values for HepG2 and Huh7 cells were 2.28 ± 0.23 and 4.31 ± 0.39 μM, respectively.

In **Table 2** we list the IC_{50} values for compounds **4k–4r** for RalA/B and HepG2, Hep3B, Huh-7, and SMMC-7721 HCC cell proliferation. Compound **4p** demonstrated the best RalA and RalB inhibitory activities with IC_{50} values of 0.22 and 0.41 μM, respectively. All eight compounds displayed good to moderately good inhibitory effects on RalA/B and HepG2 cell proliferation. Compounds **4l**, **4m**, and **4p** exhibited potent cellular proliferation inhibitory capacities on the HCC cell lines. In the current study, HepG2 was the most sensitive cell line with IC_{50} values of 6.01, 9.15, and 2.28 μM for compounds **4l**, **4m**, and **4p,** respectively. Therefore, **4p** was selected as the best compound to increase the understanding of its RalA binding and its potential molecular mechanisms against HCC in subsequent experiments.

The 3D contours of **4p** bounded to RalA allosteric sites are shown in **Figure 4**. We observed that the cyano group of **4p** formed a hydrogen bond with the RalA Glu73 residue. The benzene ring at the R^1 position and the pyrazole ring formed a π–π conjugation system with RalA Tyr82 residues, which might strengthen the stable binding. A cation–π interaction between **4p** p-trifluoromethyl benzenesulfonyl fragment and RalA Arg79 residue was also detected.

GST pulldown assays were performed to assess **4p** RalA/B inhibitory capacities. 2.0 μM of compound **4p** significantly suppressed activated RalA and RalB protein expression levels. Only activated RalA was suppressed after incubation with 0.5 μM of compound **4p** (**Figure 5A**). Additionally, total RalA expression was unchanged, which suggested that **4p** potentially interfered with RalBP1's binding to RalA/B.

Several reports have characterized RalA/B potential regulatory roles in autophagy (Zhang et al., 2019; Pang et al., 2020; Zhang et al., 2020). Considering the dual effect of HCC autophagy, we assessed changes in HepG2 cell autophagy levels after the addition of 0.5 or 2.0 μM of **4p**, before incubation. Based on HepG2 cells' TEM images with or without **4p** (**Figure 5B**), autophagy vacuoles per cell decreased in the **4p**-treated group ($p < 0.01$). After **4p** treatments, LC3-II and ATG5 protein levels declined and SQSTM1 increased. These results suggested that **4p** suppressed the autophagy flux in HepG2 cells (**Figure 5C**). In GFP-LC3–transfected HepG2 cells, cytoplasm LC3 fluorescent puncta numbers also declined after **4p** treatments. These results indicated that the **4p** addition suppressed autophagy in HepG2 cells. The *in vivo* antitumor capacities of **4p** were determined on a HepG2 subcutaneous xenograft model. The **4p** intraperitoneal injections were set to 15 mg/kg and 60 mg/kg, according to *in vitro* results. We observed that at a high dosage, the treatment group presented superior tumor growth inhibition (TGI) (63%), compared to the low-dosage group (39%) (**Figure 6A**). Moreover, mean tumor weights in both high- and low-dosage groups notably declined compared to the control ($p < 0.01$) without significant changes in body weights (**Figures 6B,C**). The potential **4p** molecular mechanisms were further validated using immunofluorescence and IHC analyses of tissue sections stained by antibodies against TUNEL, Ki-67, RalA, LC3-II, and SQSTM1. In the **4p** therapy groups, we found that a high **4p** dosage group induced declined suppression levels of Ki-67 positive cells ($p < 0.01$), induced increased TUNEL and SQSTM1 levels, and decreased LC3-II expression ($p < 0.01$). No clear changes in total RalA levels were detected (**Figure 6D**). Therefore, the *in vivo* results were consistent with *in vitro* experiments.

CONCLUSION

Overall, we reported design, synthesis, and biologically based evaluation details of 6-sulfonamide-pyrano[2,3-c]-pyrazole as a novel RalA inhibitor against HCC, both *in vitro* and *in vivo*. Compound **4p** was the most effective compound tested. It significantly inhibited cell proliferation and suppressed autophagy in HepG2 cells. These results can be a solid base for further exploration and development of novel RalA inhibitor candidates.

EXPERIMENTAL

General Information

Reactions were monitored using TLC purchased from a commercial supplier. Melting points were determined using a Reichert Thermovar apparatus. Proton nuclear magnetic resonance (^{1}H NMR, 400 MHz) spectra and carbon nuclear magnetic resonance (^{13}C NMR, 100 MHz) spectra were recorded on a Bruker Avance III NMR spectrometer. TMS (tetramethylsilane) was used as the internal standard and chloroform-d or DMSO-d_6 was used to dissolve samples. Chemical shifts (d) were marked in ppm. ESI-HRMS spectrum data were collected using a Waters TOF-MS instrument (Waters, Milford, MA, United States). Nitrogen was used as the nebulizing gas, desolvation gas, and cone curtain gas. Chemicals received from commercial sources were used without further purification. Column chromatography was performed on silica gel (400–500 mesh) eluting with ethyl acetate and petroleum ether. TLC was performed on glass-backed silica plates. UV light and I_2 were used to visualize products.

Reagents, Antibodies, and Cell Cultures

The antibodies recognizing LC3, p62/SQSTM1, RalA, RalB, and GAPDH were purchased from Proteintech (Wuhan, China). HCC cell lines, including HepG2, Hep3B, Huh-7, and SMMC-7721, were obtained from the Chinese Center for Type Culture Collection (Wuhan, China) and cultured in DMEM (Dulbecco's modified Eagle's medium) with 10% FBS (fetal bovine serum) and streptomycin. Cytotoxicity assays were performed by using the MTT method as previously described.

Biochemical and *In Vitro* Bioassays

The *in vitro* RalA/B bioactivity assays were performed following methods outlined in previous reports. (Yan et al., 2016; Zhang et al., 2018; Walsh et al., 2019; Bum-Erdene et al., 2020). In brief, the lysates of the test compound or vehicle-treated cells were cleared using cold centrifugation, and supernatants were collected. An RalBP1 solution was added to 96-well plates and incubated for 1–2 h, and then the plates were washed thrice using ELISA buffer. Next, cellular lysates were added, and samples were incubated overnight at 4°C. Then, ice-cold mouse anti-FLAG antibody was added, and samples were incubated for one more hour. After subsequent washing with ELISA buffer thrice, the HRP-conjugated anti-mouse antibody was added, and samples were incubated for another hour. Then, the HRP substrate was added. Antigen–antibody reactions were quenched by the addition of sulfuric acid (2 mol/L). Remaining RalA/B was detected by the OD450 values which were collected by using a plate reader. Cell proliferation assays, colony formation assays, apoptosis assays, GST pulldown, and Western blotting were used following methods outlined in our previous reports. (Zhou et al., 2015; Zhang et al., 2016; Yang et al., 2017; He et al., 2019). Autophagy levels and protein immunoblotting were used following the methods mentioned in our previous reports (Pan et al., 2018; Wang et al., 2018; Hao et al., 2019; Wang et al., 2019; Peng et al., 2020). Detailed experimental procedures are described in supporting materials.

Xenograft Models and *In Vivo* Evaluation

Female Balb/c nude mice aged 6–8 weeks were purchased from Beijing Huafukang Co. Ltd. (Beijing, China). Animal-based experiments complied with the guidelines of the Animal Ethics Committee (Sichuan University), and all aspects were approved by the Animal Ethics Committee of West China Hospital of Sichuan University (China). In brief, HepG2 cells were injected subcutaneously in the dorsal flank of Balb/c nude mice ($5*10^5$ cells per mice). Tumor volumes were recorded every 2 days post cancer cell injection. After the therapeutic endpoint, all mice were euthanized, and tumor tissues were stripped, fixed in formalin, embedded in paraffin, and sectioned. The IHC and immunofluorescent staining methods were performed following methods as per our previous research, (Zhang et al., 2019; Pan et al., 2020; Pang et al., 2020; Zhang et al., 2020), and detailed experimental procedures are also described in supporting materials.

General Procedure of Method for the Synthesis of 4a-4ag

To achieve the desired compound 2-benzylidenemalononitrile (**1a**), the following steps were completed. First, a mixture of benzaldehyde (10.0 mmol, 1.06 g), malononitrile (10.0 mmol, 0.66 g), sodium acetate (5.0 mmol, 0.41 g), and acetic acid (10 ml) was stirred overnight at room temperature. TLC was used to monitor whether or not the reaction was complete. When the basic reaction of raw materials was complete, ethyl acetate (30 ml) was added after the stirring was stopped, and glacial acetic acid was neutralized by $NaHCO_3$ until pH values up to 7.0 were observed. The organic layer was separated and concentrated, and the crude product was purified using silica gel column chromatography using a mixed solvent of petroleum ether/ethylacetate (4:1) to give compound **1a**.

To achieve the desired compound 2-benzylidene-malononitrile (**2b**), the following steps were completed. First, a mixture of 4-chlorophenylhydrazine salt (20 mmol, 3.6 g) and ethyl acetoacetate (30 mmol, 3.8 ml) was dissolved in 30 ml of glacial acetic acid and refluxed for 4 h. TLC was used to monitor whether or the reaction was complete. When the basic reaction of raw materials was complete, ethyl acetate (30 ml) was added on when the stirring was stopped. Then, glacial acetic acid was neutralized by $NaHCO_3$ to a pH value = 7. The organic layer was separated and concentrated, and the crude product was purified using silica gel column chromatography using a mixed solvent of petroleum ether/ethylacetate (6:1) to give compound **2b**.

6-Amino-3-methyl-1,4-diphenyl-1,4-dihydropyrano[2,3c]-pyrazole-5-carbonitrile (3a):A mixture of **1a** (5 mmol, 0.77 g), **2a** (5 mmol, 1.04 g) and morpholine (2.5 mmol, 0.22 g) in 10 ml methanol was stirred at 40°C for 30 min. The reaction mixture was filtered and washed with a small amount of ice-cold methanol to give the crude product, and then the crude product was purified using silica gel column chromatography using a mixed solvent of petroleum ether/ethylacetate (5:1) to give the compound **3a**. Yield: 90%, white power solid, m. p. 170–172°C. ^{1}H NMR (400 MHz, $CDCl_3$) δ 7.65 (dt, J = 7.3, 1.4 Hz, 2H), 7.46 (tt, J = 7.5, 1.6 Hz, 2H), 7.39–7.30 (m, 3H), 7.30–7.24 (m, 3H), 4.67 (s, 2H), 4.66 (s, 1H), and 1.89 (s, 3H) ppm.

6-Amino-3-methyl-1-phenyl-4-(p-tolyl)-1,4-dihydropyrano-[2,3-c]-pyrazole-5-carbonitrile (3b): Synthesized with **1b** and **2a** according to the general procedure of **3a**. Yield: 91%, white power solid, m. p. 169–170°C. ^{1}H NMR (400 MHz, $CDCl_3$) δ 7.68–7.63 (m, 2H), 7.45 (td, J = 8.3, 1.7 Hz, 2H), 7.30 (tt, J = 7.4, 1.6 Hz, 1H), 7.16–7.11 (m, 4H), 4.66 (s, 2H), 4.62 (s, 1H), 2.34 (s, 3H), 1.90 (s, 3H) ppm.

6-Amino-4-(3-chlorophenyl)-3-methyl-1-phenyl-1,4-dihydropyrano [2,3-c]-pyrazole-5-carbonitrile (3c): Synthesized with **1c** and **2a** according to the general procedure of **3a**. Yield: 88%, white power solid, m. p. 155–157°C. ^{1}H NMR (400 MHz, DMSO-d_6) δ 7.80–7.78 (m, 2H), 7.49(tt, J = 8.6, 1.9 Hz, 2H), 7.41–7.37 (m, 3H), 7.34–7.30 (m, 3H)), 7.27–7.24 (m, 3H), 4.75 (s, 1H), 1.81 (s, 3H) ppm.

6-Amino-4-(4-bromophenyl)-3-methyl-1-phenyl-1,4-dihydropyrano [2,3-c]-pyrazole-5-carbonitrile (3d): Synthesized with **1d** and **2a** according to the general procedure of **3a**. Yield: 90%, white power solid, m. p. 181–183°C. ^{1}H NMR (400 MHz, $CDCl_3$) δ 7.67–7.62 (m, 2H), 7.51–7.42 (m, 4H), 7.32 (t, J = 7.4 Hz, 1H), 7.14 (dt, J = 8.4, 2.6 Hz, 2H), 4.72 (s, 2H), 4.64 (s, 1H), 1.89 (s, 3H) ppm.

6-Amino-4-(4-fluorophenyl)-3-methyl-1-phenyl-1,4-dihydropyrano [2,3-c]-pyrazole-5-carbonitrile (3e): Synthesized with **1e** and **2a** according to the general procedure of **3a**. Yield: 83%, yellow power solid, m. p. 173–176°C. ^{1}H NMR (400 MHz, DMSO-d_6) δ 7.79 (d, *J* = 8.0 Hz, 2H), 7.49 (t, *J* = 7.8 Hz, 2H), 7.34–7.29 (m, 3H), 7.22–7.15 (m, 4H), 4.73 (s, 1H), 1.79 (s, 3H) ppm.

6-Amino-4-(3-bromophenyl)-3-methyl-1-phenyl-1,4-dihyd ropyrano[2,3-c]-pyrazole-5-carbonitrile (3f): Synthesized with **1f** and **2a** according to the general procedure of **3a**. Yield: 87%, white power solid, m. p. 161–164°C. ^{1}H NMR (400 MHz, $CDCl_3$) δ 7.66–7.63 (m, 2H), 7.47 (tt, *J* = 6.7, 2.0 Hz, 2H), 7.42 (dt, *J* = 6.5, 2.1 Hz, 1H), 7.36–7.30 (m, 2H), 7.23–7.22 (m, 2H), 4.75 (s, 2H), 4.63 (s, 1H), 1.91 (s, 3H) ppm.

6-Amino-4-(3,4-dichlorophenyl)-3-methyl-1-phenyl-1,4-dihydropyrano[2,3-c]-pyrazole-5-carbonitrile (3g): Synthesized with **1g** and **2a** according to the general procedure of **3a**. Yield: 85%, white power solid, m. p. 198–200°C. ^{1}H NMR (400 MHz, $CDCl_3$) δ 7.66–7.63 (m, 2H), 7.49–7.42 (m, 3H), 7.34 (dt, *J* = 7.4, 1.1 Hz, 1H), 7.32 (d, *J* = 2.1 Hz, 1H), 7.13 (dd, *J* = 8.2, 2.1 Hz, 1H), 4.77 (s, 2H), 4.64 (s, 1H), 1.92 (s, 3H) ppm.

6-Amino-4-(4-bromo-2-fluorophenyl)-3-methyl-1-phenyl-1,4-dihydropyrano[2,3-c]-pyrazole-5-carbonitrile (3h): Synthesized with **1h** and **2a** according to the general procedure of **3a**. Yield: 85%, white power solid, m. p. 200–203°C. ^{1}H NMR (400 MHz, DMSO-d_6) δ 7.81–7.75 (m, 2H), 7.56 (dd, *J* = 10.1, 2.0 Hz, 1H), 7.53–7.47 (m, 2H), 7.42 (dd, *J* = 8.3, 1.9 Hz, 1H), 7.37–7.26 (m, 4H), 4.97 (s, 1H), 1.83 (s, 3H) ppm.

6-Amino-4-(4-methoxyphenyl)-3-methyl-1-phenyl-1,4-dihydropyrano[2,3-c]-pyrazole-5-carbonitrile (3i): Synthesized with **1i** and **2a** according to the general procedure of **3a**. Yield: 90%, white power solid, m. p. 176–178°C. ^{1}H NMR (400 MHz, DMSO-d_6) δ 7.82–7.76 (m, 2H), 7.49 (tt, *J* = 8.6, 2.0 Hz, 2H), 7.31 (tt, *J* = 7.4, 1.1 Hz, 2H), 7.18–7.15 (m, 4H), 6.90 (dt, *J* = 8.6, 2.0 Hz, 1H), 4.63 (s, 1H), 3.75 (s, 3H), 1.79 (s, 3H) ppm.

6-Amino-4-(furan-2-yl)-3-methyl-1-phenyl-1,4-dihydropyrano [2,3-c]-pyrazole-5-carbonitrile (3j): Synthesized with **1j** and **2a** according to the general procedure of **3a**. Yield: 60%, yellow power solid, m. p. 225.1–225.5°C. ^{1}H NMR (400 MHz, $CDCl_3$) δ 7.62 (d, *J* = 7.8 Hz, 2H), 7.45 (t, *J* = 7.9 Hz, 2H), 7.37 (d, *J* = 0.9 Hz, 1H), 7.31 (t, *J* = 7.4 Hz, 1H), 6.34 (dd, *J* = 3.0, 1.9 Hz, 1H), 6.23 (d, *J* = 3.2 Hz, 1H), 4.83 (s, 1H), 4.75 (s, 2H), 2.09 (s, 3H) ppm.

6-Amino-3-methyl-1-phenyl-4-(pyridin-3-yl)-1,4-dihydropyrano [2,3-c]-pyrazole-5-carbonitrile (3k): Synthesized with **1k** and **2a** according to the general procedure of **3a**. Yield: 80%, white power solid, m. p. 188.7–189.1°C. ^{1}H NMR (400 MHz, DMSO-d_6) δ 8.55 (d, *J* = 2.0 Hz, 1H), 8.49 (dd, *J* = 4.7, 1.5 Hz, 1H), 7.79 (d, *J* = 7.7 Hz, 2H), 7.66 (dt, *J* = 7.9, 1.8 Hz, 1H), 7.50 (t, *J* = 8.0 Hz, 2H), 7.38 (dd, *J* = 7.8, 4.8 Hz, 1H), 7.33 (t, *J* = 7.4 Hz, 1H), 7.29 (s, *J* = 7.0 Hz, 2H), 4.79 (s, 1H), 1.79 (s, 3H) ppm.

6-Amino-3-methyl-1-phenyl-4-(pyridin-4-yl)-1,4-dihydropyrano [2,3-c]-pyrazole-5-carbonitrile (3l): Synthesized with **1l** and **2a** according to the general procedure of **3a**. Yield: 80%, white power solid, m. p. 192.2–192.6°C. ^{1}H NMR (400 MHz, DMSO-d_6) δ 8.59 (dd, *J* = 4.7, 1.3 Hz, 2H), 7.83–7.77 (m, 2H), 7.52–7.48 (m, 2H), 7.40–7.31 (m, 5H), 4.79 (s, 1H), 1.82 (s, 3H) ppm.

6-Amino-3-methyl-1-phenyl-4-(thiophen-3-yl)-1,4-dihydropyrano [2,3-c]-pyrazole-5-carbonitrile (3m): Synthesized with **1m** and **2a** according to the general procedure of **3a**. Yield: 85%, yellow power solid, m. p. 178.2–178.6°C. ^{1}H NMR (400 MHz, DMSO-d_6) δ 7.81–7.75 (m, 2H), 7.53–7.45 (m, 3H), 7.37 (dd, *J* = 2.9, 1.2 Hz, 1H), 7.31 (t, *J* = 7.4 Hz, 1H), 7.18 (s, 2H), 6.95 (dd, *J* = 5.0, 1.2 Hz, 1H), 4.82 (s, 1H), 1.86 (s, 3H) ppm.

6-Amino-3-methyl-1-phenyl-4-(4-(trifluoromethyl) phenyl)-1,4-dihydropyrano[2,3-c]-pyrazole-5-carbonitrile (3n): Synthesized with **1n** and **2a** according to the general procedure of **3a**. Yield: 85%, white power solid, m. p. 162.9–163.5°C. ^{1}H NMR (400 MHz, DMSO-d_6) δ 7.79 (d, *J* = 7.8 Hz, 2H), 7.73 (d, *J* = 8.1 Hz, 2H), 7.50 (t, *J* = 8.3 Hz, 4H), 7.33 (t, *J* = 7.6 Hz, 3H), 4.85 (s, 1H), 1.79 (s, 3H) ppm.

6-Amino-1-(2-chlorophenyl)-4-(furan-2-yl)-3-methyl-1,4-dihydropyrano[2,3-c]-pyrazole-5-carbonitrile (3o): Synthesized with **1j** and **2b** according to the general procedure of **3a**. Yield: 62%, yellow power solid, m. p. 86.8–87.2°C. ^{1}H NMR (400 MHz, DMSO-d_6) δ 7.70 (dd, *J* = 7.8, 1.5 Hz, 1H), 7.59 (td, *J* = 7.5, 2.2 Hz, 2H), 7.57–7.48 (m, 2H), 7.12 (s, 2H), 6.42 (dd, *J* = 3.1, 1.9 Hz, 1H), 6.27 (d, *J* = 3.1 Hz, 1H), 4.90 (s, 1H), 1.96 (s, 3H) ppm.

6-Amino-1-(2-chlorophenyl)-3-methyl-4-(pyridin-3-yl)-1,4-dihydropyrano[2,3-c]-pyrazole-5-carbonitrile (3p): Synthesized with **1k** and **2b** according to the general procedure of **3a**. Yield: 63%, white power solid, m. p. 165.9–166.4°C. ^{1}H NMR (400 MHz, DMSO-d_6) δ 8.56–8.47 (m, 2H), 7.71 (dd, *J* = 7.7, 1.6 Hz, 1H), 7.68–7.61 (m, 2H), 7.59–7.51 (m, 2H), 7.41 (dd, *J* = 7.8, 4.8 Hz, 1H), 7.15 (s, 2H), 4.80 (s, 1H), 1.78 (s, 3H) ppm.

6-Amino-1-(2-chlorophenyl)-3-methyl-4-(pyridin-4-yl)-1,4-dihydropyrano[2,3-c]-pyrazole-5-carbonitrile (3q): Synthesized with **1l** and **2b** according to the general procedure of **3a**. Yield: 61%, white power solid, m. p. 200.1–200.7°C. ^{1}H NMR (400 MHz, DMSO-d_6) δ 8.57 (dd, *J* = 4.4, 1.5 Hz, 2H), 7.71 (dd, *J* = 7.8, 1.6 Hz, 1H), 7.66 (dd, *J* = 7.3, 2.2 Hz, 1H), 7.59–7.51 (m, 2H), 7.28 (dd, *J* = 4.5, 1.5 Hz, 2H), 7.19 (s, 2H), 4.77 (s, 1H), 1.80 (s, 3H) ppm.

6-Amino-1-(2-chlorophenyl)-3-methyl-4-(thiophen-3-yl)-1,4-dihydropyrano[2,3-c]-pyrazole-5-carbonitrile (3r): Synthesized with **1m** and **2b** according to the general procedure of **3a**. Yield: 65%, yellow power solid, m. p. 167.0–167.5°C. ^{1}H NMR (400 MHz, DMSO-d_6) δ 7.70 (dd, *J* = 7.7, 1.7 Hz, 1H), 7.62 (dd, *J* = 7.2, 2.2 Hz, 1H), 7.58–7.48 (m, 3H), 7.35 (dd, *J* = 2.8, 1.0 Hz, 1H), 7.01 (s, 2H), 6.91 (dd, *J* = 5.0, 1.1 Hz, 1H), 4.83 (s, 1H), 1.85 (s, 3H) ppm.

6-Amino-1-(2-chlorophenyl)-4-(3-methoxyphenyl)-3-methyl-1,4-dihydropyrano[2,3-c]-pyrazole-5-carbonitrile (3s): Synthesized with **1o** and **2b** according to the general procedure of **3a**. Yield: 80%, white power solid, m. p. 170.7–171.2°C. ^{1}H NMR (400 MHz, DMSO-d_6) δ 11.49 (s, 1H), 7.64–7.62 (m, 1H), 7.57–7.42 (m, 3H), 7.28 (t, *J* = 7.9 Hz, 2H), 7.16 (d, *J* = 7.2 Hz, 1H), 6.87 (dd, *J* = 8.2, 2.2 Hz, 1H), 5.85 (d, *J* = 9.2 Hz, 1H), 4.66 (d, *J* = 10.9 Hz, 1H), 3.74 (s, 3H), 2.14 (s, 3H) ppm.

6-Amino-1-(4-chlorophenyl)-3-methyl-4-phenyl-1,4-dihydropyrano [2,3-c]-pyrazole-5-carbonitrile (3t): Synthesized with **1a** and **2c**

according to the general procedure of **3a**. Yield: 80%, white power solid, m. p. 165.9–166.4°C. ^{1}H NMR (400 MHz, DMSO-d_6) δ 7.83 (dt, *J* = 8.9, 3.0 Hz, 2H), 7.53 (dt, *J* = 8.9, 3.2 Hz, 2H), 7.38–7.32 (m, 2H), 7.29–7.19 (m, 5H), 4.68 (s, 1H), 1.78 (s, 3H) ppm.

6-Amino-1-(2-chlorophenyl)-3-methyl-4-phenyl-1,4-dihydropyrano [2,3-c]-pyrazole-5-carbonitrile (3u): Synthesized with **1a** and **2b** according to the general procedure of **3a**. Yield: 75%, white power solid, m. p. 188.9–189.2°C. 1H NMR (400 MHz, DMSO-d_6) δ 11.64 (s, 1H), 7.67–7.56 (m, 3H), 7.51–7.46 (m, 3H) 7.37 (t, *J* = 7.4 Hz, 2H), 7.32–7.28 (m, 1H), 5.8 (d, *J* = 9.4 Hz, 1H), 4.70 (d, *J* = 10.2 Hz, 1H), 2.14 (s, 3H) ppm.

6-Amino-3-methyl-4-phenyl-1-(p-tolyl)-1,4-dihydropyrano-[2,3-c]-pyrazole-5-carbonitrile (3v): Synthesized with **1a** and **2d** according to the general procedure of **3a**. Yield: 90%, white power solid, m. p. 167.0–167.5°C. ^{1}H NMR (400 MHz, DMSO-d_6) δ 7.65 (dt, *J* = 8.5, 2.8 Hz, 2H), 7.35 (tt, *J* = 7.3, 1.0 Hz, 2H), 7.30–7.23 (m, 5H), 7.17 (s, 2H), 4.67 (s, 1H), 2.35 (s, 3H), 1.77 (s, 3H) ppm.

6-Amino-1-(4-methoxyphenyl)-3-methyl-4-phenyl-1,4-dihydropyrano[2,3-c]-pyrazole-5-carbonitrile (3w): Synthesized with **1a** and **2e** according to the general procedure of **3a**. Yield: 88%, white power solid, m. p. 186.2–187,3 °C. ^{1}H NMR (400 MHz, DMSO-d_6) δ 7.65 (dt, *J* = 8.5, 3.5 Hz, 2H), 7.38–7.32 (m, 2H), 7.29–7.23 (m, 3H), 7.14 (s, 2H), 7.06–7.01 (m, 2H), 4.67 (s, 1H), 3.80 (s, 3H), 1.77 (s, 3H) ppm.

6-Amino-1-(4-fluorophenyl)-3-methyl-4-phenyl-1,4-dihydropyrano [2,3-c]-pyrazole -5-carbonitrile (3x): Synthesized with **1a** and **2f** according to the general procedure of **3a**. Yield: 80%, white power solid, m. p. 162.9–163.5°C. ^{1}H NMR (400 MHz, DMSO-d_6) δ 7.84–7.77 (m, 2H), 7.37–7.31 (m, 4H), 7.29–7.24 (m, 3H), 7.19 (s, 2H), 4.68 (s, 1H), 1.77 (s, 3H) ppm.

N-(5-cyano-3-methyl-1,4-diphenyl-1,4-dihydropyrano[2,3-c]-pyrazole-6-yl)-4-methylbenzenesulfonamide (4a): A mixture of **3a** (5 mmol, 1.6 g), 4-methylbenzenesulfonyl chloride (5 mmol, 0.95 g), and N,N-dimethylpyridin-4-amine (DMAP) (5 mmol, 0.61 g) in 30 ml dichloromethane was stirred at room temperature overnight. TLC was used to monitor whether the reaction was complete. When the basic reaction of raw materials was complete, the stirring was stopped, and the reaction mixture was cooled to room temperature. The crude product was purified using silica gel column chromatography using a mixture solvent of petroleum ether/ethyl acetate (8:1) to give **4a**. Yield: 66%, white power solid, m. p. 68.3–69.7°C. ^{1}H NMR (400 MHz, $CDCl_3$) *δ* 7.50–7.42 (m, 4H), 7.41–7.38 (m, 1H), 7.35 (dt, *J* = 8.4, 2.5 Hz, 2H), 7.24–7.18 (m, 3H), 7.17–7.13 (m, 2H), 7.04 (dt, *J* = 7.7, 0.8 Hz, 2H), 4.98 (d, *J* = 9.6 Hz, 1H), 4.85 (d, *J* = 9.6 Hz, 1H), 2.37 (s, 3H), 2.15 (s, 3H) ppm; ^{13}C NMR (100 MHz, $CDCl_3$) *δ* 147.7, 147.2, 140.4, 137.1, 136.3, 130.7 (2C), 129.9, 129.4 (2C), 129.4 (2C), 128.6, 128.5 (2C), 128.0, 127.9 (2C), 123.3 (2C), 114.0, 113.9, 108.3, 40.3, 27.3, 21.7, 14.9 ppm. HRMS (ESI): calculated for $C_{27}H_{22}N_4NaO_3S^+$ [M + Na]$^+$, 505.1305; found 505.1304.

N-(5-cyano-3-methyl-1-phenyl-4-(p-tolyl)-1,4-dihydropyrano [2,3-c]-pyrazol-6-yl)-4-methylbenzenesulfonamide (4b): Synthesized with 3b according to the general procedure of **4a**. Yield: 70%, white power solid, m. p. 74.7–75.0°C. ^{1}H NMR (400 MHz, $CDCl_3$) *δ* 7.39–7.32 (m, 4H), 7.26–7.11 (m, 7H), 7.04 (d, *J* = 8.1 Hz, 2H), 4.96 (d, *J* = 9.7 Hz, 1H), 4.80 (d, *J* = 9.7 Hz, 1H), 2.37 (d, *J* = 1.7 Hz, 6H), 2.16 (s, 3H) ppm; ^{13}C NMR (100 MHz, $CDCl_3$) *δ* 147.7, 147.2, 140.4, 137.9, 137.1, 133.3, 130.7 (2C), 129.9 (2C), 129.9, 129.4 (2C), 128.5 (2C), 128.0, 127.7 (2C), 123.3 (2C), 114.0, 113.9, 108.4, 40.1, 27.3, 21.7, 21.1, 15.0 ppm. HRMS (ESI): calculated for $C_{28}H_{24}N_4NaO_3S^+$ [M + Na]$^+$, 519.1461; found 519.1462.

N-(4-(3-chlorophenyl)-5-cyano-3-methyl-1-phenyl-1,4-dihydropyrano[2,3-c]-pyrazol-6-yl)-4-methylbenzenesulfonamide (4c). Synthesized with **3c** according to the general procedure of **4a**. Yield: 68% white power solid. m. p. 68.4–69.0°C. ^{1}H NMR (400 MHz, $CDCl_3$) *δ* 7.45 (t, *J* = 1.6 Hz, 1H), 7.43–7.37 (m, 3H), 7.35 (dt, *J* = 8.4, 1.6 Hz, 2H), 7.25–7.12 (m, 5H), 7.05 (t, *J* = 7.8 Hz, 2H), 4.99 (d, *J* = 9.7 Hz, 1H), 4.81 (d, *J* = 9.7 Hz, 1H), 2.38 (s, 3H), 2.19 (s, 3H) ppm; ^{13}C NMR (100 MHz, $CDCl_3$) *δ* 148.0, 146.9, 139.9, 137.3, 137.1, 135.2, 130.4, 130.2, 129.9 (2C), 129.0, 128.8 (2C), 128.5 (2C), 128.2, 127.6, 125.9, 123.6 (2C), 112.0, 112.0, 107.0, 41.7, 27.1, 21.7, 14.3 ppm. HRMS (ESI): calculated for $C_{27}H_{21}ClN_4NaO_3S^+$ [M + Na]$^+$, 539.0915; found 539.0916.

N-(4-(4-bromophenyl)-5-cyano-3-methyl-1-phenyl-1,4-dihydropyrano[2,3-c]-pyrazol-6-yl)-4-methylbenzenesulfonamide (4d): Synthesized with **3d** according to the general procedure of **4a**. Yield: 70%, white power solid, m. p. 101.6–102.3°C. ^{1}H NMR (400 MHz, $CDCl_3$) *δ* 7.59 (dt, *J* = 8.5,2.8 Hz, 2H), 7.40–7.30 (m, 4H), 7.24–7.17 (m, 3H), 7.17–7.12 (m, 2H), 7.04 (dt, *J* = 7.8,1.8 Hz, 2H), 4.98 (d, *J* = 9.7 = Hz, 1H), 4.80 (d, *J* = 9.7 Hz, 1H), 2.37 (s, 3H), 2.17 (s, 3H) ppm; ^{13}C NMR (100 MHz, $CDCl_3$) *δ* 148.0, 146.9, 139.9, 137.1, 134.4, 132.4 (2C), 130.1, 129.9 (2C), 129.5 (2C), 128.8 (2C), 128.5 (2C), 127.6, 123.6 (2C), 122.9, 112.1, 112.1, 107.1, 41.7, 27.1, 21.8, 14.3 ppm. HRMS (ESI): calculated for $C_{27}H_{21}BrN_4NaO_3S^+$ [M + Na]$^+$, 583.0410; found 583.0410.

N-(5-cyano-4-(4-fluorophenyl)-3-methyl-1-phenyl-1,4-dihydropyrano[2,3-c]-pyrazol-6-yl)-4-methylbenzenesulfonamide (4e): Synthesized with **3e** according to the general procedure of **4a**. Yield: 70%, white power solid, m. p. 113.0–113.5°C. ^{1}H NMR (400 MHz, $CDCl_3$) *δ* 7.51–7.45 (m, 2H), 7.33 (dt, *J* = 8.4, 2.2 Hz, 2H), 7.24–7.18 (m, 3H), 7.17–7.11 (m, 4H), 7.05 (dt, *J* = 7.8, 0.8 Hz, 2H), 4.98 (d, *J* = 9.7 Hz, 1H), 4.82 (d, *J* = 9.7 Hz, 1H), 2.38 (s, 3H), 2.16 (s, 3H) ppm; ^{13}C NMR (100 MHz, $CDCl_3$) *δ* 162.1, 148.0, 146.9, 139.8, 137.1, 131.3, 130.2, 129.9 (2C), 129.7 (2C), 128.8 (2C), 128.5 (2C), 127.6, 123.7 (2C), 116.2 (2C), 112.2, 112.2, 107.4, 41.6, 27.4, 21.7, 14.3 ppm. HRMS (ESI): calculated for $C_{27}H_{21}FN_4NaO_3S^+$ [M + Na]$^+$, 523.1211; found 523.1216.

N-(4-(3-bromophenyl)-5-cyano-3-methyl-1-phenyl-1,4-dihydropyrano[2,3-c]-pyrazol-6-yl)-4-methylbenzenesulfonamide (4f): Synthesized with **3f** according to the general procedure of **4a.** Yield:75%, white power solid, m. p. 68.4–69.5°C. ^{1}H NMR (400 MHz, $CDCl_3$) *δ* 7.60 (t, *J* = 1.9 Hz, 1H), 7.54 (ddd, *J* = 8.0, 1.9, 1.0 Hz, 1H), 7.47 (ddd, *J* = 8.8, 1.9, 0.7 Hz, 1H), 7.38–7.30 (m, 3H), 7.24–7.18 (m, 3H), 7.18–7.12 (m, 2H), 7.05 (dt, *J* = 7.8, 0.8 Hz, 2H), 4.99 (d, *J* = 9.8 Hz, 1H), 4.80 (d, *J* = 9.8 Hz, 1H), 2.38 (s, 3H), 2.20 (s, 3H) ppm; ^{13}C NMR (100 MHz, $CDCl_3$) *δ* 148.0, 146.9, 139.9, 137.6, 137.1, 131.9, 131.1, 130.6, 130.1, 129.9 (2C), 128.8 (2C), 128.5 (2C), 127.6, 126.3, 123.6 (2C), 123.3, 112.0, 112.0, 107.0, 41.7, 27.1, 21.7, 14.3 ppm. HRMS (ESI): calculated for $C_{27}H_{21}BrN_4NaO_3S^+$ [M + Na]$^+$, 583.0410; found 583.0410.

N-(5-cyano-4-(3,4-dichlorophenyl)-3-methyl-1-phenyl-1,4-dihydropyrano[2,3-c]-pyrazol-6-yl)-4-methylbenzenesulfonamide (4g): Synthesized with **3g** according to the general procedure of **4a**. Yield: 69%, white power solid, m. p. 100.9–101.3°C. ^{1}H NMR (400 MHz, $CDCl_3$) δ 7.57 (d, J = 2.3 Hz, 1H), 7.55 (d, J = 8.4 Hz, 1H), 7.37 (dd, J = 8.4, 2.3 Hz, 1H), 7.33 (dt, J = 8.4, 2.3 Hz, 2H), 7.25–7.18 (m, 3H), 7.17–7.13 (m, 2H), 7.05 (dt, J = 7.7, 0.8 Hz, 2H), 4.99 (d, J = 9.9 Hz, 1H), 4.78 (d, J = 9.9 Hz, 1H), 2.38 (s, 3H), 2.21 (s, 3H) ppm; ^{13}C NMR (100 MHz, $CDCl_3$) δ 147.9, 147.0, 139.9, 137.0, 135.5, 133.5, 133.2, 131.1, 130.1, 130.1, 129.9 (2C), 128.9 (2C), 128.5 (2C), 127.7, 127.1, 123.7 (2C), 111.9, 111.8, 106.7, 41.4, 27.1, 21.8, 14.3 ppm. HRMS (ESI): calculated for $C_{27}H_{20}Cl_2N_4NaO_3S^+$ $[M + Na]^+$, 573.0525; found 573.0523.

N-(4-(4-bromo-2-fluorophenyl)-5-cyano-3-methyl-1-phen-yl-1,4-dihydropyrano[2,3-c]-pyrazol-6-yl)-4-methylbenzenesulfonamide (4h): Synthesized with **3h** according to the general procedure of **4a**. Yield: 66%, white power solid, m. p. 73.6–77.4°C. ^{1}H NMR (400 MHz, $CDCl_3$) δ 7.52 (t, J = 8.1 Hz, 1H), 7.45 (dd, J = 8.5, 1.9 Hz, 1H), 7.35 (dd, J = 9.8, 1.9 Hz, 1H), 7.30 (dt, J = 8.4, 2.2 Hz, 2H), 7.22–7.14 (m, 3H), 7.12–7.06 (m, 2H), 7.02 (dt, J = 8.5, 2.0 Hz, 2H), 5.24 (d, J = 10.9 Hz, 1H), 5.03 (d, J = 10.9 Hz, 1H), 2.37 (s, 3H), 2.32 (s, 3H) ppm; ^{13}C NMR (100 MHz, $CDCl_3$) δ 160.0, 148.4, 146.9, 139.9, 137.0, 130.0, 129.9 (2C), 129.5, 128.8 (2C), 128.5 (2C), 128.2, 127.5, 123.6 (2C), 123.3, 122.0, 120.0, 111.9, 111.9, 105.9, 35.5, 26.4, 21.7, 13.8 ppm. HRMS (ESI): calculated for $C_{27}H_{20}BrFN_4NaO_3S^+$ $[M + Na]^+$, 601.0316; found 601.0311.

N-(5-cyano-4-(4-methoxyphenyl)-3-methyl-1-phenyl-1,4-dihydropyrano[2,3-c]-pyrazol-6-yl)-4-methylbenzenesulfonamide (4i): Synthesized with **3i** according to the general procedure of **4a**. Yield: 80%, white power solid, m. p. 145.2–146.0°C. ^{1}H NMR (400 MHz, $CDCl_3$) δ 7.40 (dt, J = 8.6, 3.4 Hz, 2H), 7.34 (dt, J = 8.4, 2.2 Hz, 2H), 7.24–7.18 (m, 3H), 7.17–7.13 (m, 2H), 7.04 (dt, J = 7.7, 1.6 Hz, 2H), 6.96 (dt, J = 8.8, 3.2 Hz, 2H), 4.95 (d, J = 9.7 Hz, 1H), 4.78 (d, J = 9.7 Hz, 1H), 3.83 (s, 3H), 2.37 (s, 3H), 2.16 (s, 3H) ppm; ^{13}C NMR (100 MHz, $CDCl_3$) δ 159.4, 147.8, 147.2, 140.3, 137.1, 130.8 (2C), 129.9, 129.5 (2C), 129.2 (2C), 128.6 (2C), 128.2, 128.1, 123.3 (2C), 114.80 (2C), 114.1, 114.0, 108.6, 55.7, 39.8, 27.6, 21.7, 15.0 ppm. HRMS (ESI): calculated for $C_{28}H_{24}N_4NaO_4S^+$ $[M + Na]^+$, 535.1410; found 535.1417.

N-(5-cyano-4-(furan-2-yl)-3-methyl-1-phenyl-1,4-dihydropyrano [2,3-c]-pyrazol-6-yl)-4-methylbenzenesulfonamide (4j): Synthesized with **3j** according to the general procedure of **4a**. Yield: 55%, yellow power solid, m. p. 153.8–154.3°C. ^{1}H NMR (400 MHz, $CDCl_3$) δ 7.49 (d, J = 1.4 Hz, 1H), 7.35 (d, J = 8.4 Hz, 2H), 7.26 (s, 1H), 7.24–7.18 (m, 3H), 7.4–7.12 (m, 2H), 7.01 (d, J = 8.2 Hz, 2H), 6.52 (d, J = 3.3 Hz, 1H), 6.45 (dd, J = 3.3, 1.9 Hz, 1H), 4.98 (d, J = 8.9 Hz, 1H), 4.84 (d, J = 8.9 Hz, 1H), 2.29 (s, 3H) ppm; ^{13}C NMR (100 MHz, DMSO-d_6) δ 149.1, 147.7, 147.5, 144.1, 140.5, 136.9, 130.7 (2C), 129.7, 129.4 (2C), 128.5 (2C), 128.0, 123.2 (2C), 113.7, 113.4, 111.4, 109.3, 106.0, 35.2, 27.2, 21.7, 14.4 ppm. HRMS (ESI): calculated for $C_{25}H_{20}N_4NaO_4S^+$ $[M + Na]^+$, 495.1097; found 495.1094.

N-(5-cyano-3-methyl-1-phenyl-4-(pyridin-3-yl)-1,4-dihydropyrano [2,3-c]-pyrazol-6-yl)-4-methylbenzenesulfonamide (4k): Synthesized with **3k** according to the general procedure of **4a**. Yield: 60%, white power solid, m. p. 136.3–137.0°C. ^{1}H NMR (400 MHz, DMSO-d_6) δ 7.98 (s, 1H), 7.87 (dd, J = 8.7, 1.0 Hz, 1H), 7.58 (d, J = 8.2 Hz, 2H), 7.52–7.38 (m, 5H), 7.34 (d, J = 8.0 Hz, 3H), 7.12 (d, J = 7.8 Hz, 3H), 2.36 (s, 3H), 2.29 (s, 3H) ppm; ^{13}C NMR (100 MHz, DMSO-d_6) δ 161.6, 151.9, 148.9, 147.7, 146.0, 145.0, 144.3, 142.4, 141.8, 138.2, 129.9 (2C), 129.4, 128.6 (2C), 126.0 (2C), 125.3 (2C), 123.4, 119.8, 118.9, 62.6, 21.4, 21.2, 13.5 ppm. HRMS (ESI): calculated for $C_{26}H_{21}N_5NaO_3S^+$ $[M + Na]^+$, 506.1257; found 506.1272.

N-(5-cyano-3-methyl-1-phenyl-4-(pyridin-4-yl)-1,4-dihydropyrano [2,3-c]-pyrazol-6-yl)-4-methylbenzenesulfonamide (4l): Synthesized with **3l** according to the general procedure of **4a**. Yield: 60%, white power solid, m. p. 100.5–101.1°C. ^{1}H NMR (400 MHz, DMSO-d_6) δ 8.70 (dd, J = 4.7, 1.4 Hz, 2H), 7.48 (d, J = 5.8 Hz, 2H), 7.43 (d, J = 8.4 Hz, 2H), 7.36–7.28 (m, 3H), 7.18 (d, J = 8.1 Hz, 2H), 7.14–7.07 (m, 2H), 5.95 (d, J = 8.9 Hz, 1H), 5.09 (d, J = 8.9 Hz, 1H), 2.34 (s, 3H), 2.03 (s, 3H) ppm; ^{13}C NMR (100 MHz, DMSO-d_6) δ 150.3, 147.7, 147.4, 145.7, 140.9, 136.9, 130.7 (2C), 129.7, 129.5 (2C), 128.6 (2C), 128.1, 123.3 (2C), 123.2 (2C), 113.7, 113.6, 107.0, 100.0, 39.5, 27.0, 21.7, 14.9 ppm. HRMS (ESI): calculated for $C_{26}H_{21}N_5NaO_3S^+$ $[M + Na]^+$, 506.1257; found 506.1253.

N-(5-cyano-3-methyl-1-phenyl-4-(thiophen-3-yl)-1,4-dihydropyrano [2,3-c]-pyrazol-6-yl)-4-methylbenzenesulfonamide (4m): Synthesized with **3m** according to the general procedure of **4a**. Yield: 65%, yellow power solid, m. p. 67.8–68.4°C. ^{1}H NMR (400 MHz, DMSO-d_6) δ 7.68 (dd, J = 5.0, 2.9 Hz, 1H), 7.61–7.57 (m, 1H), 7.43 (d, J = 8.4 Hz, 2H), 7.36–7.26 (m, 3H), 7.18 (d, J = 8.1 Hz, 2H), 7.15–7.05 (m, 3H), 5.82 (d, J = 8.9 Hz, 1H), 4.94 (d, J = 8.9 Hz, 1H), 2.34 (s, 3H), 2.00 (s, 3H) ppm; ^{13}C NMR (100 MHz, DMSO-d_6) δ 147.7, 147.4, 140.4, 137.0, 136.9, 130.7 (2C), 129.8, 129.4 (2C), 128.5 (2C), 128.1, 128.0, 127.8, 123.5, 123.2 (2C), 114.0, 113.8, 108.0, 36.8, 28.0, 21.7, 14.6 ppm. HRMS (ESI): calculated for $C_{25}H_{20}N_4NaO_3S_2^+$ $[M + Na]^+$, 511.0869; found 511.0868.

N-(5-cyano-3-methyl-1-phenyl-4-(4-(trifluoromethyl)phenyl)-1,4-dihydropyrano[2,3-c]-pyrazol-6-yl)-4-methylbenzenesulfonamide (4n): Synthesized with **3n** according to the general procedure of **4a**. Yield: 73%, white power solid, m. p. 109.3–110.2°C. ^{1}H NMR (400 MHz, DMSO-d_6) δ 7.89 (d, J = 8.3 Hz, 2H), 7.70 (d, J = 8.2 Hz, 2H), 7.44 (d, J = 8.3 Hz, 2H), 7.36–7.30 (m, 3H), 7.18 (d, J = 8.2 Hz, 2H), 7.11 (dd, J = 7.6, 1.9 Hz, 2H), 5.97 (d, J = 9.3 Hz, 1H), 5.12 (d, J = 9.3 Hz, 1H), 2.34 (s, 3H), 2.07 (s, 3H) ppm; ^{13}C NMR (100 MHz, DMSO-d_6) δ 148.0, 147.1, 140.0, 139.4, 137.7, 137.0, 131.0, 130.0 (2C), 129.0 (2C), 128.5 (2C), 128.5 (2C), 127.7, 126.3 (2C), 123.8, 123.7 (2C), 112.1, 112.1, 107.0, 41.9, 27.1, 21.9, 14.4 ppm. HRMS (ESI): calculated for $C_{28}H_{21}F_3N_4NaO_3S^+$ $[M + Na]^+$, 573.1179; found 573.1176.

N-(5-cyano-3-methyl-1-phenyl-4-(4-(trifluoromethyl)phenyl)-1,4-dihydropyrano[2,3-c]-pyrazol-6-yl)thiophene-2-sulfonamide (4o): Synthesized with **3n** and 4-thiophene-2-sulfonyl chloride according to the general procedure of **4a**. Yield: 54%, white power solid, m. p. 55.9–56.7°C. ^{1}H NMR (400 MHz, DMSO-d_6) δ 8.12 (dd, J = 5.0, 1.3 Hz, 1H), 7.89 (d, J = 8.3 Hz, 2H), 7.70 (d, J = 8.2 Hz, 2H), 7.55 (dd, J = 3.9, 1.3 Hz, 1H), 7.41–7.34 (m, 3H), 7.24–7.18 (m, 2H), 7.04 (dd, J = 4.9, 4.0 Hz, 1H), 5.98 (d, J = 9.2 Hz, 1H), 5.17 (d, J = 9.2 Hz, 1H), 2.07 (s, 3H) ppm; ^{13}C NMR (100 MHz, DMSO-d_6) δ 148.1, 139.9, 139.2, 137.3, 137.0, 136.9, 131.9, 131.0, 129.2 (2C), 128.4 (2C), 128.2, 128.0, 126.3 (2C), 123.8, 123.6 (2C), 112.0, 111.9, 107.1, 41.7, 27.0, 14.5 ppm. HRMS

(ESI): calculated for $C_{25}H_{17}F_3N_4NaO_3S_2^+$ [M + Na]$^+$, 565.0586; found 565.0572.

N-(5-cyano-3-methyl-1-phenyl-4-(4-(trifluoromethyl) phenyl)-1,4-dihydropyrano[2,3-c]-pyrazol-6-yl)-4-methoxybenzenesulfonamide (4p): Synthesized with **3n** and 4-methoxybenzenesulfonyl chloride according to the general procedure of **4a**. Yield: 76%, white power solid, m. p. 72.0–72.7°C. ^{1}H NMR (400 MHz, DMSO-d_6) δ 7.89 (d, J = 8.3 Hz, 2H), 7.71 (d, J = 8.2 Hz, 2H), 7.47 (d, J = 9.0 Hz, 2H), 7.36–7.28 (m, 3H), 7.14 (dd, J = 7.8, 1.8 Hz, 2H), 6.86 (d, J = 9.0 Hz, 2H), 5.98 (d, J = 9.3 Hz, 1H), 5.15 (d, J = 9.3 Hz, 1H), 3.83 (s, 3H), 2.07 (s, 3H) ppm; ^{13}C NMR (100 MHz, DMSO-d_6) δ 165.1, 148.0, 140.2, 139.4, 137.1, 137.1, 131.0, 130.9 (2C), 129.0 (2C), 128.5 (2C), 127.8, 126.3 (2C), 123.8, 123.6 (2C), 114.6 (2C), 112.2, 112.1, 107.0, 55.9, 41.9, 27.1, 14.4 ppm. HRMS (ESI): calculated for $C_{28}H_{21}F_3N_4NaO_4S^+$ [M + Na]$^+$, 589.1128; found 589.1129.

N-(5-cyano-3-methyl-1-phenyl-4-(4-(trifluoromethyl)phenyl)-1,4-dihydropyrano[2,3-c]-pyrazol-6-yl)-4-(trifluoromethyl)-benzenesulfonamide (4q): Synthesized with **3n** and 4-(trifluoromethyl) benzenesulfonyl chloride according to the general procedure of **4a**. Yield: 62%, yellow power solid, m. p. 153.7–154.1°C. ^{1}H NMR (400 MHz, DMSO-d_6) δ 7.86 (d, J = 8.3 Hz, 2H), 7.83–7.76 (m, 5H), 7.73–7.70 (m, 4H), 7.48–7.44 (m, 2H), 6.00 (d, J = 11.3 Hz, 1H), 4.94 (d, J = 11.3 Hz, 1H), 2.24 (s, 3H) ppm; ^{13}C NMR (100 MHz, DMSO-d_6) δ 148.2, 139.7, 139.1, 136.8, 136.7, 136.7, 131.1, 129.3 (2C), 129.1 (2C), 128.3 (2C), 128.2, 126.4 (4C), 123.8, 123.6 (2C), 120.9, 111.9, 111.9, 107.3, 41.8, 27.1, 14.5 ppm. HRMS (ESI): calculated for $C_{28}H_{18}F_6N_4NaO_3S^+$ [M + Na]$^+$, 627.0896; found 627.0880.

N-(5-cyano-3-methyl-1-phenyl-4-(4-(trifluoromethyl)phenyl)-1,4-dihydropyrano[2,3-c]-pyrazol-6-yl)-2,4-difluorobenzenesulfonamide (4r): Synthesized with **3n** and 2,4-difluorobenzenesulfonyl chloride according to the general procedure of **4a**. Yield: 60%, white power solid, m. p. 65.8–66.5°C. ^{1}H NMR (400 MHz, DMSO-d_6) δ 7.89 (d, J = 8.3 Hz, 2H), 7.71 (d, J = 8.3 Hz, 2H), 7.67–7.61 (m, 1H), 7.37–7.27 (m, 4H), 7.20–7.11 (m, 3H), 5.96 (d, J = 9.0 Hz, 1H), 5.21 (d, J = 9.0 Hz, 1H), 2.05 (s, 3H) ppm; ^{13}C NMR (100 MHz, DMSO-d_6) δ 167.7, 160.5, 148.3, 139.5, 139.1, 136.8, 133.0, 132.9, 130.0, 129.2 (2C), 128.3 (2C), 128.2, 126.4 (2C), 123.8 (1C), 123.6 (2C), 112.6, 112.0, 111.8, 107.4, 106.4, 41.7, 27.0, 14.4 ppm. HRMS (ESI): calculated for $C_{27}H_{17}F_5N_4NaO_3S^+$ [M + Na]$^+$, 595.0834; found 595.0822.

N-(1-(2-chlorophenyl)-5-cyano-4-(furan-2-yl)-3-methyl-1,4-dihydropyrano[2,3-c]-pyrazol-6-yl)-4-methylbenzenesulfonamide (4s): Synthesized with **3o** according to the general procedure of **4a**. Yield: 50%, yellow power solid, m. p. 62.5–63.9°C. ^{1}H NMR (400 MHz, DMSO-d_6) δ 7.77 (d, J = 1.2 Hz, 1H), 7.50 (dd, J = 15.6, 7.7, 1.4 Hz, 2H), 7.45 (dt, J = 8.4, 1.5 Hz, 2H), 7.34 (td, J = 7.7, 1.5 Hz, 1H), 7.30 (d, J = 8.2 Hz, 2H), 7.08 (d, J = 7.1 Hz, 1H), 6.55 (dd, J = 3.2, 1.9 Hz, 1H), 6.48 (d, J = 3.2 Hz, 1H), 5.69 (d, J = 9.1 Hz, 1H), 4.88 (d, J = 9.1 Hz, 1H), 2.40 (s, 3H), 2.12 (s, 3H) ppm; ^{13}C NMR (100 MHz, DMSO-d_6) δ 149.0, 148.1, 147.6, 144.0, 141.8, 134.3, 131.4, 131.0 (2C), 130.5, 130.5, 130.4, 129.7, 128.4, 128.3 (2C), 113.5, 113.3, 111.4, 109.3, 105.2, 35.1, 27.2, 21.7, 14.3 ppm. HRMS (ESI): calculated for $C_{25}H_{19}ClN_4NaO_4S^+$ [M + Na]$^+$, 529.0708; found 529.0703.

N-(1-(2-chlorophenyl)-5-cyano-3-methyl-4-(pyridin-3-yl)-1,4-dihydropyrano[2,3-c]-pyrazol-6-yl)-4-methylbenzenesulfonamide (4t): Synthesized with **3p** according to the general procedure of **4a**. Yield: 51%, white power solid, m. p. 195.8–196.3°C. ^{1}H NMR (400 MHz, DMSO-d_6) δ 8.66 (d, J = 1.6 Hz, 1H), 8.62 (d, J = 4.6 Hz, 1H), 7.87 (d, J = 8.1 Hz, 1H), 7.54 (dd, J = 7.9, 4.8 Hz, 1H), 7.51–7.42 (m, 4H), 7.37–7.32 (m, 1H), 7.29 (d, J = 8.3 Hz, 2H), 7.14 (d, J = 7.7 Hz, 1H), 5.89 (d, J = 9.8 Hz, 1H), 5.05 (d, J = 9.8 Hz, 1H), 2.39 (s, 3H), 2.10 (s, 3H) ppm; ^{13}C NMR (100 MHz, DMSO-d_6) δ 149.6, 149.1, 147.9, 147.6, 141.7, 135.9, 134.4, 132.3, 131.4, 131.0 (2C), 130.4 (2C), 129.8, 128.5, 128.5, 128.3 (2C), 124.3, 113.6, 113.5, 106.6, 38.2, 27.3, 21.7, 14.9 ppm. HRMS (ESI): calculated for $C_{26}H_{20}ClN_5NaO_3S^+$ [M + Na]$^+$, 540.0868; found 540.0870.

N-(1-(2-chlorophenyl)-5-cyano-3-methyl-4-(pyridin-4-yl)-1,4-dihydropyrano[2,3-c]-pyrazol-6-yl)-4-methylbenzenesulfonamide (4u): Synthesized with **3q** according to the general procedure of **4a**. Yield: 53%, white power solid, m. p. 79.0–80.0°C. 1H NMR (400 MHz, DMSO-d_6) δ 8.69 (dd, J = 4.6, 1.5 Hz, 2H), 7.52–7.42 (m, 6H), 7.37–7.31 (m, 1H), 7.29 (d, J = 8.2 Hz, 2H), 7.11 (dd, J = 7.9, 1.3 Hz, 1H), 5.90 (d, J = 9.2 Hz, 1H), 5.03 (d, J = 9.2 Hz, 1H), 2.39 (s, 3H), 2.04 (s, 3H) ppm; ^{13}C NMR (100 MHz, DMSO-d_6) δ 150.5 (2C), 148.0, 147.6, 145.3, 142.0, 134.3, 131.4, 131.0 (2C), 130.4, 130.4, 130.4, 129.7, 128.4, 128.3 (2C), 123.1 (2C), 113.5, 113.5, 106.2, 39.3, 26.9, 21.7, 14.9 ppm. HRMS (ESI): calculated for $C_{26}H_{20}ClN_5NaO_3S^+$ [M + Na]$^+$, 540.0868; found 540.0867.

N-(1-(2-chlorophenyl)-5-cyano-3-methyl-4-(thiophen-3-yl)-1,4-dihydropyrano[2,3-c]-pyrazol-6-yl)-4-methylbenzenesulfonamide (4v): Synthesized with **3r** according to the general procedure of **4a**. Yield: 57%, yellow power solid, m. p. 67.4–68.8°C. ^{1}H NMR (400 MHz, DMSO-d_6) δ 7.67 (dd, J = 5.0, 2.9 Hz, 1H), 7.59–7.55 (m, 1H), 7.52–7.44 (m, 4H), 7.33 (td, J = 7.7, 1.6 Hz, 1H), 7.29 (d, J = 8.2 Hz, 2H), 7.11–7.05 (m, 2H), 5.79 (d, J = 9.3 Hz, 1H), 4.88 (d, J = 9.4 Hz, 1H), 2.40 (s, 3H), 2.00 (s, 3H) ppm; ^{13}C NMR (100 MHz, DMSO-d_6) δ 148.0, 147.6, 141.5, 136.8, 134.4, 131.3, 131.0 (2C), 130.4 (2C), 129.7, 128.4, 128.3 (2C), 128.2, 128.0, 127.8, 123.5, 113.9, 113.6, 107.1, 36.7, 27.9, 21.7, 14.6 ppm. HRMS (ESI): calculated for $C_{25}H_{19}ClN_4NaO_3S_2^+$ [M + Na]$^+$, 545.0479; found 545.0485.

N-(1-(2-chlorophenyl)-5-cyano-4-(3-methoxyphenyl)-3-methyl-1,4-dihydropyrano[2,3-c]-pyrazol-6-yl)-4-methylbenzenesulfonamide (4w): Synthesized with **3s** according to the general procedure of **4a**. Yield: 68%, white power solid, m. p. 66.4–67.7°C. ^{1}H NMR (400 MHz, $CDCl_3$) δ 7.36–7.27 (m, 7H), 7.15 (d, J = 8.2 Hz, 2H), 7.06 (d, J = 7.8 Hz, 1H), 7.05 (t, J = 1.8 Hz, 1H), 6.91 (dd, J = 8.3, 2.2 Hz, 1H), 4.93 (d, J = 10.0 Hz, 1H), 4.69 (d, J = 10.0 Hz, 1H), 3.82 (s, 3H), 2.42 (s, 3H), 2.13 (s, 3H) ppm; ^{13}C NMR (100 MHz, $CDCl_3$) δ 160.2, 148.8, 146.6, 140.6, 136.9, 134.8, 131.9, 131.0, 130.2, 130.2, 130.1, 130.1 (2C), 129.8, 128.0 (2C), 127.3, 120.3, 114.6, 113.5, 112.3, 112.0, 106.7, 5.4, 42.4, 27.1, 21.8, 14.1 ppm. HRMS (ESI): calculated for $C_{28}H_{23}ClN_4NaO_4S^+$ [M + Na]$^+$, 569.1021; found 569.1022.

N-(1-(2-chlorophenyl)-5-cyano-4-(3-methoxyphenyl)-3-methyl-1,4-dihydropyrano[2,3-c]-pyrazol-6-yl)benzenesulfonamide (4x). Synthesized with **3s** and benzenesulfonyl chloride according to the general procedure of **4a**. Yield: 70%, white power solid, m. p. 66.0–67.5°C. ^{1}H NMR (400 MHz, $CDCl_3$) δ 7.63 (t, J = 7.4 Hz, 1H), 7.49–7.44 (m, 2H), 7.41–7.26 (m, 7H), 7.05 (dd, J = 13.9, 4.9 Hz, 2H), 7.07 (d, J = 7.6 Hz, 1H), 7.03 (t, J = 2.0 Hz, 1H), 4.92 (d, J = 10.1 Hz,

1H), 4.70 (d, *J* = 10.1 Hz, 1H), 2.14 (s, 3H), 1.56 (s, 3H) ppm; ^{13}C NMR (100 MHz, DMSO-d_6) *δ* 159.9, 148.0, 141.4, 137.7, 136.4, 134.4, 133.9, 133.7, 131.6, 130.6, 130.5 (2C), 129.9, 128.6, 128.2 (2C), 128.1, 120.1, 114.2, 113.8, 113.6, 107.4, 65.7, 55.6, 46.4, 27.2, 14.8 ppm. HRMS (ESI): calculated for $C_{27}H_{21}ClN_4NaO_4S^+$ [M + Na]$^+$, 555.0864; found 555.0869.

N-(1-(2-chlorophenyl)-5-cyano-4-(3-methoxyphenyl)-3-methyl-1,4-dihydropyrano[2,3-c]-pyrazol-6-yl)-4-methoxybenzenesulfonamide (4y): Synthesized with **3s** and 4-methoxybenzenesulfonyl chloride according to the general procedure of **4a**. Yield: 64%, white power solid, m. p. 67.6–68.2°C. ^{1}H NMR (400 MHz, DMSO-d_6) *δ* 7.53–7.45 (m, 4H), 7.42–7.34 (m, 2H), 7.19–7.16 (m, 1H), 7.07–6.93 (m, 5H), 5.86 (d, *J* = 10.1 Hz, 1H), 4.86 (d, *J* = 10.2 Hz, 1H), 3.87 (s, 3H), 3.78 (s, 3H), 2.05 (s, 3H) ppm; ^{13}C NMR (100 MHz, DMSO-d_6) *δ* 165.3, 159.9, 147.9, 141.7, 137.7, 134.5, 131.5, 130.7 (2C), 130.5, 130.4, 129.9, 128.5, 124.3, 120.1, 115.8 (2C), 115.1, 114.2, 113.9, 113.7, 113.6, 107.3, 65.7, 56.6, 55.6, 27.2, 14.8 ppm. HRMS (ESI): calculated for $C_{28}H_{23}N_4NaO_5S^+$ [M + Na]$^+$, 585.0970; found 585.0973.

N-(1-(2-chlorophenyl)-5-cyano-4-(3-methoxyphenyl)-3-methyl-1,4-dihydropyrano[2,3-c]-pyrazol-6-yl)-2-nitrobenzenesulfonamide (4z): Synthesized with **3s** and 2-nitrobenzenesulfonyl chloride according to the general procedure of **4a**. Yield: 68%, white power solid. m. p. 72.6–73.7°C. ^{1}H NMR (400 MHz, $CDCl_3$) *δ* 7.83 (dd, *J* = 7.9, 1.2 Hz, 1H), 7.79 (td, *J* = 7.1, 1.4 Hz, 1H), 7.79 (td, *J* = 7.9, 1.3 Hz, 1H), 7.51 (dd, *J* = 7.9, 1.0 Hz, 1H), 7.36 (t, *J* = 8.0 Hz, 1H), 7.31 (d, *J* = 7.1 Hz, 1H), 7.26–7.17 (m, 3H), 7.07 (d, *J* = 7.5 Hz, 1H), 6.99 (t, *J* = 1.9 Hz, 1H), 6.92 (dd, *J* = 8.2, 2.2 Hz, 1H), 4.82 (d, *J* = 10.3 Hz, 1H), 4.72 (d, *J* = 10.3 Hz, 1H), 3.82 (s, 3H), 2.18 (s, 3H) ppm; ^{13}C NMR (100 MHz, DMSO-d_6) *δ* 159.9, 148.1, 147.5, 141.3, 138.2, 137.5, 134.3, 134.1, 131.8, 131.6, 131.0, 130.5, 130.4, 130.3, 129.6, 128.4, 126.4, 126.3, 122.8, 120.0, 114.1, 113.8, 113.6, 107.7, 55.6, 27.3, 14.9 ppm. HRMS (ESI): calculated for $C_{27}H_{20}N_5NaO_6S^+$ [M + Na]$^+$, 600.0715; found 600.0720.

N-(1-(2-chlorophenyl)-5-cyano-4-(3-methoxyphenyl)-3-methyl-1,4-dihydropyrano[2,3-c]-pyrazol-6-yl)-3-nitrobenzenesulfonamide (4aa): Synthesized with **3s** and 3-nitrobenzenesulfonyl chloride according to the general procedure of **4a**. Yield: 73%, white power solid, m. p. 78.9–79.2°C. ^{1}H NMR (400 MHz, $CDCl_3$) *δ* 8.44 (ddd, *J* = 8.2, 2.1, 0.9 Hz, 1H), 8.14 (t, *J* = 1.8 Hz, 1H), 7.97 (dt, *J* = 7.9, 1.0 Hz, 1H), 7.67 (t, *J* = 8.1 Hz, 1H), 7.38 (t, *J* = 8.0 Hz, 1H), 7.32 (d, *J* = 9.0 Hz, 1H), 7.26–7.18 (m, 3H), 7.05 (d, *J* = 7.7 Hz, 1H), 7.00 (t, *J* = 2.0 Hz, 1H), 6.93 (dd, *J* = 8.2, 2.2 Hz, 1H), 4.83 (d, *J* = 10.1 Hz, 1H), 4.76 (d, *J* = 10.1 Hz, 1H), 3.83 (s, 3H), 2.16 (s, 3H) ppm; ^{13}C NMR (100 MHz, DMSO-d_6) *δ* 159.9, 148.2, 141.0, 137.5, 135.2, 134.2, 134.1, 132.8, 132.4, 131.6, 130.7, 130.5, 130.4, 130.2, 129.8, 128.7, 123.8, 122.8, 120.5, 120.1, 114.2, 113.8, 113.7, 107.6, 55.6, 27.4, 14.8 ppm. HRMS (ESI): calculated for $C_{27}H_{20}N_5NaO_6S^+$ [M + Na]$^+$, 600.0715; found 600.0717.

N-(1-(2-chlorophenyl)-5-cyano-4-(3-methoxyphenyl)-3-methyl-1,4-dihydropyrano[2,3-c]-pyrazol-6-yl)-4-nitrobenzenesulfonamide (4ab). Synthesized with **3s** and 4-nitrobenzenesulfonyl chloride according to the general procedure of **4a**. Yield: 60%, white power solid, m. p. 142.5–143.6°C. ^{1}H NMR (400 MHz, $CDCl_3$) *δ* 8.16 (dt, J = 8.8, 2.2 Hz, 2H), 7.67 (dt, *J* = 8.8, 2.2 Hz, 2H), 7.37 (t, *J* = 8.0 Hz, 1H), 7.32 (dd, *J* = 7.2, 2.0 Hz, 1H), 7.28–7.24 (m, 3H), 7.04 (d, *J* = 7.7 Hz, 1H), 6.99 (t, *J* = 2.0 Hz, 1H), 6.93 (dd, *J* = 8.2, 2.3 Hz, 1H), 4.82 (d, *J* = 10.0 Hz, 1H), 4.75 (d, *J* = 10.0 Hz, 1H), 3.83 (s, 3H), 2.16 (s, 3H) ppm; ^{13}C NMR (100 MHz, DMSO-d_6) *δ* 159.9, 151.6, 148.2, 138.8, 137.4, 134.3, 131.7, 130.6, 130.5, 130.4, 130.0 (2C), 129.9, 128.6, 127.4, 125.5 (2C), 123.8, 120.1, 114.3, 113.8, 113.7, 113.6, 107.6, 55.6, 27.4, 14.9 ppm. HRMS (ESI): calculated for $C_{27}H_{21}N_5O_6S^+$ [M + H]$^+$, 578.0896; found 578.0885.

N-(1-(4-chlorophenyl)-5-cyano-3-methyl-4-phenyl-1,4-dihydropyrano[2,3-c]-pyrazol-6-yl)-4-methylbenzenesulfonamide (4ac): Synthesized with **3t** according to the general procedure of **4a**. Compound (**4ac**) was synthesized from compound (**3t**) and 4-methylbenzenesulfonyl chloride, in a manner similar to (**4a**). Yield: 75%, white power solid. m. p. 181.4–181.7°C. ^{1}H NMR (400 MHz, $CDCl_3$) *δ* 7.49–7.36 (m, 7H), 7.19–7.07 (m, 6H), 4.95 (d, *J* = 9.6 Hz, 1H), 4.82 (d, *J* = 9.6 Hz, 1H), 2.43 (s, 3H), 2.15 (s, 3H) ppm; ^{13}C NMR (100 MHz, $CDCl_3$) *δ* 148.5, 147.2, 140.1, 135.6, 135.2, 133.4, 130.7, 129.9 (2C), 129.2 (2C), 128.9 (2C), 128.7, 128.4 (2C), 127.8 (2C), 124.7 (2C), 112.2, 112.2, 108.1, 42.0, 27.2, 21.8, 14.3 ppm. HRMS (ESI): calculated for $C_{27}H_{21}ClN_4NaO_3S^+$ [M + Na]$^+$, 539.0915; found 539.0914.

N-(1-(2-chlorophenyl)-5-cyano-3-methyl-4-phenyl-1,4-dihydropyrano[2,3-c]-pyrazol-6-yl)-4-methylbenzenesulfonamide (4ad). Synthesized with **3u** according to the general procedure of **4a**. Yield: 60%, white power solid, m. p. 77.4–78.0°C. ^{1}H NMR (400 MHz, $CDCl_3$) *δ* 7.50–7.41 (m, 4H), 7.41–7.33 (m, 3H), 7.32–7.29 (m, 2H), 7.16 (d, *J* = 8.1 Hz, 2H), 4.93 (d, *J* = 9.7 Hz, 1H), 4.74 (d, *J* = 9.6 Hz, 1H), 2.43 (s, 3H), 2.10 (s, 3H) ppm; ^{13}C NMR (100 MHz, $CDCl_3$) *δ* 148.8, 146.6, 140.7, 135.4, 134.4, 131.8, 131.0, 130.2, 130.1, 130.1 (2C), 129.7, 129.2 (2C), 128.6, 128.1 (2C), 127.9 (2C), 127.3, 112.3, 112.2, 106.9, 42.2, 27.1, 21.8, 14.2 ppm. HRMS (ESI): calculated for $C_{27}H_{21}ClN_4NaO_3S^+$ [M + Na]$^+$, 539.0915; found 539.0916.

N-(5-cyano-3-methyl-4-phenyl-1-(p-tolyl)-1,4-dihydro-pyrano[2,3-c]-pyrazol-6-yl)-4-methylbenzenesulfonamide (4ae). Synthesized with **3v** according to the general procedure of **4a**. Yield: 70%, white power solid. m. p. 142.5–143.0°C. ^{1}H NMR (400 MHz, $CDCl_3$) *δ* 7.50–7.42 (m, 4H), 7.40–7.33 (m, 3H), 7.07–6.97 (m, 6H), 4.97 (d, *J* = 9.6 Hz, 1H), 4.82 (d, *J* = 9.6 Hz, 1H), 2.39 (s, 3H), 2.34 (s, 3H), 2.14 (s, 3H) ppm; ^{13}C NMR (100 MHz, $CDCl_3$) *δ* 147.9, 147.6, 141.7, 136.3, 134.5, 131.5, 131.1 (2C), 130.7, 130.6, 130.5, 129.9, 129.4 (2C), 128.6, 128.5, 128.3 (2C), 128.0 (2C), 113.9, 113.8, 107.5, 40.6, 27.3, 21.8, 21.7, 14.9 ppm. HRMS (ESI): calculated for $C_{28}H_{24}N_4NaO_3S^+$ [M + Na]$^+$, 519.1461; found 519.1461.

N-(5-cyano-1-(4-methoxyphenyl)-3-methyl-4-phenyl-1,4-dihydropyrano[2,3-c]-pyrazol-6-yl)-4-methylbenzenesulfonamide (4af): Synthesized with **3w** according to the general procedure of **4a**. Yield: 70%, white power solid, m. p. 69.0–70.4°C. ^{1}H NMR (400 MHz, $CDCl_3$) *δ* 7.50–7.42 (m, 4H), 7.41–7.35 (m, 3H), 7.11–7.03 (m, 4H), 6.70 (dt, *J* = 8.9,3.4 Hz, 2H), 4.96 (d, *J* = 9.7 Hz, 1H), 4.81 (d, *J* = 9.7 Hz, 1H), 3.81 (s, 3H), 2.40 (s, 3H), 2.14 (s, 3H) ppm; ^{13}C NMR (100 MHz, $CDCl_3$) *δ* 147.7, 147.0, 140.5, 137.8, 136.5, 134.7, 130.7 (2C), 130.3, 129.9 (2C), 129.5 (2C), 128.6, 128.6 (2C), 127.9 (2C), 123.3 (2C), 114.0, 113.9, 108.1, 40.5, 27.4, 21.8, 21.1, 14.9 ppm. HRMS (ESI): calculated for $C_{28}H_{24}N_4NaO_4S^+$ [M + Na]$^+$, 535.1410; found 535.1412.

N-(5-cyano-1-(4-fluorophenyl)-3-methyl-4-phenyl-1,4-dihydropyrano[2,3-c]-pyrazol-6-yl)-4-methylbenzenesulfonamide (4ag): Synthesized with **3x** according to the general procedure of **4a**. Yield: 68%, white power solid, m. p. 138.6–139.3°C. ^{1}H NMR (400 MHz, $CDCl_3$) δ 7.50–7.37 (m, 7H), 7.17–7.10 (m, 4H), 6.93–6.86 (m, 2H), 4.95 (d, J = 9.6 Hz, 1H), 4.82 (d, J = 9.6 Hz, 1H), 2.41 (s, 3H), 2.14 (s, 3H) ppm; ^{13}C NMR (100 MHz, $CDCl_3$) δ 161.7 (1C), 148.2, 147.1, 134.0, 135.3, 133.3 (1C), 130.6, 129.9 (2C), 129.2 (2C), 128.7, 128.4 (2C), 127.8 (2C), 125.5 (2C), 115.7 (2C), 112.3, 112.2, 107.7, 42.0, 27.2, 21.7, 14.3 ppm. HRMS (ESI): calculated for $C_{27}H_{21}FN_4NaO_3S^+$ $[M + Na]^+$, 523.1211; found 523.1210.

DATA AVAILABILITY STATEMENT

The original contributions presented in the study are included in the article/**Supplementary Material**; further inquiries can be directed to the corresponding authors.

ETHICS STATEMENT

The animal study was reviewed and approved by the Animal Ethics Committee of West China Hospital of Sichuan University.

AUTHOR CONTRIBUTIONS

All synthetic research and data analysis were carried out by YW and MH. Biological assays were carried out by YW, MH, XL, and JC. The experiment design and manuscript preparation were performed by YW, QJ, CP, GH, and WH. All experimental research was carried out in the laboratory of GH and WH. All authors have approved the submitted manuscript.

FUNDING

This research was supported by grants from the National Natural Science Foundation (Nos. 21772131, 81773890, and 82073997), the China Postdoctoral Science Foundation, the Fundamental Research Funds of Science & Technology Department of Sichuan Province (Grant Nos. 2019YFSY0004, 2017JY0226, and 2020YFH0036), and Project First-Class Disciplines Development supported by Chengdu University of Traditional Chinese Medicine (Grant No. CZYJC1902).

SUPPLEMENTARY MATERIAL

The Supplementary Material for this article can be found online at: https://www.frontiersin.org/articles/10.3389/fchem.2021.700956/full#supplementary-material

REFERENCES

Alvarado, Y., and Giles, F. J. (2007). Ras as a Therapeutic Target in Hematologic Malignancies. *Expert Opin. Emerging Drugs* 12 (2), 271–284. PubMed PMID: WOS:000247826100008. doi:10.1517/14728214.12.2.271

Bum-Erdene, K., Liu, D., Gonzalez-Gutierrez, G., Ghozayel, M. K., Xu, D., and Meroueh, S. O. (2020). Small-molecule Covalent Bond Formation at Tyrosine Creates a Binding Site and Inhibits Activation of Ral GTPases. *Proc. Natl. Acad. Sci. USA* 117 (13), 7131–7139. PubMed PMID: WOS:000523188100031. doi:10.1073/pnas.1913654117

Chen, F.-Y., Li, X., Zhu, H.-P., and Huang, W. (2020). Regulation of the Ras-Related Signaling Pathway by Small Molecules Containing an Indole Core Scaffold: A Potential Antitumor Therapy. *Front. Pharmacol.* 11, 280, 2020 . Epub 2020/04/02PubMed PMID: 32231571; PubMed Central PMCID: PMCPMC7082308. doi:10.3389/fphar.2020.00280

Ezzeldin, M., Borrego-Diaz, E., Taha, M., Esfandyari, T., Wise, A. L., Peng, W., et al. (2014). RalA Signaling Pathway as a Therapeutic Target in Hepatocellular Carcinoma (HCC). *Mol. Oncol.* 8 (5), 1043–1053. PubMed PMID: WOS:000339774900014. doi:10.1016/j.molonc.2014.03.020

Gray, J. L., Delft, F., and Brennan, P. E. (2020). Targeting the Small GTPase Superfamily through Their Regulatory Proteins. *Angew. Chem. Int. Ed.* 59 (16), 6342–6366. PubMed PMID: WOS:000523764400004. doi:10.1002/anie.201900585

Guichard, C., Amaddeo, G., Imbeaud, S., Ladeiro, Y., Pelletier, L., Maad, I. B., et al. (2012). Integrated Analysis of Somatic Mutations and Focal Copy-Number Changes Identifies Key Genes and Pathways in Hepatocellular Carcinoma. *Nat. Genet.* 44 (6), 694–698. PubMed PMID: WOS:000304551100018. doi:10.1038/ng.2256

Hamada, M., Miki, T., Iwai, S., Shimizu, H., and Yura, Y. (2011). Involvement of RhoA and RalB in Geranylgeranyltransferase I Inhibitor-Mediated Inhibition of Proliferation and Migration of Human Oral Squamous Cell Carcinoma Cells. *Cancer Chemother. Pharmacol.* 68 (3), 559–569. PubMed PMID: WOS:000294345400002. doi:10.1007/s00280-010-1520-9

Hao, D., Wen, X., Liu, L., Wang, L., Zhou, X., Li, Y., et al. (2019). Sanshool Improves UVB-Induced Skin Photodamage by Targeting JAK2/STAT3-dependent Autophagy. *Cell Death Dis* 10, 10. PubMed PMID: WOS:000456089100008. doi:10.1038/s41419-018-1261-y

He, X. H., Ji, Y. L., Peng, C., and Han, B. (2019). Organocatalytic Asymmetric Synthesis of Cyclic Compounds Bearing a Trifluoromethylated Stereogenic Center: Recent Developments. *Adv. Synth. Catal.* 361 (9), 1923–1957. doi:10.1002/adsc.201801647

Hobbs, G. A., Der, C. J., and Rossman, K. L. (2016). RAS Isoforms and Mutations in Cancer at a Glance. *J. Cel Sci.* 129 (7), 1287–1292. PubMed PMID: WOS:000374949100001. doi:10.1242/jcs.182873

Jacobson, K. A., Merighi, S., Varani, K., Borea, P. A., Baraldi, S., Aghazadeh Tabrizi, M., et al. (2018). A3Adenosine Receptors as Modulators of Inflammation: From Medicinal Chemistry to Therapy. *Med. Res. Rev.* 38 (4), 1031–1072. Epub 2017/07/07PubMed PMID: 28682469; PubMed Central PMCID: PMCPMC5756520. doi:10.1002/med.21456

Jiang, Y., Sverdlov, M. S., Toth, P. T., Huang, L. S., Du, G., Liu, Y., et al. (2016). Phosphatidic Acid Produced by RalA-Activated PLD2 Stimulates Caveolae-Mediated Endocytosis and Trafficking in Endothelial Cells. *J. Biol. Chem.* 291 (39), 20729–20738. PubMed PMID: WOS:000384574800034. doi:10.1074/jbc.M116.752485

Klose, M., Duvall, L. B., Li, W., Liang, X., Ren, C., Steinbach, J. H., et al. (2016). Functional PDF Signaling in the Drosophila Circadian Neural Circuit Is Gated by Ral A-dependent Modulation. *Neuron* 90 (4), 781–794. PubMed PMID: WOS:000376255600012. doi:10.1016/j.neuron.2016.04.002

Lim, S. M., Westover, K. D., Ficarro, S. B., Harrison, R. A., Choi, H. G., Pacold, M. E., et al. (2014). Therapeutic Targeting of Oncogenic K-Ras by a Covalent Catalytic Site Inhibitor. *Angew. Chem. Int. Ed.* 53 (1), 199–204. PubMed PMID: WOS:000328714900026. doi:10.1002/anie.201307387

Lindsay, C. R., and Blackhall, F. H. (2019). Direct Ras G12C Inhibitors: Crossing the rubicon. *Br. J. Cancer* 121 (3), 197–198. Epub 2019/06/27PubMed PMID: 31239544; PubMed Central PMCID: PMC6738074. doi:10.1038/s41416-019-0499-1

Lito, P., Solomon, M., Li, L.-S., Hansen, R., and Rosen, N. (2016). Allele-specific Inhibitors Inactivate Mutant KRAS G12C by a Trapping Mechanism. *Science* 351 (6273), 604–608. PubMed PMID: WOS:000369291600041. doi:10.1126/science.aad6204

Ostrem, J. M., Peters, U., Sos, M. L., Wells, J. A., and Shokat, K. M. (2013). K-ras (K-Ras(G12C) Inhibitors Allosterically Control GTP Affinity and Effector

Interactions. *Nature* 503 (7477), 548–551. PubMed PMID: WOS: 000327464200048. doi:10.1038/nature12796

Paludetto, M. N., Puisset, F., Chatelut, E., and Arellano, C. (2019). Identifying the Reactive Metabolites of Tyrosine Kinase Inhibitors in a Comprehensive Approach: Implications for Drug-drug Interactions and Hepatotoxicity. *Med. Res. Rev.* 39 (6), 2105–2152. Epub 2019/05/22PubMed PMID: 31111528. doi:10.1002/med.21577

Pan, Z., Chen, Y., Liu, J., Jiang, Q., Yang, S., Guo, L., et al. (2018). Design, Synthesis, and Biological Evaluation of polo-like Kinase 1/eukaryotic Elongation Factor 2 Kinase (PLK1/EEF2K) Dual Inhibitors for Regulating Breast Cancer Cells Apoptosis and Autophagy. *Eur. J. Med. Chem.* 144, 517–528. PubMed PMID: WOS:000425198100038. doi:10.1016/j.ejmech.2017.12.046

Pan, Z., Li, X., Wang, Y., Jiang, Q., Jiang, L., Zhang, M., et al. (2020). Discovery of Thieno[2,3-D]pyrimidine-Based Hydroxamic Acid Derivatives as Bromodomain-Containing Protein 4/Histone Deacetylase Dual Inhibitors Induce Autophagic Cell Death in Colorectal Carcinoma Cells. *J. Med. Chem.* 63 (7), 3678–3700. PubMed PMID: WOS:000526405300018. doi:10.1021/acs.jmedchem.9b02178

Pang, H., Wang, N., Chai, J., Wang, X., Zhang, Y., Bi, Z., et al. (2020). Discovery of Novel TNNI3K Inhibitor Suppresses Pyroptosis and Apoptosis in Murine Myocardial Infarction Injury. *Eur. J. Med. Chem.* 197, 112314. PubMed PMID: WOS:000533524000006. doi:10.1016/j.ejmech.2020.112314

Peng, F., Zhang, N., Wang, C., Wang, X., Huang, W., Peng, C., et al. (2020). Aconitine Induces Cardiomyocyte Damage by Mitigating BNIP3-dependent Mitophagy and the TNFα-NLRP3 Signalling axis. *Cell Prolif* 53 (1), 53. PubMed PMID: WOS:000492669400001. doi:10.1111/cpr.12701

Saha, S., and Giri, T. K. (2019). Breaking the Barrier of Cancer through Papaya Extract and Their Formulation. *Acamc* 19 (13), 1577–1587. PubMed PMID: WOS:000502339400002. doi:10.2174/1871520619666190722160955

Siegel, R. L., Miller, K. D., and Jemal, A. (2019). Cancer Statistics, 2019. *CA A. Cancer J. Clin.* 69 (1), 7–34. Epub 2019/01/09PubMed PMID: 30620402. doi:10.3322/caac.21551

Suzuki, S., Yonesaka, K., Teramura, T., Takehara, T., Kato, R., Sakai, H., et al. (2021). KRAS Inhibitor-Resistance in MET-Amplified KRASG12C Non-small Cell Lung Cancer Induced by RAS- and Non-RAS-mediated Cell Signaling Mechanisms. *Clin. Cancer Res.* 7, 856, 2021 . Epub 2021/08/09PubMed PMID: 34365406. doi:10.1158/1078-0432.CCR-21-0856

Tracy, K., Velentzas, P. D., and Baehrecke, E. H. (2016). Ral GTP Ase and the Exocyst Regulate Autophagy in a Tissue-specific Manner. *EMBO Rep.* 17 (1), 110–121. PubMed PMID: WOS:000369962300007. doi:10.15252/embr.201541283

Walsh, T. G., Wersäll, A., and Poole, A. W. (2019). Characterisation of the Ral GTPase Inhibitor RBC8 in Human and Mouse Platelets. *Cell Signal.* 59, 34–40. PubMed PMID: WOS:000468251000004. doi:10.1016/j.cellsig.2019.03.015

Wang, X., Wu, F., Li, G., Zhang, N., Song, X., Zheng, Y., et al. (2018). Lipid-modified Cell-Penetrating Peptide-Based Self-Assembly Micelles for Co-delivery of Narciclasine and siULK1 in Hepatocellular Carcinoma Therapy. *Acta Biomater.* 74, 414–429. PubMed PMID: WOS:000437998200032. doi:10.1016/j.actbio.2018.05.030

Wang, Y., Wen, X., Hao, D., Zhou, M., Li, X., He, G., et al. (2019). Insights into Autophagy Machinery in Cells Related to Skin Diseases and Strategies for Therapeutic Modulation. *Biomed. Pharmacother.* 113, 108775. PubMed PMID: WOS:000462864800052. doi:10.1016/j.biopha.2019.108775

Xiong, Y.-j., Song, Y.-z., Zhu, Y., Zuo, W.-q., Zhao, Y.-f., Shen, X., et al. (2020). Neuroprotective Effects of Olanzapine against Rotenone-Induced Toxicity in PC12 Cells. *Acta Pharmacol. Sin* 41 (4), 508–515. PubMed PMID: WOS: 000517740600004. doi:10.1038/s41401-020-0378-6

Xue, B., Lei, M., Shi, K., Wang, M., Hao, Y., Xiao, Y., et al. (2019). Intratumoral Injection of Norcantharidin-Loaded Poly(D,L-lactide)-b-Poly(ethylene glycol)-b-Poly(D,L-lactide) Thermosensitive Hydrogel for the Treatment of Primary Hepatocellular Carcinoma. *J. Biomed. Nanotechnol* 15 (10), 2025–2044. Epub 2019/08/30PubMed PMID: 31462369. doi:10.1166/jbn.2019.2822

Yan, C., Theodorescu, D., Miller, B., Kumar, A., Kumar, V., Ross, D., et al. (2016). Synthesis of Novel Ral Inhibitors: An *In Vitro* and *In Vivo* Study. *Bioorg. Med. Chem. Lett.* 26 (23), 5815–5818. PubMed PMID: WOS:000389519100038. doi:10.1016/j.bmcl.2016.10.021

Yan, C., and Theodorescu, D. (2018). RAL GTPases: Biology and Potential as Therapeutic Targets in Cancer. *Pharmacol. Rev.* 70 (1), 1–11. PubMed PMID: WOS:000419220700001. doi:10.1124/pr.117.014415

Yang, M.-C., Peng, C., Huang, H., Yang, L., He, X.-H., Huang, W., et al. (2017). Organocatalytic Asymmetric Synthesis of Spiro-oxindole Piperidine Derivatives that Reduce Cancer Cell Proliferation by Inhibiting MDM2-P53 Interaction. *Org. Lett.* 19 (24), 6752–6755. PubMed PMID: WOS: 000418392400074. doi:10.1021/acs.orglett.7b03516

Yu, M., Zeng, M., Pan, Z., Wu, F., Guo, L., and He, G. (2020). Discovery of Novel Akt1 Inhibitor Induces Autophagy Associated Death in Hepatocellular Carcinoma Cells. *Eur. J. Med. Chem.* 189, 112076. Epub 2020/02/03PubMed PMID: 32007668. doi:10.1016/j.ejmech.2020.112076

Zhang, N., Huang, Y., Wu, F., Zhao, Y., Li, X., Shen, P., et al. (2016). Codelivery of a miR-124 Mimic and Obatoclax by Cholesterol-Penetratin Micelles Simultaneously Induces Apoptosis and Inhibits Autophagic Flux in Breast Cancer *In Vitro* and *In Vivo*. *Mol. Pharmaceutics* 13 (7), 2466–2483. PubMed PMID: WOS:000379455800032. doi:10.1021/acs.molpharmaceut.6b00211

Zhang, N., Peng, F., Wang, Y., Yang, L., Wu, F., Wang, X., et al. (2020). Shikonin Induces Colorectal Carcinoma Cells Apoptosis and Autophagy by Targeting Galectin-1/JNK Signaling axis. *Int. J. Biol. Sci.* 16 (1), 147–161. PubMed PMID: WOS:000499624000012. doi:10.7150/ijbs.36955

Zhang, N., Zhong, Z., Wang, Y., Yang, L., Wu, F., Peng, C., et al. (2019). Competing Endogenous Network Analysis Identifies lncRNA Meg3 Activates Inflammatory Damage in UVB Induced Murine Skin Lesion by Sponging miR-93-5p/epiregulin axis. *Aging* 11 (22), 10664–10683. PubMed PMID: WOS: 000499683800046. doi:10.18632/aging.102483

Zhang, Y., Wang, C., Huang, W., Haruehanroengra, P., Peng, C., Sheng, J., et al. (2018). Application of Organocatalysis in Bioorganometallic Chemistry: Asymmetric Synthesis of Multifunctionalized Spirocyclic Pyrazolone-Ferrocene Hybrids as Novel RalA Inhibitors. *Org. Chem. Front.* 5 (14), 2229–2233. PubMed PMID: WOS:000438245300014. doi:10.1039/c8qo00422f

Zhao, Q., Peng, C., Huang, H., Liu, S.-J., Zhong, Y.-J., Huang, W., et al. (2018). Asymmetric Synthesis of Tetrahydroisoquinoline-Fused Spirooxindoles as Ras-GTP Inhibitors that Inhibit colon Adenocarcinoma Cell Proliferation and Invasion. *Chem. Commun.* 54 (60), 8359–8362. PubMed PMID: WOS: 000439702200014. doi:10.1039/c8cc04732d

Zheng, M., Zhang, X., Guo, S., Zhang, X., Min, C., Cheon, S. H., et al. (2016). Agonist-induced Changes in RalA Activities Allows the Prediction of the Endocytosis of G Protein-Coupled Receptors. *Biochim. Biophys. Acta (Bba) - Mol. Cel Res.* 1863 (1), 77–90. PubMed PMID: WOS:000366068400009. doi:10.1016/j.bbamcr.2015.10.007

Zhongqi, F., Xiaodong, S., Yuguo, C., and Guoyue, L. (2019). Can Combined Therapy Benefit Immune Checkpoint Blockade Response in Hepatocellular Carcinoma? *Acamc* 19 (2), 222–228. PubMed PMID: WOS:000469924800011. doi:10.2174/1871520618666181114112431

Zhou, F., Shang, W., Yu, X., and Tian, J. (2018). Glypican-3: A Promising Biomarker for Hepatocellular Carcinoma Diagnosis and Treatment. *Med. Res. Rev.* 38 (2), 741–767. Epub 2017/06/18PubMed PMID: 28621802. doi:10.1002/med.21455

Zhou, R., Wu, Q., Guo, M., Huang, W., He, X., Yang, L., et al. (2015). Organocatalytic cascade Reaction for the Asymmetric Synthesis of Novel Chroman-Fused Spirooxindoles that Potently Inhibit Cancer Cell Proliferation. *Chem. Commun.* 51 (66), 13113–13116. PubMed PMID: WOS:000359151100013. doi:10.1039/c5cc04968g

Conflict of Interest: The authors declare that the research was conducted in the absence of any commercial or financial relationships that could be construed as a potential conflict of interest.

Publisher's Note: All claims expressed in this article are solely those of the authors and do not necessarily represent those of their affiliated organizations, or those of the publisher, the editors, and the reviewers. Any product that may be evaluated in this article, or claim that may be made by its manufacturer, is not guaranteed or endorsed by the publisher.

frontiers in Chemistry

ORIGINAL RESEARCH
published: 21 December 2021
doi: 10.3389/fchem.2021.759714

Mathematical Modeling of a Supramolecular Assembly for Pyrophosphate Sensing

Fereshteh Emami[1], Hamid Abdollahi[2], Tsyuoshi Minami[3], Ben Peco[1] and Sean Reliford[1]*

[1]Department of Chemistry and Physics, Southeastern Louisiana University, Hammond, LA, United States, [2]Department of Chemistry, Institute for Advanced Studies in Basic Sciences, Zanjan, Iran, [3]Institute of Industrial Science, The University of Tokyo, Meguro-ku, Japan

The power of sensing molecules is often characterized in part by determining their thermodynamic/dynamic properties, in particular the binding constant of a guest to a host. In many studies, traditional nonlinear regression analysis has been used to determine the binding constants, which cannot be applied to complex systems and limits the reliability of such calculations. Supramolecular sensor systems include many interactions that make such chemical systems complicated. The challenges in creating sensing molecules can be significantly decreased through the availability of detailed mathematical models of such systems. Here, we propose uncovering accurate thermodynamic parameters of chemical reactions using better-defined mathematical modeling-fitting analysis is the key to understanding molecular assemblies and developing new bio/sensing agents. The supramolecular example we chose for this investigation is a self-assembled sensor consists of a synthesized receptor, DPA (DPA = dipicolylamine)-appended phenylboronic acid (**1**) in combination with Zn^{2+}(**1**.Zn) that forms various assemblies with a fluorophore like alizarin red S (ARS). The self-assemblies can detect multi-phosphates like pyrophosphate (PPi) in aqueous solutions. We developed a mathematical model for the simultaneous quantitative analysis of twenty-seven intertwined interactions and reactions between the sensor (**1**.Zn-ARS) and the target (PPi) for the first time, relying on the Newton-Raphson algorithm. Through analyzing simulated potentiometric titration data, we describe the concurrent determination of thermodynamic parameters of the different guest-host bindings. Various values of temperatures, initial concentrations, and starting pHs were considered to predict the required measurement conditions for thermodynamic studies. Accordingly, we determined the species concentrations of different host-guest bindings in a generalized way. This way, the binding capabilities of a set of species can be quantitatively examined to systematically measure the power of the sensing system. This study shows analyzing supramolecular self-assemblies with solid mathematical models has a high potential for a better understanding of molecular interactions within complex chemical networks and developing new sensors with better sensing effects for bio-purposes.

Keywords: mathematical modeling, supramolecules, molecular sensing, pyrophosphate, intertwined equilibria, thermodynamic parameter fitting, enthalpy, entropy

OPEN ACCESS

Edited by:
Valeria Conte,
University of Rome Tor Vergata, Italy

Reviewed by:
Giovanni La Penna,
National Research Council (CNR), Italy
Utpal Sarkar,
Assam University, India

****Correspondence:***
Fereshteh Emami
fereshteh.emami@selu.edu

Specialty section:
This article was submitted to Theoretical and Computational Chemistry, a section of the journal Frontiers in Chemistry

Received: *16 August 2021*
Accepted: *08 November 2021*
Published: *21 December 2021*

Citation:
Emami F, Abdollahi H, Minami T, Peco B and Reliford S (2021) Mathematical Modeling of a Supramolecular Assembly for Pyrophosphate Sensing. Front. Chem. 9:759714. doi: 10.3389/fchem.2021.759714

1 INTRODUCTION

The capability to precisely detect a target system and monitor its variation over time is highly desirable in various fields, including biological studies, diagnosis, and quality control. Some sensor-target combinations include equilibrium, kinetic, or intertwined equilibrium-kinetic chemical interactions like supramolecular sensors (Johnson-Buck et al., 2015). Other sensor interactions with targets may trigger chemical, electrical, and mechanical changes like hydrogel sensors (Gladman et al., 2016). Supramolecular chemistry is an emergent research field taking its roots in chemistry. Its combination with biology opens a new direction in the study of life and its origin (Vicens and Vicens, 2011). The last several years have seen substantial growth in the field, and many detection efforts have focused on the use of fluorescent supramolecular sensors in cells and tissues (Lim et al., 2005; Palmer and Tsien, 2006; Que et al., 2008; Wong et al., 2009). In many chemical and biological processes, including molecular self-assembly and protein-protein or protein-substrate recognition, noncovalent interactions are critically important (Mugridge, 2010). Drawing inspiration from such natural systems, supramolecular chemists seek to use these weak, nonbonding interactions to mediate the formation and reactivity of host-guest complexes. Sensing applications of supramolecular chemistry rely on exploiting the forces involved in the formation of non-covalent "host-guest" complexes. In all cases, having a binding site that is highly specific for an analyte "guest" in a measurable form is the critical key for the "host" molecules (Lehn, 1994; Goral et al., 2001; Boul et al., 2005; Pérez-Fuertes et al., 2006, 2007; Ayme et al., 2012; You et al., 2015). The continued development of improved sensors depends on achieving a thorough understanding of the underlying chemical properties of the available constructs.

The determination of accurate binding constants is an important prerequisite for the development of many host-guest complexes, which range from sensing to drug discovery and development (Giri et al., 2011; Meier and Beeren, 2014). Unfortunately, in current analyses of supramolecular self-assemblies, no efficient mathematical modeling is applied to obtain these constants. Regular 1:1 or 1:2 complexes, an indicator displacement assay, or an enantioselective indicator displacement assay are usually considered, and the apparent binding constants are determined (Connors, 1987; Hargrove et al., 2010; Sheff et al., 2011). While many assemblies are produced from the reactions/interactions among different species.

The pH has a crucial role in most chemical processes, and many reactions in aqueous solutions show a strong pH dependence (Maeder et al., 2003; Wilkins, 1991). Protonation equilibria are particularly complex with multidentate ligands. Several differently protonated forms of the ligand usually coexist in solution; all of these forms show different reactivities towards each other. As a result, the observed equilibria are strongly pH dependent. Therefore, pH-metric is a practical tool to gain insight into the reactivities of the supramolecular sensors. In this study, we use a simple potentiometric pH method to simultaneously determine thermodynamic constants of the interactions among a self-assembled sensor prepared from Zn^{II}–DPA (DPA = dipicolylamine)-attached phenylboronic acid (**1**·Zn) and catechol-type dye, alizarin red S (ARS) towards pyrophosphate (PPi). We have previously used these self-assemblies to detect oligophosphates in aqueous solutions (Minami et al., 2016). We considered an indicator displacement assay and determined the apparent binding constants of ARS toward **1**.Zn and phosphates toward the sensor ARS-**1**.Zn. However, different analytical measurements displayed the presence of multiple intertwined equilibria, including twenty-seven equilibrium interactions and reactions. A mixture of such complicated combinations makes it impossible for the simple curve fitting to reproduce the observed progression. We chose 1.Zn-ARS-PPi sensing system because, according to our previous studies, this self-assembly includes many interactions that make it very complicated. So, it is a great candidate to walk the readers through the mathematical equations. Although, this study can be generalized to any other self-assembly examples.

Here, to address this problem and avoid as many assumptions as possible, we develop iterative methods that allow for the rigorous modeling of binding equations with the help of the Newton-Raphson algorithm in MATLAB, describing the complete molecular behaviors. We highlight how the extraction of binding data from a network of equilibria with the help of well-defined mathematical modeling led to having equilibria information of all recognized species to study interactions in chemical systems. This method should be generally applicable so long as the supramolecular system is pH-dependent.

2 COMPUTATIONAL DETAILS

We start with an introduction to the theory of equilibria in solution, the law of mass action, the notations required for the quantitative description of the interactions, which can be rather complex, particularly in aqueous solutions. This is followed by a discussion of the types of measurements that can be carried out and the nature of the data that are delivered. Next, we introduce the computational methods are required for the analysis of the measurements. To give the reader the possibility to apply all the above concepts, we use three practical examples: the potentiometric investigation of the interactions of 1.Zn-ARS-PPi. A suite of MATLAB programs that perform the analysis of the above data sets is available from the authors.

To introduce the mathematical modeling concept, consider a species formed by only three components A, B, and C (**Eq. 1**).

$$aA + bB + cC \rightleftarrows A_aB_bC_c \quad \beta_{abc} = \frac{[A_aB_bC_c]}{[A]^a[B]^b[C]^c} \tag{1}$$

where $a, b, c = 1, 2, 3 \ldots$ and $A_aB_bC_c$ is the product of sensor and target combination. β_{abc} is the formation constant of the species $A_aB_bC_c$. The definition of the stabilities of all species as a function of the component concentrations *via* the β_{abc} values is consistent and allows the development of general, compact, and thus fast computer programs for data analysis.

Computer programs written for the analysis of measurements for equilibrium investigations contain two parts that require specific attention. The more obvious one is the algorithm for parameter fitting. Its task is to determine the optimal values for the parameters for a given measurement and model. In a titration experiment, the parameters to be fitted are usually the formation constants and, in the case of a spectrophotometric titration, additionally the molar absorption spectra of all-absorbing species. The other important part is computing all species concentrations for a given set of total component concentrations and formation constants. This calculation has to be performed for the solution after each addition of reagent during the complete titration. This second task forms the core of the data fitting and, therefore, we will discuss it first.

2.1 The Newton-Raphson Algorithm

The quantitative analysis of chemical equilibria is achieved using the Newton-Raphson algorithm that computes the species concentrations for a given set of formation constants and total concentrations of the components $[A]_{tot}$, $[B]_{tot}$, and $[C]_{tot}$. The components are the basic units that interact with each other to form the species. The basis for the computations is the law of conservation of mass. At equilibrium, different species defined in the model reach a certain concentration that obeys the mass law. It means the law of mass action relates the species concentrations to the total concentrations of the components. For instance, the concentration summation of A existing in different species forms has to equal the known total concentration $[A]_{tot}$.

The quantitative relationship between the concentrations of free components and species is defined by the formation constants:

$$[A_aB_bC_c] = \beta_{abc}\,[A]^a\,[B]^b\,[C]^c \tag{2}$$

Each species concentration is computed from the formation constants and the free component concentrations as given in **Eq. 2** for the general equilibrium (**Eq. 1**. For each of the components, A, B, and C, we can write the following equations:

$$\begin{aligned}[A]_{tot-calc} &= [A] + a[A_aB_bC_c]\\ [B]_{tot-calc} &= [B] + b[A_aB_bC_c]\\ [C]_{tot-calc} &= [C] + c[A_aB_bC_c]\end{aligned} \tag{3}$$

In a titration process, $[A]_{tot}$, $[B]_{tot}$, and $[C]_{tot}$ are the known independent variables and are computed from the reagent solutions and dilutions occurring during the titration. The total concentrations of the components are stored in the matrix $\mathbf{C_{tot}}$. These total concentrations have to equal the sums over all appropriately weighted species concentrations, **Eq. 3**. The differences between the calculated and known total concentrations are collected in the vector ***diff***. The goal of the algorithm is to determine the free component concentrations such that the differences ***diff*** are zero.

$$\begin{aligned}\boldsymbol{diff}_A &= [A]_{tot} - [A]_{tot-calc}\\ \boldsymbol{diff}_B &= [B]_{tot} - [B]_{tot-calc}\\ \boldsymbol{diff}_C &= [C]_{tot} - [C]_{tot-calc}\end{aligned} \tag{4}$$

By substituting **Eq. 2** in **Eq. 3**, each total component concentration can be calculated as below and stored in the matrix $[Component]_{tot-calc}$:

$$\begin{aligned}[A]_{tot-calc} &= \sum_{i=1}^{nspec} a\beta_{abc}\,[A]^a\,[B]^b\,[C]^c\\ [B]_{tot-calc} &= \sum_{i=1}^{nspec} b\beta_{abc}\,[A]^a\,[B]^b\,[C]^c\\ [C]_{tot-calc} &= \sum_{i=1}^{nspec} c\beta_{abc}\,[A]^a\,[B]^b\,[C]^c\end{aligned} \tag{5-1}$$

where $nspec$ is the number of species and a, b, and c are the stoichiometric coefficients. The validity of using formation constants is, however, limited to a constant temperature. A model developed on top of these parameters cannot predict the optimized assembly sensing process under various experimental conditions. To address this limitation, we used the van't Hoff equation to relate changes in the binding constants to changes in temperature, T, leading to estimate the change in enthalpy (ΔH) and entropy (ΔS) of a chemical interaction/reaction:

$$ln\beta = \frac{-\Delta H}{RT} + \frac{\Delta S}{R} \tag{6}$$

$$\begin{aligned}[A]_{tot-calc} &= \sum_{i=1}^{nspec} a\left(e^{\left(\frac{-\Delta H_{abc}}{RT}+\frac{\Delta S_{abc}}{R}\right)}\right)[A]^a\,[B]^b\,[C]^c\\ [B]_{tot-calc} &= \sum_{i=1}^{nspec} b\left(e^{\left(\frac{-\Delta H_{abc}}{RT}+\frac{\Delta S_{abc}}{R}\right)}\right)[A]^a\,[B]^b\,[C]^c\\ [C]_{tot-calc} &= \sum_{i=1}^{nspec} c\left(e^{\left(\frac{-\Delta H_{abc}}{RT}+\frac{\Delta S_{abc}}{R}\right)}\right)[A]^a\,[B]^b\,[C]^c\end{aligned} \tag{5-2}$$

where R is the ideal gas constant and equals 8.31 J/mol/K.

There are many ways of solving such a system of equations. The Newton-Raphson algorithm is usually well behaved and is relatively straightforward to implement. however, there is no guarantee for conversion and thus informative data measurements need to be introduced to deal with such cases. These computations are usually complex, and iterative algorithms have to be employed (Maeder and Neuhold, 2007). The algorithm starts with initial guesses for the free component concentrations to compute all species concentrations, and subsequently, mass conservation is checked. If there are any discrepancies, the iterative algorithm is continued. The explanations given here are insufficient for complete understanding, and more extensive definitions are beyond the scope of this study. For more details, we refer the readers to (Maeder and Neuhold, 2007). Analyzing the MATLAB codes supplied by the authors, see the end of this paper, can also assist the comprehension of the methods discussed.

2.2 The Newton-Gauss Algorithm

The next step is to obtain the correct ΔH and ΔS values of the combinations among the sensors and the targets using data measured at various conditions. The key point is any species

in the considered interactions should exist at some minimal concentrations in the measured data. To obtain the parameters, we applied the numerical Newton-Gauss method (Bevington et al., 1993; Maeder and Neuhold, 2007) and the mathematical model of the considered sensing system to analyze the constructed data through simulations as a proxy to measured data. The measured data is always corrupted by experimental errors, instrumental shortcomings, noise, etc. The purpose of data fitting is to determine a calculated set of data, which resembles the measured data as closely as possible. The data set generated by the model is defined by the model and the thermodynamic parameters ($\boldsymbol{p}$). Here, we discuss potentiometric pH titrations. The measurement is a record of the pH of the solution ($\boldsymbol{d}_{meas}$), and the data calculated by the model is –log ($[H^+]$) ($\boldsymbol{d}_{calc}$); proton is one of the computed species concentrations. The chemical model together with the parameters allows the computation of all free species concentrations as a function of the titration. This is done by the Newton-Raphson algorithm and the results of these calculations are collected in the matrix $\boldsymbol{C}$, which is a function of the non-linear parameters.

$$\boldsymbol{C} = f\,(model,\ \boldsymbol{p}) \tag{7}$$

The non-linear parameters $\boldsymbol{p}$ require an iterative algorithm that starts with initial guesses and converges towards the optimal solution in a reasonable number of iterations and amount time. The differences between the measured and calculated data are the residuals, $\boldsymbol{r}$:

$$\boldsymbol{r} = \boldsymbol{d}_{meas} - \boldsymbol{d}_{calc}\ (model,\ \boldsymbol{p}) \tag{8}$$

The measure for the quality of the fit is the sum of squares, *ssq*, which is the sum over the squares of all elements of the vector $\boldsymbol{r}$.

$$ssq = \sum_i \sum_j r_{i,j}^2 = f\,(model,\ \boldsymbol{p}) \tag{9}$$

Eq. 9 demonstrates that *ssq* is a function of the non-linear parameters $\boldsymbol{p}$ and, of course, of the model and the data themselves that define the matrix of concentration profiles, $\boldsymbol{C}$. These parameters are refined to minimize *ssq* using the Newton-Gauss method that is fast and delivers estimates for the effect of experimental noises as the standard deviations of the fitted parameters. Please see (Maeder and Neuhold, 2007) reference for more extensive explanations. The important point to notice in the fitting process is that the smaller the number of parameters, the easier the task of the fitting. Please see **Section 3.2**. for further discussions.

3 RESULTS AND DISCUSSION

3.1 Plausible Mechanism of the Supramolecular Assembly

Most examples of chemical equilibria can be seen as interactions between Lewis acids and Lewis bases. In an aqueous solution, the protons are always present, and more importantly, they are also Lewis acids, which can compete with any other Lewis acid present. The protonation equilibrium can be described analogously as $H + A \rightleftharpoons HA$, and the law of mass action states that $K_{HA} = \frac{[HA]}{[H][A]}$.

The investigated supramolecular sensing system has been first introduced by Nonaka and his coworkers (Nonaka et al., 2008) to detect multi-phosphates in aqueous solutions. The synthesized receptor, DPA (DPA = dipicolylamine)-appended phenylboronic acid (**1**) in combination with Zn^{2+} (**1**·Zn) forms various assemblies with alizarin dye in a wide range of pHs. Among the existed complexes, ARS binds favorably to the coordinated zinc (II) in the Zn^{2+}–DPA moiety. When PPi is added to the solution, it causes reorganization of the complex to produce an alternative boronate ester assembly. Traditionally, an indicator displacement assay is considered, and the apparent binding constants of ARS to **1**·Zn and PPi to ARS-**1**·Zn are determined. However, analytical evidence (Nonaka et al., 2008; Tomsho and Benkovic, 2012) displayed the presence of multiple intertwined equilibria shown in **Scheme 1**. ARS and PPi act as two- and four-protonated weak acids, H_2ARS^- and H_4PPi. Their corresponding deprotonated forms exist in a wide pH scale. **1**·Zn ($H_2$1.Zn^{3+}) has a secondary aliphatic amine in the protonated form at lower pHs and a boronic acid moiety as a Lewis acid that exists as either a neutral trigonal-planar species at low pHs or a negatively charged tetrahedral boronate species at high pHs. Free ions Zn^{2+} can also participate in various equilibrium reactions with ARS, **1**·Zn, and PPi. Further, since the solvent is water, hydrolysis dissociations can occur. PPi–ARS–1·Zn desired complex ($H_4ARS1.ZnPPi_a^{2-}$) can dissociate whether to its original species- **1**·Zn, ARS, and PPi- or to PPi-**1**·Zn and ARS. The dissociation of PPi from the boronic acid moiety of **1**·Zn and eventually from the ternary complex, PPi–ARS–**1**·Zn, is another event. Also, an excess amount of **1**·Zn is capable of binding to the anion PPi. The mixture of such very complicated combinations that are not limited to this example makes it definitely impossible for the simple curve fitting to reproduce the observed progression. We used this self-assembly sensing example in the following sections as stepwise guides for researchers interested in incorporating mathematical modeling into the development of molecular sensors.

3.2 Separable Interactions/Reactions of ARS-1·Zn-PPi Assemblies

It is important to develop a nomenclature that uniquely describes all the species formed in solution with their appropriate equilibrium constants. Let us concentrate on the example of ARS-**1**.Zn-PPi equilibrium study in aqueous solution. After having reviewed the chemical mechanism of ARS-**1**.Zn-PPi assemblies, the next step is to determine the key chemical players and how they will interact. This step is particularly important, as it sets the stage for how complex our model will ultimately become. Using the nomenclature commonly employed in coordination chemistry, here, five components, ARS^{3-}, 1^-, PPi^{4-}, H^+, and Zn^{2+}, react with each other to form any complexity of species, and makes such confusing mechanism (**Scheme 1**). Note the expressions used: the components are the basic units that interact with each other to form the species; it is convenient to include the components in the list of species. Each of the species is formed by the appropriate number of

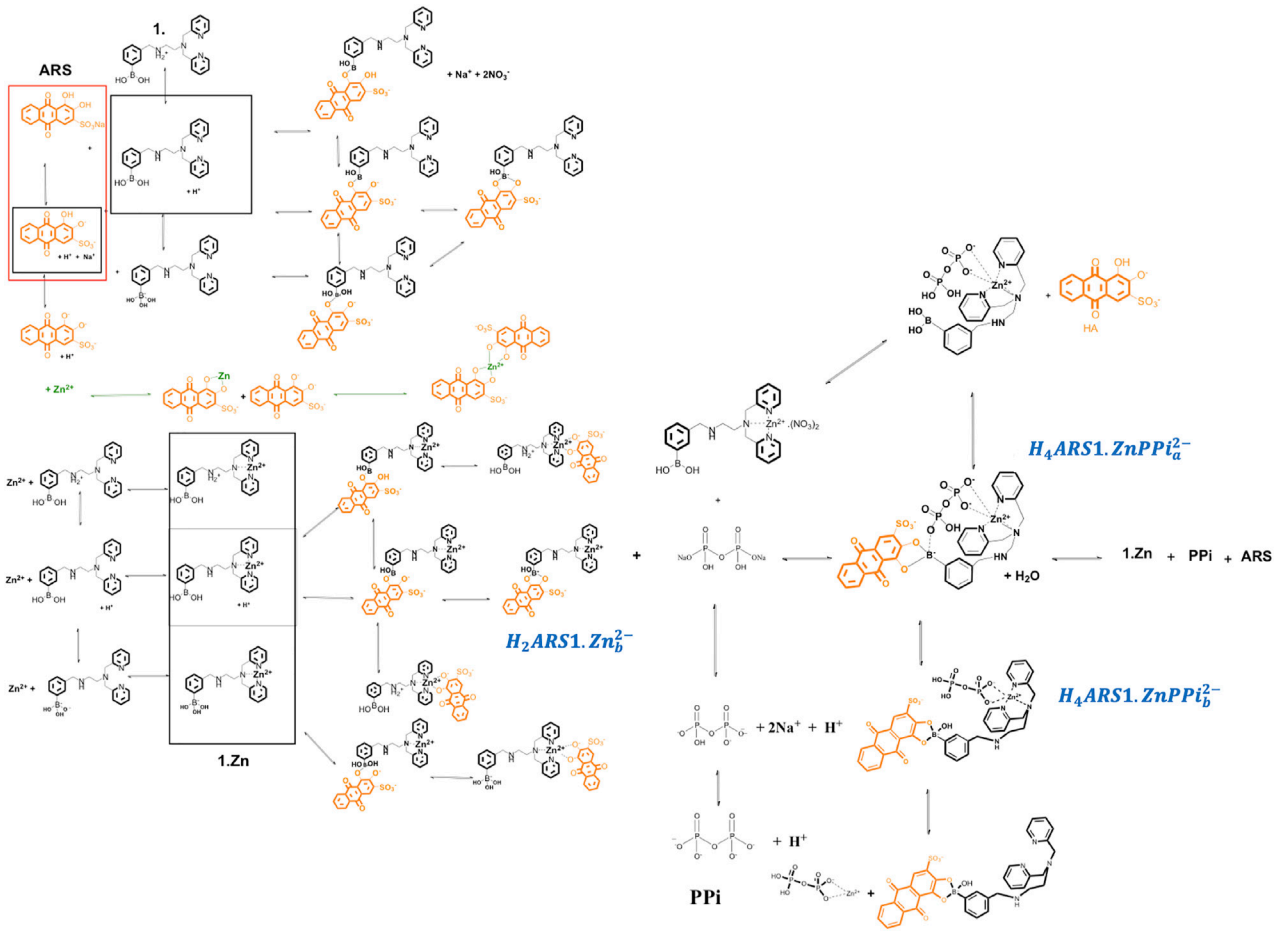

SCHEME 1 | Plausible mechanism related to different interactions among 1.Zn, ARS and PPi.

components, and the quantitative relationship between the component and species concentrations is defined by the formation constant. The notation for equilibrium modelling of ARS-**1**.Zn-PPi example is represented in **Table 1**.

To have a model that can be generalized to any new complex molecular mechanism, we assumed none of the thermodynamic constants associated with the combinations/dissociations among these components are known. The first step is recognizing the interactions/reactions that can be modeled independently. In this case, some of the parameters of interest to the study can be obtained separately, which makes fitting the final model simpler by decreasing the number of unknown parameters. Accordingly, we broke the mechanism shown in **Scheme 1** into ten sub mechanisms for independent investigations, **Sections 3.2.1–3.2.9**. Each sub-model is then followed by **Eqs 3–6** to simulate the concentration profiles of the species and **Eqs 7–9** to fit the thermodynamic parameters.

3.2.1 Equilibria of ARS/1

ARS^{3-} and 1^- act as two-protonated acids and convert to their protonated forms by changing the pH from 12 to 2. Each can be modeled and investigated by potentiometric titrations at different temperatures to compute the thermodynamic constants (ΔH and ΔS) of H_2ARS^-, $HARS^{2-}$, $H_2\mathbf{1}^+$, $H\mathbf{1}$ species:

$$
\begin{aligned}
&H^+ + X \rightleftarrows HX \qquad \beta_{HX} = \frac{[HX]}{[H^+][X]} = \frac{1}{K_{a-HX}} \\
&2H^+ + X \rightleftarrows H_2X \qquad \beta_{H_2X} = \frac{[H_2X]}{[H^+]^2[X]} = \frac{1}{K_{a-H_2X} \times K_{a-HX}} \\
&\qquad\qquad X = ARS^{3-} \text{ or } \mathbf{1}^-
\end{aligned}
\tag{10}
$$

For the components X and H^+, the following equations define the calculated total concentrations based on the law of mass action:

$$
\begin{aligned}
[X]_{tot-calc} &= [X] + [HX] + [H_2X] \\
[H]_{tot-calc} &= [H^+] + [HX] + 2[H_2X] - [OH^-]
\end{aligned}
\tag{11}
$$

Simulation of the species concentration profiles based on the above mathematical model is done using initial concentrations for X and proton, thermodynamic constants, and Newton-Raphson algorithm.

TABLE 1 | Notation for equilibrium modeling of the investigated mechanism in **Scheme 1**.

Species	Notation					Formation constant
	ars	**1**	ppi	**h**	**zn**	
ARS^{-2}	1	0	0	0	0	$\beta_{10000} = 1$
1	0	1	0	0	0	$\beta_{01000} = 1$
PPi^{-4}	0	0	1	0	0	$\beta_{00100} = 1$
H^{+}	0	0	0	1	0	$\beta_{00010} = 1$
Zn^{2+}	0	0	0	0	1	$\beta_{00001} = 1$
HARS^{-}	1	0	0	1	0	$\beta_{10010} = [\mathbf{HARS}^{-}]/[\boldsymbol{H}^{+}][\mathbf{ARS}^{-2}]$
H$_2$ARS	1	0	0	2	0	$\beta_{10020} = [\mathbf{H_2ARS}]/[\boldsymbol{H}^{+}]^2[\mathbf{ARS}^{-2}]$
H1	0	1	0	1	0	$\beta_{01010} = [\mathbf{H}1]/[\boldsymbol{H}^{+}][1]$
H$_2$1^{1+}	0	1	0	2	0	$\beta_{01020} = [\mathbf{H_2}1^{+}]/[\boldsymbol{H}^{+}]^2[1]$
HPPi^{3-}	0	0	1	1	0	$\beta_{00110} = [\mathbf{HPPi}^{3-}]/[\boldsymbol{H}^{+}][\boldsymbol{PPi}^{-4}]$
H$_2$PPi^{2-}	0	0	1	2	0	$\beta_{00120} = [\mathbf{H_2PPi}^{2-}]/[\boldsymbol{H}^{+}]^2[\boldsymbol{PPi}^{-4}]$
H$_3$PPi^{-}	0	0	1	3	0	$\beta_{00130} = [\mathbf{H_3PPi}^{-}]/[\boldsymbol{H}^{+}]^3[\boldsymbol{PPi}^{-4}]$
H$_4$PPi	0	0	1	4	0	$\beta_{00140} = [\mathbf{H_4PPi}]/[\boldsymbol{H}^{+}]^4[\boldsymbol{PPi}^{-4}]$
ZnARS	1	0	0	0	1	$\beta_{10001} = [\boldsymbol{ZnARS}]/[\boldsymbol{Zn}^{2+}][\mathbf{ARS}^{-2}]$
ZnARS$_2^{2-}$	2	0	0	0	1	$\beta_{20001} = [\boldsymbol{ZnARS_2}^{2-}]/[\boldsymbol{Zn}^{2+}][\mathbf{ARS}^{-2}]^2$
1***Zn***$^{2+}$	0	1	0	0	1	$\beta_{01001} = [1\boldsymbol{Zn}^{2+}]/[\boldsymbol{Zn}^{2+}][1]$
H1***Zn***$^{3+}$	0	1	0	1	1	$\beta_{01011} = [\boldsymbol{H}1\boldsymbol{Zn}^{3+}]/[\boldsymbol{H}^{+}][\boldsymbol{Zn}^{2+}][1]$
H$_2$1***Zn***$^{4+}$	0	1	0	2	1	$\beta_{01021} = [\boldsymbol{H}1\boldsymbol{Zn}^{3+}]/[\boldsymbol{H}^{+}]^2[\boldsymbol{Zn}^{2+}][1]$
ZnPPi^{2-}	0	0	1	0	1	$\beta_{00101} = [\boldsymbol{ZnPPi}^{2-}]/[\boldsymbol{Zn}^{2+}][\boldsymbol{PPi}^{-4}]$
ZnOHPPi^{3-}	0	0	1	−1	1	$\beta_{001-11} = [\boldsymbol{ZnOHPPi}^{3-}]/[\boldsymbol{Zn}^{2+}][\boldsymbol{OH}^{-}][\boldsymbol{PPi}^{-4}]$
ZnHPPi^{-}	0	0	1	1	1	$\beta_{00111} = [\boldsymbol{ZnHPPi}^{3-}]/[\boldsymbol{Zn}^{2+}][\boldsymbol{H}^{+}][\boldsymbol{PPi}^{-4}]$
H$_3$1***ZnPPi***$^{-}$	0	1	1	3	1	$\beta_{01131} = [\boldsymbol{H}_3\boldsymbol{1ZnPPi}^{-}]/[\boldsymbol{H}^{+}]^3[1][\boldsymbol{Zn}^{2+}][\boldsymbol{PPi}^{-4}]$
H$_3$ARS1^{+}	1	1	0	3	0	$\beta_{11030} = [\boldsymbol{H}_3\boldsymbol{ARS}1^{+}]/[\boldsymbol{H}^{+}]^3[\mathbf{ARS}^{-2}][1]$
H$_2$ARS1$_a$	1	1	0	2	0	$\beta_{11020} = [\boldsymbol{H_2ARS}1_a]/[\boldsymbol{H}^{+}]^2[\mathbf{ARS}^{-2}][1]$
H$_2$ARS1$_b$	1	1	0	2	0	$\beta_{11020} = [\boldsymbol{H_2ARS}1_b]/[\boldsymbol{H}^{+}]^2[\mathbf{ARS}^{-2}][1]$
HARS1^{-}	1	1	0	1	0	$\beta_{11010} = [\boldsymbol{HARS}1_b]/[\boldsymbol{H}^{+}][\mathbf{ARS}^{-2}][1]$

3.2.2 Pyrophosphate Protonation Equilibria

PPi can exists in four protonated forms $HPPi^{3-}$, H_2PPi^{2-}, H_3PPi^{-}, and H_4PPi from basic to acidic pHs.

$$
\begin{aligned}
&H^+ + PPi^{4-} \rightleftarrows HPPi^{3-} \quad \beta_{HPPi} = \frac{[HPPi^{3-}]}{[H^+][PPi^{4-}]} = \frac{1}{K_{a-HPPi}}\\
&2H^+ + PPi^{4-} \rightleftarrows H_2PPi^{2-} \quad \beta_{H_2PPi} = \frac{[H_2PPi^{2-}]}{[H^+]^2[PPi^{4-}]}\\
&\qquad = \frac{1}{K_{a-H_2PPi} \times K_{a-HPPi}}\\
&3H^+ + PPi^{4-} \rightleftarrows H_3PPi^{-} \quad \beta_{H_3PPi} = \frac{[H_3PPi^{-}]}{[H^+]^3[PPi^{4-}]}\\
&\qquad = \frac{1}{K_{a-H_3PPi} \times K_{a-H_2PPi} \times K_{a-HPPi}}\\
&4H^+ + PPi^{4-} \rightleftarrows H_4PPi \quad \beta_{H_4PPi} = \frac{[H_4PPi]}{[H^+]^4[PPi^{4-}]}\\
&\qquad = \frac{1}{K_{a-H_4PPi} \times K_{a-H_3PPi} \times K_{a-H_2PPi} \times K_{a-HPPi}}
\end{aligned}
\tag{12}
$$

The mass balances regarding PPi^{4-} and H^+ components are as follows:

$$
\begin{aligned}
[PPi]_{tot-calc} &= [PPi^{4-}] + [HPPi^{3-}] + [H_2PPi^{2-}] + [H_3PPi^{-}] + [H_4PPi]\\
[H]_{tot-calc} &= [H^+] + [HPPi^{3-}] + 2[H_2PPi^{2-}] + 3[H_3PPi^{-}] + 4[H_4PPi]\\
&\quad - [OH^-]
\end{aligned}
\tag{13}
$$

3.2.3 Assemblies of Zinc-Pyrophosphate

The combination of PPi with Zn^{2+} can produce 1:1 complexes of $ZnPPi^{2-}$, $ZnHPPi^{-}$, and $ZnOHPPi^{3-}$ (Moe and Wiest, 1977). We modeled these new products according to the following equations:

$$
\begin{aligned}
&Zn^{2+} + PPi^{4-} \rightleftarrows ZnPPi^{2-} \quad \beta_{ZnPPi} = \frac{[ZnPPi^{2-}]}{[Zn^+][PPi^{4-}]} = K_{ZnPPi}\\
&Zn^{2+} + PPi^{4-} + H^+ \rightleftarrows ZnHPPi^{-} \quad \beta_{ZnHPPi} = \frac{[ZnHPPi^{-}]}{[Zn^+][PPi^{4-}][H^+]}\\
&\qquad = \frac{K_{ZnHPPi}}{K_{a-HPPi}}\\
&Zn^{2+} + PPi^{4-} + OH^- \rightleftarrows ZnOHPPi^{3-} \; \beta_{ZnOHPPi}\\
&\qquad = \frac{[ZnOHPPi^{3-}]}{[Zn]^{2+}[PPi^{4-}][OH^-]} = K_{ZnPPi} \times K_{ZnOHPPi}
\end{aligned}
\tag{14}
$$

The equations of conservation mass of this equilibria system used in the algorithm during the titration of pyrophosphate and zinc with HCl are:

$$
\begin{aligned}
[PPi]_{tot-calc} &= [PPi^{4-}] + [HPPi^{3-}] + [H_2PPi^{2-}] + [H_3PPi^{-}]\\
&\quad + [H_4PPi] + [ZnPPi^{2-}] + [ZnHPPi^{-}] + [ZnOHPPi^{3-}]\\
[H]_{tot-calc} &= [H^+] + [HPPi^{3-}] + 2[H_2PPi^{2-}] + 3[H_3PPi^{-}]\\
&\quad + 4[H_4PPi] + [ZnHPPi^{-}] + [ZnOHPPi^{3-}] - [OH^-]\\
[Zn]_{tot-calc} &= [Zn^{2+}] + [ZnPPi^{2-}] + [ZnHPPi^{-}]\\
&\quad + [ZnOHPPi^{3-}]
\end{aligned}
\tag{15}
$$

3.2.4 Interactions of Zinc and ARS

Zinc ions are capable of interacting with ARS in two steps to have 1:2 coordination complexes. The core structure of ARS—1,2-dihydroxyanthraquinone—serves as new lead structures for ratiometric probes for zinc ions (Kaushik et al., 2015; Zhang et al., 2007). According to the Newton-Raphson algorithm language, the reactions between ARS^{3-} and Zn^{2+} can be written as

$$Zn^{2+} + ARS^{3-} \rightleftarrows ZnARS^{-} \quad \beta_{ZnARS} = \frac{[ZnARS^{-}]}{[Zn^{2+}][ARS^{3-}]} = K_{ZnARS}$$

$$Zn^{2+} + 2ARS^{3-} \rightleftarrows ZnARS_2^{4-} \quad \beta_{ZnARS_2} = \frac{[ZnARS_2^{4-}]}{[Zn^{2+}][ARS^{3-}]^2} = K_{ZnARS} \times K_{ZnARS_2} \tag{16}$$

Mass equations corresponding to ARS equilibria and its combinations with Zn^{2+} are

$$\begin{aligned}[ARS]_{tot-calc} &= [ARS^{3-}] + [HARS^{2-}] + [H_2ARS^{-}] + [ZnARS^{2-}] + [ZnARS_2^{4-}] \\ [H]_{tot-calc} &= [H^+] + [HARS^{2-}] + 2[H_2ARS^{-}] - [OH^-] \\ [Zn]_{tot-calc} &= [Zn^{2+}] + [ZnARS^{-}] + [ZnARS_2^{4-}]\end{aligned} \tag{17}$$

3.2.5 Zinc and 1 Complexes

The three nitrogens of the DPA ligand can coordinate strongly to Zn^{2+} cation, with an association constant around $10^7\ M^{-1}$ in water. Having three de/protonated forms in the pH 2-12 area (**Eq. 10**), molecule **1** can have three different combinations with Zn^{2+} with probably close binding constants (**Scheme 1**) (Gruenwedel, 1968; O'Neil and Smith, 2006; Wong et al., 2009):

$$\begin{aligned}&Zn^{2+} + \mathbf{1}^{-} \rightleftarrows \mathbf{1}.Zn^{+} \quad \beta_{1.Zn} = \frac{[\mathbf{1}.Zn^{+}]}{[Zn^{2+}][\mathbf{1}^{-}]} = K_{\mathbf{1}.Zn} \\ &Zn^{2+} + H^+ + \mathbf{1}^{-} \rightleftarrows H\mathbf{1}.Zn^{2+} \quad \beta_{H1.Zn} = \frac{[H\mathbf{1}.Zn^{2+}]}{[Zn^{2+}][H^+][\mathbf{1}^{-}]} = \frac{K_{H1.Zn}}{K_{a-H1}} \\ &Zn^{2+} + 2H^+ + \mathbf{1}^{-} \rightleftarrows H_2\mathbf{1}.Zn^{3+} \quad \beta_{H_2\mathbf{1}.Zn} = \frac{[H_2\mathbf{1}.Zn^{3+}]}{[Zn^{2+}][H^+]^2[\mathbf{1}.^{-}]} = \frac{K_{H_2\mathbf{1}.Zn}}{K_{a-H\mathbf{1}} \times K_{a-H_2\mathbf{1}}}\end{aligned} \tag{18}$$

The corresponding mass equations are:

$$\begin{aligned}[\mathbf{1}]_{tot-calc} &= [\mathbf{1}^{-}] + [H\mathbf{1}] + [H_2\mathbf{1}^{+}] + [\mathbf{1}.Zn^{+}] + [H\mathbf{1}.Zn^{2+}] + [H_2\mathbf{1}.Zn^{3+}] \\ [H]_{tot-calc} &= [H^+] + [H\mathbf{1}] + 2[H_2\mathbf{1}^{+}] + [H\mathbf{1}.Zn^{2+}] + 2[H_2\mathbf{1}.Zn^{3+}] - [OH^-] \\ &[Zn^{2+}] + [\mathbf{1}.Zn^{+}] + [H\mathbf{1}.Zn^{2+}] + [H_2\mathbf{1}.Zn^{3+}]\end{aligned} \tag{19}$$

3.2.6 $H_3$1.ZnPPi Complex

The other event from **Scheme 1** that can be considered separately is the interaction of $H\mathbf{1}.Zn^{2+}$ with H_2PPi^{2-}:

$$Zn^{2+} + 3H^+ + \mathbf{1}^{-} + PPi^{4-} \rightleftarrows H_3\mathbf{1}.ZnPPi \quad \beta_{H_3\mathbf{1}.ZnPPi} = \frac{[H_3\mathbf{1}.ZnPPi]}{[Zn^{2+}][H^+]^3[PPi^{4-}][1^{-}]} = \frac{K_{H_3\mathbf{1}.ZnPPi}}{K_{a-H\mathbf{1}} \times K_{a-HPPi} \times K_{a-H_2PPi}} \tag{20}$$

Here we have four components and their related mass balances are as:

$$\begin{aligned}[1]_{tot-calc} &= [1^{-}] + [H\mathbf{1}] + [H_2\mathbf{1}^{+}] + [\mathbf{1}.Zn^{+}] + [H\mathbf{1}.Zn^{2+}] + [H_2\mathbf{1}.Zn^{3+}] + [H_3\mathbf{1}.ZnPPi] \\ [PPi]_{tot-calc} &= [PPi^{4-}] + [HPPi^{3-}] + [H_2PPi^{2-}] + [H_3PPi^{-}] + [H_4PPi] + [ZnPPi^{2-}] + [ZnHPPi^{-}] + [ZnOHPPi^{3-}] + [H_3\mathbf{1}.ZnPPi] \\ [H]_{tot-calc} &= [H^+] + [H\mathbf{1}] + 2[H_2\mathbf{1}^{+}] + [H\mathbf{1}.Zn^{2+}] + 2[H_2\mathbf{1}.Zn^{3+}] + 3[H_3\mathbf{1}.ZnPPi] - [OH^-] \\ [Zn]_{tot-calc} &= [Zn^{2+}] + [\mathbf{1}.Zn^{+}] + [H\mathbf{1}.Zn^{2+}] + [H_2\mathbf{1}.Zn^{3+}] + [H_3\mathbf{1}.ZnPPi]\end{aligned} \tag{21}$$

3.2.7 Assemblies of ARS and 1

The next consideration was the study of the binding affinities of **1** for ARS (Tomsho and Benkovic, 2012) in solutions of varying pHs. The corresponding mass balances are

$$\begin{aligned}[\mathbf{1}]_{tot-calc} &= [\mathbf{1}^{-}] + [H\mathbf{1}] + [H_2\mathbf{1}^{+}] + [H_3ARS\mathbf{1}_a^{-}] + [H_2ARS\mathbf{1}_a^{2-}] + [H_2ARS\mathbf{1}_b^{2-}] + [HARS\mathbf{1}_a^{3-}] \\ [ARS]_{tot-calc} &= [ARS^{3-}] + [HARS^{2-}] + [H_2ARS^{-}] + [H_3ARS\mathbf{1}_a^{-}] + [H_2ARS\mathbf{1}_a^{2-}] + [H_2ARS\mathbf{1}_b^{2-}] + [HARS\mathbf{1}_a^{3-}] \\ [H]_{tot-calc} &= [H^+] + [H\mathbf{1}] + 2[H_2\mathbf{1}^{+}] + [HARS^{2-}] + 2[H_2ARS^{-}] + 3[H_3ARS\mathbf{1}_a^{-}] + 2[H_2ARS\mathbf{1}_a^{2-}] + 2[H_2ARS\mathbf{1}_b^{2-}] + [HARS\mathbf{1}_a^{3-}] - [OH^-]\end{aligned} \tag{22}$$

As can be seen in **Scheme 1**, **1** and ARS interactions led to ten different forms of species.

3.2.8 Assemblies of ARS and 1·Zn

The existence of zinc in the structure of **1** makes a new moiety for a binding competition of anions like ARS. We assumed the actual binding ability of boronic acid in **1** with ARS to form $H_3ARS1_a^{-}$, $H_2ARS1_a^{2-}$, $H_2ARS1_b^{2-}$, and $HARS1_a^{3-}$ species is not different from that in **1**-ARS assemblies (Nonaka et al., 2008; Tomsho and Benkovic, 2012).

TABLE 2 | Obtained thermodynamic constants for the simulated pH datasets corresponding to ARS, **1** and PPi.

Species	Used to construct data		Calculated		
	ΔH (J/mole)	ΔS (J/mole.K)	ΔH (J/mole)	ΔS (J/mole.K)	Ssq
HARS^{2-}	54,334	393	54,289 ± 126[a] (–0.08%)[b]	393 ± 0.44 (–0.04%)	3.32×10^{-4}
H_2ARS^{-}	52,047	500	51,875 ± 143 (–0.33%)	499 ± 0.50 (–0.12%)	
H1	44,813	326	44,762 ± 91 (–0.11%)	326 ± 0.31 (–0.05%)	3.42×10^{-4}
$H_2$1^{+}	64,878	531	64,787 ± 113 (–0.14%)	530 ± 0.39 (–0.06%)	
HPPi^{3-}	55,206	369	55,143.9 ± 113 (–0.11%)	368 ± 0.39 (–0.06%)	8.50×10^{-4}
H_2PPi^{2-}	115,430	704	115,202 ± 145 (–0.20%)	703 ± 0.50 (–0.11%)	
H_3PPi^{-}	101,380	700	100,435 ± 475 (–0.93%)	697 ± 1.63 (–0.46%)	
H_4PPi	123,460	806	127,597 ± 2,693 (3.35%)	820 ± 9.02 (1.72%)	

[a]*The standard errors associated with the fitted parameters (σ_p) were calculated as*

$$\sigma_P = \sigma_R = \sqrt{d_{i,i}}$$

where σ_R represents the estimated SD of the measurement error in $\boldsymbol{d_{meas}}$.

$$\sigma_R = \sqrt{\frac{ssq}{df}}$$

where df is the degree of freedom, which is defined as the number of experimental values m (elements of $\boldsymbol{d}$), subtracted by the number of optimized parameters np, $df = m - np$.$d_{i,i}$ is the i-th diagonal element of the inverted Hessian matrix $\boldsymbol{H}^{-1}$. Hessian matrix is the variance-covariance matrix of the parameters. The diagonal elements contain information on the parameter variances and the off-diagonal elements the covariances.

$$\boldsymbol{H}^{-1} = \left(\boldsymbol{J}^t\boldsymbol{J}\right)^{-1}$$

The Newton-Gauss algorithm for *ssq* minimization requires the computation of the derivatives of the residuals with respect to the parameters. These derivatives are collected in the Jacobian $\boldsymbol{J}$.

$$\boldsymbol{J} = \frac{\partial \boldsymbol{r}}{\partial \boldsymbol{p}}$$

Please see (Maeder and Neuhold, 2007) for more extensive explanations.

$$Accuracy = \left(\frac{\boldsymbol{P}_{real} - \boldsymbol{P}_{calculated}}{\boldsymbol{P}_{real}}\right) \times 100$$

where $\boldsymbol{P}_{real}$ are the thermodynamic parameters used to construct data and $\boldsymbol{P}_{calculated}$ are the thermodynamic parameters calculated using the fitting procedure.

$$\begin{aligned}
[\mathbf{1}]_{tot-calc} &= [\mathbf{1}^-] + [H\mathbf{1}] + [H_2\mathbf{1}^+] + [\mathbf{1}.Zn^+] + [H\mathbf{1}.Zn^{2+}] \\
&+ [H_2\mathbf{1}.Zn^{3+}] + [H_3ARS\mathbf{1}.Zn_a^+] + [H_3ARS\mathbf{1}.Zn_b^+] \\
&+ [H_2ARS\mathbf{1}.Zn_a^{2-}] + [H_2ARS\mathbf{1}.Zn_b^{2-}] \\
&+ [H_2ARS1.Zn_c^{2-}] + [HARS1.Zn_a^{3-}] \\
&+ [HARS1.Zn_b^{3-}] \\
[ARS]_{tot-calc} &= [ARS^{3-}] + [HARS^{2-}] + [H_2ARS^-] + [ZnARS^{2-}] \\
&+ [ZnARS_2^{4-}] + [H_3ARS\mathbf{1}.Zn_a^+] \\
&+ [H_3ARS\mathbf{1}.Zn_b^+] + [H_2ARS\mathbf{1}.Zn_a^{2-}] \\
&+ [H_2ARS\mathbf{1}.Zn_b^{2-}] + [H_2ARS\mathbf{1}.Zn_c^{2-}] \\
&+ [HARS\mathbf{1}.Zn_a^{3-}] + [HARS\mathbf{1}.Zn_b^{3-}] \\
[H]_{tot-calc} &= [H^+] + [H\mathbf{1}.] + 2[H_2\mathbf{1}^+] + [H\mathbf{1}.Zn^{2+}] \\
&+ 2[H_2\mathbf{1}.Zn^{3+}] + [HARS^{2-}] + 2[H_2ARS^-] \\
&+ 3[H_3ARS\mathbf{1}.Zn_a^+] + 3[H_3ARS\mathbf{1}.Zn_b^+] \\
&+ 2[H_2ARS\mathbf{1}.Zn_a^{2-}] + 2[H_2ARS\mathbf{1}.Zn_b^{2-}] \\
&+ 2[H_2ARS1.Zn_c^{2-}] + [HARS1.Zn_a^{3-}] \\
&+ [HARS\mathbf{1}.Zn_b^{3-}] - [OH^-] \\
[Zn]_{tot-calc} &= [Zn^{2+}] + [\mathbf{1}.Zn^+] + [H\mathbf{1}.Zn^{2+}] + [H_2\mathbf{1}.Zn^{3+}] \\
&+ [ZnARS^{2-}] + 2[ZnARS_2^{4-}] + [H_3ARS1.Zn_a^+] \\
&+ [H_3ARS1.Zn_b^+] + [H_2ARS1.Zn_a^{2-}] \\
&+ [H_2ARS1.Zn_b^{2-}] + [H_2ARS1.Zn_c^{2-}] \\
&+ [HARS1.Zn_a^{3-}] + [HARS1.Zn_b^{3-}]
\end{aligned} \tag{23}$$

According to **Scheme 1**, the species that are new and should be taken into account here are $H_3ARS1.Zn_b^+$, $H_2ARS1.Zn_c^{2-}$, and $HARS1.Zn_b^{3-}$.

3.2.9 $H_2ARS1.Zn_b^{2-}$-H_2PPi^{2-} Interactions

The final consideration is the interactions between PPi and the formed sensor $H_2ARS1.Zn_b^{2-}$ meaning the last piece of the entire **Scheme 1**. Therefore, in addition to the all species noticed in previous **Sections 3.2.1–3.2.8**, the new species $H_4ARS1.ZnPPi_a^{2-}$ and $H_4ARS1.ZnPPi_b^{-}$ were included in our mathematical model.

TABLE 3 | Obtained affinity thermodynamic constants for the simulated pH datasets corresponding to binding affinities of Zn^{2+} to PPi, ARS and **1**.

Species	Used to construct data		Calculated		
	ΔH (J/mole)	ΔS (J/mole.K)	ΔH (J/mole)	ΔS (J/mole.K)	ssq
$\boldsymbol{ZnPPi}^{2-}$	86,322	441	86,146 ± 189[a] (–0.20%)[b]	439 ± 0.65 (–0.21%)	3.18×10^{-4}
$\boldsymbol{ZnOHPPi}^{3-}$	99,370	326	98,711 ± 349 (–0.80%)	323 ± 1.20 (–0.20%)	
$\boldsymbol{ZnHPPi}^{-}$	104,390	625	104,133 ± 190 (–0.25%)	624 ± 0.65 (–0.66%)	
$\boldsymbol{ZnARS}^{-}$	102,380	522	102,731 ± 549 (0.34%)	523 ± 1.89 (0.04%)	3.36×10^{-3}
$\boldsymbol{ZnARS}_2^{4-}$	34,127	406	34,329 ± 638 (0.59%)	406 ± 2.20 (–0.01%)	
$1.\boldsymbol{Zn}^{+}$	80,299	413	80,440 ± 761 (0.18%)	413 ± 2.63 (0.12%)	3.19×10^{-4}
$\boldsymbol{H}1.\boldsymbol{Zn}^{2+}$	120,450	709	120,467 ± 782 (0.01%)	709 ± 2.70 (0.01%)	
$\boldsymbol{H}_2 1.\boldsymbol{Zn}^{3+}$	100,370	726	100,281 ± 1,155 (–0.09%)	725 ± 3.98 (–0.04%)	
$\boldsymbol{H}_3 1.\boldsymbol{ZnPPi}$	100,370	949	100,938 ± 6,993 (0.56%)	950 ± 24 (0.20%)	1.92×10^{-3}

[a]*The standard errors associated with the fitted parameters (σ_p).*
[b]*Accuracy associated with the fitted parameters.*

$$
\begin{aligned}
[\mathbf{1}]_{tot-calc} &= [\mathbf{1}^-] + [H\mathbf{1}] + [H_2\mathbf{1}^+] + [\mathbf{1}.Zn^+] + [H\mathbf{1}.Zn^{2+}] \\
&+ [H_2\mathbf{1}.Zn^{3+}] + [H_3ARS\mathbf{1}.Zn_a^+] + [H_3ARS\mathbf{1}.Zn_b^+] \\
&+ [H_2ARS\mathbf{1}.Zn_a^{2-}] + [H_2ARS\mathbf{1}.Zn_b^{2-}] \\
&+ [H_2ARS\mathbf{1}.Zn_c^{2-}] + [HARS\mathbf{1}.Zn_a^{3-}] \\
&+ [HARS\mathbf{1}.Zn_b^{3-}] + [H_4ARS\mathbf{1}.ZnPPi_a^{2-}] \\
&+ [H_4ARS\mathbf{1}.ZnPPi_b^-] \\
[ARS]_{tot-calc} &= [ARS^{3-}] + [HARS^{2-}] + [H_2ARS^-] + [ZnARS^{2-}] \\
&+ [ZnARS_2^{4-}] + [H_3ARS\mathbf{1}.Zn_a^+] \\
&+ [H_3ARS\mathbf{1}.Zn_b^+] + [H_2ARS\mathbf{1}.Zn_a^{2-}] \\
&+ [H_2ARS\mathbf{1}.Zn_b^{2-}] + [H_2ARS\mathbf{1}.Zn_c^{2-}] \\
&+ [HARS\mathbf{1}.Zn_a^{3-}] + [HARS\mathbf{1}.Zn_b^{3-}] \\
&+ [H_4ARS\mathbf{1}.ZnPPi_a^{2-}] + [H_4ARS\mathbf{1}.ZnPPi_b^-] \\
[H]_{tot-calc} &= [H^+] + [H\mathbf{1}] + 2[H_2\mathbf{1}^+] + [H\mathbf{1}.Zn^{2+}] \\
&+ 2[H_2\mathbf{1}.Zn^{3+}] + [HARS^{2-}] + 2[H_2ARS^-] \\
&+ 3[H_3ARS\mathbf{1}.Zn_a^+] + 3[H_3ARS\mathbf{1}.Zn_b^+] \\
&+ 2[H_2ARS\mathbf{1}.Zn_a^{2-}] + 2[H_2ARS\mathbf{1}.Zn_b^{2-}] \\
&+ 2[H_2ARS\mathbf{1}.Zn_c^{2-}] + [HARS\mathbf{1}.Zn_a^{3-}] \\
&+ [HARS\mathbf{1}.Zn_b^{3-}] + 4[H_4ARS\mathbf{1}.ZnPPi_a^{2-}] \\
&+ 4[H_4ARS\mathbf{1}.ZnPPi_b^-] - [OH^-][\\
Zn]_{tot-calc} &= [Zn^{2+}] + [\mathbf{1}.Zn^+] + [H\mathbf{1}.Zn^{2+}] + [H_2\mathbf{1}.Zn^{3+}] \\
&+ [ZnARS^{2-}] + 2[ZnARS_2^{4-}] + [H_3ARS1.Zn_a^+] \\
&+ [H_3ARS\mathbf{1}.Zn_b^+] + [H_2ARS\mathbf{1}.Zn_a^{2-}] \\
&+ [H_2ARS\mathbf{1}.Zn_b^{2-}] + [H_2ARS\mathbf{1}.Zn_c^{2-}] \\
&+ [HARS\mathbf{1}.Zn_a^{3-}] + [HARS\mathbf{1}.Zn_b^{3-}] \\
&+ [H_4ARS\mathbf{1}.ZnPPi_a^{2-}] + [H_4ARS\mathbf{1}.ZnPPi_b^-]
\end{aligned}
\tag{24}
$$

We mathematically defined the entire interactions with any order in **Scheme 1** using the concept in **Table 1**. Each species concentration is computed from the notation in **Table 1**, the formation thermodynamic constants, and the free component concentrations of H-PPi–ARS–1-Zn.

3.3 Guidance on the Interaction Between Mathematical Models and Experiments

With the mathematical models in place, it is now time to begin the process of using them in concert with experiments to study the molecular sensing system. Unknown thermodynamic parameters are fit by comparing model output with data, and the model itself can be assessed by predicting an unexpected experimental outcome (Banwarth-Kuhn and Sindi, 2020). To show how this step works, we simulated different data using the model and thermodynamic parameters mentioned as "used to construct data" in **Tables 2**, **3**, **6** with noise as a proxy to measured data for each separated part of the mechanism in **Scheme 1**. For each recognized sub mechanism, we optimized the physicochemical conditions of the simulated potentiometric data so that any species of the considered interactions exists at some minimal concentrations in the data. For some sub-mechanisms, regardless of initial guesses of the thermodynamic parameters being far from the used ones, we reached the results with low precision and accuracy errors like equilibria of ARS/1. However, for cases that required fitting more parameters, we had to come up with initial guesses closer to the real ones, which led to a longer fitting process. One way to avoid this problem is to collect less noisy, more informative data about all species present in the equilibria. The designed experiments for the investigation of the equilibrium network consist of a series of sample solutions with different known total concentrations of the components. The samples are titrated with a strong acid (HCl) at different temperatures to produce pH data under various conditions. There is no limit to the number of possible experiments. Apart from simple cases, pH titration will always include more data than minimally required to determine a particular parameter. It increases the robustness of the analysis and help deliver statistical information about the results, such as standard deviations of the fitted parameters. Here, the hydroxide ion is defined as negative proton concentration $[OH^-] = -[H^+]$, since in an aqueous solution, the addition of x moles of OH^- is equivalent to

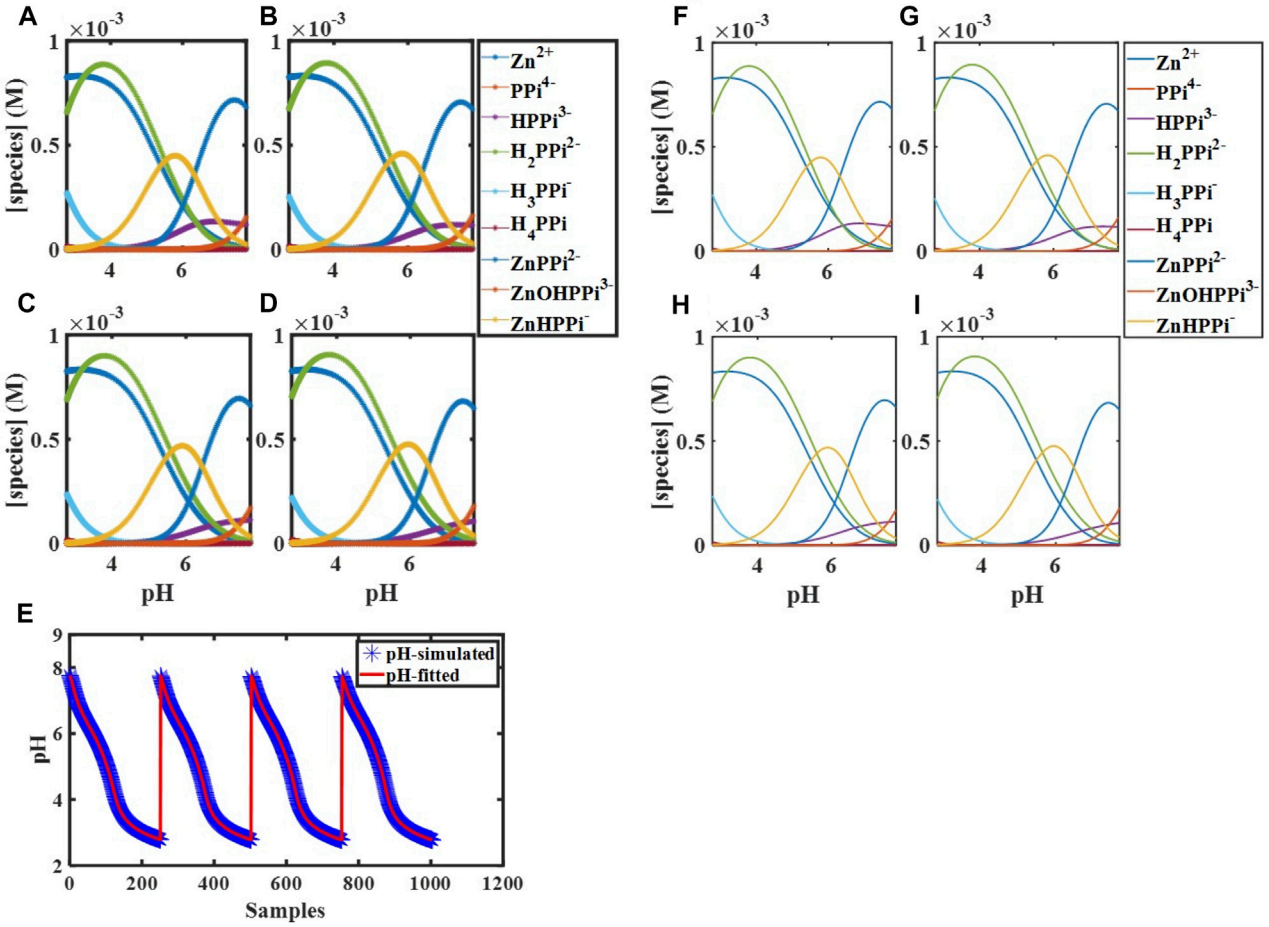

FIGURE 1 | Simulated concentration profiles for $[PPi]^0_{tot} = 9.9 \times 10^{-4}$ M, $[Zn]^0_{tot} = 8.7 \times 10^{-4}$ M, and $[H]^0_{tot} = 0$ M at **(A)** 283 K, **(B)** 288 K, **(C)** 293 K, and **(D)** 298 K; **(E)** Simulated and fitted pH for $[\boldsymbol{d}^{283}_{PPi-Zn}; \boldsymbol{d}^{288}_{PPi-Zn}; \boldsymbol{d}^{293}_{PPi-Zn}; \boldsymbol{d}^{298}_{PPi-Zn}]$; Concentration profiles of species obtained using global analysis corresponding to **(F)** 283 K, **(G)** 288 K, **(H)** 293 K, and **(I)** 298 K.

removing x moles of H^+. Its formation constant is the equilibrium constant of water K_w (or methanol for molecule **1**). Thermodynamic constants of water were kept fixed during all fitting processes. Of the different conditions examined, the optimized ones that lead to accurate and precise thermodynamic parameters are described in the following sections.

3.3.1 Fitting Thermodynamic Parameters of ARS/1 Equilibria

Concentration profiles were simulated based on the equilibrium model (**Eqs 1–11**), different initial concentrations for X and proton, thermodynamic constants, and Newton-Raphson algorithm (**Supplementary Figures S1A–D**). Taking the optimized initial concentrations of the components, $[E]^0_{tot}$ = 1 mM, $[H]^0_{tot}$ = 0 ($[H]^0_{tot}$ = 1 mM), titration is achieved by a strong acid causing change pH from ~11 to ~3. The total concentrations of the components at each titration point conveniently collected for both components X and H^+. pH changes during the titration process are used as the proxy to the measured data for fitting and acquiring equilibria information (**Supplementary Figure S1E**). These simulated data are collected in four augmented vectors of pH values at four different temperatures 283, 288, 293, and 298 K, $[\boldsymbol{d}^{283}_X; \boldsymbol{d}^{288}_X; \boldsymbol{d}^{293}_X; \boldsymbol{d}^{288}_X]$. To more rigorously test the analysis, random errors with mean zero and SD equal to 0.002 (a realistic value for pH meters) were added to the simulated data. All measurements corresponding to each system (ARS and **1**) were thus analyzed using global analysis. The analysis process results in not only the fitted formation thermodynamic constants (the purpose) but also the matrix of concentrations for all hidden species. **Supplementary Figures S1F–I** displays the acquired concentration profiles for species from the fitting, which are fully matched to the simulated profiles. The augmented data at four different temperatures for each system resulted in well-defined parameters with low standard deviations (**Table 2**).

3.3.2 Fitting Thermodynamic Parameters of Pyrophosphate Protonation Equilibria

According to the equilibria for PPi and vant's Hoff definition, there are eight thermodynamic constants corresponding to the species to

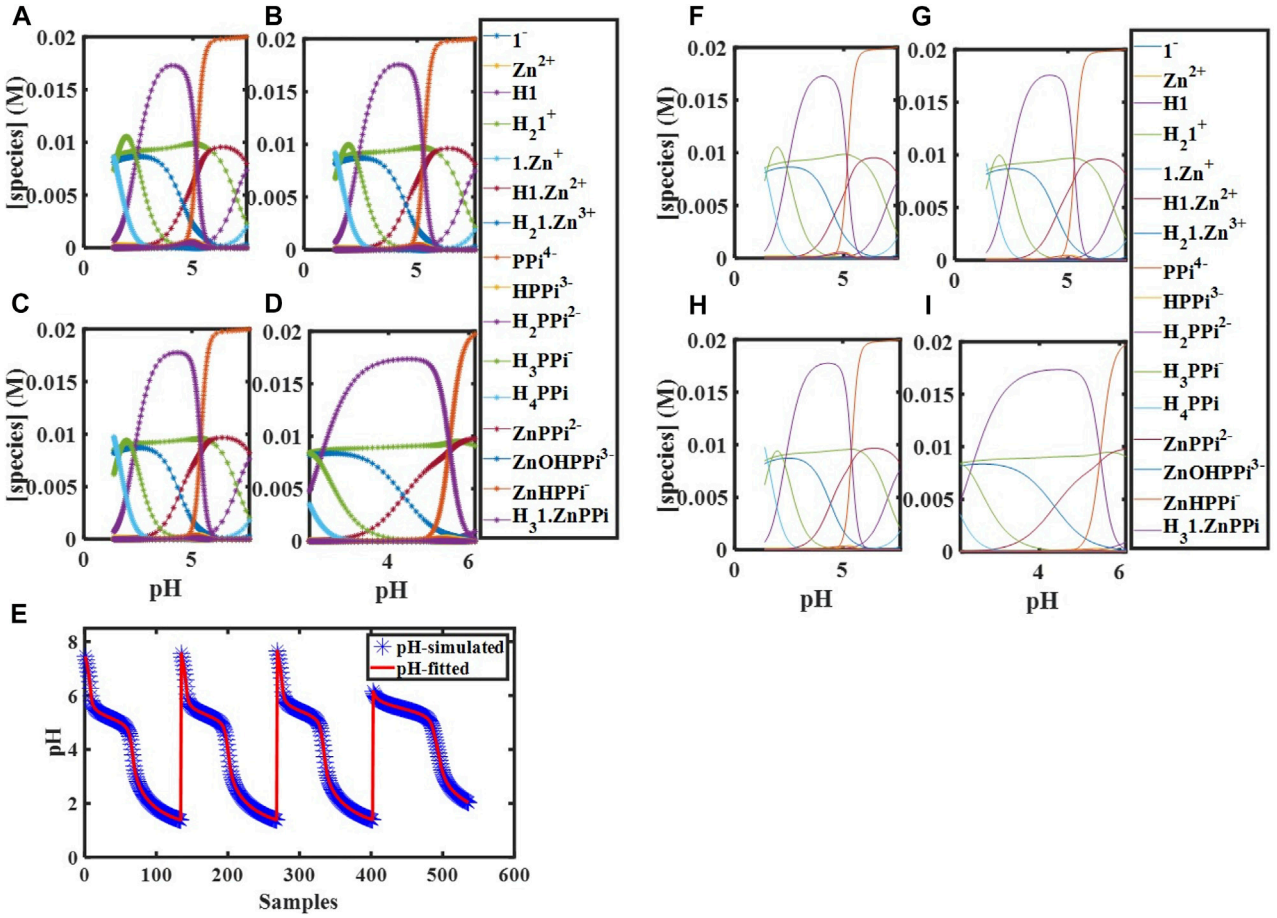

FIGURE 2 | Simulated concentration profiles for $[Zn]^0_{tot}$ = $[PPi]^0_{tot}$ = 20.00 mM, $[1]^0_{tot}$ = 10.00 mM, $[H]^0_{tot}$ = 0 at **(A)** 283 K, **(B)** 288 K, **(C)** 293 K, and **(D)** for $[Zn]^0_{tot}$ = $[PPi]^0_{tot}$ = 20.00 mM, $[1]^0_{tot}$ = 10.00 mM, $[H]^0_{tot}$ = 10.00 mM at 298 K; **(E)** Simulated and fitted pH for $[\boldsymbol{d}^{283}_{1-Zn-PPi}; \boldsymbol{d}^{288}_{1-Zn-PPi}; \boldsymbol{d}^{293}_{1-Zn-PPi}; \boldsymbol{d}^{298}_{1-Zn-PPi}]$; Concentration profiles of species obtained using global analysis corresponding to **(F)** 283 K, **(G)** 288 K, **(H)** 293 K, and **(I)** 298 K.

be determined. The enhanced number of unknown parameters needs finding experiment conditions that have sufficient equilibrium information. Similar to the previous section, simulation of concentration profiles based on the mathematical model (**Eqs 1–9**, **12–13**) requires initial concentrations for the components (*PPi* and *H*) and thermodynamic constants (Alberty, 1969) and subsequently calls the Newton-Raphson algorithm. The pH data was generated by calculating the minus logarithm of the simulated proton concentration profiles from the model. White noise with a SD of 0.002 was added to the data. The titration of solutions with initial concentrations of $[PPi]^0_{tot} = 9.90 \times 10^{-4}$ M, $[H]^0_{tot} = 0$ at the temperatures 283, 288, 293, and 298 K with a strong acid gave pH changes from ~11 to ~2. Fitting the model to the constructed data at these conditions showed around 11% accuracy error for thermodynamic parameters of H_4PPi associated with the low contribution of this species to the data (**Supplementary Figures S2A–D**). At 303 K and $[PPi]^0_{tot} = 9.90 \times 10^{-4}$ M, and $[H]^0_{tot} = 2.00 \times 10^{-4}$ M, another titration with pH variation 4.70–1.65 has been attained and added to the previous data (**Supplementary Figure S2E**). H_4PPi concentration is more noticeable at the new pH window. The fitting procedure on the five augmented data $[\boldsymbol{d}^{283}_{PPi}; \boldsymbol{d}^{288}_{PPi}; \boldsymbol{d}^{293}_{PPi}; \boldsymbol{d}^{288}_{PPi}; \boldsymbol{d}^{303}_{PPi}]$ delivered thermodynamic parameters with low errors and the acquired concentration profiles of species (**Table 2**, **Supplementary Figures S2F–K**).

TABLE 4 | The pH presence window for the species of **Scheme 1**.

Species	pH	Species	pH
ARS^{2-}	8–11.5	$\boldsymbol{ZnARS}^{4-}_2$	5–11
$HARS^-$	4.5–11.5	$1.\boldsymbol{Zn}^+$	6–11
H_2ARS	4.5–7.5	$\boldsymbol{H}1.\boldsymbol{Zn}^{2+}$	3–11
1^-	7–11.5	$\boldsymbol{H}_2 1.\boldsymbol{Zn}^{3+}$	2–8
H1	5–11	$\boldsymbol{ZnPPi}^{2-}$	4–11
$H_2 1^+$	4–8	$\boldsymbol{ZnOHPPi}^{3-}$	6–11
$\boldsymbol{PPi}^{4-}$	7–11	$\boldsymbol{ZnHPPi}^-$	3–9
$HPPi^{3-}$	4–10	$\boldsymbol{H}_3 1.\boldsymbol{ZnPPi}$	2–6
$H_2\boldsymbol{PPi}^{2-}$	2–9	$\boldsymbol{H}_3\boldsymbol{ARS}1^-_a$	4–8
$H_3\boldsymbol{PPi}^-$	0.5–5	$\boldsymbol{H}_2\boldsymbol{ARS}1^{2-}_a$	5–11
$H_4\boldsymbol{PPi}$	0.5–4	$\boldsymbol{H}_2\boldsymbol{ARS}1^{2-}_b$	5–11
Zn^{2+}	1.5–10	$\boldsymbol{HARS}1^{3-}_a$	8–11.5
$\boldsymbol{ZnARS}^-$	2–10.5	—	—

TABLE 5 | Conditions of the simulated datasets related to ARS and **1** titration with a strong acid.

Data	Temperature (K)	$[ARS]_{tot}$ (M)	$[H]_{tot}$ (M)	$[1]_{tot}$ (M)	$[H]_{titrant}$ (M)
d^{278}_{1-ARS}	278	1.00×10^{-3}	2.00×10^{-11}	1.00×10^{-3}	18.00×10^{-2}
d^{284}_{1-ARS}	284				8.00×10^{-2}
d^{298}_{1-ARS}	298				18.00×10^{-2}
$d^{308}_{1-ARS_1}$	308				
$d^{308}_{1-ARS_2}$	308		1.90×10^{-3}		

TABLE 6 | Obtained affinity thermodynamic constants for the simulated pH datasets corresponding to binding affinities of ARS, **1**, Zn, and PPi.

Species	Used to construct data		Calculated		
	ΔH (J/mole)	ΔS (J/mole.K)	ΔH (J/mole)	ΔS (J/mole.K)	ssq
H_3ARS1^+	104,350	880	104,350 ± 10,883[a] (0.00%)[b]	889 ± 37 (0.64%)	2.29×10^{-3}
H_2ARS1_a	71,633	691	71,633 ± 2,718 (–0.00)	691 ± 7.93 (0.001%)	
H_2ARS1_b	37,845	571	37,845 ± 4,620 (–0.004%)	571 ± 18.17 (0.002%)	
$HARS1^-_a$	28,935	351	28,935 ± 350 (0.001%)	351 ± 1.23 (0.004%)	
$H_2ARS1.Zn^{2-}_c$	100,370	846	96,900 ± 51 (–1.45%)	834 ± 18.21 (–3.45%)	1.81×10^{-3}
$H_4ARS1.ZnPPi^{2-}_a$	100,370	1,269	99,145 ± 2,820 (–1.22%)	1,264 ± 11.11 (–0.37%)	1.80×10^{-3}
$H_4ARS1.ZnPPi_b$	130,490	1,364	128,836 ± 6,068 (–1.27%)	1,359 ± 16.97 (–0.32%)	

[a]*The standard errors associated with the fitted parameters (σ_p).*
[b]*Accuracy associated with the fitted parameters.*

3.3.3 Fitting Thermodynamic Parameters of Assemblies of Zinc-Pyrophosphate

Having the total concentrations of PPi^{4-}, Zn^{2+}, and H^+ and the thermodynamic constants (Moe and Wiest, 1977), free concentrations of species in **Eqs 14, 15** are calculated *via* the model and Newton–Raphson solution. Again, pH changes during the titration process are used as the measured data for fitting and acquiring equilibria information. The concentrations of pyrophosphate and zinc ions in the potentiometric titrations were 9.9×10^{-4} M and 8.7×10^{-4} M, respectively. Higher concentrations of zinc and pyrophosphate were not considered because the precipitation of $ZnHPPi^-$ becomes a serious problem (Moe and Wiest, 1977). The simulated data are collected in four vectors of pH values at temperatures 283, 288, 293, and 298 K, with white noise along to SD of 0.002. pH changes at these conditions are from ~8 to ~3. Here, our fitting purpose was only computing zinc-pyrophosphate thermodynamic constants. Thermodynamic parameters of pyrophosphate protonation equilibria were kept known in the model obtained from **Section 3.3.2**. The simulated data and fitting results are given in **Figures 1A–I** and **Table 3**.

3.3.4 Fitting Thermodynamic Parameters of Zinc and ARS Interactions

Concentration profiles were simulated based on the generalized equilibrium model (**Eqs 16, 17**) at the same temperatures and initial concentrations we used for ARS (**Section 3.3.1**) along with $[Zn]^0_{tot} = 5.00 \times 10^{-4}$ M (Kaushik et al., 2015; Zhang et al., 2007). Next, pH changes during the titration process with white noise along to SD of 0.002 were used as the measured data [d^{283}_{ARS-Zn}; d^{288}_{ARS-Zn}; d^{293}_{ARS-Zn}; d^{298}_{ARS-Zn}] for fitting and acquiring equilibria information of **Eq. 14**. Thermodynamic constants of ARS protonation are kept known in the model, since they were already computed from **Eqs 10, 11** in **Section 3.3.1**. We collected promising fitting results in **Supplementary Figures S3A–I**, and **Table 3**.

3.3.5 Fitting Thermodynamic Parameters of Zinc and 1 Complexes

Using the total concentrations of $[1]_{tot}$, $[H]_{tot}$, and $[Zn]_{tot}$ and the formation constants derived from their thermodynamic parameters (Gruenwedel, 1968; O'Neil and Smith, 2006; Wong et al., 2009), free concentrations of all species can be calculated *via* **Eq. 19** and Newton–Raphson solution at each titration point. To obtain ΔH and ΔS related to each species, the temperatures used for molecule **1** titrations (**Section 3.3.1**) and $[Zn]^0_{tot} = [1]^0_{tot} =$ 1.00 mM and $[H]^0_{tot} = 0$ are used to generate different pH measurements based on the mentioned model with white noise (SD 0.002). The fitting results of this global analysis for this equilibrium system eventuate accurately defined parameters with the acceptable standard deviations and hidden concentrations of the involved species (**Supplementary Figure S4**, **Table 3**).

3.3.6 Fitting Thermodynamic Parameters of $H_31.ZnPPi$ Complex

Concentration profiles were simulated based on the equilibrium model for two different initial concentrations of components, $[Zn]^0_{tot} = [PPi]^0_{tot} = 20.00$ mM, $[1]^0_{tot} = 10.00$ mM, $[H]^0_{tot} = 0$ at 283, 288, and 293 K showing pH changes from ~7.50 to 1.50 and $[Zn]^0_{tot} = [PPi]^0_{tot} = 20.00$ mM, $[1]^0_{tot} = 10.00$ mM, $[H]^0_{tot} =$ 10.00 mM at 298 K with pH changes from ~6.00 to 2.00. According to the modeled concentration profiles (**Figure 2**), $H_31.ZnPPi$ presents mostly in the pH range 6.00–2.00. The

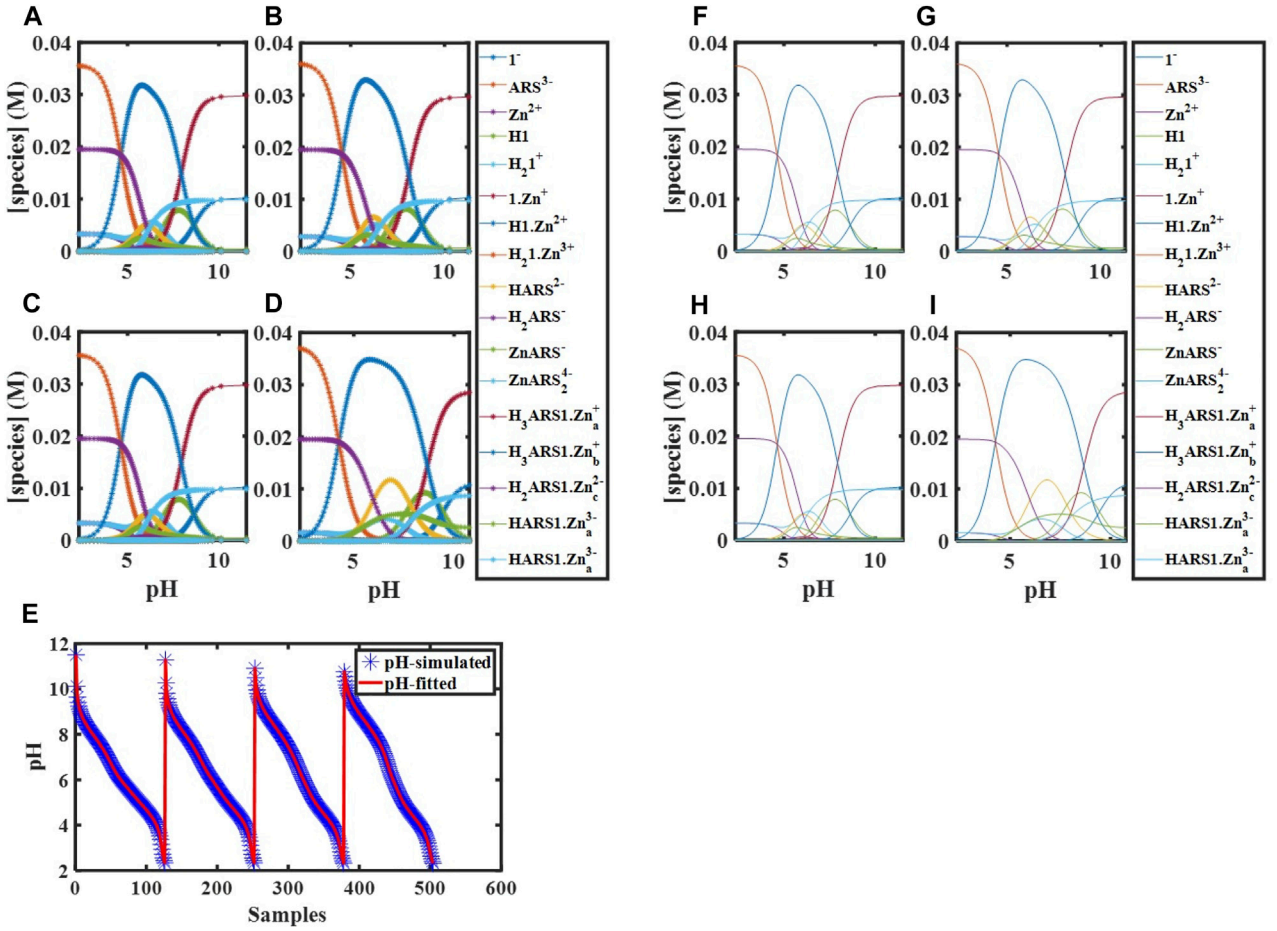

FIGURE 3 | Simulated concentration profiles for $[Zn]^0_{tot}$ = $[1]^0_{tot}$ = 40.00 mM, $[ARS]^0_{tot}$ = 20.00 mM, $[OH]^0_{tot}$= 5 × 10^{-4} M at **(A)** 278 K, **(B)** 284 K, **(C)** 298 K, and **(D)** 308 K; **(E)** Simulated and fitted pH for [$\boldsymbol{d}^{278}_{1-Zn-ARS}$; $\boldsymbol{d}^{284}_{1-Zn-ARS}$; $\boldsymbol{d}^{298}_{1-Zn-ARS}$; $\boldsymbol{d}^{308}_{1-Zn-ARS}$]; Concentration profiles of species obtained using global analysis corresponding to **(F)** 278 K, **(G)** 284 K, **(H)** 298 K, and **(I)** 308 K.

simulated datasets were again the pH profiles along to white noise with a SD 0.002. Here, the only unknown parameters were the thermodynamic constants corresponding to $H_31.ZnPPi$ species since the rest fitted before, using **Eqs 11, 13, 15, 19**. The fitting procedure delivers these parameters precisely (**Figure 2**, **Table 3**).

3.3.7 Fitting Thermodynamic Parameters of Assemblies of ARS and 1

The next consideration was the determination of the binding affinities of **1** to ARS in solutions of varying pHs. As can be seen in **Scheme 1**, ten different forms (species and components) are involved in their interactions. The thermodynamic parameters associated with H_2ARS^-, $HARS^{2-}$, H_21^+, and $H1$ were previously determined by separate experiment designs. The point about the rest species, $H_2ARS1^{2-}_a$, $H_2ARS1^{2-}_b$, and $HARS1^{3-}_a$, is they convert each other in a triangular path. The changes in the concentrations of $H_2ARS1^{2-}_a$ and $H_2ARS1^{2-}_b$ are dependent to each other with a fully overlapped presence window of pH (**Table 4**). Also, the binding constants related to these species are fully correlated. Species that are formed from different ways, but, with the same components are correlated. This comes from the fact that in the final mass balance equation of $[H]_{tot-calc}$, there is a new constant, which equals to the summation of equilibrium constants of the correlated species. Based on previous reports (Parczewski and Kateman, 1994), two completely correlated parameters cannot be computed in a chemical model because an increase or decrease of one parameter is compensated by the other. One way to solve such instances is the parameter value of one of the correlated parameters should be fixed and hence not involved in the fitting process. But, in most cases both parameter values are completely unknown and therefore, fixing one is not a viable option. In our previous study, we discovered that coupled equilibrium-kinetic mechanisms can also solve this problem (Emami et al., 2015). Here, we explored that simulating pH data at different temperatures, and initial concentrations of components and augmenting them as one dataset [$\boldsymbol{d}^{278}_{1-ARS}$; $\boldsymbol{d}^{284}_{1-ARS}$; $\boldsymbol{d}^{298}_{1-ARS}$; $\boldsymbol{d}^{308}_{1-ARS_1}$; $\boldsymbol{d}^{308}_{1-ARS_2}$], global analysis (**Table 5**), allows obtaining the fully

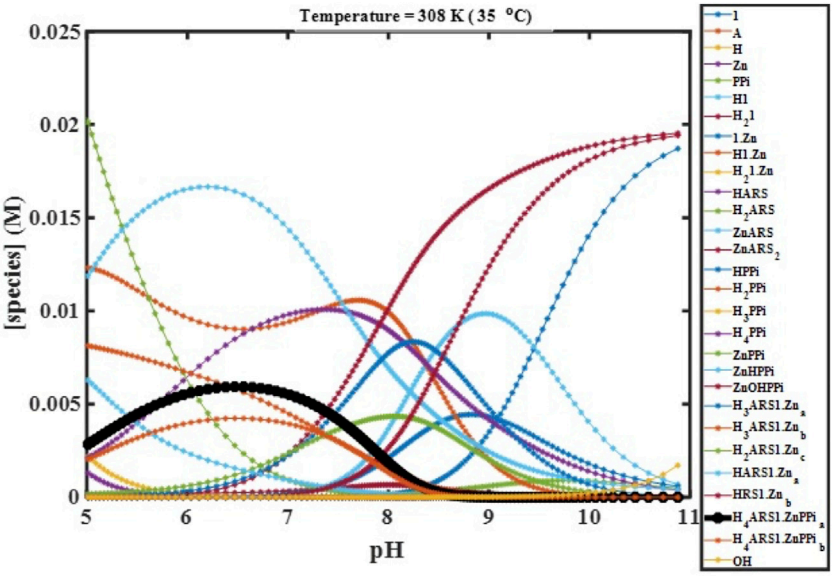

FIGURE 4 | Concentration profiles of all species in the reaction mechanism (**Scheme 1**) at different pHs obtained using the developed model and Newton-Raphson Algorithm.

correlated binding constants (**Supplementary Figure S5**, **Table 6**). Different experiment conditions and the global analysis eliminated the full correlation between binding constants in the assemblies of ARS and 1 and led to earning their thermodynamic constants correctly. Clearly, experimental conditions have to be chosen carefully. Any species needs to exist at some minimal concentration somewhere during the titration for which the thermodynamic constants are to be determined.

3.3.8 Fitting Thermodynamic Parameters of Assemblies of ARS and 1·Zn

According to **Scheme 1**, the species that are new and should be considered here are $H_3ARS1.Zn_b^+$, $H_2ARS1.Zn_c^{2-}$, and $HARS1.Zn_b^{3-}$. We simulated several pH data at different experimental conditions for the fitting purpose. In the best conditions, using the initial concentrations of 20 mM ARS and 40 mM 1·Zn at six different temperatures with pH range 2–11, the concentrations of $H_3ARS1.Zn_b^+$ and $HARS1.Zn_b^{3-}$ do not exceed ~1.00×10^{-6} and 1.00×10^{-8}, respectively. Having these low amounts, the change in pH is less affected by these species, and so obtaining their thermodynamic parameters is impossible. The model fitting is thereby truncated by ignoring their participants, and the only considered thermodynamic parameters were related to $H_2ARS1.Zn_c^{2-}$. At the mentioned initial concentrations and temperatures 278, 284, 298, and 308 K, ΔH and ΔS of $H_2ARS1.Zn_c^{2-}$have been obtained with acceptable accuracy and precision (**Figure 3**, **Table 6**).

3.3.9 $H_2ARS1.Zn_b^{2-}$-H_2PPi^{2-} Interactions

With the thermodynamic values for the species considered before in hand, further pH titrations were performed to determine the ΔH and ΔS constants of the new species, $H_4ARS1.ZnPPi_a^{2-}$ and $H_4ARS1.ZnPPi_b^-$. We simulated the concentration profiles of species stated in **Eq. 24**. The obtained pH values from 12 to 2 were examined to probe the associations of ARS, **1**, and Zn, with the two-protonated form of PPi. Finally, the data from conditions containing 40 mM ARS and Zn, and 20 mM **1** and PPi at four different temperatures, 278, 284, 308, and 318 K, with pH range ~5–12 were used to determine the parameters. Simulated and calculated pH for the augmented datasets is shown in **Supplementary Figure S6**, **Table 6**. A good agreement between the simulated and calculated pHs by the model further supports our new suggestion method to obtain all equilibrium constants correctly just using the pH data. The interesting point is the possibility of target sensing by the very simple pH metric approach.

3.4 Predict Optimum Conditions for Pyrophosphate Monitoring Using the Developed Mathematical Model

With fit thermodynamic parameters, the mathematical model could be probed for parameter sensitivity and can predict what should happen under particular initial conditions. When we measure data, it is often only possible to experimentally observe a subset of the state variables of interest. For example, here, only the proton concentration in the form of pH can be visualized. The mathematical model can reveal the "hidden" concentrations of all other species too.

We performed computer simulations at fitted values of binding constants, different temperatures, initial concentrations, and starting pHs using the constructed mathematical model, which describes the complete molecular behavior. These simulations enabled the visualization of the experimental variables' effects on the desired combination ($H_4ARS1.ZnPPi_a^{2-}$) that produces high-intensity fluorescence response leading to PPi detection. For instance, simulation at initial concentrations 40 mM ARS, and 20 mM **1**.Zn,

OH, and PPi, temperature 308 K (35°C), and pH 5–11 shows the concentration of the desired combination peaks at pH ranges from 6.2 to 7 (**Figure 4**). This scenario provides directions to reach the maximum possible sensitivity and selectivity of **1**.Zn-ARS assemblies towards PPi as our target by fine-tuning different experimental conditions. This mathematical model can be used to study how sensitive one output of interest is to increasing or decreasing the quantity of other factors. The mathematical model can also be used to aid in the design of new experiments. It should be pointed that the values of extracted thermodynamic parameters should be in favor of the target combination to have a practical sensing system. In case of weak interactions, tuning the extracted equilibrium constants of different combinations among the species can also enhance the desired result. For example, changing physicochemical conditions like ionic strength and/or adding/removing a component to the system can alter the values of the thermodynamic constants in favor of the desired combination in which the sensitivity increases.

4 CONCLUSION

Using mathematical modeling and the proposed stepwise experiment design, we showed how to quantitatively determine the association of the entire identified interactions among **1** Zn, ARS, PPi and their combinations. After the mathematical algorithm is written in MATLAB, we determined the thermodynamic parameters constants, ΔH and ΔS, quickly and accurately without having to rely on the assumptions that are inherent in many other common treatment methods. Various values of temperatures, initial concentrations, and starting pHs were considered to optimize the measurement conditions in the use of potentiometric assessments for thermodynamic studies. As a result, we computed all free species concentrations as a function of pH titration using the numerical Newton-Raphson algorithm, and therefore evaluation of multiple simultaneous equations is achieved. This method should be generally applicable so long as the supramolecular system is pH dependent.

Our results demonstrate the power of potentiometric titrations when used in conjunction with mathematical modeling methods to reveal details of the mechanisms of the complex fluorescent sensors used widely in biological chemistry. The significance of this subject can be very much enhanced by the possibility of easily describing mathematically the behavior of complex systems and fine-tuning them for different applications. The very important point in gaining potentiometric data is the pH changes related to the presence region of each species should have adequate titration points. Based on these insights, we highlight how the extraction of binding data from a network of equilibria using mathematical modeling can produce optimum conditions for real-time oligophosphate monitoring. General speaking, the results represent a significant step forward in elucidating the chemistry of complex fluorescent probes and provide a paradigm for future work in this area.

DATA AVAILABILITY STATEMENT

The original contributions presented in the study are included in the article/**Supplementary Material**, further inquiries can be directed to the corresponding author.

AUTHOR CONTRIBUTIONS

FE developed the model, performed the calculations, wrote the manuscript, and directed the research. HA advised on developing the model. TM advised on figuring the details of the supramolecular mechanism. BP and SR helped to achieve the simulations and analyze the data.

FUNDING

We gratefully acknowledge research reported in this publication is based upon work supported by the National Institute of General Medical Sciences of the National Institutes of Health under Award Number R15GM134492. The content is solely the responsibility of the authors and does not necessarily represent the official views of the National Institutes of Health.

SUPPLEMENTARY MATERIAL

The Supplementary Material for this article can be found online at: https://www.frontiersin.org/articles/10.3389/fchem.2021.759714/full#supplementary-material

REFERENCES

Alberty, R. A. (1969). Standard Gibbs Free Energy, Enthalpy, and Entropy Changes as a Function of pH and pMg for Several Reactions Involving Adenosine Phosphates. *J. Biol. Chem.*, 244(12), 3290–3302. doi:10.1016/S0021-9258(18)93127-3

Anslyn, E. V. (2007). Supramolecular Analytical Chemistry. *J. Org. Chem.* 72 (3), 687–699. doi:10.1021/jo0617971

Ayme, J.-F., Beves, J. E., Leigh, D. A., McBurney, R. T., Rissanen, K., and Schultz, D. (2012). A Synthetic Molecular Pentafoil Knot. *Nat. Chem* 4 (1), 15–20. doi:10.1038/NCHEM.1193

Banwarth-Kuhn, M., and Sindi, S. (2020). How and Why to Build a Mathematical Model: A Case Study Using Prion Aggregation. *J. Biol. Chem.* 295 (15), 5022–5035. doi:10.1074/jbc.REV119.009851

Bevington, P. R., Robinson, D. K., Blair, J. M., Mallinckrodt, A. J., and McKay, S. (1993). Data Reduction and Error Analysis for the Physical Sciences. *Comput. Phys.* 7 (4), 415–416. doi:10.1063/1.4823194

Boul, P. J., Reutenauer, P., and Lehn, J.-M. (2005). Reversible Diels–Alder Reactions for the Generation of Dynamic Combinatorial Libraries. *Org. Lett.* 7 (1), 15–18. doi:10.1021/ol048065k

Connors, K. A. (1987). *Binding Constants: The Measurement of Molecular Complex Stability*. Wiley-Interscience.

Emami, F., Maeder, M., and Abdollahi, H. (2015). Model-based Analysis of Coupled Equilibrium-Kinetic Processes: Indirect Kinetic Studies of Thermodynamic Parameters Using the Dynamic Data. *Analyst* 140 (9), 3121–3135. doi:10.1039/C4AN02279C

Giri, J., Diallo, M. S., Simpson, A. J., Liu, Y., Goddard, W. A., Kumar, R., et al. (2011). Interactions of Poly(amidoamine) Dendrimers with Human Serum

Albumin: Binding Constants and Mechanisms. *Acs Nano* 5 (5), 3456–3468. doi:10.1021/nn1021007

Goral, V., Nelen, M. I., Eliseev, A. V., and Lehn, J.-M. (2001). Double-level "orthogonal" Dynamic Combinatorial Libraries on Transition Metal Template. *Proc. Natl. Acad. Sci.* 98 (4), 1347–1352. doi:10.1073/pnas.98.4.1347

Gruenwedel, D. W. (1968). Multidentate Coordination Compounds. Chelating Properties of Aliphatic Amines Containing .alpha.-pyridyl Residues and Other Aromatic Ring Systems as Donor Groups. *Inorg. Chem.* 7 (3), 495–501. doi:10.1021/ic50061a022

Hargrove, A. E., Zhong, Z., Sessler, J. L., and Anslyn, E. V. (2010). Algorithms for the Determination of Binding Constants and Enantiomeric Excess in Complex Host : Guest Equilibria Using Optical Measurements. *New J. Chem.* 34 (2), 348–354. doi:10.1039/B9NJ00498J

Johnson-Buck, A., Su, X., Giraldez, M. D., Zhao, M., Tewari, M., and Walter, N. G. (2015). Kinetic Fingerprinting to Identify and Count Single Nucleic Acids. *Nat. Biotechnol.* 33 (7), 730–732. doi:10.1038/nbt.3246

Kaushik, R., Kumar, P., Ghosh, A., Gupta, N., Kaur, D., Arora, S., et al. (2015). Alizarin Red S-Zinc(ii) Fluorescent Ensemble for Selective Detection of Hydrogen Sulphide and Assay with an H2S Donor. *RSC Adv.* 5 (97), 79309–79316. doi:10.1039/C5RA11901D

Lehn, J.-M. (1994). Supramolecular Chemistry. *Proc. Indian Acad. Sciences-Chemical Sci.* 106, 915–922.

Lim, N. C., Freake, H. C., and Brückner, C. (2005). Illuminating Zinc in Biological Systems. *Chem. - A Eur. J.* 11 (1), 38–49. doi:10.1002/chem.200400599

Maeder, M., and Neuhold, Y.-M. (2007). *Practical Data Analysis in Chemistry*, Vol. 26. (Newcastle, Australia: Elsevier).

Maeder, M., Neuhold, Y.-M., Puxty, G., and King, P. (2003). Analysis of Reactions in Aqueous Solution at Non-constant pH: No More Buffers? *Phys. Chem. Chem. Phys.* 5 (13), 2836–2841. doi:10.1039/B301488F

Martínez-Máñez, R. (2014). Virtual Issue:Molecular Sensors. Wiley Online Library. Nicosia, New Jersey

Meier, S., and Beeren, S. R. (2014). Simultaneous Determination of Binding Constants for Multiple Carbohydrate Hosts in Complex Mixtures. *J. Am. Chem. Soc.* 136 (32), 11284–11287. doi:10.1021/ja506130q

Minami, T., Emami, F., Nishiyabu, R., Kubo, Y., and Anzenbacher, P. (2016). Quantitative Analysis of Modeled ATP Hydrolysis in Water by a Colorimetric Sensor Array. *Chem. Commun.* 52 (50), 7838–7841. doi:10.1039/C6CC02923J

Moe, O. A., and Wiest, S. A. (1977). Determination of Stability Constants for Zinc-Pyrophosphate Complexes. *Anal. Biochem.* 77 (1), 73–78. doi:10.1016/0003-2697(77)90291-3

Mugridge, J. S. (2010). *Supramolecular Host-Guest Interactions, Dynamics And Structure [PhD Thesis]*. UC Berkeley.

Nonaka, A., Horie, S., James, T. D., and Kubo, Y. (2008). Pyrophosphate-induced Reorganization of a Reporter-Receptor Assembly *via* Boronate Esterification; a New Strategy for the Turn-On Fluorescent Detection of Multi-Phosphates in Aqueous Solution. *Org. Biomol. Chem.* 6 (19), 3621–3625. doi:10.1039/B808027E

O'Neil, E. J., and Smith, B. D. (2006). Anion Recognition Using Dimetallic Coordination Complexes. *Coord. Chem. Rev.* 250 (23–24), 3068–3080. doi:10.1016/j.ccr.2006.04.006

Palmer, A. E., and Tsien, R. Y. (2006). Measuring Calcium Signaling Using Genetically Targetable Fluorescent Indicators. *Nat. Protoc.* 1 (3), 1057–1065. doi:10.1038/nprot.2006.172

Parczewski, A., and Kateman, G. (1994). Prediction and Visualization of Correlations between Parameters of the Mathematical Models of Processes. *Chemometrics Intell. Lab. Syst.* 25 (2), 265–283. doi:10.1016/0169-7439(94)85047-X

Pérez-Fuertes, Y., Kelly, A. M., Johnson, A. L., Arimori, S., Bull, S. D., and James, T. D. (2006). Simple Protocol for NMR Analysis of the Enantiomeric Purity of Primary Amines. *Org. Lett.* 8 (4), 609–612. doi:10.1021/ol052776g

Que, E. L., Domaille, D. W., and Chang, C. J. (2008). Metals in Neurobiology: Probing Their Chemistry and Biology with Molecular Imaging. *Chem. Rev.* 108 (5), 1517–1549. doi:10.1021/cr078203u

Sheff, J. T., Lucius, A. L., Owens, S. B., and Gray, G. M. (2011). Generally Applicable NMR Titration Methods for the Determination of Equilibrium Constants for Coordination Complexes: Syntheses and Characterizations of Metallacrown Ethers with α,ω-Bis(phosphite)-polyether Ligands and Determination of Equilibrium Binding Constants to Li+. *Organometallics* 30 (21), 5695–5709. doi:10.1021/om200580t

Sydney Gladman, A., Matsumoto, E. A., Nuzzo, R. G., Mahadevan, L., and Lewis, J. A. (2016). Biomimetic 4D Printing. *Nat. Mater* 15 (4), 413–418. doi:10.1038/NMAT4544

Tomsho, J. W., and Benkovic, S. J. (2012). Elucidation of the Mechanism of the Reaction between Phenylboronic Acid and a Model Diol, Alizarin Red S. *J. Org. Chem.* 77 (5), 2098–2106. doi:10.1021/jo202250d

Vicens, J., and Vicens, Q. (2011). Emergences of Supramolecular Chemistry: From Supramolecular Chemistry to Supramolecular Science. *J. Incl Phenom Macrocycl Chem.* 71 (3), 251–274. doi:10.1007/s10847-011-0001-z

Wilkins, R. G. (1991). *Kinetics and Mechanisms of Reactions of Transition Metal Complexes*. (VeinHeim (Federal Republic of Germany): VCH Publishers). doi:10.1002/3527600825

Wong, B. A., Friedle, S., and Lippard, S. J. (2009). Solution and Fluorescence Properties of Symmetric Dipicolylamine-Containing Dichlorofluorescein-Based Zn2+ Sensors. *J. Am. Chem. Soc.* 131 (20), 7142–7152. doi:10.1021/ja900980u

You, L., Zha, D., and Anslyn, E. V. (2015). Recent Advances in Supramolecular Analytical Chemistry Using Optical Sensing. *Chem. Rev.* 115 (15), 7840–7892. doi:10.1021/cr5005524

Zhang, L., Dong, S., and Zhu, L. (2007). Fluorescent Dyes of the Esculetin and Alizarin Families Respond to Zinc Ions Ratiometrically. *Chem. Commun.* 19, 1891–1893. doi:10.1039/B618413H

Conflict of Interest: The authors declare that the research was conducted in the absence of any commercial or financial relationships that could be construed as a potential conflict of interest.

Publisher's Note: All claims expressed in this article are solely those of the authors and do not necessarily represent those of their affiliated organizations, or those of the publisher, the editors and the reviewers. Any product that may be evaluated in this article, or claim that may be made by its manufacturer, is not guaranteed or endorsed by the publisher.

frontiers in Chemistry

REVIEW
published: 07 January 2022
doi: 10.3389/fchem.2021.816266

Facing Diseases Caused by Trypanosomatid Parasites: Rational Design of Pd and Pt Complexes With Bioactive Ligands

Dinorah Gambino and Lucía Otero**

Área Química Inorgánica, DEC, Facultad de Química, Universidad de la República, Montevideo, Uruguay

Human African Trypanosomiasis (HAT), Chagas disease or American Trypanosomiasis (CD), and leishmaniases are protozoan infections produced by trypanosomatid parasites belonging to the kinetoplastid order and they constitute an urgent global health problem. In fact, there is an urgent need of more efficient and less toxic chemotherapy for these diseases. Medicinal inorganic chemistry currently offers an attractive option for the rational design of new drugs and, in particular, antiparasitic ones. In this sense, one of the main strategies for the design of metal-based antiparasitic compounds has been the coordination of an organic ligand with known or potential biological activity, to a metal centre or an organometallic *core*. Classical metal coordination complexes or organometallic compounds could be designed as multifunctional agents joining, in a single molecule, different chemical species that could affect different parasitic targets. This review is focused on the rational design of palladium(II) and platinum(II) compounds with bioactive ligands as prospective drugs against trypanosomatid parasites that has been conducted by our group during the last 20 years.

Keywords: antiparasitic agents, rational design, trypanosomatid parasites, palladium, platinum

OPEN ACCESS

Edited by:
Valeria Conte,
University of Rome Tor Vergata, Italy

Reviewed by:
Rubem Figueiredo Sadok Menna-Barreto,
Oswaldo Cruz Foundation (Fiocruz), Brazil
Samuel M. Meier-Menches,
University of Vienna, Austria

****Correspondence:***
Dinorah Gambino
dgambino@fq.edu.uy
Lucía Otero
luotero@fq.edu.uy

Specialty section:
This article was submitted to Medicinal and Pharmaceutical Chemistry, a section of the journal Frontiers in Chemistry

Received: *16 November 2021*
Accepted: *15 December 2021*
Published: *07 January 2022*

Citation:
Gambino D and Otero L (2022) Facing Diseases Caused by Trypanosomatid Parasites: Rational Design of Pd and Pt Complexes With Bioactive Ligands. Front. Chem. 9:816266. doi: 10.3389/fchem.2021.816266

INTRODUCTION

Seventeen infectious diseases have been named by the World Health Organization (WHO) as Neglected Tropical Diseases (NTDs), mainly due to low pharmaceutical industry investment in drug research because of the low associated revenue. Consequently, most of the efforts related to the search of new chemotherapeutics against these diseases has come from the academy. More than 20% of the world's population lives in regions where these diseases are endemic. The impact of NTDs on the affected countries is enormous because of mortality and morbidity that causes important economic losses (World Health Organization, 2012; De Rycker et al., 2018; Chami and Bundy, 2019; World Health Organization, 2021a).

Human African Trypanosomiasis (HAT), Chagas disease or American Trypanosomiasis (CD), and leishmaniases are protozoan infections produced by trypanosomatid parasites belonging to the kinetoplastid order. These are among the most important neglected diseases and constitute an urgent health problem in developing countries. They are often co-endemic in certain regions of the world (Leishmaniasis and Chagas' disease in South America and Leishmaniasis and HAT in Africa) and they have span worldwide because of globalization caused by human migration. Despite being some of the most life-threatening infective diseases, only a poor and inadequate chemotherapy is available (De Rycker et al., 2018; Santos et al., 2020; Kourbeli et al., 2021).

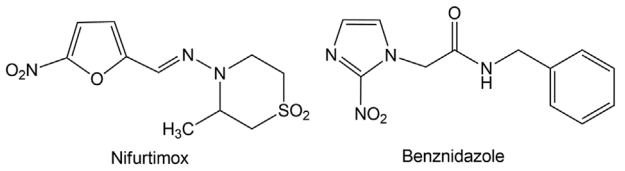

FIGURE 1 | Structure of Nifurtimox and Benznidazole.

American trypanosomiasis also called Chagas' disease after its discoverer, the Brazilian scientist Carlos Chagas, is endemic in Latin America where there are 7–8 million infected people, 10,000 annual deaths and 25 million people at risk of infection. In the last decades, the number of cases in non-endemic regions, like United States, Australia, Europe and Japan, has increased due to migration flows. The disease is caused by the protozoan parasite *Trypanosoma cruzi* (*T. cruzi*) that is mainly transmitted to mammalian hosts by infected blood-sucking bugs. In addition, other modes of transmission, responsible of the spreading of the disease to non-endemic regions, involve blood transfusion, organ transplant and congenital transmission. The parasite shows a complex life cycle that involves stages in the host and in the biological vector. Stages in the host show different susceptibility to drugs, which hampers the development of an effective chemotherapy (Santos et al., 2020; World Health Organization, nd).

The available chemotherapy includes drugs developed more than 50 years ago, Benznidazole and Nifurtimox (**Figure 1**), which proved to be toxic, require long treatments, are not effective in chronic stage of the disease, and often develop resistance.

Many natural products and synthetic inorganic and organic compounds have been successful assayed against *T. cruzi* and some of them entered clinical trials but finally did not reach the clinics (Paucar et al., 2016; Chatelain and Ioset, 2018; Scarim et al., 2018; Francisco et al., 2020).

Leishmaniases are a group of diseases caused by various *Leishmania* species. The insect vector that transmits the disease through its bite is a female phlebotomine sandfly. Leishmaniasis affect 350 million people in 98 countries, in four continents. There are three main forms of the disease: cutaneous, visceral and mucocutaneous with different levels of severity. In addition, Leishmania–HIV co-infection has been reported leading to more severe forms that are also more difficult to face (Nagle et al., 2014; Burza et al., 2018; Kwofie

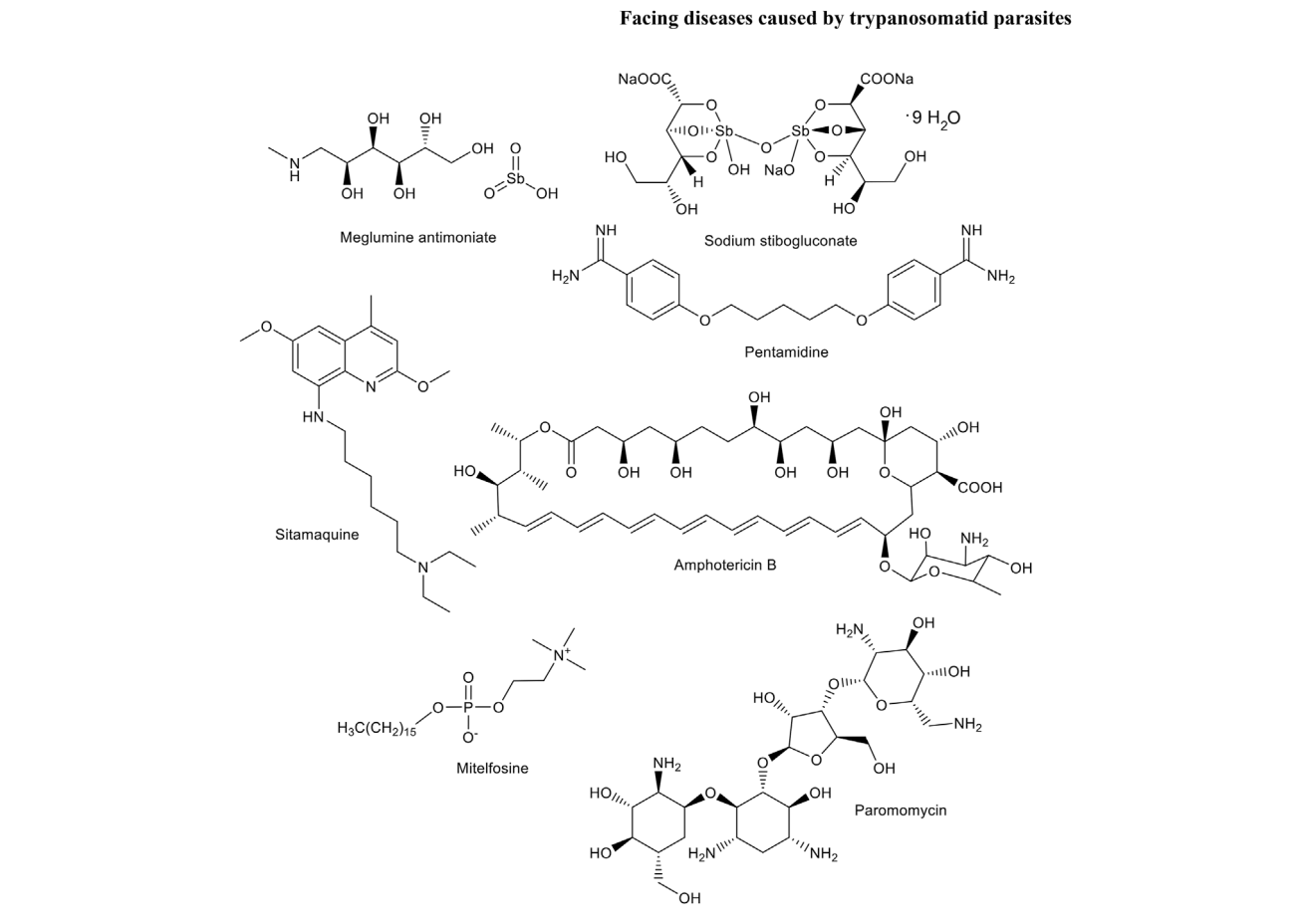

FIGURE 2 | Some current drugs for the treatment of Leishmaniasis.

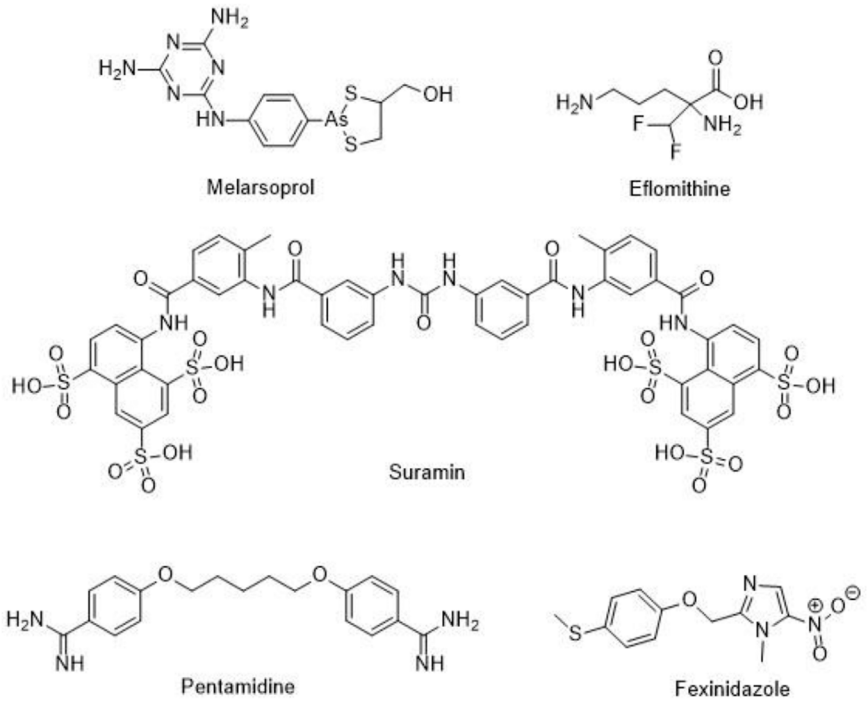

FIGURE 3 | Drugs for the treatment of HAT.

et al., 2020; Brindha et al., 2021; World Health Organization, 2021b). Some current drugs for the treatment of this disease are shown in **Figure 2**.

HAT mainly occurs in the sub-Saharan regions of Africa and it is transmitted through the bite of a tsetse fly. During the 20th century, the epidemics of this disease was devasting being people living in rural areas the most affected ones. Despite control efforts have reduced the number of annual cases, the relax of surveillance policies, the lack of new drugs for its treatment and the emergence of resistance to the old ones, have contributed to the reappearance of the disease. The protozoan parasite causing this disease is *Trypanosoma brucei* (*T. brucei*) and in particular, *Trypanosoma brucei gambiense* and *Trypanosoma brucei rhodesiense* subspecies. Most cases of chronic-like infections are caused by *T. b. gambiense* while *T. b. rhodesiense* causes the most serious form of the disease. In the late stage of this illness the parasites enter the central nervous system leading to profound sleep effects that give rise to the common name of HAT, sleeping sickness. A similar disease, called Nagana importantly affects cattle since antiquity but, interestingly, humans are resistant to the trypanosome species causing it. All forms of HAT are fatal if they are not properly treated. Five drugs are currently recommended: pentamidine, melarsoprol, eflornithine, suramin, and fexinidazole (**Figure 3**). Nifurtimox-eflornithine combination therapy is currently a first line treatment for HAT.

However, most of these drugs show toxicity problems and their efficacy is variable depending on the type and stage of the disease. Although the mortality rates for HAT have decreased substantially in the last years with less than 1,000 cases found in 2019, the development of improved drugs bearing high bioavailability and low toxicity is crucial to definitively fight HAT (Nagle et al., 2014; Kourbeli et al., 2021; World Health Organization, 2021c).

Even though in the last years public-private consortia have pushed forward the drug discovery process, in general, no new drugs to treat diseases caused by kinetoplastids have been registered in more than 30 years. As previously stated, current chemotherapy against diseases caused by trypanosomatid parasites is very deficient so more research is urgently needed to discover safe and effective therapies (Nagle et al., 2014; Rao et al., 2019; Kayode et al., 2020).

During the preclinical development of new prospective drugs, it is important to know that these parasites exhibit complicated lifecycles alternating between stages in the insect vectors gut and in the mammalian host. This knowledge is relevant since it is well known that these different stages show different biological properties and, most importantly, different susceptibility to drugs. Shortly, *T. cruzi* is transmitted to the vertebrate host by the release of metacyclic trypomastigote form of the parasite in the feces of an infected triatome insect vector during its bite. Once inside the host, the parasite converts into the infective blood circulating trypomastigote stage that invades the tissues. Intracellularly, the amastigote form emerges that divides by binary fission and produces cell´s lysis. The released amastigotes convert into blood circulating trypomastigotes. After an insect meal they infect new insects and close the life cycle by converting into the non-infective epimastigote stage that only exists inside the gut of the insect. A similar scenario is

observed in the lifecycle of *T. brucei* that shows four main developmental stages that occur in the infected insect and in the mammalian host, epimastigotes and procyclic forms, slender metacyclic trypomastigotes, and stumpy bloodstream proliferative metacyclic trypomastigotes, being the last one the most relevant form in the development of therapeutic agents. In contrast to other trypanosomatids, the part of the life cycle of *T. brucei* in the mammalian host occurs completely in the extracellular space. During the lifecycle of *Leishmania sp* the parasite alternates between the infective promastigote stage generated in the intestine of the insect vector and the replicative amastigote form inside the host macrophages (Brindha et al., 2021; Kourbeli et al., 2021).

Although these trypanosomatid protozoan parasites show important differences, they are transmitted by different insect vectors and are responsible for clinically different human diseases, it has been demonstrated that they show relevant similarities related to their biology. Their genomes have been sequenced in 2005 and they are available in a database for parasites of the family *Trypanosomatidae* (TriTrypDB, http://tritrypdb.org) (El-Sayed et al., 2005; Aslett et al., 2010). These studies showed that *Leishmania* spp, *T. cruzi* and *Trypanosoma brucei* have many common features, like gene conservation, genome architecture, high synteny, identical amino acid sequences in proteins and common subcellular structures like kinetoplasts. In particular, they show more than 6,100 closely related genes codifying proteins of a total of 8,000–12,000 genes. This paves the way for planning the development of broad-spectrum compounds that could be trypanosomatid-specific, affecting the three main parasites instead of affecting only one of them. This could lead to drugs that affect common targets in the different parasites showing activity against *Leishmania* spp, *T. cruzi* and *T. brucei* (Stuart et al., 2008; Ilari et al., 2018).

Metal-based medicines have been used since ancient times. However, the discovery of the potent anti-tumor activity of cisplatin, $[PtCl_2(NH_3)_2]$ determined the beginning of the modern era of Medicinal inorganic chemistry, accompanied by a huge impact of metal compounds in modern medicine. By exploiting the unique properties of metal ions, Medicinal inorganic chemistry currently offers an attractive option for the rational design of new drugs, looking for defined targets and activities, and new diagnostic and theranostic tools (Zhang and Sadler, 2017; Hanif and Hartinger, 2018; Englinger et al., 2019; Kostelnik and Orvig, 2019; Soldevila-Barreda and Metzler-Nolte, 2019; WahsnerGale et al., 2019; Wang et al., 2019; Anthony et al., 2020; Chamberlain et al., 2020; Chellan and Sadler, 2020; Imberti et al., 2020; Murray and Dyson, 2020; Cirri et al., 2021; Karges and Cohen, 2021; Lin et al., 2021; Silva et al., 2021; Yousuf et al., 2021). In the last decades, the development of metal-based drugs has proven to be a promising approach in the search for new therapeutic tools against parasitic diseases. As a result of the research performed by several academic groups, a great number of classical coordination compounds and organometallics bearing antiparasitic activity were developed (Sánchez-Delgado et al., 2004; Navarro, 2009; Navarro et al., 2010; Gambino, 2011; Gambino and Otero, 2012; Salas et al., 2013; Tahghighi, 2014; Brown and Hyland, 2015; Pessoa et al., 2015; Camarada et al., 2016; Gambino and Otero, 2018; Marcelino et al., 2018; Ravera et al., 2018; Gambino and Otero, 2019; Markwalter et al., 2019; Ong et al., 2019; Mbaba et al., 2020; Păunescu et al., 2021).

STRATEGIES FOR THE RATIONAL DESIGN OF ANTIPARASITIC METAL COMPLEXES

As previously stated, current drugs for the treatment of diseases caused by trypanosomatid parasites are characterized for their severe side effects, the need for prolonged treatments, and the emergence of resistance. In the search for new improved treatment options based on organic compounds, both phenotypic and target-based approaches have been used. In a phenotypic approach, many compounds are evaluated *in vitro* against the parasites searching for a hit or lead compound and, in the target-based drug design, a specific parasite target is selected, and drugs are drawn up to affect this target specifically (Haanstra and Bakker, 2015; Field et al., 2017; Gambino and Otero, 2019).

The *phenotypic strategy* has been the method of choice for the discovery of potential metal-based drugs and, in particular, antiparasitic ones. In fact, although metal compounds have the potentiality of interacting with selected parasitic enzymes and biomolecules, they are likely to act on different targets at the same time. In addition, they are usually transformed *in vivo* into active species by ligand exchange or redox reactions which sometimes makes it difficult to design them to act on specific targets (Navarro et al., 2010; Field et al., 2017; Anthony et al., 2020).

However, metal-based classical coordination complexes or organometallic compounds could be designed as multifunctional agents joining, in a single molecule, different chemical species that could affect different parasitic targets: a bioactive metal ion or metal centre and one or more antiparasitic organic compounds included as ligands. In fact, metal complexes with compounds bearing antiparasitic activity as ligands are expected to maintain the target of the bioactive compound. In addition, the presence of some bioactive metal ions (like palladium or platinum, as will be stated below) could give rise to the appearance of other targets like DNA or parasitic enzymes (Sánchez-Delgado et al., 2004; Gambino, 2011; Gambino and Otero, 2012; Gambino and Otero, 2018; Gambino and Otero, 2019).

In this sense, the peculiar chemical properties of metal complexes impart them the ability to interact with different biomolecules including proteins, enzymes, small peptides, nucleic acids, carbohydrates, among many others. To avoid unspecific toxicity, the design of metal-based compounds bearing antiparasitic activity should include specific targets like proteins or enzymes that are essential for the parasites and are not present in the host (like NADH-fumarate reductase, see below). When the mode of action of metal compounds are involved in metabolic pathways or targets that are common between parasite and mammals, specificity in the toxic action could also be achieved by taking advantage of other differences like the presence of specific organelles in the parasites or the poor mechanisms of detoxification of some toxic species as will be stated in the following sections (Gambino and Otero, 2019).

In particular, DNA is not a specific parasitic target as it is for metal-based antitumor compounds. However, parasites and cancer cells have some common features like their capacity for rapid cell division, some immune evasion and defense strategies, high rate of aerobic glycolysis with key glycolytic enzymes, need of nucleic acid biosynthesis, etc. These similarities noy only support DNA as a valid target for antiparasitic metal-based drugs but also the selection of metal centres that have proved to be useful in cancer therapy, like platinum or palladium (see below) (Williamson and Scott-Finnigan, 1975; Kinnamon et al., 1979; Fuertes et al., 2008; Dorosti et al., 2014; Sullivan et al., 2015).

In the framework of these general features, one of the main strategies for the design of metal-based antiparasitic compounds has been the coordination of an organic ligand with known or potential biological activity, to a metal centre or an organometallic *core*. The activity of the selected ligand could be enhanced because of metal complexation and its pharmacological properties could be improved as the stabilization of the organic drug may allow it to have a better performance in reaching and affecting the biological targets. In addition, the potential toxicity of the metal may be reduced because the organic ligand may limit the ability of the metal to interact with biomolecules that leads to toxicity. This approach could also be useful to circumvent drug resistance, as the metal complex would mask the organic drug. Finally, as stated, these metallodrugs would be capable of affecting multiple parasitic targets simultaneously (Sánchez-Delgado et al., 2004; Gambino and Otero, 2012; Ong et al., 2019; Navarro and Visbal, 2021).

For a metal compound to be able to accomplish an adequate pharmacological behavior, a very strict control of all its chemical features should be considered. The selection of the nature and oxidation state of the metal, the nature and number of coordinated ligands and the coordination geometry are essential for controlling complexes' reactivity and tuning their thermodynamic and kinetic stability. In addition, other physicochemical properties like lipophilicity, solubility or protein interaction can also be tuned by the choice of the metal ion, its oxidation state, and the inclusion of auxiliary co-ligands (Barry and Sadler, 2014; Ong et al., 2019; Czarnomysy et al., 2021; Mjos and Orvig, 2014).

This review is focused on the rational design of palladium(II) and platinum(II) compounds with bioactive ligands as prospective antiparasitic drugs that has been conducted by our group during the last 20 years. The selection of these metal ions is based on the resemblance between tumour cells and parasites as stated above. In this sense, the current treatment of cancer is based on platinum complexes, alone or in combination with other chemotherapeutic agents. In addition, most efforts related to the development of more effective and less toxic anticancer agents have been devoted to platinum compounds. On the other hand, complexes containing palladium are closely related to their platinum analogues. Therefore, Pd(II) has been selected as an alternative to Pt(II) in the search of new compounds for cancer therapy. The most significant resemblances are related to their coordination chemistry and, in particular, to the coordination number (four) and geometry (square planar) of their compounds. However, the ligand exchange kinetics of Pd(II) compounds is

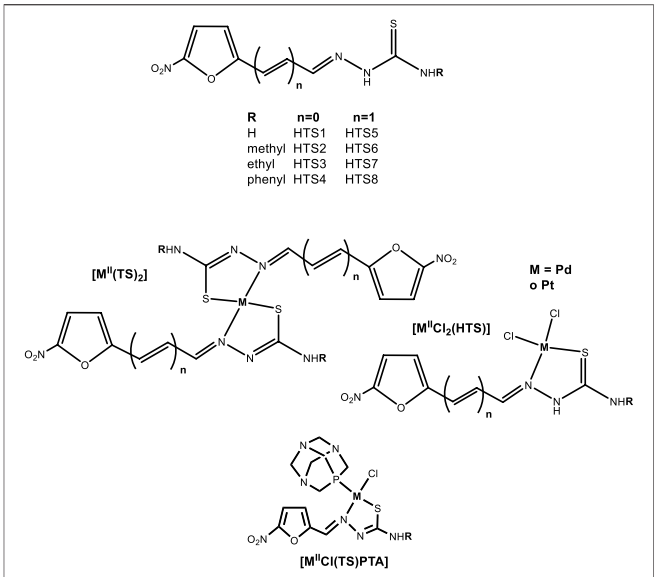

FIGURE 4 | Bioactive 5-nitrofuryl-containing thiosemicarbazones (HTS) and their Pt(II) and Pd(II) complexes.

10^4–10^5 times faster than that of the Pt(II) analogues. This means that Pd(II) compounds are much more reactive in solution which could lead to a higher toxicity and a different biological behaviour. However, the adequate selection of ligands could be able to stabilize Pd(II) complexes affecting their reactivity and imparting substitution inertness (Jahromi et al., 2016; Lazarević et al., 2017; Cirri et al., 2021; Czarnomysy et al., 2021; Yousuf et al., 2021).

PALLADIUM AND PLATINUM COMPLEXES WITH BIOACTIVE LIGANDS

In the search of ligands bearing anti *T. cruzi* activity, we had developed 5-nitrofuryl-containing thiosemicarbazones (HTS) maintaining the 5-nitrofuryl moiety that has proved to be the pharmacophore group of Nifurtimox (**Figure 4**). HTS were more active *in vitro* against *T. cruzi* than this reference drug. These compounds were designed to act on *T. cruzi* by the same mechanism than Nifurtimox: the generation of toxic reactive oxygen species (ROS) through the reduction of the nitro moiety followed by redox cycling. In addition, they have proved to affect the activity of trypanothione reductase parasitic specific enzyme through the nitrofuran group as well as to inhibit the main parasitic cysteine protease, cruzipain, through the thiosemicarbazone moiety (Aguirre et al., 2004; Rigol et al., 2005; Otero et al., 2008).

In order to address the effect of palladium and platinum complexation on the anti *T. cruzi* activity of these organic compounds, a large series of complexes with different stoichiometries and including different co-ligands was developed (**Figure 4**).

Thirty two analogous platinum and palladium complexes of the formula $[MCl_2(HTS)]$ and $[M(TS)_2]$ with M = Pd(II) and

Pt(II) were obtained. Most of them were, *in vitro*, equally or more active than Nifurtimox against *T. cruzi* (epimastigote form, Tulahuen 2 strain). For palladium complexes, the activity of the ligands was maintained or increased as a consequence of metal complexation. Although, the obtained IC_{50} differences between the assayed species were quite low (IC_{50}/5 days between 3 and 6 μM), a general trend was found: $[PdCl_2(HTS)]$ > HTS > $[Pd(TS)_2]$. However, no similar trend was observed for platinum compounds showing, in most cases, lower activity than the palladium counterparts and the free ligands. Some platinum compounds were also tested against Dm28c epimastigotes and trypomastigotes of *T. cruzi*. Indeed, the infective trypomastigote form of the parasite resulted more susceptible to most of the tested Pt compounds than the epimastigote form, being these compounds more active on trypomastigotes than Nifurtimox (Otero et al., 2006; Vieites et al., 2008a; Vieites et al., 2009).

On the other hand, eight new palladium(II) and platinum(II) complexes of formula [MCl(TS)(PTA)] with PTA (1,3,5-triaza-7-phosphaadamantane) as co-ligand were obtained. PTA was included with the aim of modulating the solubility and lipophilicity of the new species. Most [MCl(TS)(PTA)] complexes showed similar activities against *T. cruzi* (trypomastigote form, Dm28c clone) to those of the corresponding HTS ligands and $[PtCl_2(HTS)]$ complexes. In contrast to what was observed for $[MCl_2(HTS)]$ compounds, no significant differences between palladium and platinum complexes were observed. However, for the most active compound, [MCl(TS4)(PTA)], the selectivity index (SI) was higher for the platinum complex (SI =20) than for the palladium one (SI = 10). It also should be noted that for the whole series of compounds, no correlation between the anti *T. cruzi* activity and the nature of substituent in the thiosemicarbazone chain was observed (Cipriani et al., 2014).

All prepared palladium and platinum complexes with the 5-nitrofuryl-containing thiosemicarbazones as bioactive ligands were supposed to show various mechanisms of action i.e., affecting the same targets or processes than the bioactive ligands or maintaining those mechanisms related to the PTA co-ligand and/or to the metal ions. Therefore, different studies were performed in order to sustain the proposed targets and to look into the potential mode of action of the metal compounds. Related to the bioactive ligands, the reduction of the nitro moiety had been demonstrated to be the first step of their mechanism of anti *T. cruzi* action. The nitro anion formed would be responsible of generating other toxic radical species through a redox cycling process. Therefore, the effect of metal complexation on the redox potential of the nitro moiety was studied using cyclic voltammetry. This potential slightly changed because of both palladium or platinum complexes formation (ΔE = 0.05–0.1 V) and no significant differences were observed between both metal ions. However, it should be stated that the nitro moiety of all compounds resulted more easily reducible than that of Nifurtimox, and, therefore, the capacity of generating toxic free radicals would be better for the complexes. The production of free radicals inside the parasite cells was assessed by ESR spectroscopy using 5,5-dimethyl-1-pirroline-N-oxide (DMPO) for spin trapping of radical species having short half-lives. A 10–13 lines spectral pattern was observed for all the studied complexes which is consistent with the intracellular generation of the hydroxyl radical and the nitroheterocyclic radical of the complexes. So, the mechanism of anti *T. cruzi* action of the HTS compounds seems to remain in the obtained complexes. However, only for $[PdCl_2(HTS)]$ and $[Pd(TS)_2]$ series, a good correlation between the concentration of the detected radicals (measured through the EPR signal intensities) and the IC_{50} values for the anti *T. cruzi* activity was observed. On the other hand, the described redox cycling processes should increase the parasite oxygen consumption. Thus, the parasite oxygen uptake in the presence of the compounds was determined. In general, complexes increased oxygen consumption which confirms that redox cycling processes are occurring inside the parasites treated with the complexes (Otero et al., 2006; Vieites et al., 2008a; Cipriani et al., 2014).

On the other hand, trypanothione reductase and cruzipain inhibition was also observed for some of the obtained metal compounds but no correlation with the anti *T. cruzi* activity was observed (Otero et al., 2006; Cipriani et al., 2014).

DNA was also tested as a potential target for the developed palladium and platinum compounds. The binding of $[MCl_2(HTS)]$ and $[M(TS)_2]$ compounds was studied by combining quantification of the bound metal by atomic absorption spectrometry and quantification of DNA by electronic absorption measurements. The amount of metal bound to DNA for platinum complexes was comparable to that previously reported for cytotoxic metal complexes and it was lower than the one determined for palladium complexes (Otero et al., 2006; Vieites et al., 2008a; Vieites et al., 2009).

$[MCl_2(HTS)]$ interaction with DNA was characterized by using gel electrophoresis, DNA viscosity measurements, circular dichroism (CD) and atomic force microscopy (AFM). Electrophoresis results showed that all complexes caused the loss of DNA superhelicity and modifications in the shape of plasmid DNA were observed in AFM studies. The effect on DNA was more significant for palladium complexes than for platinum analogues. In addition, CD results showed that while palladium complexes induce modifications in calf thymus DNA structure, no effect was observed for platinum ones. Finally, either Pd or Pt complexes increased the viscosity of DNA which agrees with an intercalative mode of interaction. An explanation for the observed differential intensity of the effect on DNA between palladium and platinum complexes could be the differences in exchange reactions kinetics between both metal ions (Vieites et al., 2011).

Similar results were obtained for [MCl(TS)(PTA)] complexes (**Figure 4**). The effect of these compounds on DNA was characterized by gel electrophoresis and ethidium bromide fluorescence experiments. Results of both experiments are in accordance with an intercalating-like mode of interaction between DNA and these compounds. However, the intensity of the effect on DNA was dependent on the nature of the metal ion. In fact, all Pd complexes showed a more significant effect on DNA than the platinum ones. In fact, some palladium

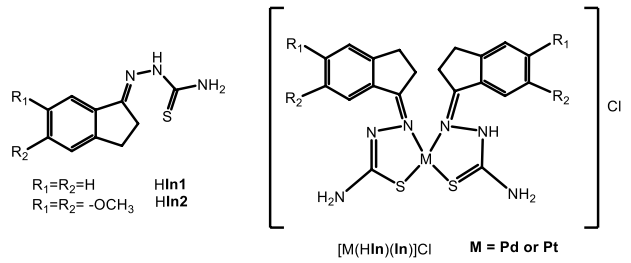

FIGURE 5 | Bioactive thiosemicarbazones derived from 1-indanones (HIn) and their Pt(II) and Pd(II) complexes.

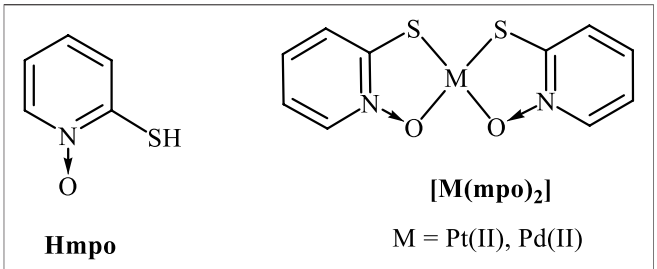

FIGURE 6 | pyridine-2-thiol *N*-oxide (Hmpo) and their Pt(II) and Pd(II) complexes.

compounds induce decomposition of DNA at high DNA/complex molar ratios (Cipriani et al., 2014).

It is interesting to note that no correlation between the anti *T. cruzi* activity and DNA binding was observed for the different series of palladium and platinum compounds. In fact, theoretical calculations performed for $[MCl_2(HTS)]$ complexes suggested that, in the cell, these complexes would not interact with DNA because they would react with the cell content before accessing to DNA. In addition, the potency and mode of interaction of both HTS and their metal complexes with *T. cruzi* cruzipain and trypanothione reductase enzymes was also studied using molecular docking. Results showed that the mode of action of these compounds involved multiple mechanisms and that, depending on the nature of the species, one mode of action would be predominant over others (Merlino et al., 2011).

Other thiosemicarbazone containing bioactive ligands were selected to study the effect of palladium and platinum complexation on the anti *T. cruzi* activity. Eight Pd(II) and Pt(II) complexes, $[MCl_2(HIn)]$ and [M(HIn)(In)]Cl with HIn = thiosemicarbazones derived from 1-indanones were obtained (**Figure 5**; Gómez et al., 2011).

The *in vitro* activity on *T. cruzi* (epimastigote form, Tulahuen 2 strain) and the unspecific cytotoxicity on red blood cells, were studied. All compounds showed higher activity than the corresponding free ligands with IC_{50} values in the low micromolar range. Most palladium compounds showed higher trypanosomicidal activity than their platinum counterparts. A quite good correlation between lipophilicity and antiproliferative activity was observed for these complexes. On one hand, lipophilicity was enhanced as a consequence of metal complexation and, in most cases, anti *T. cruzi* activity was also increased. In addition, being most palladium complexes more lipophilic than platinum ones, they showed higher anti *T. cruzi* activity. Unfortunately, obtained complexes showed low selectivity for the antiparasitic action, being less selective than the free ligands. In this case, coordination to Pd and Pt led to an increase in bioactivity but had a deleterious effect on unspecific cytotoxicity.

On the other hand, obtained complexes were tested for their antitumoral activity. Free ligands had no cytotoxic effect, but platinum and palladium complexes showed anti-leukemia properties and induced apoptosis. However, in this case no clear correlation between antitrypanosomal and antitumoral activities could be detected (Gómez et al., 2011; Santos et al., 2012).

Using the same approach, palladium and platinum compounds with pyridine-2-thiol *N*-oxide (2-mercaptopyridine *N*-oxide, Hmpo) as bioactive ligand were studied as potential antitrypanosomal agents (**Figure 6**). Mpo had shown a high anti *T. cruzi* activity against all forms of the parasite and no unspecific toxicity on mammalian cells. The antiparasitic action of mpo was related to the inhibition of NADH-fumarate reductase enzyme which is responsible for producing succinate from fumarate in the parasite. The lack of this enzyme in mammalian cells makes it a promising target for the development of antichagasic compounds. In addition, mpo, as similar amine *N*-oxides do, could suffer bioreduction leading to the release of radical species that are toxic for the parasite (Vieites et al., 2008b).

$[Pd(mpo)_2]$ and $[Pt(mpo)_2]$ compounds were synthesized and fully characterized. Both complexes showed very high *in vitro* growth inhibition activity of *T. cruzi* (epimastigote form, Tulahuen 2 strain) with IC_{50} values in the nanomolar range (IC_{50}/5 days = 0.067 and 0.200 μM for palladium and platinum complexes, respectively). They were 39–115 times more active than Nifurtimox. In addition, the palladium complex showed an approximately threefold enhancement of the activity compared with the free mpo while only a low increase in the activity was observed for the platinum compound. In addition, owing to their low unspecific cytotoxicity on mammalian macrophages, the complexes showed a highly selective antiparasitic activity.

These complexes were also good candidates for a multi-target activity. In this sense, free-radical production, inhibition of the parasite-specific enzymes trypanothione reductase and NADH-fumarate reductase were studied. Additionally, studies on DNA interaction were performed.

Although radical species could be obtained electrochemically for both metal complexes, no free radical species were detected when they were incubated with the epimastigote form of *T. cruzi*. In addition, neither trypanothione reductase inhibition nor DNA interaction could be observed.

However, in the assayed conditions, both complexes have an inhibitory effect on NADH fumarate reductase. $[Pd(mpo)_2]$ showed the highest inhibition levels while the effect of $[Pt(mpo)_2]$ on the anzyme was similar to that of the free ligand. A similar behaviour was observed when analysing the IC_{50} values of these compounds which strongly suggest the

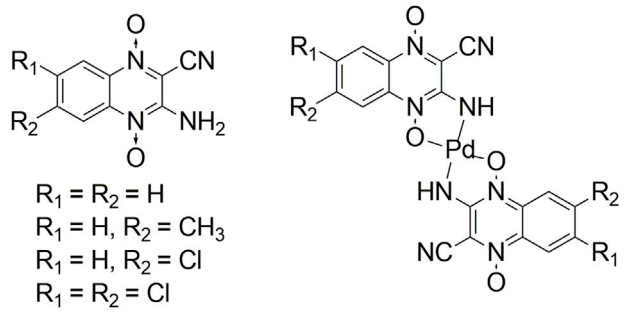

FIGURE 7 | Trypanocidal 3-aminoquinoxaline-2- carbonitrile 1,4-dioxides (quino) and their Pd(II) complexes.

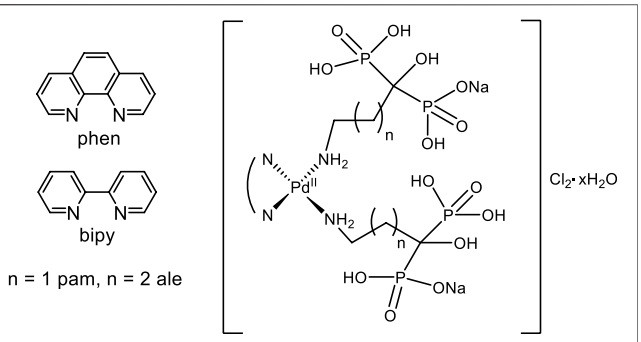

FIGURE 8 | Pamidronate (pam) and alendronate (ale) mixed-ligand Pd(II) compounds.

involvement of this enzyme in the mode of action of the obtained complexes.

On the other hand, homology modelling combined with enzyme-cofactor docking were used to propose tertiary structures for NADH-dependent *T. cruzi* fumarate reductase. This model was used to explain the inhibitory effect and the binding modes of Pd- and Pt-mpo complexes. In fact, obtained theoretical inhibition constants (K_i values) showed a good correlation with the experimental data. Both complexes bind to the enzyme into the cleft between domains 2 and 3, near to the nicotinamide ring of the NADH cofactor. However, $[Pd(mpo)_2]$ seems to bind closer to the cofactor which could affect the orientation of the nicotinamide ring for a proper position for catalysis, explaining the better inhibitory capacity displayed by this complex (Merlino et al., 2014).

Quinoxalines (3-aminoquinoxaline-2-carbonitrile 1,4-dioxides) are a family of compounds that had shown anti *T. cruzi* activity. Previous QSAR studies had shown that these compounds' activity was dependent on the electronic characteristics of the substituents as well as on the volume at the 3-amino level of the compounds. However, the low activities displayed by some derivatives could be the result of their low solubilities in the physiological media. In this sense, $[Pd(quino)_2]$ complexes were obtained in order to improve on one hand, the volume at the 3-amino level (**Figure 7**) and on the other hand, the bioavailability of the organic ligands. Results showed that the antitrypanosomal activity (epimastigote form, Tulahuen 2 strain) of the quinoxalines was improved upon complexation. The parent ligands having poor trypanosomicidal activity became 20- to 80-times more active upon complexation with palladium (Urquiola et al., 2009; Benítez et al., 2012).

In order to diminish the costs of developing new drugs, "repositioning" was used as one of the strategies for obtaining new antiparasitic compounds. Biphosphonates are examples of this approach. These compounds are the most prescribed drugs for osteoporosis and other bone diseases. Among bisphosphonates, those containing nitrogen (NBPs) have proved to inhibit farnesyl diphosphate synthase (FPPS) enzyme of the osteoclastic cells as their main mode of action. This enzyme is also present in trypanosomatid parasites. In addition, the specificity of the anti *T. cruzi* action of NBPs could be facilitated by the presence in parasites of specific organelles called acidocalcisomes. Acidocalcisomes are acidic structures involved in the storage and metabolism of phosphorous and calcium in parasites. Their composition is equivalent to the bone mineral so accumulation of bisphosphonates in these organelles would facilitate their antiparasitic action (Gambino and Otero, 2019). Therefore, bisphosphonates were selected as bioactive ligands for our multi-target based approach. In this sense, complexes of the formula $[Pd(NBP)_2(NN)]$ with NBP = commercial bisphosphonates (alendronate (ale) or pamidronate (pam)) and NN = 1,10 phenanthroline (phen) or 2,2′-bipyridine (bpy) were obtained (**Figure 8**). The selection of palladium as metal ion and the NN compounds as co-ligands points at DNA as target. In fact, besides the potential covalent interaction of Pd ion with DNA, metal complexes with these planar aromatic ligands could interact with DNA through intercalation between nucleobases. Additionally, parasitic enzymes of the mevalonate pathway (like FPPS) would also be a potential target for these compounds as they are for the NBP ligands.

All the obtained compounds showed an increased anti-*T. cruzi* activity (amastigotes, CL strain) when compared to the free NBP ligands showing only slight signs of unspecific toxicity at high concentrations. In addition, Pd–NBP–phen complexes (IC_{50}/3 days = 1.30 and 1.44 μM for ale and pam, respectively) resulted 15 times more active than the corresponding bpy analogues (IC_{50}/3 days = 17.4 and 21.4 μM for ale and pam, respectively). However, all the complexes were able to similarly inhibit *T. cruzi* farnesyl diphosphate synthase and solanesyl diphosphate synthase enzymes suggesting that enzymatic inhibition would not be responsible for the observed differences in the biological activity. On the contrary, differences in the anti *T. cruzi* activity could be explained through the interaction of the complexes with DNA. As expected, the nature of the NN ligand determined the complexes' interaction with DNA. In fact, both Pd–NBP–phen complexes showed a much higher affinity for DNA in the fluorescent ethidium bromide displacement experiments than Pd–NBP–bpy analogues. It should be noted that, for these complexes, a good correlation between the antiparasitic and antitumor activities was observed. Additionally, the compounds were tested for their

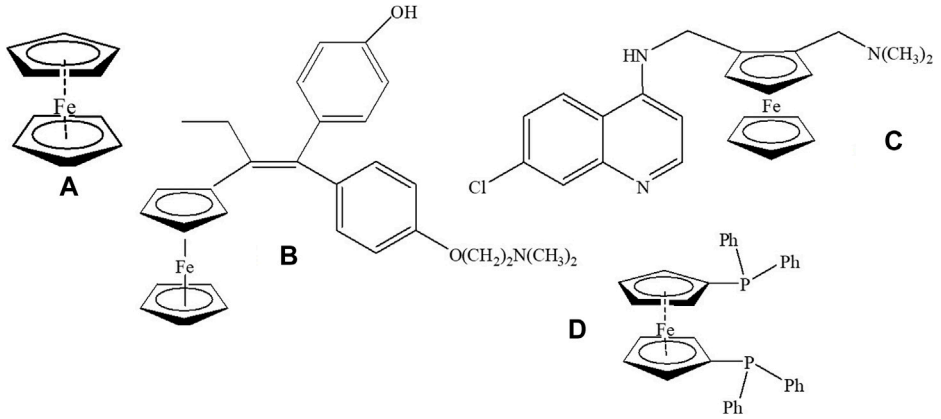

FIGURE 9 | (A) ferrocene moiety; **(B)** ferrocifen **(C)** ferroquine **(D)** 1,1'-bis(dipheny1phosphino) ferrocene, dppf.

antitumoral activities. The cytotoxicity of the complexes on MG-63 osteosarcoma cells was dependent on the nature of the NBP as expected but for the A549 lung adenocarcinoma cells, Pd–NBP–phen compounds showed the highest cytotoxicities (Cipriani et al., 2020).

FERROCENYL DERIVATIVES

Organometallic compounds, characterized by showing at least one σ metal-carbon bond, offer a promising opportunity for the rational design of novel metal-based drugs. They show a wide structural diversity, their lability can be modulated leading to kinetically stable compounds, and they show adequate lipophilicity which favors their *in vivo* behavior (Allardyce et al., 2005; Hartinger and Dyson, 2009; Noffke et al., 2012; Zhang and Sadler, 2017; Chellan and Sadler, 2020).

In particular, the "sandwich type" ferrocene moiety has shown high potentiality in the development of novel organometallic drugs (**Figure 9**).

For instance, compounds including it, like ferrocifen, an analogue of the antitumoral drug tamoxifen, and ferroquine, an analogue of the antimalarial drug chloroquine, have achieved clinical or preclinical trials (**Figure 9**). In general, ferrocene derivatives are low cost, they are stable both in air and in solution and they are easy to derivatize. In addition, they are hardly not cytotoxic and have adequate lipophilicity. Furthermore, ferrocene derivatives show improved bioaccumulation when compared to the ionic forms of iron. In addition, ferrocenes are able to undergo one electron oxidation which could catalyze the generations of radicals in a Fenton-like manner, leading to the oxidation of macromolecules. The formation of ROS could be significant for antiparasitic therapy because trypanosomatids have a very primitive system of radical species detoxification (Biot, 2004; Dubar et al., 2008; Biot et al., 2010; Braga and Silva, 2013; Jaouen et al., 2015; Gambino and Otero, 2018).

In order to further address the therapeutic potential of palladium and platinum compounds with the selected bioactive ligands, we followed the rational design strategy previously delineated by including a ferrocene moiety in the new structures (**Figure 9**). Instead of coupling, as usual, the ferrocene scaffold to an organic skeleton as in ferroquine or ferrocifen, our synthetic strategy was to include the ferrocene fragment as a coligand in the platinum or palladium coordination sphere. The selected coligand, 1,1'-bis(dipheny1phosphino) ferrocene, dppf (**Figure 9**), acts as bidentate ligand binding to the metal center through the two phosphorus donor atoms and leaving the two extra coordination positions of the metal centre able to coordinate to the selected bioactive bidentate ligand (**Figure 10**). Accordingly, the twenty-four structurally related ferrocenyl compounds shown in **Figure 10** were synthesized and fully characterized in the solid state and in solution and they were evaluated on trypanosomes as well as on mammalian cell models. Their effect on some selected molecular targets was studied and omic studies were performed for the most promising pyridine-2-thiolato-1-oxide (mpo) compounds. In general, the inclusion of the ferrocene moiety led to interesting effects on the biological profile of the compounds (Rodríguez Arce et al., 2015; Mosquillo et al., 2018a; Mosquillo et al., 2018b; Rivas et al., 2018; Rivas et al., 2019; Rodríguez Arce et al., 2019; Mosquillo et al., 2020; Rivas et al., 2021).

At a first stage $[M(dppf)(L)](PF_6)$ compounds with L = pyridine-2-thiolato-1-oxide (mpo) as bioactive ligand were synthesized and characterized and their biological behavior compared with the previously developed classical coordination compounds $[M(mpo)_2]$ (**Figure 11**; Rodríguez Arce et al., 2015). Both ferrocenyl compounds showed IC_{50} values in the nanomolar range on *T. cruzi* epimastigotes (Dm28c strain) as well as low cytotoxicity on VERO epithelial cells (ATCC CCL81) as mammalian cell model, leading to good selectivity towards the parasite (**Table 1**). The complexes were about 10–20 times more active than the antitrypanosomal drug Nifurtimox (IC_{50}/5 days = 6.0 μM) and two- to five-fold more active than mpo sodium salt. Moreover, epimastigotes of CL Brener strain (type VI) resulted more

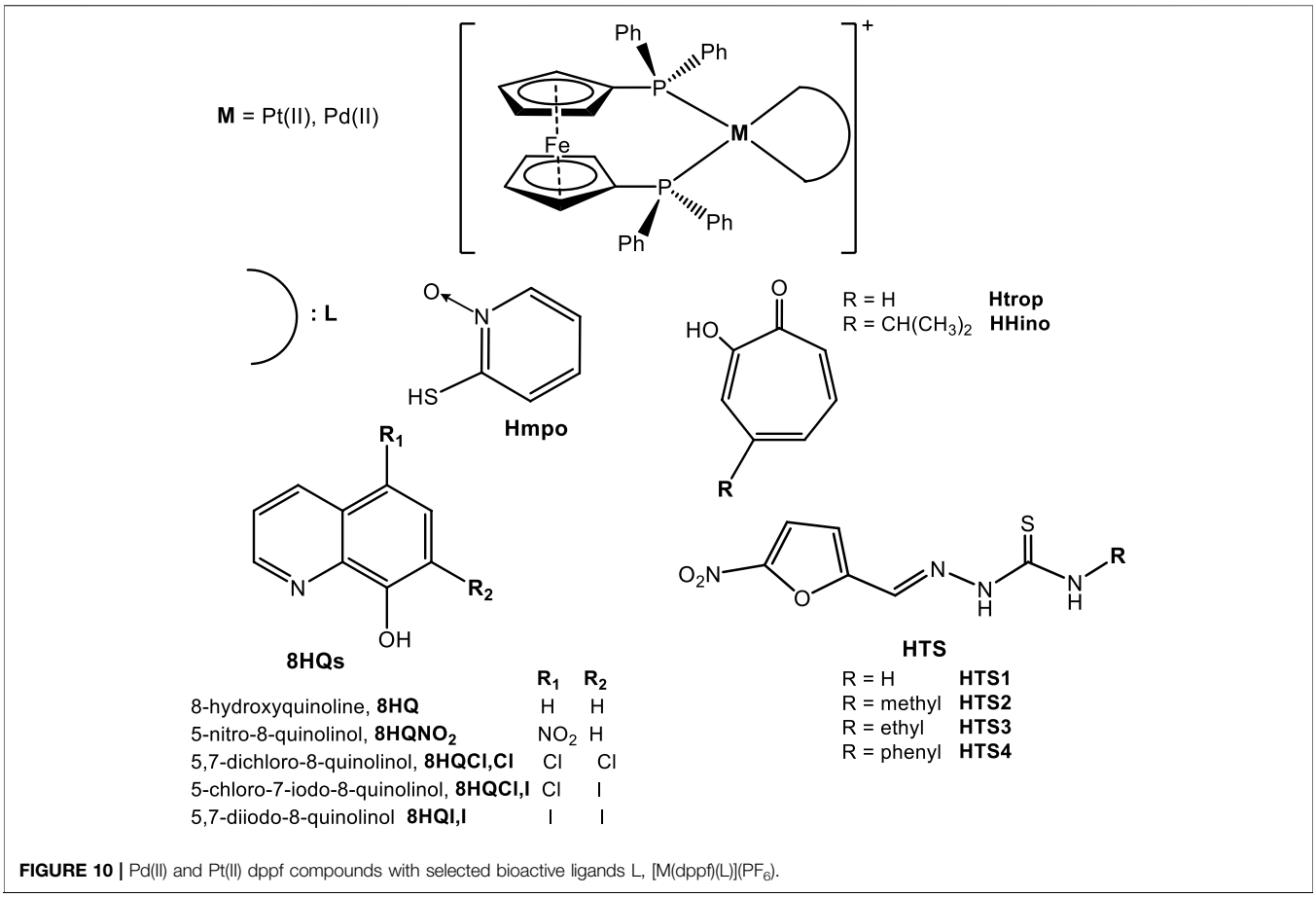

FIGURE 10 | Pd(II) and Pt(II) dppf compounds with selected bioactive ligands L, $[M(dppf)(L)](PF_6)$.

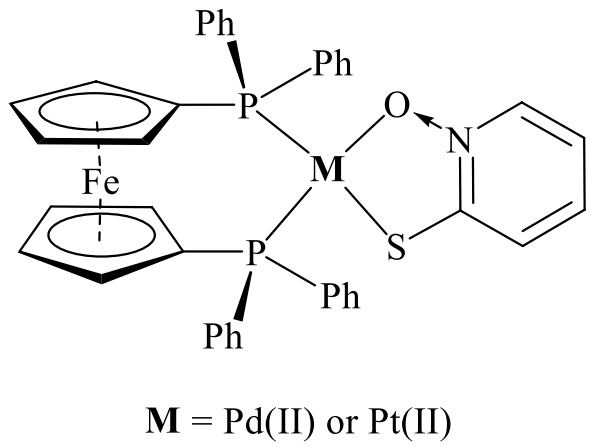

FIGURE 11 | Structure of $[M(dppf)(mpo)]$ (PF_6) compounds, where M = Pd or Pt, mpo = pyridine-2-thiolato-1-oxide.

susceptible to the compounds than the type I Dm28c strain (**Table 1**). It is well known that genetic diversity of the parasite can lead to different susceptibility to drugs.

The compounds induce necrosis after 24 h of parasite incubation. Both complexes also affected the trypomastigote infection process as well as the number of amastigotes per cell. As expected, these dppf compounds showed lower unspecific cytotoxicity on mammalian cells than the $[M(mpo)_2]$ compounds (**Table 1**; Mosquillo et al., 2018a; Mosquillo et al., 2018b).

Molecular docking studies conducted on a model structure of the *T. cruzi* NADH fumarate reductase (TcFR) together with experimental *in vitro* studies on *T. cruzi* protein extracts demonstrated the inhibitory effect of the compounds on TcFR. As a consequence of palladium and platinum complexation, an increase in the inhibitory effect in respect to the free mpo was observed. Interestingly, the Pt compound had both the highest inhibition values and the highest activity against *T. cruzi* suggesting that TcFR could be involved in the mode of action of the compounds. Additionally, theoretical calculations confirmed that both compounds could be able to undergo oxidation at the ferrocene moiety which could aid to the biological activity. The generation of radical species inside the parasite cells by the action of M-dppf-mpo compounds was confirmed through EPR experiments (unpublished results) (Gambino and Otero, 2018).

These compounds resulted highly promising deserving further studies. The identification of molecular targets and the understanding of the mode of action of drug candidates are essential data for their clinical development. This knowledge is commonly elusive for metal-based drugs due to complicated

TABLE 1 | Activity against trypanosomes of M-dppf-L compounds.

Compound	*T. brucei* IC_{50}/24 h/μM	SI[a]	*T. cruzi* IC_{50}/μM	SI[a]
Pt-dppf-mpo	—	—	0.28[b]/0.060[c]	18/85 (Vero cells)
Pd-dppf-mpo	—	—	0.64[b]/0.30[c]	39/83 (Vero cells)
Pt-dppf-trop	2.1	18 (J774)	—	—
Pd-dppf-trop	1.3	8 (J774)	—	—
Pt-dppf-hino	4.5	>22	—	—
Pd-dppf-hino	1.2	3	—	—
Pt-dppf-TS1	0.77	>65 (EA.hy926)	3.11[d]	>16 (EA.hy926)
Pd-dppf-TS1	0.9	>55 (EA.hy926)	7.58[d]	>7 (EA.hy926)
Pt-dppf-TS2	0.60	>83 (EA.hy926)	0.79[d]	>63 (EA.hy926)
Pd-dppf-TS2	0.93	>54 (EA.hy926)	1.42[d]	>35 (EA.hy926)
Pt-dppf-TS3	0.52	>56 (EA.hy926)	0.76[d]	>66 (EA.hy926)
Pd-dppf-TS3	0.98	>51 (EA.hy926)	3.6[d]	>14 (EA.hy926)
Pt-dppf-TS4	1.01	>50 (EA.hy926)	1.32[d]	>38 (EA.hy926)
Pd-dppf-TS4	1.56	>32 (EA.hy926)	29.4[d]	>2 (EA.hy926)
Pt-dppf-8HQ	0.3	11.3 (J774)	—	—
Pd-dppf-8HQ	0.9	9.4 (J774)	—	—
Pt-dppf-8HQNO_2	0.93	27.7 (J774)	—	—
Pd-dppf-8HQNO_2	0.33	102.4 (J774)	—	—
Pt-dppf-8HQCl,Cl	0.22	15.5 (J774)	—	—
Pd-dppf-8HQCl,Cl	4.5	4.4 (J774)	—	—
Pt-dppf-8HQCl,I	0.14	47.8 (J774)	—	—
Pd-dppf-8HQCl,I	4.8	6.3 (J774)	—	—
Pt-dppf-8HQI,I	0.22	29.1 (J774)	—	—
Pd-dppf-8HQI,I	7	7.2 (J774)	—	—
Nifurtimox	15	10 (J774)	6 (Dm28c epimastigotes) 2.8 (CL Brener epimastigotes) 20 (Dm28c trypomastigotes)	—

[a]*SI = IC_{50} mammalian cells/IC_{50} parasite.*
[b]*Dm28c strain epimastigotes, 24 h incubation.*
[c]*CL Brener strain epimastigotes, 24 h incubation.*
[d]*Dm28c strain tripomastigotes, 24 h incubation; EA.hy926 endothelial cell line: permanent human cell line derived by fusing human umbilical vein endothelial cells-HUVEC with human lung cells-A549; VERO cells, VERO kidney epithelial cells from African green monkey (ATCC CCL81); J774, J774 murine macrophages.*

mechanisms of action involving the interaction of metal compounds with multiple targets and biomolecules. Inorganic medicinal chemists have traditionally tried to identify and characterize, using *in vitro* approaches, molecular targets of a metal-based drug that mainly depend on the nature of the organic ligands and the metal center. Omic studies are relevant tools for uncovering the whole mechanism of action of metal-based drugs. Up and down regulated cellular proteins due to effects of drug and molecular targets interactions, identified and quantified by proteomics, together with cell uptake and subcellular distribution, quantified by metallomics, and changes in gene expression, determined by transcriptomics, allow to get a deeper insight into what occurs in the cells after administering a metallodrug. The knowledge achieved is a useful income for the rational design of novel metallodrugs (Wang et al., 2020).

High-throughput omic studies have proved to be powerful tools for going further into the basic biology of parasites like *T. cruzi* and also for the validation of drug targets (Atwood et al., 2005; Chávez et al., 2017; García-Huertas et al., 2017; Van den Kerkhof et al., 2020). Although these studies have been also used to explore organic drugs action in kinetoplastid parasites, similar studies for metal-based drugs were not reported until part of our group recently performed a high throughput omic study on *T. cruzi* for the two analogous Pt and Pd organometallic hit compounds $[M^{II}(dppf)(mpo)](PF_6)$ (Mosquillo et al., 2018a; Mosquillo et al., 2018b; Mosquillo et al., 2020).

Metallomic studies showed a high Pt and Pd uptake by parasite epimastigotes. For the same dose a higher nanomolar uptake per 10^6 parasites was determined for Pt-dppf-mpo than for Pd-dppf-mpo. A similar pattern of metal distribution among the four analyzed macromolecules fractions (DNA, RNA, soluble proteins and insoluble proteins including membrane lipids) was found, with a preferential association to DNA. It is well known that metal complexes often could suffer reactions in biological media. Therefore, to evaluate if the M-dppf-mpo compounds are taken up intact by the parasites, the M (Pd or Pt) and Fe (present in the dppf moiety) levels were quantified in the selected parasite fractions at the same time. A 1:1 stoichiometric relationship between Fe and M in each fraction was obtained which would be consistent with the presence of the intact M-dppf-mpo species bound to the selected macromolecules (Mosquillo et al., 2018a; Mosquillo et al., 2018b). Proteomic and transcriptomic analyses allowed to identify differentially expressed transcripts and proteins in the treated parasites. The number of differentially expressed proteins was 342 for Pd-dppf-mpo and 411 for Pt-dppf-mpo. In addition, the number of soluble and insoluble proteins modified after treatment with both compounds was similar. The effect of Pd-dppf-mpo treatment showed more modulated transcripts (2,327

of 10,785 identified transcripts) than Pt-dppf-mpo treatment (201 of 10,773 identified transcripts). These results suggest that the mechanism of action for Pd-dppf-mpo is at the transcriptome level. Differentially expressed transcripts were functionally categorized which allowed to identify the cellular processes and pathways that were affected by the treatment with the compounds. Transcripts involved in DNA binding, protein metabolism, transmembrane transport (ABC transporters related with *T. cruzi* response and resistance to drugs, among others), oxidative defense, and the biosynthesis of ergosterol pathways were found to be modulated by the presence of the compounds. The whole set of data obtained allowed to suppose that the antitrypanosomal mechanism of action of Pd-dppf-mpo and Pt-dppf-mpo is multimodal. Interestingly, significant biological differences were assessed for both structurally analogous compounds showing the significance of the nature of the metal center on the biological behavior. In particular, metallomic studies allowed to assess that the Pt(II) compound showed higher cellular uptake than the Pd one. In addition, proteomic and transcriptomic studies showed different biological effects of both chemically analogous compounds. Both metals belong to the same group of the periodic table allowing to expect many chemical and physicochemical similarities between their compounds. Nevertheless, differences are expected based on the differential lability of the metal centers. The omic work performed gives details about the biological implications emerging of these chemical differences (Mosquillo et al., 2020).

As previously discussed, NADH-fumarate reductase, a specific parasite enzyme absent in the host, had been previously identified as a potential target for both M-dppf-mpo compounds (Mosquillo et al., 2018a). Although proteomic analysis agrees with this previous finding showing that, the amount of enzyme is modified in the treated parasites respect to untreated control parasites, omic studies unveiled, in addition, several down and up regulated proteins and a wide range of pathways affected by the compounds. Another remarkable point is that *in vitro* target identification should be in agreement with observed cellular uptake and subcellular localization. In the case of the M-dppf-mpo compounds, DNA was not considered for the *in vitro* target identification as an important biological target to be tested but metallomics showed a high accumulation of the complexes in the parasite DNA fraction. Globally, this study constitutes the first omic contribution to unravel the whole scenario of effects involved in the mechanism of action of potential metal-based drugs for the treatment of Chagas disease.

Following the promising results obtained with the M-dppf-mpo compounds and in an attempt to get broad spectrum Pd and Pt dppf compounds that could affect both *T. brucei* and *T. cruzi* parasites, four 5-nitrofuryl containing thiosemicarbazones (HTS) were coordinated as bioactive bidentate ligands to the {M-dppf} centers leading to eight new heterobimetallic $[M^{II}(TS)(dppf)](PF_6)$ Pt(II) or Pd(II) compounds (**Figure 10**). IC_{50} values for most compounds were in the low micromolar or submicromolar range against both parasites, having the platinum compounds higher activities than the corresponding palladium ones (**Table 1**). Their activities were significantly higher than those of the free thiosemicarbazone ligands, showing a 3- to 24-fold increase for *T. cruzi* and up to 99-fold increase for *T. brucei*. The presence of the organometallic dppf co-ligand also seems to be responsible for a lower toxicity on mammalian cells and higher selectivity towards both parasites when compared to the free thiosemicarbazone compounds. In addition, new compounds showed higher activity and selectivity than the several groups of Pd and Pt classical coordination complexes with 5-nitrofuryl thiosemicarbazones previously described in this review.

The M-dppf-TS compounds resulted up to 26 times more active on *T. cruzi* than Nifurtimox (IC_{50}/24 h = 20 μM) and up to 30 times (IC_{50}/24 h = 15 μM) on *T. brucei*. These Pd and Pt compounds demonstrated to affect the redox metabolism of *T. cruzi* seeming to retain the mechanism of anti-*T. cruzi* action of the free ligands previously described in this review. However, no correlation between oxygen uptake and the generation of free oxygen radical species in the parasite, and the anti-*T. cruzi* activity was observed. Additionally, these compounds demonstrated to interact with DNA. Fluorescence results showed that ethidium bromide (EB) was displaced from the {DNA–EB} adduct as a result of the interaction of the Pd and Pt complexes with the biomolecule. This effect could be related to an intercalative-like mode of interaction or to the generation of DNA conformational changes causing the disruption of EB binding (Log K_{SV} 4.3–5.0, with K_{SV} = Stern Volmer quenching constant). Obtained K_{SV} values could be related to a high affinity of the compounds for DNA. However, no correlation between the interaction with DNA and the biological activity was observed, discarding this biomolecule as a main target.

Zebrafish (*Danio rerio*) is employed as a toxicological model, among others, for evaluating *in vivo* toxicity in drug development. The most active and selective compound of the new series, [Pt(dppf)(TS3)] (PF_6), showed no *in vivo* toxicity in zebrafish embryos. All embryos were alive in the 1–100 μM concentration range examined, and no apparent toxicity was observed after 48 h of treatment (Rodríguez Arce et al., 2019).

Based on the very nice results obtained for these complexes on both, *T. cruzi* and *T. brucei*, other ferrocenyl compounds, [M(dppf)(L)](PF_6), with M=Pd(II) or Pt(II) and HL=tropolone (HTrop) or hinokitiol (HHino), were obtained and evaluated against the bloodstream form of *T. brucei* and *L. infantum* amastigotes (**Figure 10**; Rivas et al., 2018). Tropolones and their derivatives were selected as bioactive ligands because they are considered lead-like natural products. The tropolone moiety shows high possibilities for derivatization including improvements in the metal binding abilities. Tropolone, hinokitiol and their derivatives as well as the metal complexes with these compounds as ligands have shown various biological activities, for example antimicrobial one (Ononye et al., 2013; Saniewski et al., 2014; El Hachlafi et al., 2021).

The obtained complexes showed IC_{50}/24 h values in the range 1.2–4.5 μM against *T. brucei* together with a significant increase of the activity against this parasite with respect to the free ligands (**Table 1**). In addition, obtained heterobimetallic compounds showed higher selectivity indexes towards the parasite than the free ligands. Platinum complexes were more selective than palladium ones. Moreover, coordination of the bioactive ligands to the {M-dppf} moiety also led to a slight increase of

the anti-leishmanial potency. Studies performed to unravel the mechanism of action of the compounds indicated that no effect on the thiol-redox homeostasis of the parasites is produced by the complexes' action. On the other hand, fluorescence measurements of displacement of ethidium bromide from the adduct {DNA-EB} showed that DNA could be a probable, but not main, target of these compounds.

Later on, the series of structurally related Pd and Pt dppf compounds was expanded with ten new compounds that include five 8-hydroxyquinoline derivatives (8HQs) as bioactive bidentate co-ligands (**Figure 10**; Rivas et al., 2019; Rivas et al., 2021). These compounds showed IC_{50} values against bloodstream *T. brucei* form, in the submicromolar or micromolar range (IC_{50}/24 h: Pt compounds 0.14–0.93 μM; Pd compounds 0.33–1.2 μM). In addition, they displayed good to very good selectivity towards the parasite (SI: Pt compounds 11–48; Pd compounds 4–102) with respect to murine macrophages (cell line J774) (**Table 1**). In most cases, an increase of the activity (11- to 41-fold) was observed as a consequence of coordination of the bioactive 8HQs to the {Pt-dppf} moiety. Only part of the Pd compounds were more active than the corresponding 8HQ ligands and most of the Pd compounds were less active than their Pt analogues. It should be stated that, the palladium compounds were 2- to 45-fold more potent than the drug Nifurtimox while platinum complexes resulted 16- to 107-fold more potent than the same reference drug. All the complexes interacted with DNA (Pt compounds Log K_{SV} 3.3–3.9; Pd compounds Log K_{SV} 3.8–4.6) but the Pd compounds show higher Log K_{SV} values than the Pt analogues. In addition, the most active Pt ones induced reactive oxygen species (ROS) formation in tumor cells. Results suggest that the mechanism of action for these complexes against *T. brucei* may be mediated by interaction with DNA and additionally oxidative stress for the Pt compounds.

An exploratory pre-clinical therapeutic efficacy study was performed in an acute murine model for Human African Trypanosomiasis (HAT) for the most promising Pt compound, Pt-dppf-8HQ Cl,I, (IC_{50}/24 h = 0.14 μM, SI = 48) using mice infected with a bioluminescent cell line of *T. brucei* that allows *in vivo* mice imaging. Although preliminary, the *in vivo* study showed that the assayed compound does not show acute toxicity to animals. In addition, results suggested that although the compound exerts an anti-proliferative activity that prolongs animal survival, it does not exert a curative effect (Rivas et al., 2021).

Having developed a long series of twenty-two structurally related M-dppf-L compounds with different bioactive ligands L (**Figure 10**) that had been evaluated against bloodstream *T. brucei* and with the aim of understanding and assessing the main structural parameters that determine the anti-*T. brucei* activity, a quantitative structure–activity relationships (QSAR) study was performed (Rivas et al., 2021). For this study, the dependent variable was the $\log_{10}$ of the IC_{50} values on *T. brucei*. As independent variables, different physicochemical characteristics including lipophilic, electronic, and steric/topological properties were considered (Hansch et al., 1963). Lipophilicity was indirectly determined by a reverse phase TLC method adequate for non-soluble in water compounds that led to experimental R_f and calculated R_M values. As electronic parameter a signal of the ^{1}H NMR spectra of the studied compounds was selected. Owing to the chemical variability of the studied compounds, i.e. palladium or platinum and three different families of ligands, the cyclopentadienyl-moiety was selected as common feature to determine the contribution of the compounds' electronic effect on the measured anti *T. brucei* activities. The displacement δ of the ^{1}H NMR signals of the protons of the cyclopentadienyl-framework resulted indicative of the coordination and the nature of compound. Consequently, Δδ defined as the largest difference between δ of cyclopentadienyl-framework protons in the complexes and δ of cyclopentadienyl-framework protons without coordination was used as electronic descriptor. Additionally, an indicator variable, IV_{Pd}, was defined that adopts value 1 for palladium compounds or 0 for platinum complexes. According to the QSAR study, ligands with electron withdrawing substituents and with high lipophilicity and having platinum as central atom would result in complexes with increased anti *T. brucei* activity. Among all these descriptors, the electronic properties and the nature of the metal ion were the most relevant ones. QSAR studies are relevant to guide the rational design of further bioactive compounds. However, they are not common in inorganic medicinal chemistry due to the need of having numerous structurally related compounds to perform them (Rivas et al., 2021).

CONCLUDING REMARKS

The development of metal-based compounds for the treatment of diseases caused by trypanosomatid parasites has evolved from rather isolated serendipitous efforts to a more rational and systematic strategy. In this sense, the development of palladium and platinum compounds described in this review constitute an example of this rational phenotypic approach. In fact, from the selection of the metal centers and the bioactive ligands to the inclusion of different co-ligands, the design was based on both chemical and biological arguments. The establishment of structure-activity relationships and the deep insight into the molecular modes of action of the metallic compounds also aided to redesign new compounds with improved pharmacological properties. In this sense, the development of structurally related series of compounds has let us perform quantitative structure activity relationship (QSAR) studies that are not common in Medicinal Inorganic Chemistry.

On the other hand, all the data previously discussed clearly show that the strategy of combining, in a single molecule, palladium or platinum with ligands bearing activity against parasites produce, in most cases, an enhancement of the activity of the ligand and/or a reduction in toxicity. In addition, it was demonstrated that this approach could lead to multifunctional compounds generating single chemical entities that can act simultaneously on multiple targets. In this sense, the omic approach, also new for metal-based antiparasitic drug

development, allowed us to go further into the study of the whole mechanism of action of the prospective antiparasitic agents.

In the process of rational design of palladium and platinum complexes bearing antiparasitic activity, the selection of dppf as co-ligand deserves to be highlighted. The inclusion of a bioactive ligand in the {M-dppf} moiety gave the most promising results as most developed ferrocenyl derivatives not only showed low IC_{50} values in both *T. cruzi* and *T. brucei* but also excellent selectivity index values. In particular, the hypothesis of developing broad spectrum drugs that affect more than one trypanosomatid parasite, based on the discovery of common genomic features for *T. cruzi*, *T. brucei* and *L. major*, was verified in the case of the 5-nitrofurylthiosemicarbazone M-dppf-L complexes. These compounds showed IC_{50} values in the submicromolar or micromolar range on both, *T. cruzi* and *T. brucei*. Some of these compounds were good candidates for *in vivo* studies. Currently, our group is working on the development of delivery systems based on different nano-systems with the aim of avoiding or diminishing usual toxicity and solubility problems of metal-based drugs and to improve bioavailability.

AUTHOR CONTRIBUTIONS

DG and LO are responsible of conceptualization, original draft preparation, writing, review and editing the manuscript. Both authors have read and agreed to the published version of the manuscript.

REFERENCES

Aguirre, G., Boiani, L., Cerecetto, H., González, M., Denicola, A., Otero, L., et al. (2004). *In Vitro* activity and Mechanism of Action against the Protozoan Parasite Trypanosoma Cruzi of 5-nitrofuryl Containing Thiosemicarbazones. *Bioorg. Med. Chem.* 12, 4885–4893. doi:10.1016/j.bmc.2004.07.003

Allardyce, C. S., Dorcier, A., Scolaro, C., and Dyson, P. J. (2005). Development of Organometallic (Organo-Transition Metal) Pharmaceuticals. *Appl. Organometal. Chem.* 19, 1–10. doi:10.1002/aoc.725

Anthony, E. J., Bolitho, E. M., Bridgewater, H. E., Carter, O. W. L., Donnelly, J. M., Imberti, C., et al. (2020). Metallodrugs Are Unique: Opportunities and Challenges of Discovery and Development. *Chem. Sci.* 11, 12888–12917. doi:10.1039/D0SC04082G

Aslett, M., Aurrecoechea, C., Berriman, M., Brestelli, J., Brunk, B. P., Carrington, M., et al. (2010). TriTrypDB: A Functional Genomic Resource for the Trypanosomatidae. *Nucleic Acids Res.* 38, D457. doi:10.1093/nar/gkp851

Atwood, J. A., Weatherly, D. B., Minning, T. A., Bundy, B., Cavola, C., Opperdoes, F. R., et al. (2005). The Trypanosoma Cruzi Proteome. *Science* 309, 473–476. doi:10.1126/science.1110289

Barry, N. P. E., and Sadler, P. J. (2014). 100 Years of Metal Coordination Chemistry: from Alfred Werner to Anticancer Metallodrugs. *Pure Appl. Chem.* 86, 1897–1910. doi:10.1515/pac-2014-0504

Benítez, D., Lavaggi, M. L., Gambino, D., Torre, M. H., Cerecetto, H., and González, M. (2012). Effect of Complexation of 3-Aminoquinoxaline-2-Carbonitrile 1,4-dioxides with Palladium and Copper on Their Anti-T. Cruzi Activity. *Med. Chem. Res.* 21, 1439–1444. doi:10.1007/s00044-011-9660-y

Biot, C., and Dive, D. (2010). "Bioorganometallic Chemistry and Malaria," in *Medicinal Organometallic Chemistry*. Editors G. Jaouen and N. Metzler-Nolte (Berlin, Heidelberg: Springer), 32, 155–193. doi:10.1007/978-3-642-13185-1_7

Biot, C. (2004). Ferroquine: A New Weapon in the Fight against Malaria. *Cmcaia* 3, 135–147. doi:10.2174/1568012043354008

Braga, S. S., and Silva, A. M. S. (2013). A New Age for Iron: Antitumoral Ferrocenes. *Organometallics* 32, 5626–5639. doi:10.1021/om400446y

Brindha, J., Balamurali, M., and Chanda, K. (2021). An Overview on the Therapeutics of Neglected Infectious Diseases-Leishmaniasis and Chagas Diseases. *Front. Chem.* 9, 1–19. doi:10.3389/fchem.2021.622286

Brown, R. W., and Hyland, C. J. T. (2015). Medicinal Organometallic Chemistry - an Emerging Strategy for the Treatment of Neglected Tropical Diseases. *Med. Chem. Commun.* 6, 1230–1243. doi:10.1039/c5md00174a

Burza, S., Croft, S. L., and Boelaert, M. (2018). Leishmaniasis. *Lancet* 392, 951–970. doi:10.1016/s0140-6736(18)31204-2

Camarada, M. B., Echeverria, C., and Ramirez-Tagle, R. (2016). Medicinal Organometallic Compounds with Anti-chagasic Activity. *Med. Chem. Commun.* 7, 1307–1315. doi:10.1039/c6md00200e

Chamberlain, S., Cole, H. D., Roque, J., III, Bellnier, D., McFarland, S. A., and Shafirstein, G. (2020). TLD1433-mediated Photodynamic Therapy with an Optical Surface Applicator in the Treatment of Lung Cancer Cells *In Vitro*. *Pharmaceuticals* 13, 137. doi:10.3390/ph13070137

Chami, G. F., and Bundy, D. A. P. (2019). More Medicines Alone Cannot Ensure the Treatment of Neglected Tropical Diseases. *Lancet Infect. Dis.* 19, e330. doi:10.1016/S1473-3099(19)30160-4

Chatelain, E., and Ioset, J.-R. (2018). Phenotypic Screening Approaches for Chagas Disease Drug Discovery. *Expert Opin. Drug Discov.* 13, 141–153. doi:10.1080/17460441.2018.1417380

Chávez, S., Eastman, G., Smircich, P., Becco, L. L., Oliveira-Rizzo, C., Fort, R., et al. (2017). Transcriptome-wide Analysis of the Trypanosoma Cruzi Proliferative Cycle Identifies the Periodically Expressed mRNAs and Their Multiple Levels of Control. *PLoS One* 12, e0188441. doi:10.1371/journal.pone.0188441

Chellan, P., and Sadler, P. J. (2020). Enhancing the Activity of Drugs by Conjugation to Organometallic Fragments. *Chemistry* 26, 8676–8688. doi:10.1002/chem.201904699

Cipriani, M., Rostán, S., León, I., Li, Z.-H., Gancheff, J. S., Kemmerling, U., et al. (2020). Multi-Target Heteroleptic Palladium Bisphosphonate Complexes. *J. Biol. Inorg. Chem.* 25, 509–519. doi:10.1007/s00775-020-01779-y

Cipriani, M., Toloza, J., Bradford, L., Putzu, E., Vieites, M., Curbelo, E., et al. (2014). Effect of the Metal Ion on the Anti *T. cruzi* Activity and Mechanism of Action of 5-Nitrofuryl-Containing Thiosemicarbazone Metal Complexes. *Eur. J. Inorg. Chem.* 2014, 4677–4689. doi:10.1002/ejic.201402614

Cirri, D., Bartoli, F., Pratesi, A., Baglini, E., Barresi, E., and Marzo, T. (2021). Strategies for the Improvement of Metal-Based Chemotherapeutic Treatments. *Biomedicines* 9, 504. doi:10.3390/biomedicines9050504

Czarnomysy, R., Radomska, D., Szewczyk, O. K., Roszczenko, P., and Bielawski, K. (2021). Platinum and Palladium Complexes as Promising Sources for Antitumor Treatments. *Ijms* 22, 8271. doi:10.3390/ijms22158271

De Rycker, M., Baragaña, B., Duce, S. L., and Gilbert, I. H. (2018). Challenges and Recent Progress in Drug Discovery for Tropical Diseases. *Nature* 559, 498–506. doi:10.1038/s41586-018-0327-4

Dorosti, Z., Yousefi, M., Sharafi, S. M., and Darani, H. Y. (2014). Mutual Action of Anticancer and Antiparasitic Drugs: Are There Any Shared Targets? *Future Oncol.* 10, 2529–2539. doi:10.2217/fon.14.65

Dubar, F., Khalife, J., Brocard, J., Dive, D., and Biot, C. (2008). Ferroquine, an Ingenious Antimalarial Drug -Thoughts on the Mechanism of Action. *Molecules* 13, 2900–2907. doi:10.3390/molecules13112900

El Hachlafi, N., Lakhdar, F., Khouchlaa, A., Bakrim, S., El Omari, N., Balahbib, A., et al. (2021). Health Benefits and Pharmacological Properties of Hinokitiol. *Processes* 9, 1680. doi:10.3390/pr9091680

El-Sayed, N. M., Myler, P. J., Blandin, G., Berriman, M., Crabtree, J., Aggarwal, G., et al. (2005). Comparative Genomics of Trypanosomatid Parasitic Protozoa. *Science* 309 (5733), 404–409. doi:10.1126/science.1112181

Englinger, B., Pirker, C., Heffeter, P., Terenzi, A., Kowol, C. R., Keppler, B. K., et al. (2019). Metal Drugs and the Anticancer Immune Response. *Chem. Rev.* 119, 1519–1624. doi:10.1021/acs.chemrev.8b00396

Field, M. C., Horn, D., Fairlamb, A. H., Ferguson, M. A. J., Gray, D. W., Read, K. D., et al. (2017). Anti-Trypanosomatid Drug Discovery: An Ongoing challenge and

a Continuing Need. *Nat. Rev. Microbiol.* 15, 217–231. doi:10.1038/nrmicro.2016.193

Francisco, A. F., Jayawardhana, S., Olmo, F., Lewis, M. D., Wilkinson, S. R., Taylor, M. C., et al. (2020). Challenges in Chagas Disease Drug Development. *Molecules* 25, 1–14. doi:10.3390/molecules25122799

Fuertes, M. A., Nguewa, P. A., Castilla, J., Alonso, C., and Pérez, J. M. (2008). Anticancer Compounds as Leishmanicidal Drugs: Challenges in Chemotherapy and Future Perspectives. *Curr. Med. Chem.* 15, 433–439. doi:10.2174/092986708783503221

Gambino, D., and Otero, L. (2019). Metal Compounds in the Development of Antiparasitic Agents: Rational Design from Basic Chemistry to the Clinic. *Met. Ions Life Sci.* 19, 331–358. doi:10.1515/9783110527872-019

Gambino, D., and Otero, L. (2012). Perspectives on what Ruthenium-Based Compounds Could Offer in the Development of Potential Antiparasitic Drugs. *Inorg. Chim. Acta* 393, 103–114. doi:10.1016/j.ica.2012.05.028

Gambino, D. (2011). Potentiality of Vanadium Compounds as Anti-Parasitic Agents. *Coord. Chem. Rev.* 255, 2193–2203. doi:10.1016/j.ccr.2010.12.028

Gambino, D., and Otero, L. (2018). Design of Prospective Antiparasitic Metal-Based Compounds Including Selected Organometallic Cores. *Inorg. Chim. Acta* 472, 58–75. doi:10.1016/j.ica.2017.07.068

García-Huertas, P., Mejía-Jaramillo, A. M., González, L., and Triana-Chávez, O. (2017). Transcriptome and Functional Genomics Reveal the Participation of Adenine Phosphoribosyltransferase inTrypanosoma cruziResistance to Benznidazole. *J. Cell Biochem.* 118, 1936–1945. doi:10.1002/jcb.25978

Gómez, N., Santos, D., Vázquez, R., Suescun, L., Mombrú, Á., Vermeulen, M., et al. (2011). Synthesis, Structural Characterization, and Pro-apoptotic Activity of 1-Indanone Thiosemicarbazone Platinum(II) and Palladium(II) Complexes: Potential as Antileukemic Agents. *ChemMedChem* 6, 1485–1494. doi:10.1002/cmdc.201100060

Haanstra, J. R., and Bakker, B. M. (2015). Drug Target Identification through Systems Biology. *Drug Discov. Today Tech.* 15, 17–22. doi:10.1016/j.ddtec.2015.06.002

Hanif, M., and Hartinger, C. G. (2018). Anticancer Metallodrugs: Where is the Next Cisplatin? *Future Med. Chem.* 10, 615–617. doi:10.4155/fmc-2017-0317

Hansch, C., Muir, R. M., Fujita, T., Maloney, P. P., Geiger, F., and Streich, M. (1963). The Correlation of Biological Activity of Plant Growth Regulators and Chloromycetin Derivatives with Hammett Constants and Partition Coefficients. *J. Am. Chem. Soc.* 85, 2817–2824. doi:10.1021/ja00901a033

Hartinger, C. G., and Dyson, P. J. (2009). Bioorganometallic Chemistry-From Teaching Paradigms to Medicinal Applications. *Chem. Soc. Rev.* 38, 391–401. doi:10.1039/b707077m

Ilari, A., Genovese, I., Fiorillo, F., Battista, T., De Ionna, I., Fiorillo, A., et al. (2018). Toward a Drug against All Kinetoplastids: From LeishBox to Specific and Potent Trypanothione Reductase Inhibitors. *Mol. Pharmaceutics* 15, 3069–3078. doi:10.1021/acs.molpharmaceut.8b00185

Imberti, C., Zhang, P., Huang, H., and Sadler, P. J. (2020). New Designs for Phototherapeutic Transition Metal Complexes. *Angew. Chem. Int. Ed.* 59, 61–73. doi:10.1002/anie.201905171

Jahromi, E. Z., Divsalar, A., Saboury, A. A., Khaleghizadeh, S., Mansouri-TorshiziKostova, H. I., and Kostova, I. (2016). Palladium Complexes: New Candidates for Anti-Cancer Drugs. *J. Iran Chem. Soc.* 13, 967–989. doi:10.1007/s13738-015-0804-8

Jaouen, G., Vessières, A., and Top, S. (2015). Ferrocifen Type Anti Cancer Drugs. *Chem. Soc. Rev.* 44, 8802–8817. doi:10.1039/c5cs00486a

Karges, J., and Cohen, S. (2021). Metal Complexes as Antiviral Agents for SARS-CoV-2. *ChemBioChem* 22, 1–9. doi:10.1002/cbic.202100186

Kayode, O. T., Lele, C. K., and Kayode, A. A. A. (2020). Trypanosomiasis: Recent Advances in Strategies for Control. *Glob. J. Infect. Dis. Clin. Res.* 6, 37–41. doi:10.17352/2455-5363.000033

Kinnamon, K. E., Steck, E. A., and Rane, D. S. (1979). Activity of Antitumor Drugs Against African Trypanosomes. *Antimicrob. Agents Chemother.* 15, 157–160. doi:10.1128/aac.15.2.157

Kostelnik, T. I., and Orvig, C. (2019). Radioactive Main Group and Rare Earth Metals for Imaging and Therapy. *Chem. Rev.* 119, 902–956. doi:10.1021/acs.chemrev.8b00294

Kourbeli, V., Chontzopoulou, E., Moschovou, K., Pavlos, D., Mavromoustakos, T., and Papanastasiou, I. P. (2021). An Overview on Target-Based Drug Design against Kinetoplastid Protozoan Infections: Human African Trypanosomiasis, Chagas Disease and Leishmaniases. *Molecules* 26, 4629. doi:10.3390/molecules26154629

Kwofie, S. K., Broni, E., Dankwa, B., Enninful, K. S., Kwarko, G. B., Darko, L., et al. (2020). Outwitting an Old Neglected Nemesis: A Review on Leveraging Integrated Data-Driven Approaches to Aid in Unraveling of Leishmanicides of Therapeutic Potential. *Curr. Top. Med. Chem.* 20, 349–366. doi:10.2174/1568026620666200128160454

Lazarević, T., Rilak, A., and Bugarčić, Ž. D. (2017). Platinum, Palladium, Gold and Ruthenium Complexes as Anticancer Agents: Current Clinical Uses, Cytotoxicity Studies and Future Perspectives. *Eur. J. Med. Chem.* 142, 8–31. doi:10.1016/j.ejmech.2017.04.007

Lin, Y., Betts, H., Keller, S., Cariou, K., and Gasser, G. (2021). Recent Developments of Metal-Based Compounds Against Fungal Pathogens. *Chem. Soc. Rev.* 50, 10346–10402. doi:10.1039/d0cs00945h

Marcelino, P. R. F., Moreira, M. B., Lacerda, T. M., and da Silva, S. S. (2018). "Metal-Based Drugs for Treatment of Malaria," in *Biomedical Applications of Metals*. Editors M. Rai, A. P. Ingle, and S. Medici (Zurich, Switzerland: Springer International Publishing AG, part of Springer Nature), 167–193. doi:10.1007/978-3-319-74814-6_8

Markwalter, C. F., Kantor, A. G., Moore, C. P., Richardson, K. A., and Wright, D. W. (2019). Inorganic Complexes and Metal-Based Nanomaterials for Infectious Disease Diagnostics. *Chem. Rev.* 119, 1456–1518. doi:10.1021/acs.chemrev.8b00136

Mbaba, M., Golding, T. M., and Smith, G. S. (2020). Recent Advances in the Biological Investigation of Organometallic Platinum-Group Metal (Ir, Ru, Rh, Os, Pd, Pt) Complexes as Antimalarial Agents. *Molecules* 25, 5276. doi:10.3390/molecules25225276

Merlino, A., Otero, L., Gambino, D., and Laura Coitiño, E. (2011). In Search of Patterns over Physicochemical Properties and Pharmacological Activities for a Set of [MCl2(thiosemicarbazone)] Complexes (M=Pt/Pd): Support for Multiple Mechanisms of Antichagasic Action Excluding DNA-Bonding *In Vivo*? *Eur. J. Med. Chem.* 46, 2639–2651. doi:10.1016/j.ejmech.2011.03.046

Merlino, A., Vieites, M., Gambino, D., and Laura Coitiño, E. (2014). Homology Modeling of *T. cruzi* and *L. major* NADH-dependent Fumarate Reductases: Ligand Docking, Molecular Dynamics Validation, and Insights on Their Binding Modes. *J. Mol. Graph. Model.* 48, 47–59. doi:10.1016/j.jmgm.2013.12.001

Mjos, K. D., and Orvig, C. (2014). Metallodrugs in Medicinal Inorganic Chemistry. *Chem. Rev.* 114, 4540–4563. doi:10.1021/cr400460s

Mosquillo, M. F., Bilbao, L., Hernández, F., Machado, I., Gambino, D., Garat, B., et al. (2018). Effect of a New Anti-T. Cruzi Metallic Compound Based on Palladium. *BioMetals* 31, 961–974. doi:10.1007/s10534-018-0140-4

Mosquillo, M. F., Bilbao, L., Hernández, F., Tissot, F., Gambino, D., Garat, B., et al. (2018). Trypanosoma Cruzibiochemical Changes and Cell Death Induced by an Organometallic Platinum-Based Compound. *Chem. Biol. Drug Des.* 92, 1657–1669. doi:10.1111/cbdd.13332

Mosquillo, M. F., Smircich, P., Ciganda, M., Lima, A., Gambino, D., Garat, B., et al. (2020). Comparative High-Throughput Analysis of the Trypanosoma Cruzi Response to Organometallic Compounds. *Metallomics* 12, 813–828. doi:10.1039/d0mt00030b

Murray, B. S., and Dyson, P. J. (2020). Recent Progress in the Development of Organometallics for the Treatment of Cancer. *Curr. Opin. Chem. Biol.* 56, 28–34. doi:10.1016/j.cbpa.2019.11.001

Nagle, A. S., Khare, S., Kumar, A. B., Supek, F., Buchynskyy, A., Mathison, C. J. N., et al. (2014). Recent Developments in Drug Discovery for Leishmaniasis and Human African Trypanosomiasis. *Chem. Rev.* 114, 11305–11347. doi:10.1021/cr500365f

Navarro, M., and Visbal, G. (2021). *Metal-Based Antiparasitic Therapeutics*. Cambridge, MA: MIT Press.

Navarro, M., Gabbiani, C., Messori, L., and Gambino, D. (2010). Metal-based Drugs for Malaria, Trypanosomiasis and Leishmaniasis: Recent Achievements and Perspectives. *Drug Discov. Today* 15, 1070–1078. doi:10.1016/j.drudis.2010.10.005

Navarro, M. (2009). Gold Complexes as Potential Anti-parasitic Agents. *Coord. Chem. Rev.* 253, 1619–1626. doi:10.1016/j.ccr.2008.12.003

Noffke, A. L., Habtemariam, A., Pizarro, A. M., and Sadler, P. J. (2012). Designing Organometallic Compounds for Catalysis and Therapy. *Chem. Commun.* 48, 5219–5246. doi:10.1039/c2cc30678f

Ong, Y. C., Roy, S., Andrews, P. C., and Gasser, G. (2019). Metal Compounds Against Neglected Tropical Diseases. *Chem. Rev.* 119, 730–796. doi:10.1021/acs.chemrev.8b00338

Ononye, S. N., VanHeyst, M. D., Oblak, E. Z., Zhou, W., Ammar, M., Anderson, A. C., et al. (2013). Tropolones as Lead-Like Natural Products: The Development of Potent and Selective Histone Deacetylase Inhibitors. *ACS Med. Chem. Lett.* 4, 757–761. doi:10.1021/ml400158k

Otero, L., Maya, J. D., Morello, A., Rigol, C., Barriga, G., Rodríguez, J., et al. (2008). Insight into the Bioreductive Mode of Action of Antitrypanosomal 5-nitrofuryl Containing Thiosemicarbazones. *Med. Chem.* 4, 11–17. doi:10.2174/157340608783331470

Otero, L., Vieites, M., Boiani, L., Denicola, A., Rigol, C., Opazo, L., et al. (2006). Novel Antitrypanosomal Agents Based on Palladium Nitrofurylthiosemicarbazone Complexes: DNA and Redox Metabolism as Potential Therapeutic Targets. *J. Med. Chem.* 49, 3322–3331. doi:10.1021/jm0512241

Paucar, R., Moreno-Viguri, E., and Pérez-Silanes, S. (2016). Challenges in Chagas Disease Drug Discovery: A Review. *Cmc* 23, 3154–3170. doi:10.2174/0929867323999160625124424

Păunescu, E., Boubaker, G., Desiatkina, O., Anghel, N., Amdouni, Y., Hemphill, A., et al. (2021). The Quest of the Best - A SAR Study of Trithiolato-Bridged Dinuclear Ruthenium(II)-Arene Compounds Presenting Antiparasitic Properties. *Eur. J. Med. Chem.* 222, 113610. doi:10.1016/j.ejmech.2021.113610

Pessoa, J. C., Etcheverry, S., and Gambino, D. (2015). Vanadium Compounds in Medicine. *Coord. Chem. Rev.* 301–302, 24–48. doi:10.1016/j.ccr.2014.12.002

Rao, S. P. S., Barrett, M. P., Dranoff, G., Faraday, C. J., Gimpelewicz, C. R., Hailu, A., et al. (2019). Drug Discovery for Kinetoplastid Diseases: Future Directions. *ACS Infect. Dis.* 5, 152–157. doi:10.1021/acsinfecdis.8b00298

Ravera, M., Moreno-Viguri, E., Paucar, R., Pérez-Silanes, S., and Gabano, E. (2018). Organometallic Compounds in the Discovery of New Agents against Kinetoplastid-Caused Diseases. *Eur. J. Med. Chem.* 155, 459–482. doi:10.1016/j.ejmech.2018.05.044

Rigol, C., Olea-Azar, C., Mendizábal, F., Otero, L., Gambino, D., González, M., et al. (2005). Electrochemical and ESR Study of 5-Nitrofuryl-Containing Thiosemicarbazones Antiprotozoal Drugs. *Spectrochim. Acta A Mol. Biomol. Spectrosc.* 61, 2933–2938. doi:10.1016/j.saa.2004.11.003

Rivas, F., Medeiros, A., Comini, M., Suescun, L., Rodríguez Arce, E., Martins, M., et al. (2019). Pt-Fe Ferrocenyl Compounds With Hydroxyquinoline Ligands Show Selective Cytotoxicity on Highly Proliferative Cells. *J. Inorg. Biochem.* 199, 110779. doi:10.1016/j.jinorgbio.2019.110779

Rivas, F., Medeiros, A., Quiroga, C., Benítez, D., Comini, M., Rodríguez-Arce, E., et al. (2021). New Pd-Fe Ferrocenyl Antiparasitic Compounds with Bioactive 8-hydroxyquinoline Ligands: a Comparative Study with Their Pt-Fe Analogues. *Dalton Trans.* 50, 1651–1665. doi:10.1039/d0dt03963b

Rivas, F., Medeiros, A., Rodríguez Arce, E., Comini, M., Ribeiro, C. M., Pavan, F. R., et al. (2018). New Heterobimetallic Ferrocenyl Derivatives: Evaluation of Their Potential as Prospective Agents against Trypanosomatid Parasites and *Mycobacterium tuberculosis*. *J. Inorg. Biochem.* 187, 73–84. doi:10.1016/j.jinorgbio.2018.07.013

Rodríguez Arce, E., Mosquillo, M. F., Pérez-Díaz, L., Echeverría, G. A., Piro, O. E., Merlino, A., et al. (2015). Aromatic Amine N-Oxide Organometallic Compounds: Searching for Prospective Agents against Infectious Diseases. *Dalton Trans.* 44, 14453–14464. doi:10.1039/c5dt00557d

Rodríguez Arce, E., Putzu, E., Lapier, M., Maya, J. D., Olea Azar, C., Echeverría, G. A., et al. (2019). New Heterobimetallic Ferrocenyl Derivatives are Promising Antitrypanosomal Agents. *Dalton Trans.* 48, 7644–7658. doi:10.1039/c9dt01317b

Sánchez-Delgado, R. A., Martínez, A. A., and Suárez, L. (2004). "Metal Ions and Their Complexes in Medication," in *Metal Ions in Biological Systems*. Editors A. Sigel and H. Sigel (New York: Marcel Dekker), 379.

Salas, P. F., Herrmann, C., and Orvig, C. (2013). Metalloantimalarials. *Chem. Rev.* 113, 3450–3492. doi:10.1021/cr3001252

Saniewski, M., Horbowicz, M., and Kanlayanarat, S. (2014). The Biological Activities of Troponoids and Their Use in Agriculture A Review. *J. Hortic. Res.* 22, 5–19. doi:10.2478/johr-2014-0001

Santos, D., Parajón-Costa, B., Rossi, M., Caruso, F., Benítez, D., Varela, J., et al. (2012). Activity on Trypanosoma Cruzi, Erythrocytes Lysis and Biologically Relevant Physicochemical Properties of Pd(II) and Pt(II) Complexes of Thiosemicarbazones Derived from 1-indanones. *J. Inorg. Biochem.* 117, 270–276. doi:10.1016/j.jinorgbio.2012.08.024

Santos, S. S., de Araújo, R. V., Giarolla, J., Seoud, O. E., and Ferreira, E. I. (2020). Searching for Drugs for Chagas Disease, Leishmaniasis and Schistosomiasis: a Review. *Int. J. Antimicrob. Agents* 55, 105906. doi:10.1016/j.ijantimicag.2020.105906

Scarim, C. B., Jornada, D. H., Chelucci, R. C., de Almeida, L., Dos Santos, J. L., and Chung, M. C. (2018). Current Advances in Drug Discovery for Chagas Disease. *Eur. J. Med. Chem.* 155, 824–838. doi:10.1016/j.ejmech.2018.06.040

Silva, M. J. S. A., Gois, P. M. P., and Gasser, G. (2021). Unveiling the Potential of Transition Metal Complexes for Medicine: Translational *In Situ* Activation of Metal-Based Drugs from Bench to *In Vivo* Applications. *ChemBioChem* 22, 1740–1742. doi:10.1002/cbic.202100015

Soldevila-Barreda, J. J., and Metzler-Nolte, N. (2019). Intracellular Catalysis with Selected Metal Complexes and Metallic Nanoparticles: Advances toward the Development of Catalytic Metallodrugs. *Chem. Soc. Rev.* 119, 829–869. doi:10.1021/acs.chemrev.8b00493

Stuart, K., Brun, R., Croft, S., Fairlamb, A., Gürtler, R. E., McKerrow, J., et al. (2008). Kinetoplastids: Related Protozoan Pathogens, Different Diseases. *J. Clin. Invest.* 118, 1301–1310. doi:10.1172/jci33945

Sullivan, J. A., Tong, J. L., Wong, M., Kumar, A., Sarkar, H., Ali, S., et al. (2015). Unravelling the Role of SNM1 in the DNA Repair System ofTrypanosoma Brucei. *Mol. Microbiol.* 96, 827–838. doi:10.1111/mmi.12973

Tahghighi, A. (2014). Importance of Metal Complexes for Development of Potential Leishmanicidal Agents. *J. Organomet. Chem.* 770, 51–60. doi:10.1016/j.jorganchem.2014.08.007

Urquiola, C., Vieites, M., Torre, M. H., Cabrera, M., Lavaggi, M. L., Cerecetto, H., et al. (2009). Cytotoxic Palladium Complexes of Bioreductive Quinoxaline N1,N4-Dioxide Prodrugs. *Bioorg. Med. Chem.* 17, 1623–1629. doi:10.1016/j.bmc.2008.12.064

Van den Kerkhof, M., Sterckx, Y. G., Leprohon, P., Maes, L., and Caljon, G. (2020). Experimental Strategies to Explore Drug Action and Resistance in Kinetoplastid Parasites. *Microorganisms* 8, 1–24. doi:10.3390/microorganisms8060950

Vieites, M., Otero, L., Santos, D., Olea-Azar, C., Norambuena, E., Aguirre, G., et al. (2009). Platinum-based Complexes of Bioactive 3-(5-nitrofuryl)acroleine Thiosemicarbazones Showing Anti-trypanosoma Cruzi Activity. *J. Inorg. Biochem.* 103, 411–418. doi:10.1016/j.jinorgbio.2008.12.004

Vieites, M., Otero, L., Santos, D., Toloza, J., Figueroa, R., Norambuena, E., et al. (2008). Platinum(II) Metal Complexes as Potential Anti-trypanosoma Cruzi Agents. *J. Inorg. Biochem.* 102, 1033–1043. doi:10.1016/j.jinorgbio.2007.12.005

Vieites, M., Smircich, P., Pagano, M., Otero, L., Fischer, F. L., Terenzi, H., et al. (2011). DNA as Molecular Target of Analogous Palladium and Platinum Anti-trypanosoma Cruzi Compounds: a Comparative Study. *J. Inorg. Biochem.* 105, 1704–1711. doi:10.1016/j.jinorgbio.2011.07.018

Vieites, M., Smircich, P., Parajón-Costa, B., Rodríguez, J., Galaz, V., Olea-Azar, C., et al. (2008). Potent *In Vitro* Anti-trypanosoma Cruzi Activity of Pyridine-2-Thiol N-Oxide Metal Complexes Having an Inhibitory Effect on Parasite-specific Fumarate Reductase. *J. Biol. Inorg. Chem.* 13, 723–735. doi:10.1007/s00775-008-0358-7

WahsnerGale, J. E. M., Gale, E. M., Rodríguez-Rodríguez, A., and Caravan, P. (2019). Chemistry of MRI Contrast Agents: Current Challenges and New Frontiers. *Chem. Rev.* 119, 957–1057. doi:10.1021/acs.chemrev.8b00363

Wang, H., Zhou, Y., Xu, X., Li, H., and Sun, H. (2020). Metalloproteomics in Conjunction with Other Omics for Uncovering the Mechanism of Action of Metallodrugs: Mechanism-Driven New Therapy Development. *Curr. Opin. Chem. Biol.* 55, 171–179. doi:10.1016/j.cbpa.2020.02.006

Wang, X., Wang, X., Jin, S., Muhammad, N., and Guo, Z. (2019). Stimuli-Responsive Therapeutic Metallodrugs. *Chem. Rev.* 119, 1138–1192. doi:10.1021/acs.chemrev.8b00209

Williamson, J., and Scott-Finnigan, T. J. (1975). Trypanocidal Activity of Antitumour Antibodies and Other Metabolic Inhibitors. *Trans. R. Soc. Trop. Med. Hyg.* 69, 1–2.

World Health Organization (nd). Chagas Disease (American Trypanosomiasis). Available at: https://www.who.int/health-topics/chagas-disease#tab=tab_1 (Accessed September 15, 2021).

World Health Organization (2021). Leishmaniasis. Available at: https://www.who.int/es/news-room/fact-sheets/detail/leishmaniasis (Accessed Sepember 15, 2021).

World Health Organization (2021). Maintenance Break. Available at: http://www.who.int/trypanosomiasis_african/ (Accessed September 15, 2021).

World Health Organization (2021). Neglected Tropical Diseases. Available at: https://www.who.int/news-room/q-a-detail/neglected-tropical-diseases (Accessed September 15, 2021).

World Health Organization (2012). Why Are Some Tropical Diseases Called 'neglected'? Available at: https://www.who.int/features/qa/58/en/ (Accessed September 15, 2021).

Yousuf, I., Bashir, M., Arjmand, F., and Tabassum, S. (2021). Advancement of Metal Compounds as Therapeutic and Diagnostic Metallodrugs: Current Frontiers and Future Perspectives. *Coord. Chem. Rev.* 445, 214104. doi:10.1016/j.ccr.2021.214104

Zhang, P., and Sadler, P. J. (2017). Advances in the Design of Organometallic Anticancer Complexes. *J. Organomet. Chem.* 839, 5–14. doi:10.1016/j.jorganchem.2017.03.038

Conflict of Interest: The authors declare that the research was conducted in the absence of any commercial or financial relationships that could be construed as a potential conflict of interest.

frontiers in Chemistry

MINI REVIEW
published: 12 January 2022
doi: 10.3389/fchem.2021.812098

Illuminating the Effect of the Local Environment on the Performance of Organic Sunscreens: Insights From Laser Spectroscopy of Isolated Molecules and Complexes

Natalie G. K. Wong† *and Caroline E. H. Dessent**†

Department of Chemistry, University of York, York, United Kingdom

Sunscreens are essential for protecting the skin from UV radiation, but significant questions remain about the fundamental molecular-level processes by which they operate. In this mini review, we provide an overview of recent advanced laser spectroscopic studies that have probed how the local, chemical environment of an organic sunscreen affects its performance. We highlight experiments where UV laser spectroscopy has been performed on isolated gas-phase sunscreen molecules and complexes. These experiments reveal how pH, alkali metal cation binding, and solvation perturb the geometric and hence electronic structures of sunscreen molecules, and hence their non-radiative decay pathways. A better understanding of how these interactions impact on the performance of individual sunscreens will inform the rational design of future sunscreens and their optimum formulations.

Keywords: sunscreens, lasers, pH, solvent, rational design, photochemistry, photophysics

OPEN ACCESS

Edited by:
Rene A. Nome,
State University of Campinas, Brazil

Reviewed by:
Natércia Das Neves Rodrigues,
The Lubrizol Corporation, United States
Joaquim C. G. Esteves Da Silva,
University of Porto, Portugal

****Correspondence:***
Caroline E. H. Dessent
caroline.dessent@york.ac.uk

†ORCID:
Natalie G. K. Wong
orcid.org/0000-0002-3154-038X
Caroline E. H. Dessent
orcid.org/0000-0003-4944-0413

Specialty section:
This article was submitted to Physical Chemistry and Chemical Physics, a section of the journal Frontiers in Chemistry

Received: *09 November 2021*
Accepted: *20 December 2021*
Published: *12 January 2022*

Citation:
Wong NGK and Dessent CEH (2022) Illuminating the Effect of the Local Environment on the Performance of Organic Sunscreens: Insights From Laser Spectroscopy of Isolated Molecules and Complexes. Front. Chem. 9:812098. doi: 10.3389/fchem.2021.812098

INTRODUCTION

The incidence of melanoma skin cancer has reached epidemic proportions globally, with cases predicted to continue rising by 2.5% year on year. Against this background, considerable effort is being made towards developing more efficient broad-spectrum sunscreens that protect against both UVA and high-energy UVB rays (Forestier, 2008; Campos et al., 2017). Despite the importance of sunscreens to human health remarkably little was known until very recently about how photoactive organic sunscreens function in terms of their detailed molecular potential energy surfaces (Karsili et al., 2014; Baker et al., 2017). An organic sunscreen molecule works by absorbing damaging UV radiation, and dispersing it into less harmful forms of energy (Forestier, 2008; Karsili et al., 2014; Baker et al., 2017; Losantos et al., 2018). One key requisite for such molecules to act as chemical sunscreens is that they should not undergo chemical change or induce unwanted toxicity upon exposure to UV light (Forestier, 2008). However, the extent to which a molecule's structure remains intact after absorbing UV light depends not only on its intrinsic photochemistry, but also on how that photochemistry is affected by external chemical and physical influences such as pH, aggregation between components in a mixture, and the effects of phase change.

Commercial sunscreen lotions are complex multicomponent mixtures of organic and inorganic substances dispersed in a mixture of solvents (Osterwalder et al., 2014). This complexity means that individual organic sunscreen molecules can experience a range of different intermolecular

interactions within the suncream formulation, including interactions with solvent, counterions and other organic sunscreen molecules. All of these interactions have the potential to perturb the electronic structure of the organic sunscreen, and hence its intrinsic photochemistry. Sunscreen development in commercial laboratories tends to focus on achieving an acceptable bulk formulation without considering such molecular-level interactions (Acker et al., 2014). However, it is clear that a better fundamental understanding of how intermolecular interactions can impact on the performance of organic sunscreens could be beneficial in the rational design of new and improved sunscreens and their optimum formulations (Serpone, 2021). Over recent years, laser spectroscopy techniques have been applied to better understand how intermolecular interactions (e.g., with solvent molecules) and the local environment (pH) affect sunscreen photochemistry. These studies have either been performed in highly simplified mixtures (i.e., one sunscreen molecule and one solvent) or on individual molecules and their complexes in the gas phase (Tan et al., 2014; Rodrigues and Stavros, 2018). In this review, we provide an overview of recent work in this area and illustrate how such studies are beginning to impact on the development of new sunscreen agents.

Before moving to discuss the impact of the molecular-level environment on sunscreen photochemistry, it is useful to review the molecular properties that are linked to good sunscreen action. The majority of organic sunscreen molecules are composed of structures that contain aromatic rings conjugated to carbonyl groups, with examples including cinnamates, salicylates, oxybenzone and avobenzone (Forestier, 2008). All of these molecules provide photoprotection through a combination of a high absorption cross-section for UV light coupled with high internal conversion (IC) efficiency (Forestier, 2008; Baker et al., 2017; Rodrigues and Stavros, 2018). UV electronic excitation is therefore followed by rapid conversion to vibrational energy which is dissipated as heat to the molecule's surroundings. The extent to which the UV energy absorbed is converted to benign heat is a measure of the suitability of the molecule as a sunscreen, since it ensures that the molecule is able to absorb and dissipate repeated UV photons. Ideally, a sunscreen molecule should be able to dissipate excited state energy through IC (i.e., non-radiatively) on a rapid timescale (femtoseconds-picoseconds), to reduce the possibility of harmful side reactions such as the formation of triplet states, and/or molecular fragmentation (Serpone et al., 2007).

Common organic sunscreen molecules display a range of IC pathways that allow them to dissipate absorbed UV energy. For cinnamates, their side chains contain C=C double bonds that photoisomerize following UV absorption, thus opening an excited state pathway towards a conical intersection which facilitates IC (Peperstraete et al., 2016). Oxybenzone illustrates a different type of IC pathway: It contains an H atom donor on a hydroxyl group adjacent to a carbonyl oxygen acceptor group, allowing intramolecular hydrogen transfer. Following UV photoexcitation, excited state hydrogen transfer, which drives enol-keto tautomerisation, and leads to a slower rotation about the C-C bond which in turn facilitates IC back to the electronic ground state through an S_1/S_0 conical intersection (Baker et al., 2015). High-level computational studies of the ground and excited state potential energy surfaces of these sunscreen molecules confirm the pathways outlined here, with the oxybenzone system having been studied by Domcke and co-workers (Karsili et al., 2014), and the cinnamates by Cui and co-workers and Ebata and co-workers (Chang et al., 2015; Kinoshita et al., 2021). Any geometric change of the key functional groups involved in accessing the conical intersection for IC has the potential to perturb the optimum decay dynamics of the sunscreen molecule. Thus, our focus in this review will be to explore at molecular-level detail, whether local environmental effects (i.e., solvent molecules, counterions) can lead to geometric structural modifications at the key molecular functional groups, and hence perturb the molecule's electronic structure to impact its photophysical behaviour.

THE EFFECT OF pH ON ORGANIC SUNSCREENS

Despite the significant growth in fundamental studies of sunscreens over the last decade, surprisingly little attention appears to have been paid to the effect of the pH environment on sunscreen performance (De Laurentiis et al., 2013; Ignasiak et al., 2015; Li et al., 2016). From a chemical perspective, the question to be addressed is straightforward, namely how do the properties of the protonated or deprotonated sunscreen molecule differ from those of the neutral? Li et al. (2016) recently performed a series of oxybenzone photolysis studies in pure water, which revealed that while the neutral form of oxybenzone is stable over long timescales, the anionic form is not. This is potentially a key issue since commercial sunscreens typically involve complex mixtures including water and alcoholic solvents. Moreover, in common usage, sunscreens are exposed to acidic and alkaline environments, with chlorinated swimming pools and the ocean being alkaline (Kulthanan et al., 2013), while human skin and sweat are typically mildly acidic (Proksch, 2018).

Laser-interfaced mass spectrometry (LIMS) is an excellent experimental method for exploring the spectroscopy and photochemistry of protonated and deprotonated forms of the same molecular system (Matthews and Dessent, 2018; Matthews et al., 2018; Uleanya et al., 2020). Since experiments are conducted on isolated, mass-selected ions, the charged system under investigation is unambiguous, and any complications of the bulk environment are removed. The technique allows the measurement of the gas-phase absorption profile of the charged molecule, along with the photon-energy dependent production profile of any ionic photoproducts (Matthews et al., 2016). We have applied this approach over recent years to a number of protonated and deprotonated forms of organic sunscreens (Matthews and Dessent, 2017; Wong et al., 2019b; Wong et al., 2019a; Wong et al., 2021a; Wong et al., 2021b; Berenbeim et al., 2020b).

LIMS was first applied in 2019 to the protonated and deprotonated forms of an organic UV filter, oxybenzone (Wong et al., 2019b). **Figure 1** displays the gas-phase

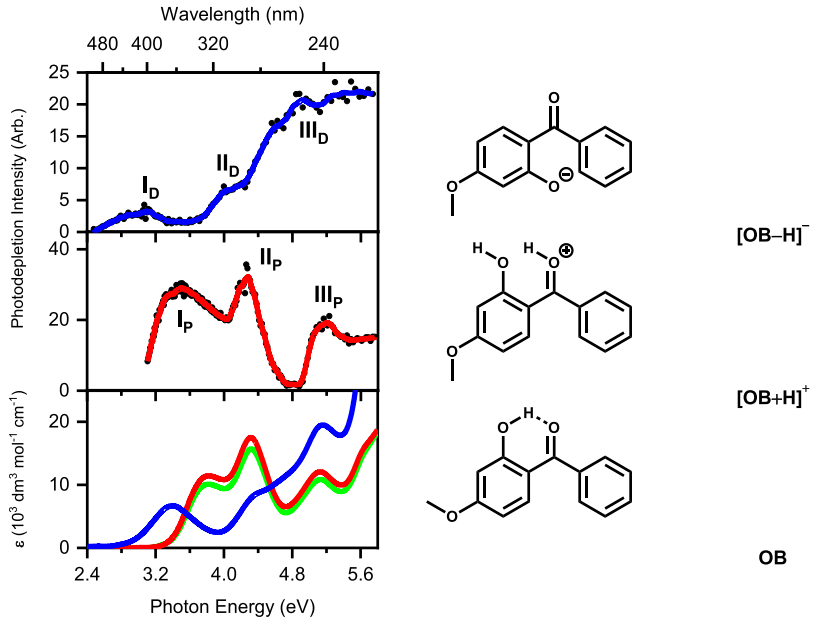

FIGURE 1 | (Top) Gas-phase photodepletion (absorption) spectrum of deprotonated oxybenzone ([OB–H]$^-$). (Middle) Gas-phase photodepletion spectrum of protonated oxybenzone ([OB + H]$^+$). The solid lines are a 5-point adjacent average of the data points. A schematic of the lowest-energy isomers of [OB–H]$^-$ and [OB + H]$^+$ are shown alongside their respective spectra. (Bottom) Solution-phase absorption spectra of OB under alkaline (blue), neutral (green), and acidic (red) conditions. Data reproduced from (Wong et al., 2019b) with permission from the PCCP owner societies.

absorption spectra of the protonated and deprotonated forms of oxybenzone, along with the solution-phase UV-VIS spectra. From the spectra displayed in **Figure 1**, it is clear that the protonation state has a dramatic effect on the absorption properties. While the UV absorption profile (400–216 nm) of oxybenzone was only modestly affected by protonation, deprotonated oxybenzone displays a considerably modified absorption spectrum, with very low absorption in the UVA region between 370–330 nm.

The photodissociation pathways of oxybenzone are also found to be affected by the protonation state, with the protonated form photofragmenting primarily by rupture of the bonds on either side of the central carbonyl group, with a significant number of additional photofragments also observed. Intriguingly, the production spectra of these various photofragments fell into two distinctive groups, in terms of their excitation energy production profiles. This revealed that two distinctive decay pathways are accessible to protonated oxybenzone across this region, possibly due to coupling of the initially accessed π-π* transition with an energetically similar charge-transfer state (Dean et al., 2014). In addition, analysis of the photofragments provided information on the nature of the excited-state decay dynamics, revealing that one of these pathways was not associated with ultrafast IC decay. This result is important as it indicates that the protonated form of oxybenzone is a non-ideal sunscreen over the UVA region, and would be likely to undergo enhanced photodegradation under acidic conditions.

Deprotonated oxybenzone photofragments in a completely different way to the protonated form, photodissociating with either loss of a methyl free radical, or a methane molecule from the starting molecule. These results for the isolated deprotonated oxybenzone ion are consistent with the results of Li et al. (2016) who observed oxybenzone acting as a photosensitiser under alkaline conditions, since the free radical photoproducts we observe in the gas-phase system could initiate the observed photosensitiser behaviour in solution.

The potential energy surfaces on which neutral oxybenzone relaxes back to the ground state after UV absorption are well-characterised following advanced quantum-chemical calculations. Domcke and co-workers found that excited-state decay involves proton transfer from the enol to keto forms, followed by rapid internal conversion (Karsili et al., 2014). The expected geometric forms of protonated and deprotonated oxybenzone predict that the keto-enol site is the protonation/deprotonation location, so it is entirely unsurprising to find that the ultrafast decay mechanism is significantly perturbed in alkaline or acidic media. Indeed, this is the key finding from the series of deprotonated and protonated sunscreen molecules we have studied *via* LIMS, which include avobenzone, 2-phenylbenzimidazole-5-sulfonic acid, and benzophenone-4 (Wong et al., 2019a; Berenbeim et al., 2020b; Wong et al., 2021a). Protonation/deprotonation will impact on the ultrafast decay mechanisms if a geometric change occurs at a structural location involved in the pathway by which the excited state accesses the conical intersection. This occurs upon protonation of avobenzone (Berenbeim et al., 2020b), but not upon deprotonation of benzophenone-4 (Wong et al., 2021a), illustrating the importance of considering the pK_a/pK_b's of the sunscreen functional groups, alongside an assessment of these

TABLE 1 | Summary of Isolated (Gas-Phase) Sunscreen Molecules Studied in their Protonated or Deprotonated Forms.

Sunscreen	Protonated (P) Or Deprotonated (D)	Technique	Reference
Oxybenzone	P and D	LIMS[a]	Wong et al. (2019b)
Avobenzone	P	LIMS[a]	Berenbeim et al. (2020b)
2-phenylbenzimidazole-5-sulfonic acid	D	LIMS[a]	Wong et al. (2019a)
benzophenone-4	D	LIMS[a]	Wong et al. (2021a)
para-aminobenzoic acid (PABA)	P	LIMS[a]	Matthews and Dessent, 2017
trans-para-coumaric acid	D	LIMS[a]	Wong et al. (2021b)
trans-caffeic acid	D	LIMS[a]	Wong et al. (2021b)
trans-ferulic acid	D	LIMS[a]	Wong et al. (2021b)
para-coumaric acid	D	TRPES[b]	Bull et al. (2020)
para-coumaric acid	D	TRPES[b]	Henley et al. (2018)
para-coumaric acid	D	LP-IMMS[c]	Bull et al. (2019)

[a]*LIMS: Laser Interfaced Mass Spectrometry.*
[b]*TRPES: Time Resolved Photoelectron Spectroscopy.*
[c]*LP-IMMS: Laser Photodissociation Ion Mobility Mass Spectrometry.*

functional group's involvement in the ultrafast photodecay pathway.

Finally, we note that a growing number of deprotonated/protonated sunscreen molecules have recently been studied in the gas-phase. **Table 1** provides an overview of these recent studies, highlighting the sunscreens studied and the techniques used.

SODIUM CATION BINDING CAN DISRUPT SUNSCREEN ACTION

Alkali metal cations are common constituents of commercial sunscreen mixtures, where they are typically coupled to pH buffered anions. They are also commonly encountered in high concentrations in environments were sunscreens are used, such as swimming pools and the sea. Given that protonation can impact on the function of an organic sunscreen at the molecular level, it is clearly important to understand if cation binding could produce a similar effect. To investigate this, a series of experiments were performed on isolated complexes, M^+·OB, where alkali metal cations (M^+ = Na^+, K^+ and Rb^+) were bound to the sunscreen oxybenzone, OB (Berenbeim et al., 2020a).

The electronic spectrum of the Na^+·OB complex was found to be strikingly different from those of K^+·OB and Rb^+·OB, indicating that the Na^+ cation binds to OB with a different binding motif than K^+ and Rb^+. Infrared multiphoton dissociation (IRMPD) spectroscopy conducted at the FELIX free electron facility and computational calculations revealed that the cation-dependent UV spectra could be traced to the compact Na^+ ion breaking the intramolecular hydrogen bond in OB, and adopting the position normally taking by the hydrogen atom in the most stable form of OB. In contrast, K^+ and Rb^+ appear to prefer to bind above the aromatic rings, leaving the intramolecular hydrogen bond intact. This is an important result in terms of the UV filtering ability of OB, since the disruption of the intramolecular hydrogen bond that occurs upon Na^+ binding blocks the non-radiative relaxation mechanism that relies on excited state electron driven hydrogen atom transfer. A number of other common organic sunscreens (e.g., dioxybenzone and octyl salicylate) relay on similar intramolecular hydrogen bonding for non-radiative relaxation. The results found for the Na^+·OB complex suggest that close coordination to Na^+ may jeopardize the photostability of these molecules, both in sunscreen mixtures with significant sodium ion concentrations, but also in locations such as swimming pools and the sea.

In considering the potential impact of sodium ion cationization on sunscreen molecules, it is important to acknowledge that the organic sunscreen molecules are frequently present in an oil phase of the sunscreen formulation, which is suspended in an aqueous phase. As such, the sunscreens are in limited contact with metal cations which can be expected to be largely contained in the aqueous phase in the pure formulations. The extent to which phase mixing allows direct contact of cations and sunscreens will be dynamic, as well as location/climate dependent. Nonetheless, a possible enhanced degradation pathway is suggested by the results described above that merits future investigation.

To our knowledge, our study of the effect of alkali metal complexation on oxybenzone is the first to directly probe how cation binding can affect the photodynamics of a sunscreen molecule. However, our results were mirrored by other subsequent studies where metal cation binding has been reported to significantly perturb the excited-state behaviour of an aromatic molecule (Marlton et al., 2021; Robertson et al., 2021), indicating that cation coordination may have widespread photochemical importance.

HOW DOES CHANGING THE SOLVENT AFFECT SUNSCREEN PERFORMANCE?

Microsolvation studies of sunscreen chromophores have been conducted to determine how individual solvent molecules can affect the excited state dynamics, and hence the effectiveness of

the chromophores as sunscreen filters. Buma and co-workers investigated the effect of complexation of one water molecule on the UVB photodynamics of the cinnamate sunscreen, 2-ethylhexyl-(2*E*)-3-(4-methoxyphenyl)prop-2-enoate (EHMC) by probing the behaviour of a modified form of EHMC, methyl-4-methoxycinnamate (MMC) (Tan et al., 2014). In these experiments, they used resonance enhanced multiphoton ionization spectroscopy of an $MMCH_2O$ complex formed in a supersonic molecular beam to probe the photodynamics. For bare MMC, they found that absorption of UVB light was not immediately followed by rapid non-radiative decay, as would ideally be the case since photoexcitation resulted in internal conversion to an $n\pi^*$ state which impeded fast dissipation of the damaging UV light. However, upon H_2O complexation, the ordering of the key $n\pi^*$ and $\pi\pi^*$ states were reversed so that the bottleneck to ultrafast decay was removed. This led to the conclusion that the microenvironment was intrinsically promoting efficient ultrafast decay for this sunscreen. More recently, Buma and co-workers have used resonance enhanced multiphoton ionization to investigate an isolated complex of the UV filter methyl sinapate with a single water molecule (Fan et al., 2021), again observing how solvent complexation perturbs the electronic properties.

One of the considerable advantages of such gas-phase studies is that they allow direct comparison with high-level computational chemistry calculations. A number of computational studies were performed on cinnamates after the initial MMC study described above, supporting the conclusion that the individual water molecule led to energetic reversal of the crucial $n\pi^*$ and $\pi\pi^*$ states (Xie et al., 2016; Kinoshita et al., 2019).

A detailed insight into how individual water molecules affect sunscreen structure has been obtained using microwave spectroscopy (Domingos and Schnell, 2018). They assigned the global minimum geometry of oxybenzone and identified the two primary water-binding sites formed at either the enol or keto group, measuring their relative stability and internal dynamics. Intriguingly, the water-docking site influences the relative energies of the keto-enol structures that are directly involved in ultrafast energy dissipation. The results show that local structural changes in sunscreen molecules can lead to selective changes in electronic strcture.

Over the last decade, ultrafast transient absorption spectroscopy has been widely applied to probe the fundamental photodynamics of organic sunscreens in solutions. This work complements the gas-phase work described above since it provides insight into how bulk solvation impacts on the intrinsic sunscreen photophysics. A study of diethylamino hydroxybenzoyl in four different solvents (i.e., methanol, dimethyl sulfoxide, acetonitrile, and cyclohexane) by Orr-Ewing and co-workers provides a recent example (Kao et al., 2021). Work in this area has been previously reviewed by Stavros and co-workers (Rodrigues and Stavros, 2018; Holt et al., 2020) so we refer the reader to the reviews for further information.

SYNERGISTIC EFFECTS THROUGH AGGREGATION OF ORGANIC SUNSCREENS

A recent observation of increased performance of organic sunscreens in the presence of lignin molecules provides further insight into the importance of the local, molecular-level environment on sunscreen efficiency. In a series of experiments, Qian et al. (2016) investigated how the performance of the sunscreens avobenzone and octinoxate changed when they were mixed with organosolv lignin (a mixture of small lignin segments). They observed that the absorption of the mixed solutions increased dramatically, to the extent that the absorption of the mixed solutions was much greater than the sum of the individual component's absorption. In addition, there were concomitant shifts in the absorption profiles into the UVA region, which is highly notable given how challenging it has proven to identify effective UVA sunscreens. Qian et al. attributed these effects to J-aggregation (a form of π-π^* stacking where the angle between the centre of the chromophores is less than 54.7°) between the lignin and the chemical sunscreen molecule (Deng et al., 2011). J-aggregation is known to result in an excitation energy decrease for a π-π^* transition, thus producing a substantial redshift in the UV spectrum of the organic sunscreens. It would be important to further characterise the fundamental photophysics associated with these results through gas-phase measurements of complexes of lignin molecular units such as *p*-coumaryl, coniferyl or sinapyl alcohols with organic sunscreen molecules such as avobenzone or octinoxate. Measurements would be possible using either laser-interfaced mass spectrometry or resonance enhanced multiphoton ionization techniques, and could be conducted alongside infrared spectroscopy measurements to verify whether an intermolecular geometry associated with a J-aggregate geometry is present.

In the context of this discussion, recent work from Kohler and co-workers on the photophysics of eumelanin is notable (Grieco et al., 2020). Eumelanin is a biological pigment with sunscreen function and has represented a photophysical puzzle for decades due to uncertainty over the mechanism by which it delivers sunscreen action. Kohler and co-workers have been able to demonstrate that aggregation of chromophore units with diverse oxidation states is key to eumelanin's ability to dissipate UV radiation.

CONCLUSION

Experiments that probe the function of organic sunscreen molecules at the detailed, molecular level have already delivered a much-improved understanding of their safety and photostability. What is particularly striking about these experiments is the extent to which the local chemical environment that the sunscreen molecule interacts with has the ability to significantly perturb sunscreen action. This knowledge has the potential to drive the rational development of new, effective, safe sunscreens and their formulations (Karsili

et al., 2014), thus paving the way for a reduction in future melanoma cases. A recent study from Bardeen and co-workers is relevant in this context. They found that encapsulation of avobenzone into sodium dodecylsulfate micelles considerably enhances its photostability (Hanson et al., 2020). This was attributed to the micelle creating an enhanced polar microenvironment, which reduces the propensity of avobenzone to diketonize and hence photodegrade. Further work on the encapsulation of organic sunscreens into rationally designed gels or nanoparticles may well provide a pathway further between to and improved performance (Qiu et al., 2018; Song et al., 2021).

AUTHOR CONTRIBUTIONS

CEHD conceived the article. NGKW and CEHD wrote, revised, and reviewed the article. Both authors approved the submitted version.

FUNDING

This work was funded through the Leverhulme Trust Research Project Grant RPG-2017-147.

ACKNOWLEDGMENTS

We thank the University of York and the Department of Chemistry for provision of funds for the OPO laser system used in the studies described. We are also grateful for the computational support from the University of York High Performance Computing service, Viking, and the Research Computing team. We also acknowledge use of the York Centre of Excellence in Mass Spectrometry, which was created thanks to a major capital investment through Science City York, supported by Yorkshire Forward with funds from the Northern Way Initiative, and has more recently received additional support from the EPSRC and BBSRC.

REFERENCES

Acker, S., Hloucha, M., and Osterwalder, U. (2014). The Easy Way to Make a Sunscreen. *SOFW-Journal* 7, 24–30.

Baker, L. A., Horbury, M. D., Greenough, S. E., Coulter, P. M., Karsili, T. N. V., Roberts, G. M., et al. (2015). Probing the Ultrafast Energy Dissipation Mechanism of the Sunscreen Oxybenzone after UVA Irradiation. *J. Phys. Chem. Lett.* 6, 1363–1368. doi:10.1021/acs.jpclett.5b00417

Baker, L. A., Marchetti, B., Karsili, T. N. V., Stavros, V. G., and Ashfold, M. N. R. (2017). Photoprotection: Extending Lessons Learned from Studying Natural Sunscreens to the Design of Artificial Sunscreen Constituents. *Chem. Soc. Rev.* 46, 3770–3791. doi:10.1039/C7CS00102A

Berenbeim, J. A., Wong, N. G. K., Cockett, M. C. R., Berden, G., Oomens, J., Rijs, A. M., et al. (2020a). Sodium Cationization Can Disrupt the Intramolecular Hydrogen Bond that Mediates the Sunscreen Activity of Oxybenzone. *Phys. Chem. Chem. Phys.* 22, 19522–19531. doi:10.1039/D0CP03152F

Berenbeim, J. A., Wong, N. G. K., Cockett, M. C. R., Berden, G., Oomens, J., Rijs, A. M., et al. (2020b). Unravelling the Keto-Enol Tautomer Dependent Photochemistry and Degradation Pathways of the Protonated UVA Filter Avobenzone. *J. Phys. Chem. A.* 124, 2919–2930. doi:10.1021/acs.jpca.0c01295

Bull, J. N., Anstöter, C. S., and Verlet, J. R. R. (2020). Fingerprinting the Excited-State Dynamics in Methyl Ester and Methyl Ether Anions of Deprotonated Para-Coumaric Acid. *J. Phys. Chem. A.* 124, 2140–2151. doi:10.1021/acs.jpca.9b11993

Bull, J. N., Silva, G. d., Scholz, M. S., Carrascosa, E., and Bieske, E. J. (2019). Photoinitiated Intramolecular Proton Transfer in Deprotonated Para-Coumaric Acid. *J. Phys. Chem. A.* 123, 4419–4430. doi:10.1021/acs.jpca.9b02023

Chang, X.-P., Li, C.-X., Xie, B.-B., and Cui, G. (2015). Photoprotection Mechanism of P-Methoxy Methylcinnamate: A CASPT2 Study. *J. Phys. Chem. A.* 119, 11488–11497. doi:10.1021/acs.jpca.5b08434

De Laurentiis, E., Minella, M., Sarakha, M., Marrese, A., Minero, C., Mailhot, G., et al. (2013). Photochemical Processes Involving the UV Absorber Benzophenone-4 (2-Hydroxy-4-Methoxybenzophenone-5-Sulphonic Acid) in Aqueous Solution: Reaction Pathways and Implications for Surface Waters. *Water Res.* 47, 5943–5953. doi:10.1016/j.watres.2013.07.017

Dean, J. C., Kusaka, R., Walsh, P. S., Allais, F., and Zwier, T. S. (2014). Plant Sunscreens in the UV-B: Ultraviolet Spectroscopy of Jet-Cooled Sinapoyl Malate, Sinapic Acid, and Sinapate Ester Derivatives. *J. Am. Chem. Soc.* 136, 14780–14795. doi:10.1021/ja5059026

Deng, Y., Feng, X., Zhou, M., Qian, Y., Yu, H., and Qiu, X. (2011). Investigation of Aggregation and Assembly of Alkali Lignin Using Iodine as a Probe. *Biomacromolecules* 12, 1116–1125. doi:10.1021/bm101449b

Domingos, S. R., and Schnell, M. (2018). Wet Sunscreens in the Gas Phase: Structures of Isolated and Microsolvated Oxybenzone. *J. Phys. Chem. Lett.* 9, 4963–4968. doi:10.1021/acs.jpclett.8b02029

Fan, J., Roeterdink, W., and Buma, W. J. (2021). Excited-state Dynamics of Isolated and (Micro)solvated Methyl Sinapate: the Bright and Shady Sides of a Natural Sunscreen. *Mol. Phys.* 119, e1825850. doi:10.1080/00268976.2020.1825850

Fang, Y.-G., Li, C.-X., Chang, X.-P., Cui, G., García-Iriepa, C., Campos, P. J., et al. (2018). Photophysics of a UV-B Filter 4-Methylbenzylidene Camphor: Intersystem Crossing Plays an Important Role. *ChemPhysChem* 19, 744–752. doi:10.1002/cphc.201701230

Forestier, S. (2008). Rationale for Sunscreen Development. *J. Am. Acad. Dermatol.* 58, S133–S138. doi:10.1016/j.jaad.2007.05.047

Grieco, C., Kohl, F. R., Hanes, A. T., and Kohler, B. (2020). Probing the Heterogeneous Structure of Eumelanin Using Ultrafast Vibrational Fingerprinting. *Nat. Commun.* 11, 4569. doi:10.1038/s41467-020-18393-w

Hanson, K. M., Cutuli, M., Rivas, T., Antuna, M., Saoub, J., Tierce, N. T., et al. (2020). Effects of Solvent and Micellar Encapsulation on the Photostability of Avobenzone. *Photochem. Photobiol. Sci.* 19, 390–398. doi:10.1039/C9PP00483A

Henley, A., Patel, A. M., Parkes, M. A., Anderson, J. C., and Fielding, H. H. (2018). Role of Photoisomerization on the Photodetachment of the Photoactive Yellow Protein Chromophore. *J. Phys. Chem. A.* 122, 8222–8228. doi:10.1021/acs.jpca.8b07770

Holt, E. L., Krokidi, K. M., Turner, M. A. P., Mishra, P., Zwier, T. S., Rodrigues, N. d. N., et al. (2020). Insights into the Photoprotection Mechanism of the UV Filter Homosalate. *Phys. Chem. Chem. Phys.* 22, 15509–15519. doi:10.1039/D0CP02610G

Ignasiak, M. T., Houée-Levin, C., Kciuk, G., Marciniak, B., Pedzinski, T., Houée-Levin, C., et al. (2015). A Reevaluation of the Photolytic Properties of 2-Hydroxybenzophenone-Based UV Sunscreens: Are Chemical Sunscreens Inoffensive? *ChemPhysChem* 16, 628–633. doi:10.1002/cphc.201402703

Kao, M.-H., Venkatraman, R. K., Sneha, M., Wilton, M., and Orr-Ewing, A. J. (2021). Influence of the Solvent Environment on the Ultrafast Relaxation Pathways of a Sunscreen Molecule Diethylamino Hydroxybenzoyl Hexyl Benzoate. *J. Phys. Chem. A.* 125, 636–645. doi:10.1021/acs.jpca.0c10313

Karsili, T. N. V., Marchetti, B., Ashfold, M. N. R., and Domcke, W. (2014). Ab Initio Study of Potential Ultrafast Internal Conversion Routes in Oxybenzone, Caffeic Acid, and Ferulic Acid: Implications for Sunscreens. *J. Phys. Chem. A.* 118, 11999–12010. doi:10.1021/jp507282d

Kinoshita, S.-n., Harabuchi, Y., Inokuchi, Y., Maeda, S., Ehara, M., Yamazaki, K., et al. (2021). Substitution Effect on the Nonradiative Decay and Trans → Cis

Photoisomerization Route: a Guideline to Develop Efficient Cinnamate-Based Sunscreens. *Phys. Chem. Chem. Phys.* 23, 834–845. doi:10.1039/D0CP04402D

Kinoshita, S.-n., Inokuchi, Y., Onitsuka, Y., Kohguchi, H., Akai, N., Shiraogawa, T., et al. (2019). The Direct Observation of the Doorway 1nπ* State of Methylcinnamate and Hydrogen-Bonding Effects on the Photochemistry of Cinnamate-Based Sunscreens. *Phys. Chem. Chem. Phys.* 21, 19755–19763. doi:10.1039/C9CP02914A

Kulthanan, K., Nuchkull, P., and Varothai, S. (2013). The pH of Water from Various Sources: an Overview for Recommendation for Patients with Atopic Dermatitis. *Asia Pac. Allergy* 3, 155. doi:10.5415/apallergy.2013.3.3.155

Li, Y., Qiao, X., Zhou, C., Zhang, Y.-n., Fu, Z., and Chen, J. (2016). Photochemical Transformation of Sunscreen Agent Benzophenone-3 and its Metabolite in Surface Freshwater and Seawater. *Chemosphere* 153, 494–499. doi:10.1016/j.chemosphere.2016.03.080

Losantos, R., Funes-Ardoiz, I., Aguilera, J., Herrera-Ceballos, E., García-Iriepa, C., Campos, P. J., et al. (2017). Rational Design and Synthesis of Efficient Sunscreens to Boost the Solar Protection Factor. *Angew. Chem. Int. Ed.* 56, 2632–2635. doi:10.1002/anie.201611627

Marlton, S. J. P., McKinnon, B. I., Hill, N. S., Coote, M. L., and Trevitt, A. J. (2021). Electrostatically Tuning the Photodissociation of the Irgacure 2959 Photoinitiator in the Gas Phase by Cation Binding. *J. Am. Chem. Soc.* 143, 2331–2339. doi:10.1021/jacs.0c11978

Matthews, E., Cercola, R., and Dessent, C. (2018). Protomer-Dependent Electronic Spectroscopy and Photochemistry of the Model Flavin Chromophore Alloxazine. *Molecules* 23, 2036. doi:10.3390/molecules23082036

Matthews, E., and Dessent, C. E. H. (2017). Experiment and Theory Confirm that UV Laser Photodissociation Spectroscopy Can Distinguish Protomers Formed via Electrospray. *Phys. Chem. Chem. Phys.* 19, 17434–17440. doi:10.1039/c7cp02817b

Matthews, E., and Dessent, C. E. H. (2018). Observation of Near-Threshold Resonances in the Flavin Chromophore Anions Alloxazine and Lumichrome. *J. Phys. Chem. Lett.* 9, 6124–6130. doi:10.1021/acs.jpclett.8b02529

Matthews, E., Sen, A., Yoshikawa, N., Bergström, E., and Dessent, C. E. H. (2016). UV Laser Photoactivation of Hexachloroplatinate Bound to Individual Nucleobases In Vacuo as Molecular Level Probes of a Model Photopharmaceutical. *Phys. Chem. Chem. Phys.* 18, 15143–15152. doi:10.1039/c6cp01676f

Osterwalder, U., Sohn, M., and Herzog, B. (2014). Global State of Sunscreens. *Photodermatol. Photoimmunol. Photomed.* 30, 62–80. doi:10.1111/phpp.12112

Peperstraete, Y., Staniforth, M., Baker, L. A., Rodrigues, N. D. N., Cole-Filipiak, N. C., Quan, W.-D., et al. (2016). Bottom-up Excited State Dynamics of Two Cinnamate-Based Sunscreen Filter Molecules. *Phys. Chem. Chem. Phys.* 18, 28140–28149. doi:10.1039/C6CP05205C

Proksch, E. (2018). pH in Nature, Humans and Skin. *J. Dermatol.* 45, 1044–1052. doi:10.1111/1346-8138.14489

Qian, Y., Qiu, X., and Zhu, S. (2016). Sunscreen Performance of Lignin from Different Technical Resources and Their General Synergistic Effect with Synthetic Sunscreens. *ACS Sustain. Chem. Eng.* 4, 4029–4035. doi:10.1021/acssuschemeng.6b00934

Qiu, X., Li, Y., Qian, Y., Wang, J., and Zhu, S. (2018). Long-Acting and Safe Sunscreens with Ultrahigh Sun Protection Factor via Natural Lignin Encapsulation and Synergy. *ACS Appl. Bio Mater.* 1, 1276–1285. doi:10.1021/acsabm.8b00138

Robertson, P. A., Bishop, H. M., and Orr-Ewing, A. J. (2021). Tuning the Excited-State Dynamics of Acetophenone Using Metal Ions in Solution. *J. Phys. Chem. Lett.* 12, 5473–5478. doi:10.1021/acs.jpclett.1c01466

Rodrigues, N. D. N., and Stavros, V. G. (2018). From Fundamental Science to Product: A Bottom-Up Approach to Sunscreen Development. *Sci. Prog.* 101, 8–31. doi:10.3184/003685018X15166183479666

Serpone, N., Dondi, D., and Albini, A. (2007). Inorganic and Organic UV Filters: Their Role and Efficacy in Sunscreens and Suncare Products. *Inorg. Chim. Acta* 360, 794–802. doi:10.1016/j.ica.2005.12.057

Serpone, N. (2021). Sunscreens and Their Usefulness: Have We Made Any Progress in the Last Two Decades? *Photochem. Photobiol. Sci.* 20, 189–244. doi:10.1007/s43630-021-00013-1

Song, J., Chen, S., Zhao, X., Cheng, J., Ma, Y., Ren, S., et al. (2021). Simple, green, Ultrasound-Assisted Preparation of Novel Core-Shell Microcapsules from Octyl Methoxycinnamate and Oligomeric Proanthocyanidins for UV-Stable Sunscreen. *RSC Adv.* 11, 6374–6382. doi:10.1039/D0RA09116B

Tan, E. M. M., Hilbers, M., and Buma, W. J. (2014). Excited-State Dynamics of Isolated and Microsolvated Cinnamate-Based UV-B Sunscreens. *J. Phys. Chem. Lett.* 5, 2464–2468. doi:10.1021/jz501140b

Uleanya, K. O., Cercola, R., Nikolova, M., Matthews, E., Wong, N. G. K., and Dessent, C. E. H. (2020). Observation of Enhanced Dissociative Photochemistry in the Non-native Nucleobase 2-Thiouracil. *Molecules* 25, 3157. doi:10.3390/molecules25143157

Wong, N. G. K., Berenbeim, J. A., and Dessent, C. E. H. (2019a). Direct Observation of Photochemical Free Radical Production from the Sunscreen 2-Phenylbenzimidazole-5-Sulfonic Acid via Laser-Interfaced Mass Spectrometry. *ChemPhotoChem* 3, 1231–1237. doi:10.1002/cptc.201900149

Wong, N. G. K., Berenbeim, J. A., Hawkridge, M., Matthews, E., and Dessent, C. E. H. (2019b). Mapping the Intrinsic Absorption Properties and Photodegradation Pathways of the Protonated and Deprotonated Forms of the Sunscreen Oxybenzone. *Phys. Chem. Chem. Phys.* 21, 14311–14321. doi:10.1039/C8CP06794E

Wong, N. G. K., Rankine, C. D., and Dessent, C. E. H. (2021a). Linking Electronic Relaxation Dynamics and Ionic Photofragmentation Patterns for the Deprotonated UV Filter Benzophenone-4. *J. Phys. Chem. Lett.* 12, 2831–2836. doi:10.1021/acs.jpclett.1c00423

Wong, N. G. K., Rankine, C. D., and Dessent, C. E. H. (2021b). Measurement of the Population of Electrosprayed Deprotomers of Coumaric Acids Using UV-Vis Laser Photodissociation Spectroscopy. *J. Phys. Chem. A.* 125, 6703–6714. doi:10.1021/acs.jpca.1c04880

Xie, X.-Y., Li, C.-X., Fang, Q., and Cui, G. (2016). Mechanistic Photochemistry of Methyl-4-Hydroxycinnamate Chromophore and its One-Water Complexes: Insights from MS-CASPT2 Study. *J. Phys. Chem. A.* 120, 6014–6022. doi:10.1021/acs.jpca.6b05899

Conflict of Interest: The authors declare that the research was conducted in the absence of any commercial or financial relationships that could be construed as a potential conflict of interest.

Publisher's Note: All claims expressed in this article are solely those of the authors and do not necessarily represent those of their affiliated organizations, or those of the publisher, the editors and the reviewers. Any product that may be evaluated in this article, or claim that may be made by its manufacturer, is not guaranteed or endorsed by the publisher.

frontiers in Chemistry

ORIGINAL RESEARCH
published: 25 January 2022
doi: 10.3389/fchem.2021.815827

Silver(I)-Tazobactam Frameworks with Improved Antimicrobial Activity

Daniela R. Ferreira[1,2], *Paula C. Alves*[1,2], *Alexander M. Kirillov*[1], *Patrícia Rijo*[3,4] *and Vânia André*[1,2]*

[1]*Centro de Química Estrutural, Instituto Superior Técnico, Universidade de Lisboa, Lisboa, Portugal,* [2]*Associação do Instituto Superior Técnico para a Investigação e Desenvolvimento (IST-ID), Lisboa, Portugal,* [3]*Universidade Lusófona's Research Center for Biosciences and Health Technologies (CBIOS), Lisboa, Portugal,* [4]*Faculty of Pharmacy, Research Institute for Medicines (iMed. ULisboa), Universidade de Lisboa, Lisboa, Portugal*

Tazobactam (TazoH) is a penicillinate sulfone β-lactamase inhibitor with negligible antimicrobial activity, commonly used with other antibiotics to provide an effective combination against many susceptible organisms expressing β-lactamases. Two novel Ag(I)-tazobactam frameworks ([Ag(I)-Tazo] and [Ag(I)-$Tazo_2$]) prepared by mechanochemistry are presented herein as alternative forms to improve the antimicrobial activity of tazobactam by exploring synergistic effects with silver, being the first crystal structures reported of tazobactam coordinating to a metal site. The topological analysis of the 3D ([Ag(I)-Tazo]) and 2D+1D ([Ag(I)-$Tazo_2$]) frameworks revealed underlying nets with the **cbs** (CrB self-dual) and decorated **sql** topologies, respectively. These novel frameworks are stable and show an enhanced antimicrobial activity when compared to tazobactam alone. Amongst the tested microorganisms, *Pseudomonas aeruginosa* is the most sensitive to tazobactam and the new compounds. This study thus unveils novel facets of tazobactam chemistry and opens up its application as a multifunctional linker for the design of antibiotic coordination frameworks and related materials.

Keywords: mechanochemistry, supramolecular chemistry, tazobactam, silver, antibiotic coordination frameworks

OPEN ACCESS

Edited by:
Hicham Fennirii,
Northeastern University, United States

Reviewed by:
Jianqiang Liu,
Guangdong Medical University, China
Peter Cragg,
University of Brighton,
United Kingdom

***Correspondence:**
Vânia André
vaniandre@tecnico.ulisboa.pt

Specialty section:
This article was submitted to Supramolecular Chemistry, a section of the journal Frontiers in Chemistry

Received: *15 November 2021*
Accepted: *16 December 2021*
Published: *25 January 2022*

Citation:
Ferreira DR, Alves PC, Kirillov AM, Rijo P and André V (2022) Silver(I)-Tazobactam Frameworks with Improved Antimicrobial Activity. Front. Chem. 9:815827. doi: 10.3389/fchem.2021.815827

INTRODUCTION

The development of antibiotics was one of the most significant medical achievements in the treatment of microbial infections, and therefore has saved numerous lives. Nevertheless, the inappropriate use of antibiotics is one of the causes of the emerging antimicrobial resistance (AMR), which represents a major threat to modern society and makes most of the commercially available antimicrobial drugs ineffective (Tooke et al., 2019).

Amongst the different classes of antibiotics, β-lactams encompass several of the most used antimicrobial agents, such as penicillins, cephalosporins, carbapenems and monobactams. The first β-lactam antibiotic, penicillin G, was developed to treat bacterial infections. As these compounds affect the biosynthesis of the bacterial cell wall and demonstrated high efficiency, there has been an increase in the search, development and production of similar penicillin derivatives (Drawz and Bonomo 2010; Bozcal and Dagdeviren 2017; Tooke et al., 2019). In particular, the emergence of β-lactamase-mediated resistance can compromise β-lactam antibiotics efficiency. One of the strategies explored to circumvent this problem concerns the development of selective β-lactamase inhibitors for co-administration with β-lactam antibiotics (Drawz and Bonomo 2010; Docquier and Mangani 2018).

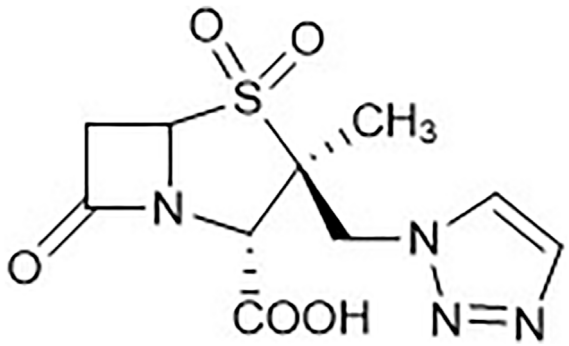

FIGURE 1 | Tazobactam (TazoH) representation.

Tazobactam (**Figure 1**) is an effective inhibitor of β-lactamase against several susceptible organisms expressing various classes of β-lactamases (Fisher et al., 1980; Drawz and Bonomo 2010). It is a penicillinate sulfone, with similarities to the structure of penicillin, however when used as a drug alone it has low antibacterial activity. This compound has been widely used in combination with β-lactam antibiotics in clinical use (Drawz and Bonomo 2010). One of the latest combination therapies with tazobactam relies on its combination with ceftolozane, an antipseudomonal cephalosporin.

Frequently, patients susceptible to Gram-negative bacilli, such as *Pseudomonas aeruginosa* and *Enterobacterales*, are diagnosed with bacterial pneumonia. The therapeutic combination ceftolozane/tazobactam is widely used in the treatment of multidrug-resistant (MDR) *P. aeruginosa* infections. This Gram-negative bacterium is an especially important nosocomial pathogen with intrinsic resistance to several classes of antimicrobial agents (Jacqueline et al., 2017; Sheffield et al., 2020; Karlowsky et al., 2021). Another possible therapy combines piperacillin and tazobactam (P/T) which is used in the treatment of *P. aeruginosa* and methicillin-resistant *Staphylococcus aureus* (MRSA) (Asai et al., 2021). This P/T combination is recommended for clinical use by the World Health Organization Model List of Essential Medicines [22nd List (2021)] as the first choice for severe intra-abdominal infections, high-risk febrile neutropenia, acquired pneumonia at the hospital and necrotizing fasciitis (World Health Organization 2021).

In order to face the microbial (multi) resistance to drugs/antibiotics, several approaches have been developed and tested to augment or improve the arsenal of tools to battle this health growing problem. One of the strategies that could lead to considerable results is the application of nanoporous materials due to their high specific surface area and correlations between the structure and surface characteristics. Metal-organic frameworks (MOFs) belong to this family of materials and represent one of the most current advances in coordination chemistry and supramolecular engineering (Tanaka 2020). MOFs are hybrid extended networks derived from inorganic units (as isolated cations, chains, clusters) and organic polydentate ligands, building a flexible family of crystalline compounds with an extraordinary variety of applications in chemical and material sciences (Rojas et al., 2019), including gas storage (Qasem et al., 2018), catalysis (Hong et al., 2021), luminescence (Huang et al., 2019; Liu et al., 2021a), electrochemistry (Wen et al., 2012; Wang et al., 2020), and separation (Kadioglu and Keskin 2018). MOFs with biomedical and pharmaceutical properties have been reported as carriers for the controlled delivery of different active species (Mileo et al., 2021), for cutaneous and cosmetic treatments (Duan et al., 2021), and as contrast agents for magnetic resonance imaging (Zhang et al., 2018; Hu et al., 2021), not disregarding the potential biomedical/pharmaceutical applications in cancer (Zhang et al., 2018; Li et al., 2020; Liu et al., 2021b; Liu et al., 2021c) and antimicrobial (André et al., 2021; Liu et al., 2021d) therapies.

MOFs based on bioactive components (BioMOFs) are an emerging subclass of MOFs, constructed from a variety of metals and ligands such as amino acids, peptides, nucleobases, saccharides, active pharmaceutical ingredients, and enzyme inhibitors (Rojas et al., 2017; An et al., 2019; Cai et al., 2019; Quaresma et al., 2020). Due to the low steric hindrance, low toxicity, and good biocompatibility of bioligands, BioMOFs are currently widely studied for possible applications in several areas including biomedicine (Sun et al., 2020) and biocatalysis (Celik et al., 2018). Within BioMOFs, the approach to use antibiotics for the direct coordination to biocompatible metal centers, giving rise to antibiotic coordination frameworks (ACFs), has been demonstrated to be a valid strategy to increase the efficiency of already commercially available antibiotics against some microorganisms (André et al., 2019; Quaresma et al., 2021).

Given a virtually unexplored coordination chemistry of tazobactam, the main goal of the present study consisted in probing its potential for the generation of new ACFs. Hence, two novel Ag(I)-tazobactam frameworks, [Ag(I)-Tazo] and [Ag(I)-Tazo$_2$], were synthesized by mechanochemistry, a "green" synthetic route that has already shown its potential for such type of synthesis (Friščic et al., 2020; Zábranský et al., 2021). To the best of our knowledge, the obtained compounds are the first crystal structures reporting the coordination of tazobactam to metal sites. The choice of silver as a cation in these studies lies in its well-recognized antibacterial action (Alexander 2009), allowing use to be made of potential synergistic effects between both ACFs components. The ultimate goal of this study was to improve the antimicrobial activity of tazobactam from the synergy with silver, since this drug is frequently used in the treatment of bacterial infections. Hence, the synthesis, full characterization, structural features, and antimicrobial activity of the obtained ACFs, [Ag(I)-Tazo] and [Ag(I)-Tazo$_2$], are described in the present work.

RESULTS AND DISCUSSION

Two new Ag(I)-tazobactam coordination frameworks $[Ag_2(\mu_3\text{-Tazo})(\mu_4\text{-Tazo})]_n$ (abbreviated as [Ag(I)-Tazo]) and $\{[Ag(\mu\text{-Tazo})(\mu\text{-TazoH})][Ag(\mu\text{-Tazo})(TazoH)]\}_n$ (abbreviated as [Ag(I)-Tazo$_2$]) were synthesized from tazobactam (TazoH) and silver(I) oxide, using 1:1 and 1:2 Ag:tazobactam ratios.

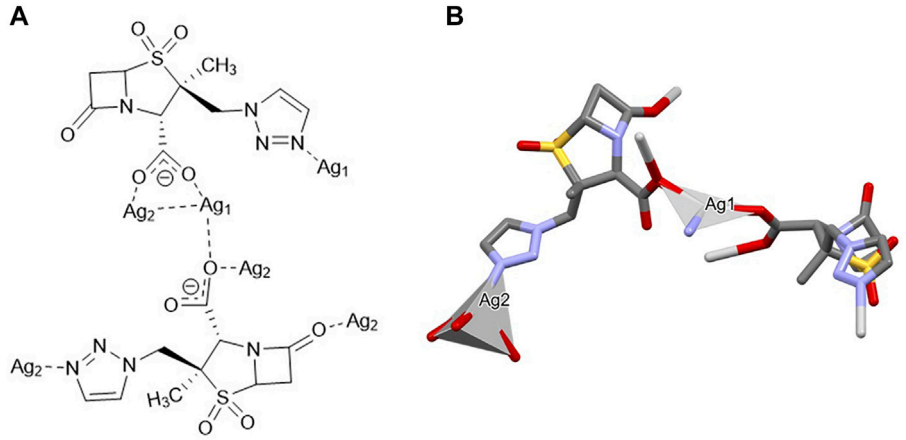

FIGURE 2 | Schematic representation of **(A)** the coordination sites and **(B)** the coordination geometry around the Ag(I) sites (hydrogen atoms have been omitted for clarity reasons) for [Ag(I)-Tazo].

Despite the successful synthesis of both compounds by different methods, liquid-assisted grinding (LAG) performed in a vibrational ball mill was the preferred procedure, due to the low amount of solvent required (η = 0.5 μL/mg) (Do and Friščić 2017), a reduced reaction time, and an ease of the process without compromising high purity and yield.

Powder X-ray Diffraction (PXRD) analysis confirmed the purity of product samples obtained via the slurry reaction, manual grinding, and ball milling methods by comparing the diffractograms with those simulated from the single crystal data of [Ag(I)-Tazo] and [Ag(I)-$Tazo_2$] (**Supplementary Figures S1, S2**). The purity of both compounds was also confirmed by elemental analysis: [Ag(I)-Tazo]: C, 29.5% calc/29.73% found; H, 2.72% calc/found 2.35%; N, 13.76% calc/13.69% found; S, 7.87% calc/8.08% found; [Ag(I)-$Tazo_2$]: C, 34% calc/34.39% found; H, 3.14% calc/2.98% found; N, 15.86% calc/15.82% found; S, 9.08% calc/9.16% found.

The structural elucidation, and the physicochemical characterization are presented and discussed for both compounds, [Ag(I)-Tazo] and [Ag(I)-$Tazo_2$]. Antimicrobial assays were also carried out to prove the enhanced antimicrobial activity of both compounds unveiled herein.

Structural Characterization

$[Ag_2(\mu_3\text{-}Tazo)(\mu_4\text{-}Tazo)]_n$ {[Ag(I)-Tazo]}. Despite the 1:1 ratio, the asymmetric unit of [Ag(I)-Tazo] is formed by two crystallographically independent deprotonated tazobactam moieties (μ_3-and μ_4-$Tazo^-$) and two Ag(I) sites, Ag1 and Ag2. The μ_3-$Tazo^-$ ligand coordinates to two Ag1 sites via the carboxylate [2.229 (5) Å] and the triazole [2.281 (5) Å] functionalities, and to one Ag2 via the other O of the carboxylate group [2.297 (5) Å]. The μ_4-$Tazo^-$ coordinates to Ag1 via the carboxylate group [2.263 (5) Å] and to three different Ag2 via the other O of the carboxylate [2.607 (5) Å], the carbonyl [2.627 (5) Å] and the triazole [2.276 (5) Å] moieties. The Ag sites assume distorted trigonal planar [Ag1, NC = 3, Ag1 deviation from the plane of 0.196 (4) Å] and tetrahedral (Ag2, NC = 4) coordination geometries (**Figure 2**).

The presence of different coordination sites gives rise to an extended 3D non-porous metal-organic framework (**Figure 3**), with the consecutive alternation of Ag1 and Ag2 metal sites via the μ_3-and μ_4-$Tazo^-$ linkers. Even though no classical hydrogen bonds are present in the supramolecular arrangement of [Ag(I)-Tazo], two S-O···π [2.780 (6) Å, 60.2 (2) º and 3.545 (6) Å, 83.9 (2) º] and five π···π interactions [3.681(4)—4.813(5) Å] are responsible for the interactions within the framework (**Supplementary Table S2**), resulting in a high packing efficiency (74.2%).

From the topological analysis, it is possible to conclude that the 3D metal-organic net is built from the 3 and 4-connected Ag1/Ag2 nodes, and the 3 and 4-connected μ_3-and μ_4-$Tazo^-$ nodes (**Figure 4**). The resulting underlying network can be classified as a dinodal 3,4-linked net with a **cbs** (CrB self-dual) topology and a point symbol of (6^3) (6^6).

$\{[Ag(\mu\text{-}Tazo)(\mu\text{-}TazoH)][Ag(\mu\text{-}Tazo)(TazoH)]\}_n$ {[Ag(I)-$Tazo_2$]}. The asymmetric unit of [Ag(I)-$Tazo_2$] is formed by two crystallographically independent tazobactam molecules (TazoH), two deprotonated tazobactam anions (μ-$Tazo^-$) and two Ag(I) centers, fulfilling a 1:2 stoichiometry. Both Ag1 and Ag2 centers are bound by two triazole moieties [2.208 (8) and 2.209 (8) Å for Ag1, 2.168 (9) and 2.176 (9) Å for Ag2]. Ag1 is further coordinated by two carboxylate groups from μ-$Tazo^-$/μ-TazoH [2.435 (7) and 2.441 (7) Å]. The Ag2 is only coordinated by the carboxylate group one μ-$Tazo^-$ linker (2.504 (8) Å). Despite the different coordination patterns in [Ag(I)-$Tazo_2$], the Ag sites also adopt distorted trigonal planar (Ag1, NC = 3) and tetrahedral (Ag2, NC = 4) coordination geometries (**Figure 5**).

The structure of [Ag(I)-$Tazo_2$] reveals two independent 2D and 1D coordination networks (**Figure 6**). The 2D net is formed by the crystallographically independent μ-$Tazo^-$ and μ-TazoH moieties that act as linkers for Ag1 centers. The 1D chain is based on Ag2 centers and comprises the terminal TazoH ligands and

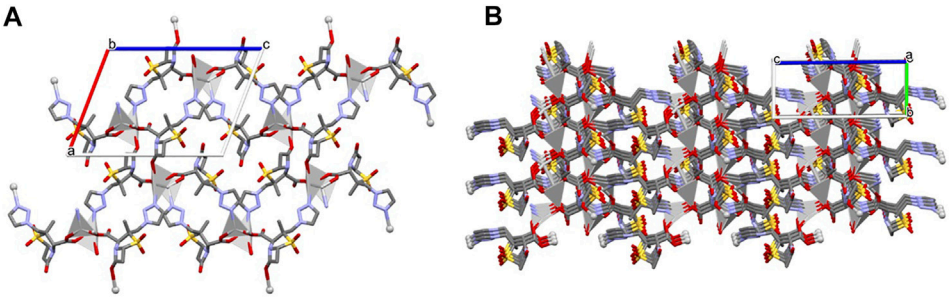

FIGURE 3 | Crystal packing of [Ag(I)-Tazo], depicting **(A)** the view along the *b* axis, and **(B)** the formation of the 3D metal-organic framework.

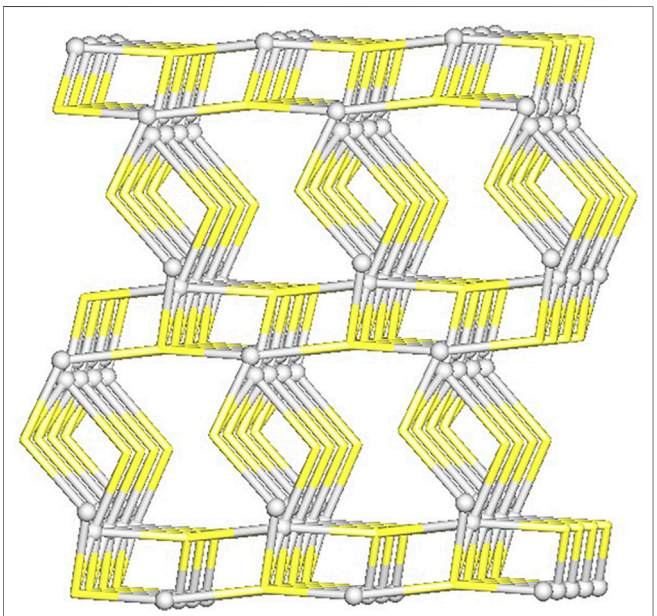

FIGURE 4 | Topological representation of a dinodal 3,4-linked net in [Ag(I)-Tazo] with a **cbs** (CrB self-dual) topology; rotated view along the *b* axis; Ag1/Ag2 centers (gray balls), centroids of μ_3-and μ_4-Tazo$^-$ moieties (yellow).

μ-Tazo$^-$ linkers. An overall structure of [Ag(I)-Tazo$_2$] can be defined as a 2D+1D coordination polymer wherein 1D chains (based on Ag2 atoms) are interdigitated into 2D layers (based on Ag1 atoms) (**Figure 6**). Each of these motifs is reinforced by hydrogen bonds between COOH/COO$^-$ groups of tazobactam ligands [O–H···O 2.421 (11) and 2.469 (12) Å] (**Table 1**); however, there are no classical hydrogen bonds between the 1D and 2D networks. Several weaker interactions are also established (**Supplementary Table S2**). This structure has a packing efficiency of 69.6%. From a topological perspective, the resulting underlying network can be classified as a 4-linked **sql** [Shubnikov tetragonal plane net] layer decorated with the chains of 2C1 topology (**Figure 7** and **Supplementary Figure S3**). The **sql** layer is composed of the 4-connected Ag1 centers and μ-Tazo$^-$ linkers, leading to a $(4^4.6^2)$ point symbol.

The study of the packing interactions is complemented by the analysis of the Hirshfeld surfaces and the corresponding two-dimensional fingerprint plots (**Figure 8**). The O-H interactions are the most abundant in both compounds, but the presence of hydrogen bonds in [Ag(I)-Tazo$_2$] is responsible for a higher percentage of this type of interactions in [Ag(I)-Tazo$_2$] than in [Ag(I)-Tazo] (44.3 *vs* 36.5%, respectively). The two spikes in the 2D fingerprint plots corresponding to the O-H interactions are sharper in [Ag(I)-Tazo$_2$], due to the presence of hydrogen bonds and shorter distances. The O-H interactions can be identified as red regions in the d_{norm} representation, supporting the interactions previously described. The H-H interactions appear in the middle-scattered points in the 2D fingerprint map and are the second most relevant type of interactions {23 and 28.1% for [Ag(I)-Tazo] and [Ag(I)-Tazo$_2$], respectively}. The N-H interactions are also significant, representing 10.8 and 5.5% of the total Hirshfeld surface for [Ag(I)-Tazo] and [Ag(I)-Tazo$_2$], respectively, as well as Ag-O {8.6 and 5.2% for [Ag(I)-Tazo] and [Ag(I)-Tazo$_2$], respectively}. Apart from these, π···π (C–C) contacts are observed in [Ag(I)-Tazo] corresponding to 1.7%, but they are not present in [Ag(I)-Tazo$_2$], with lone-pair···π (O–C) interactions being also higher in [Ag(I)-Tazo] than in [Ag(I)-Tazo$_2$] (1.8 *vs* 1%). On the other hand, the lone-pair···lone-pair (O–O) interactions are higher in [Ag(I)-Tazo$_2$], corresponding respectively to 5.6% *vs* 3% in [Ag(I)-Tazo]. All the other interactions are present in minor percentages (see supplementary material for full details, **Supplementary Figures S4–S6**).

FTIR-ATR analysis of tazobactam, [Ag(I)-Tazo] and [Ag(I)-Tazo$_2$] (**Supplementary Figure S7** and **Supplementary Table S3**) makes evident that the stretching vibrations of the C-SO$_2$-C and N=N groups are visible in TazoH (C-SO$_2$-C:1140, 1190, 1313 cm^{-1}; N=N: 1238, 1455 cm^{-1}) as well as in both compounds [Ag(I)-Tazo] (C-SO$_2$-C: 1139, 1206, 1311 cm^{-1}; N=N: 1233, 1446 cm^{-1}) and [Ag(I)-Tazo$_2$] (C-SO$_2$-C: 1142, 1188, 1321 cm^{-1}; N=N: 1241, 1455 cm^{-1}) without significant changes. Differences in the bands associated with the carboxylic moiety of tazobactam can be detected. The peaks concerning the carbonyl group from the amide are found at 1795, 1791 and 1773 cm^{-1} for TazoH, [Ag(I)-Tazo] and [Ag(I)-Tazo$_2$], respectively. The main differences in the three spectra correspond to the peaks at around 1610 and 1380 cm^{-1}, characteristic of carboxylate moieties present in both structures. The carbonyl group stretching from the carboxylic acid moiety

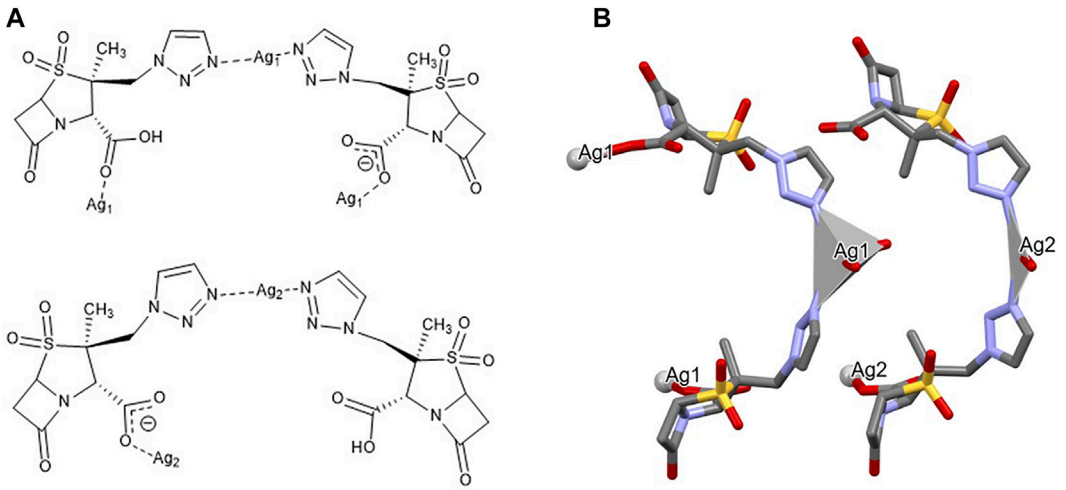

FIGURE 5 | Schematic representation of **(A)** the coordination sites and **(B)** the coordination geometry around the Ag(I) sites (hydrogen atoms have been omitted for clarity reasons) for [Ag(I)-Tazo$_2$].

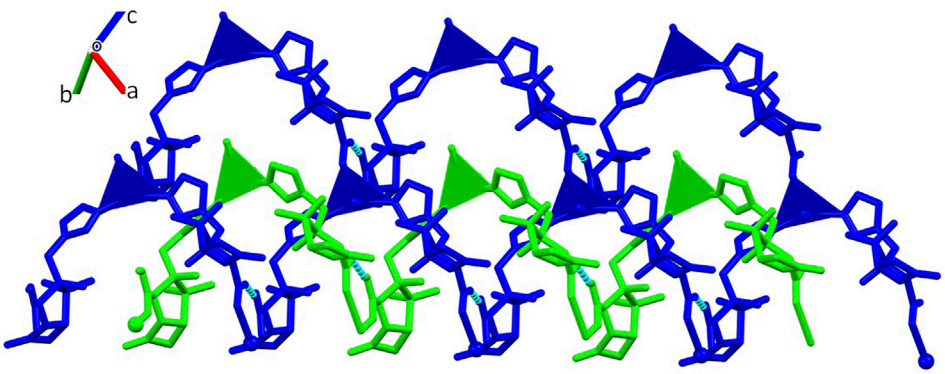

FIGURE 6 | Crystal packing of [Ag(I)-Tazo$_2$] depicting the 2D (blue) and 1D (green) coordination networks.

TABLE 1 | List of the main hydrogen bonds found for compound [Ag(I)-Tazo$_2$].

Sym. Op	D–H···A	*d* (D–H) (Å)	*d* (H···A) (Å)	*d* (D···A) (Å)	(DHA) (deg)
-1+x, y, -1+z	O_7–H_{70}···O_1	0.82	1.71	2.421 (11)	143
-1+x, y, -1+z	O_{17}–H_{170}···O_{11}	0.82	1.73	2.469 (12)	148

detected at 1702 cm^{-1} in TazoH, is not seen in [Ag(I)-Tazo] due to the fully deprotonated Tazo$^-$ linkers, with the characteristic peaks of the carboxylate being detected at 1373 and 1599 cm^{-1}. In [Ag(I)-Tazo$_2$], the protonated tazobactam gives rise to the peak at 1702 cm^{-1}, while the deprotonated Tazo$^-$ moiety is identified by the peaks at 1384 and 1610 cm^{-1}.

Stability of the Compounds

The stability of the compounds is a very important factor to be controlled, especially for medical/pharmaceutical applications. Considering the PXRD diffractograms of the obtained compounds monitored along time, it can be concluded that no degradation of these silver-organic frameworks under shelf storage conditions is detected, as the patterns remain unchanged for at least 5 months (**Supplementary Figures S8–S13**).

Regarding thermal stability, DSC/TGA data are very similar for both [Ag(I)-Tazo] and [Ag(I)-Tazo$_2$] (**Figure 9** and **Supplementary Figure S14**), showing their stability until 155°C, temperature at which melting, and decomposition

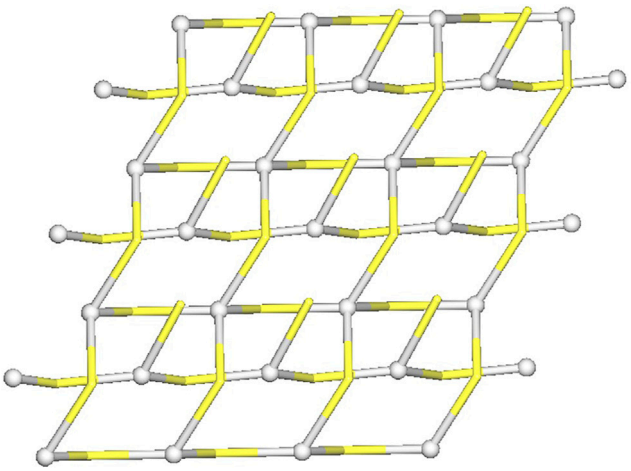

FIGURE 7 | Topological representation of a mononodal 4-linked metal-organic layer in [Ag(I)-Tazo$_2$] with a **sql** topology, decorated with 2C1 chains; rotated view along the *b* axis; Ag1/Ag2 centers (gray balls), centroids of TazoH/Tazo$^-$ moieties (yellow).

begin. These observations are confirmed by hot-stage microscopy (HSM) data.

Antimicrobial Activity Assays

A microbial screening for the assessment of the antimicrobial activity of the new Ag(I)-tazobactam frameworks was carried out by the determination of their minimum inhibitory concentration (MIC) median values via the microdilution method (Clinical and Laboratory Standards Institute 2018; Alves et al., 2020).

The results obtained (**Table 2** and **Figure 10**) show that, in comparison with free tazobactam, both [Ag(I)-Tazo] and [Ag(I)-Tazo$_2$] are more active against Gram-negative (*E. coli* and *P. aeruginosa*) and Gram-positive (*S. aureus MRSA*, *S. aureus*, *E. faecalis*, *M. smegmatis*) bacteria, with [Ag(I)-Tazo] being also more active against the *C. albicans* and *S. cerevisiae* yeasts, benefiting a possible synergistic effect between Ag(I) and tazobactam components (Alexander 2009; Lu et al., 2014).

Among the two Ag(I)-tazobactam frameworks, [Ag(I)-Tazo] is generally more active, with MIC values lower than [Ag(I)-Tazo$_2$], except for *P. aeruginosa* and *S. aureus*, for which that both new compounds present the same MIC value.

From the list of microorganisms tested in this study, the yeasts were the least sensitive to tazobactam and its frameworks, with [Ag(I)-Tazo] being slightly more active.

Regarding the MIC values for the tested bacteria, generally, tazobactam and its silver derivatives are more efficient against Gram-negative bacteria. In fact, *P. aeruginosa* shown to be the most sensitive to tazobactam, [Ag(I)-Tazo] and [Ag(I)-Tazo$_2$]. As previously reported, *P. aeruginosa* isolates were considered highly susceptible to the ceftolozane/tazobactam β-lactam–β-lactamase inhibitor combination, displaying MIC values lower than 4 μg/ml (Karlowsky et al., 2021). Both novel Ag(I) compounds unveiled herein also display very low MIC value (0.98 μg/ml) against this bacterium, showing a promising activity. The MIC values obtained for the new complexes are lower than not also tazobactam, but also lower that silver oxide itself.

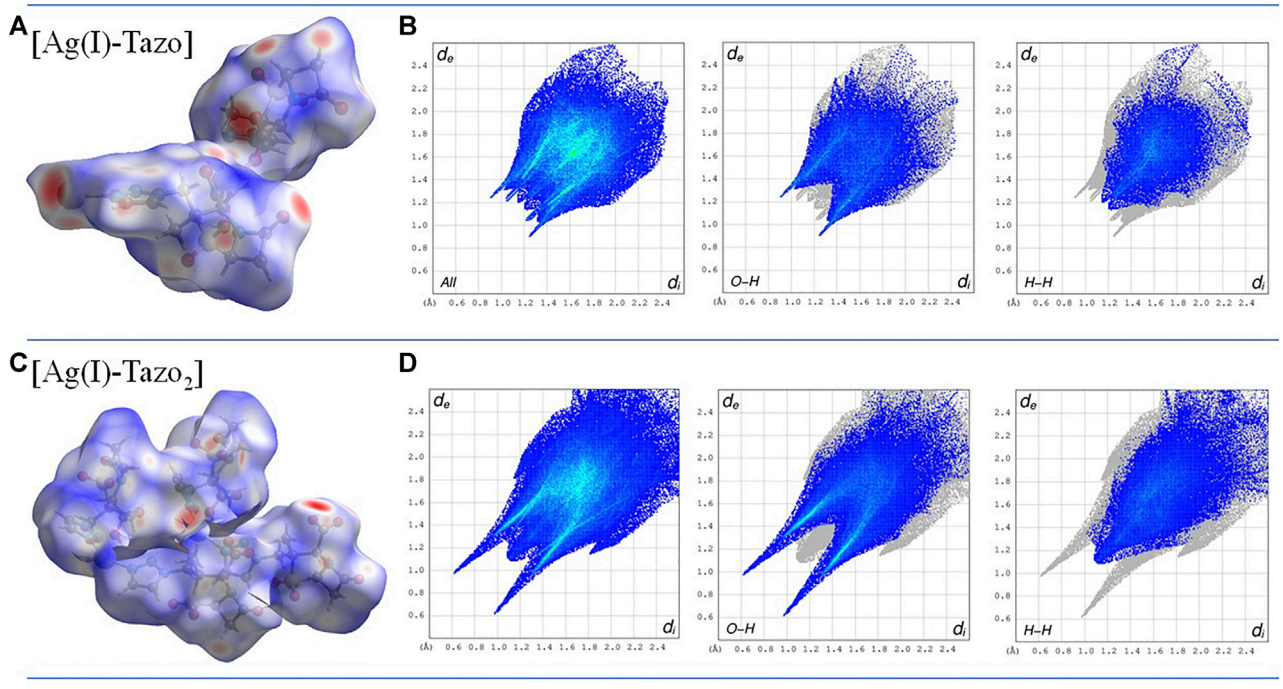

FIGURE 8 | Hirshfeld surface mapped with d_{norm}, with surfaces shown as transparent to allow the visualization of the compound **(A)** and two-dimensional fingerprint plots **(B)** for the most relevant interactions in [Ag(I)-Tazo] **(C)** and [Ag(I)-Tazo$_2$] **(D)**.

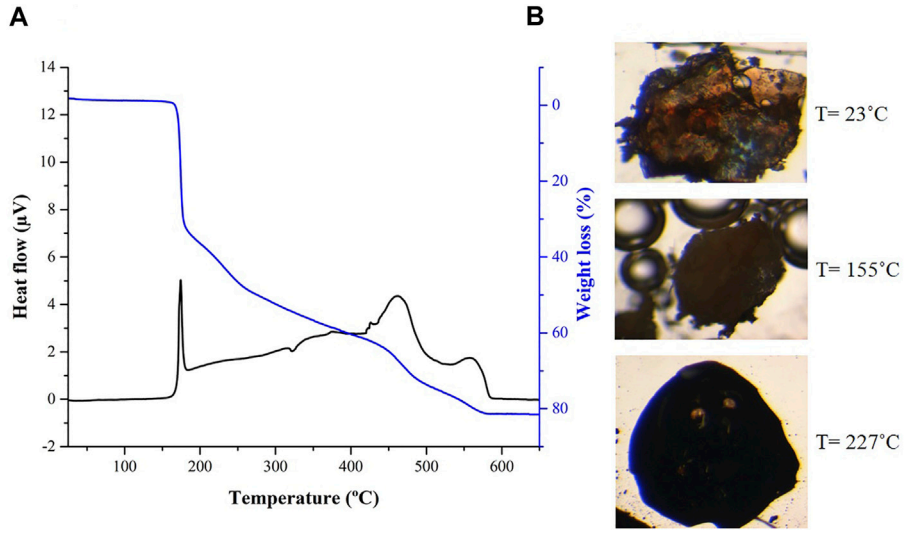

FIGURE 9 | (A) Differential scanning calorimetry (DSC) and thermogravimetry (TGA) and **(B)** hot-stage microscopy (HSM) images at 23, 155 and 227°C for compound [Ag(I)-$Tazo_2$].

TABLE 2 | Determination of the minimum inhibitory concentration values (MIC, μg/mL) of the synthesized compounds, and the starting materials for *Candida albicans* and *Saccharomyces cerevisiae* (yeasts), *Escherichia coli* and *Pseudomonas aeruginosa* (Gram-negative bacteria) and *Staphylococcus aureus*, *Enterococcus faecalis* and *Mycobacterium smegmatis* (Gram-positive bacteria) after 24 h for bacteria and 48 h for yeasts.

Microorganisms		Ag_2O	Tazobactam	[Ag(I)-Tazo]	[Ag(I)-$Tazo_2$]	Positive control	Negative control
Yeasts	*C. albicans*	6.88	62.50	31.25	62.50	3.91 (Nys)	125.00
	S. cerevisiae	6.88	>62.50	31.25	>62.50	3.91 (Nys)	62.50
Gram-negative bacteria	*E. coli*	1.72	31.25	7.81	11.72	<0.49 (Nor)	62.50
	P. aeruginosa	1.66	15.63	0.98	0.98	<0.49 (Nor)	62.50
Gram-positive bacteria	*S. aureus MRSA*	6.88	62.50	7.81	31.25	0.98 (Van)	125.00
	S. aureus	13.75	31.25	15.63	15.63	3.91 (Van)	125.00
	E. faecalis	5.16	>125.00	15.63	31.25	<0.49 (Van)	125.00
	M. smegmatis	11.78	46.88	15.63	19.53	<0.49 (Van)	125.00

Legend: Positive controls: Nys—nystatin; Nor—norfloxacin; Van—vancomycin. Negative control: DMSO.
Note: The antimicrobial effect activity of tazobactam is limited by the effect of DMSO, for S. cerevisiae *and* E. faecalis.

Interesting results were obtained from the assay with two different strains of *S. aureus* (MRSA CIP 106760 and ATCC 25923). Both [Ag(I)-Tazo] and [Ag(I)-$Tazo_2$] display higher activity than tazobactam against both strains, with an important note for the fact that [Ag(I)-Tazo] is even more active against the methicillin-resistant *S. aureus* (MRSA) strain than the *S. aureus* (ATCC).

It is worth noting that bacterial infections caused by both *P. aeruginosa* and *S. aureus* are commonly treated using β-lactams (Foster 2017; Gherardi et al., 2019). Meanwhile, the emergence of resistant strains to the usual therapy motivated the search for new ways to deal with these very important infections.

The obtained results highlight the importance of the synergy between tazobactam and silver metal centers that possess a well-recognized antimicrobial efficiency (Alexander 2009; Lu et al., 2014). Moreover, these striking, and very promising findings provide a sustainable and fast strategy to reuse the available antibiotics and obtain new and powerful ACFs to battle bacteria like *P. aeruginosa* and *S. aureus*, which are responsible for several nosocomial infections and highly capable to develop resistance mechanisms to the existing antibiotics (Foster 2017; Pang et al., 2019).

MATERIALS AND METHODS

Reagents

The following reagents and solvents were purchased from commercial sources and used without further purification: tazobactam ($C_{10}H_{12}N_4O_5S$, Carbosynth Ltd.); silver(I) oxide (Ag_2O, 99%, Alfa Aesar) and dimethyl sulfoxide (DMSO, 99%, Fluka).

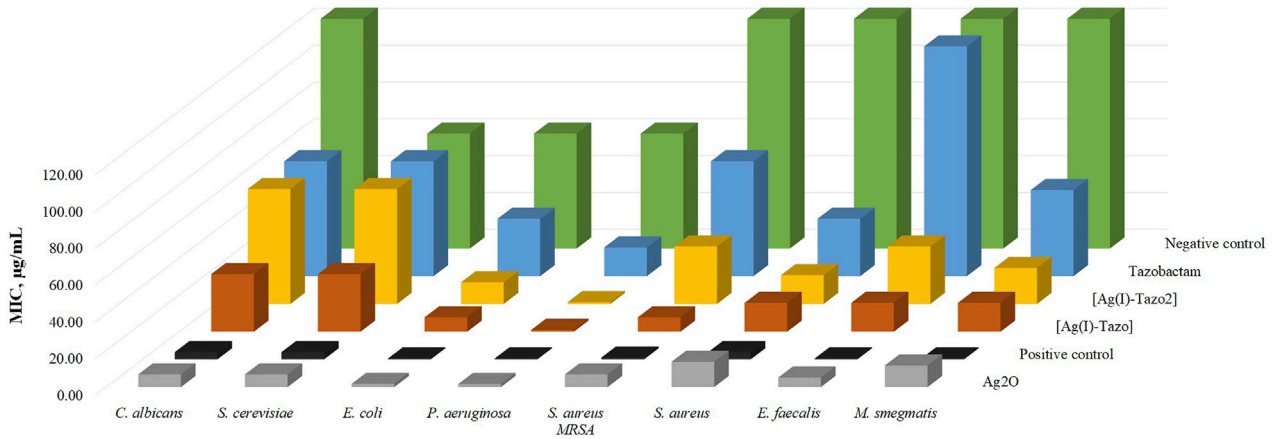

FIGURE 10 | Minimum inhibitory concentration values (MIC, μg/ml) of the synthesized compounds {[Ag(I)-Tazo] and [Ag(I)-$Tazo_2$]} and the starting materials for *Candida albicans* and *Saccharomyces cerevisiae* (yeasts), *Escherichia coli* and *Pseudomonas aeruginosa* (Gram-negative bacteria) and *Staphylococcus aureus*, *Enterococcus faecalis* and *Mycobacterium smegmatis* (Gram-positive bacteria) after 24 h for bacteria and 48 h for yeasts. DMSO was used as negative control and nystatin, norfloxacin and vancomycin were used as positive controls for yeasts, Gram-negative and Gram-positive bacteria, respectively.

TABLE 3 | Experimental conditions for the synthesis of compounds [Ag(I)-Tazo] and [Ag(I)-$Tazo_2$].

Compound	Method	Tazobactam	Ag_2O	Tazobactam:Ag ratio	Time	Solvent (H_2O)	η (μL/mg)
[Ag(I)-Tazo]	Ball milling	144.7 mg 0.4806 mmol	55.8 mg 0.2403 mmol	1:1	5 min	100	0.499
	Manual grinding	72.3 mg 0.2403 mmol	27.8 mg 0.1201 mmol		15 min	100	1.00
	Suspension	72.2 mg 0.2403 mmol	28.0 mg 0.1201 mmol		48 h	2000	20.0
[Ag(I)-$Tazo_2$]	Ball milling	167.7 mg 0.5583 mmol	32.4 mg 0.1396 mmol	2:1	5 min	100	0.500
	Manual grinding	83.9 mg 0.2792 mmol	16.3 mg 0.0698 mmol		10 min	100	1.00
	Suspension	83.8 mg 0.2792 mmol	16.2 mg 0.0698 mmol		48 h	2000	20.0

Synthesis

The new compounds $[Ag_2(\mu_3\text{-Tazo})(\mu_4\text{-Tazo})]_n$ (abbreviated as [Ag(I)-Tazo]) and $\{[Ag(\mu\text{-Tazo})(\mu\text{-TazoH})][Ag(\mu\text{-Tazo})(TazoH)]\}_n$ (abbreviated as [Ag(I)-$Tazo_2$]) were synthesized by reacting tazobactam (TazoH) and Ag_2O in two different stoichiometries and using the liquid-assisted grinding (LAG) mechanochemical method in the presence of catalytic amounts of water for different periods of time (**Table 3**). The ball milling reactions were carried out in a Retsch MM400 ball mill at a frequency of 20 Hz, in 15 ml stainless steel snap closure jars containing two 7 mm stainless steel balls (approximately 2.7340 g). Both compounds could also be obtained by manual grinding and suspension methods, however more reaction time is needed as indicated in **Table 3**. The resulting powder was then dissolved in water, and colorless single crystals of [Ag(I)-Tazo] were grown by slow evaporation of the solvent after 3 weeks at room temperature. With respect to form [Ag(I)-$Tazo_2$], the resulting powder was also dissolved in water and orange single crystals were grown by slow evaporation of solvent after 3 weeks at room temperature.

Powder X-Ray Diffraction

Powder X-ray Diffraction data were collected in a D8 Advance Bruker AXS θ-2θ diffractometer (Bruker, Karlsruhe, Germany), equipped with a LYNXEYE-XE detector, copper radiation source (Cu Kα, λ = 1.5406 Å), operated at 40 kV and 30 mA, with the following data collection parameters: 3–60° 2θ range, step size of 0.02° and 1.5 s per step. The diffractograms were used to analyze the purity of compounds [Ag(I)-Tazo] and [Ag(I)-$Tazo_2$] by comparing the experimental PXRD data with the patterns simulated from SCXRD data, using MERCURY 2021.2.0 (Macrae et al., 2008).

Single Crystal X-Ray Diffraction

Crystals suitable for single X-ray diffraction studies were mounted on a loop with Fomblin© protective oil. Data for [Ag(I)-Tazo] and [Ag(I)-$Tazo_2$] was collected on a Bruker

TABLE 4 | Crystallographic data for compounds [Ag(I)-Tazo] and [Ag(I)-$Tazo_2$].

	[Ag(I)-Tazo]	[Ag(I)-$Tazo_2$]
Chemical formula	$C_{20}H_{22}Ag_2N_8O_{10}S_2$	$C_{20}H_{23}AgN_8O_{10}S_2$
Formula weight	808.00	707.45
Crystal form, colour	Needle, colourless	Plate, colourless
Crystal size (mm)	0.20 × 0.04 × 0.04	0.16 × 0.10 × 0.05
Crystal system	Monoclinic	Monoclinic
Space group	$P2_1$	$P2_1$
a (Å)	12.4747 (13)	10.404 (3)
b (Å)	6.4407 (7)	25.480 (8)
c (Å)	16.9538 (16)	10.538 (3)
β (°)	110.961 (5)	109.793 (9)
V (Å^3)	1272.0 (2)	2,628.5 (13)
Z	2	4
d (mg.cm^{-3})	2.126	1.788
μ (mm^{-1})	1.778	0.997
θ range (°)	3.266–26.493	2.080–28.833
Reflections collected/unique	10,530/4,978	24,760/12,766
R_{int}	0.0487	0.0912
GoF	1.028	1.004
Final R indices[a,b] [$I > 2\sigma(I)$]	R_1 = 0.0380, wR_2 = 0.0828	R_1 = 0.0663, wR_2 = 0.0873

[a] $R_1 = \Sigma||F_o|-|F_c||/\Sigma|F_o|$.
[b] $wR_2 = \{\Sigma[w\ (F_o^2-F_c^2)^2]/\Sigma[w\ (F_o^2)^2]\}^{1/2}$.

D8Quest diffractometer, with graphite-monochromated radiation (Mo Kα, λ = 0.71073 Å) at 293 K. X-ray generator was operated at 50 kV and 30 mA and APEX3 (Bruker 2016) program monitored data collection. Data were corrected for Lorentzian polarization and absorption effects using SAINT (Bruker 2014) and SADABS (Bruker 2014) programs. SHELXT 2014/4 (Sheldrick 2015b) was used for structure solution and SHELXL 2014/7 (Sheldrick 2015a) was used for full matrix least-squares refinement on F^2. These two programs are included in the WINGX-Version 2014.1 (Farrugia 1999; Farrugia 2012) program package. A full-matrix least-squares refinement was used for the non-hydrogen atoms with anisotropic thermal parameters. The H_{CH} were inserted in idealized positions and allowed to refine in the parent carbon atom. The hydrogen atoms of the COOH groups of [Ag(I)-$Tazo_2$] were located from the electron density and inserted in idealized positions in the respective parent atoms and allowed to refine in the parent oxygen atom. MERCURY 2021.2.0 (Macrae et al., 2008) was used for packing diagrams and for polyhedral representation. PLATON (Spek and Anthony, 2018) was used for the determination of hydrogen bond interactions. **Table 4** summarizes the data collection and refinement details for [Ag(I)-Tazo] and [Ag(I)-$Tazo_2$]. Crystallographic data of compounds [Ag(I)-Tazo] and [Ag(I)-$Tazo_2$] were deposited at the Cambridge Crystallographic Data Centre (Groom et al., 2016) (CCDC 2121840-2121841).

Topological Analysis

Topological analysis of the obtained silver(I) coordination frameworks (Blatov 2006; Blatov et al., 2014) was performed by using a concept of underlying (simplified) net (O'Keeffe and Yaghi 2012; Li et al., 2014). Such networks were generated by reducing the ligands to the respective centroids while preserving their connectivity with silver(I) centers. Weak intermolecular interactions, such as hydrogen bonds, and argentophilic contacts, were not considered.

Hot-Stage Microscopy

Hot-stage microscopy experiments were carried out using a Linkam TP94 device connected to a Linkam LTS350 platinum plate, using a 10°C/min heating rate. Images were collected, via the imaging software Cell D (Olympus United Kingdom Ltd., Hertfordshire, United Kingdom), with an Olympus SZX10 stereomicroscope. The observations were conducted under Fomblin© oil with crystals that were previously indexed and whose cell parameters are similar to the previously determined crystal structures.

Attenuated Total Reflection-Fourier Transform Infrared Spectroscopy

Fourier Transform Infrared Spectroscopy (FTIR) measurements were recorded on a Thermo Nicolet 6,700 spectrometer (Waltham, MA, United States) with attenuated total reflectance (ATR) mode by averaging 32 scans at a maximum resolution of 4 cm^{-1}, registering the spectra at a wavelength interval of 4,000–650 cm^{-1}.

Elemental Analysis

Data were performed in a Fisons CHNS/O analyzer Carlo Erba Instruments EA-1108 equipment at the Instituto Superior Técnico Analyses Laboratory. Anal. Calculated for [Ag(I)-Tazo]: C, 29.5%; H, 2.72%; N, 13.76%; S, 7.87%. Found: C, 29.73%; H, 2.35%; N, 13.69%; S, 8.08%. Anal. Calculated for [Ag(I)-Tazo]$_2$: C, 34%; H, 3.14%; N, 15.86%; S, 9.08%. Found: C, 34.39%; H, 2.98%; N, 15.82%; S, 9.16%.

Differential Scanning Calorimetry and Thermogravimetry Analysis

Combined measurements were carried out on a SETARAM TG-DTA 92 thermobalance under a nitrogen flow with a heating rate of 10°C/min. The sample masses were in the range from 5 to 10 mg.

Antimicrobial Activity Assays

The synthesized compounds and respective starting materials were tested against yeasts (*Candida albicans* ATCC 10231 and *Saccharomyces cerevisiae* ATCC 2601), Gram-negative (*Escherichia coli* ATCC 25922 and *Pseudomonas aeruginosa* ATCC 27853) and Gram-positive bacteria (*Staphylococcus aureus* (MRSA CIP 106760 and ATCC 25923), *Enterococcus faecalis* ATCC 29212 and *Mycobacterium smegmatis* ATCC 607) for the determination of their minimum inhibitory concentration (MIC) values. These values were determined by the microdilution method (Clinical and Laboratory Standards Institute 2018; Alves et al., 2020). Briefly, 100 μL of Mueller-Hinton (for bacteria) or Sabouraud Dextrose (for yeasts) liquid culture medium were added to all the 96-wells of the microtiter plates. Then, 100 μL of the testing compounds at a concentration of 1 mg/mL in DMSO were added to the first well. Serial dilutions of (1:2) were performed and 10 μL of bacterial inoculum was added to each well. The microtiter plates were incubated at 37°C for 24 and 48 h for bacteria and yeasts, respectively, and their growth was assessed through the analysis of the optical density of cultures at 620 nm using a Thermo Scientific Multiskan FC (Loughborough, United Kingdom) microplate reader.

CONCLUSIONS

Two new Ag(I)-tazobactam coordination compounds were prepared by LAG, which revealed to be the most advantageous synthetic technique regarding time, yield and purity. The structural elucidation of the new compounds revealed a 3D metal-organic framework in [Ag(I)-Tazo] and an intricate combination of 2D+1D networks in [Ag(I)-$Tazo_2$]. The obtained products are stable on shelf storage and up to 155°C, fundamental requisites for prospective pharmaceutical applications.

Despite the antimicrobial resistance to β-lactams, this class of antibiotics remains an important tool to treat infectious diseases. Importantly, the results disclosed herein show that both [Ag(I)-Tazo] and [Ag(I)-$Tazo_2$] have greater antimicrobial activity than tazobactam alone, making it clear that if co-administered tazobactam were to be replaced by either MOF, the antimicrobial outcomes should be better. Nevertheless, this theory needs to be confirmed by *in vivo* and *in vitro* tests.

The coordination to the metal in both new compounds is established by the binding sites of tazobactam that are known to interact with enzymes (β-lactamases) in the human body and that may affect the interaction of tazobactam within the MOFs, leading to a different activity. Also, the potential release of labile silver cations certainly leads to synergistic effects promoting higher antimicrobial efficiency.

Furthermore, these results highlight the use of ACFs as a sustainable and valid alternative to circumvent the emergence of resistance mechanisms to the available antibiotics. As [Ag(I)-Tazo] and [Ag(I)-$Tazo_2$] represent the first structurally characterized coordination compounds of tazobactam, this study also unveils new facets of tazobactam chemistry and will stimulate its application as a multifunctional linker for designing ACFs and related materials with higher antimicrobial efficiency.

DATA AVAILABILITY STATEMENT

The datasets presented in this study can be found in online repositories. The names of the repository/repositories and accession number(s) can be found below: https://www.ccdc.cam.ac.uk/ CCDC 2121840-2121841.

AUTHOR CONTRIBUTIONS

VA, and PA contributed to conception and design of the study. DF performed the synthesis, and general characterization of the compounds. VA performed the structural elucidation. PA and PR performed the antimicrobial activity tests. AK performed the topological analysis. DF and PA wrote the first draft of the manuscript. VA and AK wrote sections of the manuscript. All authors contributed to manuscript revision, read, and approved the submitted version.

ACKNOWLEDGMENTS

The authors acknowledge funding from Fundação para a Ciência e a Tecnologia (projects UIDB/00100/2020, UIDP/00100/2020, UIDB/04567/2020, UIDP/04567/2020, and PTDC/QUI-OUT/30988/2017; contract under CEECIND program—CEECIND/00283/2018) and FEDER, Portugal 2020 and Lisboa 2020 (project LISBOA-01-0145-FEDER-030988 and contract under DL No. 57/2016 regulation). Also COST Action CA18112 is acknowledged for fruitful discussions. Auguste Fernandes is acknowledged for the IR and TGA/DSC data.

SUPPLEMENTARY MATERIAL

The Supplementary Material for this article can be found online at: https://www.frontiersin.org/articles/10.3389/fchem.2021.815827/full#supplementary-material

REFERENCES

Alexander, J. W. (2009). History of the Medical Use of Silver. *Surg. Infections* 10, 9941. doi:10.1089=sur.2008.994110.1089/sur.2008.9941

An, H., Li, M., Gao, J., Zhang, Z., Ma, S., and Chen, Y. (2019). Incorporation of Biomolecules in Metal-Organic Frameworks for Advanced Applications. *Coord. Chem. Rev.* 384, 90–106. doi:10.1016/j.ccr.2019.01.001

André, V., Alves, P. C., and Duarte, M. T. (2021). Exploring Antibiotics as Ligands in Metal-Organic and Hydrogen Bonding Frameworks: Our Novel Approach towards Enhanced Antimicrobial Activity (Mini-review). *Inorg. Chim. Acta* 525 (September), 120474. doi:10.1016/j.ica.2021.120474

André, V., da Silva, A. R. F., Fernandes, A., Frade, R., Garcia, C., Rijo, P., et al. (2019). Mg- and Mn-MOFs Boost the Antibiotic Activity of Nalidixic Acid. *ACS Appl. Bio Mater.* 2 (6), 2347–2354. doi:10.1021/acsabm.9b00046

Asai, N., Suematsu, H., Ohashi, W., Shibata, Y., Sakanashi, D., Kato, H., et al. (2021). Ceftriaxone versus Tazobactam/Piperacillin and Carbapenems in the Treatment of Aspiration Pneumonia: A Propensity Score Matching Analysis. *J. Infect. Chemother.* 27 (10), 1465–1470. doi:10.1016/j.jiac.2021.06.011

Blatov, V. A. (2006). IUCr Computing Commission Newsletter. Available at: http://www-structmed.cimr.cam.ac.uk/.

Blatov, V. A., Shevchenko, A. P., and Proserpio, D. M. (2014). Applied Topological Analysis of Crystal Structures with the Program Package Topospro. *Cryst. Growth Des.* 14 (7), 3576–3586. doi:10.1021/cg500498k

Bozcal, E., and Dagdeviren, M. (2017). "Toxicity of β-Lactam Antibiotics: Pathophysiology, Molecular Biology and Possible Recovery Strategies," in *Poisoning - from Specific Toxic Agents to Novel Rapid and Simplified Techniques for Analysis* (Rijeka, Croatia: InTech), 87–105. doi:10.5772/intechopen.70199

Bruker (2014). *Bruker Analytical Systems*. Madison, WI: Bruker.

Bruker (2016). *Bruker Analytical Systems*. Madison, WI: Bruker.

Cai, H., Huang, Y.-L., and Li, D. (2019). Biological Metal-Organic Frameworks: Structures, Host-Guest Chemistry and Bio-Applications. *Coord. Chem. Rev.* 378, 207–221. doi:10.1016/j.ccr.2017.12.003

C. Alves, P., Rijo, P., Bravo, C., Antunes, A. M. M., and André, V. (2020). Bioactivity of Isostructural Hydrogen Bonding Frameworks Built from Pipemidic Acid Metal Complexes. *Molecules* 25 (10), 2374. doi:10.3390/molecules25102374

Celik, C., Tasdemir, D., Demirbas, A., Katı, A., Gul, O. T., Cimen, B., et al. (2018). Formation of Functional Nanobiocatalysts with a Novel and Encouraging Immobilization Approach and Their Versatile Bioanalytical Applications. *RSC Adv.* 8, 25298–25303. doi:10.1039/c8ra03250e

Clinical and Laboratory Standards Institute (2018). *Methods for Dilution Antimicrobial Susceptibility Tests for Bacteria that Grow Aerobically. 11th Ed. Vol. 38*. Malvern, PA: Clinical and Laboratory Standards Institute.

Do, J.-L., and Friščić, T. (2017). Mechanochemistry: A Force of Synthesis. *ACS Cent. Sci.* 3 (1), 13–19. doi:10.1021/acscentsci.6b00277

Docquier, J.-D., and Mangani, S. (2018). An Update on β-lactamase Inhibitor Discovery and Development. *Drug Resist. Updates* 36, 13–29. doi:10.1016/j.drup.2017.11.002

Drawz, S. M., and Bonomo, R. A. (2010). Three Decades of β-Lactamase Inhibitors. *Clin. Microbiol. Rev.* 23, 160–201. doi:10.1128/CMR.00037-09

Duan, W., Qiao, S., Zhuo, M., Sun, J., Guo, M., Xu, F., et al. (2021). Multifunctional Platforms: Metal-Organic Frameworks for Cutaneous and Cosmetic Treatment. *Chem* 7 (2), 450–462. doi:10.1016/j.chempr.2020.11.018

Farrugia, L. J. (2012). WinGXandORTEP for Windows: an Update. *J. Appl. Cryst.* 45 (4), 849–854. doi:10.1107/S0021889812029111

Farrugia, L. J. (1999). WinGXsuite for Small-Molecule Single-crystal Crystallography. *J. Appl. Cryst.* 32, 837–838. doi:10.1107/s0021889899006020

Fisher, J., Belasco, J. G., Charnas, R. L., Khosla, S., and Knowles, J. R. (1980). Beta-lactamase Inactivation by Mechanism-Based Reagents. *Philos. Trans. R. Soc. Lond. B Biol. Sci.* 289, 309–319. doi:10.1098/rstb.1980.0048

Foster, T. J. (2017). Antibiotic Resistance in Staphylococcus Aureus. Current Status and Future Prospects. *FEMS Microbiol. Rev.* 41, 430–449. doi:10.1093/femsre/fux007

Friščić, T., Mottillo, C., and Titi, H. M. (2020). Mechanochemistry for Synthesis. *Angew. Chem. Int. Ed.* 59, 1018–1029. doi:10.1002/anie.201906755

Gherardi, G., Linardos, G., Pompilio, A., Fiscarelli, E., and Di Bonaventura, G. (2019). Evaluation of *In Vitro* Activity of Ceftolozane-Tazobactam Compared to Other Antimicrobial Agents against Pseudomonas Aeruginosa Isolates from Cystic Fibrosis Patients. *Diagn. Microbiol. Infect. Dis.* 94 (3), 297–303. doi:10.1016/j.diagmicrobio.2019.01.012

Groom, C. R., Bruno, I. J., Lightfoot, M. P., and Ward, S. C. (2016). The Cambridge Structural Database. *Acta Crystallogr. Sect B* 72 (2), 171–179. doi:10.1107/S2052520616003954

Hong, D. H., Shim, H. S., Ha, J., and Moon, H. R. (2021). MOF-on-MOF Architectures: Applications in Separation, Catalysis, and Sensing. *Bull. Korean Chem. Soc.* 42, 956–969. doi:10.1002/bkcs.12335

Hu, J., Chen, Y., Zhang, H., Chen, Z., Ling, Y., Yang, Y., et al. (2021). TEA-assistant Synthesis of MOF-74 Nanorods for Drug Delivery and *In-Vitro* Magnetic Resonance Imaging. *Microporous Mesoporous Mater.* 315 (February), 110900. doi:10.1016/j.micromeso.2021.110900

Huang, W.-H., Ren, J., Yang, Y.-H., Li, X.-M., Wang, Q., Jiang, N., et al. (2019). Water-Stable Metal-Organic Frameworks with Selective Sensing on Fe3+ and Nitroaromatic Explosives, and Stimuli-Responsive Luminescence on Lanthanide Encapsulation. *Inorg. Chem.* 58 (2), 1481–1491. doi:10.1021/acs.inorgchem.8b02994

Jacqueline, C., Howland, K., and Chesnel, L. (2017). *In Vitro* Activity of Ceftolozane/Tazobactam in Combination with Other Classes of Antibacterial Agents. *J. Glob. Antimicrob. Resist.* 10 (September), 326–329. doi:10.1016/j.jgar.2017.04.003

Kadioglu, O., and Keskin, S. (2018). Efficient Separation of Helium from Methane Using MOF Membranes. *Separat. Purif. Technol.* 191, 192–199. doi:10.1016/j.seppur.2017.09.031

Karlowsky, J. A., Lob, S. H., Young, K., Motyl, M. R., and Sahm, D. F. (2021). Activity of Ceftolozane/tazobactam against Gram-Negative Isolates from Patients with Lower Respiratory Tract Infections - SMART United States 2018-2019. *BMC Microbiol.* 21 (1), 74. doi:10.1186/s12866-021-02135-z

Li, D., Yang, Y., Chen, B., Guo, X., Gao, S., Wang, M., et al. (2020). MOF Regulates TNK2 Transcription Expression to Promote Cell Proliferation in Thyroid Cancer. *Front. Pharmacol.* 11 (December), 607605. doi:10.3389/fphar.2020.607605

Li, M., Li, D., O'Keeffe, M., and Yaghi, O. M. (2014). Topological Analysis of Metal-Organic Frameworks with Polytopic Linkers And/or Multiple Building Units and the Minimal Transitivity Principle. *Chem. Rev.* 114, 1343–1370. doi:10.1021/cr400392k

Liu, J., YangYang, L. Y., and Luo, F. (2021a). A New Zn-Triazole MOF Showing Very Long-Lived Luminescence up to 3 s. *J. Solid State. Chem.* 301 (September), 122369. doi:10.1016/j.jssc.2021.122369

Liu, W., Pan, Y., Zhong, Y., Li, B., Ding, Q., Xu, H., et al. (2021c). A Multifunctional Aminated UiO-67 Metal-Organic Framework for Enhancing Antitumor Cytotoxicity through Bimodal Drug Delivery. *Chem. Eng. J.* 412 (May), 127899. doi:10.1016/j.cej.2020.127899

Liu, W., Yan, Q., Xia, C., Wang, X., Kumar, A., Wang, Y., et al. (2021b). Recent Advances in Cell Membrane Coated Metal-Organic Frameworks (MOFs) for Tumor Therapy. *J. Mater. Chem. B* 9, 4459–4474. doi:10.1039/d1tb00453k

Liu, Y., Zhou, L., Dong, Y., Wang, R., Pan, Y., Zhuang, S., et al. (2021d). Recent Developments on MOF-Based Platforms for Antibacterial Therapy. *RSC Med. Chem.* 12, 915–928. doi:10.1039/d0md00416b

Lu, X., Ye, J., Zhang, D., Xie, R., Bogale, R. F., Sun, Y., et al. (2014). Silver Carboxylate Metal-Organic Frameworks with Highly Antibacterial Activity and Biocompatibility. *J. Inorg. Biochem.* 138, 114–121. doi:10.1016/j.jinorgbio.2014.05.005

Macrae, C. F., Bruno, I. J., Chisholm, J. A., Edgington, P. R., McCabe, P., Pidcock, E., et al. (2008). Mercury CSD 2.0- New Features for the Visualization and Investigation of crystal Structures. *J. Appl. Cryst.* 41, 466–470. doi:10.1107/S0021889807067908

Mileo, P. G. M., Gomes, D. N., Gonçalves, D. V., and Lucena, S. M. P. (2021). Mesoporous Metal-Organic Framework MIL-100(Fe) as Drug Carrier. *Adsorption* 27, 1123–1135. doi:10.1007/s10450-021-00343-7

O'Keeffe, M., and Yaghi, O. M. (2012). Deconstructing the Crystal Structures of Metal-Organic Frameworks and Related Materials into Their Underlying Nets. *Chem. Rev.* 112, 675–702. doi:10.1021/cr200205j

Pang, Z., Raudonis, R., Glick, B. R., LinLin, T.-J., and Cheng, Z. (2019). Antibiotic Resistance in Pseudomonas Aeruginosa: Mechanisms and Alternative Therapeutic Strategies. *Biotechnol. Adv.* 37, 177–192. doi:10.1016/j.biotechadv.2018.11.013

Qasem, N. A. A., Ben-Mansour, R., and Habib, M. A. (2018). An Efficient CO2 Adsorptive Storage Using MOF-5 and MOF-177. *Appl. Energ.* 210 (January), 317–326. doi:10.1016/j.apenergy.2017.11.011

Quaresma, S., Alves, P. C., Rijo, P., Duarte, M. T., and André, V. (2021). Antimicrobial Activity of Pyrazinamide Coordination Frameworks Synthesized by Mechanochemistry. *Molecules* 26 (7), 1904. doi:10.3390/molecules26071904

Quaresma, S., André, V., Antunes, A. M. M., Vilela, S. M. F., Amariei, G., Arenas-Vivo, A., et al. (2020). Novel Antibacterial Azelaic Acid BioMOFs. *Cryst. Growth Des.* 20 (1), 370–382. doi:10.1021/acs.cgd.9b01302

Rojas, S., Arenas-Vivo, A., and Horcajada, P. (2019). Metal-Organic Frameworks: A Novel Platform for Combined Advanced Therapies. *Coord. Chem. Rev.* 388, 202–226. doi:10.1016/j.ccr.2019.02.032

Rojas, S., Devic, T., and Horcajada, P. (2017). Metal Organic Frameworks Based on Bioactive Components. *J. Mater. Chem. B* 5, 2560–2573. doi:10.1039/C6TB03217F

Sheffield, M., Nelson, D., O'Neal, M., Gould, A. P., Bouchard, J., Nicolau, D., et al. (2020). Use of Continuous-Infusion Ceftolozane/Tazobactam for Resistant Gram-Negative Bacterial Infections: A Retrospective Analysis and Brief Review of the Literature. *Int. J. Antimicrob. Agents* 56 (5), 106158. doi:10.1016/j.ijantimicag.2020.106158

Sheldrick, G. M. (2015a). Crystal Structure Refinement with SHELXL. *Acta Crystallogr. C* 71 (January), 3–8. doi:10.1107/S2053229614024218

Sheldrick, G. M. (2015b). SHELXT- Integrated Space-Group and crystal-structure Determination. *Acta Cryst. Sect A.* 71 (1), 3–8. doi:10.1107/S2053273314026370

Spek, A. L., and Anthony, L. (2018). What Makes a Crystal Structure Report Valid? *Inorg. Chim. Acta* 470 (January), 232–237. doi:10.1016/j.ica.2017.04.036

Sun, Y., Zheng, L., Yang, Y., Qian, X., Fu, T., Li, X., et al. (2020). Metal-Organic Framework Nanocarriers for Drug Delivery in Biomedical Applications. *Nano-micro Lett.* 12, 103. doi:10.1007/s40820-020-00423-3

Tanaka, S. (2020). Mechanochemical Synthesis of MOFs. *Metal-Organic Frameworks Biomed. Appl.* 2020, 197–222. doi:10.1016/b978-0-12-816984-1.00012-3

Tooke, C. L., Hinchliffe, P., Bragginton, E. C., Colenso, C. K., Hirvonen, V. H. A., Takebayashi, Y., et al. (2019). β-Lactamases and β-Lactamase Inhibitors in the 21st Century. *J. Mol. Biol.* 431, 3472–3500. doi:10.1016/j.jmb.2019.04.002

Wang, J., Li, N., Xu, Y., and Pang, H. (2020). Two-Dimensional MOF and COF Nanosheets: Synthesis and Applications in Electrochemistry. *Chem. Eur. J.* 26, 6402–6422. doi:10.1002/chem.202000294

Wen, L., Zhao, J., Lv, K., Wu, Y., Deng, K., Leng, X., et al. (2012). Visible-Light-Driven Photocatalysts of Metal-Organic Frameworks Derived from Multi-Carboxylic Acid and Imidazole-Based Spacer. *Cryst. Growth Des.* 12 (3), 1603–1612. doi:10.1021/cg2016512

World Health Organization (2021). *World Health Organization Model List of Essential Medicines, 22nd List*. Geneva, Switzerland: World Health Organization.

Zábranský, M., Alves, P. C., Bravo, C., Duarte, M. T., and André, V. (2021). From Pipemidic Acid Molecular Salts to Metal Complexes and BioMOFs Using Mechanochemistry. *CrystEngComm* 23 (5), 1099–1109. doi:10.1039/d0ce01533d

Zhang, L., Liu, C., Gao, Y., Li, Z., Xing, J., Ren, W., et al. (2018). ZD2-Engineered Gold Nanostar@Metal-Organic Framework Nanoprobes for T1 -Weighted Magnetic Resonance Imaging and Photothermal Therapy Specifically toward Triple-Negative Breast Cancer. *Adv. Healthc. Mater.* 7 (24), 1801144. doi:10.1002/adhm.201801144

Conflict of Interest: The authors declare that the research was conducted in the absence of any commercial or financial relationships that could be construed as a potential conflict of interest.

Publisher's Note: All claims expressed in this article are solely those of the authors and do not necessarily represent those of their affiliated organizations, or those of the publisher, the editors, and the reviewers. Any product that may be evaluated in this article, or claim that may be made by its manufacturer, is not guaranteed or endorsed by the publisher.

frontiers in Chemistry

ORIGINAL RESEARCH
published: 27 January 2022
doi: 10.3389/fchem.2021.784625

SOMSpec as a General Purpose Validated Self-Organising Map Tool for Rapid Protein Secondary Structure Prediction From Infrared Absorbance Data

Marco Pinto Corujo[1†], *Adewale Olamoyesan*[2†], *Anastasiia Tukova*[2], *Dale Ang*[2], *Erik Goormaghtigh*[3], *Jason Peterson*[4], *Victor Sharov*[4], *Nikola Chmel*[1] *and Alison Rodger*[1,2*]

[1]Department of Chemistry, University of Warwick, Coventry, United Kingdom, [2]Department of Molecular Sciences, Macquarie University, Sydney, NSW, Australia, [3]Center for Structural Biology and Bioinformatics, Laboratory for the Structure and Function of Biological Membranes, Campus Plaine, Université Libre de Bruxelles, Brussels, Belgium, [4]BioPharmaSpec Inc., Malvern, PA, United States

OPEN ACCESS

Edited by:
Cosimino Malitesta,
University of Salento, Italy

Reviewed by:
Federico Marini,
Sapienza University of Rome, Italy
Laura Bonati,
University of Milano-Bicocca, Italy

***Correspondence:**
Alison Rodger
alison.rodger@mq.edu.au

[†]These authors have contributed equally to this work and share first authorship

Specialty section:
This article was submitted to Analytical Chemistry, a section of the journal Frontiers in Chemistry

Received: 28 September 2021
Accepted: 06 December 2021
Published: 27 January 2022

Citation:
Pinto Corujo M, Olamoyesan A, Tukova A, Ang D, Goormaghtigh E, Peterson J, Sharov V, Chmel N and Rodger A (2022) SOMSpec as a General Purpose Validated Self-Organising Map Tool for Rapid Protein Secondary Structure Prediction From Infrared Absorbance Data. Front. Chem. 9:784625. doi: 10.3389/fchem.2021.784625

A protein's structure is the key to its function. As protein structure can vary with environment, it is important to be able to determine it over a wide range of concentrations, temperatures, formulation vehicles, and states. Robust reproducible validated methods are required for applications including batch-batch comparisons of biopharmaceutical products. Circular dichroism is widely used for this purpose, but an alternative is required for concentrations above 10 mg/mL or for solutions with chiral buffer components that absorb far UV light. Infrared (IR) protein absorbance spectra of the Amide I region (1,600–1700 cm^{-1}) contain information about secondary structure and require higher concentrations than circular dichroism often with complementary spectral windows. In this paper, we consider a number of approaches to extract structural information from a protein infrared spectrum and determine their reliability for regulatory and research purpose. In particular, we compare direct and second derivative band-fitting with a self-organising map (SOM) approach applied to a number of different reference sets. The self-organising map (SOM) approach proved significantly more accurate than the band-fitting approaches for solution spectra. As there is no validated benchmark method available for infrared structure fitting, SOMSpec was implemented in a leave-one-out validation (LOOV) approach for solid-state transmission and thin-film attenuated total reflectance (ATR) reference sets. We then tested SOMSpec and the thin-film ATR reference set against 68 solution spectra and found the average prediction error for helix ($\alpha + 3_{10}$) and β-sheet was less than 6% for proteins with less than 40% helix. This is quantitatively better than other available approaches. The visual output format of SOMSpec aids identification of poor predictions. We also demonstrated how to convert aqueous ATR spectra to and from transmission spectra for structure fitting. Fourier self-deconvolution did not improve the average structure predictions.

Keywords: protein, secondary structure, infrared absorbance, validation, self-organising map

INTRODUCTION

Proteins are biomolecules with characteristic 3D shapes that determine their functions, e.g., structural, immune response, enzyme catalysis, and regulation (Lesk, 2010). In addition, there has been a growing interest in proteins as therapeutic agents over the past 20 years (Leurs et al., 2015). For a protein to be functional, it needs to be in a certain conformation; however, purification procedures often induce structural changes. To ensure the correct structure is retained/obtained during protein production and formulation, robust analysis methods must be used for regulatory as well as research purposes (Leurs et al., 2015).

Optical spectroscopic methods have the major advantage of not requiring a protein to form crystals, and they can be applied to any size molecules from peptide to high molecular weight assemblies. Circular dichroism (CD) spectroscopy is routinely used to estimate the secondary structure of unknown proteins and for batch-to-batch comparison of biopharmaceutical products (Woody, 1994; Sklepari et al., 2016; Spencer and Rodger, 2021). CD has the advantage of being relatively straightforward both to implement and to interpret. However, it has a number of limitations largely following from the need to keep the sample absorbance below a maximum of 2.5 at all wavelengths of interest and the need to know the concentration and path length. In aqueous solution, the protein concentration range is therefore practically limited to approximately 0.01—10 mg/ml protein. This is further restricted for biopharmaceuticals which are often formulated with high concentrations of non-protein absorbing components such as amino acids and chloride ions.

An alternative spectroscopic method to CD is mid-infrared absorption spectroscopy as the differential patterns in H-bonds and geometrical orientations of amide bonds in different secondary structure motifs affect the frequencies and intensities of vibrations. Protein IR spectra contain nine separate bands, referred to as Amide A, B, and I–VII (Kong and Yu, 2007; Rygula et al., 2013). It is generally accepted that the Amide I band (1,600–1700 cm^{-1}) carries the most direct link to secondary structure content. Its vibrational contribution is from the C=O stretching of the amide group coupled with the in-phase bending of the N–H bond and stretching of the C–N bond (Krimm and Bandekar, 1986; Bandekar, 1992). Some side chains also absorb in the region; however, in this work, we ignore side-chain contributions because Venyaminov and Kalnin (Venyaminov and Kalnin, 1990) and Oberg (Oberg et al., 2004) found that subtracting side chain contributions provided only a moderate improvement to secondary structure determination. A great deal of work has been done on protein IR spectroscopy, but the best way to extract secondary structure information for regulatory or research purposes remains unclear.

The Amide I band is usually a featureless broad band so curve fitting methods, often preceded by band-narrowing, have been implemented to facilitate structure fitting (Kauppinen et al., 1981; Maddams and Tooke, 1982; Susi and Byler, 1983; Byler and Susi, 1986). Byler and Susi (Byler and Susi, 1986) developed a band-fitting method involving first a deconvolution procedure and then band-shape fitting with the Gaussian bands centred at the maximum (negative) values of the second derivative of the spectrum. They decided, after empirical analysis of over 20 proteins, that the relative areas under bands assigned to α-helix (~1,654 cm^{-1}), β-sheet (~1,631 ± 7 cm^{-1} and ~1,678 cm^{-1}), and everything else corresponded to their relative secondary structure contents. (This has been assumed by other workers.) They found a fairly good match of their predictions with the Levitt and Greer's algorithm for extracting secondary structure from crystal data (Levitt and Greer, 1977). However, Levitt and Greer noted in their original work that their approach significantly over-estimates β-structure, making Byler and Susi's IR predictions a significant over-estimate of β-structure as deemed by other annotation approaches. The more recent consensus, e.g., (Kong and Yu, 2007; Yang et al., 2015), is that 1,620–1,640 cm^{-1} is attributed to β-sheet, 1,640–1,650 cm^{-1} to Other structures, 1,650–1,656 cm^{-1} to α-helix, and 1,670–1,685 cm^{-1} to turns. However, as noted by Oberg et al. (2004), band fitting usually requires a series of subjective decisions that can dramatically affect both result and interpretation. The authors arguably making the strongest claims for the efficacy of a band fitting approach (Yang et al., 2015) refer to their previous work on cytochrome-*c* (Dong et al., 1992) and to a paper by Kalnin et al. (1990). However, the Dong cytochrome-*c* result, while good for α-helix, has a 21–25% error in β-sheet content and Kalnin et al. (1990) used a reference set of proteins of known structure as their fitting approach rather than band fitting.

Various factor analysis methods have been applied to proteins using different reference sets. Lee et al. (1990), using a reference set of 18 protein IR spectra, concluded that they could predict protein secondary structure with standard errors of 4% for α-helix and 8% for β-sheet. Pancoska Keiderling and others used a reference set as well as principal component and factor analysis methodologies for both vibrational CD and IR spectra (Pancoska et al., 1991; Baumruk et al., 1996). Further refinement of the data through Fourier self-deconvolution did not improve their structure estimates (Wi et al., 1998). Dukor et al. and BioTools (Jupiter, US) have developed this approach into an easy-to-use fitting program by complementing the approach with their IR reference set and integrating it with data collection on their instrument. The resulting program *Prota*^{TM} provides reasonably good structure estimates, but the details of the fittings cannot be interrogated by the user. Oberg et al. (2004) have extensively explored the application of a partial least squares analysis (PLS) with a 50-protein reference set and concluded that the most important factor is the quality of the reference set—it must cover the structure-space of interest.

Oberg et al. (2004) also considered application of the CD structure fitting program SELCON (Sreerama and Woody, 2000) to IR data which proved to give similar performance to the PLS analysis. They observed that larger reference sets usually do not perform better than smaller ones, as they may include more "anomalous" spectra—so it is important to be able to interrogate results rather than simply accept a number. Goormaghtigh et al. (2006) had significant success with an approach which identifies three key wavenumbers for the three structural features that can

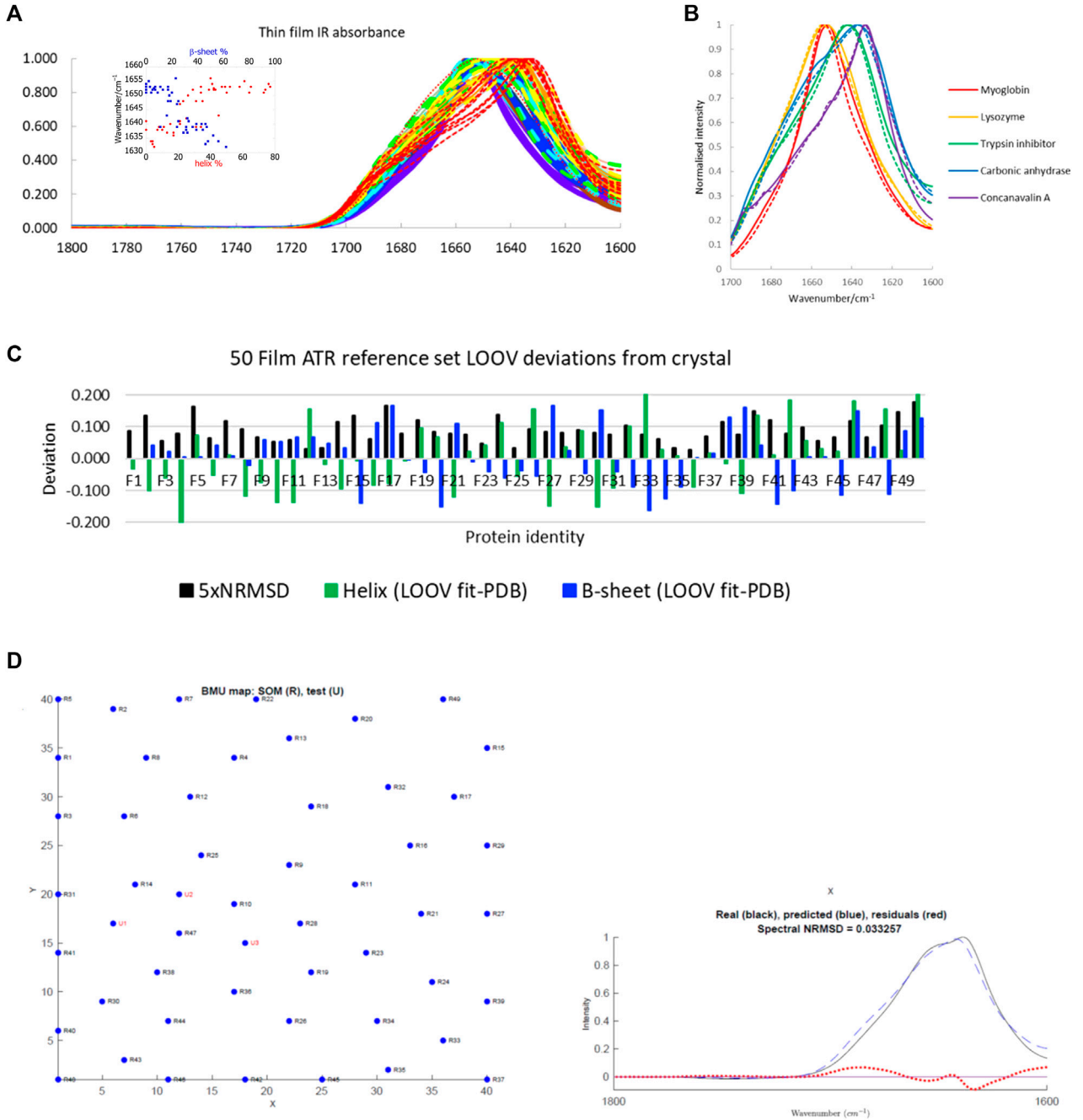

FIGURE 1 | (A) A 50-protein thin-film ATR reference set (see **Supplementary Table S1** for list of proteins). Inset: Amide I maxima plotted versus total α-helix red and β-sheet blue content. Proteins F1–F7 (>60% helix) are purple; F8–14 (45–59% helix) are blue; F15–21 (34–44% helix) are turquoise; F22–F28 (26–33% helix) are green; F29–F33, F36, F38 (17–25% helix) are yellow; F34, F35, F37, F39, F40 (10–16% helix) are orange; F41–F50 (<10% helix) are red with the unfolded F50 dotted. **(B)** Overlay of some normalised ATR thin-film (solid lines) and aqueous transmission (dashed lines) spectra. **(C)** LOOV deviations of SS prediction from PDB structures for helix (α-helix + 3_{10}-helix) and β-sheet for the Amide I 50-protein thin-film reference set in order of decreasing helix content from left to right. 5 × NRMSD of the spectral fit is overlaid. Other category deviations are minus the sum of helix and β-sheet deviations. **(D)** Phosphoglycerate kinase (F17) LOOV SOMSpec output from 50-protein film reference set for a relatively poor quality example. In the map, U1, U2, U3 are the best matching nodes for the test protein. These can be expressed as linear combinations of their neighbouring reference set nodes. The proteins can be identified from **Supplementary Table S1** in the SM, by noting that the test protein is F17 in the reference set, so proteins R1–R16 correspond to F1–F16, and R17–R49 correspond to F18–F50. The *real* spectrum is F17's input data, and the *predicted* spectrum is the SOMSpec output.

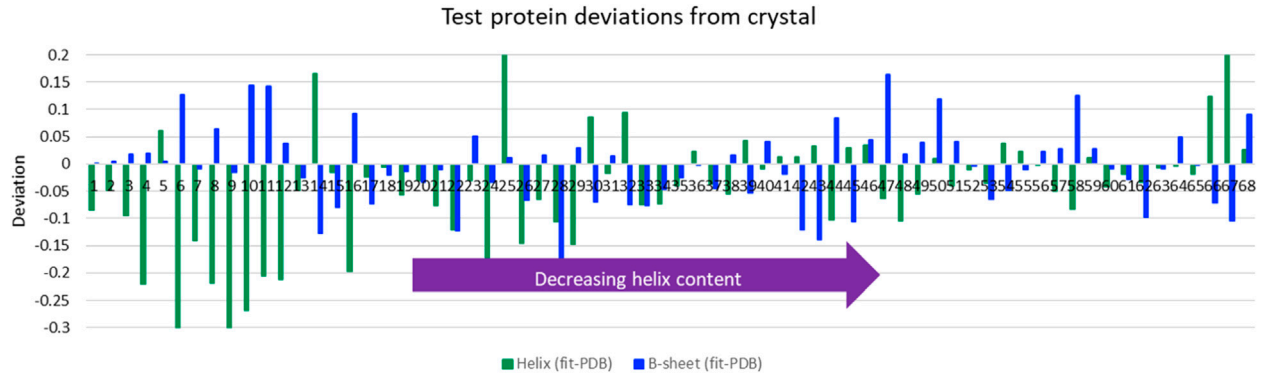

FIGURE 2 | Deviations of predictions from PDB structures for average helix (α-helix + 3_{10}-helix) and β-sheet for Amide I of 68 aqueous test proteins presented in order of decreasing helix content from left to right. Other category deviations are minus the sum of helix and β-sheet deviations.

be distinguished in the IR spectrum. Their ascending stepwise method identifies the relevance of each wavenumber of the infrared spectrum for the prediction of a given secondary structure and yields a particularly simple method for computing the secondary structure content. The original work has been successfully extended to high throughput secondary structure determination by collecting data in an array format (De Meutter and Goormaghtigh, 2021). However, the preference for a data point in the Amide II band is a concern for biopharmaceutical samples as we have observed that the magnitude of this band varies significantly with formulation vehicle. A different choice of optimal wavenumbers could make the analysis more universal.

Our experience of using CD for the analysis of biopharmaceutical protein structure has convinced us that the most important aspect of a structure fitting approach is to know its limitations. Extensive work has been done to validate methods that determine structure from CD spectra of unknowns. The most widely used methods for CD analysis, e.g., CDsstr (Johnson, 1988) and SELCON3 (Sreerama and Woody, 2000), all use a reference set of spectra of proteins of known secondary structures. Our self-organising map approach (Hall et al., 2014a; Hall et al., 2014b) uses a different approach from CDsstr and SELCON, but we have shown it is equally reliable and it has the advantage that it produces output that enables the user to interrogate what is behind secondary structure estimates. When we needed to develop robust methods for analyzing protein infrared absorbance spectra, we therefore adapted our self-organising map analysis, now called SOMSpec, to be used for structure fitting from Amide I IR spectra (Corujo et al., 2018) and found it seemed to work well for the few examples we considered, though it depended on the reference set of spectra and structure assignments. SOMSpec is described in the Materials and Methods section and the Supplementary Material. The goal of this work was to develop an easy-to-use protein IR spectra analysis platform based on the SOMSpec program and to determine how well it works for various datasets of transmission, Fourier self-deconvolved spectra, and attenuated total reflectance (ATR) spectra. We also provide the means to transform ATR spectra into transmission for slightly improved secondary structure predictions against a transmission reference set. The endpoint of the work is a clear idea of how reliable SOMSpec is for this application and where the user must interrogate the output for further information.

MATERIALS AND METHODS

Secondary Structure Annotation

The hydrogen-bonding pattern-based Dictionary of Secondary Structure of Proteins (DSSP) which divides protein secondary structure into 8 major classes abbreviated as follows: 3_{10}-helix (G), α-helix (H), π-helix (I), β-sheet (E), β-bridge (B), turn (T), bend (S), and coil (C) is used in this work. The different reference sets combine the categories differently to reduce the number of classes (Wi et al., 1998). Annotations may be found in http://2struc.cryst.bbk.ac.uk [(Whitmore and Wallace, 2004) and (Oberg et al., 2003)]. Based on the results of reference (Spencer and Rodger, 2021) for CD spectroscopy and reference (Oberg et al., 2004) for IR, we limited our final discussions to three categories which we refer to as α-helix or helix (which includes α-helix and 3_{10}-helix), β-sheet, and other (which is the combination of the rest of secondary structure types). As any residue belongs either to the helix or sheet or Other category, we only explicitly present the helix and sheet results in our figures. The deviations for Other are simply minus the sum of the helix and sheet deviations.

Self-Organising Map Spectral Fitting

SOMSpec Operates in Three Steps

i) *Training the map*: in the first step, an unsupervised self-organising (or Kohonen) map approach creates a 2D square array and organises the reference set protein IR spectra to cluster them in terms of spectral similarity, with the similarity being represented by distances. Each node of the map has a spectrum allocated to it. Unless a reference spectrum sits on a node, a distance-weighted mean of neighbouring reference spectra is assigned to each node. A trained map can be used

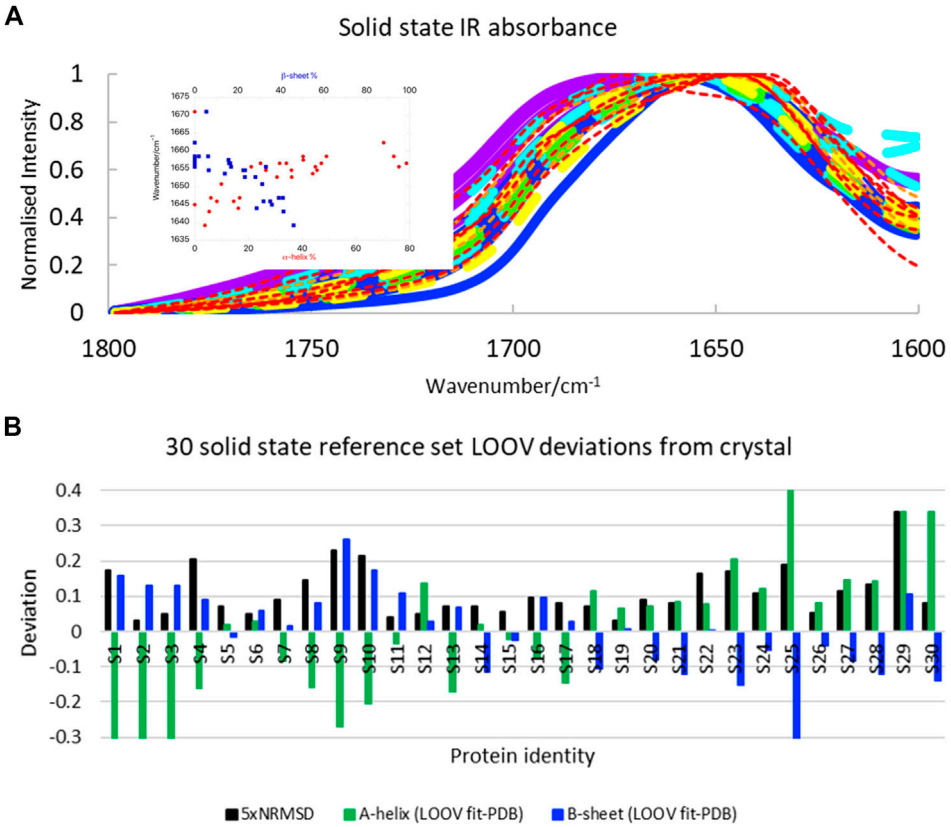

FIGURE 3 | (A) Amide I transmission IR spectra of 30 solid-state proteins normalised to 1. Proteins with α-helix content >45% are indicated with broad lines and have maxima above 1,650 cm^{-1}. Papain and lysozyme are broad dashed lines (see text). Colour coding of spectra is the same as in **Figure 1**: >60% helix purple; 45–59% helix blue; 34–44% helix turquoise; 26–33% helix green; 17–25% helix yellow; 10–16% helix orange; <10% helix red. Inset: Amide I maxima plotted against α-helix and β-sheet content. **(B)** LOOV deviations of SS prediction from PDB structures for α-helix and β-sheet for the Amide I of 30-protein solid-state reference set presented in order of decreasing helix content from left to right (for protein identities see Supplementary Material). Other category deviations are minus the sum of helix and β-sheet deviations.

repeatedly as long as the wavenumber range of the test spectrum is the same as the reference spectra. For the leave-one-out validations (LOOV, see below), we trained for 20,000 steps and for full reference sets for 50,000 steps. The optimal map dimension (Hall et al., 2013) is somewhat lower than the reference set size, so we used 20 × 20 for the solid-state reference set and 40 × 40 for the film one.

ii) *Structure assignment*: in the second step, a vector which summarises the secondary structure of the spectrum assigned to a node is also assigned to the node. Reference spectra nodes take the reference spectra secondary structure vector. Nodes with distance-weighted sum spectra have secondary structure assigned in the same way.

iii) *Test*: unknown spectra are tested against the map by identifying nodes that are the best matching units (BMU) for the unknowns in terms of the distance in the spectral space. The secondary structure of the test spectrum is determined by a distance-weighted average of secondary structure of the top 5 or 3 best matching nodes or units (BMUs) in terms of the Euclidean distance on the map.

SOMSpec input files are created as comma-separated txt files. For an *N*-member reference set, the training file consist of *N* vertical columns of spectral data, separated by commas, with the corresponding structural data placed below. The test files are in the same format but without the structural information. The files were either created manually using Excel (*via* the basic .csv output format then renamed with the. txt extension) or automatically produced by a MATLab™ code.

SOMSpec output includes Normalised Root Mean Square Deviations (NRMSD, see Supplementary Materials for details) between experimental and predicted spectra, a plot of the trained map and the overlay of experimental and predicted spectra, the secondary structure predictions, and all the files to enable the plots to be regenerated.

More details about SOMSpec are given in the Supplementary Material which also contains a summary of the input and output information used below. The SOMSpec App [coded in

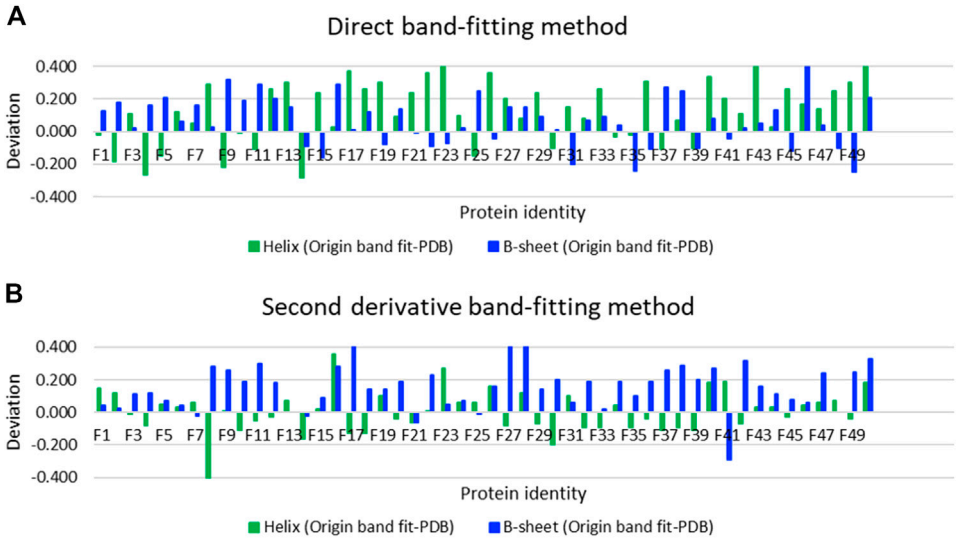

FIGURE 4 | Deviations of secondary structure prediction from PDB structures for helix and β-sheet for the Amide I band of the 50-protein film reference set presented in order of decreasing helix content from left to right for **(A)** direct Gaussian band-fitting and **(B)** the second derivative fitting approach reported in reference (Yang et al., 2015). See Supplementary Material for protein identities. Deviations of the Other category deviations are minus the sum of helix and β-sheet deviations.

MATLab™ (MathWorks, Chatswood, Australia)] and example input and output files may be found in the data repository which can be accessed via the **Supplementary Material**.

Leave-One-Out Validation

In LOOV testing the spectra and secondary structure assignments of N–1 proteins out of N proteins in an IR reference set are used as the training set to generate a SOM. Then, the Nth spectrum is tested against that SOM. This is repeated N times. The SOMSpec LOOV training files consist of N–1 vertical columns of spectral data, separated by commas, with the corresponding structural data placed below. The test files for the LOOV are a single column of spectral data. The results of the N LOOV tests give an indication of performance of the method–reference set combination.

Spectra Transformations

ATR to transmission and transmission to ATR: We used the methodology developed in reference (Rodger et al., 2020) to convert ATR spectra into transmission spectra and inverted the methodology to convert transmission spectra into what would be collected on the same sample with a 45° incidence zinc selenide (ZnSe) ATR crystal. In summary (see Supplementary Material for more details), the relationships between ATR and transmission spectra we used are

$$A_{protein}^{ATR} = (\varepsilon C)_{protein}\left(ad_pf\right)\left(1-\left(ln\,10d_pf\right)(\varepsilon C)_{water}\right)$$

$$A_{protein}^{Transmission} = \frac{A_{protein}^{ATR}\ell}{\left(\left(d_pf\right)\left(1-\left(ln\,10d_pf\right)(\varepsilon C)_{water}\right)\right)}$$

where $A_{protein}^{ATR}$ denotes the protein's ATR absorbance, d_pf is the penetration depth times the light intensity factor and $\varepsilon C = A/\ell$ is the protein's extinction coefficient times its concentration, where ℓ is the transmission path length. As the protein absorbance is much smaller than that of water in our experiments, we used d_pf for water. Given the above equation is linear in $(\varepsilon C)_{protein}$, we do not need to know the protein concentration or extinction coefficient or path length if we ultimately plan to normalise the spectra for structure fitting.

Fourier self-deconvolution (FSD): OriginPro 2021 (Originlab, 2021) was used to perform FSD with the gamma and smoothing factor parameters varied. Each deconvolved spectrum was re-zeroed and re-normalised to 1 at its maximum value.

Band Fitting

Two different band fitting approaches were undertaken. The first uses peak deconvolution within Origin Pro (Originlab, 2021) to fit the absorption bands directly to Gaussians after baselining the Amide 1 band by drawing a straight line from 1,600 cm^{-1}–1700 cm^{-1}. The secondary structure was identified by normalising the total area under the bands to 1 and then summing the areas of the bands that occurred in the accepted wavelength regions for each type of secondary structure: 1,620–1,640 cm^{-1} for β-sheet and 1,650–1,656 cm^{-1} for α-helix. If the answers were obviously wrong, the wavelength range was expanded slightly to favour the band-fitting approach. The approach outlined in (Yang et al., 2015) which involves taking the second derivative then band-fitting was also attempted. OriginPro 2021 (Originlab, 2021) was used to take second derivatives and to perform band fitting to Gaussians of minus the second derivative spectrum. The OriginPro fitting methodologies used in this work are detailed in the Supplementary

Material, and the OriginPro files are provided in the data repository.

Materials and Data Collection

All the proteins used in this work were purchased from Sigma Aldrich (Poole, United Kingdom) or available in-house. Using 2 different Jasco J-4200 (Jasco, Hachioji, Japan) spectrometers, spectra were collected with 64–1,000 scans with 4 cm^{-1} resolution, cosine apodization, and wavenumber range from 400 to 4,000 cm^{-1}. The instruments were flushed with nitrogen (N_2) at ~30 L/min flow rate for 10 min to stabilise the water vapour contribution. The sample chamber flow rate was decreased to 5 L min^{-1} during data collection, and the interferometer was closed to the nitrogen flow. We collected 30 solid-state transmission spectra (see below), 19 aqueous transmission spectra (see below), and 2 aqueous ATR spectra. Baseline water spectra (18.2 MΩ Milli-Q water) were subtracted from the aqueous protein spectra to produce a flat line in the 2,100 cm^{-1} libration band region. A small scaling factor was sometimes required. If the spectrum could not be made flat in that region, the data were discarded. The integrated absorbance of the 1717–1772 cm^{-1} or 3,800–3,900 cm^{-1} regions were used to guide water vapour subtraction where necessary (Max and Chapados, 2009). A vapour spectrum was collected by first purging the instrument with N_2, collecting a spectrum, then stopping the N_2 flow (which allows a small increase in water vapour in the light beam) and collecting a second spectrum. The difference between the two spectra was used for water vapour correction. In practice, the need for water vapour correction was minimised by collecting a baseline water spectrum directly before each protein spectrum—so both spectra had similar water vapour contributions. Protein spectra were normalised to 1 at the Amide I maximum.

Solid-state data were collected using samples prepared by grinding proteins to a fine powder before mixing with separately grounded potassium bromide (KBr) to obtain a 1–10% w/w dilution of the protein. The KBr/protein mixture was compressed by means of a Manual Hydraulic Press (Specac, Orpington, UK) using 5–10 kpsi for about a minute to produce a pellet which was held between sodium chloride (NaCl) windows in a PIKE Technologies cell (Fitchburg, United States). Since liquid water absorption was detected, a scaled water spectrum collected separately with calcium fluoride (CaF_2) windows was subtracted to give a flat spectrum in the 2,100 cm^{-1} region (Max and Chapados, 2009).

Aqueous protein solutions were prepared by dissolving lyophilised protein powders in 18.2 MΩ *cm* Milli-Q water in concentrations ranging from 10 to 80 mg ml^{-1}. Insoluble residues were removed by centrifugal filtration with Teflon disk filters (0.22 μm pore size). Solution transmission spectra were collected using a Specac (Orpington, United Kingdom) transmission cell with CaF_2 windows and no spacer making an estimated 1 μm path length. About 40 μl of sample was placed on one of the windows and the other was slid over it, making sure no air bubbles got trapped in the process. Two high β-sheet aqueous proteins samples were collected in ATR mode using a Pike Miracle™ ATR unit.

In addition, a 50-protein reference set previously obtained using ATR with thin films that were made by slowly evapourating aqueous protein solutions containing 100 μg of protein under a stream of N_2 (Goormaghtigh et al., 2006) was used as the main reference set for this work. The proteins in the 50-protein thin-film set were selected to cover structure and fold space (Oberg et al., 2003; Goormaghtigh et al., 2006). A 47-spectra normalised aqueous transmission reference set provided by BioTools (Jupiter, USA) was used as an additional test set.

RESULTS

The goal of this work was to determine how we could optimise and validate the accuracy and reliability of secondary structure predictions for proteins from good quality protein IR absorbance spectra. A key goal was to have a procedure that required no intelligent intervention until the final analysis of the results. For validation of protein secondary structure fitting methods, the key questions to be answered are:

i) when can the fitting be trusted (most relevant for day-to-day applications)
ii) if the fitting is poor, why? (most relevant for method assessment).

What is presented here is the largest consideration of protein IR data that has been performed to date. We have worked with the reference-set based method SOMSpec, which we designed for CD, to extract structure information for an unknown protein spectrum by finding combinations of known proteins that most resemble the unknown using a self-organising map. We undertook a leave-one-out validation within a large reference set and then tested against a larger set of unknowns from different sources. We also considered to what extent the band shape enhancement of FSD facilitates how SOMSpec extracts information from the broad largely featureless bands of protein IR spectra. The structure information content of solid-state IR spectra, which are even broader than aqueous spectra, is assessed, as is whether transmission and ATR Amide I spectra can be compared. We also perform direct and second derivative band-fitting estimates on the same reference set in order to be able to compare the performance of the approaches most commonly used in the literature relative to an approach using the information in a reference set.

Film Protein IR Spectra LOOV

The main protein IR reference set used in this work is a large one available in the literature (**Figure 1A**, see **Supplementary Table S1** in the Supplementary Material for list of proteins and spreadsheets with SOMSpec input and output data). It is a 50-protein film reference set designed to give structure and fold coverage (Oberg et al., 2003; Goormaghtigh et al., 2006). The data for 50 proteins were collected by drying aqueous protein samples on an ATR unit to a thin film (we refer to this as the 50-

protein thin film reference set). This approach has the advantage that the water absorbance of the spectra, which needs to be removed to give the protein contribution, is small rather than dominating the signal. However, it raises the question whether the spectra are an appropriate reference set for aqueous spectra. We expected the ATR film spectra to have the same spectral shape as transmission spectra based on reference (Jang and Miller, 1993) (if the proteins are folded the same). However, we were concerned that the film spectra might be less structured than solution spectra as is observed for solid-state data (see below). **Figure 1B** contains the overlay of some film and solution spectra for a few proteins of different secondary structure content. The spectra differ no more than independently collected aqueous transmission spectra vary which gave us the confidence to use this reference set as the main training set for SOMSpec IR in this work.

The correlation between intensity maximum position and helix or sheet content for the 50-protein thin film reference set is illustrated in the **Figure 1A** inset. On a simple level, there is a correlation between peak position and low α-helix/high β-sheet content, which is the basis for the band-fitting approaches. Peak position enables high, medium, and low α-helical and β-sheet proteins to be directly identified.

To test the performance of SOMSpec with proteins whose data were collected in an entirely consistent manner, LOOV analysis was performed. The deviations of the predicted fractions of α-helix and β-sheet from the Protein data bank (PDB) (Berman et al., 2000) DSSP are summarised in **Figure 1C** where the difference between the SOMSpec prediction and the DSSP annotation is plotted for helix ($\alpha + 3_{10}$) and β-sheet. The deviation for Other structures is minus the sum of these two (as both prediction and DSSP content sum to 1). The LOOV average helix ($\alpha + 3_{10}$) prediction error is 8% and the average β-sheet error is 7% (when the unfolded metallothionein II (F50) is excluded).

Figure 1D shows the LOOV graphical output for phosphoglycerate kinase (protein F17). The top graph illustrates the trained SOM with the BMUs for the test protein overlaid. Although there are 1,600 nodes in the map, only those corresponding to the 49 LOOV training set proteins are shown as blue dots with black labels. In this case, the fit is poor as shown by the BMUs not clustering (which indicates the test spectrum does not resemble spectra in any area of the map), a high spectral NRMSD, and poor maximum intensity wavenumber match. If the training is repeated, the map may look different with nodes moved, but the BMUs and structure predictions are almost the same because the nodes' relationships are regenerated.

For practical application of any fitting method to unknown spectra, an estimate of the error for that specific sample is needed. The spectral NRMSD (5×NRMSD is plotted in **Figure 1C** to aid visualisation) gives an indication of how well the test spectrum overlays the best spectrum generated from the combination of spectra from the other $N-1$ spectra in the reference set. This together with the accuracy of the predicted *versus* experimental wavenumber maximum are guides to fit-quality. To get a more detailed picture of the reliability of SOMSpec, all helix and sheet errors above 10% were individually analysed. Caveats to emerge are:

i) Poor water or water vapour correction causes problems (e.g., F48). If this was a test spectrum, the data should be discarded. As it is part of a published reference set we retained it.
ii) Metallo-proteins whose ligand IR signals contribute to the Amide I region of the spectrum cause secondary structure prediction errors both for their own analysis and where they are BMUs (e.g., F10, F12, F26).
iii) 77% helix F4 (haemoglobin) and 41% helix F12 (cytochrome c) have almost identical spectra so any fit involving either of these as a BMU can only be concluded to have helix >40%.
iv) Predicted and original spectra that have a poor match of a high wavenumber maxima >1,650 cm^{-1} and/or miss significant high wavenumber intensity indicate helix secondary structure errors.
v) Predicted and original spectra that have a poor match of a low wavenumber maxima (<1,645 cm^{-1}) and/or miss significant low wavenumber intensity indicate β-sheet secondary structure errors.
vi) Immunoglobulins (F42) only give good fits when an immunoglobulin is present in the reference set.
vii) F46 and F50 both have ~70% random structure which is underestimated by ~40% and causes problems when they are BMUs.

The poor protein fits in the LOOV for the 50-protein film reference set are annotated in the final column of **Supplementary Table S1**.

Aqueous Test Spectra of Known Structure

The LOOV results gave guidance for the use of SOMSpec with unknowns. We therefore tested SOMSpec on a further 68 transmission spectra of various proteins with known secondary structure content using a SOMSpec map trained for the 50-protein thin-film reference set (the trained map is available *via* the Supplementary Material). Nineteen of the test spectra were collected in transmission mode, 2 were collected by ATR and transformed computationally to transmission (see methods and Supplementary Material spreadsheet), and 47 were from the commercial BioTools reference set. The average total helix and sheet errors were 8 and 5%, respectively (see **Figure 2** for deviations from PDB structures), with the major contributions to the helix error being for high helix content proteins. When only the results for proteins of helix content <48% are considered, the helix and sheet average errors are both 5–6%, leading us to conclude that high helix proteins contribute disproportionately to the absolute helix errors. In general, the SOMSpec output plots present warnings where needed as listed above.

Fourier Self-Deconvolution

It is widely accepted for IR spectroscopy applications that FSD can improve analysis. This is partly visual, which is important in most band fitting approaches, but may perhaps also be because it can remove noise from a spectrum. The effects of different parameters are illustrated in the Supplementary Material (**Supplementary Figure S1**) for bovine serum albumin. LOOV

testing of the BioTools 47-protein reference set with a range of FSD parameters made significant improvements in the spectral NRMSDs, e.g., γ = 25 and smoothing factor = 0.5 together with re-zeroing and re-normalising improved average spectral NRMSDs by ~30%; however, disconcertingly, the average error of structure predictions from PDB structures for these parameters increased marginally (1–2%). Less dramatic parameters, e.g., γ = 10, smoothing factor = 0.25, showed a marginal average improvement in secondary structure estimates, though this probably correlates with the noise reduction of the FSD process.

Fitting ATR Spectra With a Transmission Reference Set

Because we often wish to study proteins in their native environment and aqueous ATR experiments are much easier to perform than transmission, we also investigated the quality of the secondary structure predictions for aqueous ATR spectra. Due to the instrument to instrument and sample to sample (e.g., concentration and buffer components) differences of ATR spectra, we decided that we should use a reference set that was instrument independent (in this case, the 50-protein thin film reference set). We produced ATR test spectra by transforming our transmission spectra for 21 aqueous test proteins to ATR following the equations given in the Supplementary Material which are based on reference (Rodger et al., 2020) (assuming a single bounce 45° incidence ZnSe crystal). The average SOMSpec helix prediction for the ATR spectra was somewhat worse than the corresponding transmission tests at 8 versus 6% for this subset of proteins, but the sheet prediction was marginally (1%) better. Again, visual inspection of output made problems obvious.

Solid-State Protein IR Spectra LOOV

We were interested to test how well SOMSpec worked with Amide I solid-state data, since solid-state proteins are more likely to have the same structures as those used for crystallography and the protein absorbance is not dominated by the water signal. The solid-state spectra (**Figure 3A**, see Supplementary Material for list of proteins and spreadsheets with SOMSpec input and output data) are broader and less structured than the 50-protein film reference set (**Figure 1A**). The correlation between position of the intensity maximum and helix or sheet content is slightly worse for the solid-state protein set than for the 50-protein film reference set.

The SOMSpec LOOV results for the 30-protein solid-state reference set are summarised in **Figure 3B** (see Supplementary Material for input and output details) in terms of deviations of α-helix and *β*-sheet content from PDB values. The NRMSD levels (plotted as 5×NRMSD) are generally a guide to the quality of the fit. Overall, SOMSpec gave reasonable estimates of secondary structure content with a few notable exceptions. The average deviations are 17% for α-helix and 10% for β-sheet. If we remove three types of problematic proteins from the average error calculation the average errors reduce to 11 and 8% respectively. The problem classes are again 1) high helix content proteins especially those with papain (S19) and/or lysozyme (S12) among their BMUs (the helix content is significantly underestimated), 2) β_{II} proteins in particular trypsin (S24) and chymotrypsin (S25), and 3) the largely unfolded bungarotoxin (S30). Interestingly, both lysozyme and papain CD spectra (Whitmore et al., 2011; Olamoyesan et al., 2021) have β_{II} characteristics suggesting this is a key to the problems with the first two types.

Overall, the solid state SOMSpec LOOV analysis can be described as being indicative of the secondary structure of the test protein as the errors are quite high. The increased accuracy when high helix, high sheet, and β_{II} proteins are removed flags a warning for the quality of the fitting for these classes of proteins. It should be noted that some of the reduced accuracy of the fits with the solid-state rather than film or solution proteins will be the result of the smaller reference set used. However, the space coverage of this reference set is fairly good so we attribute most of the increased error to the broader peaks.

Gaussian Band-Fitting to Determine Secondary Structure

Using SOMSpec takes more effort than a simple band-fitting approach so we assessed whether the extra effort was worth it by making estimates of the secondary structures of the 50-protein thin-film reference set using both a direct Gaussian fitting and second derivative spectra fitting implemented in OriginPro. The differences between the predicted fractions of α-helix and β-sheet and the Protein data bank (PDB) (Berman et al., 2000) DSSP values (referred to as deviations) are plotted in **Figure 4A** for direct band-fitting and in **Figure 4B** for the Yang method *via* the second derivative spectra. The proteins have been plotted in order of helical content decreasing from left to right. The results of the direct fitting were average helix and sheet errors of 19 and 13%, respectively, whereas fitting *via* second derivatives gave average errors of 10 and 16%. We could see no patterns or common signatures of poor secondary structure estimates to help guide answering either question (i) or (ii) above.

CONCLUSION

The main goal of this work was to establish a robust and reproducible approach, whose limitations are clear, to extract secondary structure information from Amide I protein IR spectra. In summary, we implemented our reference-set based self-organising map approach, SOMSpec, with a 50-protein thin-film reference set in both LOOV and on 68 other test proteins. We showed that the thin-film ATR spectra could be used as a reference set for transmission spectra aqueous proteins. The average SOMSpec prediction errors were 7% for both helix and sheet content for aqueous protein samples. High helix (>40–50%) estimates are of variable quality due e.g., to the high similarity of cytochrome-*c*'s spectrum (41% helix) and hemoglobin's (77% helix). If high helix proteins are removed from the average, then the errors reduce to 5–6%. Due to the cause of the helix errors, adding more proteins to the reference set will not resolve it.

Problematic results were able to be identified by inspection of the SOMSpec outputs. In particular, shifts of wavelength maxima

and loss of spectral intensity at high wavenumbers or low wavenumbers indicate, respectively, low helix and low sheet content in the prediction. We also found that proteins such as lysozyme and papain which have β_{II} characteristics in their CD spectra (Whitmore et al., 2011; Olamoyesan et al., 2021) have helix-like IR spectra. Finally, proteins with prosthetic groups which absorb in the Amide I region such as flavins and hemes may also cause errors in secondary structure predictions. Despite these caveats, a key advantage of the SOMSpec approach is that the fitting process is entirely reproducible so it can be used for batch-to-batch comparisons. The attraction of the 50-protein thin-film reference set is that the spectra mirror the shape of transmission spectra as illustrated in **Figure 3C** but are easier to collect and perform baseline correction than aqueous transmission spectra so the reference set itself is more reliable.

We also estimated the secondary structures of the 50-protein thin-film reference set using two band-fitting approaches and found that the errors can be significant and variable. This work and previous work by (Oberg et al., 2004) on applications of SELCON to IR data suggests that the key advantage of SOMSpec is that it is based on using a reference-set to provide secondary structure information. Thus, it (or e.g., SELCON3) is dependent on the quality of the reference set. SOMSpec has the additional advantage that it enables the user to interrogate the input and output regarding the quality of the fit.

A SOMSpec LOOV analysis of solid-state spectra suggests that there is enough information in solid-state spectra for useful secondary structure fitting, but that the 30-protein reference set is too small.

In accord with the results of Wi et al. (1998), we found that FSD does not improve structure fitting with the reference-set based SOM approach, though the spectral NRMSDs improved in a misleading manner. This is in accordance with FSD not actually increasing the information content of any spectrum.

Finally, ATR data collection is extremely attractive for aqueous protein samples as it is much simpler to mount the sample and simpler to perform the baseline correction. Although we have previously shown it is relatively straightforward to convert ATR spectra to transmission as summarised in the Supplementary Material (Rodger et al., 2020), many users find it attractive to be able to ignore the differences. Our conclusion for ATR data is that if the protein of interest either has high β-sheet content or an extra 2% average helix error is acceptable, then normalised ATR data can be used directly with a transmission (or ATR thin film as in this work) reference set, and conversely. As quality protein ATR data collection is much easier to achieve than with transmission, this innovation addresses some of the challenges of protein structure fitting from IR data.

DATA AVAILABILITY STATEMENT

The original contributions presented in the study are included in the article/**Supplementary Materials**, further inquiries can be directed to the corresponding author.

AUTHOR CONTRIBUTIONS

AR conceptualised the project; DA designed and wrote the analysis code; MC, EG, JP, and VS collected data; NC supervised data collection; MC, AO, AT, and AR undertook data analysis; and MC, AO, and AR wrote a draft manuscript. All authors contributed to the reviewing and editing.

FUNDING

This work was supported by funding from the Engineering and Physical Sciences Research Council *via* the Molecular Analytical Sciences Centre for Doctoral Training for MP (No. EP/L015307/1), the European Marie Curie Initial Training Network scheme for DLA, and Macquarie University (Research Excellence Scholarship) for AO.

ACKNOWLEDGMENTS

Discussions with Andrew Reason on the relevance of this work to biopharmaceutical products are gratefully acknowledged. The contributions of the reviewers to the quality of this manuscript are gratefully acknowledged.

SUPPLEMENTARY MATERIAL

The Supplementary Material for this article can be found online at: https://www.frontiersin.org/articles/10.3389/fchem.2021.784625/full#supplementary-material

Supplementary Data Sheet S1 | Supplementary material text (including details of SOMSpec, protein identities and band fitting methods).

Supplementary Data Sheet S2 | Film 50 set input and LOOV output inc band fitting with plots at side.

Supplementary Data Sheet S3 | 30-solid state Input data and output predictions plots at side.

Supplementary Data Sheet S4 | Aq trans & ATR 21&47 output tested against 50-film map with test plot.

REFERENCES

Bandekar, J. (1992). Amide Modes and Protein Conformation. *Biochim. Biophys. Acta (Bba) - Protein Struct. Mol. Enzymol.* 1120, 123–143. doi:10.1016/0167-4838(92)90261-b

Baumruk, V., Pancoska, P., and Keiderling, T. A. (1996). Predictions of Secondary Structure Using Statistical Analyses of Electronic and Vibrational Circular Dichroism and Fourier Transform Infrared Spectra of Proteins in H2O. *J. Mol. Biol.* 259, 774–791. doi:10.1006/jmbi.1996.0357

Berman, H. M., Westbrook, J., Feng, Z., Gilliland, G., Bhat, T. N., Weissig, H., et al. (2000). The Protein Data Bank. *Nucleic Acids Res.* 28, 235–242. doi:10.1093/nar/28.1.235

Byler, D. M., and Susi, H. (1986). Examination of the Secondary Structure of Proteins by Deconvolved FTIR Spectra. *Biopolymers* 25, 469–487. doi:10.1002/bip.360250307

Corujo, M. P., Sklepari, M., Ang, D. L., Millichip, M., Reason, A., Goodchild, S. C., et al. (2018). Infrared Absorbance Spectroscopy of Aqueous Proteins: Comparison of Transmission and ATR Data Collection and Analysis for Secondary Structure Fitting. *Chirality* 30, 957–965. doi:10.1002/chir.23002

De Meutter, J., and Goormaghtigh, E. (2021). FTIR Imaging of Protein Microarrays for High Throughput Secondary Structure Determination. *Anal. Chem.* 93, 3733–3741. doi:10.1021/acs.analchem.0c03677

Dong, A., Huang, P., and Caughey, W. S. (1992). Redox-dependent Changes in .beta.-extended Chain and Turn Structures of Cytochrome C in Water Solution Determined by Second Derivative Amide I Infrared Spectra. *Biochemistry* 31, 182–189. doi:10.1021/bi00116a027

Goormaghtigh, E., Ruysschaert, J.-M., and Raussens, V. (2006). Evaluation of the Information Content in Infrared Spectra for Protein Secondary Structure Determination. *Biophysical J.* 90, 2946–2957. doi:10.1529/biophysj.105.072017

Hall, V., Nash, A., Hines, E., and Rodger, A. (2013). Elucidating Protein Secondary Structure with Circular Dichroism and a Neural Network. *J. Comput. Chem.* 34, 2774–2786. doi:10.1002/jcc.23456

Hall, V., Nash, A., and Rodger, A. (2014a). SSNN, a Method for Neural Network Protein Secondary Structure Fitting Using Circular Dichroism Data. *Anal. Methods* 6, 6721–6726. doi:10.1039/c3ay41831f

Hall, V., Sklepari, M., and Rodger, A. (2014b). Protein Secondary Structure Prediction from Circular Dichroism Spectra Using a Self-Organizing Map with Concentration Correction. *Chirality* 26, 471–482. doi:10.1002/chir.22338

Jang, W. H., and Miller, J. D. (1993). Verification of the Internal Reflection Spectroscopy Adsorption Density Equation by Fourier Transform Infrared Spectroscopy Analysis of Transferred Langmuir-Blodgett Films. *Langmuir* 9, 3159–3165. doi:10.1021/la00035a068

Johnson, W. C. (1988). Secondary Structure of Proteins through Circular Dichroism Spectroscopy. *Annu. Rev. Biophys. Biophys. Chem.* 17, 145–166. doi:10.1146/annurev.bb.17.060188.001045

Kalnin, N. N., Baikalov, I. A., and Venyaminov, S. Y. (1990). Quantitative IR Spectrophotometry of Peptide Compounds in Water (H2O) Solutions. III. Estimation of the Protein Secondary Structure. *Biopolymers* 30, 1273–1280. doi:10.1002/bip.360301311

Kauppinen, J. K., Moffatt, D. J., Mantsch, H. H., and Cameron, D. G. (1981). Fourier Self-Deconvolution: A Method for Resolving Intrinsically Overlapped Bands. *Appl. Spectrosc.* 35, 271–276. doi:10.1366/0003702814732634

Kong, J., and Yu, S. (2007). Fourier Transform Infrared Spectroscopic Analysis of Protein Secondary Structures. *Acta Biochim. Biophys. Sinica* 39, 549–559. doi:10.1111/j.1745-7270.2007.00320.x

Krimm, S., and Bandekar, J. (1986). Vibrational Spectroscopy and Conformation of Peptides, Polypeptides, and Proteins. *Adv. Protein Chem.* 38, 181–364. doi:10.1016/s0065-3233(08)60528-8

Lee, D. C., Haris, P. I., Chapman, D., and Mitchell, R. C. (1990). Determination of Protein Secondary Structure Using Factor Analysis of Infrared Spectra. *Biochemistry* 29, 9185–9193. doi:10.1021/bi00491a012

Lesk, A. M. (2010). *Introduction to Protein Science*. Oxford: Oxford University Press.

Leurs, U., Mistarz, U. H., and Rand, K. D. (2015). Getting to the Core of Protein Pharmaceuticals - Comprehensive Structure Analysis by Mass Spectrometry. *Eur. J. Pharmaceutics Biopharmaceutics* 93, 95–109. doi:10.1016/j.ejpb.2015.03.012

Levitt, M., and Greer, J. (1977). Automatic Identification of Secondary Structure in Globular Proteins. *J. Mol. Biol.* 114, 181–239. doi:10.1016/0022-2836(77)90207-8

Maddams, W. F., and Tooke, P. B. (1982). Quantitative Conformational Studies on Poly(vinyl Chloride). *J. Macromolecular Sci. A - Chem.* 17, 951–968. doi:10.1080/00222338208056495

Max, J.-J., and Chapados, C. (2009). Isotope Effects in Liquid Water by Infrared Spectroscopy. III. H2O and D2O Spectra from 6000to0cm−1. *J. Chem. Phys.* 131, 184505. doi:10.1063/1.3258646

Oberg, K. A., Ruysschaert, J.-M., and Goormaghtigh, E. (2003). Rationally Selected Basis Proteins: A New Approach to Selecting Proteins for Spectroscopic Secondary Structure Analysis. *Protein Sci.* 12, 2015–2031. doi:10.1110/ps.0354703

Oberg, K. A., Ruysschaert, J.-M., and Goormaghtigh, E. (2004). The Optimization of Protein Secondary Structure Determination with Infrared and Circular Dichroism Spectra. *Eur. J. Biochem.* 271, 2937–2948. doi:10.1111/j.1432-1033.2004.04220.x

Olamoyesan, A., Ang, D., and Rodger, A. (2021). Circular Dichroism for Secondary Structure Determination of Proteins with Unfolded Domains Using a Self-Organising Map Algorithm SOMSpec. *RSC Adv.* 11, 23985–23991. doi:10.1039/d1ra02898g

Originlab (2021). *Northampton.* , US: OriginLab Corporation.

Pancoska, P., Yasui, S. C., and Keiderling, T. A. (1991). Statistical Analyses of the Vibrational Circular Dichroism of Selected Proteins and Relationship to Secondary Structures. *Biochemistry* 30, 5089–5103. doi:10.1021/bi00234a036

Rodger, A., Steel, M. J., Goodchild, S. C., Chmel, N. P., and Reason, A. (2020). Transformation of Aqueous Protein Attenuated Total Reflectance Infra-red Absorbance Spectroscopy to Transmission. *QRB Discov.* 1, e8. doi:10.1017/qrd.2020.11

Rygula, A., Majzner, K., Marzec, K. M., Kaczor, A., Pilarczyk, M., and Baranska, M. (2013). Raman Spectroscopy of Proteins: a Review. *J. Raman Spectrosc.* 44, 1061–1076. doi:10.1002/jrs.4335

Sklepari, M., Rodger, A., Reason, A., Jamshidi, S., Prokes, I., and Blindauer, C. A. (2016). Biophysical Characterization of a Protein for Structure Comparison: Methods for Identifying Insulin Structural Changes. *Anal. Methods* 8, 7460–7471. doi:10.1039/c6ay01573e

Spencer, S. E. F., and Rodger, A. (2021). Bayesian Inference Assessment of Protein Secondary Structure Analysis Using Circular Dichroism Data – How Much Structural Information Is Contained in Protein Circular Dichroism Spectra. *Anal. Methods* 13, 359–368. doi:10.1039/d0ay01645d

Sreerama, N., and Woody, R. W. (2000). Estimation of Protein Secondary Structure from Circular Dichroism Spectra: Comparison of CONTIN, SELCON, and CDSSTR Methods with an Expanded Reference Set. *Anal. Biochem.* 287, 252–260. doi:10.1006/abio.2000.4880

Susi, H., and Michael Byler, D. (1983). Protein Structure by Fourier Transform Infrared Spectroscopy: Second Derivative Spectra. *Biochem. Biophysical Res. Commun.* 115, 391–397. doi:10.1016/0006-291x(83)91016-1

Venyaminov, S. Y., and Kalnin, N. N. (1990). Quantitative IR Spectrophotometry of Peptide Compounds in Water (H2O) Solutions. II. Amide Absorption Bands of Polypeptides and Fibrous Proteins in ?-, ?-, and Random Coil Conformations. *Biopolymers* 30, 1259–1271. doi:10.1002/bip.360301310

Whitmore, L., and Wallace, B. A. (2004). DICHROWEB, an Online Server for Protein Secondary Structure Analyses from Circular Dichroism Spectroscopic Data. *Nucleic Acids Res.* 32, W668–W673. doi:10.1093/nar/gkh371

Whitmore, L., Woollett, B., Miles, A. J., Klose, D. P., Janes, R. W., and Wallace, B. A. (2011). PCDDB: the Protein Circular Dichroism Data Bank, a Repository for Circular Dichroism Spectral and Metadata. *Nucleic Acids Res.* 39, D480–D486. doi:10.1093/nar/gkq1026

Wi, S., Pancoska, P., and Keiderling, T. A. (1998). Predictions of Protein Secondary Structures Using Factor Analysis on Fourier Transform Infrared Spectra: Effect of Fourier Self-Deconvolution of the Amide I and Amide II Bands. *Biospectroscopy* 4, 93–106. doi:10.1002/(sici)1520-6343(1998)4:2<93:aid-bspy2>3.0.co;2-t

Woody, R. W. (1994). "Circular Dichroism of Peptides and Proteins," in *Circular Dichroism Principles and Applications*. Editors K. Nakanishi, N. Berova, and R. W. Woody (New York: VCH).

Yang, H., Yang, S., Kong, J., Dong, A., and Yu, S. (2015). Obtaining Information about Protein Secondary Structures in Aqueous Solution Using Fourier Transform IR Spectroscopy. *Nat. Protoc.* 10, 382–396. doi:10.1038/nprot.2015.024

Conflict of Interest: JP and VS were employed by BioPharmaSpec Inc.

The remaining authors declare that the research was conducted in the absence of any commercial or financial relationships that could be construed as a potential conflict of interest.

Publisher's Note: All claims expressed in this article are solely those of the authors and do not necessarily represent those of their affiliated organizations, or those of the publisher, the editors and the reviewers. Any product that may be evaluated in this article, or claim that may be made by its manufacturer, is not guaranteed or endorsed by the publisher.

frontiers in Chemistry

PERSPECTIVE
published: 07 February 2022
doi: 10.3389/fchem.2022.821020

Design Principles and Applications of Selective Lanthanide-Based Receptors for Inorganic Phosphate

Valérie C. Pierre and Randall K. Wilharm*

Department of Chemistry, University of Minnesota, Minneapolis, MN, United States

Phosphate is an anion of both environmental and medical significance. The increase in phosphate levels in surface waters due primarily to run-offs from fertilized agricultural fields causes widespread eutrophication and increasingly large dead-zones. Hyperphosphatemia, a condition in which blood phosphate levels are elevated, is a primary cause of increased mortality and morbidity in chronic or advanced kidney disease. Resolving both of these issues require, in part, new technology that could selectively sequester phosphate in water at neutral pH. The high hydration energy of phosphate, which prevents organic receptors from functioning in water with sufficient affinity, can be overcome via coordination to a hard metal ion. The hardness, oxophilicity and lability of lanthanide ions make them excellent candidates for the design of high affinity phosphate receptors. In this perspective, we discuss how the principles of lanthanide coordination chemistry can be exploited to design sensitive and selective receptors for phosphate. Unlike many supramolecular systems, these hosts do not recognize their anionic guests via directed electrostatic and hydrogen bonding interactions. Instead, the selectivity of our fluxional receptors is governed entirely by acid-base chemistry and electrostatic forces. Parameters that affect the affinity and selectivity of the receptors include the basicities of the coordinating ligand and of the targeted anion, the acidity of the lanthanide ion, and the geometry of the ligand. Uniquely, their affinity for phosphate can be readily tuned by orders of magnitude either by peripheral interactions or by the lanthanide ion itself without affecting their exquisite selectivity over competing anions such as bicarbonate and chloride.

Keywords: phosphate, receptor, lanthanide, luminescence, supramolecular, recognition

OPEN ACCESS

Edited by:
Valeria Conte,
University of Rome Tor Vergata, Italy

Reviewed by:
David Esteban-Gómez,
University of A Coruña, Spain

****Correspondence:***
Valérie C. Pierre
pierre@umn.edu

Specialty section:
This article was submitted to Inorganic Chemistry, a section of the journal Frontiers in Chemistry

Received: *23 November 2021*
Accepted: *11 January 2022*
Published: *07 February 2022*

Citation:
Pierre VC and Wilharm RK (2022) Design Principles and Applications of Selective Lanthanide-Based Receptors for Inorganic Phosphate. Front. Chem. 10:821020. doi: 10.3389/fchem.2022.821020

INTRODUCTION–NEED AND REQUIREMENTS FOR PHOSPHATE RECEPTORS

Phosphate, a tetrahedral oxyanion with one of the largest hydration energy ($\Delta G_{hydration}$ $H_2PO_4^-$ = -465 kJ mol^{-1}), (Marcus, 1991), has received much attention in supramolecular chemistry due to its significance in both environmental and medical applications. Environmentally, phosphate is the leading cause of eutrophication due to agricultural run-offs into lakes, rivers and coastal waters. (Schindler et al., 2008; Wang and Wang, 2009; Ménesguen et al., 2018). Efforts to clean up or attenuate these damages would benefit from the development of novel technology that can selectively remove and recover phosphate from wastewaters. Medically, the poor ability of dialysis to remove the highly hydrated anion leads to accumulation of phosphate in patients with advanced or chronic

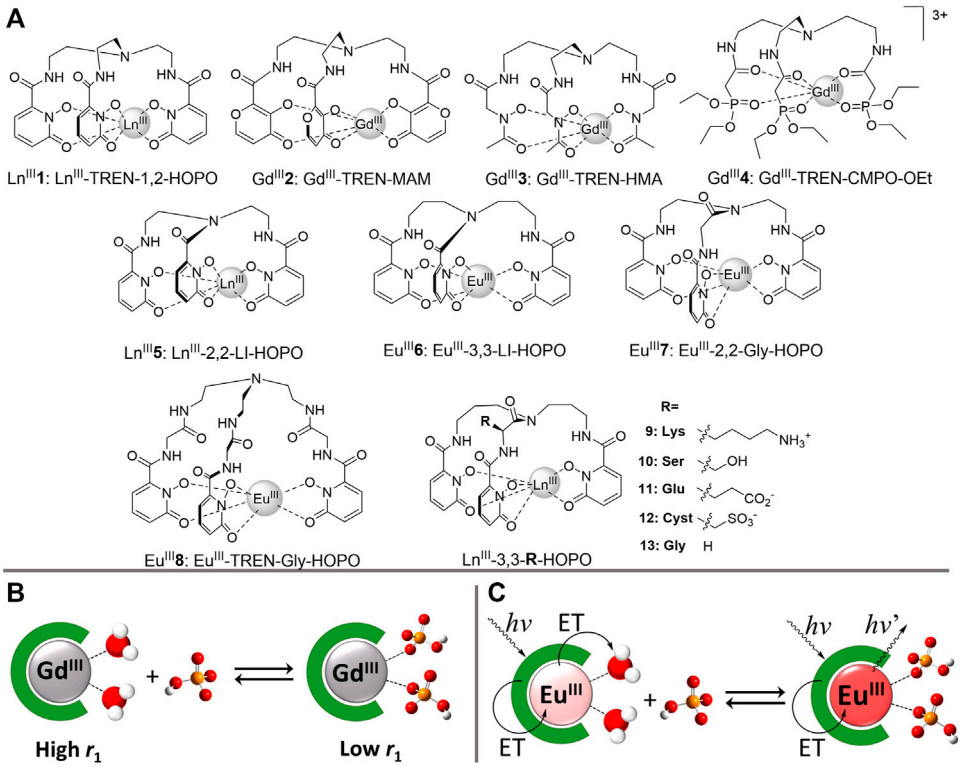

FIGURE 1 | (A) Chemical structures of phosphate receptors **(B)** Relaxivity response of Gd^{III} receptors to phosphate binding. Rapidly exchanging water molecules bound to Gd^{III} enhance the proton relaxation of the bulk water, resulting in high longitudinal relaxivity (r_1). Bound phosphate anions prevent coordination of water molecules, thereby reducing the proton relaxation of the bulk solvent and decreasing the relaxivity (r_1) **(C)** Luminescence response of Eu^{III} receptors to phosphate binding. Coordinated water molecules efficiently quench Eu^{III} luminescence. Phosphate anions displace the inner-sphere water molecules upon coordination, which increases the Eu^{III}-centered luminescence intensity and lifetime.

kidney diseases. (Sherman, 2016). With time, this accumulation leads to vascular calcification with significant increased risk of mortality and morbidity. (Block et al., 1998; Ganesh et al., 2001; Block et al., 2004). Phosphate binders such as lanthanum carbonate, which are taken orally at large doses, lead to significant side effects and have shown limited efficacy at managing this conditions. (Floege, 2016; Biruete et al., 2020).

Both of these problems could be addressed with efficacious supramolecular receptors that could sequester excess phosphate from complex aqueous media. There are similarities in the requirements for both of these applications, including efficacy in water at neutral pH and extremely high selectivity over other anions present in higher concentration, notably bicarbonate and chloride. There are also differences. Because the target phosphate level in blood is 1.5 mM, phosphate receptors with relatively low affinity will suffice as long as they are highly selective and highly stable. For environmental applications, prevention of eutrophication and algae blooms requires decreasing phosphate levels to below 1 μM, (Great Lakes Water Quality Agreement, 2012), requiring receptors with substantially higher affinity for the anion.

Many receptors for phosphate have been reported and reviewed. (Hargrove et al., 2011; Pal et al., 2020; Ramakrishnam Raju et al., 2020). Most are organic molecules inspired by phosphate binding proteins and follow the traditional lock-and-key principles of supramolecular chemistry. In these cases, phosphate recognition is contingent on pre-organized hydrogen-bonding and electrostatic interactions, which are too weak to overcome the very high hydration energy of phosphate. As a result, they perform poorly or not at all in aqueous media. Overcoming the hydration energy of phosphate, a hard anion, is best achieved by enabling the anion to coordinate a hard metal. Some success has been achieved with zinc(II) and copper (II), although the affinity and selectivity of these receptors remain insufficient for the intended medical and environmental applications. Lanthanide complexes, on the other hand, offer the possibility to achieve not only very high selectivity and sensitivity, as required for both of these applications, but also the ability to tune the affinity for phosphate as desired. Herein we discuss how and why our group has achieved this unique control.

LANTHANIDE-BASED RECEPTORS FOR PHOSPHATE

The affinity of lanthanide complexes with one or more open coordination sites for inorganic phosphate in water is well known. All clinical gadolinium-based magnetic resonance imaging (MRI)

contrast agents have at least some affinity for phosphate. (Burai et al., 1997). Many lanthanide-based probes for smaller anions such as HCO_3^- are not perfectly selective over phosphate despite their more crowded open coordination sites that disfavors coordination of the bulkier tetrahedral anion. (Bretonniere et al., 2004; Pierre et al., 2006a; Pálinkás et al., 2009; Smith et al., 2012). It thus follows from these observations that one could design lanthanide complexes that have good affinity for phosphate simply by opening up at least one coordination site. (Ramakrishnam Raju et al., 2020). Importantly, one should note that for lanthanide receptors in water and in the absence of anions, these open coordination sites are occupied by loosely bound and rapidly exchanging water molecules. Selectivity over other anions, most of which are smaller (i e., F^-, HCO_3^-), is more difficult to engineer since it cannot be achieved by steric means. Instead, this selectivity that is so crucial to both medical and environmental applications has to be incorporated by modifying the nature of the coordinating ligand L.

Insight into how selectivity can be engineered also comes from the field of MRI contrast agents and luminescent probes. Europium(III) complexes of TREN-1,2-hydroxypyridinonate (**1, Figure 1A**, **Table 1**), are known to have no affinity for phosphate despite their flexible coordination geometry that leaves two sterically unhindered open coordination sites. (Jocher et al., 2007). They thus differ from their less basic polyaminocarboxylate counterparts that also bind oxyanions such as phosphate and bicarbonate. This difference is rational. Since the filled 5s and 5p orbitals efficiently shield the partially filled 4f orbitals of the lanthanides, bonding to lanthanide ions is almost entirely ionic. Unlike transition metal complexes, there is negligible overlap between the molecular orbitals of the lanthanide ion and those of the coordinating ligands. Coordination to lanthanide ions is thus primarily an acid-base interaction. There is thus, predictably, a well-established relationship between the basicity of the coordinating ligand L and the stability of $Gd^{III}L$ complexes. The more basic the ligand, the more stable the complex, up to a point near $\Sigma pK_a \approx 35$ beyond which the trend reverses. (Kumar et al., 1993; Doble et al., 2003; Pierre et al., 2004).

We postulated that this same trend could be used to rationally design selective lanthanide receptors for phosphate. Since phosphate is not just the guest of the lanthanide host but also one of its ligands, it would thus follow that the basicity of the ligand L should impact the affinity of the $Gd^{III}L$ complex for phosphate and other anions. TREN-1,2-hydroxypyridinonate (**1**) ligands, which have a $\Sigma pK_a \approx 35$, already fulfill the needs of the gadolinium(III) ion. Coordination of a basic oxyanion guest would increase the sum of the basicity for all coordinating ligands, which is thermodynamically unfavorable. The opposite is true for complexes that use less basic ligands. For those, coordination of an additional oxyanion would be thermodynamically favored because it would increase the ΣpK_a.

Indeed, we have demonstrated that if the geometry of the ligand and the charge of the complex are constant, and in the absence of steric hindrance at the open coordination sites, the affinity of gadolinium(III) complexes for anions is directly determined by only two factors: the stability of the complex, which is itself a function of the basicity of the ligand, and the basicity of the anionic guest. (Ramakrishnam Raju et al., 2019). The more stable the $Gd^{III}L$ complex, the lower the affinity of the lanthanide for the anion. The most stable Gd^{III} complex has no affinity for any anions (**Table 1**). The lanthanide complexes with intermediate stability form ternary ($Ln^{III}L{\cdot}anion$) or quaternary ($Ln^{III}L{\cdot}anion_2$) assemblies with anions. For weakly stable complexes, however, phosphate and other anions readily compete with and displace the ligands L, resulting in the formation of $Ln^{III}{\cdot}anion_x$ precipitates. Advantageously, these equilibriums can be readily monitored by relaxivity. Since the relaxivity (r_1) of $Gd^{III}L$ complexes is directly proportional to the number of inner-sphere water molecules (**Figure 1B**), unbound $Gd^{III}L$ receptors have significantly higher r_1 than those for which the inner-sphere water molecules have been displaced by coordinating anions.

The reverse—selectivity between different anions for a given lanthanide complex—follows the same rules. In the absence of steric hindrance at the coordination site, the affinity of Gd^{III} complexes for anions always follows the trend in the basicity of the anions: phosphate > arsenate > bicarbonate > fluoride. (Ramakrishnam Raju et al., 2019). That basicity, and not Pearson's hardness, governs the selectivity between anions is due to the purely ionic nature of lanthanide coordination. Indeed, under basic conditions, significantly softer but also more basic anions such as CN^- also coordinate lanthanide ions. (Huang and Pierre, 2018).

The ligand TREN-MAM (**2**) is slightly less basic than TREN-HOPO (**1**). (Puerta et al., 2006). As a result, even though Gd^{III}-TREN-HOPO has no affinity for anions, Gd^{III}-TREN-MAM has high affinity for phosphate and good, although not sufficient, selectivity over bicarbonate and fluoride. (Harris et al., 2017; **Table 1**). Predictably, given the role of basicity on anion coordination, this coordination is pH dependent. Gd^{III}-TREN-MAM binds phosphate with high affinity at neutral pH but not at all at pH 2. This behavior, which is common to the entire class of lanthanide-based phosphate receptors, is key to pH-driven catch-and-release process that, advantageously, enable recycling of the receptor over numerous cycles. (Harris et al., 2017).

It is important to note that the above trends are only valid in so much as there is no significant steric hindrance at the open coordination sites. This is not the case, for instance, for macrocyclic polyaminocarboxylate (DOTA-type) complexes. Crystal structures of lanthanide complexes of the class of tris-bidentate ligands indicate that their open coordination sites, filled with solvent molecules in the absence of anions, are far apart from each other. (Xu et al., 2004; Jocher et al., 2007). There is no steric hindrance preventing anion coordination. Moreover, in the absence of ligand-field stabilization and with non-rigid ligands such as the ones discussed herein, lanthanide complexes are highly fluxional, interconverting rapidly between different isomers close in energy. This rapid interconversion between numerous isomers, which is faster than the NMR time-scale, is apparent for both the unbound (free) and the phosphate-bound form of the complexes. It is evident that this class of fluxional lanthanide hosts does not follow the standard lock-and-key geometric standards of supramolecular chemistry articulated

TABLE 1 | Inorganic phosphate ternary complex stoichiometry, affinity, selectivity, and mode of detection for phosphate receptors.

Receptor	Stoichiometry (LnL:Pi)	Affinity (logβ)[a]	Interfering anions (logβ)[a]	Mode of detection	Ref
Eu^{III}**1**	No binding	—	—	luminescence	20
Gd^{III}**1**				relaxivity	24
Gd^{III}**2**	1:2	17	arsenate (7.8) bicarbonate (2.7) fluoride (2.0)	relaxivity	24
Gd^{III}**3**	transmetallation	6.1	arsenate (11) bicarbonate (3.0) fluoride (2.6)	relaxivity	24
Gd^{III}**4**	transmetallation	29	arsenate (4.7) bicarbonate (3.0) fluoride (3.1)	relaxivity	24
Sm^{III}**5**	1:2	10.4	not tested	luminescence	35
Eu^{III}**5**	1:2	10.4	none	luminescence	29
Gd^{III}**5**	1:2	12.6	not tested	luminescence	35
Eu^{III}**6**	No binding	—	—	luminescence	29
Eu^{III}**7**	No binding	—	—	luminescence	29
Eu^{III}**8**	No binding	—	—	luminescence	29
Eu^{III}**9**	1:2	11.3	none	luminescence	38
Eu^{III}**10**	1:3	15.9	none	luminescence	38
Eu^{III}**11**	No binding	—	—	luminescence	38
Eu^{III}**12**	No binding	—	—	luminescence	38
Sm^{III}**13**	1:3	14.7	not tested	luminescence	35
Eu^{III}**13**	1:3	14.5	none	luminescence	29
Gd^{III}**13**	1:3	17.0	not tested	luminescence	35

[a]*Overall association constant for the indicated anion, which corresponds to the equilibrium* $Ln^{III}L + nA^- \rightleftharpoons Ln^{III}L{\cdot}A_n$ *where* $\beta = [Ln^{III}L{\cdot}A_n]/([Ln^{III}L][A^-]^n)$, A^- *is the indicated anion and* n *is the total number of anions found to bind to the receptor.*

by Emil Fischer whereby recognition of the phosphate guest is reliant on pre-organized hydrogen-bonding and electrostatic interactions. Instead, the affinity and selectivity for phosphate is entirely governed by the highly ionic lanthanide(III)-OPO_3H bond.

Gd^{III}-TREN-MAM demonstrated the potential to rebrand failed gadolinium-based MRI contrast agents as phosphate sequestration agents, but its insufficient selectivity over bicarbonate does not make it the receptor of choice for both medical and environmental applications. Based on the above discussion, a complex of stability intermediate between TREN-MAM and TREN-HOPO should offer the necessary selectivity. Given the limited choice in podands, a simpler approach to achieve this goal than changing the podand is to slightly destabilize the Gd^{III}-TREN-HOPO complex by marginally modifying its geometry. With that goal in mind, we synthesized five more tripodal Eu^{III}-HOPO complexes bearing different ligand caps (**Figure 1A**). (Huang et al., 2020) Europium(III) was chosen for this study instead of gadolinium(III) due to the lower solubility of the lanthanide HOPO complexes that is incompatible with the insensitive nature of relaxometric measurements. The high efficiency by which HOPO sensitizes Eu^{III} emission, on the other hand, enables facile determination of anion coordination by time-resolved luminescence spectroscopy (**Figure 1C**).

Of the six Eu^{III}-HOPO complexes synthesized, four have eight-coordinate, q = 2 ground states (Eu^{III}**1**, Eu^{III}**5**, Eu^{III}**6**, and Eu^{III}**7**), whereas two have nine-coordinate, q = 3 ground states (Eu^{III}**8** and Eu^{III}**13**), where q is the number of open coordination sites initially filled by water molecules. This observation is in line with prior reports that demonstrated that the 8 and 9 coordination states of the HOPO-class of complexes are very close in energy such that minor modification in ligand geometry is sufficient to favor one or the other state. (Pierre et al., 2006b). Two of these complexes: the 8-coordinate Eu^{III}-2,2-LI-HOPO (Eu^{III}**5**) and the 9-coordinate Eu^{III}-3,3-Gly-HOPO (Eu^{III}**13**) bind phosphate with very high affinity in water at neutral pH. Predictably, the Eu^{III} complex with two open coordination sites binds two phosphate anions, thereby forming a $Ln^{III}L{\cdot}Pi2$ assembly, whereas the one with three open coordination sites binds three phosphate anions, forming $Ln^{III}L{\cdot}Pi3$. Importantly, both complexes showed not only high affinity for phosphate, but also exquisite selectivity over other anions, notably bicarbonate, fluoride and carboxylates. As such, they both fulfill all the prerequisites noted above for both environmental and medical applications of phosphate sequestration.

This study yielded two important conclusions. The first is that there is no relationship between the number of open coordination sites and the affinity of the complex for anions. Some highly stable complexes with three open coordination sites have no affinity for phosphate or any other anions. Some slightly less stable complexes with only two open coordination sites do have high affinity for phosphate. The second is that there is, however, a strong relationship between the quantum yields of europium complexes of 1,2-HOPO and their affinity for phosphate. Indeed, the only two complexes that bind phosphate have noticeably lower quantum yields. Raymond previously reported that lower quantum yields of some 1,2-HOPO Eu^{III} complexes are due in part to the effect to the increased distance separating the HOPO

sensitizer from the Eu^{III} ion. (Abergel et al., 2009; Daumann et al., 2016). Decreasing the effectiveness by which one or more 1,2-HOPO podand coordinates Eu^{III} is what leads to increase affinity of the receptor for phosphate. Unfortunately, it is not yet possible to predict or compute which ligand will or will not destabilize the complex, that is, which ligand cap will decrease the effectiveness by which 1,2-HOPO coordinates Eu^{III} as necessary to enable phosphate coordination.

Altogether, these studies demonstrate that highly sensitive and selective receptor for phosphate that function in water at neutral pH can be successfully designed by optimizing the stability of the lanthanide coordination sphere. A common theme in achieving our goal was the importance of the basicity of both the coordinating ligand L and the anions. It thus follows that the nature of the lanthanide ion, which affects its Lewis acidity, should also have an effect on the stability of the complex and, by extension, on the affinity of the receptor for phosphate.

The most important periodic trend across the lanthanide series is their gradual contraction, with a 16% reduction in the ionic radii of the lanthanides from La^{III} to Lu^{III}. (Shannon, 1976). This contraction results in a progressive increase in the acidity of the lanthanides across the series from a pK_a of 9.24 for La^{III} to 7.52 for Lu^{III}. (Klungness and Byrne, 2000). Our NMR studies demonstrated that these tris-bidentate ligands are highly fluxional suggesting that steric hindrance does not impede lanthanide coordination. Given that the stability of gadolinium(III) complexes is a function of the basicity of the ligand, we anticipated a linear progression in stability of Ln^{III}-2,2-LI-HOPO complexes across the series. Indeed, we observed significant and progressive increase in pM values from La^{III} to Lu^{III} indicating that for complexes of this class of ligand, steric components do not hinder coordination of even the smallest lanthanides. (Wilharm et al., 2021). The extreme difference in pM values between Lu^{III} and La^{III}, ΔpM = 7.5, which is substantially more than that observed with other ligands, suggest that this class of ligands also holds potential for separation of rare earth elements.

The same periodic trend is observed for the affinity of lanthanide complexes for phosphate. The affinity for phosphate of both Ln^{III}-2,2-LI-HOPO and Ln^{III}-3,3-Gly-HOPO increases significantly from La^{III} to Lu^{III}, with a difference in affinity (Δlogβ) for the oxyanion of at least 5.2 and 2.5 between the first and last lanthanide complexes of those two ligands, respectively. (Wilharm et al., 2021). As predicted, the affinity of the lanthanide receptors for phosphate can be tuned as desired by orders of magnitude simply by moving left or right on the periodic table. Advantageously, increased efficacy does not come at the detriment of complex stability. lutetium(III) has the highest affinity for phosphate and also forms the most stable 1,2-HOPO complexes. It thus holds particular potential for translational applications for both medical and environmental applications since it is even less likely, given its stability, to leach from the receptor.

The unique ability to design lanthanide complexes that bind phosphate with high affinity and selectivity stems from the purely ionic nature of the lanthanide-ligand interactions. By extension, this ionic nature of lanthanide coordination stipulates that, even in water, peripheral electrostatic charges would have a significant effect on the affinity of the receptor for the oxyanion. We previously exploited this behavior to distinguish between ATP, ADP and AMP and monitor enzymatic reactions of kinases. (Weitz et al., 2012; Weitz et al., 2013). The extreme magnitude of this effect was demonstrated with a series of five amino-acid derivatives, Eu^{III}-3,3-AA-HOPO (Eu^{III}**9**–Eu^{III}**13**), that differed in the incorporation of a single positively charged (lysine), negatively charged (glutamate and cysteate) or neutral (serine) pendant group capable of hydrogen bonding (**Figure 1A** and **Table 1**). (Huang et al., 2019) In the absence of phosphate, all five of these complexes are nine-coordinate with three inner-sphere water molecules. The two negatively-charged complexes, Eu^{III}-3,3-Glu-HOPO (Eu^{III}**11**) and Eu^{III}-3,3-Cyst-HOPO (Eu^{III}**12**) have no affinity whatsoever for phosphate at neutral pH: addition of 10 equivalents of the anion does not increase either the luminescence intensity nor the luminescence lifetime of the probe. Addition of a single alcohol group that can hydrogen bond to phosphate and stabilize its coordination to the lanthanide center increases the affinity of the complex for the oxyanion by 20-fold. Whereas the two neutral complexes Eu^{III}-3,3-Gly-HOPO (Eu^{III}**13**) and Eu^{III}-3,3-Ser-HOPO (Eu^{III}**10**) each bind three phosphates, one for each open coordination site, the positively charged complex Eu^{III}-3,3-Lys-HOPO (Eu^{III}**9**) only binds two. The pendant primary amine of the lysine derivative strongly stabilizes one of the inner-sphere water molecules. As a result, the Eu^{III}-3,3-Lys-HOPO·Pi_2 adduct retains one inner-sphere water molecule even in the presence of an excess of phosphate. Similar behavior has been observed with other gadolinium(III) 1-Me-3,2-HOPO complexes. (Pierre et al., 2006b). Nonetheless, even though Eu^{III}-3,3-Lys-HOPO only binds two phosphates, which accounts for its lower increase in luminescence intensity and luminescence lifetime upon anion coordination, both the first and second association constant for phosphate increases over two orders of magnitude compared to the parent neutral glycine derivative. One can thus dramatically increase the affinity of a lanthanide receptor for phosphate by orders of magnitude by adding either peripheral positive charges or stabilizing hydrogen-bonding moieties. The presence of a single negative charge, on the other hand, is sufficient to eliminate all affinity for phosphate. Significantly, increasing or decreasing the affinity via peripheral interactions does not affect the exquisite selectivity of these receptors.

CONCLUSION AND OUTLOOK

The above discussion highlighted the principles behind the design of lanthanide-based receptors with high affinity for phosphate and high selectivity over other common competing anions in water at neutral pH, notably bicarbonate. The high selectivity of these receptors is notable given the absence of steric hindrance at the open coordination sites and the lack of pre-organized hydrogen-bonding or electrostatic interactions. In these aspects, lanthanide-based receptors distinguish themselves from the majority of supramolecular hosts for anion recognition. The high stability of the complexes ensures that the metal will likely not leach into either a biological or environmental media, as prerequisite for any phosphate sequestration technologies. Future work will focus on immobilizing these receptors on polymers or materials and testing these unique filtration technologies in application such as the treatment of hyperphosphatemia and phosphate sequestration from wastewaters.

AUTHOR CONTRIBUTIONS

All authors listed have made a substantial, direct, and intellectual contribution to the work and approved it for publication.

FUNDING

This work was supported by the National Institutes of Health provided by R01 DK124333-01A1.

REFERENCES

Abergel, R. J., D'Aléo, A., Ng Pak Leung, C., Shuh, D. K., and Raymond, K. N. (2009). Using the Antenna Effect as a Spectroscopic Tool: Photophysics and Solution Thermodynamics of the Model Luminescent Hydroxypyridonate Complex [EuIII(3,4,3-Li(1,2-Hopo))]−. *Inorg. Chem.* 48, 10868–10870. doi:10.1021/ic9013703

Biruete, A., Hill Gallant, K. M., Lindemann, S. R., Wiese, G. N., Chen, N. X., and Moe, S. M. (2020). Phosphate Binders and Nonphosphate Effects in the Gastrointestinal Tract. *J. Ren. Nutr.* 30, 4–10. doi:10.1053/j.jrn.2019.01.004

Block, G. A., Klassen, P. S., Lazarus, M. J., Ofsthun, N., Lowrie, E. G., Chertow, G. M., et al. (2004). Mineral Metabolism, Mortality, and Morbidity in Maintenance Hemodialysis. *J. Am. Soc. Nephrol.* 15, 2208–2218. doi:10.1097/01.ASN.0000133041.27682.A2

Block, G., Hulbert-Shearon, T., Levin, N., and Port, F. (1998). Association of Serum Phosphorus and Calcium X Phosphate Product with Mortality Risk in Chronic Hemodialysis Patients: A National Study. *Am. J. Kidney Dis.* 31, 607–617. doi:10.1053/ajkd.1998.v31.pm9531176

Bretonniere, Y., Cann, M. J., Parker, D., and Slater, R. (2004). Design, Synthesis and Evaluation of Ratiometric Probes for Hydrogencarbonate Based on Europium Emission. *Org. Biomol. Chem.* 2, 1624–1632. doi:10.1039/b400734b

Burai, L., Hietapelto, V., Király, R., Tóth, é., and Brücher, E. (1997). Stability Constants and1H Relaxation Effects of Ternary Complexes Formed between Gd-Dtpa, Gd-Dtpa-Bma, Gd-Dota, and Gd-Edta and Citrate, Phosphate, and Carbonate Ions. *Magn. Reson. Med.* 38, 146–150. doi:10.1002/mrm.1910380120

Daumann, L. J., Tatum, D. S., Andolina, C. M., Pacold, J. I., D'Aléo, A., Law, G.-l., et al. (2016). Effects of Ligand Geometry on the Photophysical Properties of Photoluminescent Eu(III) and Sm(III) 1-Hydroxypyridin-2-One Complexes in Aqueous Solution. *Inorg. Chem.* 55, 114–124. doi:10.1021/acs.inorgchem.5b01927

Doble, D. M. J., Melchior, M., O'Sullivan, B., Siering, C., Xu, J., Pierre, V. C., et al. (2003). Toward Optimized High-Relaxivity MRI Agents: The Effect of Ligand Basicity on the Thermodynamic Stability of Hexadentate Hydroxypyridonate/Catecholate Gadolinium(III) Complexes. *Inorg. Chem.* 42, 4930–4937. doi:10.1021/ic026240s

Floege, J. (2016). Phosphate Binders in Chronic Kidney Disease: a Systematic Review of Recent Data. *J. Nephrol.* 29, 329–340. doi:10.1007/s40620-016-0266-9

Ganesh, S. K., Stack, A. G., Levin, N. W., Hulbert-Shearon, T., and Port, F. K. (2001). Association of Elevated Serum PO4, Ca × PO4Product, and Parathyroid Hormone with Cardiac Mortality Risk in Chronic Hemodialysis Patients. *Jasn* 12, 2131–2138. doi:10.1681/asn.v12102131

Hargrove, A. E., Nieto, S., Zhang, T., Sessler, J. L., and Anslyn, E. V. (2011). Artificial Receptors for the Recognition of Phosphorylated Molecules. *Chem. Rev.* 111, 6603–6782. doi:10.1021/cr100242s

Harris, S. M., Nguyen, J. T., Pailloux, S. L., Mansergh, J. P., Dresel, M. J., Swanholm, T. B., et al. (2017). Gadolinium Complex for the Catch and Release of Phosphate from Water. *Environ. Sci. Technol.* 51, 4549–4558. doi:10.1021/acs.est.6b05815

Huang, S.-Y., and Pierre, V. C. (2018). A Turn-On Luminescent Europium Probe for Cyanide Detection in Water. *Chem. Commun.* 54, 9210–9213. doi:10.1039/c8cc05114c

Huang, S.-Y., Qian, M., and Pierre, V. C. (2019). A Combination of Factors: Tuning the Affinity of Europium Receptors for Phosphate in Water. *Inorg. Chem.* 58, 16087–16099. doi:10.1021/acs.inorgchem.9b02650

Huang, S.-Y., Qian, M., and Pierre, V. C. (2020). The Ligand Cap Affects the Coordination Number but Not Necessarily the Affinity for Anions of Tris-Bidentate Europium Complexes. *Inorg. Chem.* 59, 4096–4108. doi:10.1021/acs.inorgchem.0c00137

Jocher, C. J., Moore, E. G., Xu, J., Avedano, S., Botta, M., Aime, S., et al. (2007). 1,2-Hydroxypyridonates as Contrast Agents for Magnetic Resonance Imaging: TREN-1,2-HOPO. *Inorg. Chem.* 46, 9182–9191. doi:10.1021/ic700985j

Klungness, G. D., and Byrne, R. H. (2000). Comparative Hydrolysis Behavior of the Rare Earths and Yttrium: the Influence of Temperature and Ionic Strength. *Polyhedron* 19, 99–107. doi:10.1016/s0277-5387(99)00332-0

Kumar, K., Chang, C. A., and Tweedle, M. F. (1993). Equilibrium and Kinetic Studies of Lanthanide Complexes of Macrocyclic Polyamino Carboxylates. *Inorg. Chem.* 32, 587–593. doi:10.1021/ic00057a017

Marcus, Y. (1991). Thermodynamics of Solvation of Ions. Part 5.-Gibbs Free Energy of Hydration at 298.15 K. *J. Chem. Soc. Faraday Trans.* 87, 2995–2999. doi:10.1039/ft9918702995

Ménesguen, A., Desmit, X., Dulière, V., Lacroix, G., Thouvenin, B., Thieu, V., et al. (2018). How to Avoid Eutrophication in Coastal Seas? A New Approach to Derive River-specific Combined Nitrate and Phosphate Maximum Concentrations. *Sci. Total Environ.* 628–629, 400–414. doi:10.1016/j.scitotenv.2018.02.025

Pal, S., Ghosh, T. K., Ghosh, R., Mondal, S., and Ghosh, P. (2020). Recent Advances in Recognition, Sensing and Extraction of Phosphates: 2015 Onwards. *Coord. Chem. Rev.* 405, 213128. doi:10.1016/j.ccr.2019.213128

Pálinkás, Z., Roca-Sabio, A., Mato-Iglesias, M., Esteban-Gómez, D., Platas-Iglesias, C., de Blas, A., et al. (2009). Stability, Water Exchange, and Anion Binding Studies on Lanthanide (III) Complexes with a Macrocyclic Ligand Based on 1, 7-diaza-12-crown-4: Extremely Fast Water Exchange on the Gd3+ Complex. *Inorg. Chem.* 48, 8878–8889. doi:10.1021/ic9011197

Pierre, V. C., Botta, M., Aime, S., and Raymond, K. N. (2006). Substituent Effects on Gd(III)-Based MRI Contrast Agents: Optimizing the Stability and Selectivity of the Complex and the Number of Coordinated Water Molecules1. *Inorg. Chem.* 45, 8355–8364. doi:10.1021/ic061262q

Pierre, V. C., Botta, M., Aime, S., and Raymond, K. N. (2006). Tuning the Coordination Number of Hydroxypyridonate-Based Gadolinium Complexes: Implications for MRI Contrast Agents. *J. Am. Chem. Soc.* 128, 5344–5345. doi:10.1021/ja057805x

Pierre, V. C., Melchior, M., Doble, D. M. J., and Raymond, K. N. (2004). Toward Optimized High-Relaxivity MRI Agents: Thermodynamic Selectivity of Hydroxypyridonate/Catecholate Ligands1. *Inorg. Chem.* 43, 8520–8525. doi:10.1021/ic0493447

Puerta, D. T., Botta, M., Jocher, C. J., Werner, E. J., Avedano, S., Raymond, K. N., et al. (2006). Tris(pyrone) Chelates of Gd(III) as High Solubility MRI-CA. *J. Am. Chem. Soc.* 128, 2222–2223. doi:10.1021/ja057954f

Ramakrishnam Raju, M. V., Harris, S. M., and Pierre, V. C. (2020). Design and Applications of Metal-Based Molecular Receptors and Probes for Inorganic Phosphate. *Chem. Soc. Rev.* 49, 1090–1108. doi:10.1039/c9cs00543a

Ramakrishnam Raju, M. V., Wilharm, R. K., Dresel, M. J., McGreal, M. E., Mansergh, J. P., Marting, S. T., et al. (2019). The Stability of the Complex and the Basicity of the Anion Impact the Selectivity and Affinity of Tripodal Gadolinium Complexes for Anions. *Inorg. Chem.* 58, 15189–15201. doi:10.1021/acs.inorgchem.9b02133

Schindler, D. W., Hecky, R. E., Findlay, D. L., Stainton, M. P., Parker, B. R., Paterson, M. J., et al. (2008). Eutrophication of Lakes Cannot Be Controlled by Reducing Nitrogen Input: Results of a 37-year Whole-Ecosystem experiment. *Proc. Natl. Acad. Sci.* 105, 11254–11258. doi:10.1073/pnas.0805108105

Shannon, R. D. (1976). Revised Effective Ionic Radii and Systematic Studies of Interatomic Distances in Halides and Chalcogenides. *Acta Cryst. Sect A.* 32, 751–767. doi:10.1107/s0567739476001551

Sherman, R. A. (2016). Hyperphosphatemia in Dialysis Patients: Beyond Nonadherence to Diet and Binders. *Am. J. Kidney Dis.* 67, 182–186. doi:10.1053/j.ajkd.2015.07.035

Smith, D. G., Pal, R., and Parker, D. (2012). Measuring Equilibrium Bicarbonate Concentrations Directly in Cellular Mitochondria and in Human Serum Using Europium/Terbium Emission Intensity Ratios. *Chem. Eur. J.* 18, 11604–11613. doi:10.1002/chem.201201738

Great Lakes Water Quality Agreement (2012). Oakbrook Terrace: International Joint Commission.

Wang, H., and Wang, H. (2009). Mitigation of lake Eutrophication: Loosen Nitrogen Control and Focus on Phosphorus Abatement. *Prog. Nat. Sci.* 19, 1445–1451. doi:10.1016/j.pnsc.2009.03.009

Weitz, E. A., Chang, J. Y., Rosenfield, A. H., Morrow, E. A., and Pierre, V. C. (2013). The Basis for the Molecular Recognition and the Selective Time-Gated Luminescence Detection of ATP and GTP by a Lanthanide Complex. *Chem. Sci.* 4, 4052. doi:10.1039/c3sc51583d

Weitz, E. A., Chang, J. Y., Rosenfield, A. H., and Pierre, V. C. (2012). A Selective Luminescent Probe for the Direct Time-Gated Detection of Adenosine Triphosphate. *J. Am. Chem. Soc.* 134, 16099–16102. doi:10.1021/ja304373u

Wilharm, R. K., Huang, S.-Y., Gugger, I. J., and Pierre, V. C. (2021). A Walk across the Lanthanide Series: Trend in Affinity for Phosphate and Stability of Lanthanide Receptors from La(III) to Lu(III). *Inorg. Chem.* 60, 15808–15817. doi:10.1021/acs.inorgchem.1c02462

Xu, J., Churchill, D. G., Botta, M., and Raymond, K. N. (2004). Gadolinium(III) 1,2-Hydroxypyridonate-Based Complexes: Toward MRI Contrast Agents of High Relaxivity1. *Inorg. Chem.* 43, 5492–5494. doi:10.1021/ic049028s

Conflict of Interest: The authors declare that the research was conducted in the absence of any commercial or financial relationships that could be construed as a potential conflict of interest.

Publisher's Note: All claims expressed in this article are solely those of the authors and do not necessarily represent those of their affiliated organizations, or those of the publisher, the editors and the reviewers. Any product that may be evaluated in this article, or claim that may be made by its manufacturer, is not guaranteed or endorsed by the publisher.

frontiers in Chemistry

ORIGINAL RESEARCH
published: 08 March 2022
doi: 10.3389/fchem.2022.827530

Electron Transport Lipids Fold Within Membrane-Like Interfaces

*Margaret M. Braasch-Turi[1†], Jordan T. Koehn[1†], Kateryna Kostenkova[1], Cameron Van Cleave[1], Jacob W. Ives[1], Heide A. Murakami[1], Dean C. Crick[2,3] and Debbie C. Crans[1,2]**

[1]Chemistry Department, Colorado State University, Fort Collins, CO, United States, [2]Cell and Molecular Biology Program, Colorado State University, Fort Collins, CO, United States, [3]Microbiology, Immunology, and Pathology Department, Colorado State University, Fort Collins, CO, United States

OPEN ACCESS

Edited by:
Parasuraman Jaisankar, Indian Institute of Chemical Biology (CSIR), India

Reviewed by:
Sumit Sharma, Ohio University, United States
Makoto Kawamukai, Shimane University, Japan
Alokmay Datta, University of Calcutta, India

***Correspondence:**
Debbie C. Crans
debbie.crans@colostate.edu

[†]These authors have contributed equally to this work and share first authorship

Specialty section:
This article was submitted to Chemical Biology, a section of the journal Frontiers in Chemistry

Received: 06 December 2021
Accepted: 07 January 2022
Published: 08 March 2022

Citation:
Braasch-Turi MM, Koehn JT, Kostenkova K, Van Cleave C, Ives JW, Murakami HA, Crick DC and Crans DC (2022) Electron Transport Lipids Fold Within Membrane-Like Interfaces. Front. Chem. 10:827530. doi: 10.3389/fchem.2022.827530

Lipoquinones, such as ubiquinones (UQ) and menaquinones (MK), function as essential lipid components of the electron transport system (ETS) by shuttling electrons and protons to facilitate the production of ATP in eukaryotes and prokaryotes. Lipoquinone function in membrane systems has been widely studied, but the exact location and conformation within membranes remains controversial. Lipoquinones, such as Coenzyme Q (UQ-10), are generally depicted simply as "Q" in life science diagrams or in extended conformations in primary literature even though specific conformations are important for function in the ETS. In this study, our goal was to determine the location, orientation, and conformation of UQ-2, a truncated analog of UQ-10, in model membrane systems and to compare our results to previously studied MK-2. Herein, we first carried out a six-step synthesis to yield UQ-2 and then demonstrated that UQ-2 adopts a folded conformation in organic solvents using ^{1}H-^{1}H 2D NOESY and ROESY NMR spectroscopic studies. Similarly, using ^{1}H-^{1}H 2D NOESY NMR spectroscopic studies, UQ-2 was found to adopt a folded, U-shaped conformation within the interface of an AOT reverse micelle model membrane system. UQ-2 was located slightly closer to the surfactant-water interface compared to the more hydrophobic MK-2. In addition, Langmuir monolayer studies determined UQ-2 resided within the monolayer water-phospholipid interface causing expansion, whereas MK-2 was more likely to be compressed out and reside within the phospholipid tails. All together these results support the model that lipoquinones fold regardless of the headgroup structure but that the polarity of the headgroup influences lipoquinone location within the membrane interface. These results have implications regarding the redox activity near the interface as quinone vs. quinol forms may facilitate locomotion of lipoquinones within the membrane. The location, orientation, and conformation of lipoquinones are critical for their function in generating cellular energy within membrane ETS, and the studies described herein shed light on the behavior of lipoquinones within membrane-like environments.

Keywords: lipoquinone, ubiquinone, menaquinone, folded conformation, 2D NMR, electron transport, membrane interface, Langmuir monolayer

1 INTRODUCTION

Molecular conformations are paramount to the physical and chemical properties that dictate recognition and function of molecules within biological systems. The location and conformation of lipoquinones within biological membranes is not well understood and highly debated (Kingsley and Feigenson, 1981; Michaelis and Moore, 1985; Ulrich et al., 1985; Salgado et al., 1993; Soderhall and Laaksonen, 2001; Afri et al., 2004; Galassi and Arantes, 2015; Quirk et al., 2016; Koehn et al., 2018b; Koehn et al., 2019). Lipoquinones are hydrophobic membrane-bound molecules consisting of a redox-active quinone headgroup and an isoprenyl side chain. There are three major structural subgroups of lipoquinones which differ only in the structure of the headgroup. Ubiquinones (UQ), such as Ubiquinone-10 (UQ-10, **Figure 1A**), comprise of a benzoquinone ring with two methoxy substituents, plastoquinones (PQ) with a dimethylbenzoquinone, such as plastoquinone-9 (PQ-9), and menaquinones (MK), such as menaquinone-9 (MK-9, **Figure 1B**), contain a methylnaphthoquinone ring. Lipoquinones function as essential components of the respiratory electron transport system (ETS), where they shuttle electrons and protons between membrane-bound protein complexes, ultimately ending in the production of ATP (Nowicka and Kruk, 2010; Kawamukai, 2018). UQ and MK are involved in the ETS of oxidative phosphorylation in mammalian and bacterial cells, but PQ is involved in photosynthetic ETS in plants and photosynthetic bacteria (Kawamukai, 2018). For the purpose of this study, we will focus on UQ and MK. Even though the ETS is vital for life through the production of ATP, the role of lipoquinones is commonly distilled to an abbreviation within a diagram, such as "Q" for Coenzyme Q (UQ-10), the major electron transport agent in eukaryotes (Trumpower, 1981; Kawamukai, 2018), ignoring the conformation and location of these molecules as a whole. Similar to lipoquinones, polyprenyl compounds have been known to adopt preorganized, folded conformations presumably due to hydrophobic effect and π-π interactions (Woodward and Bloch, 1953; Murgolo et al., 1989). The synthesis of cholesterol relies on the preorganized conformation of squalene epoxide to produce a single stereochemical outcome out of 256 (2^8) possible conformations (Woodward and Bloch, 1953). Moreover, dolichol-19 adopts a coiled conformation (Murgolo et al., 1989). A handful of computational studies have investigated the dihedral angle (φ) about the C2C3CβCγ bond (as shown in red in **Figure 1C**) in UQs (Nilsson et al., 2001b; Ceccarelli et al., 2003; Galassi and Arantes, 2015; Eddine et al., 2020), MKs (Eddine et al., 2020), and plastoquinones (Nilsson et al., 2001a; Jong et al., 2015; Eddine et al., 2020), which determined φ was ~90°, 100°, and 90°, respectively. In this study we determined the location, orientation, and conformation of UQ-2 (**Figure 1C**), a truncated, representative analog for native UQ-10, using 1D and 2D NMR spectroscopic methods in organic solvents and in biological model membrane systems comprised of AOT reverse micelles (RM) (Van Horn et al., 2008). This analysis will allow us to compare the location and conformation of UQ-2 with MK-2 (**Figure 1D**) (Koehn et al., 2018b) in membrane-like environments to shed light on the controversies regarding the location and conformation of lipoquinones in cellular membranes.

The location of UQ-10 within the membrane has been widely studied using experimental and computational methods, but it continues to be controversial. Briefly, there is no consensus regarding the location of UQ-10 with its locations spanning the entire width of the membrane bilayer leaflet. Out of these studies, three schools of thought have emerged; the quinone headgroup is located: 1) at or near the lipid headgroups (Kingsley and Feigenson, 1981; Stidham et al., 1984; Lenaz et al., 1992; Salgado et al., 1993; Galassi and Arantes, 2015; Gómez-Murcia et al., 2016; Kaurola et al., 2016; Quirk et al., 2016; Teixeira and Arantes, 2019), 2) within the acyl chains (Michaelis and Moore, 1985; Cornell et al., 1987; Chazotte

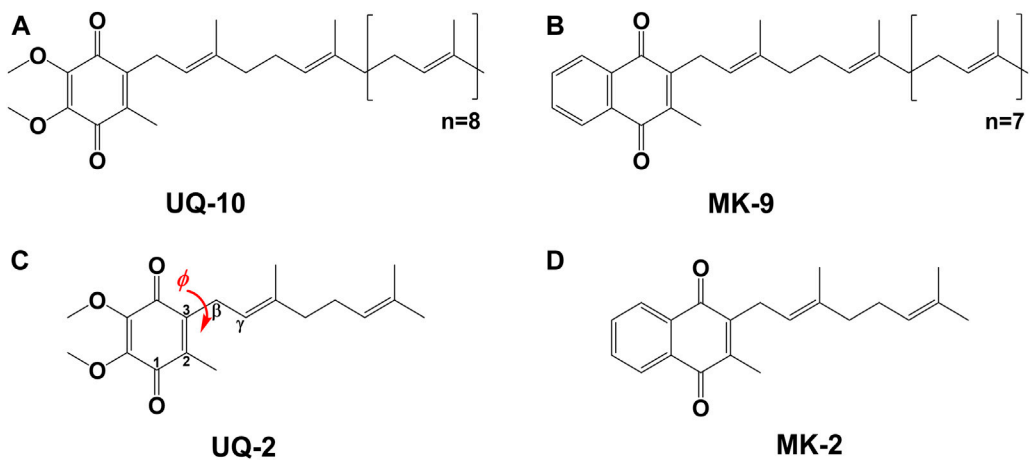

FIGURE 1 | Schematic structures of native lipoquinones: **(A)** Ubiquinone-10 (UQ-10), and **(B)** Menaquinone-9 (MK-9). Schematic structures of truncated lipoquinone analogs: **(C)** Ubiquinone-2 (UQ-2) with the C2C3CβCγ bond indicated in red with dihedral angle, φ, and **(D)** Menaquinone-2 (MK-2).

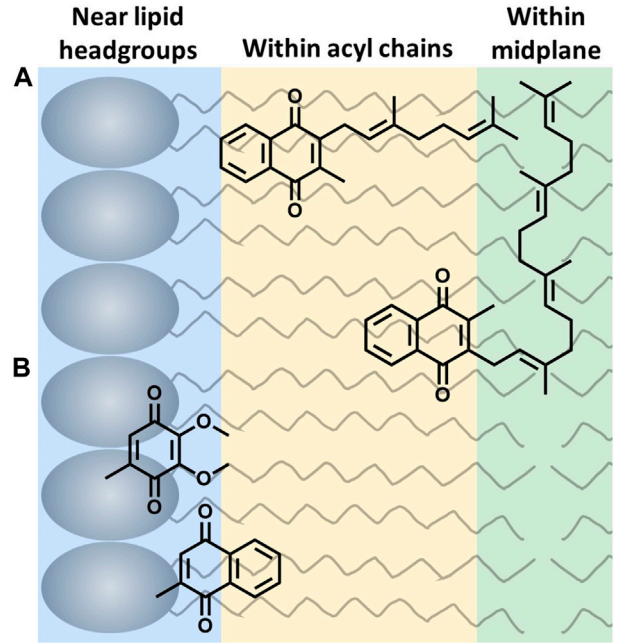

FIGURE 2 | Three possible locations of lipoquinone headgroup: **(A)** Example of the influence of the isoprenyl side chain length on location of the quinone headgroup. MK-2 and MK-4 are shown as a 2D schematics. MK-2 has been determined to fold in membrane-like interfaces (Koehn et al., 2018b). **(B)** Relative placement based on headgroup polarity (side chain omitted for clarity) (Van Cleave et al., 2020; Van Cleave et al., 2021).

et al., 1991; Salgado et al., 1993; Metz et al., 1995; Afri et al., 2004; Hauss et al., 2005), or 3) within the bilayer midplane (Ulrich et al., 1985; Ondarroa and Quinn, 1986; Soderhall and Laaksonen, 2001) (**Figure 2**). Even though the location of the headgroup is controversial, the field does seem to agree that at least part of the isoprenyl side chain is embedded within the bilayer midplane, and the headgroup is thought to extend into one of the membrane leaflets. This bend (~90° turn) in the isoprenyl side chain allows UQ-10 to be accommodated within the bilayer, which addresses the fact that UQ-10 is roughly the same length as a typical phospholipid bilayer if UQ-10 were in fully-extended conformation (Trumpower, 1981).

Two hypotheses have been reported to explain the headgroup position within the membrane. First, the length of the isoprenyl side chain was reported to affect the position of the quinone headgroup by pulling the headgroup closer to the midplane as the side chain length increases. For example, the quinone headgroup of MK-4 would be found closer to the midplane than MK-2 (**Figure 2A**). On the other hand, the polarity of the headgroup is also thought to anchor its location within the membrane. Recent computational studies by Arantes and coworkers determined UQ associates with the lipid headgroups (Galassi and Arantes, 2015; Teixeira and Arantes, 2019). Together, we recently showed for the series of MK-1, MK-2, MK-3, and MK-4 that the location of the headgroup remained constant as the side chain length increased using both experimental and computational techniques (Van Cleave et al., 2020). As a consequence of the latter, one would anticipate a difference in the location of the more polar UQ headgroup compared to the more hydrophobic MK headgroup as illustrated in **Figure 2B** (Van Cleave et al., 2020). Lipoquinone headgroup is also linked to diffusive motion. "Swimming" lipoquinones are associated with the phospholipid headgroups, and "diving" are found near the midplane. A few computational and experimental studies determined UQ and various analogs are stabilized in the swimming position (Soderhall and Laaksonen, 2001; Hoyo et al., 2017). A recent computational study determined the lipoquinone position depends on the local protein content of the membrane (Singharoy et al., 2020). If the region is lipid-rich, swimming lipoquinone is the dominant species, and diving lipoquinones are the most common in the vicinity of protein complexes (Gupta et al., 2020; Singharoy et al., 2020).

Although lipoquinone conformation is likely to be critical for function and recognition, the topic of conformation of the UQ and MK headgroup relative to the isoprenyl side chain is curiously ignored in the literature aside from a handful of computational studies (Joela et al., 1997; Bernardo et al., 1998; Lenaz et al., 1999; Nilsson et al., 2001a; Nilsson et al., 2001b; Soderhall and Laaksonen, 2001; Ceccarelli et al., 2003; Tekin and Erkoc, 2010; Galassi and Arantes, 2015; Jong et al., 2015; Ismail et al., 2016; Kaurola et al., 2016; Eddine et al., 2020; Feng et al., 2021). Additionally, a few of the computational studies investigating the location of lipoquinones in the membrane contained figures suggesting φ was ~90° (Joela et al., 1997; Bernardo et al., 1998; Lenaz et al., 1999; Soderhall and Laaksonen, 2001; Tekin and Erkoc, 2010; Ismail et al., 2016; Kaurola et al., 2016; Feng et al., 2021), leading to the expectation of a folded conformation. However, there was no discussion regarding the conformation of the headgroup relative to the isoprenyl side chain prior to our work in 2018 (Koehn et al., 2018b). The implications of conformation on lipoquinone locomotion were hypothesized by Joela and coworkers (Joela et al., 1997). Therein, they speculated the quinone headgroup is located close to the enzyme active site and moves between membrane and enzyme binding pocket by rotating about the C2C3CβCγ bond. They describe this limited movement with a stationary side chain and a mobile headgroup as if the "tail is wagging the dog." The isoprenyl chain would serve to the anchor the quinone headgroup location. Since we previously found that the side chain did not dictate the headgroup location for MK-1 through MK-4, we hypothesized that the anchoring of the headgroup drives the extension of the side chain, and that the more polar UQ-2 headgroup will be closer to the interface than the more hydrophobic headgroup of MK-2. Hence, we carried out studies in which the location and conformation of UQ-2 were elucidated in environments that allow direct comparison to previously reported MK-2, which folds within model membrane interfaces (Koehn et al., 2018b). This study will illuminate how headgroup structure changes the position, orientation, and conformation, which are critical to recognition and function, of prominent lipoquinones within membrane-like environments.

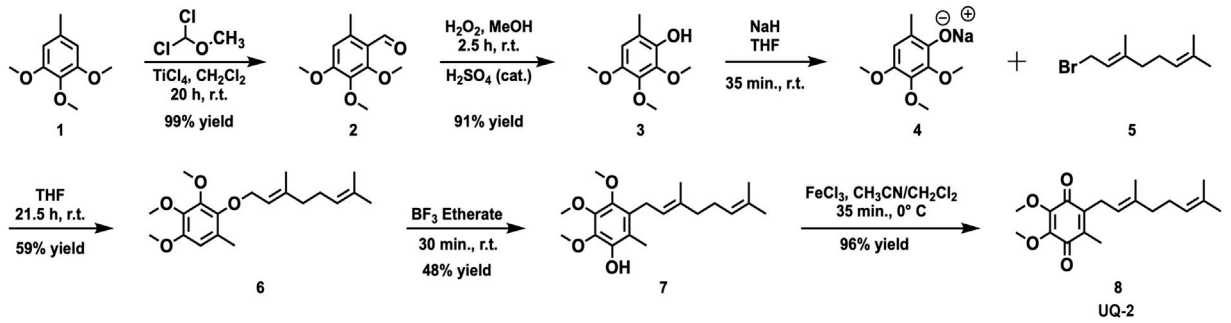

SCHEME 1 | Synthetic scheme for the six-step synthesis to obtain UQ-2 **8** from 3,4,5-trimethoxytoluene **1** using modified protocols as reported (Matsumoto et al., 1984; Lu and Chen, 2004; Bovicelli et al., 2008).

2 RESULTS AND DISCUSSION

2.1 Synthesis of UQ-2

UQ-2 **8** was prepared using a 6-step synthesis (**Scheme 1**) starting from commercially available 3,4,5-trimethoxytoluene **1**. The synthetic route has been reported in literature (Lu and Chen, 2004; Bovicelli et al., 2008); however, we scaled up the reactions and used modified procedures and conditions to overcome synthetic challenges encountered. The aldehyde **2** was prepared efficiently and was practically pure upon workup using a Rieche formylation reaction with $TiCl_4$, which is the traditional Lewis acid catalyst for this reaction. Efforts to achieve this reaction using $AlCl_3$ as the Lewis acid catalyst were low yielding and resulted in impure compound in our hands. An acid-catalyzed Dakin oxidation reaction was used to afford phenol **3** in excellent yield even after chromatographic purification (Matsumoto et al., 1984). The geranyl ether **6** was prepared via an S_N2 reaction between phenolate **4** and geranyl bromide **5** in a modest yield. Efforts to achieve the allylic rearrangement to yield compound **7** close to yields reported in literature (Bovicelli et al., 2008) was met with limited success. A 48% yield was the highest yield we obtained compared to 73% in literature (Bovicelli et al., 2008). Attempts to improve this yield failed, and reactions times longer than 30 min decreased the yield and appeared to increase the amount of unknown side products. While compound **7** was efficiently oxidized to **8** using $FeCl_3{\cdot}6H_2O$ in a mixture of dichloromethane and acetonitrile at 0°C, attempts to follow a published procedure (Bovicelli et al., 2008) using $FeCl_3$ in a mixture of ethanol and H_2O at ambient temperature yielded only starting material.

2.2 1D ^{1}H NMR Spectroscopic Studies of UQ-2 in Organic Solvents

To establish that UQ conformation is sensitive to its surrounding environment, UQ-2 was first characterized using 1D ^{1}H NMR spectroscopy. **Figure 3** shows the 1D ^{1}H NMR spectra of UQ-2 in isooctane (2,2,4-trimethylpentane), d_6-benzene, d_5-pyridine, d_6-DMSO, d_3-acetonitrile, and D_2O. The observed chemical shifts of UQ-2 vary dramatically in the different solvents shown. Different spectroscopic trends are observed in the hydrophobic (isooctane, d_5-pyridine, and d_6-benzene) and the hydrophilic

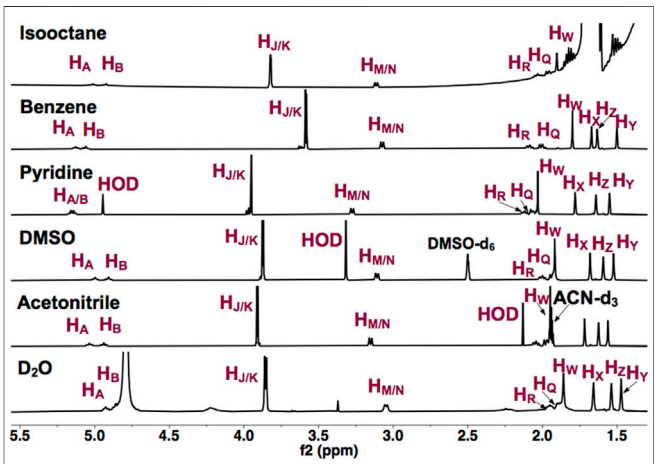

FIGURE 3 | ^{1}H NMR (400 MHz) spectra of UQ-2 in hydrophobic (isooctane (2,2,4-trimethtylpentane), d_6-benzene, and d_5-pyridine) and hydrophilic (d_6-DMSO, d_3-acetonitrile, and D_2O) solvents.

(d_3-acetonitrile, d_6-DMSO, and H_2O/D_2O) solvent environments. For example, the isoprenyl protons H_M/H_N and methoxy protons H_J/H_K are observed at significantly different chemical shifts between the two different classes of solvents. The observations could be described by conformational changes of UQ-2 in the various solvent environments investigated, alterations of the electronic state due to interaction with the solvent, or most likely, a combination of both. There were similarities and differences among the investigated solvents. For the hydrophobic solvents, protons H_M/H_N have similar chemical shifts in isooctane and benzene, but they appear more downfield in pyridine, whereas they appear in similar chemical shifts in the hydrophilic solvents. The chemical shifts for H_J and H_K are in different locations in each solvent, which suggests the methoxy groups are changing environments in the different solvents (Nilsson et al., 2001b). The chemical shifts of the vinyl protons H_A and H_B are increasingly more downfield as the polarity of the hydrophobic solvents increases. In the hydrophilic solvents, H_A and H_B are found in

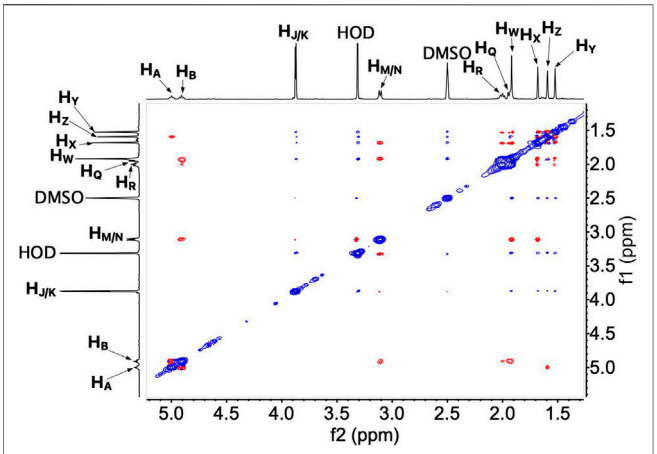

FIGURE 4 | Full ^{1}H-^{1}H 2D NOESY spectrum of UQ-2 in DMSO.

similar chemical shifts aside from D_2O where they appear slightly upfield and obscured by the HOD peak.

2.3 ^{1}H-^{1}H 2D NOESY and ^{1}H-^{1}H 2D ROESY NMR Spectroscopic Studies of UQ-2 in d_6-DMSO, d_3-Acetonitrile, d_6-Benzene, and d_5-Pyridine

To determine the conformation of UQ-2 in organic solvents, we utilized two complementary 2D NMR methods, ^{1}H-^{1}H 2D NOESY and ^{1}H-^{1}H 2D ROESY (Jones et al., 2011). We chose to highlight the NOESY and ROESY spectra of UQ-2 in d_6-DMSO for direct comparison to our previous work with MK-2 (Koehn et al., 2018b). The corresponding spectra for d_3-acetonitrile, d_6-benzene, and d_5-pyridine can be found in **Supplementary Figures S15–S23** in the Supplementary Material. Looking at the structure of UQ-2, a folded conformation, which is defined by a ~90° dihedral angle about the C2C3CβCγ bond, would be indicated by cross peaks between the headgroup and particular protons on the isoprenyl side chain such as the methyl protons H_W and protons further down the side chain, such as H_A, H_Y, and H_Z. In the full NOESY spectrum in d_6-DMSO, there is a cross peak observed between H_W and vinyl protons, H_A and H_B (**Figure 4** and proton labeling scheme is shown in **Figure 5A**). The proton H_B is close enough to H_W have NOE interactions; however, H_A would be too far away to have NOE interactions unless the molecule is in a folded conformation. In addition, there are cross peaks that confirm the 1D ^{1}H NMR spectra assignments along the isoprenyl tail, such as H_W and allylic protons H_M and H_N and between H_A/H_B and methyl protons H_X, H_Y, and H_Z. The folded conformation is also suggested by the cross peaks observed between methyl protons H_W and methyl protons, H_X, H_Y and H_Z (**Figure 5B**). These cross peaks are also observed in the ROESY spectrum (**Figures 5C,D**. Enlarged full ROESY spectrum is also shown in the Supplementary Materials: **Supplementary Figure S13**). These cross peaks are indicative of a U-shaped conformation (example shown in **Figure 6**), placing the terminal methyl groups over the quinone headgroup for UQ-2 in d_6-DMSO.

In the case of the 2D NOESY and ROESY spectra of UQ-2 in d_3-acetonitrile (**Supplementary Figures S16, S17**), there are cross peaks observed between H_W and vinyl protons, H_A and H_B, and methyl protons, H_X, H_Y, and H_Z, similar to d_6-DMSO. Together these suggest a folded, U-shaped conformation, but the results are somewhat inconclusive. The reference peak for d_3-acetonitrile, 1.93 ppm, is close to H_W (1.94 ppm) and almost overlapping. Therefore, it is hard to conclude if the cross peaks observed are a result of intramolecular NOE interactions or interactions with the solvent. For 2D NOESY and ROESY spectra of UQ-2 in d_6-benzene (**Supplementary Figures S19, S20**), there are cross peaks observed between H_W and H_X, and H_M/H_N. In both the flat-extended and folded-extended conformations (example shown in **Figure 6**), H_X, and H_M/H_N are all within the 5 Å NOE range of H_W. To distinguish between the two, we looked for cross peaks between H_W and the terminal methyl protons, H_Y and H_Z. In the folded-extended conformation, the average distance between H_W and H_Y is approximately 5.1 Å. In the ROESY spectrum, there are cross peaks present between H_W and H_Y and H_Z (**Supplementary Figure S20**) and they are present in the corresponding NOESY (**Supplementary Figure S19**). Therefore, the presence of a cross peak between H_W and H_Y in the NOESY (**Supplementary Figure S19**) suggests H_Y is inside the NOE range and therefore indicates a folded, open U-shaped conformation in d_6-benzene. Similar observations were found for 2D NOESY and ROESY spectra for UQ-2 in d_5-pyridine (**Supplementary Figures S22, S23**). There are cross peaks observed between H_W and H_A/H_B, H_X, and H_M/H_N, but there is a cross peak observed between H_W and H_Y. Similar to benzene, this together suggests UQ-2 adopts a folded, open U-shaped conformation in d_5-pyridine.

2.4 Illustrating UQ-2 Conformations Determined by NMR Using Molecular Mechanics

UQ-2 has a short repeating isoprenyl chain (C_{10}) but enough carbons with numerous degrees of rotational freedom; therefore, even the truncated version of UQ-10, UQ-2, can assume many different specific conformations and still be considered folded by our definition. We created 3D conformations (**Figure 7**) of UQ-2 for visualization using Molecular Mechanics where intramolecular distances between specific protons obtained from 2D NOESY/ROESY NMR spectra (**Supplementary Table S1**) were used as geometric constraints. While the exact position of the isoprenyl side chain varies slightly from solvent to solvent, UQ-2 adopts a folded conformation in all four solvents examined in the 2D NMR studies, where the dihedral angle about the C2C3CβCγ bond (**Figure 1C**) is ~90°.

To understand the differences between the conformations of UQ-2 and MK-2, we first had to determine the distances between the protons on the isoprenyl side chain and the headgroup methyl proton H_W. We used the volume integrals from the 2D NOESY spectra and correlated them to intramolecular distances. The

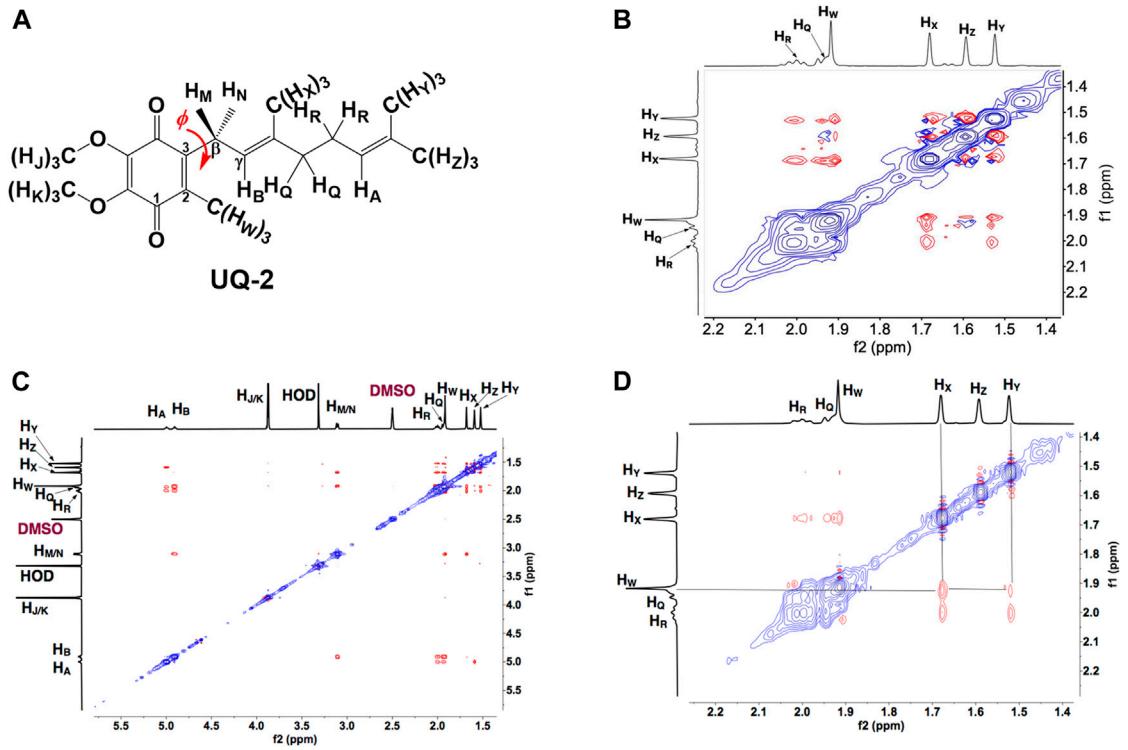

FIGURE 5 | (A) Proton labeling scheme for UQ-2. **(B)** Partial ^{1}H-^{1}H 2D NOESY spectrum of UQ-2 in DMSO. **(C)** A larger ^{1}H-^{1}H 2D ROESY spectrum of UQ-2 in DMSO. Full ROESY spectrum can also be found in the Supplementary Material, **Supplementary Figure S13**. **(D)** Partial ^{1}H-^{1}H 2D ROESY spectrum of UQ-2 in DMSO.

volume integral of the H_W and H_M/H_N cross peak, which has a known intramolecular distance of ~3.5 Å, was set to 1, and each volume integral was standardized against it. From here, the values obtained were used to determine if the cross peaks were strong (>1.5), medium (0.6–1.5), or weak (<0.6). These intensities were translated to distance in Ångstroms accordingly: 1) strong (<3 Å), 2) medium (3–4 Å), and 3) weak (>4 Å). The intramolecular distances were then used to construct the conformations, and MMFF94 minimization calculations were performed to correct bond lengths. The distances in **Supplementary Table S1** reflect the intramolecular distances post minimization.

DMSO and pyridine were chosen due to the distinctly different 1D ^{1}H NMR spectra to better illustrate the differences in conformation (Koehn et al., 2018b). Since NOESY and ROESY spectra are products of an average conformation, the intramolecular distances generated are representative of the most abundant conformation. As described previously, the interactions between headgroup methyl protons H_W and protons along the isoprenyl side chain, such as vinyl protons H_A and methyl protons H_X, H_Y, and H_Z, are critical to evaluate UQ-2 conformation in organic solvents. The distances between H_W and H_A, H_X, H_Y, and H_Z imply there is a folded conformation about the C2C3βCγ bond, and the position of the terminal methyl protons H_Y and H_Z relative to H_W suggest differences in the position of the end of the isoprenyl side chain: U-shaped or folded-extended conformation.

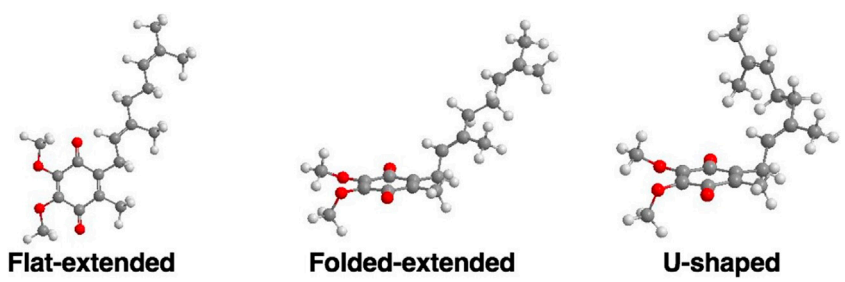

FIGURE 6 | Examples of three possible classes of UQ-2 conformations: Flat-extended, Folded-extended, and U-shaped (Koehn et al., 2018b; Koehn et al., 2019).

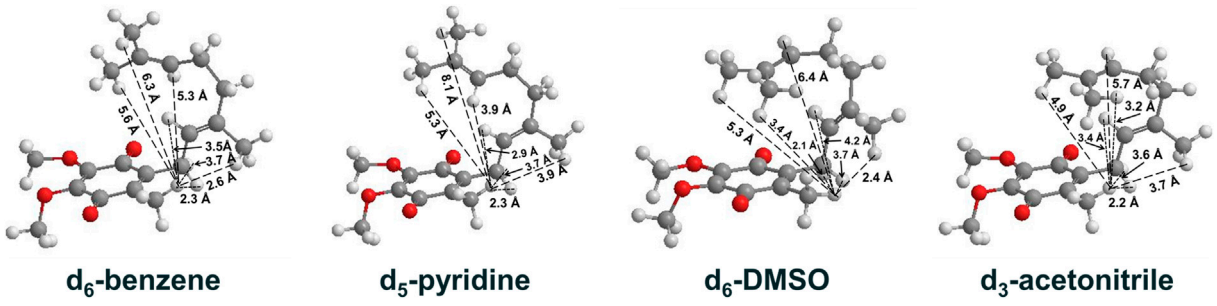

FIGURE 7 | UQ-2 conformations generated using 2D NMR data distance constraints and MMFF94 calculations to illustrate the conformations elucidated in d_6-benzene, d_5-pyridine, d_6-DMSO, and d_3-acetonitrile. Intramolecular distances (Å) between H_W and select protons on the side chain are shown (dashed lines).

For UQ-2 in d_5-pyridine, the intramolecular distance between H_W and H_X is shown to be 3.9 Å. The distance between H_W and vinyl proton, H_A, 3.9 Å, supports a folded conformation. The intramolecular distances between H_W and H_Y and H_Z were found to be 8.1 Å and 5.3 A, respectively. Although these values are outside the range of NOE influence, cross peaks were observed in the 2D NOESY and ROESY spectra (**Figures 4**, **5C**, respectively). Therefore, we cannot preclude the possibility that UQ-2 adopts both a folded-extended or a more open U-shaped conformation in d_5-pyridine. These results are in line with MK-2 in d_5-pyridine, which was previously found to adopt a folded-extended conformation (Koehn et al., 2018b).

We superimposed the conformations of UQ-2 in d_3-acetonitrile and d_6-DMSO to better visualize the minute differences observed between conformations (**Figure 8**). The superimposed conformations of UQ-2 in d_6-benzene and d_5-pyridine are found in the Supplementary Material (**Supplementary Figure S25**). In **Figure 8A**, UQ-2 in d_3-acetonitrile and d_6-DMSO are shown in green and purple, respectively. With the headgroups aligned, there is a slight variation in the dihedral angle along the C2C3CβCγ bond, and the trend continues along the sidechain through the second isoprene unit. This accounts for the differences observed in intramolecular distances toward the end of the isoprenyl side chain. The terminal methyl groups of UQ-2 in d_6-DMSO appear directly above the headgroup leading to a U-shaped conformation. The same methyl groups in d_3-acetonitrile appear to be above but not centered over the headgroup, which is consistent with the possibility of U-shaped or folded-extended conformation. In **Figure 8B**, the conformation of UQ-2 and MK-2 in d_6-DMSO are superimposed to visualize how the headgroup structure affects the conformation. The C2C3CβCγ bond in both UQ-2 and MK-2 are nearly identical to one another, but the conformation along the side chain starts to deviate past the first alkene. Taking into consideration the many degrees of freedom about the isoprenyl side chain, it is not unexpected to see deviations in conformation along the side chain.

The folded conformations observed for UQ-2 are likely a result of non-covalent interactions. Firstly, UQ-2 is folding upon itself to minimize interactions with the solvent due to the hydrophobic effect. This is especially apparent in the U-shaped conformations of UQ-2 in the hydrophilic solvents, DMSO and acetonitrile, whereas the hydrophobic solvents, pyridine and benzene, afford an open U-shaped or folded-extended conformation. Additionally, the folded conformation is likely reinforced by π-π interactions between the π bonds in the quinone headgroup and the isoprenyl side chain. This idea is supported by the work done on farnesol, where farnesol does not adopt a folded conformation, regardless of the increased number of degrees of freedom along the molecule (Zahn et al., 2000). Therefore, the presence of the quinone headgroup plays a significant role in the ability of the lipoquinone to adopt a folded conformation, but we only saw modest differences between the folded UQ-2 and MK-2 conformations. In addition to the presence of the lipoquinone headgroup, a study suggests the methyl proton, H_W, on the quinone also plays an important

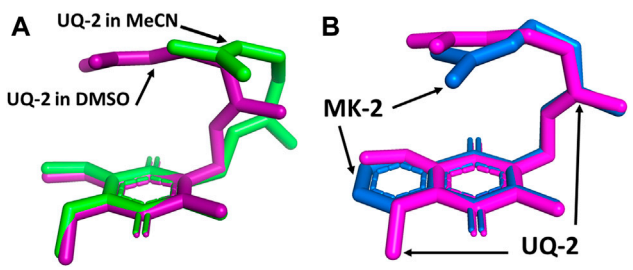

FIGURE 8 | Superimposed 3D conformations of **(A)** UQ-2 based on the 2D NMR data in d_3-acetonitrile (green) and d_6-DMSO (purple) and **(B)** UQ-2 (pink) and MK-2 (blue) based on the 2D NMR data in d_6-DMSO.

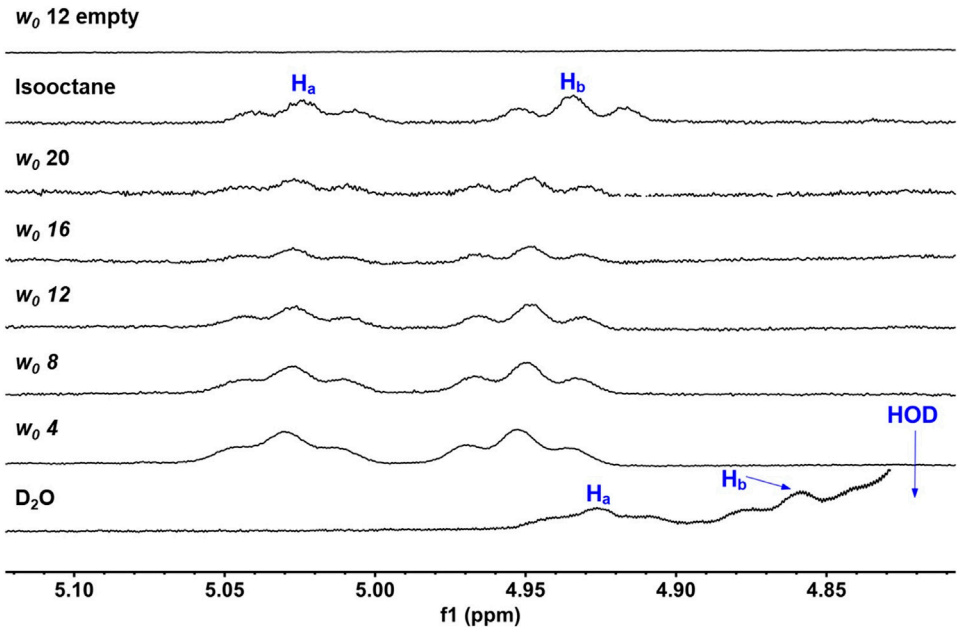

FIGURE 9 | 1D ^{1}H NMR (400 MHz) spectra of UQ-2's alkene protons, H_A and H_B, in D_2O, isooctane, and different sized RMs. An empty RM lacking UQ-2 is also shown for comparison. Peak labelling corresponds to the proton labelling scheme key in **Figure 5A**.

role in influencing a folded conformation (Eddine et al., 2020). The quinone methyl group serves as a rotational barrier by preventing the side chain from freely rotating between folded and flat conformations.

2.5 1D ^{1}H NMR Spectroscopic Studies of UQ-2 in RMs

Our ultimate objective was to determine how UQ-2 behaved with respect to membrane-like interfaces. We used a system comprised of nanosized water droplets encased in AOT surfactant to create reverse micelles (RMs) inside an isooctane (hydrophobic) solvent. This simple model system will provide useful information regarding location, orientation, and conformation of UQ-2 at an interface using NMR spectroscopy with minimal overlap between surfactant proton peaks and key UQ-2 proton peaks. 1D ^{1}H NMR spectra of varying RM sizes were collected in D_2O (w_0: 4, 8, 12, 16, 20, where $w_0 = [D_2O]/[AOT]$), shown in **Figure 9**. The placement of the UQ-2 molecules inside the membrane system was determined via the changes in chemical shift that UQ-2 protons undergo as the RM size changes. Typically, aromatic protons often offer ideal peaks to compare and analyze shifts, as they lie far from any AOT peaks. However, as there are no aromatic protons to observe in UQ-2, we instead observed the vinyl protons peaks (H_A/H_B), which are both triplet peaks that are easily discernable from the AOT peaks. The peak locations for H_A and H_B respectively are 5.02 and 4.93 ppm for isooctane, 5.03 and 4.95 ppm for w_0 20, 5.03 and 4.95 ppm for w_0 16, 5.03 and 4.95 ppm for w_0 12, 5.03 and 4.95 ppm for w_0 8, 5.03 and 4.95 ppm for w_0 4, 4.93 and 4.86 ppm for D_2O. The chemical shifts of these peaks do not change significantly enough as the RM changes in size to reliably indicate where in the RM interface the UQ-2 resides. However, the large shift between the D_2O sample and the RM samples (−0.10 ppm for H_A and −0.09 ppm for H_B from w_0 4 to D_2O) compared to the much smaller shift between the isooctane sample and the RM samples (0.01 ppm for H_a and 0.02 ppm for H_b from isooctane to w_0 20) would indicate that the UQ-2 does not reside within the bulk water or in the isooctane of the RM system, and thus UQ-2 must reside somewhere in the RM interface. However, 2D NMR studies will enable the exact location, orientation, and conformation of UQ-2 in RMs to be identified.

Dynamic Light Scattering (DLS) was used to determine the hydrodynamic radius of RMs containing UQ-2 and verify that RMs formed in the samples used and that the properties and stability of the samples were consistent with previous studies (see Section V of the **Supplementary Material**). DLS samples were prepared following the sample preparation method used for NMR spectroscopic studies except that DDI H_2O was used instead of D_2O. The results showed that RMs formed and that the sizes of the RMs made were in excellent agreement with that of the literature (Maitra, 1984). These results indicate that the introduction of UQ-2 into the RM system does not significantly affect the size or stability of the RMs.

2.6 ^{1}H-^{1}H 2D NOESY NMR Spectroscopic Studies of UQ-2 in a RM Model Membrane System

To determine the exact location, orientation, and conformation of UQ-2 within RMs, we obtained an ^{1}H-^{1}H 2D NOESY NMR of UQ-2 in a w_0 12 RM (**Figure 10**). **Figure 10A** shows a full NOESY spectrum. To elucidate the location and orientation of UQ-2 within the RM, we looked for the interactions of UQ-2 with AOT (**Figure 10C**). Methoxy protons H_J and H_K and

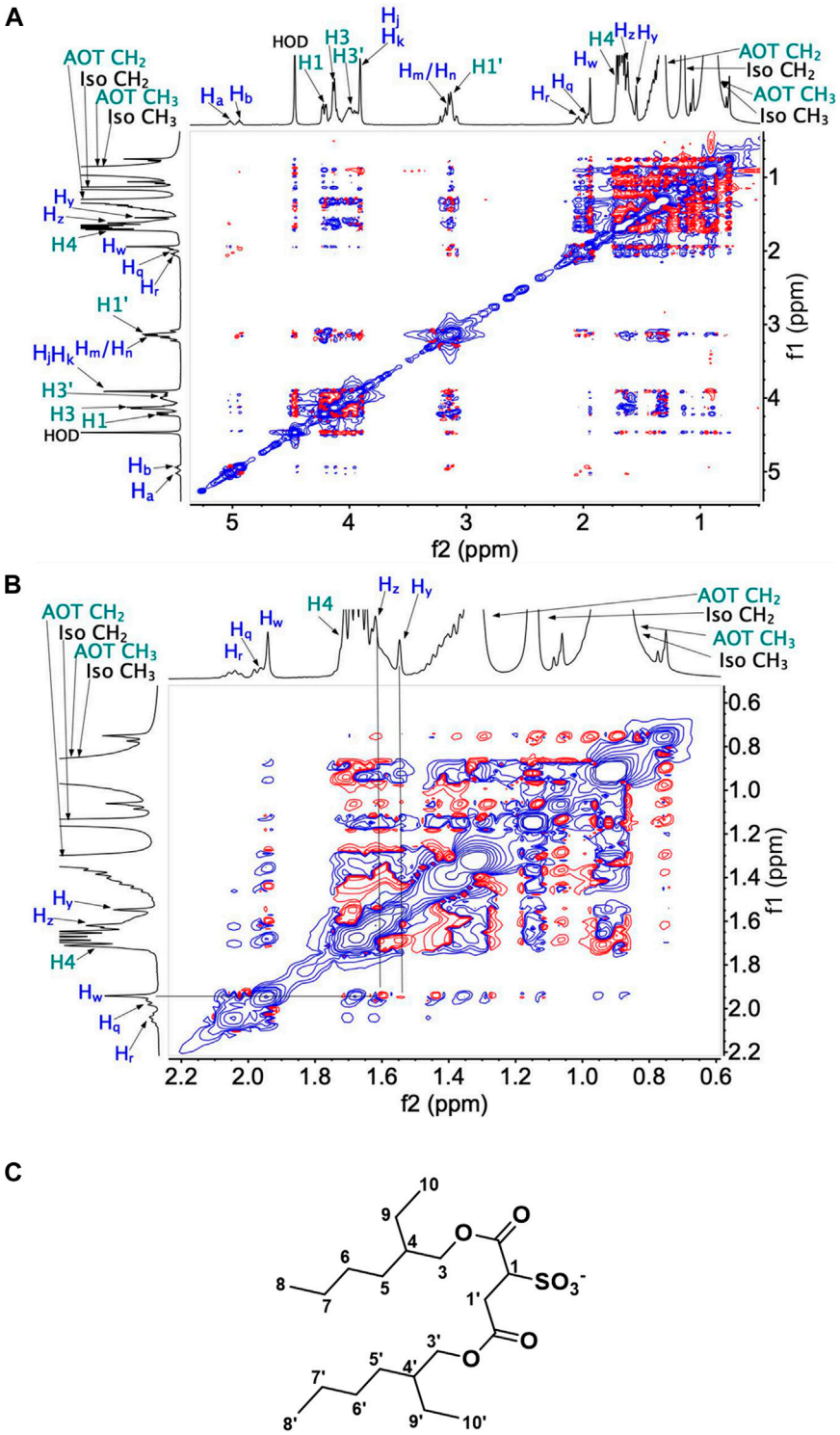

FIGURE 10 | ^{1}H-^{1}H 2D NOESY NMR spectra of UQ-2 in w_0 12 AOT-RM: **(A)** full spectrum, **(B)** partial spectrum. **(C)** Labeled structure of AOT. Blue text labels correspond to UQ-2 protons and teal text labels to AOT protons.

benzoquinone methyl protons H_W are shown to have cross peaks with AOT between H1′, H4, AOT-CH_2, and AOT-CH_3. Additionally, H_W shows cross peaks with H1, H3', and H3 of AOT. Vinyl protons H_A/H_B were found to have cross peaks with H1, H3, and H3'. Allylic protons H_M/H_N were found to have interactions with H1, H3, H3′ and AOT-CH_2, and H_Q/H_R were

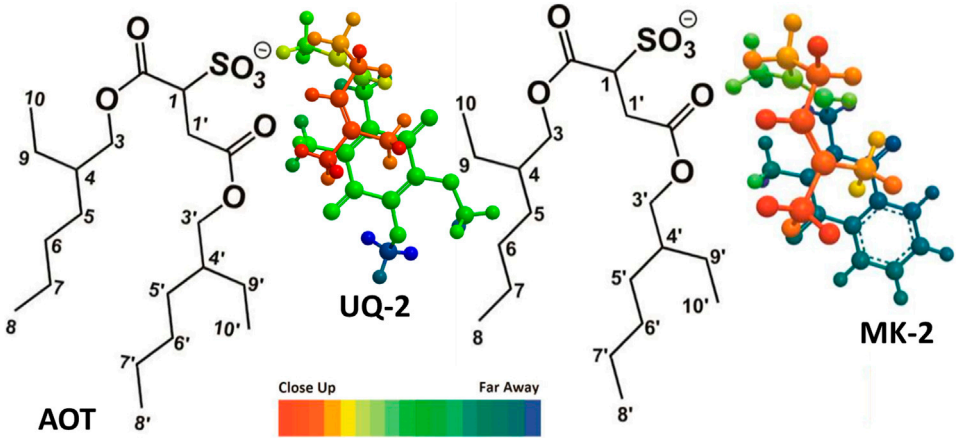

FIGURE 11 | Illustration of UQ-2 and MK-2's proposed folded, U-shaped conformations and placement within the RM interface. The arrangements are consistent with ^{1}H-^{1}H 2D NOESY and ROESY NMR spectral data obtained in a w_0 12 RM. Color depth gradient shows dark red as closer in distance and the dark blue as farther in distance from the reader. AOT proton labeling scheme key is shown.

found to have interactions with H1′. Although UQ-2 is less hydrophobic than MK-2, it is still shown to penetrate the AOT-water interface. The 2D NOESY cross peaks illustrate that UQ-2 is positioned near the interface of AOT with the methoxy groups of the headgroup oriented towards the alkyl chains of AOT (**Figure 11**). This orientation is similar to that of MK-2 (Koehn et al., 2018b), however the interactions between H_W and H_J/H_K with H1-H4 indicate the molecule is positioned closer to the interface than MK-2, which is in agreement with our previous work showing the UQ headgroup is closer to the water pool than MK-2 in phospholipid bilayers (Koehn et al., 2018b; Van Cleave et al., 2020; Van Cleave et al., 2021). The cross peaks observed between H_W and H_Y/H_Z and H_A/H_B indicate UQ-2 is in a folded conformation, specifically a U-shaped conformation. This conformation would not be possible unless the isoprenyl side chain was positioned over the headgroup (**Figure 10B**). Using methods described above in **Section 2.4**, the interproton distances of UQ-2 in a w_0 12 AOT-RM system were determined between H_W and protons along the sidechain (**Supplementary Table S2**). The intramolecular distance between H_W and H_X is shown to be 2.6 Å. Additionally, the distance between H_W and H_Y and H_Z were found to be 4.6 Å and 3.7 Å, respectively. Together this supports a U-shaped conformation for UQ-2 in AOT-RMs. As a confirmatory measure, 1D NOE experiments were performed to confirm the interactions of H_A/H_B with H_W, H_Z and H1′ within the w_0 12 AOT-RM system (**Supplementary Figure S24**). Additionally, the 2D NOESY NMR experiment in AOT-RMs was repeated multiple times, and the same conclusions were made regarding location, orientation, and conformation of UQ-2 in the interface of the AOT-RM system.

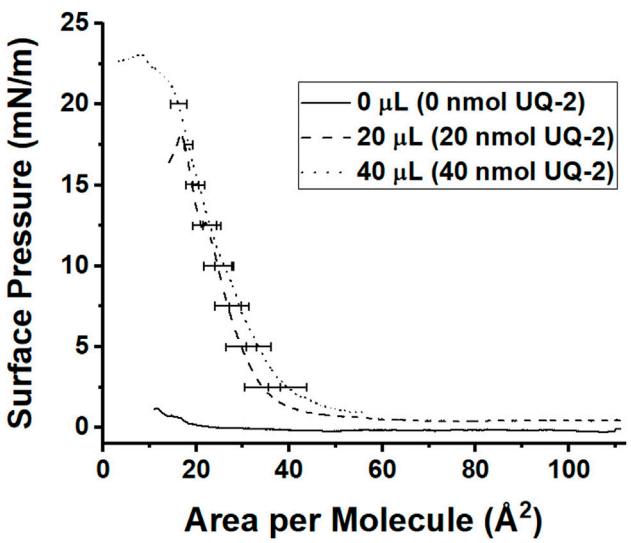

FIGURE 12 | Compression isotherms of different amounts of 1 mM UQ-2. The solid black curve represents pure phosphate buffer with no UQ-2 present, the dashed curve represents an injection of 20 µl of UQ-2, and the dotted curve represents an injection of 40 µl of UQ-2. Curves are the average of at least three measurements. Standard deviations of the area were calculated for every 5 mN/m of surface pressure.

2.7 Interaction of UQ-2 With Langmuir Phospholipid Monolayers

2.7.1 Compression Isotherms of Pure and Mixed Monolayers

Finally, we wanted to understand how UQ-2 interacted with the interface of a phospholipid-based membrane monolayer and compare these results to the RM system. UQ-2 was found to have a collapse pressure of 21 mN/m in this study (**Figure 12**). Our value was obtained by taking the second derivative of area per molecule with respect to surface pressure, with the lowest point representing the collapse pressure. Reported literature values varied widely, with some as high as 35 mN/m and others reporting that UQ-2 dissolved into the subphase (Quinn and Esfahani, 1980; Bernard et al., 2000; Hoyo et al.,

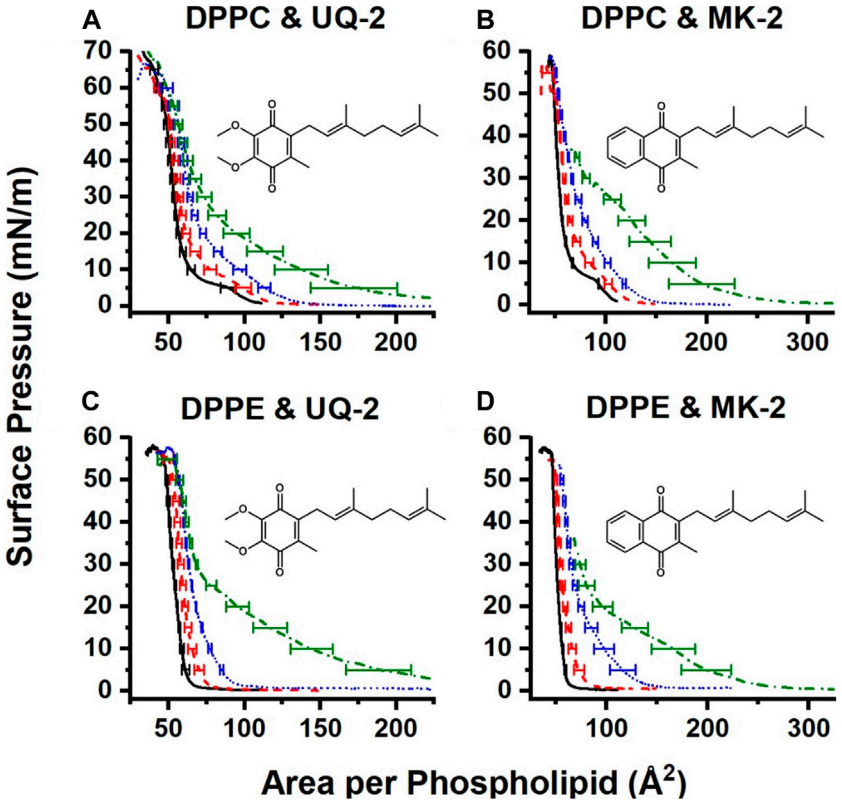

FIGURE 13 | Normalized compression isotherms of mixed monolayers of UQ-2 **(A and C)** or MK-2 **(B and D)** and either DPPC **(A and B)** or DPPE **(C and D)**. Solid black curves represent pure phospholipid monolayers, red dashed curves represent 75:25 lipid:lipoquinone films, blue dotted curves represent 50:50 lipid:lipoquinone films, and green dash-dot curves represent 25:75 lipid:lipoquinone films. Curves are the average of at least three measurements. Error bars are the standard deviation of the area at every 5 mN/m of surface pressure. MK-2 data were reproduced with permission from Koehn et al. 2018b).

2017). These discrepancies may be due to the slightly soluble nature of UQ-2, differences in the composition of the subphase, and even stirring of the subphase.

Pure films of DPPC and DPPE were in line with the literature (Patterson et al., 2016; Hoyo et al., 2017), with DPPC exhibiting its signature gas-liquid transition between 0 and 5 mN/m and its liquid-liquid condensed transition from 5 to 10 mN/m of surface pressure. The gas-liquid transition disappears upon the addition of UQ-2. The normalized 75:25 DPPC:UQ-2 curve does not overlap with the control curve. However, the variability in our measurements makes it impossible to draw a solid conclusion on whether UQ-2 is compressed out of the DPPC monolayer. Regardless, compression modulus analysis showed that increasing amounts of UQ-2 caused the DPPC monolayer to become more elastic (**Supplementary Figure S26**).

Compression isotherms with DPPE did not exhibit a significant difference in collapse pressure, as seen in **Figure 13**. The 25:75 and 50:50 DPPE:UQ-2 monolayers exhibited a liquid condensed phase, which suggests a reorganization of the monolayer. All mixed DPPE monolayers demonstrated at least a 9% increase in area per molecule at physiological surface pressure (Jones and Chapman, 1995) (30–35 mN/m) without the normalized curves overlapping with the control (see **Supplementary Tables S3, S4**). This indicates that UQ-2 is in the interface and spreading the DPPE molecules apart. UQ-2 was not compressed out of the monolayer at physiological surface pressure for DPPE.

2.7.2 Comparison of UQ-2 and MK-2 in Langmuir Monolayers

Interestingly, UQ-2 remains in the DPPC interface at physiological surface pressure, whereas MK-2 was likely to be compressed out. There is also a more distinct hump in the 25:75 DPPC:MK-2 curve at 25 mN/m than that of the 25:75 DPPC:UQ-2. In combination with the fact that mixed DPPC:UQ-2 curves do not overlap the control; we might conclude that UQ-2 is more likely to reside in the interface than MK-2. This is logical, as MK is more hydrophobic than UQ.

Both UQ-2 and MK-2 induce a liquid-condensed phase in DPPE, but it appears with a smaller mole fraction of MK-2 than UQ-2. As with DPPC, UQ-2 is always present in the interface as the mixed monolayers are at least 9% more expanded at physiological surface pressure than the DPPE control. Again, the hydrophobicity of the naphthoquinone headgroup of MK-2 is greater than that of the benzoquinone headgroup of UQ-2 which likely explains these differences. In summary, both UQ-2 and MK-2 associated with the Langmuir monolayer interface, but

UQ-2 resided closer to the interfacial water than MK-2 due to MKs more hydrophobic nature, consistent with the RM model membrane studies.

3 CONCLUSION

UQs and MKs are critical components of the ETS. UQs are found in bacteria, fungi, plants, and mammals, and MKs are mainly found in gram positive bacteria. While the interactions of these electron transport lipids with the membrane-bound protein complexes along the ETS is well-known, surprisingly their exact location and conformation within the membrane is still widely debated. In this study, we determined the location, orientation, and conformation of UQ-2, a truncated, representative analog for native UQ-10, using 1D and 2D NMR spectroscopic methods in organic solution and biological membrane-like environments. We then compared the UQ-2 results to the previously studied MK-2 to understand fundamentally how the class of lipoquinone molecules behave within membranes.

The 1D and 2D NMR studies showed that different solution environments slightly change the observed folded conformation of UQ-2. In all four solvents examined in this study (DMSO, acetonitrile, pyridine, and benzene), UQ-2 was found to adopt a folded, U-shaped conformation with a ~90° dihedral angle about the C2C3CβCγ. On the other hand, UQ-2 adopts a more open U-shaped conformation in the hydrophobic solvents, benzene and pyridine, which documents the fact that the environment will impact the conformation of the UQ-2 side chain. Once we established that UQ-2 folded in solution, we wanted to determine if a folded conformation was also adopted in a membrane-like interface. Using 2D NMR spectroscopy, we determined that UQ-2 interacts similarly to MK-2 with the RM model membrane system. Both UQ-2 and MK-2 adopt a folded, U-shaped conformation but reside at slightly different places in the membrane-like interface. Not surprisingly, and consistent with other studies (Van Cleave et al., 2020; Van Cleave et al., 2021), UQ-2 resides closer to the AOT-water interface than the more hydrophobic MK-2. Both lipoquinone molecules were oriented in a manner that allowed the side chain to fold back over the quinone moiety and be accommodated in the surfactant tails. It appears that regardless of lipoquinone headgroup structure, lipoquinones adopt folded conformations at membrane-like interfaces. Langmuir monolayer studies examining the interaction of UQ-2 with DPPC and DPPE phospholipids supported the results of the RM studies. Both UQ-2 and MK-2 were found to associate with the monolayer water-lipid interface, but MK-2 was more easily compressed out of the interface, which indicates UQ-2 resides closer to the interface than MK-2.

In summary, lipoquinones UQ-2 and MK-2 adopted folded conformations in solution and within membrane-like interfaces. The more polar UQ-2 was found to reside slightly closer to the water-surfactant interface, which was supported by both the RM and Langmuir monolayer studies. It appears that the presence of a lipoquinone headgroup is important for anchoring the lipoquinone in the membrane interface and for allowing the isoprenyl side chain to adopt some variation of a folded conformation that can be accommodated within the lipid tails due to the orientation of the lipoquinone within the interface. Varying the structure of the lipoquinone (UQ vs. MK) only modestly changed the location while residing in the RM interface. However, since lipoquinones are redox-active and the polarity of the headgroup changes upon reduction to the quinol form, structural differences in the headgroup likely facilitate locomotion of headgroup within the interface between membrane-bound enzymes in the ETS (Van Cleave et al., 2020). Taken together, the results of this study and others support a model where the headgroups of the longer, native lipoquinones, such as UQ-10 and MK-9, reside close to the water-lipid interface with the side chains folded but penetrating through the acyl tails into the midplane of the membrane bilayer. The location, orientation, and conformation of lipoquinones are critical for their function in generating cellular energy within membrane ETS and the studies described herein shed light on the behavior of lipoquinones within membrane-like environments.

4 EXPERIMENTAL

4.1 General Materials

The following chemicals were used without further purification for the synthetic work: Ultra-high purity argon (99.9%, Airgas), 3,4,5-trimethoxytoluene (97%, Aldrich), α,α-dichloromethyl methyl ether (98%, Aldrich), Dichloromethane (DCM, Stabilized, 99.9%, Fisher Scientific), $TiCl_4$ (99.9%, Aldrich), *n*-pentane (98%, Merck), Ethyl Acetate (99.9%, Fisher), Diethyl ether (≥99.0%, Merck), $NaHCO_3$ (99.7%, Merck), NaCl (Fisher), Na_2SO_4 (Fisher), Methanol (Aldrich), 30% aq. H_2O_2 solution (Sigma-Aldrich), H_2SO_4 (Fisher), SiO_2 (SiliCycle® SilicaFlash® F60, 43–60 μm 60 Å), 60% NaH dispersion in mineral oil (Aldrich), THF (Fisher), Geranyl Bromide (95%, Aldrich), NH_4Cl (99.7%, Fisher), BF_3 diethyl etherate (≥46.5%, Aldrich), $MgSO_4$ (98%, Merck), Acetonitrile (99.9%, Fisher) and $FeCl_3$ hexahydrate (99.9%, Fisher). The following chemicals were used without further purification for the spectroscopic studies: D_2O (99.9%, Cambridge Isotope Laboratories), d_1-chloroform (99.8%, Cambridge Isotope Laboratories), d_3-acetonitrile (99.8%, Aldrich), d_6-DMSO (99.9%, Cambridge Isotope Laboratories), d_5-pyridine (99.8%, Merck), d_6-benzene (99.5%, Cambridge Isotope Laboratories), isooctane (99.8%, Aldrich), and AOT (≥99%, Aldrich). The following materials were used for the trough work: Sodium phosphate monobasic monohydrate (≥98%) and chloroform (≥99.8%) were purchased from Sigma Aldrich. Sodium phosphate dibasic anhydrous (≥99%) and methanol (≥99.9%) were purchased from Fisher Scientific. 1,2-dipalmitoyl-*sn*-glycero-3-phosphocholine (DPPC, >99%) and 1,2-dipalmitoyl-sn-glycero-3-phosphoethanolamine (DPPE, >99%) were purchased from Avanti Polar Lipids. Distilled deionized water (DDI H_2O) was purified with a Barnsted E-pure system (~18 MΩ-cm).

4.2 General Methods

All reactions were carried out under argon atmosphere unless otherwise noted. All reagents were used as purchased unless otherwise noted. Solvents were dried by passing through an alumina drying column (Solv-Tek Inc.) under argon pressure (DCM, THF, diethyl ether).

4.3 Syntheses

4.3.1 Preparation of 2,3,4-Trimethoxy-6-Methylbenzaldehyde (2)

To a dry 500 ml round bottom Schlenk flask was added dry dichloromethane (DCM) (150 ml) followed by 3,4,5-trimethoxytoluene **1** (9.97 g, 54.7 mmol) and α,α-dichloromethyl methyl ether (12.58 g, 109.5 mmol, 2 eq.) and then cooled to 0°C. Then, $TiCl_4$ (273.6 mmol, 137 ml, 2.0 M in dry DCM, 2.5 eq. to α,α-dichloromethyl methyl ether) was added dropwise over 30 min via a 250 ml addition funnel under argon at 0°C. After addition was complete, the red reaction mixture was stirred at ambient temperature for 20 h. Thin layer chromatography (TLC) (9:1 *n*-pentane/EtOAc) showed the reaction was complete. The reaction was then very slowly quenched with ice until the reaction color turned light blue-gray. The DCM was removed under reduced pressure at ambient temperature and the resulting off-yellow liquid was extracted with diethyl ether (3 × 100 ml). The combined organic extracts were washed with sat. $NaHCO_3$ (200 ml), washed with brine (3 × 100 ml), dried over anhydrous Na_2SO_4, and then the solvent was removed under reduced pressure at ambient temperature. The product was dried under reduced pressure (~125 Torr) for 1 h, which yielded an off-white crystalline solid (11.40 g, 54.2 mmol, 99.1%) that was pure. ^{1}H NMR (400 MHz, $CDCl_3$) δ: 10.40 (s, 1H), 6.50 (s, 1H), 3.98 (s, 3H), 3.92 (s, 3H), 3.86 (s, 3H), 2.56 (s, 3H). ^{13}C NMR (101 MHz, $CDCl_3$) δ: 191.18, 158.46, 157.78, 139.80, 138.26, 121.48, 110.53, 62.50, 61.12, 56.15, 21.91. HRMS (ESI, OTOF) m/z: $[(M + H)^+]$ Calcd for $C_{11}H_{15}O_4$ 211.0965; Found 211.0965.

4.3.2 Preparation of 2,3,4-Trimethoxy-6-Methylphenol (3)

To a 250 ml round bottom Schlenk flask was added 2,3,4-trimethoxy-6-methylbenzaldehyde **2** (11.37 g, 54.1 mmol), MeOH (110 ml), and 30% aq. H_2O_2 solution (7.97 g, 70.3 mmol, 1.3 eq.). Then, conc. H_2SO_4 (1.08 ml) was added dropwise resulting in a red-orange reaction mixture. After 2.5 h of stirring at ambient temperature under argon, the ^{1}H NMR spectrum showed no aldehyde peak present. The reaction mixture was poured into sat. $NaHCO_3$ (100 ml) and then extracted with DCM (3 × 100 ml). The combined organic extracts were washed sat. $NaHCO_3$ (100 ml), washed with brine (100 ml), dried over anhydrous Na_2SO_4, and the solvent was evaporated under reduced pressure (~125 Torr) at ambient temperature to yield 10.55 g crude red oil. The product was then purified by flash column chromatography (7:1 *n*-pentane/EtOAc, 600 ml SiO_2, 70 mm column) to yield the desired product as an off-white crystalline solid (9.75 g, 49.2 mmol, 90.9%). ^{1}H NMR ($CDCl_3$) δ: 6.43 (s, 1H), 5.43 (s, 1H), 3.95 (s, 3H), 3.86 (s, 3H), 3.80 (s, 3H), 2.21 (s, 3H). ^{13}C NMR (101 MHz, $CDCl_3$) δ:146.17, 141.24, 140.14, 140.09, 118.08, 109.63, 61.34, 61.11, 56.75, 15.65. HRMS (ESI, OTOF) m/z: $[(M + H)^+]$ Calcd for $C_{10}H_{15}O_4$ 199.0965; Found 199.0951.

4.3.3 Preparation of Geranyl 2,3,4-Trimethoxy-6-Methylphenyl Ether (6)

NaH (2.95 g of 60% NaH dispersion in mineral oil washed with *n*-pentane that was first dried over activated neutral alumina, 73.8 mmol) was added to a dry 500 ml round bottom Schlenk flask containing a solution of 2,3,4-trimethoxy-6-methylphenol **3** (9.75 g, 49.2 mmol) dissolved in dry THF (150 ml). The mixture was stirred at ambient temperature for 35 min. The solvent was removed under reduced pressure at 25°C until an off-white powder was obtained. To a dry 500 ml round-bottom Schlenk flask was added the crude powder dissolved in anhydrous THF (75 ml) and then the mixture was cooled in an ice-H_2O bath. Then, a solution of geranyl bromide (16.02 g, 73.8 mmol, 1.5 eq.) in dry THF (75 ml) was added dropwise over 15 min via an addition funnel under argon. The mixture was then warmed to ambient temperature and stirred for 21.5 h under argon. The resulting yellow reaction mixture was slowly quenched with 5% aq. NH_4Cl solution (100 ml) and then extracted with diethyl ether (3 × 100 ml). The combined yellow organic extracts were washed with sat. $NaHCO_3$ (100 ml), washed with brine (100 ml), dried over anhydrous Na_2SO_4, and then the solvent was removed under reduced pressure (~125 Torr) at ambient temperature to yield 22.4 g crude yellow oil. The crude oil was purified by flash column chromatography (9:1 *n*-pentane/EtOAc, 1,200 ml SiO_2, 70 mm column) to yield a light-yellow oil (9.75 g, 29.2 mmol, 59.4%). ^{1}H NMR ($CDCl_3$) δ: 6.44 (s, 1H), 5.55 (t, J = 7.2 Hz, 1H), 5.10 (t, J = 6.3 Hz, 1H), 4.45 (d, J = 7.1 Hz, 2H), 3.93 (s, 3H), 3.86 (s, 3H), 3.81 (s, 3H), 2.22 (s, 3H), 2.04–2.12 (m, 4H), 1.69 (s, 6H), 1.61 (s, 3H). ^{13}C NMR (101 MHz, $CDCl_3$) δ: 149.19, 147.42, 144.52, 141.48, 140.97, 131.81, 126.54, 124.11, 120.48, 108.45, 69.74, 61.37, 61.23, 56.28, 39.79, 26.53, 25.83, 17.83, 16.47, 16.43. HRMS (ESI, QTOF) m/z: $[(M + H)^+]$ Calcd for $C_{20}H_{31}O_4$ 335.2217; Found 335.2220.

4.3.4 Preparation of 5-Geranyl-2,3,4-Trimethoxy-6-Methyl-Phenol (7)

To a 500 ml round bottom Schlenk flask was added geranyl 2,3,4-trimethoxy-6-methylphenyl ether **6** (9.73 g, 29.1 mmol) dissolved in dry diethyl ether (120 ml). Then, the mixture was treated with fresh BF_3 etherate (36.9 ml, 46.5% BF_3 etherate solution, 291.0 mmol, 10 eq.) added dropwise over 5 min and then stirred under argon at ambient temperature for 30 min. After exactly 30 min, the brown colored reaction was quenched with sat. NaCl (100 ml) very slowly over 8 min and then the mixture was extracted with diethyl ether (3 × 100 ml). The combined light yellow organic extracts were washed with sat. $NaHCO_3$ (50 ml, releases CO_2), washed with brine (100 ml), dried over anhydrous $MgSO_4$, vacuum filtered, and then the solvent was removed under reduced pressure (~125 Torr) at ambient temperature to yield 9.41 g crude brown oil. The product was purified by flash column chromatography (9:1 *n*-pentane/EtOAc, 800 ml SiO_2, 70 mm) to yield the desired product (4.67 g, 14.0 mmol, 48.1%) as a light-yellow oil. ^{1}H NMR

($CDCl_3$) δ: 5.60 (s, 1H), 5.05 (q, J = 6.5, 2H), 3.93 (s, 3H), 3.91 (s, 3H), 3.75 (s, 3H), 3.33 (d, J = 6.5, 2H), 2.13 (s, 3H), 2.07 (q, J = 7.2, 2H), 1.98 (m, 2H), 1.76 (s, 3H), 1.65 (s 3H), 1.57 (s, 3H). ^{13}C NMR (101 MHz, $CDCl_3$) δ: 144.49, 143.61, 143.44, 137.85, 135.12, 131.48, 129.82, 124.43, 123.18, 117.68, 61.44, 61.32, 60.92, 39.83, 26.78, 25, 82, 25.66, 17.82, 16.34, 11.48. HRMS (ESI, QTOF) m/z: [$(M + Na)^+$] Calcd for $C_{20}H_{31}O_4Na$ 357.2036; Found 357.2004.

4.3.5 Preparation of Ubiquinone-2 (8)

To a 50 ml round bottom flask was added 5-geranyl-2,3,4-trimethoxy-6-methylphenol 7 (0.137 g, 0.410 mmol), followed by DCM (2 ml) and ACN (2 ml) and then cooled to 0°C. An excess of $FeCl_3$ (1.11 g, 4.10 mmol, 10 eq.) dissolved in ACN (4 ml) was then added. The open atmosphere mixture was stirred at 0°C for 35 min. Then, DDI H_2O (30 ml) and sat. aq. $NaHCO_3$ (30 ml) were added to the orange reaction mixture and then extracted with diethyl ether (3 × 100 ml). The combined organic extracts were washed with sat. $NaHCO_3$ (50 ml), washed with brine (50 ml), dried over anhydrous Na_2SO_4, and then the solvent was removed under reduced pressure at ambient temperature to yield UQ-2 as a red oil and practically pure (0.125 g, 0.393 mmol, 95.9%). ^{1}H NMR ($CDCl_3$) δ: 5.03 (t, J = 6.8, 1H), 4.92 (t, J = 7.0, 1H), 3.99 (s, 3H), 3.98 (s, 3H), 3.18 (d, J = 7.0, 2H), 2.01 (m, 8H), 1.72 (s, 3H), 1.64 (s, 3H), 1.57 (s, 3H). ^{13}C NMR (101 MHz, $CDCl_3$) δ: 184.91, 184.05, 144.53, 144.38, 141.84, 139.01, 137.66, 131.68, 124.13, 199.08, 61.28, 39.82, 26.66, 25.81, 25.43, 17.82, 16.43, 12.07. HRMS (DART) m/z: [$(M + H)^+$] Calcd for $C_{19}H_{27}O_4$ 319.1904; Found 319.1935.

4.4 Mass Spectrometry

High resolution mass spectrometry (HRMS) experiments were carried out using one of the following instruments: 1) an Agilent 6220 TOF LC/MS ("OTOF") interfaced to an Agilent 1200 HPLC, 2) a Maxis QTOF ("QTOF") with electrospray (ESI) mode, and 3) a Maxis QTOF in positive DART mode (DART) using jeffamine as an internal calibration standard.

4.5 NMR Spectroscopic Studies

1D and 2D ^{1}H studies were carried out both in organic solvents and a RM system. ^{1}H and ^{13}C spectra were recorded using either a Varian Model MR400 or Model Inova400 operating at 400 and 101 MHz, respectively. Chemical shift values (δ) are reported in ppm and referenced against the internal solvent peaks in ^{1}H NMR ($CDCl_3$, δ at 7.26 ppm; d_3-acetonitrile δ at 1.94 ppm; d_6-DMSO, δ at 2.50 ppm; d_6-benzene, δ at 7.16 ppm; d_5-pyridine, δ at 8.74 ppm; D_2O, δ at 4.79 ppm) and in ^{13}C NMR (d_6-DMSO, δ at 39.52 ppm; d_6-benzene, δ at 128.06 ppm). All NMR spectra were recorded at either 22°C or 26°C. When samples were prepared for RM NMR experiments, deuterium oxide was used instead of H_2O, and the pH was adjusted to consider the presence of deuterium (pD = 0.4 + pH) (Samart et al., 2014).

For 1D and 2D NMR spectroscopic studies, a sample for analytical characterization of UQ-2 was prepared by using normal phase preparative thin layer chromatography (TLC) (10:1 *n*-pentane/EtOAc). First, ~10 mg of UQ-2 (dissolved in minimal amount of DCM) was loaded onto a preparative TLC plate and then eluted (10:1 *n*-pentane/EtOAc, 45 min). The plate was briefly dried of eluent solvent and eluted a second time (10:1 *n*-pentane/EtOAc, 45 min). The orange band was illuminated under UV light and while illuminated, the band was divided into a top half and a bottom half. The bottom half was carefully removed with a razor blade, extracted with DCM, filtered through a disposable Pasteur pipette filled with glass wool (pre-rinsed with DCM) and concentrated under reduced pressure at ambient temperature to provide 6 mg of UQ-2 as a red oil for NMR spectroscopic studies.

4.5.1 Solution 1D ^{1}H NMR Spectroscopic Studies of UQ-2

Samples were prepared by dissolving 5.0 mg of UQ-2 in 0.5 ml of either d_1-chloroform, d_6-DMSO, d_5-pyridine, d_3-acetonitrile, and d_6-benzene, respectively. The NMR instrument was locked onto the respective deuterium signal in the deuterated solvent used. NMR spectra were then collected using 32 scans for each sample. The data was processed using MestReNova NMR processing software version 10.0.1. The spectra were manually phased and then the baseline was corrected using a Bernstein Polynomial Fit (polynomial order 3). The obtained spectra were referenced to the internal solvent peak.

4.5.2 Sample Preparation for ^{1}H-^{1}H 2D NOESY and ^{1}H-^{1}H 2D ROESY NMR Spectroscopic Studies of UQ-2

To prepare the samples in d_5-pyridine, d_3-acetonitrile, and d_6-DMSO, 3.2 mg of UQ-2 was dissolved in 0.5 ml of solvent to yield a 20 mM solution of UQ-2. The NMR tubes containing the UQ-2 solution were purged with argon prior to data collection. To prepare a 100 mM solution of UQ-2 in $CDCl_3$, 15.9 mg of UQ-2 was dissolved in 0.5 ml $CDCl_3$. To prepare a 20 mM sample, 3.2 mg of UQ-2 was dissolved in 0.5 ml of each respective solvent (d_1-chloroform, d_6-DMSO, d_5-pyridine, d_3-acetonitrile, and d_6-benzene).

4.5.3 ^{1}H-^{1}H 2D NOESY and ^{1}H-^{1}H 2D ROESY NMR Spectroscopic Solution Experiments of UQ-2

^{1}H-^{1}H 2D NOESY NMR and ^{1}H-^{1}H 2D ROESY NMR spectroscopic experiments were conducted using a 400 MHz Varian MR400 NMR at 26°C. A standard NOESY pulse sequence was used consisting of 256 transients with 16 scans in the f1 domain using a 500 ms mixing time, 45° pulse angle, and a 1.5 s relaxation delay. A standard ROESYAD pulse sequence was used consisting of 256 transients with 16 scans in the f1 domain using a 400 ms mixing time, 45° pulse angle, and a 2.0 s relaxation delay. The NMR was locked onto either d_5-pyridine, d_6-benzene, d_3-acetonitrile, or d_6-DMSO. The resulting spectrum was processed using MestReNova NMR software version 10.0.1 (see **Supplementary Material** for details). The spectra were referenced to the internal solvent peak.

4.5.4 Sample Preparation for RM NMR Spectroscopic Studies of UQ-2

A 0.50 M AOT stock solution was made by dissolving AOT (5.56 g, 12.5 mmol) in isooctane (25.0 ml). Empty RMs were made by mixing 0.50 M AOT stock solution with a D_2O water pool, and then vortexed. UQ-2 RMs were made in a similar matter. The only difference being a

14.3 mM for UQ-2 stock solution was made by dissolving 45.4 mg of UQ-2 in 10.0 ml of 0.50 M AOT/isooctane solution. The RMs were then prepared using the UQ-2 stock solution. First, 2.0 ml samples were made using specific amounts of the 14.3 mM UQ-2 stock solution and then diluting the sample with the 500 mM AOT/isooctane solution. From the 2.0 ml solutions, 1.0 ml RM samples were prepared using the designated amounts of 2.0 ml sample and then adding the proper amount of D_2O with pH 7.0 (see **Section 4.2** for pH measurements) for UQ-2 to form the desired size RM. The samples were then vortexed until clear. The overall concentrations for 1.0 ml UQ-2 RM samples are as follows: w_0 4, 13.8 mM; w_0 8, 6.4 mM; w_0 12, 3.5 mM; w_0 16, 2.0 mM; and w_0 20, 1.4 mM.

4.5.5 1D ^{1}H NMR Spectroscopic Studies of AOT/Isooctane RMs Containing UQ-2

NMR spectra of various size RMs and in isooctane and D_2O were obtained using a Varian Inova 400 MHz instrument at 22°C using routine parameters (pulse angle: 45°, relaxation delay of 1 s) using 64 scans. The NMR instrument was locked onto 10% D_2O signal for the RM samples and D_2O for the sample in D_2O. The 1D ^{1}H spectra of UQ-2 in isooctane were doped with 5% d_6-benzene for the NMR instrument to lock onto and to achieve properly shimmed spectra. The spectral data was processed using MestReNova NMR processing software version 10.0.1. The spectra were manually phased and then the baseline was corrected using a multipoint baseline correction (cubic splines). The spectrum in D_2O was referenced to the internal D_2O peak and the spectra in isooctane and RM samples were referenced to the isooctane methyl peak (0.904 ppm) as previously reported (Samart et al., 2014).

4.5.6 Sample Preparation for ^{1}H-^{1}H 2D NOESY and ROESY NMR Spectroscopic Studies of UQ-2 in AOT/Isooctane RMs

A 0.50 M AOT stock solution was made by dissolving AOT (5.56 g, 12.5 mmol) in isooctane (25.0 ml). A 1 ml stock solution of 112 mM UQ-2 in AOT/isooctane was made by dissolving 35.7 mg of UQ-2 in 1 ml isooctane/AOT stock solution. To make a w_0 12 RM, 893 µl of 112 mM UQ-2 AOT/isooctane stock solution and 107 µl of D_2O at pH 7 were mixed together and then vortexed. This final mixture results in a w_0 12 RM microemulsion with an overall concentration of UQ-2 being ~100 mM (~29 molecules per RM).

4.5.7 ^{1}H-^{1}H 2D NOESY NMR Spectroscopic Studies of UQ-2 in a w_0 12 AOT/Isooctane RM

2D NMR spectra were obtained using similar conditions used previously (Peters et al., 2016; Koehn et al., 2018b) using a 400 MHz Varian NMR at 26°C. A standard NOESY pulse sequence was used consisting of 256 transients with 16 scans in the f1 direction using a 200 ms mixing time, 45° pulse angle, and a relaxation delay of 1.5 s. The NMR instrument was locked onto 10% D_2O signal. The resulting spectrum was processed using MestReNova NMR software version 10.0.1. (see **Supplementary Material** for details). The spectrum was referenced to the isooctane methyl peak at 0.904 ppm as previously reported (Samart et al., 2014; Koehn et al., 2018a). The 3D structure illustration within a RM was drawn using ChemBioD Ultra 12.0 and ChemBio3D Ultra 12.0 based on spectral parameters described under results.

4.6 Langmuir Monolayer Compression Isotherm Methods

4.6.1 Instrument and Cleaning

All Langmuir monolayer studies were performed on a Kibron µTrough XS equipped with a Teflon ribbon barrier (hydrophobic) as described previously (Van Cleave et al., 2021). The trough bed was cleaned between runs by scrubbing three times with isopropanol, then scrubbing three times with absolute EtOH, and then rinsing with DDI H_2O. The ribbon was cleaned by a rinse with isopropanol, a rinse with absolute EtOH, and then a rinse with DDI H_2O.

4.6.2 Preparation of the Subphase

The subphase consisted of approximately 50 ml of 20 mM sodium phosphate buffer (pH 7.40 ± 0.02). The pH was adjusted using 1.0 M HCl or NaOH. The subphase surface was cleaned with vacuum aspiration until the surface pressure remained at 0.0 ± 0.5 mN/m throughout a quick compression.

4.6.3 Preparation of Lipid Solutions

Phospholipid solutions were prepared by dissolving powdered lipid (0.018 g DPPC, 0.017 g DPPE) into 25 ml of 9:1 chloroform/MeOH (v/v) to yield a 1 mM phospholipid stock solution. A 1 mM UQ-2 solution was prepared the same as the phospholipids, but with 0.0016 g UQ-2 dissolved into 5 ml of the chloroform/methanol solution. Stock solutions were stored at −20°C. Mixed monolayer were prepared immediately before experiments by adding appropriate amount of phospholipid stock and UQ-2 stock to a small glass vial and vortexing for ~30 s. Mixed monolayers consisted of 25:72, 50:50, and 75:25 UQ-2:phospholipid (mol fraction).

4.6.4 Formation and Compression of Monolayers

Monolayers consisted of pure DPPC, pure DPPE, pure UQ-2, or varying phospholipid:UQ-2 molar fractions (25:75, 50:50, 75:25). Films were prepared by adding 20 µl lipid stock solutions or mixtures (40 µl were used for UQ-2 and 75:25 UQ-2:phospholipid to obtain full compression) drop-wise to the surface of the subphase and were equilibrated for 15 min. Monolayers were compressed at a speed of 10 mm/min (5 mm/min from two sides). Surface pressure measurements were made via a modified Wilhelmy plate method where a wire probe was used instead of a plate. Surface pressure was calculated from surface tension with **Eq. 1**, where π is surface pressure (mN/m), γ_o is the surface tension of the subphase (72.8 mN/m), and γ is the surface tension after the addition of the monolayer.

$$\pi = \gamma_o - \gamma. \quad (1)$$

The averages of triplicate isotherms were worked up in Excel. The averages were then normalized to the amount of phospholipid according to **Eq. 2**, where A_N is the normalized area per phospholipid (Å^2), A is the experimental area per molecule (Å^2) (Van Cleave et al., 2021), and x is the mol fraction of phospholipid (0.25, 0.5, or 0.75). This method of analysis was developed from a previous study (Quinn and Esfahani, 1980).

$$A_N = A\left(x^{-1}\right). \quad (2)$$

Normalized isotherms were plotted with Origin 2021. Reported error bars are the standard deviations of the experimental area.

DATA AVAILABILITY STATEMENT

The original contributions presented in the study are included in the article/**Supplementary Material**, further inquiries can be directed to the corresponding author.

AUTHOR CONTRIBUTIONS

Project conception JK; Project management DC (Crans); Experimental design JK, DC (Crans), CC; Experiments JK, JI, CC, KK, HM; Verification MB-T, JK, DC (Crans); Manuscript preparation MB-T, JK, DC (Crans); Editing MB-T, JK, DC (Crans), KK, CC, HM; Preparation of grant funding DC (Crans) and DC (Crick). All authors helped edit and have approved the submitted manuscript.

FUNDING

DC (Crans) and DC (Crick) thank NSF for funding (Grant #CHE-1709564). DC (Crans) also thanks the Arthur Cope Foundation administered by the American Chemical Society for partial support.

ACKNOWLEDGMENTS

The authors wish to thank the Analytical Resources Core at Colorado State University for instrument access, training, and assistance with sample analysis. Additionally, the authors would like to thank Drs. Michele Mailhot and Christopher D. Rithner for experimental consultation for NMR spectroscopy.

SUPPLEMENTARY MATERIAL

The Supplementary Material for this article can be found online at: https://www.frontiersin.org/articles/10.3389/fchem.2022.827530/full#supplementary-material

REFERENCES

Afri, M., Ehrenberg, B., Talmon, Y., Schmidt, J., Cohen, Y., and Frimer, A. A. (2004). Active Oxygen Chemistry within the Liposomal Bilayer. *Chem. Phys. Lipids* 131, 107–121. doi:10.1016/j.chemphyslip.2004.04.007

Bernard, S., Roche, Y., Etienne, F., and Peretti, P. (2000). Interaction between Ubiquinones and Dipalmitoylphosphatidylcholine in Mixed Langmuir Monolayers. *Mol. Crystals Liquid Crystals Sci. Techn. Section A. Mol. Crystals Liquid Crystals* 338, 207–221. doi:10.1080/10587250008024431

Bovicelli, P., Borioni, G., Fabbrini, D., and Barontini, M. (2008). New Efficient Synthesis of Ubiquinones. *Synth. Commun.* 38, 391–400. doi:10.1080/00397910701771066

Ceccarelli, M., Procacci, P., and Marchi, M. (2003). Anab Initio Force Field for the Cofactors of Bacterial Photosynthesis. *J. Comput. Chem.* 24, 129–142. doi:10.1002/jcc.10198

Chazotte, B., Wu, E.-S., and Hackenbrock, C. R. (1991). The Mobility of a Fluorescent Ubiquinone in Model Lipid Membranes. Relevance to Mitochondrial Electron Transport. *Biochim. Biophys. Acta (Bba) - Bioenerg.* 1058, 400–409. doi:10.1016/s0005-2728(05)80136-7

Cornell, B. A., Keniry, M. A., Post, A., Robertson, R. N., Weir, L. E., and Westerman, P. W. (1987). Location and Activity of Ubiquinone 10 and Ubiquinone Analogs in Model and Biological Membranes. *Biochemistry* 26, 7702–7707. doi:10.1021/bi00398a025

de Jong, D. H., Liguori, N., van den Berg, T., Arnarez, C., Periole, X., and Marrink, S. J. (2015). Atomistic and Coarse Grain Topologies for the Cofactors Associated with the Photosystem II Core Complex. *J. Phys. Chem. B* 119, 7791–7803. doi:10.1021/acs.jpcb.5b00809

Di Bernardo, S., Fato, R., Casadio, R., Fariselli, P., and Lenaz, G. (1998). A High Diffusion Coefficient for Coenzyme Q10might Be Related to a Folded Structure. *FEBS Lett.* 426, 77–80. doi:10.1016/s0014-5793(98)00313-5

Feng, S., Wang, R., Pastor, R. W., Klauda, J. B., and Im, W. (2021). Location and Conformational Ensemble of Menaquinone and Menaquinol, and Protein-Lipid Modulations in Archaeal Membranes. *J. Phys. Chem. B* 125, 4714–4725. doi:10.1021/acs.jpcb.1c01930

Galassi, V. V., and Arantes, G. M. (2015). Partition, Orientation and Mobility of Ubiquinones in a Lipid Bilayer. *Biochim. Biophys. Acta (Bba) - Bioenerg.* 1847, 1560–1573. doi:10.1016/j.bbabio.2015.08.001

Gómez-Murcia, V., Torrecillas, A., De Godos, A. M., Corbalán-García, S., and Gómez-Fernández, J. C. (2016). Both idebenone and Idebenol Are Localized Near the Lipid-Water Interface of the Membrane and Increase its Fluidity. *Biochim. Biophys. Acta (Bba) - Biomembranes* 1858, 1071–1081. doi:10.1016/j.bbamem.2016.02.034

Gupta, C., Khaniya, U., Chan, C. K., Dehez, F., Shekhar, M., Gunner, M. R., et al. (2020). Charge Transfer and Chemo-Mechanical Coupling in Respiratory Complex I. *J. Am. Chem. Soc.* 142, 9220–9230. doi:10.1021/jacs.9b13450

Hauss, T., Dante, S., Haines, T. H., and Dencher, N. A. (2005). Localization of Coenzyme Q10 in the center of a Deuterated Lipid Membrane by Neutron Diffraction. *Biochim. Biophys. Acta* 1710, 57–62. doi:10.1016/j.bbabio.2005.08.007

Hoyo, J., Guaus, E., and Torrent-Burgués, J. (2017). Tuning Ubiquinone Position in Biomimetic Monolayer Membranes. *Eur. Phys. J. E* 40, 62. doi:10.1140/epje/i2017-11552-2

Ismail, A., Leroux, V., Smadja, M., Gonzalez, L., Lombard, M., Pierrel, F., et al. (2016). Coenzyme Q Biosynthesis: Evidence for a Substrate Access Channel in the FAD-dependent Monooxygenase Coq6. *Plos Comput. Biol.* 12, e1004690–27. doi:10.1371/journal.pcbi.1004690

Joela, H., Kasa, S., Lehtovuori, P., Bech, M., Mellikov, E., Niinistö, L., et al. (1997). EPR, ENDOR and TRIPLE Resonance and MO Studies on Ubiquinones (Q-N): Comparison of Radical Anions and Cations of Coenzymes Q-10 and Q-6 with the Model Compounds Q-2 and Q-0. *Acta Chem. Scand.* 51, 233–241. doi:10.3891/acta.chem.scand.51-0233

Jones, C. R., Butts, C. P., and Harvey, J. N. (2011). Accuracy in Determining Interproton Distances Using Nuclear Overhauser Effect Data from a Flexible Molecule. *Beilstein J. Org. Chem.* 7, 145–150. doi:10.3762/bjoc.7.20

Jones, M. N., and Chapman, D. (1995). *Micelles, Monolayers, and Biomembranes*. New York: Wiley-Liss, Inc.

Kaurola, P., Sharma, V., Vonk, A., Vattulainen, I., and Róg, T. (2016). Distribution and Dynamics of Quinones in the Lipid Bilayer Mimicking the Inner Membrane of Mitochondria. *Biochim. Biophys. Acta (Bba) - Biomembranes* 1858, 2116–2122. doi:10.1016/j.bbamem.2016.06.016

Kawamukai, M. (2018). Biosynthesis and Applications of Prenylquinones. *Biosci. Biotechnol. Biochem.* 82, 963–977.

Kingsley, P. B., and Feigenson, G. W. (1981). 1H-NMR Study of the Location and Motion of Ubiquinones in Perdeuterated Phosphatidylcholine Bilayers. *Biochim. Biophys. Acta (Bba) - Bioenerg.* 635, 602–618. doi:10.1016/0005-2728(81)90117-1

Koehn, J. T., Beuning, C. N., Peters, B. J., Dellinger, S. K., Van Cleave, C., Crick, D. C., et al. (2019). Investigating Substrate Analogues for Mycobacterial MenJ: Truncated and Partially Saturated Menaquinones. *Biochemistry* 58, 1596–1615. doi:10.1021/acs.biochem.9b00007

Koehn, J. T., Crick, D. C., and Crans, D. C. (2018a). Synthesis and Characterization of Partially and Fully Saturated Menaquinone Derivatives. *ACS Omega* 3, 14889–14901. doi:10.1021/acsomega.8b02620

Koehn, J. T., Magallanes, E. S., Peters, B. J., Beuning, C. N., Haase, A. A., Zhu, M. J., et al. (2018b). A Synthetic Isoprenoid Lipoquinone, Menaquinone-2, Adopts a Folded Conformation in Solution and at a Model Membrane Interface. *J. Org. Chem.* 83, 275–288. doi:10.1021/acs.joc.7b02649

Lenaz, G., Samorì, B., Fato, R., Battino, M., Parenti Castelli, G., and Domini, I. (1992). Localization and Preferred Orientations of Ubiquinone Homologs in Model Bilayers. *Biochem. Cel Biol* 70, 504–514. doi:10.1139/o92-078

Lenaz, G., Fato, R., Di Bernardo, S., Jarreta, D., Costa, A., Genova, M. L., et al. (1999). Localization and Mobility of Coenzyme Q in Lipid Bilayers and Membranes. *BioFactors* 9, 87–93. doi:10.1002/biof.5520090202

Lu, L., and Chen, F. (2004). A Novel and Convenient Synthesis of Coenzyme Q1. *Synth. Commun.* 34, 4049–4053. doi:10.1081/scc-200036578

Maitra, A. (1984). Determination of Size Parameters of Water-Aerosol OT-Oil Reverse Micelles from Their Nuclear Magnetic Resonance Data. *J. Phys. Chem.* 88, 5122–5125. doi:10.1021/j150665a064

Matsumoto, M., Kobayashi, K., and Hotta, Y. (1984). Acid-Catalyzed Oxidation of Benzaldehydes to Phenols by Hydrogen Peroxide. *J. Org. Chem.* 49, 4740–4741. doi:10.1021/jo00198a037

Metz, G., Howard, K. P., van Liemt, W. B. S., Prestegard, J. H., Lugtenburg, J., and Smith, S. O. (1995). NMR Studies of Ubiquinone Location in Oriented Model Membranes: Evidence for a Single Motionally-Averaged Population. *J. Am. Chem. Soc.* 117, 564–565. doi:10.1021/ja00106a078

Michaelis, L., and Moore, M. J. (1985). Location of Ubiquinone-10 (CoQ-10) in Phospholipid Vesicles. *Biochim. Biophys. Acta* 821, 121–129. doi:10.1016/0005-2736(85)90162-2

Murgolo, N. J., Patel, A., Stivala, S. S., and Wong, T. K. (1989). The Conformation of Dolichol. *Biochemistry* 28, 253–260. doi:10.1021/bi00427a035

Nilsson, J. A., Eriksson, L. A., and Laaksonen, A. (2001a). Molecular Dynamics Simulations of Plastoquinone in Solution. *Mol. Phys.* 99, 247–253. doi:10.1080/00268970010010204

Nilsson, J. A., Lyubartsev, A., Eriksson, L. A., and Laaksonen, A. (2001b). Molecular Dynamics Simulations of Ubiquinone; a Survey over Torsional Potentials and Hydrogen Bonds. *Mol. Phys.* 99, 1795–1804. doi:10.1080/00268970110072403

Nowicka, B., and Kruk, J. (2010). Occurrence, Biosynthesis and Function of Isoprenoid Quinones. *Biochim. Biophys. Acta (Bba) - Bioenerg.* 1797, 1587–1605. doi:10.1016/j.bbabio.2010.06.007

Ondarroa, M., and Quinn, P. J. (1986). Proton Magnetic Resonance Spectroscopic Studies of the Interaction of Ubiquinone-10 with Phospholipid Model Membranes. *Eur. J. Biochem.* 155, 353–361. doi:10.1111/j.1432-1033.1986.tb09498.x

Patterson, M., Vogel, H. J., and Prenner, E. J. (2016). Biophysical Characterization of Monofilm Model Systems Composed of Selected Tear Film Phospholipids. *Biochim. Biophys. Acta (Bba) - Biomembranes* 1858, 403–414. doi:10.1016/j.bbamem.2015.11.025

Peters, B. J., Groninger, A. S., Fontes, F. L., Crick, D. C., and Crans, D. C. (2016). Differences in Interactions of Benzoic Acid and Benzoate with Interfaces. *Langmuir* 32, 9451–9459. doi:10.1021/acs.langmuir.6b02073

Quinn, P. J., and Esfahani, M. A. (1980). Ubiquinones Have Surface-Active Properties Suited to Transport Electrons and Protons across Membranes. *Biochem. J.* 185, 715–722. doi:10.1042/bj1850715

Quirk, A., Lardner, M. J., Tun, Z., and Burgess, I. J. (2016). Surface-Enhanced Infrared Spectroscopy and Neutron Reflectivity Studies of Ubiquinone in Hybrid Bilayer Membranes under Potential Control. *Langmuir* 32, 2225–2235. doi:10.1021/acs.langmuir.5b04263

Salgado, J., Villalain, J., and Gomez-Fernandez, J. C. (1993). Magic Angle Spinning 13C-NMR Spin-Lattice Relaxation Study of the Location and Effects of A-Tocopherol, Ubiquinone-10, and Ubiquinol-10 in Unsonicated Model Membranes. *Eur. Biophys. J.* 22, 151–155. doi:10.1007/bf00196919

Samart, N., Beuning, C. N., Haller, K. J., Rithner, C. D., and Crans, D. C. (2014). Interaction of a Biguanide Compound with Membrane Model Interface Systems: Probing the Properties of Antimalaria and Antidiabetic Compounds. *Langmuir* 30, 8697–8706. doi:10.1021/la501600s

Seif Eddine, M., Biaso, F., Rendon, J., Pilet, E., Guigliarelli, B., Magalon, A., et al. (2020). 1,2H Hyperfine Spectroscopy and DFT Modeling Unveil the Demethylmenasemiquinone Binding Mode to *E. coli* Nitrate Reductase A (NarGHI). *Biochim. Biophys. Acta (Bba) - Bioenerg.* 1861, 148203. doi:10.1016/j.bbabio.2020.148203

Singharoy, A., Maffeo, C., Delgado-Magnero, K. H., Swainsbury, D. J. K., Sener, M., Kleinekathöfer, U., et al. (2020). Atoms to Phenotypes: Molecular Design Principles of Cellular Energy Metabolism. *Cell* 179, 1098–e23. doi:10.1016/j.cell.2019.10.021

Söderhäll, J. A., and Laaksonen, A. (2001). Molecular Dynamics Simulations of Ubiquinone inside a Lipid Bilayer. *J. Phys. Chem. B* 105, 9308–9315. doi:10.1021/jp011001w

Stidham, M. A., Mcintosh, T. J., and Siedow, J. N. (1984). On the Localization of Ubiquinone in Phosphatidylcholine Bilayers. *Biochim. Biophys. Acta (Bba) - Bioenerg.* 767, 423–431. doi:10.1016/0005-2728(84)90040-9

Teixeira, M. H., and Arantes, G. M. (2019). Effects of Lipid Composition on Membrane Distribution and Permeability of Natural Quinones. *RSC Adv.* 9, 16892–16899. doi:10.1039/c9ra01681c

Tekin, E. D., and Erkoc, S. (2010). Structural and Electronic Features of the Ubiquinone and Ubiquinol Molecules: Molecular Dynamics and Quantum Chemical Treatments. *Mol. Simulation* 36, 763–771. doi:10.1080/08927021003752838

Trumpower, B. L. (1981). New Concepts on the Role of Ubiquinone in the Mitochondrial Respiratory Chain. *J. Bioenerg. Biomembr* 13, 1–24. doi:10.1007/bf00744743

Ulrich, E. L., Girvin, M. E., Cramer, W. A., and Markley, J. L. (1985). Location and Mobility of Ubiquinones of Different Chain Lengths in Artificial Membrane Vesicles. *Biochemistry* 24, 2501–2508. doi:10.1021/bi00331a016

Van Cleave, C., Koehn, J. T., Pereira, C. S., Haase, A. A., Peters, B. J., Croslow, S. W., et al. (2021). Interactions of Truncated Menaquinones in Lipid Monolayers and Bilayers. *Int. J. Mol. Sci.* 22, 1–22. doi:10.3390/ijms22189755

Van Cleave, C., Murakami, H. A., Samart, N., Koehn, J. T., Maldonado, P., Kreckel, H. D., et al. (2020). Location of Menaquinone and Menaquinol Headgroups in Model Membranes. *Can. J. Chem.* 98, 307–317. doi:10.1139/cjc-2020-0024

Van Horn, W. D., Ogilvie, M. E., and Flynn, P. F. (2008). Use of Reverse Micelles in Membrane Protein Structural Biology. *J. Biomol. NMR.* 40, 203–211. doi:10.1007/s10858-008-9227-5

Woodward, R. B., and Bloch, K. (1953). The Cyclization of Squalene in Cholesterol Synthesis. *J. Am. Chem. Soc.* 75, 2023–2024. doi:10.1021/ja01104a535

Zahn, T. J., Eilers, M., Guo, Z., Ksebati, M. B., Simon, M., Scholten, J. D., et al. (2000). Evaluation of Isoprenoid Conformation in Solution and in the Active Site of Protein-Farnesyl Transferase Using Carbon-13 Labeling in Conjunction with Solution- and Solid-State NMR. *J. Am. Chem. Soc.* 122, 7153–7164. doi:10.1021/ja000860f

Conflict of Interest: The authors declare that the research was conducted in the absence of any commercial or financial relationships that could be construed as a potential conflict of interest.

Publisher's Note: All claims expressed in this article are solely those of the authors and do not necessarily represent those of their affiliated organizations, or those of the publisher, the editors and the reviewers. Any product that may be evaluated in this article, or claim that may be made by its manufacturer, is not guaranteed or endorsed by the publisher.

frontiers in Chemistry

ORIGINAL RESEARCH
published: 09 March 2022
doi: 10.3389/fchem.2022.842190

A Stoichiometric Solvent-Free Protocol for Acetylation Reactions

Francesca Valentini[1], *Pierluca Galloni*[1,2], *Diana Brancadoro*[2], *Valeria Conte*[1] and *Federica Sabuzi*[1,2]*

[1]Department of Chemical Science and Technologies, University of Rome Tor Vergata, Rome, Italy, [2]BT-InnoVaChem Srl, Rome, Italy

Considering the remarkable relevance of acetylated derivatives of phenols, alcohols, and aryl and alkyl thiols in different areas of biology, as well as in synthetic organic chemistry, a sustainable solvent-free approach to perform acetylation reactions is proposed here. Acetylation reactions are classically performed using excess of acetic anhydride (Ac_2O) in solvent-free conditions or by eventually working with stoichiometric amounts of Ac_2O in organic solvents; both methods require the addition of basic or acid catalysts to promote the esterification. Therefore, they usually lead to the generation of high amounts of wastes, which sensibly raise the E-factor of the process. With the aim to develop a more sustainable system, a solvent-free, stoichiometric acetylation protocol is, thus, proposed. The naturally occurring phenol, thymol, can be converted to the corresponding—biologically active—ester with good yields, in the presence of 1% of $VOSO_4$. Interestingly, the process can be efficiently adopted to synthesize other thymyl esters, as well as to perform acetylation of alcohols and aryl and alkyl thiols. Remarkably, a further improvement has been achieved replacing Ac_2O with its greener alternative, isopropenyl acetate (IPA).

Keywords: acetylation, acetic anhydride, isopropenyl acetate, sustainability, thymol, phenols, alcohols, thiols

OPEN ACCESS

Edited by:
Jason B. Harper,
University of New South Wales, Australia

Reviewed by:
Marta Feroci,
Sapienza University of Rome, Italy
Stojan Stavber,
Institut Jožef Stefan (IJS), Slovenia

***Correspondence:**
Federica Sabuzi
federica.sabuzi@uniroma2.it

Specialty section:
This article was submitted to Organic Chemistry, a section of the journal Frontiers in Chemistry

Received: *23 December 2021*
Accepted: *08 February 2022*
Published: *09 March 2022*

Citation:
Valentini F, Galloni P, Brancadoro D, Conte V and Sabuzi F (2022) A Stoichiometric Solvent-Free Protocol for Acetylation Reactions. Front. Chem. 10:842190. doi: 10.3389/fchem.2022.842190

INTRODUCTION

In the framework of organic transformations, acetylation is a common and versatile reaction, extensively used both on laboratory and industrial scale. In fact, acetate is usually exploited as an effective protective group for phenols, alcohols, thiols, and amines in several multistep syntheses, including drug preparation (Carey et al., 2006). Moreover, acetylation of bioactive molecules, such as natural phenols, confers enhanced lipophilicity, eventually leading to an improved bioactivity (Su et al., 2020; Floris et al., 2021). The key role of such a reaction is particularly highlighted in the case of Aspirin®, where acetylation is fundamental to allow safe drug administration (Vane and Botting, 2003). Therefore, it is particularly important to find sustainable methodologies to perform acetylation reactions in good yields. Acetic anhydride (Ac_2O) is amongst the most used acetylating reagent (Larionov and Zipse, 2011), but basic or acid catalysts are needed to activate it. Yet, 4-(dimethylamino)pyridine (DMAP) (Steglich and Hofle, 1969; Mandai et al., 2018), triethylamine, and tributylphosphine (Vedejs et al., 1993) are generally used as basic catalysts for Ac_2O activation in chlorinated solvents. Analogously, several Lewis acid complexes with hard anions (Chandra et al., 2002; Reddy et al., 2006) that significantly enhance metal acidity, such as triflates (Ishihara et al., 1995; Barrett and Braddock, 1997; Chauhan et al., 1999; Saravanan and Singh, 1999; Chen et al., 2001; Orita et al., 2001; Das and Chakraborty, 2011; Kumar et al., 2014), perchlorates (Bartoli et al., 2003), and chlorides (De, 2004), have been adopted in acetylation

TABLE 1 | Thymol acetylation. Reaction conditions: thymol = 6.7 mmol (1 g), T = r. t., and t = 24 h.

Entry	V-Cat	V-Cat (%)	Ac_2O (eq)	Isolated Yield (%)	E-factor[d]
1	$VOSO_4$	5%	8	85	8.7
2	$VO(acac)_2$	5%	8	85	8.7
3	$VOSO_4$	1%	8	80	9.2
4	$VO(acac)_2$	1%	8	74	10.0
5	$VOSO_4$	0.5%	8	71	10.5
6	$VOSO_4$	1%	3.2	85	5.6
7	$VOSO_4$	1%	1.2	83	4.5
8	$VOSO_4$	1%	1.0	83	4.4
9[a]	$VOSO_4$	1%	1.0	87	1.3
10[b]	$VOSO_4$	1%	1.0	97	0.6
11	—	—	1.0	3[c]	146.9

[a]*Reaction performed on 10 g of thymol.*
[b]*Reaction performed on 50 g of thymol.*
[c]*GC-MS yield.*
[d]*Solvent contribution not included (Sabuzi et al., 2015).*

reactions with Ac_2O, showing high catalytic activity. Interestingly, acetylation of tertiary alcohols, which generally show slow rates and unsatisfactory yields, has been successfully obtained by merging together the catalytic activity of $Sc(OTf)_3$ and DMAP (Zhao et al., 1998). However, several disadvantages are associated with these catalysts, such as the moisture sensitivity as well as their high prices. Furthermore, chlorinated solvents, high reaction temperatures, and inert atmosphere are usually required.

In the last years, the chemistry community has been committed to find new sustainable approaches to perform organic transformations, preferring environment-friendly methodologies. Such task results particularly relevant for industrial processes (Sarkar et al., 2016). In this respect, acetylation of phenols, alcohols, amines, and thiols has been extensively investigated, with the goal of improving sustainability through homogenous (Lugemwa et al., 2013; Singha and Ray, 2016; Temperini et al., 2017; Kuciński and Hreczycho, 2018; Zhu et al., 2018; Jain et al., 2019; Chutia and Chetia, 2020; Pantawane et al., 2021) and heterogenous catalysis (Rajabi and Luque, 2014; Bajracharya and Shrestha, 2018; Behera and Patra, 2021; Hlatshwayo et al., 2021). Indeed, earth-abundant transition metals (Zhu et al., 2018; Jain et al., 2019), solvent-free conditions (Rajabi and Luque, 2014; Behera and Patra, 2021), and safe acylating reagents (Singha and Ray, 2016; Temperini et al., 2017; Pantawane et al., 2021) have been employed. Among transition metal complexes, vanadium covers a chief role as an environment-friendly catalyst for several organic transformations, including oxidation and halogenation reactions (Conte and Floris, 2010; Galloni et al., 2013; Floris et al., 2017; Coletti et al., 2018; Sabuzi et al., 2019; Sabuzi et al., 2021; Valentini et al., 2021). Moreover, various inorganic and organic vanadium (IV) complexes have been studied as catalysts in acetylation of alcohols, thiols, and amines, with high excess of acetic anhydride, eventually adding organic solvents (Chen et al., 2001; Oskooie et al., 2008; Taghavi et al., 2011).

In this study, vanadium (IV)-based catalysts have been employed in the sustainable esterification of thymol (2-isopropyl-5-methylphenol, 1), a natural phenolic compound, particularly known at the industrial level for its peculiar biological properties. Notably, functionalization allows to access different thymol derivatives characterized by even more improved bioactivity (Galloni et al., 2018; Piombino et al., 2020; Floris et al., 2021). To this purpose, over the last years, we have been involved in the synthesis of differently functionalized thymol-based products for applications in the biological and cosmetical fields (Sabuzi et al., 2015; Galloni et al., 2018; Piombino et al., 2020). In addition, many studies demonstrated that thymyl acetate resulted more effective than thymol against different pathogenic fungi and several bacterial strains (Floris et al., 2021); other thymyl esters have been recently highlighted for their promising biological and pharmacological activities (Chauhan et al., 2017; Tharamak et al., 2020; Floris et al., 2021). Therefore, considering the growing interest in such valuable compounds, a sustainable method for thymol esterification, even extended for the esterification of other phenols, aliphatic alcohols, and thiols, is presented here.

METHODS

All commercial reagents and solvents were purchased from Sigma-Aldrich/Merck Life Science, with the highest degree of purity, and they were used without any further purification. GC-MS analyses have been performed with a Shimadzu GCMS QP2010 Ultra system. ^{1}H-NMR experiments have been performed with Bruker Avance 700 MHz.

General Procedure for the Synthesis of Thymyl Acetate and Esters 3a–d

In a round-bottom flask, $VOSO_4{\cdot}5H_2O$ was suspended in the proper volume of the anhydride. After 10 min, 6.6 mmol (1 g) of thymol was added. The reaction was kept under stirring for 2 or 24 h at room temperature. The reaction was quenched with the addition of 50 ml of distilled H_2O, and it was kept under stirring for about 15 min. 10 ml of $NaHCO_3$ (s s.) were then added to the aqueous phase to neutralize the carboxylic acid formed as by-product. The aqueous phase was extracted with 100 ml of ethyl acetate. The organic phase was washed with 100 ml of water until neutrality was reached, dried over anhydrous Na_2SO_4, and filtered, and the solvent was removed under reduced pressure. The oil was purified by using a chromatography column (SiO_2, DCM: petroleum ether 2:3 *v:v*).

Synthesis of Thymyl Acetate on a 10 g Scale

168 mg of $VOSO_4{\cdot}5H_2O$ (0.66 mmol) was suspended in 6.4 ml of Ac_2O (0.068 mol). After 10 min, 10 g of thymol (0.067 mol) was added, and the reaction was kept under stirring for 24 h at room temperature. 150 ml of H_2O was added, and the aqueous phase was extracted with 2 × 100 mL of ethyl acetate. The organic phase was washed with 2 × 50 mL of 1 M NaOH solution to remove unreacted thymol and then with water. The organic phase was dried over anhydrous Na_2SO_4 and filtered, and the solvent was evaporated. The product was obtained as a colorless oil. Purity

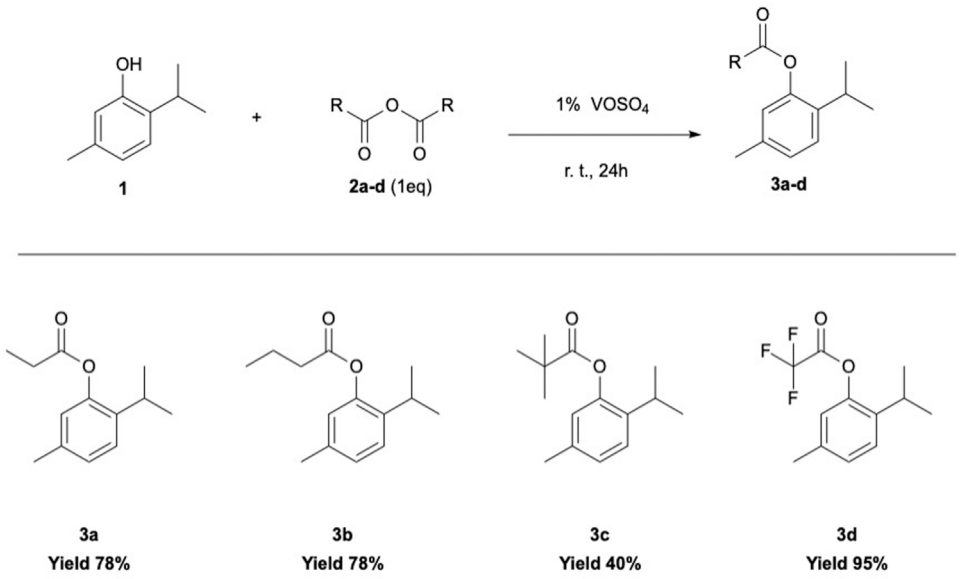

[a] Reaction conditions: thymol = 6.7 mmol, anhydrides = 6.7 mmol, $VOSO_4$ = 0.06 mmol, r.t., 24h.
[b] Isolated yield are reported.

FIGURE 1 | Thymol acetylation reaction using different anhydrides as the acetylating agent.

was checked by TLC and ^{1}H NMR analyses. Yield = 87% (11.2 g, 0.058 mol).

Synthesis of Thymyl Acetate on a 50 g Scale

50 g of thymol (0.33 mol) was added to a solution of 32 ml of acetic anhydride (0.34 mol) containing 835 mg of $VOSO_4{\cdot}5H_2O$ (3.3 mmol). The reaction was kept under stirring for 24 h at room temperature. The reaction was quenched with the addition of 200 ml of H_2O. Being non-soluble in water, the synthesized product has been separated from the aqueous phase through a separatory funnel. The product was diluted with 50 ml of ethyl acetate extracted with 2 × 50 mL of 1 M NaOH solution to remove unreacted thymol and then with water. Then, it was dried over anhydrous Na_2SO_4 and filtered, and the solvent was removed under reduced pressure. The product was obtained as a colorless oil. Purity was checked by TLC and ^{1}H NMR analyses. Yield = 97% (62.3 g, 0.32 mol).

Synthesis of Esters and Thioesters 5a–h

In a 5 ml round-bottom flask, 1 g of 4a–h was added to an equimolar amount of acetic anhydride containing 1% of $VOSO_4{\cdot}5H_2O$. The reaction was kept under stirring for 2 or 24 h at room temperature. The reaction was then quenched with 50 ml of H_2O and kept under stirring for about 15 min. 10 ml of $NaHCO_3$ (s s.) was then added to the aqueous phase, and it was extracted with 100 ml of ethyl acetate. The organic phase was then washed with 100 ml of distilled water until neutrality was reached. The organic phase was dried over anhydrous Na_2SO_4, filtered, and evaporated. The obtained product was purified by using a chromatography column.

Products have been characterized with GC-MS, ^{1}H NMR, and ^{13}C-NMR analyses. Data are included in **Supplementary Material S1**.

General Procedure for *O*-Acetylation With Isopropenyl Acetate

In a 5 ml round-bottom flask, 1% of $VOSO_4{\cdot}5H_2O$ was dissolved in 1 eq. of isopropenyl acetate. After 10 min, 1 g of substrate was added. The reaction was kept under magnetic stirring at 60°C for 24 h. An aliquot of 4 μL was taken and diluted in 5 ml with a solution 10 mM decane in ethyl acetate and analyzed with GC-MS. Results are reported in **Supplementary Table S7** and **Figure 3**.

RESULTS AND DISCUSSION

Thymol acetylation was initially explored using acetic anhydride as an acetylating reagent. Ac_2O activation was promoted by V(IV)-based catalysts, namely, vanadyl sulfate ($VOSO_4$) and vanadyl acetylacetonate ($VO(acac)_2$). To minimize waste production, thus increasing process sustainability, reactions have been carried out in solvent-free conditions. Consequently, Ac_2O has been exploited as a reagent and solvent. Results are reported in **Table 1**.

Results show that reactions performed at room temperature, with 5% of $VOSO_4$ or $VO(acac)_2$ and 8 equivalents of acetic anhydride, led to 85% of isolated product, and no difference between the catalysts has been observed (entries 1–2). Catalyst

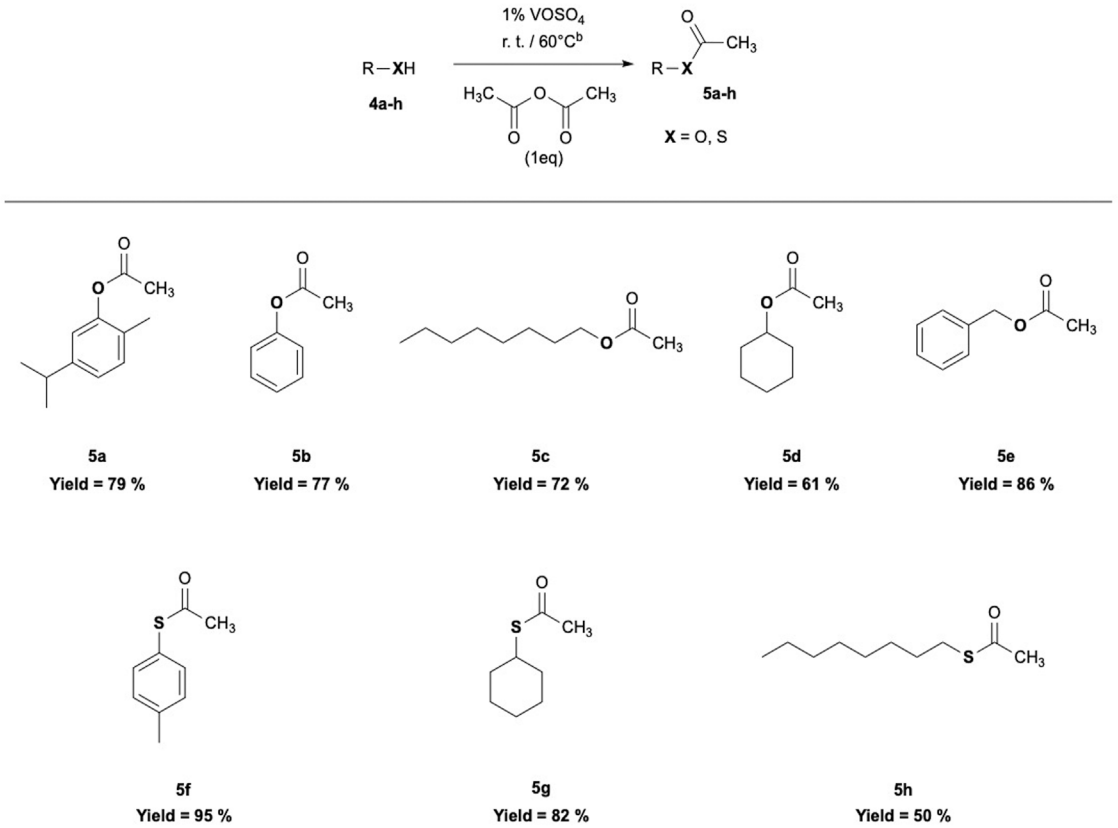

[a]Isolated yields are reported. Reaction conditions: substrate = 1 g, acetic anhydride = 1 eq, $VOSO_4$ = 1%, t = 24 h.
[b]S-acetylation was carried out at 60°C.

FIGURE 2 | *O,S*-acetylation reactions: substrate scope investigation.

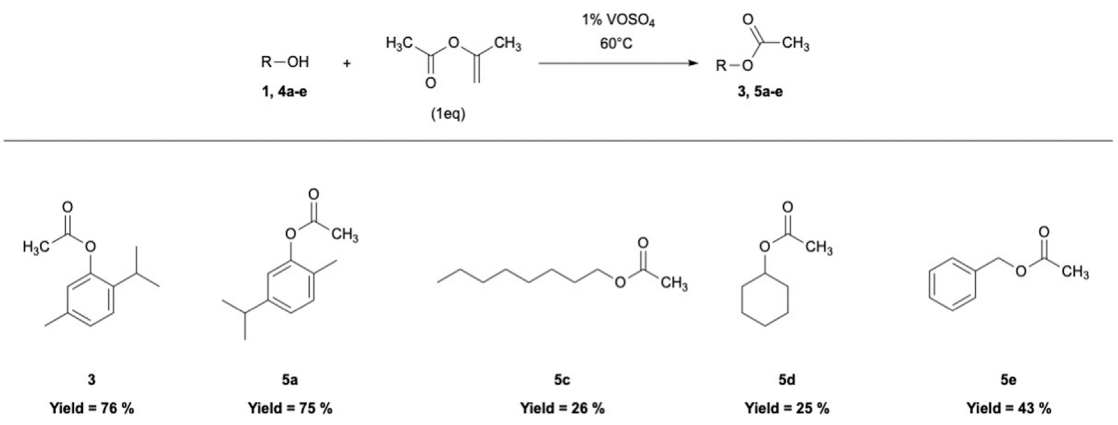

[a]GC-MS yields are reported.
[b]Reaction conditions: substrate = 1 g, isopropenyl acetate = 1 eq, VOSO4 = 1%, T = 60°C, t = 24h.

FIGURE 3 | *O*-acetylation with isopropenyl acetate.

loading was then decreased to 1% (entries 3–4), and $VOSO_4$ showed higher catalytic performance than $VO(acac)_2$. In particular, thymyl acetate was obtained with 80% yield in 24 h at room temperature, and a further decrease of the catalyst to 0.5% led to only a slight decrease of the yield (entry 5). Thus, 1% of vanadyl sulfate has been chosen for further experiments. Interestingly, with respect to the other catalysts commonly used for acetylation reactions such as amines (Steglich and Hofle, 1969; Mandai et al., 2018), phosphines (Vedejs et al., 1993), and Lewis acid complexes with hard anions (Chandra et al., 2002; Reddy et al., 2006), environmental and human health risks associated with the use of $VOSO_4$ are reduced, being non-toxic for humans, non-flammable, or non-corrosive. Therefore, $VOSO_4$ is considered a safe and biocompatible catalyst; recently, the pharmacological benefits associated with its assumption have been highlighted (Ścibior et al., 2020).

In order to further improve the sustainability of such process, the amount of Ac_2O was gradually decreased, and its effect on product yield has been investigated (entries 6–8): reduction of Ac_2O up to 1 equivalent (620 μL per gram of thymol) does not affect product yield, which still results higher than 80% (entry 8). The remarkable progress reported here is the $VOSO_4$ reduction to 1% and the stoichiometric amount of Ac_2O. In fact, in previously optimized processes, 50% excess of the reactant and higher catalyst loadings (5% mol) were required (Oskooie et al., 2008). Such a result greatly improves the E-factor (Sheldon, 2008) of the process, since a 1:1 stoichiometric ratio between the reactants is preferred to avoid large amount of wastes (Sarkar et al., 2016). Interestingly, reactions performed on a larger scale (i.e., on 10 and 50 g of substrate) led to even more improved yields and strongly reduced E-factor values because of the simplified workup (entries 9–10). In particular, 97% of thymyl acetate was isolated performing the reaction on a 50 g scale, likely anticipating promising results for further scale-ups. To note, all the reactions led to the selective formation of thymyl acetate, and blank experiments showed only 3% of the product (entry 11).

Considering the biological relevance of thymyl esters, the optimized reaction conditions have been exploited to perform thymol esterification with different anhydrides (**Figure 1**). Remarkably, thymyl esters 3a–3d were obtained in moderate to very good yields at room temperature, working with a stoichiometric amount of reactants and 1% of $VOSO_4$ (**Supplementary Table S1**). Notably, by increasing the acylating reagent side chain length, a slight decrease in product yield was observed (**Supplementary Table S1**, entries 1–4), while with trimethyl acetic anhydride (TMA) (**Supplementary Table S1**, entries 5–6), only 40% of the product was obtained after 24 h. As a matter of fact, both steric hindrance and inductive effect of the three alkyl groups likely deactivate TMA toward a nucleophilic attack (Chen et al., 2001). Conversely, trifluoroacetic anhydride resulted more reactive than the others; indeed, a significant increase in the yield was observed, reaching 90% of isolated product in 2 h and 95% in 24 h (**Supplementary Table S1**, entries 7–8).

Given the very good results achieved in thymol esterification, substrate scope has been investigated using acetic anhydride as a model reagent. *O*- or *S*-acetylation of phenols, alcohols, and aryl and alkyl thiols has been performed, using a stoichiometric amount of acetic anhydride and 1% of vanadyl sulfate (**Figure 2**, **Supplementary Tables S3, S4**).

Carvacryl and phenyl acetates (5a–b) were obtained with good yields, comparable to that of thymyl acetate in the same conditions, and 86% yield was achieved with benzyl acetate (5e) in 24 h at room temperature. Also, 1-octanol and cyclohexanol were converted to their corresponding esters (5c–d) with a good but slightly lower yield. On the contrary, *S*-acetylation of alkyl and aryl thiols required higher reaction temperature (**Supplementary Table S4**). Still, 4-methylphenyl thioacetate (5f) has been obtained with 95% yield at 60°C, while alkyl thiols, such as cyclohexanethiol and 1-octanethiol, were converted to their corresponding thioacetate with 68 and 50% of isolated yield, respectively, likely indicating that both substrate nucleophilicity and steric hindrance affect reaction outcome.

In the context of acetylation reactions, isopropenyl acetate (IPA) is recently emerging as a new green acetylating reagent for alcohols (Barry, et al., 1988; Temperini et al., 2017; Zhu et al., 2018; Rigo et al., 2020), thiols (Kuciński and Hreczycho, 2018), and amines (Pelagalli et al., 2012). The main advantage of IPA is related with the formation of acetone as the only by-product, which can be easily removed from the reaction mixture through distillation. On the contrary, acetylation reactions performed with Ac_2O lead to the formation of acetic acid, which must be removed through acid–base extractions. In one of the first reported examples concerning IPA application in acetylation reactions, 20% mol K_2CO_3 was the catalyst (Barry et al., 1988). Although the reaction proceeded with an almost quantitative yield at room temperature, the environmental impact of the process was negatively influenced by the strong basicity and high amount of the base. In fact, after reaction, high volumes of water were possibly needed to neutralize the K_2CO_3 solution, thus making the process less sustainable and raising disposal budgets. Such treatments are absent in $VOSO_4$-catalyzed reactions. Thus, 1% of vanadyl sulfate has been used as the catalyst in the *O*-acetylation of alcohols and phenols, using isopropenyl acetate as both reagent and solvent in a stoichiometric amount (**Figure 3**). However, at room temperature, *O*-acetylation did not occur with satisfactory yields; therefore, reactions have been carried out at 60°C. Remarkably, thymol and carvacrol acetylation were accomplished with ca. 75% yield, which is in line with the results achieved with Ac_2O; conversely, octyl, cyclohexyl, and benzyl acetate were obtained in lower amounts, and the reaction performed on aryl and alkyl thiols led to poor yields and lacked in selectivity (**Supplementary Table S7**).

CONCLUSION

In this study, a sustainable procedure to carry out acylation reactions has been proposed. Thymol has been adopted as model substrate, as its ester derivatives are particularly known for their biological properties. Results showed that it is possible to successfully perform thymol acetylation using a stoichiometric amount of acetic anhydride in solvent-free conditions. The activation of acetic anhydride is promoted by the addition of

1% of $VOSO_4$. Here, thymyl acetate can be isolated in 80% yield in 24 h at room temperature. The optimized process shows an E-factor decisively lower than that of the classical acylation reactions, which requires the use of a large excess of acetic anhydride and organic solvents. The advantages of the process have been confirmed by preliminary scale-up studies, which showed that the 50 g scale reaction proceeds with an almost quantitative substrate conversion. Furthermore, the optimized conditions can be efficiently adopted for the synthesis of thymyl esters using different anhydrides, as well as for the acylation of other phenols, alkyl alcohols, and alkyl and aryl thiols.

Interestingly, a further improvement of the sustainability of the process was achieved by carrying out the reaction with a stoichiometric amount of isopropenyl acetate, which is a "greener" alternative to acetic anhydride, as the only by-product is acetone, which is easily removed from the reaction mixture through distillation. Again, good results in phenol acetylation have been obtained at 60°C, although the reaction is worth to be further optimized for alkyl alcohols and thiols.

DATA AVAILABILITY STATEMENT

The original contributions presented in the study are included in the article/**Supplementary Material**, further inquiries can be directed to the corresponding author.

AUTHOR CONTRIBUTIONS

PG and FS developed the idea and designed the experiments; FV and DB performed the experiments and analyzed data; FS supervised the experimental work; FV wrote the manuscript draft; and FS, PG, and VC reviewed and edited the manuscript.

FUNDING

This research was funded by Lazio Innova—Regione Lazio Progetti Gruppi di Ricerca 2020 (POR FESR LAZIO 2014-2020), Grant No. A0375-2020-36654 BeeO-GEL Project.

ACKNOWLEDGMENTS

The authors thank Mr. Lorenzo Tommasi for preliminary experiments.

SUPPLEMENTARY MATERIAL

The Supplementary Material for this article can be found online at: https://www.frontiersin.org/articles/10.3389/fchem.2022.842190/full#supplementary-material

REFERENCES

Bajracharya, G. B., and Shrestha, S. S. (2018). Unprecedented Acetylation of Phenols Using a Catalytic Amount of Magnesium Powder. *Synth. Commun.* 48, 1688–1693. doi:10.1080/00397911.2018.1459721

Barrett, A. G. M., and Christopher Braddock, D. (1997). Scandium(III) or Lanthanide(III) Triflates as Recyclable Catalysts for the Direct Acetylation of Alcohols with Acetic Acid. *Chem. Commun.* 4, 351–352. doi:10.1039/A606484A

Barry, J., Bram, G., and Petit, A. (1988). Organic Syntheses without Solvent: Base-Catalysed Ester Interchange. *Tetrahedron Lett.* 29, 4567–4568. doi:10.1016/S0040-4039(00)80548-1

Bartoli, G., Bosco, M., Dalpozzo, R., Marcantoni, E., Massaccesi, M., and Sambri, L. (2003). $Zn(ClO_4)_2{\cdot}6H_2O$ as a Powerful Catalyst for a Practical Acylation of Alcohols with Acid Anhydrides. *Eur. J. Org. Chem.* 2003, 4611–4617. doi:10.1002/ejoc.200300458

Behera, S., and Patra, B. N. (2021). An Efficient, Economical and Eco-Friendly Acylation of Alcohols and Amines by Alum Doped Nanopolyaniline under Solvent Free Condition. *Appl. Catal. A: Gen.* 623, 118288–118295. doi:10.1016/j.apcata.2021.118288

Carey, J. S., Laffan, D., Thomson, C., and Williams, M. T. (2006). Analysis of the Reactions Used for the Preparation of Drug Candidate Molecules. *Org. Biomol. Chem.* 4, 2337–2347. doi:10.1039/b602413k

Chandra, K. L., Saravanan, P., Singh, R. K., and Singh, V. K. (2002). Lewis Acid Catalyzed Acylation Reactions: Scope and Limitations. *Tetrahedron* 58, 1369–1374. doi:10.1016/S0040-4020(01)01229-7

Chauhan, K. K., Frost, C. G., Love, I., and Waite, D. (1999). Indium Triflate: An Efficient Catalyst for Acylation Reactions. *Synlett* 1999, 1743–1744. doi:10.1055/s-1999-2941

Chauhan, K. R., Le, T. C., Chintakunta, P. K., and Lakshman, D. K. (2017). Phyto-Fungicides: Structure Activity Relationships of the Thymol Derivatives against *Rhizoctonia Solani*. *Jacen* 06, 175–185. doi:10.4236/jacen.2017.64012

Chen, C.-T., Kuo, J.-H., Li, C.-H., Barhate, N. B., Hon, S.-W., Li, T.-W., et al. (2001). Catalytic Nucleophilic Acyl Substitution of Anhydrides by Amphoteric Vanadyl Triflate. *Org. Lett.* 3, 3729–3732. doi:10.1021/ol016684c

Chutia, R., and Chetia, B. (2020). Acetylation of Alcohols, Phenols and Amines Using Waste Plant Extract. *SN Appl. Sci.* 2, 1564–1572. doi:10.1007/s42452-020-03353-2

Coletti, A., Sabuzi, F., Floris, B., Galloni, P., and Conte, V. (2018). Efficient and Sustainable V-Catalyzed Oxidative Desulfurization of Fuels Assisted by Ionic Liquids. *J. Fuel Chem. Technol.* 46, 1121–1129. doi:10.1016/S1872-5813(18)30045-8

Conte, V., and Floris, B. (2010). Vanadium Catalyzed Oxidation with Hydrogen Peroxide. *Inorg. Chim. Acta* 363, 1935–1946. doi:10.1016/j.ica.2009.06.056

Das, R., and Chakraborty, D. (2011). Silver Triflate Catalyzed Acetylation of Alcohols, Thiols, Phenols, and Amines. *Synthesis* 2011, 1621–1625. doi:10.1055/s-0030-1259999

De, S. K. (2004). Ruthenium(III) Chloride Catalyzed Acylation of Alcohols, Phenols, Thiols, and Amines. *Tetrahedron Lett.* 45, 2919–2922. doi:10.1016/j.tetlet.2004.02.071

Floris, B., Sabuzi, F., Coletti, A., and Conte, V. (2017). Sustainable Vanadium-Catalyzed Oxidation of Organic Substrates with H_2O_2. *Catal. Today* 285, 49–56. doi:10.1016/j.cattod.2016.11.006

Floris, B., Galloni, P., Conte, V., and Sabuzi, F. (2021). Tailored Functionalization of Natural Phenols to Improve Biological Activity. *Biomolecules* 11, 1325–1388. doi:10.3390/biom11091325

Galloni, P., Mancini, M., Floris, B., and Conte, V. (2013). A Sustainable Two-phase Procedure for V-Catalyzed Toluene Oxidative Bromination with H_2O_2-KBr. *Dalton Trans.* 42, 11963–11970. doi:10.1039/c3dt50907a

Galloni, P., Conte, V., Sabuzi, F., Migliore, L., Thaller, M. C., and Matteucci, G. (2018). *Sustainable Process for the Preparation of Highly Pure 4-bromothymol and its Applications as Antimicrobial Agent*. Geneva, Switzerland : European Patent Office. WO 2018/046584 A1.

Hlatshwayo, X. S., Ndolomingo, M. J., Bingwa, N., and Meijboom, R. (2021). Molybdenum-modified Mesoporous SiO_2 as an Efficient Lewis Acid Catalyst for the Acetylation of Alcohols. *RSC Adv.* 11, 16468–16477. doi:10.1039/d1ra02134f

Ishihara, K., Kubota, M., Kurihara, H., and Yamamoto, H. (1995). Scandium Trifluoromethanesulfonate as an Extremely Active Acylation Catalyst. *J. Am. Chem. Soc.* 117, 4413–4414. doi:10.1021/ja00120a030

Jain, I., Sharma, R., and Malik, P. (2019). Manganese-Mediated Acetylation of Alcohols, Phenols, Thiols, and Amines Utilizing Acetic Anhydride. *Synth. Commun.* 49, 1–9. doi:10.1080/00397911.2019.1650282

Kuciński, K., and Hreczycho, G. (2018). S-Acetylation of Thiols Mediated by Triflic Acid: A Novel Route to Thioesters. *Org. Process. Res. Dev.* 22, 489–493. doi:10.1021/acs.oprd.7b00378

Kumar, N. U., Reddy, B. S., Reddy, V. P., and Bandichhor, R. (2014). Zinc Triflate Catalyzed Acylation of Alcohols, Phenols, and Thiophenols. *Tetrahedron Lett.* 55, 910–912. doi:10.1016/j.tetlet.2013.12.039

Larionov, E., and Zipse, H. (2011). Organocatalysis: Acylation Catalysts. *Wires Comput. Mol. Sci.* 1, 601–619. doi:10.1002/wcms.48

Lugemwa, F., Shaikh, K., and Hochstedt, E. (2013). Facile and Efficient Acetylation of Primary Alcohols and Phenols with Acetic Anhydride Catalyzed by Dried Sodium Bicarbonate. *Catalysts* 3, 954–965. doi:10.3390/catal3040954

Mandai, H., Fujii, K., and Suga, S. (2018). Recent Topics in Enantioselective Acyl Transfer Reactions with Dialkylaminopyridine-Based Nucleophilic Catalysts. *Tetrahedron Lett.* 59, 1787–1803. doi:10.1016/j.tetlet.2018.03.016

Orita, A., Tanahashi, C., Kakuda, A., and Otera, J. (2001). Highly Powerful and Practical Acylation of Alcohols with Acid Anhydride Catalyzed by $Bi(OTf)_3$. *J. Org. Chem.* 66, 8926–8934. doi:10.1021/jo0107453

Oskooie, H. A., Baghernezhad, B., Heravi, M. M., and Beheshtiha, Y. S. (2008). Vanadyl Sulfate ($VOSO_4{\cdot}3H_2O$). An Efficient Catalyst for Acylation of Alcohols and Phenols under Solvent Free Condition. *J. Chin. Chem. Soc.* 55, 713–715. doi:10.1002/jccs.200800107

Pantawane, A. R., Thul, M., Lin, Y.-J., Lin, M., Lin, W., Julakanti, S. R., et al. (2021). Mild and Efficient Tunable Brønsted Acidic Ionic Liquid Catalyzed *O*-Acetylation and *O*-Trimethylsilylation with Trimethylsilyl Acetate (TMSOAc) and Hexamethyldisilazane (HMDS). *Catalysts* 11, 825–838. doi:10.3390/catal11070825

Pelagalli, R., Chiarotto, I., Feroci, M., and Vecchio, S. (2012). Isopropenyl Acetate, a Remarkable, Cheap and Acylating Agent of Amines under Solvent- and Catalyst-free Conditions: a Systematic Investigation. *Green. Chem.* 14, 2251–2255. doi:10.1039/c2gc35485c

Piombino, C., Lange, H., Sabuzi, F., Galloni, P., Conte, V., and Crestini, C. (2020). Lignosulfonate Microcapsules for Delivery and Controlled Release of Thymol and Derivatives. *Molecules* 25, 866–882. doi:10.3390/molecules25040866

Rajabi, F., and Luque, R. (2014). Solventless Acetylation of Alcohols and Phenols Catalyzed by Supported Iron Oxide Nanoparticles. *Catal. Commun.* 45, 129–132. doi:10.1016/j.catcom.2013.11.003

Reddy, T. S., Narasimhulu, M., Suryakiran, N., Mahesh, K. C., Ashalatha, K., and Venkateswarlu, Y. (2006). A Mild and Efficient Acetylation of Alcohols, Phenols and Amines with Acetic Anhydride Using $La(NO_3)_3{\cdot}6H_2O$ as a Catalyst under Solvent-free Conditions. *Tetrahedron Lett.* 47, 6825–6829. doi:10.1016/j.tetlet.2006.07.059

Rigo, D., Calmanti, R., Perosa, A., and Selva, M. (2020). A Transesterification-Acetalization Catalytic Tandem Process for the Functionalization of Glycerol: the Pivotal Role of Isopropenyl Acetate. *Green. Chem.* 22, 5487–5496. doi:10.1039/d0gc01775b

Sabuzi, F., Churakova, E., Galloni, P., Wever, R., Hollmann, F., Floris, B., et al. (2015). Thymol Bromination - A Comparison between Enzymatic and Chemical Catalysis. *Eur. J. Inorg. Chem.* 2015, 3519–3525. doi:10.1002/ejic.201500086

Sabuzi, F., Pomarico, G., Floris, B., Valentini, F., Galloni, P., and Conte, V. (2019). Sustainable Bromination of Organic Compounds: A Critical Review. *Coord. Chem. Rev.* 385, 100–136. doi:10.1016/j.ccr.2019.01.013

Sabuzi, F., Pomarico, G., Conte, V., and Galloni, P. (2021). in *Peroxo-vanadium Complexes as Sustainable Catalysts in Oxidations, Halogenations and Other Organic Transformations*. Editors M. Sutradhar, J. L. A. L. da Silva, and A. J. L. Pombeiro (London, UK: RSC), 97–110.

Saravanan, P., and Singh, V. K. (1999). An Efficient Method for Acylation Reactions. *Tetrahedron Lett.* 40, 2611–2614. doi:10.1016/S0040-4039(99)00229-4

Sarkar, A., Santra, S., Kundu, S. K., Hajra, A., Zyryanov, G. V., Chupakhin, O. N., et al. (2016). A Decade Update on Solvent and Catalyst-free Neat Organic Reactions: a Step Forward towards Sustainability. *Green. Chem.* 18, 4475–4525. doi:10.1039/C6GC01279E

Ścibior, A., Pietrzyk, Ł., Plewa, Z., and Skiba, A. (2020). Vanadium: Risks and Possible Benefits in the Light of a Comprehensive Overview of its Pharmacotoxicological Mechanisms and Multi-Applications with a Summary of Further Research Trends. *J. Trace Elem. Med. Biol.* 61, 126508. doi:10.1016/j.jtemb.2020.126508

Sheldon, R. A. (2008). E Factors, Green Chemistry and Catalysis: an Odyssey. *Chem. Commun.* 44, 3352–3365. doi:10.1039/b803584a

Singha, R., and Ray, J. K. (2016). Selective Acetylation of Primary Alcohols by Ethyl Acetate. *Tetrahedron Lett.* 57, 5395–5398. doi:10.1016/j.tetlet.2016.10.088

Steglich, W., and Höfle, G. (1969). N,N-Dimethyl-4-Pyridinamine, a Very Effective Acylation Catalyst. *Angew. Chem. Int. Ed. Engl.* 8, 981. doi:10.1002/anie.196909811

Su, Y., Sun, C., Sun, X., Wu, R., Zhang, X., and Tu, Y. (2020). Acetylresveratrol as a Potential Substitute for Resveratrol Dragged the Toxic Aldehyde to Inhibit the Mutation of Mitochondrial DNA. *Appl. Biochem. Biotechnol.* 191, 1340–1352. doi:10.1007/s12010-020-03279-w

Taghavi, S. A., Moghadam, M., Mohammadpoor-Baltork, I., Tangestaninejad, S., Mirkhani, V., and Khosropour, A. R. (2011). Investigation of Catalytic Activity of High-Valent Vanadium(IV) Tetraphenylporphyrin: A New, Highly Efficient and Reusable Catalyst for Acetylation of Alcohols and Phenols with Acetic Anhydride. *Inorg. Chim. Acta* 377, 159–164. doi:10.1016/j.ica.2011.07.036

Temperini, A., Minuti, L., Morini, T., Rosati, O., and Piazzolla, F. (2017). Isopropenyl Acetate: A Cheap and General Acylating Agent of Alcohols under Metal-free Conditions. *Tetrahedron Lett.* 58, 4051–4053. doi:10.1016/j.tetlet.2017.09.007

Tharamak, S., Yooboon, T., Pengsook, A., Ratwatthananon, A., Kumrungsee, N., Bullangpoti, V., et al. (2020). Synthesis of Thymyl Esters and Their Insecticidal Activity against *Spodoptera Litura* (Lepidoptera: Noctuidae). *Pest Manag. Sci.* 76, 928–935. doi:10.1002/ps.5598

Valentini, F., Ferracci, G., Galloni, P., Pomarico, G., Conte, V., and Sabuzi, F. (2021). Sustainable Highly Selective Toluene Oxidation to Benzaldehyde. *Catalysts* 11, 262–277. doi:10.3390/catal11020262

Vane, J. R., and Botting, R. M. (2003). The Mechanism of Action of Aspirin. *Thromb. Res.* 110, 255–258. doi:10.1016/S0049-3848(03)00379-7

Vedejs, E., Bennett, N. S., Conn, L. M., Diver, S. T., Gingras, M., Lin, S., et al. (1993). Tributylphosphine-Catalyzed Acylations of Alcohols: Scope and Related Reactions. *J. Org. Chem.* 58, 7286–7288. doi:10.1021/jo00077a064

Zhao, H., Pendri, A., and Greenwald, R. B. (1998). General Procedure for Acylation of 3° Alcohols: Scandium Triflate/DMAP Reagent. *J. Org. Chem.* 63, 7559–7562. doi:10.1021/jo981161c

Zhu, X., Qian, B., Wei, R., Huang, J.-D., and Bao, H. (2018). Protection of COOH and OH Groups in Acid, Base and Salt Free Reactions. *Green. Chem.* 20, 1444–1447. doi:10.1039/c8gc00037a

Conflict of Interest: Authors DB, PG, and FS are employed by BT-InnoVaChem srl.

The remaining authors declare that the research was conducted in the absence of any commercial or financial relationship that could be construed as a potential conflict of interest.

frontiers in Chemistry

ORIGINAL RESEARCH
published: 22 March 2022
doi: 10.3389/fchem.2022.856832

The Synthesis of Picolinamide-Supported Tetracoordinated Organoboron Complexes with Aggregation-Induced Emission Property

Gaoqiang You, Liang Xu and Yu Wei**

Key Laboratory for Green Processing of Chemical Engineering of Xin-Jiang Bingtuan, School of Chemistry and Chemical Engineering, Shihezi University, Shihezi, China

The picolinamide-supported tetracoordinated organoboron complexes containing diaryl boronyl segments have been synthesized for the first time. Aryl trifluoroborates were utilized as the BAr_2 sources to introduce different aryl motifs with diverse functional groups. The optical experiments discovered these five-membered boron-containing complexes were aggregation-induced emission (AIE) active, thus affording a new class of AIE molecules.

Keywords: tetracoordinated organoboron, AIE, picolinamide, potassium trifluoroborate, manganese

OPEN ACCESS

Edited by:
Jamal Rafique, Federal University of Mato Grosso do Sul, Brazil

Reviewed by:
Zhao Chen, Jiangxi Science and Technology Normal University, China
Dario Pasini, University of Pavia, Italy

****Correspondence:***
Liang Xu
xuliang4423@shzu.edu.cn
Yu Wei
yuweichem@shzu.edu.cn

Specialty section:
This article was submitted to Organic Chemistry, a section of the journal Frontiers in Chemistry

Received: *17 January 2022*
Accepted: *21 February 2022*
Published: *22 March 2022*

Citation:
You G, Xu L and Wei Y (2022) The Synthesis of Picolinamide-Supported Tetracoordinated Organoboron Complexes with Aggregation-Induced Emission Property. Front. Chem. 10:856832. doi: 10.3389/fchem.2022.856832

INTRODUCTION

Taking advantage of the vacant *p*-orbitals of the boron atoms, the chelating complexation between π-conjugated ligands and -BR_2 units will generate tetracoordinated organoboron complexes containing X→B dative bonds that are able to lock the π-conjugated ligands. These modifications will enhance the molecular rigidity, extend the π-conjugation system, and thus afford molecules with superior photoluminescence properties (Chen et al., 2017; Dou et al., 2017; Mellerup and Wang, 2019; Yan et al., 2019; Huang et al., 2020). Therefore, over the past decades, the synthesis, improvement, and application of these tetracoordinated organoboron complexes have attracted a continuing interest from organic and materials communities. However, the emission of these planar structures in aggregates or the solid-state is usually spoiled due to the aggregation-caused quenching (ACQ) effects. This limits their applications in organic optoelectronic materials or other situations that demand solid-state emissions, such as organic lasers and organic light-emitting diodes (OLEDs), which necessitates the development of new series of these complexes with high solid-state luminescence efficiency.

Since the conceptualization of the aggregation-induced emission (AIE) effect by the Tang group in 2001 (Luo et al., 2001; Mei et al., 2015), many types of AIE-active compounds/units have been developed. In recent years, a number of AIE-active tetracoordinated organoboron complexes have been synthesized and applied as aggregate-state emitters (Virgili et al., 2013; Liu et al., 2019; Nitti et al., 2020; Ito et al., 2021; Yin et al., 2021; Min et al., 2022). These AIE-active complexes, which are usually obtained *via* linking AIE-active units such as tetraphenylethylene (TPE) or introducing rotational aryls onto the chelating backbones, mostly contain BF_2 segments. The introduction of BAr_2 segments, which had two bulky aryl rings on boron atoms, has been utilized to disrupt the intermolecular π–π stacking in aggregate states and thus enable more efficient AIE effects (**Figure 1**). Based on our survey, most of the known AIE-active complexes with BAr_2 segments were six-

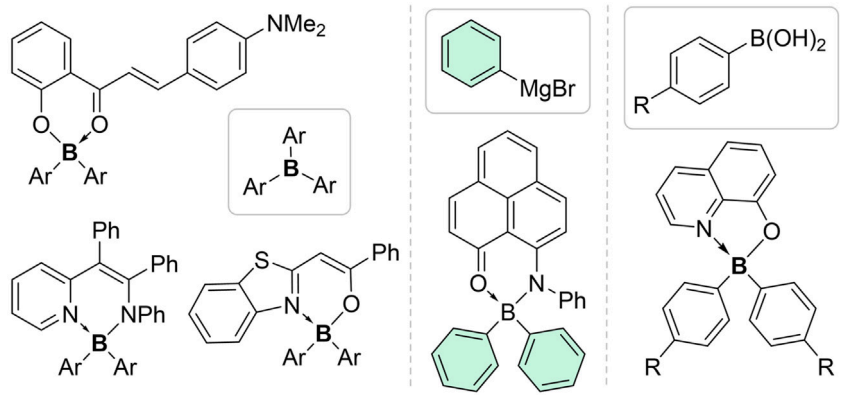

FIGURE 1 | The tetracoordinated organoboron complexes containing BAr_2 segments with AIE properties. The aryl precursors are indicated in the boxes.

TABLE 1 | Optimization of reaction conditions[a].

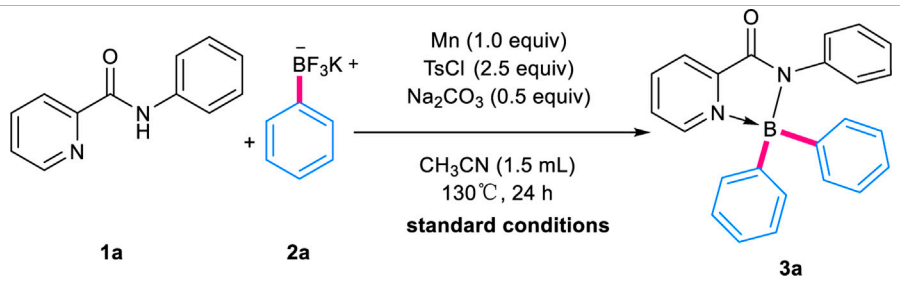

Entry	Variations from the standard conditions	Yields (%)[b]
1	None	99
2	Without Mn	81
3	Without TsCl	N.R.
4	Without Na_2CO_3	24
5	DMF instead of MeCN	Trace
6	DMA instead of MeCN	Trace
7	THF instead of MeCN	Trace
8	NMP instead of MeCN	Trace
9	DMSO instead of MeCN	Trace
10	HFIP instead of MeCN	Trace
11	90°C instead of 130°C	N.R.
12	110°C instead of 130°C	66
13	K_3PO_4 instead of Na_2CO_3	24
14	Cs_2CO_3 instead of Na_2CO_3	27
15	LiOH instead of Na_2CO_3	41
16	$PhBF_3K$ (4.0 equiv)	41
17	$PhBF_3K$ (3.0 equiv)	23

[a]*Reaction conditions:* ***1a*** *(0.15 mmol),* ***2a*** *(0.75 mmol, 5 equiv), air, CH_3CN (1.5 ml), 130°C, 24 h.*
[b]*Isolated yields.*

membered. To the best of our knowledge, the only AIE-active five-membered cases have been disclosed very recently by Yang and Zou group (Qi et al., 2021). This was surprising since five-membered tetracoordinated organoboron compounds were very commonly encountered in organoboron-based molecules and materials. Moreover, BAr_2 segments were usually introduced via Ar_3B or aryl organometallic reagents (Kubota et al., 2012; Yan et al., 2014; Gong et al., 2015; Wang et al., 2015; Wu et al., 2015), limiting the accessibility and diversity of the target molecules (Yang et al., 2021).

On the other hand, innumerable chelating backbones have been applied in the complexation formation of tetracoordinated organoboron, to fine-tune the desirable luminescence properties. In this regard, it is surprising that picolinamide, one of the most available and widely-used chelating ligands in coordination chemistry, has never been used in the preparation of

TABLE 2 | Optimization of reaction conditions[a].

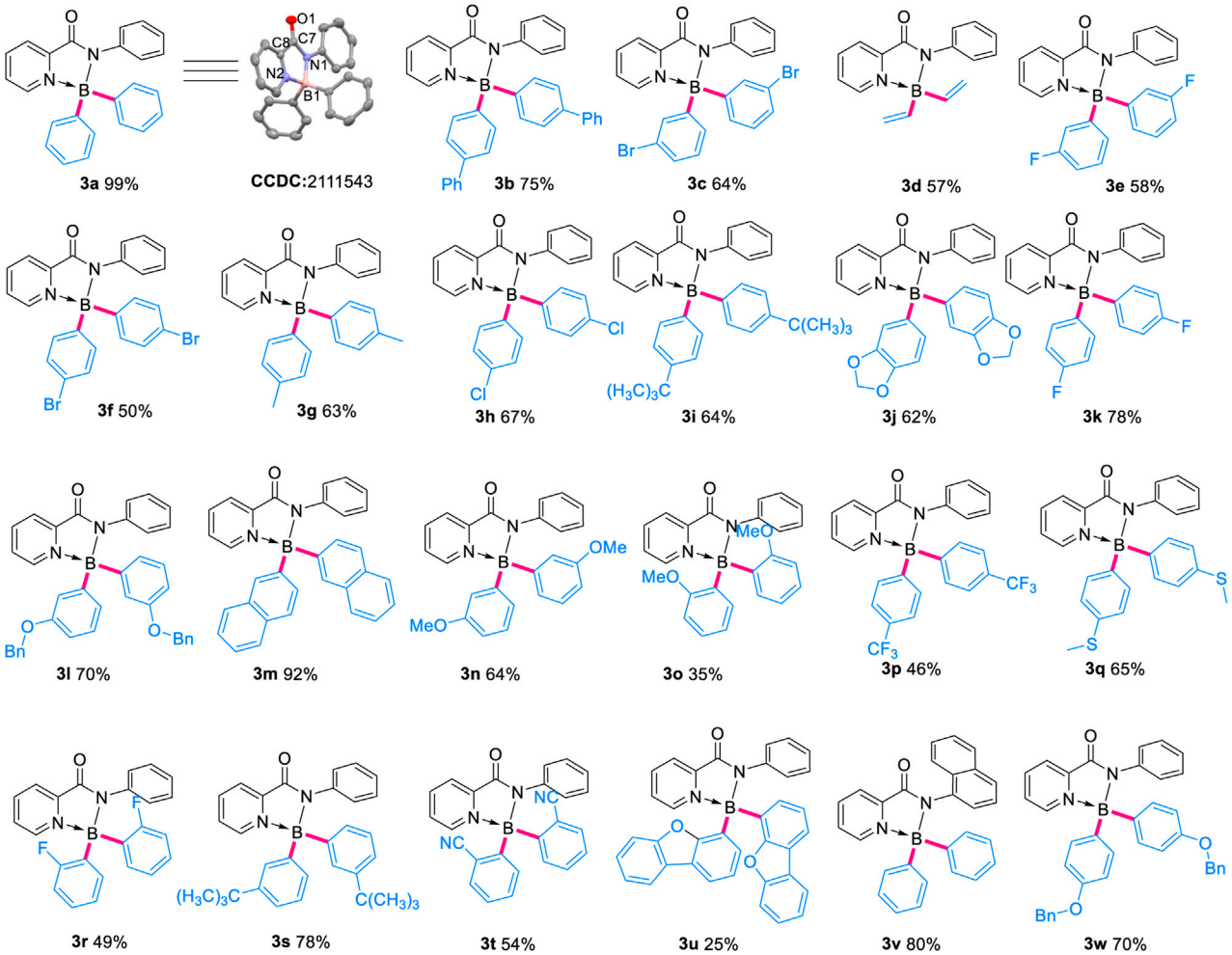

[a]*Reaction conditions: pyridinecarboxamide* ***1*** *(0.15 mmol), potassium aryl trifluoroborate* ***2*** *(0.75 mmol, 5 equiv), air, CH_3CN (1.5 ml), 130°C, 24 h.*

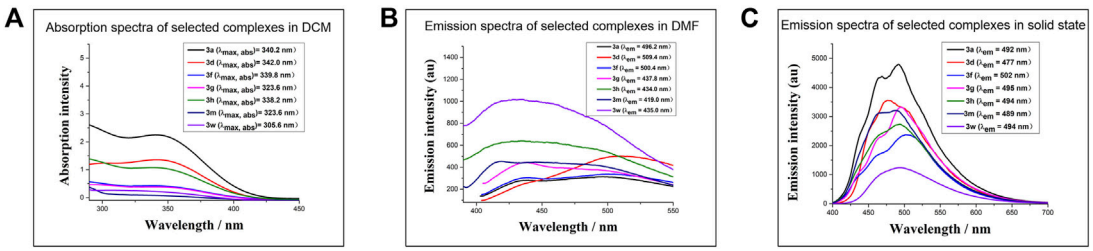

FIGURE 2 | The absorption and emission spectra of selected complexes.

tetracoordinated organoboron, to the best of our knowledge (Yang et al., 2021). Thus, we hypothesized that complexation between picolinamide and BAr_2 segments would afford a new series of tetracoordinated organoboron molecules. These complexes should adopt propeller structures and be consisted of electron-deficient pyridyl, electron-rich anilino groups, and the spiro linker centers of boron atoms, which potentially circumvent the trade-off between the complexation stability and the solid-

TABLE 3 | Luminescence quantum yield and lifetime of selected complexes.

	3a	3d	3f	3g	3h	3m	3w
Φ_{liquid} (%)[a]	0.31	0.39	0.39	0.64	0.59	1.02	1.09
τ_{liquid} (ns)[a]	1.99	1.86	1.91	1.76	2.03	1.86	2.01
Φ_{solid} (%)	78.38	82.46	44.26	89.54	97.83	82.96	31.48
τ_{solid} (ns)	3.64	4.29	3.01	3.84	3.31	2.98	3.29

[a]*Sample concentration 10^{-4} M.*

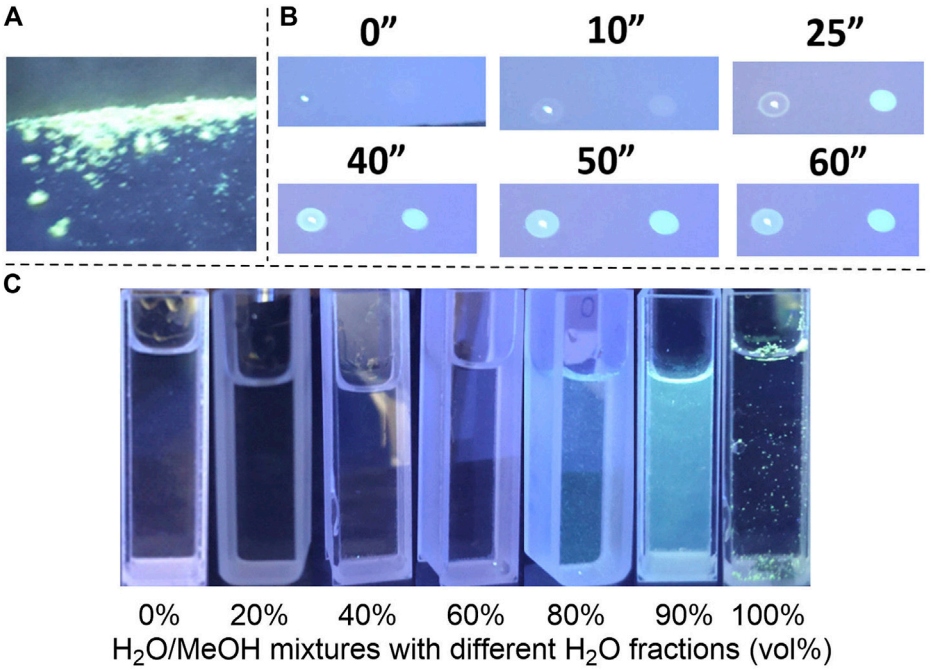

FIGURE 3 | AIE behaviours of **3a**. **(A) 3a** solid at 365 nm. **(B)** Fluorescence comparison of **3a** solution at 365 nm at different time. **(C)** Fluorescence comparison of **3a** at 365 nm in different ratios of water/methanol.

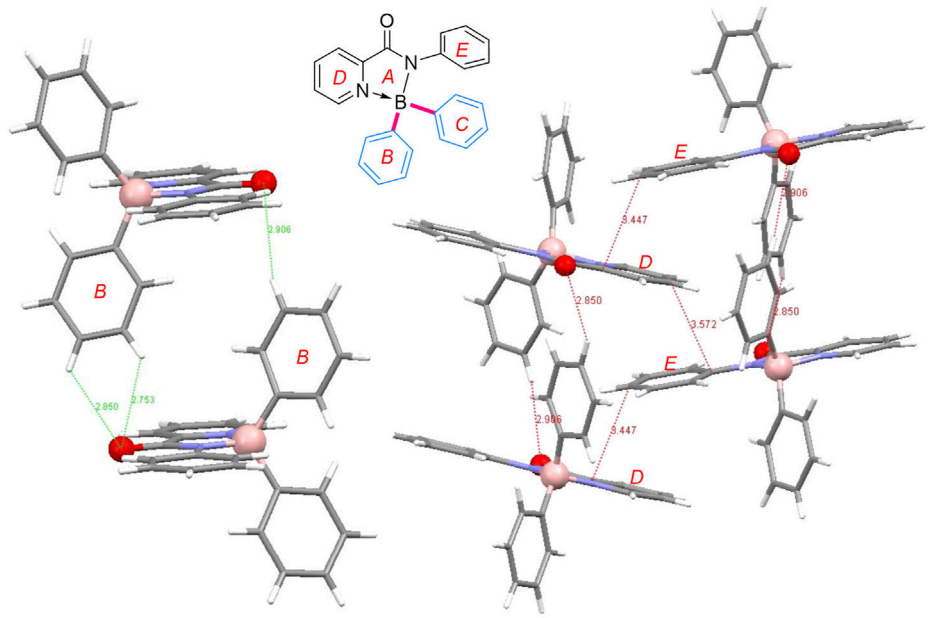

FIGURE 4 | The crystal structure of **3a**.

state luminescence, leading to some special light-emitting molecules (Shiu et al., 2016). The proposal would pose at least two major challenges: 1) to properly introduce the relatively flexible picolinamide ligands and 2) to bypass the traditional organometallic BAr_2 incorporation pathways.

RESULTS AND DISCUSSION

With these considerations in mind, the investigation was initiated by exploring the reaction between *N*-phenylpyridinecarboxamide **1a** and potassium phenyltrifluoroborate **2a** (Sawazaki et al., 2018; Wang

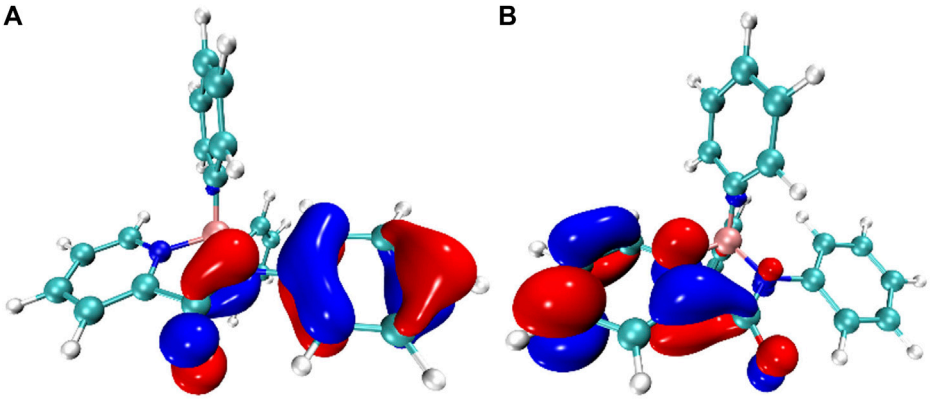

FIGURE 5 | The calculated HOMO **(A)** and LUMO **(B)** orbitals of **3a**.

et al., 2019), which has been demonstrated to be a competent BPh_2 provider recently by Song group (Yang et al., 2018) and our group (Zu et al., 2020) (**Table 1**). After systematic evaluation of reaction variables, to our delight, under similar reaction conditions with our previous work (Zu et al., 2020), the target product **3a** could be isolated in 99% yield by using Mn (1.0 equiv), *p*-toluenesulfonyl chloride (TsCl, 2.5 equiv) and Na_2CO_3 (0.5 equiv) in acetonitrile (CH_3CN) at 130°C for 24 h (entry 1). The propeller structure of **3a** was confirmed unambiguously *via* X-ray diffraction analysis of its crystals (**Table 2**).

Subsequently, control experiments were performed to elucidate the function of Mn, TsCl and Na_2CO_3 in these conditions (entry 2–4). It was found TsCl played a vital role in the formation of **3a**, in view that its absence would suppress the reaction totally. Omitting Mn from the conditions, still, 81% isolated yield of **3a** could be obtained, while the omission of Na_2CO_3 led to the formation of **3a** in only 24% yield. Further evaluation revealed the choice of solvent was also critical (entry 5–10). Other commonly-used organic solvents, including DMF, THF and DMSO, afforded only a trace amount of product **3a**. Moreover, the test of the reaction temperature showed the yield dropped sharply while lowering the temperature (entries 11–12). The investigation of a variety of bases showed that Na_2CO_3 performed best (entries 13–15). The reduction of the amount of **2a** also affected the yields remarkably (entries 16–17).

With the optimal conditions in hand, the substrate scope of this methodology was then investigated (**Table 2**). A broad scope of aryl trifluoroborates containing *para- ortho-* and *meta-*substituents were applied in the reactions successfully. Generally, the *ortho*-substituted aryl trifluoroborates gave lower isolated yields, in comparison with their *para-* and *meta*-substituted analogs, mainly due to the steric effect (**3e**, 58% vs. **3k**, 78% vs. **3r**, 49%; **3n**, 64% vs. **3o**, 35%). The reaction tolerated bromides and chlorides well (**3c**, **3f, 3h**), allowing the formation of halogenated products and thus leaving ample space for further decorations. No matter electron-withdrawing (-CF_3, -halides, -CN) or -donating (-OMe, -^{t}Bu, -OBn) groups were on the aryl trifluoroborates, the target boronyl complexes could be obtained in moderate to good yields. While aryl substrates containing π-extended systems were applied, products with more congested BAr_2 segments, like **3b**, **3m** and **3u**, were obtained. Notably, potassium vinyl fluoroborate proceeded smoothly to provide **3d** in moderate yields. When the *N*-substituent of pyridinecarboxamide was changed to 1-naphthyl, 80% of **3v** could be isolated.

Then, photophysical properties of the obtained complexes in solvent and in the solid-state were measured. As shown in **Figure 2** and **Table 3**, the selected complexes possessed very weak luminescence in organic solvent DMF along with very low quantum yield ($\Phi_{liquid} < 0.015$), probably due to the non-radiative process in the solvent induced by intramolecular rotation. In contrast, the solid-state spectra of the BAr_2-species showed intense emission bands centered around 490 nm with high quantum yield (Φ_{solid}: 31–98%), indicating the existence of AIE phenomenon and the absence of strong intermolecular π-π interactions in the solid-state.

Furthermore, the emission properties of **3a** were investigated in detail to prove its AIE behaviors (**Figure 3**). Firstly, under irradiation with a UV lamp at 365 nm, solid **3a** showed macroscopical fluorescence (**Figure 3A**). Then, **3a** was dissolved in H_2O/MeOH mixtures with different H_2O content (**Figure 3C**). When the H_2O content is lower than 60%, **3a** was dissolved totally and the solution was transparent without observable fluorescence. As the water content increased from 80 to 90%, **3a** became insoluble in the solvents and began to aggregate. Correspondingly, the turbidity and luminescence (at 365 nm) of the solution increased, which could be observed with the naked eyes. **3a** would disperse in the pure water with its aggregation showing the same luminescence as the solid-state. The AIE behavior of **3a** was further verified by observing the fluorescent changes during the evaporation of MeOH and THF solution of **3a** (**Figure 3B**). On a thin-layer chromatography plate, as the solvent evaporated and **3a** molecules aggregated, a clear increase in the fluorescence was observed under UV irradiation at 365 nm.

In order to better understand the AIE properties of these complexes, X–ray crystallographic analysis of **3a** was performed. As shown in **Figure 4**, the boron atoms of **3a** adopted a typical

tetrahedral geometry to form *N,N*–chelated five-membered rings. The pyridyl N→B bond lengths are around 0.03 Å longer than the amide N–B bonds. As anticipated, **3a** adopt twisted conformations and the two phenyl rings on the boron atom were not coplanar. The dihedral angles of A and B, A and C, B and C were 76.50°, 78.02° and 61.95°, respectively. As for the packing mode, to take advantage of the capacious space around the planar picolinamide motif, two **3a** molecules could assemble in the head-to-tail mode. The aryl hydrogens on the B rings could interact with the carbonyl oxygens of the other molecule to form H-bonding (O1 ... H1, 2.85 Å; O1 ... H2, 2.75 Å; O2 ... H3, 2.91 Å). The aforementioned dimers would interlace zigzag to form weak intermolecular π–π interactions. The shortest distances between the aryl D and E rings were around 3.5 Å. These weak intermolecular interactions, like H-bonding and π–π stacking, were able to fix the molecular conformations in the solid-state, thus inhibiting the internal rotations and non-radiative relaxation and inducing the AIE property.

To gain additional insight, density functional theory (DFT) and time-dependent density functional theory calculations (TD-DFT) (Adamo and Jacquemin, 2013) of **3a** were performed with Gaussian09 suite of programs (Frisch et al., 2009). The combination of m062x/6–311 g** was applied in both cases (Zhao and Truhlar, 2008). As shown in **Figure 5**, both the HOMO and LUMO orbitals were delocalized over the picolinamide backbone. However, the electron density distribution of HOMO and LUMO was mainly localized at acyl aniline motif and pyridyl group, respectively. The electron-density contribution of boron in both orbitals were negligible, being 0.80% (HOMO) and 0.48% (LUMO). The HOMO and LUMO orbitals were spatially separated by the boron atom, rendering limited overlap between these two orbitals. Then, TD-DFT calculations on the DFT-optimized structure suggested that lowest energy transition (S0→S1) involves mostly the HOMO and the LUMO orbitals, indicating a possible ligand-to-ligand charge transfer character.

In conclusion, using readily available and stable aryl trifluoroborates as the BAr_2 sources, the picolinamide-based diaryl boronyl complexes have been synthesized for the first time. These propeller-type five-membered complexes exhibit very weak fluorescence in organic solvents and intense fluorescence in their aggregation/solid-state, showing classical AIE properties, which should originate from the confinement of molecular conformations and the inhibited internal rotations when these molecules assemble.

EXPERIMENTAL SECTION

General Information

Unless otherwise noted, all reactions were carried out under an air atmosphere. Analytical thin-layer chromatography (TLC) was performed on glass plates coated with 0.25 mm 230–400 mesh silica gel containing a fluorescent indicator. Visualization was accomplished by exposure to a UV lamp. All the products in this article are compatible with standard silica gel chromatography. Column chromatography was performed on silica gel (200–300 mesh). Eluent generally contained ethyl acetate (EA), petroleum ether (PE) and triethylamine (TEA).

NMR spectra were measured on a Bruker Ascend 400 spectrometer and chemical shifts (δ) are reported in parts per million (ppm). ^{1}H NMR spectra were recorded at 400 MHz in NMR solvents and referenced internally to corresponding solvent resonance, and ^{13}C NMR spectra were recorded at 101 MHz and referenced to corresponding solvent resonance. Coupling constants are reported in Hz with multiplicities denoted as s (singlet), d (doublet), t (triplet), q (quartet), m (multiplet) and br (broad). Infrared spectra were collected on a Thermo Fisher Nicolet 6700 FT-IR spectrometer using ATR (Attenuated Total Reflectance) method. Absorption maxima (ν max) are reported in wavenumbers (cm^{-1}). High resolution mass spectra (HRMS) were acquired on Thermo Scientific LTQ Orbitrap XL with an ESI source. Melting points were measured with a micro-melting point apparatus.

Commercial reagents, including picolinoyl chloride hydrochloride, aniline, naphthalen-1-amine, Mn, *p*-toluenesulfonyl chloride, Na_2CO_3 and All potassium trifluoroborate, were purchased from commercial sources and used as received unless otherwise stated.

Preparation of 2-Pyridinecarboxamide

*N-phenylpicolinamide **(1a)**.* The target product was prepared according to a literature procedure (Li et al., 2014). The product was isolated by flash chromatography as a white solid (1.64 g, 90%): ^{1}H NMR (400 MHz, $CDCl_3$) δ 10.03 (s, 1H), 8.62 (d, J = 4.4 Hz, 1H), 8.31 (d, J = 7.6 Hz, 1H), 7.96–7.87 (m, 1H), 7.82–7.76 (m, 2H), 7.51–7.45 (m, 1H), 7.43–7.36 (m, 2H), 7.15 (t, J = 7.2 Hz, 1H). ^{13}C{^{1}H} NMR (101 MHz, $CDCl_3$) δ 162.0, 149.9, 148.0, 137.8, 137.7, 129.1, 126.5, 124.3, 122.4, 119.7, 77.4, 77.1, 76.7.

N-(naphthalen-1-yl)picolinamide ***(1v)***. The target product was prepared according to a literature procedure.[14] The product was isolated by flash chromatography as a white solid (2.03 g, 89%): ^{1}H NMR (400 MHz, $CDCl_3$) δ 10.77 (s, 1H), 8.75–8.70 (m, 1H), 8.46–8.34 (m, 2H), 8.11 (d, J = 8.4 Hz, 1H), 7.98–7.89 (m, 2H), 7.71 (d, J = 8.4 Hz, 1H), 7.63–7.50 (m, 4H). ^{13}C{^{1}H} NMR (101 MHz, $CDCl_3$) δ 162.3, 150.1, 148.2, 137.8, 134.1, 132.4, 128.9, 126.6, 126.4, 126.3, 126.3, 126.0, 126.0, 125.9, 125.1, 122.5, 120.8, 120.5, 119.0, 118.6, 109.7, 77.4, 77.1, 76.7.

Typical Experimental Procedures

General Procedure A

A flame-dried 25 ml vial was placed with a magnetic stir bar. Then, *N*-phenylpicolinamide (29.7 mg, 0.15 mmol, 1.0 equiv), potassium trifluoro(phenyl)borate (138.0 mg, 0.75 mmol, 5.0 equiv), Mn (82.0 mg, 0.15 mmol, 1.0 equiv), *p*-toluenesulfonyl chloride (71.5 mg, 0.375 mmol, 2.5 equiv) and Na_2CO_3 (79.5 mg, 0.075 mmol, 0.50 equiv) as a base, and react with acetonitrile as the reaction solvent at 130°C for 24 h. After the completion of the reaction and concentration, the crude product was purified by column chromatography (silica gel) to give the target product, using PE/EtOAc/DCM the eluent.

Preparation and characterization data for isolated products:

Compounds **3a**—**3w** are unknown compounds. $^{1}H/^{13}C$ NMR, melting point, IR, data HRMS (ESI) m/z for these compounds are provided herein.

1,1,2-triphenyl-1,2-dihydro-3H-1λ⁴,8λ⁴-[1,3,2]diazaborolo[1,5-a]pyridin-3-one ***(3a)***. The product was isolated by flash chromatography as a yellow-green solid (53.8 mg, 99%): mp: 186.4–189.4°C; ^{1}H NMR (400 MHz, $CDCl_3$) δ 8.41–8.34 (m, 2H), 8.19 (td, *J* = 8.0, 1.2 Hz, 1H), 7.58 (dd, *J* = 12.4, 6.4 Hz, 1H), 7.55–7.51 (m, 2H), 7.37 (dd, *J* = 7.6, 4.0 Hz, 4H), 7.27–7.20 (m, 6H), 7.16 (t, *J* = 7.9 Hz, 2H), 7.02 (dd, *J* = 1.2, 7.6 Hz, 1H). $^{13}C\{^{1}H\}$ NMR (101 MHz, $CDCl_3$) δ 161.4, 142.4, 141.6, 140.0, 135.8, 133.7, 128.4, 127.9, 127.3, 127.2, 125.0, 124.8, 122.5, 77.5, 77.2, 76.8. HRMS (ESI), m/z calcd for $C_{24}H_{19}BN_2ONa^+$ $(M + Na)^+$ 385.1483, found 385.1485. IR (cm^{-1}): 3,074, 3,009, 1,663, 1,489, 1,348, 762, 702.

1,1-di([1,1′-biphenyl]-4-yl)-2-phenyl-1,2-dihydro-3H-1λ⁴,8λ⁴-[1,3,2]diazaborolo[1,5-a]pyridin-3-one ***(3b)***. The product was isolated by flash chromatography as a yellow-green solid (57.9 mg, 75%): mp: 289.0–290.7°C; ^{1}H NMR (400 MHz, $CDCl_3$) δ 8.46 (dd, *J* = 15.6, 5.6 Hz, 2H), 8.28 (t, *J* = 7.2 Hz, 1H), 7.72–7.68 (m, 1H), 7.65–7.57 (m, 6H), 7.53–7.47 (m, 8H), 7.44–7.39 (m, 4H), 7.34–7.29 (m, 2H), 7.22 (dd, *J* = 7.6, 2.0 Hz, 2H), 7.06 (t, *J* = 7.2 Hz, 1H). $^{13}C\{^{1}H\}$ NMR (101 MHz, $CDCl_3$) δ 161.3, 148.9, 142.4, 141.6, 141.2, 139.9, 139.8, 134.1, 128.7, 128.4, 127.2, 127.1, 127.0, 126.5, 125.0, 124.6, 122.5, 77.4, 77.2, 76.7. HRMS (ESI), m/z calcd for $C_{36}H_{27}BN_2ONa^+$ $(M + Na)^+$ 537.2109, found 537.2111. IR (cm^{-1}): 3,058, 3,015, 1,680, 1,495, 1,348, 740, 686.

1,1-bis(3-bromophenyl)-2-phenyl-1,2-dihydro-3H-1λ⁴,8λ⁴-[1,3,2]diazaborolo[1,5-a]pyridin-3-one ***(3c)*** The product was isolated by flash chromatography as a yellow-green solid (49.9 mg, 64%): mp: 203.5–204.5°C; ^{1}H NMR (400 MHz, $CDCl_3$) δ 8.48–8.40 (m, 1H), 8.38–8.28 (m, 3H), 7.78–7.72 (m, 2H), 7.43–7.35 (m, 6H), 7.25–7.19 (m, 2H), 7.17–7.08 (m, 3H). $^{13}C\{^{1}H\}$ NMR (101 MHz, $CDCl_3$) δ 161.2, 148.6, 143.1, 141.6, 139.0, 135.9, 135.8, 132.0, 130.5, 129.8, 128.6, 127.6, 125.6, 124.9, 122.9, 77.4, 77.1, 76.8. HRMS (ESI), m/z calcd for $C_{24}H_{17}BBr_2N_2ONa^+$ $(M + Na)^+$ 542.9672, found 542.9680. IR (cm^{-1}): 3,058, 1,674, 1,489, 1,348, 762, 692.

2-phenyl-1,1-divinyl-1,2-dihydro-3H-1λ⁴,8λ⁴-[1,3,2]diazaborolo[1,5-a]pyridin-3-one ***(3d)*** The product was isolated by flash chromatography as a yellow-green solid (22.4 mg, 57%): mp: 78.9–80.0°C; ^{1}H NMR (400 MHz, $CDCl_3$) δ 8.40 (d, *J* = 5.6 Hz, 1H), 8.34–8.22 (m, 2H), 7.93–7.85 (m, 2H), 7.75 (t, *J* = 6.0 Hz, 1H), 7.38–7.31 (m, 2H), 7.14 (t, *J* = 7.2 Hz, 1H), 6.30 (dd, *J* = 19.6, 13.2 Hz, 2H), 5.57 (dd, *J* = 13.2, 3.2 Hz, 2H), 5.32 (dd, *J* = 19.6, 3.6 Hz, 2H). $^{13}C\{^{1}H\}$ NMR (101 MHz, $CDCl_3$) δ 160.6, 149.0, 142.1, 141.0, 140.3, 128.4, 126.5, 124.7, 124.6, 123.7, 122.3, 77.4, 77.1, 76.8. HRMS (ESI), m/z calcd for $C_{16}H_{15}BN_2ONa^+$ $(M + Na)^+$ 285.1170, found 285.1173. IR (cm^{-1}): 3,047, 2,928, 1,668, 1,495, 1,360, 757, 686.

1,1-bis(3-fluorophenyl)-2-phenyl-1,2-dihydro-3H-1λ⁴,8λ⁴-[1,3,2]diazaborolo[1,5-a]pyridin-3-one ***(3e)*** The product was isolated by flash chromatography as a yellow-green solid (34.6 mg, 58%): mp: 152.3–154.6°C; ^{1}H NMR (400 MHz, $CDCl_3$) δ 8.43 (d, *J* = 8.0 Hz, 1H), 8.37–8.27 (m, 2H), 7.72 (t, *J* = 6.4 Hz, 1H), 7.44 (d, *J* = 7.6 Hz, 2H), 7.25–7.16 (m, 4H), 7.13–7.04 (m, 3H), 7.00 (dd, *J* = 10.4, 1.2 Hz, 2H), 6.92 (td, *J* = 8.4, 2.0 Hz, 2H). $^{13}C\{^{1}H\}$ NMR (101 MHz, $CDCl_3$) δ 164.0, 161.6, 161.2, 148.8, 143.0, 141.5, 139.3, 129.6, 129.5, 128.9, 128.9, 128.5, 127.4, 125.4, 124.8, 122.8, 119.8, 119.6, 114.3, 114.1, 77.4, 77.1, 76.8. ^{19}F NMR (376 MHz, $CDCl_3$) δ -113.78. HRMS (ESI), m/z calcd for $C_{24}H_{17}BF_2N_2ONa^+$ $(M + Na)^+$ 421.1294, found 421.1297. IR (cm^{-1}): 3,068, 1,680, 1,495, 1,354, 762, 702.

1,1-bis(4-bromophenyl)-2-phenyl-1,2-dihydro-3H-1λ⁴,8λ⁴-[1,3,2]diazaborolo[1,5-a]pyridin-3-one ***(3f)*** The product was isolated by flash chromatography as a yellow-green solid (39.0 mg, 50%): mp: 250.0–251.3°C; ^{1}H NMR (400 MHz, $CDCl_3$) δ 8.42 (d, *J* = 8.0 Hz, 1H), 8.34–8.28 (m, 2H), 7.72 (t, *J* = 6.4 Hz, 1H), 7.47–7.41 (m, 2H), 7.36 (d, *J* = 8.0 Hz, 4H), 7.23–7.16 (m, 6H), 7.07 (t, *J* = 7.6 Hz, 1H). $^{13}C\{^{1}H\}$ NMR (101 MHz, $CDCl_3$) δ 161.1, 148.8, 142.9, 141.4, 139.3, 135.2, 131.0, 128.5, 127.4, 125.4, 124.6, 122.8, 121.9, 77.4, 77.1, 76.7. HRMS (ESI), m/z calcd for $C_{24}H_{17}BBr_2N_2ONa^+$ $(M + Na)^+$ 542.9672, found 542.9680. IR (cm^{-1}): 3,068, 1,674, 1,489, 1,354, 762, 698.

2-phenyl-1,1-di-p-tolyl-1,2-dihydro-3H-1λ⁴,8λ⁴-[1,3,2]diazaborolo[1,5-a]pyridin-3-one ***(3g)*** The product was isolated by flash chromatography as a yellow-green solid (36.9 mg, 63%): mp: 240.9–241.9°C; ^{1}H NMR (400 MHz, $CDCl_3$) δ 8.41–8.35 (m, 2H), 8.24–8.18 m, 1H), 7.64–7.56 (m, 1H), 7.28 (d, *J* = 8.0 Hz, 4H), 7.20–7.14 (m, 2H), 7.07 (d, *J* = 7.6 Hz, 4H), 7.05–7.00 (m, 1H), 2.31 (s, 6H). $^{13}C\{^{1}H\}$ NMR (101 MHz, $CDCl_3$) δ 161.2, 148.8, 142.2, 141.5, 140.1, 136.6, 133.7, 128.6, 128.2, 127.0, 124.8, 124.6, 122.3, 77.4, 77.1, 76.8, 21.3. HRMS (ESI), m/z calcd for $C_{26}H_{23}BN_2ONa^+$ $(M + Na)^+$ 413.1796, found 413.1799. IR (cm^{-1}): 3,020, 1,674, 1,489, 1,348, 768, 686.

1,1-bis(4-chlorophenyl)-2-phenyl-1,2-dihydro-3H-1λ⁴,8λ⁴-[1,3,2]diazaborolo[1,5-a]pyridin-3-one ***(3h)*** The product was isolated by flash chromatography as yellow-green solid (43.3 mg, 67%): mp: 202.0–206.3°C; ^{1}H NMR (400 MHz, DMSO-*d6*) δ 8.74 (d, *J* = 5.6 Hz, 1H), 8.56 (t, *J* = 7.6 Hz, 1H), 8.42 (d, *J* = 7.8 Hz, 1H), 7.99 (t, *J* = 6.4 Hz, 1H), 7.47 (d, *J* = 8.0 Hz, 2H), 7.35–7.25 (m, 8H), 7.19 (t, *J* = 7.6 Hz, 2H), 7.02 (t, *J* = 7.2 Hz, 1H). $^{13}C\{^{1}H\}$ NMR (101 MHz, DMSO-*d6*) δ 161.6, 147.3, 145.0, 142.8, 140.3, 135.5, 132.5, 129.5, 128.7, 128.1, 124.9, 124.1, 123.0, 40.6, 40.4, 40.2, 40.0, 39.8, 39.6, 39.4. HRMS (ESI), m/z calcd for $C_{24}H_{17}BCl_2N_2ONa^+$ $(M + Na)^+$ 453.0703, found 453.0707. IR (cm^{-1}): 3,080, 1,674, 1,489, 1,360, 1,082, 768.

1,1-bis(4-(tert-butyl)phenyl)-2-phenyl-1,2-dihydro-3H-1λ⁴,8λ⁴-[1,3,2]diazaborolo[1,5-a]pyridin-3-one ***(3i)*** The product was isolated by flash chromatography as a yellow-green solid (45.5 mg, 64%): mp: 222.6–223.4°C; ^{1}H NMR (400 MHz, $CDCl_3$) δ 8.42–8.34 (m, 2H), 8.17 (td, *J* = 8.0, 1.2 Hz, 1H), 7.62–7.54 (m, 3H), 7.32 (d, *J* = 8.4 Hz, 4H), 7.28–7.23 (m, 4H), 7.20–7.13 (m, 2H), 7.05–6.97 (m, 1H), 1.29 (s, 18H). $^{13}C\{^{1}H\}$ NMR (101 MHz, $CDCl_3$) δ 161.3, 149.7, 148.7, 142.1, 141.7, 140.2, 133.5, 128.2, 126.9, 124.7, 124.6, 124.6, 122.2, 77.4, 77.1, 76.8, 34.4, 31.4. HRMS (ESI) m/z calcd for $C_{32}H_{35}BN_2ONa^+$ $(M + Na)^+$ 497.2735, found 497.2740. IR (cm^{-1}): 3,080, 2,966, 1,674, 1,489, 1,354, 762, 686.

1,1-bis(benzo[d][1,3]dioxol-5-yl)-2-phenyl-1,2-dihydro-3H-1λ⁴,8λ⁴-[1,3,2]diazaborolo[1,5-a]pyridin-3-one ***(3j)*** The product was isolated by flash chromatography as a yellow-green solid (41.9 mg, 62%): mp: 227.6–229.4°C; ^{1}H NMR (400 MHz, $CDCl_3$) δ 8.37–8.33 (m, 2H), 8.20 (td, *J* = 8.0, 0.8 Hz, 1H), 7.65–7.59 (m, 1H), 7.58–7.52 (m, 2H),

7.23–7.16 (m, 2H), 7.04 (t, *J* = 7.6 Hz, 1H), 6.85 (dd, *J* = 7.6, 1.2 Hz, 2H), 6.79 (d, *J* = 1.2 Hz, 2H), 6.71 (d, *J* = 8.0 Hz, 2H), 5.85 (s, 4H). $^{13}C\{^1H\}$ NMR (101 MHz, $CDCl_3$) δ 161.1, 148.6, 147.3, 146.8, 142.5, 141.5, 139.8, 128.3, 127.1, 125.0, 124.6, 122.4, 113.1, 108.2, 100.4, 77.4, 77.1, 76.8. HRMS (ESI) m/z calcd for $C_{26}H_{19}BN_2O_5Na^+$ $(M + Na)^+$ 473.1279, found 473.1281. IR (cm^{-1}): 3,063, 2,884, 1,680, 1,484, 1,348, 1,234, 1,039, 768.

1,1-bis(4-fluorophenyl)-2-phenyl-1,2-dihydro-3H-1λ⁴,8λ⁴-[1,3,2] diazaborolo[1,5-a]pyridin-3-one ***(3k)*** The product was isolated by flash chromatography as a yellow-green solid (46.6 mg, 78%): mp: 176.1–177.9°C; ^1H NMR (400 MHz, $CDCl_3$) δ 8.40 (d, *J* = 7.6 Hz, 1H), 8.33 (d, *J* = 5.6 Hz, 1H), 8.31–8.24 (m, 1H), 7.71–7.65 (m, 1H), 7.49–7.44 (m, 2H), 7.34–7.27 (m, 4H), 7.22–7.15 (m, 2H), 7.08–7.02 (m, 1H), 6.96–6.90 (m, 4H). $^{13}C\{^1H\}$ NMR (101 MHz, $CDCl_3$) δ 163.8, 161.3, 161.1, 148.7, 142.7, 141.4, 139.7, 135.2, 135.1, 128.7, 128.4, 127.3, 125.2, 124.6, 122.6, 114.9, 114.7, 77.4, 77.1, 76.8. ^{19}F NMR (376 MHz, $CDCl_3$) δ -113.78. HRMS (ESI) m/z calcd for $C_{24}H_{17}BF_2N_2ONa^+$ $(M + Na)^+$ 421.1294, found 421.1298. IR(cm^{-1}): 3,042, 1,680, 1,495, 1,364, 1,164, 774.

1,1-bis(3-(benzyloxy)phenyl)-2-phenyl-1,2-dihydro-3H-1λ⁴,8λ⁴-[1,3,2]diazaborolo[1,5-a]pyridin-3-one ***(3l)*** The product was isolated by flash chromatographyas a yellow-green solid (60.3 mg, 70%): mp: 72.6–74.2°C; ^1H NMR (400 MHz, $CDCl_3$) δ 8.36 (d, *J* = 7.6 Hz, 1H), 8.26 (d, *J* = 5.6 Hz, 1H), 8.20 (td, *J* = 8.0, 1.2 Hz, 1H), 7.59–7.50 (m, 3H), 7.38–7.27 (m, 10H), 7.23–7.15 (m, 4H), 7.07 (t, *J* = 7.2 Hz, 1H), 6.98–6.94 (m, 4H), 6.90–6.84 (m, 2H), 4.97–4.89 (m, 4H). $^{13}C\{^1H\}$ NMR (101 MHz, $CDCl_3$) δ 161.2, 158.3, 148.7, 142.4, 141.6, 139.9, 137.3, 128.9, 128.5, 128.4, 127.8, 127.6, 127.1, 126.3, 125.1, 124.9, 122.4, 120.0, 113.5, 77.4, 77.1, 76.8, 69.8. HRMS (ESI) m/z calcd for $C_{38}H_{31}BN_2O_3Na^+$ $(M + Na)^+$ 597.2320, found 597.2322. IR (cm^{-1}): 3,063, 3,030, 1,680, 1,489, 1,348, 1,229, 762, 692.

1,1-di(naphthalen-2-yl)-2-phenyl-1,2-dihydro-3H-1λ⁴,8λ⁴-[1,3,2] diazaborolo[1,5-a]pyridin-3-one ***(3m)*** The product was isolated by flash chromatography as a yellow-green solid (63.8 mg, 92%): mp: 215.5–217.0°C; ^1H NMR (400 MHz, $CDCl_3$) δ 8.44 (dd, *J* = 4.8, 4.0 Hz, 2H), 8.20 (td, *J* = 7.6, 0.8 Hz, 1H), 7.98–7.95 (m, 2H), 7.83–7.78 (m, 2H), 7.77–7.71 (m, 4H), 7.65–7.61 (m, 2H), 7.60–7.55 (m, 1H), 7.51 (dd, *J* = 8.4, 1.2 Hz, 2H), 7.48–7.40 (m, 4H), 7.19–7.12 (m, 2H), 7.05–6.98 (m, 1H). $^{13}C\{^1H\}$ NMR (101 MHz, $CDCl_3$) δ 161.4, 148.9, 142.5, 141.7, 139.9, 133.5, 133.4, 133.0, 131.0, 128.4, 128.1, 127.6, 127.1,127.1, 125.7, 125.6, 125.1, 124.8, 122.6, 77.4, 77.1, 76.8. HRMS (ESI) m/z calcd for $C_{32}H_{23}BN_2ONa^+$ $(M + Na)^+$ 485.1796, found 485.1797. IR (cm^{-1}): 3,047, 1,668, 1,495, 1,354, 762, 469.

1,1-bis(3-methoxyphenyl)-2-phenyl-1,2-dihydro-3H-1λ⁴,8λ⁴-[1,3,2] diazaborolo[1,5-a]pyridin-3-one ***(3n)*** The product was isolated by flash chromatography as a yellow-green solid (40.5 mg, 64%): mp: 170.9–172.2°C; ^1H NMR (400 MHz, $CDCl_3$) δ 8.378 (t, *J* = 5.2 Hz, 2H), 8.20 (td, *J* = 400, 1.2 Hz, 1H), 7.64–7.58 (m, 1H), 7.55–7.49 (m, 2H), 7.21–7.15 (m, 4H), 7.07–7.01 (m, 1H), 6.96–6.89 (m, 4H), 6.79–6.75 (m, 2H), 3.67 (s, 6H). $^{13}C\{^1H\}$ NMR (101 MHz, $CDCl_3$) δ 161.3, 159.1, 148.7, 142.5, 141.7, 139.9, 128.9, 128.3, 127.1, 125.9, 125.1, 124.9, 122.4, 119.4, 112.2, 77.5, 77.1, 76.8, 55.0. HRMS (ESI) m/z calcd for $C_{26}H_{23}BN_2O_3Na^+$ $(M + Na)^+$ 445.1694, found 445.1699. IR (cm^{-1}): 3,009, 1,668, 1,343, 1,229, 762, 757.

1,1-bis(2-methoxyphenyl)-2-phenyl-1,2-dihydro-3H-1λ⁴,8λ⁴-[1,3,2] diazaborolo[1,5-a]pyridin-3-one ***(3o)*** The product was isolated by flash chromatography as a yellow-green solid (22.2 mg, 35%): mp: 249.1–250.7°C; ^1H NMR (400 MHz, $CDCl_3$) δ 9.13 (d, *J* = 5.6 Hz, 1H), 8.29 (d, *J* = 7.6 Hz, 1H), 8.15 (t, *J* = 6.8 Hz, 1H), 7.62 (d, *J* = 7.6 Hz, 2H), 7.55 (t, *J* = 6.0 Hz, 1H), 7.43–7.39 (m, 2H), 7.23–7.18 (m, 2H), 7.12 (t, *J* = 7.6 Hz, 2H), 6.95 (t, *J* = 7.6 Hz, 1H), 6.84 (t, *J* = 7.2 Hz, 2H), 6.76 (d, *J* = 8.0 Hz, 2H), 3.48 (s, 6H). $^{13}C\{^1H\}$ NMR (101 MHz, $CDCl_3$) δ 162.7, 162.3, 149.6, 142.7, 141.3, 140.9, 137.2, 128.6, 127.9, 125.9, 124.1, 124.0, 121.3, 120.3, 110.4, 77.4, 77.1, 76.8, 54.8. HRMS (ESI) m/z calcd for $C_{26}H_{23}BN_2O_3Na^+$ $(M + Na)^+$ 445.1694, found 445.1695. IR (cm^{-1}): 3,058, 2,933, 1,674, 1,495, 1,360, 1,234, 757.

2-phenyl-1,1-bis(4-(trifluoromethyl)phenyl)-1,2-dihydro-3H-1λ⁴,8λ⁴-[1,3,2]diazaborolo[1,5-a]pyridin-3-one ***(3p)*** The product was isolated by flash chromatography as a yellow-green solid (34.4 mg, 46%): mp: 230.3–232.0°C; ^1H NMR (400 MHz, $CDCl_3$) δ 8.47 (d, *J* = 7.6 Hz, 1H), 8.37 (dd, *J* = 7.6, 1.2 Hz, 1H), 8.35–8.31 (m, 1H), 7.79–7.74 (m, 1H), 7.50 (d, *J* = 8.0 Hz, 4H), 7.46–7.40 (m, 6H), 7.24–7.18 (m, 2H), 7.09 (t, *J* = 7.6 Hz, 1H). $^{13}C\{^1H\}$ NMR (101 MHz, $CDCl_3$) δ 161.1, 148.9, 143.2, 141.4, 139.1, 133.6, 129.8, 129.4, 129.1, 128.6, 127.5, 125.7, 125.5, 124.6, 124.6, 123.0, 123.0, 77.4, 77.0, 76.7. ^{19}F NMR (376 MHz, $CDCl_3$) δ -62.58. HRMS (ESI) m/z calcd for $C_{26}H_{17}BF_6N_2ONa^+$ $(M + Na)^+$ 521.1230, found 521.1236. IR (cm^{-1}): 3,074, 3,036, 1,691, 1,327, 1,109, 762.

1,1-bis(4-(methylthio)phenyl)-2-phenyl-1,2-dihydro-3H-1λ⁴,8λ⁴-[1,3,2]diazaborolo[1,5-a]pyridin-3-one ***(3q)*** The product was isolated by flash chromatography as a yellow-green solid (44.3 mg, 65%): mp: 242.1–243.6°C; ^1H NMR (400 MHz, $CDCl_3$) δ 8.37–8.29 (m, 2H), 8.21 (td, *J* = 7.6, 0.8 Hz, 1H), 7.64–7.57 (m, 1H), 7.53–7.47 (m, 2H), 7.26–7.22 (m, 4H), 7.18–7.12 (m, 2H), 7.11–7.08 (m, 4H), 7.04–6.98 (m, 1H), 2.40 (s, 6H). $^{13}C\{^1H\}$ NMR (101 MHz, $CDCl_3$) δ 161.2, 148.7, 142.5, 141.4, 139.8, 137.2, 134.1, 128.4, 127.1, 125.9, 125.0, 124.5, 122.5, 77.4, 77.1, 76.8, 15.5. HRMS (ESI) m/z calcd for $C_{26}H_{23}BN_2OS_2Na^+$ $(M + Na)^+$ 477.1237, found 477.1238. IR (cm^{-1}): 3,063, 2,916, 1,674, 1,495, 1,375, 1,088, 762.

1,1-bis(2-fluorophenyl)-2-phenyl-1,2-dihydro-3H-1λ⁴,8λ⁴-[1,3,2] diazaborolo[1,5-a]pyridin-3-one ***(3r)*** The product was isolated by flash chromatography as a yellow-green solid (29.3 mg, 49%): mp: 222.9–224.0°C; ^1H NMR (400 MHz, $CDCl_3$) δ 8.85 (d, *J* = 6.0 Hz, 1H), 8.36 (d, *J* = 7.6 Hz, 1H), 8.25 (td, *J* = 8.0, 1.2 Hz, 1H), 7.10–766 (m, 1H), 7.65–7.60 (m, 2H), 7.48–7.42 (m, 2H), 7.25–7.20 (m, 2H), 7.20–7.15 (m, 2H), 7.06–7.01 (m, 3H), 6.92–6.86 (m, 2H). $^{13}C\{^1H\}$ NMR (101 MHz, $CDCl_3$) δ 167.3, 164.9, 161.6, 149.0, 142.5, 142.0, 140.0, 136.9, 136.8, 129.8, 129.7, 128.3, 127.2, 124.6, 123.9, 123.8, 123.8, 122.4, 115.2, 115.0, 77.4, 77.1, 76.7. ^{19}F NMR (376 MHz, $CDCl_3$) δ -103.33. HRMS (ESI) m/z calcd for $C_{24}H_{17}BF_2N_2ONa^+$ $(M + Na)^+$ 421.1294, found 421.1298. IR (cm^{-1}): 3,068, 1,668, 1,495, 1,354, 762, 746.

1,1-bis(3-(tert-butyl)phenyl)-2-phenyl-1,2-dihydro-3H-1λ⁴,8λ⁴-[1,3,2]diazaborolo[1,5-a]pyridin-3-one **(3s)** The product was isolated by flash chromatography as a yellow-green solid (55.5 mg, 78%): mp: 78.1–79.8°C; ^1H NMR (400 MHz, $CDCl_3$) δ 8.45–8.37 (m, 2H), 8.21 (td, *J* = 7.6, 0.8 Hz, 1H), 7.66–7.55 (m, 3H), 7.51–7.45 (m, 2H), 7.32–7.27 (m, 2H), 7.23–7.14 (m, 4H), 7.08–7.01 (m, 3H), 1.25 (s, 18H). $^{13}C\{^1H\}$ NMR (101 MHz, $CDCl_3$) δ 161.3, 149.9, 148.9, 142.3, 141.7, 140.0, 131.6, 130.2,

128.2, 127.4, 127.0, 125.1, 125.0, 123.9, 122.4, 77.5, 77.1, 76.8, 34.7, 31.5. HRMS (ESI) m/z calcd for $C_{32}H_{35}BN_2ONa^+$ $(M + Na)^+$ 497.2735, found 497.2740. IR (cm^{-1}): 2,966, 1,680, 1,489, 1,354, 757, 713.

2,2′-(3-oxo-2-phenyl-2,3-dihydro-1H-1λ⁴,8λ⁴-[1,3,2]diazaborolo[1,5-a]pyridine-1,1-diyl)dibenzonitrile ***(3t)*** The product was isolated by flash chromatography as a yellow-green solid (33.4 mg, 54%): mp: 252.9–253.7°C; ^1H NMR (400 MHz, $CDCl_3$) δ 8.44–8.40 (m, 1H), 8.34–8.29 (m, 2H), 7.75–7.69 (m, 1H), 7.47–7.42 (m, 2H), 7.39–7.34 (m, 4H), 7.22–7.16 (m, 6H), 7.10–7.04 (m, 1H). $^{13}C\{^1H\}$ NMR (101 MHz, $CDCl_3$) δ 161.0, 148.8, 142.9, 141.4, 139.4, 135.2, 131.0, 128.5, 127.3, 125.3, 124.6, 122.8, 121.9, 77.4, 77.1, 76.7. HRMS (ESI) m/z calcd for $C_{26}H_{18}BN_4O+$ $(M + H)^+$ 413.1568, found 413.1563. IR (cm^{-1}): 3,074, 3,025, 1,674, 1,489, 1,348, 762.

1,1-bis(dibenzo[b,d]furan-4-yl)-2-phenyl-1,2-dihydro-3H-1λ⁴,8λ⁴-[1,3,2]diazaborolo[1,5-a]pyridin-3-one ***(3u)*** The product was isolated by flash chromatography as a yellow-green solid (20.3 mg, 25%): mp: 240.3–241.9°C; ^1H NMR (400 MHz, $CDCl_3$) δ 9.12 (d, J = 5.6 Hz, 1H), 8.55 (d, J = 7.6 Hz, 1H), 8.31 (t, J = 7.6 Hz, 1H), 7.98–7.90 (m, 4H), 7.71–7.64 (m, 4H), 7.60–7.54 (m, 1H), 7.39–7.34 (m, 2H), 7.33–7.29 (m, 3H), 7.29–7.27 (m, 1H), 7.24 (d, J = 7.6 Hz, 2H), 7.15 (t, J = 7.9 Hz, 2H), 7.00 (t, J = 7.2 Hz, 1H).$^{13}C\{^1H\}$ NMR (101 MHz, $CDCl_3$) δ 162.0, 159.6, 155.5, 149.8, 142.6, 142.3, 140.3, 134.7, 128.2, 126.8, 126.5, 124.6, 124.5, 124.3, 123.2, 122.6, 122.4, 122.1, 120.4, 120.2, 111.3, 77.4, 77.1, 76.7. HRMS (ESI) m/z calcd for $C_{36}H_{23}BN_2O_3Na^+$ $(M + Na)^+$ 565.1694, found 565.1697. IR (cm^{-1}): 3,053, 1,685, 1,446, 1,348, 1,175, 762.

2-(naphthalen-1-yl)-1,1-diphenyl-1,2-dihydro-3H-1λ⁴,8λ⁴-[1,3,2]diazaborolo[1,5-a]pyridin-3-one ***(3v)*** The product was isolated by flash chromatography as a yellow-green solid (49.5 mg, 80%): mp: 251.2–252.5°C; ^1H NMR (400 MHz, $CDCl_3$) δ 8.48 (d, J = 8.0 Hz, 1H), 8.38 (d, J = 5.6 Hz, 1H), 8.30 (t, J = 7.2 Hz, 1H), 7.75–7.67 (m, 3H), 7.58–7.32 (m, 3H), 7.32–7.27 (m, 3H), 7.23–7.15 (m, 3H), 7.14–6.78 (m, 6H). $^{13}C\{^1H\}$ NMR (101 MHz, $CDCl_3$) δ 161.4, 148.9, 142.6, 142.5, 136.0, 134.2, 129.7, 128.0, 127.3, 127.1, 125.4, 125.3, 125.2, 124.2, 124.1, 122.8, 77.4, 77.1, 76.7. HRMS (ESI) m/z calcd for $C_{28}H_{21}BN_2ONa^+$ $(M + Na)^+$ 435.1639, found 435.1636. IR (cm^{-1}): 3,047, 1,674, 1,398, 1,354, 774, 702.

1,1-bis(4-(benzyloxy)phenyl)-2-phenyl-1,2-dihydro-3H-1λ⁴,8λ⁴-[1,3,2]diazaborolo[1,5-a]pyridin-3-one ***(3w)*** The product was isolated by flash chromatography as a yellow-green solid (60.3 mg, 70%): mp: 83.7–85.6°C; ^1H NMR (400 MHz, $CDCl_3$) δ 8.37 (d, J = 7.2 Hz, 2H), 8.22 (t, J = 8.0 Hz, 1H), 7.66–7.54 (m, 3H), 7.44–7.35 (m, 8H), 7.35–7.28 (m, 6H), 7.19 (t, J = 7.6 Hz, 2H), 7.05 (t, J = 7.6 Hz, 1H), 6.89 (d, J = 8.4 Hz, 4H), 5.02 (s, 4H). $^{13}C\{^1H\}$ NMR (101 MHz, $CDCl_3$) δ 161.2, 158.2, 148.8, 142.2, 141.5, 140.1, 137.3, 134.9, 128.6, 128.3, 127.9, 127.6, 127.0, 124.8, 124.6, 122.3, 114.2, 77.4, 77.2, 76.8, 69.8. HRMS (ESI) m/z calcd for $C_{38}H_{31}BN_2O_3Na^+$ $(M + Na)^+$ 597.2320, found 597.2322. IR (cm^{-1}): 3,020, 1,674, 1,592, 1,170, 698.

DATA AVAILABILITY STATEMENT

The original contributions presented in the study are included in the article/**Supplementary Material**, further inquiries can be directed to the corresponding authors. Additional ^1H and ^{13}C spectra and spectral data for all compounds are available free of charge at http://pubs.acs.org.

AUTHOR CONTRIBUTIONS

GY performed the experiments. LX and YW wrote the manuscript.

ACKNOWLEDGMENTS

We thank the financial support by the National Natural Science Foundation of China (No. 21963010), Shihezi University (CXRC201601 and CXRC201602).

SUPPLEMENTARY MATERIAL

The Supplementary Material for this article can be found online at: https://www.frontiersin.org/articles/10.3389/fchem.2022.856832/full#supplementary-material

REFERENCES

Adamo, C., and Jacquemin, D. (2013). The Calculations of Excited-State Properties with Time-Dependent Density Functional Theory. *Chem. Soc. Rev.* 42, 845–856. doi:10.1039/C2CS35394F

Chen, P.-Z., Niu, L.-Y., Chen, Y.-Z., and Yang, Q.-Z. (2017). Difluoroboron β-diketonate Dyes: Spectroscopic Properties and Applications. *Coord. Chem. Rev.* 350, 196–216. doi:10.1016/j.ccr.2017.06.026

Dou, C., Liu, J., and Wang, L. (2017). Conjugated Polymers Containing B←N Unit as Electron Acceptors for All-Polymer Solar Cells. *Sci. China Chem.* 60, 450–459. doi:10.1007/s11426-016-0503-x

Frisch, M. J., Trucks, G. W., Schlegel, H. B., Scuseria, G. E., Robb, M. A., Cheeseman, J. R., et al. (2009). *Gaussian 09, Revision A*. Wallingford, CT: Gaussian, Inc..

Gong, S., Liu, Q., Wang, X., Xia, B., Liu, Z., and He, W. (2015). AIE-active Organoboron Complexes with Highly Efficient Solid-State Luminescence and Their Application as Gas Sensitive Materials. *Dalton Trans.* 44, 14063–14070. doi:10.1039/C5DT01525A

Huang, Z., Wang, S., Dewhurst, R. D., Ignat'ev, N. V., Finze, M., and Braunschweig, H. (2020). Boron: Its Role in Energy-Related Processes and Applications. *Angew. Chem. Int. Ed.* 59, 8800–8816. doi:10.1002/anie.201911108

Ito, S., Gon, M., Tanaka, K., and Chujo, Y. (2021). Molecular Design and Application of Luminescent Materials Composed of Group 13 Elements with an Aggregation-Induced Emission Property. *Natl. Sci. Rev.* 8, nwab049. doi:10.1093/nsr/nwab049

Kubota, Y., Tanaka, S., Funabiki, K., and Matsui, M. (2012). Synthesis and Fluorescence Properties of Thiazole-Boron Complexes Bearing a β-Ketoiminate Ligand. *Org. Lett.* 14, 4682–4685. doi:10.1021/ol302179r

Li, Q., Zhang, S.-Y., He, G., Ai, Z., Nack, W. A., and Chen, G. (2014). Copper-Catalyzed Carboxamide-Directed Ortho Amination of Anilines with Alkylamines at Room Temperature. *Org. Lett.* 16, 1764–1767. doi:10.1021/ol500464x

Liu, Z., Jiang, Z., Yan, M., and Wang, X. (2019). Recent Progress of BODIPY Dyes With Aggregation-Induced Emission. *Front. Chem.* 7, 712. doi:10.3389/fchem.2019.00712

Luo, J., Xie, Z., Lam, J. W. Y., Cheng, L., Tang, B. Z., Chen, H., et al. (2001). Aggregation-induced Emission of 1-Methyl-1,2,3,4,5-Pentaphenylsilole. *Chem. Commun.*, 1740–1741. doi:10.1039/B105159H

Mei, J., Leung, N. L. C., Kwok, R. T. K., Lam, J. W. Y., and Tang, B. Z. (2015). Aggregation-Induced Emission: Together We Shine, United We Soar!. *Chem. Rev.* 115, 11718–11940. doi:10.1021/acs.chemrev.5b00263

Mellerup, S. K., and Wang, S. (2019). Boron-based Stimuli Responsive Materials. *Chem. Soc. Rev.* 48, 3537–3549. doi:10.1039/C9CS00153K

Min, X., Yi, F., Han, X.-L., Li, M., Gao, Q., Liang, X., et al. (2022). Targeted Photodynamic Therapy Using a Water-Soluble Aggregation-Induced Emission Photosensitizer Activated by an Acidic Tumor Microenvironment. *Chem. Eng. J.* 432, 134327. doi:10.1016/j.cej.2021.134327

Nitti, A., Botta, C., Forni, A., Cariati, E., Lucenti, E., and Pasini, D. (2020). Crystallization-induced Room-Temperature Phosphorescence in Fumaramides. *CrystEngComm* 22, 7782–7785. doi:10.1039/D0CE01253J

Qi, Y., Cao, X., Zou, Y., and Yang, C. (2021). Color-tunable Tetracoordinated Organoboron Complexes Exhibiting Aggregation-Induced Emission for the Efficient Turn-On Detection of Fluoride Ions. *Mater. Chem. Front.* 5, 2353–2360. doi:10.1039/D1QM00046B

Sawazaki, T., Shimizu, Y., Oisaki, K., Sohma, Y., and Kanai, M. (2018). Convergent and Functional-Group-Tolerant Synthesis of B-Organo BODIPYs. *Org. Lett.* 20, 7767–7770. doi:10.1021/acs.orglett.8b03138

Shiu, Y.-J., Cheng, Y.-C., Tsai, W.-L., Wu, C.-C., Chao, C.-T., Lu, C.-W., et al. (2016). Pyridyl Pyrrolide Boron Complexes: The Facile Generation of Thermally Activated Delayed Fluorescence and Preparation of Organic Light-Emitting Diodes. *Angew. Chem. Int. Ed.* 55, 3017–3021. doi:10.1002/anie.201509231

Virgili, T., Forni, A., Cariati, E., Pasini, D., and Botta, C. (2013). Direct Evidence of Torsional Motion in an Aggregation-Induced Emissive Chromophore. *J. Phys. Chem. C* 117, 27161–27166. doi:10.1021/jp4104504

Wang, X., Wu, Y., Liu, Q., Li, Z., Yan, H., Ji, C., et al. (2015). Aggregation-induced Emission (AIE) of Pyridyl-Enamido-Based Organoboron Luminophores. *Chem. Commun.* 51, 784–787. doi:10.1039/C4CC07451C

Wang, Z., Cheng, C., Kang, Z., Miao, W., Liu, Q., Wang, H., et al. (2019). Organotrifluoroborate Salts as Complexation Reagents for Synthesizing BODIPY Dyes Containing Both Fluoride and an Organo Substituent at the Boron Center. *J. Org. Chem.* 84, 2732–2740. doi:10.1021/acs.joc.8b03145

Wu, Y., Li, Z., Liu, Q., Wang, X., Yan, H., Gong, S., et al. (2015). High Solid-State Luminescence in Propeller-Shaped AIE-Active Pyridine-Ketoiminate-boron Complexes. *Org. Biomol. Chem.* 13, 5775–5782. doi:10.1039/C5OB00607D

Yan, N., Wang, F., Wei, J., Song, J., Yan, L., Luo, J., et al. (2019). Highly Emissive B←N Unit Containing Four-Coordinate C,N-Chelated Organoboron Compound for the Detection of Fluoride Ions. *Dyes Pigm.* 166, 410–415. doi:10.1016/j.dyepig.2019.03.057

Yan, W., Hong, C., Long, G., Yang, Y., Liu, Z., Bian, Z., et al. (2014). Synthesis, crystal Structures and Photophysical Properties of Novel boron-containing Derivatives of Phenalene with Bright Solid-State Luminescence. *Dyes Pigm.* 106, 197–204. doi:10.1016/j.dyepig.2014.03.017

Yang, K., Zhang, G., and Song, Q. (2018). Four-coordinate Triarylborane Synthesis via cascade B-Cl/C-B Cross-Metathesis and C-H Bond Borylation. *Chem. Sci.* 9, 7666–7672. doi:10.1039/C8SC02281J

Yang, T., Tang, N., Wan, Q., Yin, S.-F., and Qiu, R. (2021). Recent Progress on Synthesis of N,N′-Chelate Organoboron Derivatives. *Molecules* 26, 1401. doi:10.3390/molecules26051401

Yin, Y., Chen, Z., Li, R.-H., Yuan, C., Shao, T.-Y., Wang, K., et al. (2021). Ligand-Triggered Platinum(II) Metallacycle with Mechanochromic and Vapochromic Responses. *Inorg. Chem.* 60, 9387–9393. doi:10.1021/acs.inorgchem.1c00233

Zhao, Y., and Truhlar, D. G. (2008). The M06 Suite of Density Functionals for Main Group Thermochemistry, Thermochemical Kinetics, Noncovalent Interactions, Excited States, and Transition Elements: Two New Functionals and Systematic Testing of Four M06-Class Functionals and 12 Other Functionals. *Theor. Chem. Account.* 120, 215–241. doi:10.1007/s00214-007-0310-x

Zu, W., Day, C., Wei, L., Jia, X., and Xu, L. (2020). Dual Aminoquinolate Diarylboron and Nickel Catalysed Metallaphotoredox Platform for Carbon-Oxygen Bond Construction. *Chem. Commun.* 56, 8273–8276. doi:10.1039/D0CC03230A

Conflict of Interest: The authors declare that the research was conducted in the absence of any commercial or financial relationships that could be construed as a potential conflict of interest.

Publisher's Note: All claims expressed in this article are solely those of the authors and do not necessarily represent those of their affiliated organizations, or those of the publisher, the editors and the reviewers. Any product that may be evaluated in this article, or claim that may be made by its manufacturer, is not guaranteed or endorsed by the publisher.

frontiers | Frontiers in Chemistry

ORIGINAL RESEARCH
published: 05 May 2022
doi: 10.3389/fchem.2022.829538

The Role of a Confined Space on the Reactivity and Emission Properties of Copper(I) Clusters

Eko Adi Prasetyanto[1,2*†], *Youssef Atoini*[1†], *Loic Donato*[1], *Chien-Wei Hsu*[1] *and Luisa De Cola*[1,3*]

[1]*Institut de Science et D'Ingénierie Supramoléculaires (ISIS - UMR 7006), Université de Strasbourg, CNRS, Strasbourg, France,* [2]*Department of Pharmacy, School of Medicine and Health Sciences, Atma Jaya Catholic University of Indonesia, Jakarta, Indonesia,* [3]*Institute of Nanotechnology (INT), Karlsruhe Institut of Technology (KIT), Karlsruhe, Germany*

Metal clusters have gained a lot of interest for their remarkable photoluminescence and catalytic properties. However, a major drawback of such materials is their poor stability in air and humidity conditions. Herein we describe a versatile method to synthesize luminescent Cu(I) clusters inside the pores of zeolites, using a sublimation technique with the help of high vacuum and high temperature. The porous materials play an essential role as a protecting media against the undesirable and easy oxidation of Cu(I). The obtained clusters show fascinating luminescence properties, and their reactivity can be triggered by insertion in the pores of organic monodentate ligands such as pyridine or triphenylphosphine. The coordinating ligands can lead to the formation of Cu(I) complexes with completely different emission properties. In the case of pyridine, the final compound was characterized and identified as a cubane-like structure. A thermochromism effect is also observed, featuring, for instance, a hypsochromic effect for a phosphine derivative at 77K. The stability of the encapsulated systems in zeolites is rather enthralling: they are stable and emissive even after several months in the air.

Keywords: luminescence, confined space, copper clusters, zeolites, Cu(I), color tunability

OPEN ACCESS

Edited by:
Valeria Conte,
University of Rome Tor Vergata, Italy

Reviewed by:
Wai-Pong To,
The University of Hong Kong, Hong Kong SAR, China
Eri Sakuda,
Nagasaki University, Japan

***Correspondence:**
Eko Adi Prasetyanto
prasetyanto@atmajaya.ac.id
Luisa De Cola
luisa.decola@unimi.it

†These authors have contributed equally to this work

Specialty section:
This article was submitted to Inorganic Chemistry, a section of the journal Frontiers in Chemistry

Received: *06 December 2021*
Accepted: *15 March 2022*
Published: *05 May 2022*

Citation:
Prasetyanto EA, Atoini Y, Donato L, Hsu C-W and De Cola L (2022) The Role of a Confined Space on the Reactivity and Emission Properties of Copper(I) Clusters. Front. Chem. 10:829538. doi: 10.3389/fchem.2022.829538

INTRODUCTION

Currently, rare-earth-based phosphors are frequently used as emitters in lighting applications. (Bünzli and Piguet, 2005; Eliseeva and Bünzli, 2010). They are commercially available materials that are sufficiently photostable upon UV or blue excitation and meet all the industrial requirements regarding emission colors and efficiency. However, their very high cost and limited natural availability led researchers to find valuable alternatives. In this regard, various materials such as quantum dots based on zinc and cadmium selenides, (Raman et al., 1996; Frecker et al., 2016), have been developed with favorable spectral characteristics to replace rare-earth-based phosphors. Unfortunately, these are usually highly toxic and expensive, (Lewinski et al., 2008), and their use is not desirable. A valuable, cheaper, and a more environmentally friendly alternative is the use of metal complexes (Armaroli et al., 2007; Costa et al., 2012; Keller et al., 2018; Weber et al., 2018) and in this respect, silver has resulted in excellent luminophores with outstanding emission quantum yields when the clusters are protected by the environment. (Fenwick et al., 2016; Baekelant et al., 2019; Baekelant et al., 2020).

Amongst the use of cheaper and more abundant metals, copper is an interesting choice and many compounds have been investigated for their outstanding emission properties. (Armaroli et al., 2007; Costa et al., 2012; Keller et al., 2018; Weber et al., 2018). Indeed, M. Thompson *et al.* recently

reported Cu(I) complexes reaching almost quantitative emission quantum yields. (Hamze et al., 2019; Shi et al., 2019). Nevertheless, their stability is still a critical issue and easy oxidation as well as distortion of their geometry in the excited state are the main drawbacks of such systems. (Itoh et al., 2002; Li et al., 2006; Brühwiler et al., 2009). A possible solution to decrease the non-radiative decay is to take advantage of a pronounced thermally activated delayed luminescence exhibited by some of these complexes. (Palmer and McMillin, 1987; Deaton et al., 2010; Linfoot et al., 2014; Baranov et al., 2020). This process consists in the back population of the lowest excited singlet state from the triplet luminescent level. This process could also solve the long-lived radiative emission decay for the $T_1 \rightarrow S_0$ transitions of Cu(I) compounds, typically in the range of hundreds of μs up to ms. (Armaroli et al., 2007; Costa et al., 2012; Keller et al., 2018; Weber et al., 2018). Usually, compounds with such a long excited-state lifetime would not be well suitable as emitters in devices or in solution since quenching processes such as *e.g.,* triplet-triplet annihilation or bimolecular deactivation can easily occur.

In addition, simple compounds such as Cu(I) clusters, (Kyle et al., 1991), containing halides as bridging ligands between the Cu(I) ions, are of great potential as emitters. Still, their formation and existence are restricted to particular conditions. From such versatile species, it is possible to generate a series of emissive compounds by simple substitution of the halide with coordinating ligands such as pyridines or phosphines. (Liu et al., 2012; Parmeggiani and Sacchetti, 2012; Benito et al., 2014).

Indeed, previous work has shown that three main products from reactions of CuI and pyridine, namely $[CuI(py)]_2$ $[CuI(py)_2]_2$, and $[CuI(py)]_4$ (py = pyridine), can be formed, showing blue, green, and orange emission, respectively, in the solid-state at room temperature. (Ford et al., 1999). Phosphine molecules have also been investigated as strong ligands in the synthesis of metal clusters due to the excellent coordination properties of phosphine that can stabilize metal clusters. (Perruchas et al., 2011). In general, a way to stabilize transition metal complexes (*i.e.,* preventing oxidation and distortion) can be performed by their encapsulation inside porous nanocontainers. For instance, the successful insertion of transition metal complexes inside mesoporous silica nanoparticles was already performed by De Cola *et al.*, Costa *et al.* and Hofkens *et al.*, using Ir(III) (de Barros e Silva Botelho et al., 2011; Ezquerro et al., 2019) Pt (II) (Atoini et al., 2018) and Cu(I)complexes (Donato et al., 2018) and Ag(I) clusters. (Fenwick et al., 2016).

This work presents an alternative strategy to stabilize the Cu(I) clusters by their encapsulation in inert silica-based porous materials. We demonstrate that a straightforward sublimation of copper iodide into the pores leads to the formation of luminescent clusters. In addition, the diffusion of a ligand inside the pores results in fast coordination to the Cu(I) ion and a change in the emission color are observed.

RESULTS AND DISCUSSION

Porous silica-based materials such as zeolite L, zeolite Y, MCM-41, and SBA-15 were selected as convenient nanocontainers to be investigated as hosts for the formation of luminescent copper iodide clusters. The different materials differ in crystallinity, alumina content, charge, pore size, and order. For this work, the most relevant feature is the pore size that can influence the size and stability of the resulting clusters and their loading. Moreover, it should also play a role in the stability of the Cu(I) species since bigger pores might allow faster oxidation of the metal cation into Cu(II) due to faster oxygen diffusion inside the pores. Zeolites L (disk-shaped, 1 μm) were first filled by CuI salt by sublimation in a closed system (see experimental section) at high vacuum (10^{-9} bar) and 200 °C for 2 h (**Scheme 1**). Upon cooling, we observed a deep red luminescence coming from the zeolite L crystals.

This preliminary observation rules out the emission of the CuI salt since its weak emission is centered at 415 nm (**Supplementary Figure S1**). On the other hand, the copper clusters containing iodine as bridging ligand display a red emission similar to the one we recorded. It is important to note that the material displays the same emission *in vacuo* and after air exposure. As previously mentioned, the porous material plays a role as a stabilizing agent against the oxidation of Cu(I) into Cu(II). Moreover, the sublimation technique is not effective with complexes and clusters based on heavier transition metal ions, such as for instance platinum (II) or iridium (III), even with a longer heating time. Therefore, we can point out the quasi exclusivity of this approach for copper-based species.

In order to gain more insight into the photophysical properties of the species entrapped in the pores, excitation and emission spectra of CuI@ZeoL were recorded in the solid-state. The emission is characterized by a broad, non-structured band, with maximum of 710 nm (**Figure 1**) and an emission quantum yield of 14%.

The origin of the emission can only be assigned to a triplet "cluster-centered" (^{3}CC) excited state, which has mixed iodide-

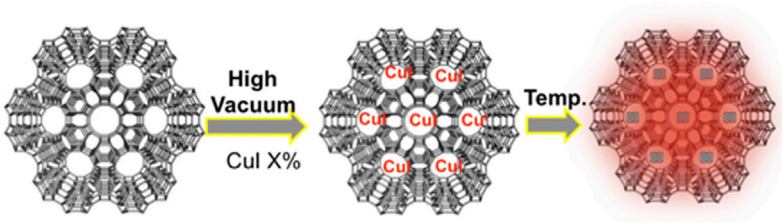

SCHEME 1 | Schematic illustration of the synthesis of CuI cluster inside zeolite.

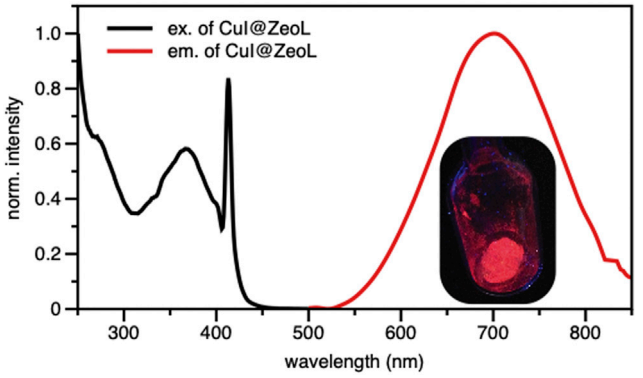

FIGURE 1 | Excitation (λ_{em} = 700 nm) and Emission (λ_{exc} = 414 nm) spectra of CuI@ZeoL in solid-state condition; inset is the photograph of CuI@ZeoL inside the glass tube. The peak at 410 nm is an artifact.

to-metal charge transfer (^{3}XMCT) and metal-centered transfer (^{3}MC: $d^{10} \rightarrow d^9S^1Cu$). The excitation spectrum recorded at λ_{em} = 710 nm shows a broad absorption at about 350 nm. The excited-state lifetime is a few microseconds (see **Table 1**), with complex multiple decay components pointing out the phosphorescence behavior of the material.

Confocal microscopy images (**Supplementary Figure S2**) clearly show that the emission originates from the zeolite crystals, emphasizing the successful encapsulation of CuI inside ZeoL, and the formation of a new emissive species. Moreover, different ratios in weight of CuI and ZeoL were studied (see supporting information) obtained by subliming different amounts of CuI in the same amount of zeolite (100 mg). In particular the ratios 10:100, CuI@ZeoL-A; 60:100 CuI@ZeoL-B; 100:100 CuI@ZeoL-C, after indicated only as CuI@ZeoL, and 200:100 CuI@ZeoL-D were prepared and the emission spectra of the obtained materials are depicted in **Figure 2A**. These data show that the emission energy is independent from the amount of CuI added to the zeolite.

Through the SEM images we can see that the morphology of the zeolite and silica material did not change before and after loading the copper source (**Supplementary Figure S3**), indicating that the loading of CuI did not destroy the porous structure of our materials. Meanwhile, we have obtained a red emission from the loaded CuI inside each host, which indicated that the copper source was successfully loaded inside the porous material. The photophysical properties of the resulting hybrid materials are discussed below.

To prove the confinement effect dictated by the porous containers, needed to obtain such a red emissive material, copper iodide powder was treated alone in the same manner (high vacuum and temperature), and after the treatment, we could not observe any red luminescence from this material. Moreover, the same procedure was performed with bulk, non-porous silica (**Supplementary Figure S1**). We clearly see the same emission as CuI alone, *i.e.,* an emission maximum at around 415 nm. This emphasizes the importance of the pores rather than the substrate to obtain emissive Cu(I) clusters. On the side, we performed nitrogen sorption experiments to show that the zeolites are indeed filled.

A comparison between the zeolites before and after sublimation of copper iodide reveals a decrease of the pore width and confirms a certain loading of the zeolites.

To understand the effect of the pore size, we have sublimed 100 mg of CuI inside materials featuring bigger pores, namely Zeolite Y (1.2 nm pore), MCM-41 (2 nm pore size), and SBA-15 (10 nm pore size), see Supplementary Materials section. The MCM-41, having 2 nm pore size and 100 nm in diameter, (Trewyn et al., 2007), and the SBA-15 mesoporous silica (SujandiPrasetyanto and Park, 2008) were synthesized following a typical sol-gel micelle-templated process. All those sublimation processes lead to the same deep red luminescence. (**Table 1**; **Figure 2B**). These results indicate the similarity of the cluster's structure, without any dependence on the host used. However, it is essential to note that the cluster inside bigger pores is less stable toward degradation since it allows a more important penetration of oxygen. In the two extreme cases, *i.e.,* zeolite L and SBA 15, the red luminescence of the former does not decrease after several months, while it only takes a few days for the latter to lose its luminescence due to the oxidation of the Cu(I). The loading of the two materials: CuI@ZeoL and CuI@ZeoY (both of them with a ratio CuI:Zeo 100:100), was determined using the ICP-MS technique. The loading of the latter (CuI@ZeoY, 28%) is

TABLE 1 | Photophysiscal properties of the different hybrid materials.

Sample	λ_{max}^{Em} (nm)	Φ_p[a] (%)/λ_{ex} (nm)	Lifetime 298K (μs)[b]		
			τ_1 (μs)/%	τ_2 (μs)/%	τ_3 (μs)/%
CuI@ZeoL	712	14/360	5.2/6	1.01/27	0.17/67
CuI@ZeoY	711	8/360	4.13/10	1.1/45	0.24/45
CuI@MCM-41	711	7.5/360	6.25/35	0.65/65	–/–
CuI@SBA-15	712	5.7/360	5.76/27	0.97/73	–/–
CuIPy@ZeoY	575	34/360	11/90	2.37/10	–/–
CuIPy@ZeoY (77K)	435	n.a	22.7/100	–/–	–/–
CuIPPh3@ZeoY	695	12/412	8/70	1.87/26	0.34/4
CuIPPh3@ZeoY (77K)	493	n.a	2.5/72	0.29/28	–/–

[a]*Absolute quantum yield was determined using an integrated sphere.*
[b]*Measured at λem = λmax (i.e. CuI@ZeoL, CuI@SBA-15: λem = 712 nm; CuI@ZeoY, CuI@MCM-41: λem = 711 nm; CuIPy@ZeoY: rt: λem = 575 nm, 77K: λem = 435 nm; CuIPPh3@ZeoY: rt: λem = 695 nm, 77K: λem = 493 nm).*

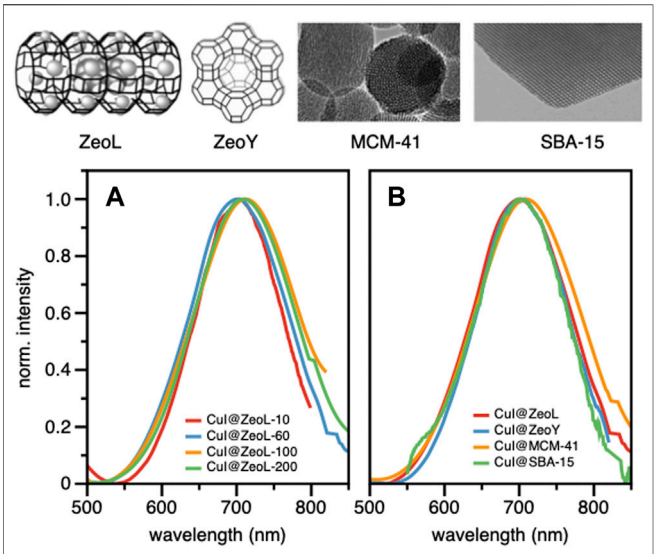

FIGURE 2 | Structure and TEM image of the different porous materials used in this work (top); emission spectra of CuI@ZeoL with different ratios of CuI:ZeoL (CuI@ZeoL-A red line; CuI@ZeoL-B: blue line; CuI@ZeoL-C: orange line; CuI@ZeoL-D: green line) **(A)**; effect of host/pore size to the emission spectra **(B)** in solid-state condition. On top of the graphs is depicted the representation of the host used in **Figure 2B** λ_{exc} = 414 nm.

higher than that of the former (CuI@ZeoL, 13%), and this difference can be easily explained by the difference in the pore size, larger in the case of ZeoY. However, we could not detect evident changes in the emission maximum or excited state lifetimes suggesting that the luminescent species are the same (see **Table1**).

Knowing that Cu(II) based species are not luminescent, we could assume that the Cu(I) cluster was not oxidized since our material is strongly luminescent. However, the hypothesis of undesirable partial oxidation cannot be disproved only by the use of photophysical studies. In order to ensure there is no Cu(II) in our material, the oxidation state of Cu was then investigated by X-ray photoelectron spectroscopy (XPS) measurements (**Supplementary Figure S5**). As a control, pure CuI gives us the $Cu2p_{3/2}$ peak at 932.9eV and $I3d_{5/2}$ at 620.0eV. The spectra from Cu clusters show the $Cu2p_{3/2}$ peak at 933.5eV and $I3d_{5/2}$ at 620.9eV. The binding energy of copper stays in the Cu(I) region compared to the other copper halogen compounds. But more importantly, the spectrum does not feature any signal around 960eV, typical for Cu(II) (satellite signal of Cu(II)).

Both the Cu and I peaks shifted to a little bit higher binding energy in the clusters, which is due to the interactions with the oxygen atoms on the zeolite channels. All the signals present only one contribution in agreement with only one chemical environment, indicating that there is no oxidation of Cu(I).

To assess the structure of the CuI cluster, the species formed inside the zeolite were analyzed by powder X-ray diffraction (PXRD), and the results were determined by Total Pattern Analysis Solutions (TOPAS) software using advanced Rietveld refinement. (Coelho, 2003). Quantitative phase analysis QPA in the TOPAS software is based on the method first described by Hill and Howard. (Hill and Howard, 1987). This method is based on the assumption that 1) all phases in the specimen are identified, 2) all phases are crystalline, and 3) the crystal structures of all phases are known. By comparing the experimental data, calculated data, and its residual (**Figure 3**), we found that the Cu(I) clusters inside the zeolite have cubic type crystal structure with F-43m space group and a = b = c = 6.056 Å, featuring a Rietveld weigh profile (Rwp) value of 7.8. By performing calculations, we obtained the crystal symmetry, lattice parameter, and we could also determine the atomic composition of the cluster. Finally, we were able to reconstruct the crystal structure of the CuI cluster, as shown in **Supplementary Figure S6**. The position of the copper cluster inside the zeolite Y was then reconstructed and shown in **Supplementary Figure S7**.

Two different organic ligands, *i.e.,* pyridine and triphenylphosphine, were inserted in CuI@porous materials. As explained here above, porous hosts have small pores. In other words, zeolites are better candidates for stability reasons.

In this work, zeolites L present too small channels to host the organic ligands. For these reasons, the material chosen for the

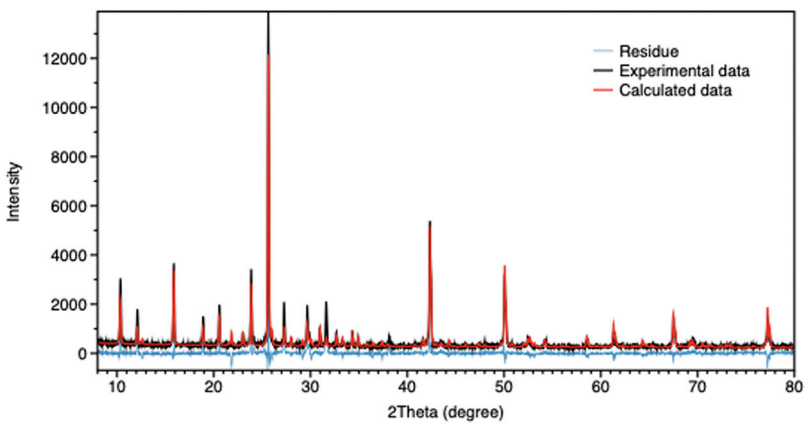

FIGURE 3 | TOPAS calculation result for CuI@ZeoL. The black curve shows the measured XRD data, the red curve shows the calculated Rietveld fitting, and the blue curve shows the difference between the former and the latter.

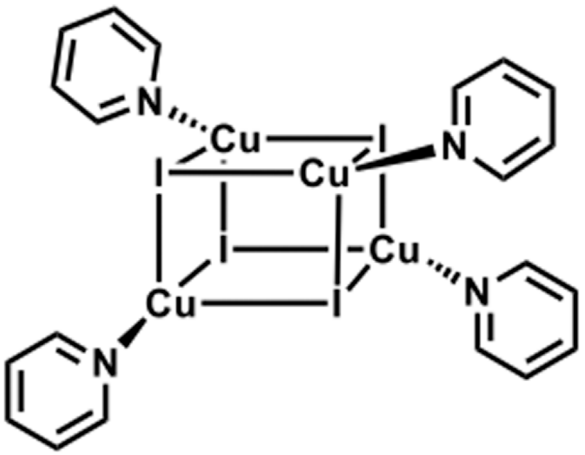

SCHEME 2 | Schematic representation of CuI cluster functionalized with pyridine ligands featuring a cubane-like structure. (Ford et al., 1999).

following of this work is zeolite Y, most likely the best candidate for such a purpose. (Yu et al., 2014; Łukarska et al., 2017). After the addition of the organic ligands into CuI@ZeoY, the characterization of the resulting materials was performed. In order to determine the structure of the resulting CuI cluster formed in zeolites, an interesting approach was to use PXRD analysis by comparing.

One of the materials we obtained with a simulation of the addition of zeolite Y and the already.

Reported $(C_5H_5CuIN)_4$ cubane cluster (**Supplementary Figure S8**). (Raston and White, 1976). PXRD studies showed a high degree of crystallinity of the materials, and again by using TOPAS software, (Coelho, 2003), we were able to identify our guest cluster as a cubane-like structure (**Scheme 2**). It is important to mention the matching between the experimental and the measured patterns, and the Rwp found is 6.5, which is a very good value for such studies.

To confirm this result, the compound was isolated from the zeolites by breaking the latter by means of a sonication process. The resulting species was characterized by ^{1}H NMR, DOSY NMR, and HR ESI-MS. NMR spectra of the CuIPy cluster were compared with that of pyridine. While ^{1}H NMR of both molecules, *i.e.*, CuIPy cluster and pyridine, have the same protons, they display similar spectra, featuring three signals in the aromatic region; the main difference relies on a downfield shift of the signals referring to CuIPy cluster, by around 0.5 ppm (**Supplementary Figure S9**).

DOSY NMR spectra (**Supplementary Figure S10**, **Supplementary Table S1**) show a diffusion coefficient of 1.46 nm s^{-1} and 2.93 nm s^{-1} for CuIPy cluster and pyridine, respectively. Hence, the molecular volumes determined for pyridine and the CuIPy cluster are respectively 21 Å^3 and 169 Å^3.

HR ESI-MS spectrum (**Supplementary Figure S11**) shows an m/z value of 1,075.51, matching perfectly the theoretical predictions of $Cu_4I_4(C_6H_5N)_4$. Thus, the isolated molecule was confirmed to be $(CuIPy)_4$.

Copper-iodine clusters were intensively studied by Peter C. Ford. In this regard, a cubic copper-iodine bearing a pyridine on each

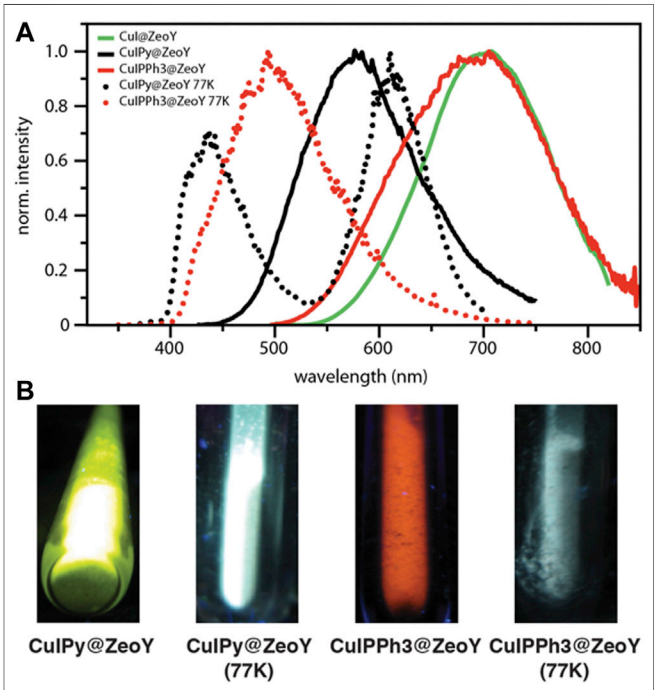

FIGURE 4 | Emission spectra of CuI@ZeoY in solid-state condition; λ_{exc} = 414 nm.

copper atom was characterized. (Liu et al., 2012). Inline of Ford's studies, our sublimation process, followed by pyridine addition, aims to obtain the same cluster inside the zeolites Y pores.

It has been noticed that both clusters containing organic ligands, *i.e.,* CuIPy@ZeoY and $CuIPPh_3$@ZeoY, feature a thermochromic behavior. In fact, in thermochromic clusters, the luminescent thermochromism is caused by a relative intensity change of two distinct emission bands. (Kitagawa et al., 2010; Perruchas et al., 2010; Fenwick et al., 2016; Tsuge et al., 2016; Baekelant et al., 2019; Baekelant et al., 2020). Hence, the emission of the materials was also measured at 77K (**Figure 4**), and a correlation could be found between the temperature and the emission profiles. Indeed, the high energy emission band at around 400–450 nm is dominant at low temperature, assigned to a halogen-to-ligand charge transfer (XLCT) transition state.

The low energy emission band at around 575 nm for CuIPy@ZeoY and 695 nm for $CuIPPh_3$@ZeoY is dominant at room temperature, which is referred to a cluster-centered excited state (^{3}CC) and can be affected by outer environments such as solid/solution state, temperature, or pressure. Regarding CuIPy@ZeoL, the photophysical data match perfectly with the cluster previosuly described eliminate in Peter Ford studies, this allows us to confirm the cubane like structure, referring to the following chemical formula: $(Cu_4I_4Py_4)$. (Kyle et al., 1991; Ford et al., 1999).

When the tube was taken out from liquid nitrogen and exposed to the irradiation of a UV lamp (365 nm), the interesting reversible thermochromic luminescence from yellow (298 K) to blue (77 K) can be easily distinguished by the naked eye or recorded by a digital camera. Solid-state luminescence performed from 298 to 77 K is in accordance with the thermochromic luminescence and the variation

of luminescent intensity. At room temperature, the maximum of the single emission is found at 575 nm with an excited state lifetime featuring a bi-exponential decay, 11 and 2.37 μs, and an emission quantum yield of 34% (**Figure 4**; **Table 1**). The long excited-state lifetime, in the microsecond range, indicates the phosphorescence behavior, which is not surprising coming from such clusters. With the decrease of temperature from room temperature to 77 K, the emission band is progressively blue-shifted from 575 to 435 nm, which is accompanied by a widening of the bandwidth and a decrease in emission intensity. This dramatic hypsochromic shift of about 140 nm makes the detection of the color change by the naked eye easier. Without the presence of an organic ligand, the origin of the emission can only be assigned to a triplet "cluster-centered" (^{3}CC) excited state, which has mixed iodide-to-metal charge transfer (^{3}XMCT) and metal-centered transfer (^{3}MC: $d^{10} \rightarrow d^9S^1$Cu). However, in the case of $Cu_4I_4L_4$, other transitions such as organic-ligand-related excited states, *i.e.,* halide to ligand charge transfers (XLCT), must be considered.

Moreover, it has been shown that the thermochromic luminescence is due to a significant change in Cu···Cu distances that decreases together with the temperature. (Ford et al., 1999). Indeed, at lower temperatures, Cu···Cu distances become shorter, and the bonding character becomes more and more obvious. The transition of the LT phase to the HT phase resulted in some shortening of Cu···Cu distances. The origin of thermochromic luminescence in CuI cluster is quite different from cubane $Cu_4I_4L_4$ cluster-based compounds, where relative intensities of ^{3}CC and XLCT emissions with the temperature are responsible for the thermochromic luminescence. (Tard et al., 2008).

CONCLUSIONS

In conclusion, we have synthesized luminescent copper iodide inside porous nanomaterials, with a relatively high photoluminescence quantum yield. The nanomaterial allow high stability due to its protection from oxygen, preventing the oxidation of Cu(I) into Cu(II). A certain correlation was also found between the pore size and the stability of the Cu(I) cluster. By adding an organic monodentate ligand after sublimation of CuI, *i.e.,* pyridine or triphenylphosphine, we are able to tune the luminescence energy, the resulting luminescence featuring an important bathochromic shift. The materials also showed a thermochromic behavior, which led to a significant hypsochromic emission shift of 140 nm. Thanks to several characterizations, among them ESI-HRMS, DOSY NMR, and PXRD experiment followed by Rietveld refinement and simulation, we were able to identify Cu(I) cluster and CuIPy cluster, the latter having a cubane like structure. This finding may lead to the use of copper, much cheaper than its transition metals counterparts, as alternative materials in applications such as lighting devices.

DATA AVAILABILITY STATEMENT

The original contributions presented in the study are included in the article/**Supplementary Material**, further inquiries can be directed to the corresponding authors.

AUTHOR CONTRIBUTIONS

All authors listed have made a substantial, direct, and intellectual contribution to the work and approved it for publication.

FUNDING

European Union FP7-SACS Project (Grant agreement no. 2012-310651). Ministry of Research, Technology and Higher Education of the Republic of Indonesia Scheme for Academic Mobility and Exchange (SAME)—"PHC-Nusantara.

ACKNOWLEDGMENTS

Cyril Antheaume and Bruno Vincent are gratefully thanked for their contribution on NMR and MS analysis.

SUPPLEMENTARY MATERIAL

The Supplementary Material for this article can be found online at: https://www.frontiersin.org/articles/10.3389/fchem.2022.829538/full#supplementary-material

REFERENCES

Armaroli, N., Accorsi, G., Cardinali, F., and Listorti, A. (2007). in *Photochemistry and Photophysics of Coordination Compounds I*. Editors V. Balzani and S. Campagna (Springer Berlin Heidelberg), 280, 69–115.

Atoini, Y., Prasetyanto, E. A., Chen, P., Silvestrini, S., Harrowfield, J., and De Cola, L. (2018). Luminescence of Amphiphilic Pt II Complexes Controlled by Confinement. *Chem. Eur. J.* 24, 12054–12060. doi:10.1002/chem.201802743

Baekelant, W., Aghakhani, S., Fron, E., Martin, C., Woong-Kim, C., Steele, J. A., et al. (2019). Luminescent Silver-Lithium-Zeolite Phosphors for Near-Ultraviolet LED Applications. *J. Mater. Chem. C* 7, 14366–14374. doi:10.1039/c9tc04674g

Baekelant, W., Romolini, G., Sun, L., De Ras, M., Fron, E., Moreira, T., et al. (2020). Tunable white Emission of Silver-Sulfur-Zeolites as Single-phase LED Phosphors. *Methods Appl. Fluoresc.* 8, 024004. doi:10.1088/2050-6120/ab7169

Baranov, A. Y., Berezin, A. S., Samsonenko, D. G., Mazur, A. S., Tolstoy, P. M., Plyusnin, V. F., et al. (2020). New Cu(I) Halide Complexes Showing TADF Combined with Room Temperature Phosphorescence: the Balance Tuned by Halogens. *Dalton Trans.* 49, 3155–3163. doi:10.1039/d0dt00192a

Benito, Q., Le Goff, X. F., Maron, S., Fargues, A., Garcia, A., Martineau, C., et al. (2014). Polymorphic Copper Iodide Clusters: Insights into the Mechanochromic Luminescence Properties. *J. Am. Chem. Soc.* 136, 11311–11320. doi:10.1021/ja500247b

Brühwiler, D., Calzaferri, G., Torres, T., Ramm, J. H., Gartmann, N., Dieu, L.-Q., et al. (2009). Nanochannels for Supramolecular Organization of Luminescent Guests. *J. Mater. Chem.* 19, 8040–8067. doi:10.1039/b907308f

Bünzli, J.-C. G., and Piguet, C. (2005). Taking Advantage of Luminescent Lanthanide Ions. *Chem. Soc. Rev.* 34, 1048–1077. doi:10.1039/b406082m

Coelho, A. A. (2003). Indexing of Powder Diffraction Patterns by Iterative Use of Singular Value Decomposition. *J. Appl. Cryst.* 36, 86–95. doi:10.1107/s0021889802019878

Costa, R. D., Ortí, E., Bolink, H. J., Monti, F., Accorsi, G., and Armaroli, N. (2012). Luminescent Ionic Transition-Metal Complexes for Light-Emitting Electrochemical Cells. *Angew. Chem. Int. Ed.* 51, 8178–8211. doi:10.1002/anie.201201471

de Barros e Silva Botelho, M., Fernandez-Hernandez, J. M., de Queiroz, T. B., Eckert, H., De Cola, L., and de Camargo, A. S. S. (2011). Iridium(iii)-surfactant Complex Immobilized in Mesoporous Silica via Templated Synthesis: a New Route to Optical Materials. *J. Mater. Chem.* 21, 8829–8834. doi:10.1039/c1jm10878f

Deaton, J. C., Switalski, S. C., Kondakov, D. Y., Young, R. H., Pawlik, T. D., Giesen, D. J., et al. (2010). E-type Delayed Fluorescence of a Phosphine-Supported Cu2(μ-NAr2)2 Diamond Core: Harvesting Singlet and Triplet Excitons in OLEDs. *J. Am. Chem. Soc.* 132, 9499–9508. doi:10.1021/ja1004575

Donato, L., Atoini, Y., Prasetyanto, E. A., Chen, P., Rosticher, C., Bizzarri, C., et al. (2018). Selective Encapsulation and Enhancement of the Emission Properties of a Luminescent Cu(I) Complex in Mesoporous Silica. *Helv. Chim. Acta* 101, e1700273. doi:10.1002/hlca.201700273

Eliseeva, S. V., and Bünzli, J.-C. G. (2010). Lanthanide Luminescence for Functional Materials and Bio-Sciences. *Chem. Soc. Rev.* 39, 189–227. doi:10.1039/b905604c

Ezquerro, C., Fresta, E., Serrano, E., Lalinde, E., García-Martínez, J., Berenguer, J. R., et al. (2019). White-emitting Organometallo-Silica Nanoparticles for Sun-like Light-Emitting Diodes. *Mater. Horiz* 6, 130–136.

Fenwick, O., Coutiño-Gonzalez, E., Grandjean, D., Baekelant, W., Richard, F., Bonacchi, S., et al. (2016). Tuning the Energetics and Tailoring the Optical Properties of Silver Clusters Confined in Zeolites. *Nat. Mater* 15, 1017–1022. doi:10.1038/nmat4652

Ford, P. C., Cariati, E., and Bourassa, J. (1999). Photoluminescence Properties of Multinuclear Copper(I) Compounds. *Chem. Rev.Compounds* 99, 3625–3648. doi:10.1021/cr960109i

Frecker, T., Bailey, D., Arzeta-Ferrer, X., McBride, J., Rosenthal, S. J., and Ecs, J. (2016). Review-Quantum Dots and Their Application in Lighting, Displays, and Biology. *ECS J. Solid State. Sci. Technol.* 5, R3019–R3031. doi:10.1149/2.0031601jss

Hamze, R., Peltier, J. L., Sylvinson, D., Jung, M., Cardenas, J., Haiges, R., et al. (2019). Eliminating Nonradiative Decay in Cu(I) Emitters: >99% Quantum Efficiency and Microsecond Lifetime. *Science* 363, 601–606. doi:10.1126/science.aav2865

Hill, R. J., and Howard, C. J. (1987). Quantitative Phase Analysis from Neutron Powder Diffraction Data Using the Rietveld Method. *J. Appl. Cryst.* 20, 467–474. doi:10.1107/s0021889887086199

Itoh, T., Yano, K., Inada, Y., and Fukushima, Y. (2002). Photostabilized Chlorophyll a in Mesoporous Silica: Adsorption Properties and Photoreduction Activity of Chlorophyll a. *J. Am. Chem. Soc.* 124, 13437–13441. doi:10.1021/ja0203059

Keller, S., Prescimone, A., Bolink, H., Sessolo, M., Longo, G., Martínez-Sarti, L., et al. (2018). Luminescent Copper(i) Complexes with Bisphosphane and Halogen-Substituted 2,2′-bipyridine Ligands. *Dalton Trans.* 47, 14263–14276. doi:10.1039/c8dt01338a

Kitagawa, H., Ozawa, Y., and Toriumi, K. (2010). Flexibility of Cubane-like Cu4I4 Framework: Temperature Dependence of Molecular Structure and Luminescence Thermochromism of [Cu4I4(PPh3)4] in Two Polymorphic Crystalline States. *Chem. Commun.* 46, 6302–6304. doi:10.1039/c0cc01434f

Kyle, K. R., Ryu, C. K., Ford, P. C., and DiBenedetto, J. A. (1991). Photophysical Studies in Solution of the Tetranuclear Copper(I) Clusters Cu4I4L4 (L = Pyridine or Substituted Pyridine). *J. Am. Chem. Soc.* 113, 2954–2965. doi:10.1021/ja00008a026

Łukarska, M., Jankowska, A., Gapiński, J., Valable, S., Anfray, C., Ménard, B., et al. (2017). Synthesis of Fluorescein by a Ship-In-A-Bottle Method in Different Zeolites. *New J. Chem.* 41, 9969–9976.

Lewinski, N., Colvin, V., and Drezek, R. (2008). Cytotoxicity of Nanoparticles. *Small* 4, 26–49. doi:10.1002/smll.200700595

Li, S., Song, H., Li, W., Ren, X., Lu, S., Pan, G., et al. (2006). Improved Photoluminescence Properties of Ternary Terbium Complexes in Mesoporous Molecule Sieves. *J. Phys. Chem. B* 110, 23164–23169. doi:10.1021/jp064509d

Linfoot, C. L., Leitl, M. J., Richardson, P., Rausch, A. F., Chepelin, O., White, F. J., et al. (2014). Thermally Activated Delayed Fluorescence (TADF) and Enhancing Photoluminescence Quantum Yields of [CuI(diimine)(diphosphine)]+ Complexes-Photophysical, Structural, and Computational Studies. *Inorg. Chem.* 53, 10854–10861. doi:10.1021/ic500889s

Liu, Z., Djurovich, P. I., Whited, M. T., and Thompson, M. E. (2012). Cu4I4 Clusters Supported by P^N-type Ligands: New Structures with Tunable Emission Colors. *Inorg. Chem.* 51, 230–236. doi:10.1021/ic2015226

Palmer, C. E. A., and McMillin, D. R. (1987). Singlets, Triplets, and Exciplexes: Complex, Temperature-dependent Emissions from (2,9-Dimethyl-1,10-Phenanthroline)bis(triphenylphosphine)copper(1+) and (1,10-phenanthroline)(triphenylphosphine)copper(1+). *Inorg. Chem.* 26, 3837–3840. doi:10.1021/ic00270a004

Parmeggiani, F., and Sacchetti, A. (2012). Preparation and Luminescence Thermochromism of Tetranuclear Copper(I)-Pyridine-Iodide Clusters. *J. Chem. Educ.* 89, 946–949. doi:10.1021/ed200736b

Perruchas, S., Le Goff, X. F., Maron, S., Maurin, I., Guillen, F., Garcia, A., et al. (2010). Mechanochromic and Thermochromic Luminescence of a Copper Iodide Cluster. *J. Am. Chem. Soc.* 132, 10967–10969. doi:10.1021/ja103431d

Perruchas, S., Tard, C., Le Goff, X. F., Fargues, A., Garcia, A., Kahlal, S., et al. (2011). Thermochromic Luminescence of Copper Iodide Clusters: the Case of Phosphine Ligands. *Inorg. Chem.* 50, 10682–10692. doi:10.1021/ic201128a

Raman, N. K., Anderson, M. T., and Brinker, C. J. (1996). Template-Based Approaches to the Preparation of Amorphous, Nanoporous Silicas. *Chem. Mater.* 8, 1682–1701. doi:10.1021/cm960138+

Raston, C. L., and White, A. H. (1976). Crystal Structure of the Copper(I) Iodide-Pyridine (1/1) Tetramer. *J. Chem. Soc. Dalton Trans.*, 2153–2156. doi:10.1039/dt9760002153

Shi, S., Jung, M. C., Coburn, C., Tadle, A., Sylvinson, M. R. D., et al. (2019). Highly Efficient Photo- and Electroluminescence from Two-Coordinate Cu(I) Complexes Featuring Nonconventional N-Heterocyclic Carbenes. *J. Am. Chem. Soc.* 141, 3576–3588. doi:10.1021/jacs.8b12397

SujandiPrasetyanto, E. A., and Park, S.-E. (2008). Synthesis of Short-Channeled Amino-Functionalized SBA-15 and its Beneficial Applications in Base-Catalyzed Reactions. *Appl. Catal. A: Gen.* 350, 244–251. doi:10.1016/j.apcata.2008.08.020

Tard, C., Perruchas, S., Maron, S., Le Goff, X. F., Guillen, F., Garcia, A., et al. (2008). Thermochromic Luminescence of Sol–Gel Films Based on Copper Iodide Clusters. *Chem. Mater.* 20, 7010–7016. doi:10.1021/cm801780g

Trewyn, B. G., Slowing, I. I., Giri, S., Chen, H.-T., and Lin, V. S.-Y. (2007). Synthesis and Functionalization of a Mesoporous Silica Nanoparticle Based on the Sol-Gel Process and Applications in Controlled Release. *Acc. Chem. Res.* 40, 846–853. doi:10.1021/ar600032u

Tsuge, K., Chishina, Y., Hashiguchi, H., Sasaki, Y., Kato, M., Ishizaka, S., et al. (2016). Luminescent Copper(I) Complexes with Halogenido-Bridged Dimeric Core. *Coord. Chem. Rev.* 306, 636–651. doi:10.1016/j.ccr.2015.03.022

Weber, M. D., Fresta, E., Elie, M., Miehlich, M. E., Renaud, J.-L., Meyer, K., et al. (2018). Rationalizing Fabrication and Design toward Highly Efficient and Stable Blue Light-Emitting Electrochemical Cells Based on NHC Copper(I) Complexes. *Adv. Funct. Mater.* 28, 1707423–1707435. doi:10.1002/adfm.201707423

Yu, Y., Mai, J., Wang, L., Li, X., Jiang, Z., and Wang, F. (2014). Ship-in-a-bottle Synthesis of Amine-Functionalized Ionic Liquids in NaY Zeolite for CO2 Capture. *Sci. Rep.* 4, 5997–6004. doi:10.1038/srep05997

Conflict of Interest: The authors declare that the research was conducted in the absence of any commercial or financial relationships that could be construed as a potential conflict of interest.

Publisher's Note: All claims expressed in this article are solely those of the authors and do not necessarily represent those of their affiliated organizations, or those of the publisher, the editors and the reviewers. Any product that may be evaluated in this article, or claim that may be made by its manufacturer, is not guaranteed or endorsed by the publisher.

Frontiers in Chemistry

Explores all fields of chemical science across the periodic table

Advances our understanding of how atoms, ions, and molecules come together and come apart. It explores the role of chemistry in our everyday lives - from electronic devices to health and wellbeing.

Discover the latest Research Topics

See more →

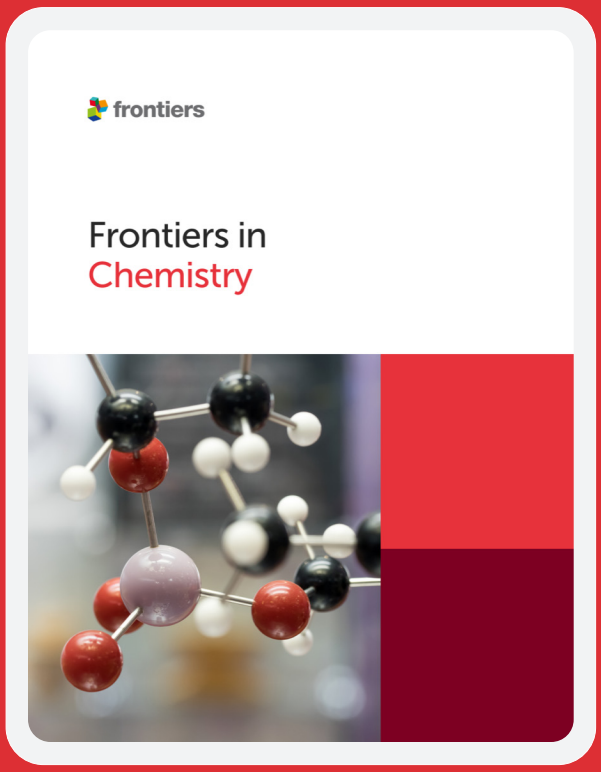

Frontiers

Avenue du Tribunal-Fédéral 34
1005 Lausanne, Switzerland
frontiersin.org

Contact us

+41 (0)21 510 17 00
frontiersin.org/about/contact